รายงานการวิจัยฉบับสมบูรณ์

สัญญาเลขที่ BRG5680006

โครงการ : วัสดุเพียโซอิเล็กทริกไร้สารตะกั่วสำหรับฮาร์ดดิสก์และอุปกรณ์บันทึกข้อมูล

รศ.ดร. นราธิป วิทยากร

ได้รับทุนสนับสนุนงานวิจัยจากสำนักงานกองทุนสนับสนุนงานวิจัย (สกว)

รหัสโครงการ BRG5680006
ชื่อโครงการ: วัสดุเพียโซอิเล็กทริกไร้สารตะกั่วสำหรับฮาร์ดดิสก์และอุปกรณ์บันทึกข้อมูล
ระยะเวลาโครงการ: 3 ปี (31 กรกฎาคม 2556–31 กรกฎาคม 2559)
งบประมาณ: 1,950,000 บาท
ชื่อหัวหน้าโครงการวิจัยผู้รับทุน: รองศาสตราจารย์ ดร. นราธิป วิทยากร
ภาควิชาเคมี คณะวิทยาศาสตร์ สถาบันเทคโนโลยีพระจอมเกล้าเจ้าคุณทหารลาดกระบัง

บทคัดย่อ

งานวิจัยนี้ทำการศึกษาวัสดุเพียโซอิเล็กทริกไร้สารตะกั่ว เพื่อนำมาทดแทนวัสดุเพียโซอิเล็กทริกที่มีตะกั่วเป็นองค์ประกอบ โดยเน้นศึกษาเซรามิกที่ประกอบด้วยระบบหลัก 3 ระบบ คือ แบเรียมไทเทเนต (BT) บิสมัทโซเดียมไทเทเนต (BNT) และโพแทสเซียมโซเดียมไนโอเบต (KNN) เพื่อสมบัติเพียโซอิเล็กทริกที่สูง จึงมีการออกแบบเซรามิกในสัดส่วนที่ประกอบด้วยเฟสร่วมระหว่างสองเฟสหรือมากกว่า โดยอาศัยหลักการของบริเวณรอยต่อระหว่างเฟส (MPB) และการเปลี่ยนเฟสแบบหลายรูป (PPT) ทั้งนี้มีการรวบรวมข้อมูลจากเอกสารอ้างอิงเพื่อสร้างเฟสไดอะแกรมเฟอร์โรอิเล็กทริกและบริเวณรอยต่อระหว่างหลายรูปวัฏภาค (PPB) จากนั้นศึกษาเอกลักษณ์เฉพาะของโครงสร้างผลึกของแต่ละเฟส โดยเทคนิคการเลี้ยวเบนของรังสีเอกซ์ (XRD) และรามานสเปคโทรสโคปี การวิเคราะห์เชิงคุณภาพของเฟสและการวิเคราะห์โครงสร้างระยะสั้น (local structure) ได้ศึกษาโดยเทคนิครีทเวลรีไฟน์เมนต์ (Rietveld analysis refinement) และเทคนิคการดูดกลืนรังสีเอกซ์ (XAS) พร้อมทั้งรายงานค่าสัมประสิทธิ์เพียโซอิเล็กทริกและค่าทางเฟอร์โรอิเล็กทริก เช่น d_{33} d_{33}^{*} K_p P_r และ E_c รวมทั้งศึกษาพฤติกรรมความล้าทางไฟฟ้า ซึ่งเป็นสมบัติสำคัญของวัสดุที่จะประยุกต์ใช้งานในฮาร์ดดิสก์ไดรฟ์

งานวิจัยได้นำเสนอเฟสไดอะแกรมเฟอร์โรอิเล็กทริกของระบบสามองค์ประกอบ BT–BZ–CT และรายละเอียดของรอยต่อระหว่างเฟส ผลการทดลองพบว่าเซรามิกที่สัดส่วนบริเวณรอยต่อระหว่างเฟสหลายรูป (PPB) แสดงสมบัติเพียโซอิเล็กทริกที่โดดเด่น เมื่อมีการเหนี่ยวนำทางไฟฟ้า เซรามิกที่สัดส่วน x = 0.06 แสดงค่าความเครียดสูงถึงร้อยละ 0.23 เมื่อใช้ค่าสนามไฟฟ้าเท่ากับ 40 กิโลโวลต์ต่อเซนติเมตร เนื่องจากเซรามิกประกอบด้วยเฟสร่วมระหว่างเฟสรอมโบฮีดรอลและเฟสเททระโกนอล ส่งผลให้ค่าสัมประสิทธิ์เพียโซอิเล็กทริกสัมพัทธ์ (S_{max}/E_{max}) มีค่าสูงถึง 1280 พิโคเมตรต่อโวลต์ ภายใต้สนามไฟฟ้าเท่ากับ 10 กิโลโวลต์ต่อเซนติเมตร เซรามิกที่สัดส่วนบริเวณรอยต่อระหว่างเฟสหลายรูป

(PPB) ยังแสดงการเสื่อมสภาพจากความล้าในระดับต่ำ ภายหลังจากการให้สนามไฟฟ้าจำนวน 10^6 รอบ นอกจากนั้น เมื่อมีการให้สนามไฟฟ้าด้านเดียว ค่าความเครียดภายใต้สนามไฟฟ้ายังไม่แสดงวงวนฮีสเทอเรสิส ณ สนามไฟฟ้าค่าสูง จากการศึกษาส่วนนี้พบว่าเซรามิกที่สัดส่วนบริเวณรอยต่อระหว่างเฟสหลายรูปข้างต้น มีความเหมาะสมต่อการนำไปประยุกต์ใช้งานด้านแอคชัวเอเตอร์

เซรามิกในระบบ BT–CT–BS ที่สัดส่วน x = 0.1000 หรือ $(Ba_{0.825+x}Ca_{0.175-x})(Ti_{1-x}Sn_x)O_3$ แสดงสมบัติเพียโซอิเล็กทริกที่โดดเด่น ค่าสัมประสิทธิ์เพียโซอิเล็กทริก (d_{33}) มีค่าเท่ากับ 515 พิโคคูลอมบ์ต่อนิวตัน และค่าสัมประสิทธิ์เพียโซอิเล็กทริก (d_{33}^*) เท่ากับ 1293 พิโคเมตรต่อโวลต์ ซึ่งค่าดังกล่าวสูงกว่าค่าที่รายงานในเซรามิกเลดเซอร์โคเนตไทเทเนตแบบอ่อน ยิ่งไปกว่านั้น ผลการวิจัยพบการผ่อนคลายทางไดอิเล็กทริก ณ อุณหภูมิ 90–150 เคลวิน ซึ่งต่ำกว่าอุณหภูมิการเปลี่ยนเฟสระหว่างเฟสรอมโบฮีดรอลกับเฟสออโธรอมบิกมาก โดยเป็นไปตามแบบจำลองของ Vogel–Fulcher แสดงค่าพลังงานก่อกัมมันต์ (E_a) ในช่วง 20 – 70 มิลลิอิเล็กตรอนโวลต์ และพบอุณหภูมิเยือกแข็ง (T_{VF}) มีค่าระหว่าง 65–85 เคลวิน สำหรับระบบที่มี BNT เป็นองค์ประกอบหลัก ได้ทำการศึกษาเซรามิก $(1–x)(0.94Bi_{0.5}Na_{0.5}TiO_3–0.06BaTiO_3)–xBaSnO_3$ หรืออักษรย่อ BNT–BT–xBSn ในสัดส่วน x = 0.00 0.02 0.04 0.06 0.08 และ 0.10 พบว่าเซรามิกที่สัดส่วน x = 0.02 แสดงค่าความเครียดสูงถึงร้อยละ 0.4 และค่าสัมประสิทธิ์เพียโซอิเล็กทริกสัมพัทธ์ (d_{33}^*) มีค่าเท่ากับ 669 พิโคเมตรต่อโวลต์ ณ อุณหภูมิห้อง ผลการศึกษาส่วนนี้แสดงว่าเซรามิกในระบบ BNT–BT–xBSn เหมาะสมสำหรับการประยุกต์ใช้ในงานแอคชัวเอเตอร์ที่ต้องการความเครียดตอบสนองที่สูง

ในระบบสุดท้ายงานวิจัยทำการศึกษาเซรามิกในระบบ$(1–x)(K_{1/2}Na_{1/2})NbO_3 – xBi(Zn_{2/3}Nb_{1/3})O_3$ [(1–x)KNN–xBZnN] ที่อัตราส่วน x = 0.01–0.10จากผลการศึกษาสมบัติไดอิเล็กทริกพบว่า อุณหภูมิในการเปลี่ยนเฟสเฟอร์โรอิเล็กทริก– พาราอิเล็กทริกมีค่าลดลงอย่างมีนัยสำคัญต่อการเจือ BZnN ในเซรามิก KNN. เซรามิกแสดงสมบัติเพียโซอิเล็กทริกและเฟอร์โรอิเล็กทริกที่โดดเด่นที่องค์ประกอบ x = 0.01 โดยให้ค่า ค่าสัมประสิทธิ์เพียโซอิเล็กทริก (d_{33}^*) เท่ากับ 498 พิโคเมตรต่อโวลต์ และ ค่าโพราไรเซชั่นคงค้าง (P_r) gmjkdy[23.3 ไมโครคูลอมต่อลูกบาศก์เซนติเมตร แสดงค่าความเครียดภายใต้สนามไฟฟ้าสูงเท่ากับ 0.3% และอุณหภูมิคูรีย์มีค่าเท่ากับ 380°C งานวิจัยนี้พบว่า เซรามิกในระบบนี้เมื่อเทียบกับเซรามิกในระบบ BT และ BNT เหมาะสมที่จะนำมาประยุกต์ใช้งานกำลังสูง หรือ แอคชัวเอเตอร์ที่ใช้งานที่อุณหภูมิสูง

คำสำคัญ : วัสดุเพียโซอิเล็กทริกไร้สารตะกั่ว แบเรียมไทเทเนต บิสมัทโซเดียมไทเทเนต โพแทสเซียมโซเดียมไนโอเบต ความล้า แอคชัวเอเตอร์ การผ่อนคลายทางไดอิเล็กทริก

Research code: BRG5680006

Research Title: Lead-free piezoelectric materials for hard disk drives and data storage applications

Researcher: Assoc. Prof. Dr. Naratip Vittayakorn

Faculty: Science **Department:** Chemistry

King Mongkut's Institute of Technology Ladkrabang

ABSTRACT

An attempt was made by this study to replace Pb-based piezoelectric ceramics with a non-toxic lead-free piezoceramic, while focusing on a perovskite structure based on 3 systems; $BaTiO_3$, $(Bi,Na)TiO_3$ and $(K,Na)NbO_3$-based ceramics. In order to achieve high piezoelectric properties, the composition that exhibits two or multiphase coexistent near room temperature was designed, based on the concept of morphotropic phase boundary (MPB) and polymorphic phase transition (PPT). Several works in the literature were reviewed in order to establish the ferroelectric phase diagram and search the polymorphic phase boundary (PPB). Phase compositions in the crystal structure were characterized by X-ray diffraction and Raman spectroscopy. The quantitative phase analysis and local structure of some systems were characterized by Rietveld analysis refinement and X-ray absorption fine structure spectroscopy (XAS). This study measured important piezoelectric and ferroelectric parameters, such as d_{33}, d_{33}^* K_p, P_r, E_c, and also focused on electric fatigue behavior, which is an important parameter for HDD applications.

The ferroelectric phase diagram was established in the BT-BZ-CT ternary system, with the PPB line being proposed. The PPB composition exhibited outstanding piezoelectric properties. A large, virtually hysteresis-free electric field induced strain of 0.23% was achieved with the composition, x = 0.06, at 40 kV/cm on the boundary between rhombohedral and tetragonal phase. This relates to an extraordinarily high and normalized piezoelectric coefficient (S_{max}/E_{max}) of 1280 pm/V, which was reached at a low electric field applied at 10 kV/cm. Fatigue measurement carried out on PPB compositions showed a small degradation in maximum strain after 10^6 cycles, when using an applied field of 20 kV/cm at 10 Hz. Furthermore, the unipolar strain curves were almost hysteresis-free at a high electric field. This study recommended the use of PPB composition for high precision actuator applications.

As a result, at x = 0.1000 in the BT-CT-BS system, the $(Ba_{0.825+x}Ca_{0.175-x})(Ti_{1-x}Sn_x)O_3$ showed outstanding piezoelectric values of d_{33} = 515 pC/N and d_{33}^* = 1293 pm/V, which were higher than those found in commercially available soft PZT. In addition, this study was the first to

report an anomalous dielectric relaxation at $T \approx 90–150$ K, which is far below that in rhombohedral to orthorhombic phase transition. This relaxation fitted the Vogel–Fulcher model with activation energy of $E_a \approx 20 - 70$ meV and freezing temperature of $T_{VF} \approx 65–85$ K.

Solid solution of $(1–x)(0.94Bi_{0.5}Na_{0.5}TiO_3–0.06BaTiO_3)–xBaSnO_3$ [abbreviated as BNT–BT–xBSn] with the compositions, x = 0.00, 0.02, 0.04, 0.06, 0.08 and 0.10 in the BNT–based system was considered. This part of the research reported that a large strain of around 0.4%, with a normalized strain value (d_{33}^*) of 669 pm/V at the composition, x = 0.02, was achieved by applying an electric field of 60 kV/cm at room temperature. The results of this study showed that a new BNT–BT–xBSn ceramic system is a very promising candidate for creating a significantly large strain response, which is sufficiently effective for actuator material applications.

In the KNN–based system, the binary system of $(1–x)(K_{1/2}Na_{1/2})NbO_3 – xBi(Zn_{2/3}Nb_{1/3})O_3$ [(1–x)KNN–*x*BZnN]; x = 0.01–0.10 was investigated. The dielectric data show that the amount of $Bi(Zn_{2/3}Nb_{1/3})O_3$ added in $(K_{1/2}Na_{1/2})NbO_3$ decreases the ferroelectric–paraelectric transition temperature progressively. Furthermore, optimum piezoelectric and ferroelectric properties were observed at the composition, x = 0.01: effective piezoelectric coefficients (d_{33}^*) = 498 pm/V, remanent polarization (P_r) = 23.3 $\mu C/cm^2$, coercive field (E_c) = 14 kV/cm, maximum strain (S_{max}) = 0.3% and Curie temperature (T_C) = 380°C. The results of this study show that KNN with a small amount of $Bi(Zn_{2/3}Nb_{1/3})O_3$ (x = 0.01) can be a candidate lead–free piezoelectric ceramic. Furthermore, when compared with the BT and BNT–based system, the KNN–based system can be a candidate lead free piezoelectric ceramic for high power or high temperature actuator applications.

Keywords : Barium Titanate, Solid solution, Phase transition, Tolerance factor, Piezoelectric properties;

ผลผลิตงานวิจัยที่ได้รับทุนวิจัย

ผลงานวิจัยที่ได้รับทุนวิจัยจากโครงการนี้ได้รับการตีพิมพ์เผยแพร่ในวารสารวิชาการระดับนานาชาติที่มีดัชนีผลกระทบการอ้างอิง (Impact Factor) ทั้งหมดรวม 25 เรื่องประกอบด้วย

1. S. Vuttivong and N. Vittayakorn "Synthesis and Morphology of $KNbO_3$ Powders via Hydrothermal Method" Integrated Ferroelectrics, 149: 25–31 (2013), Impact Factor = 0.375
2. S. Vuttivong, S. Niemcharoen, P. Seeharaj, W. Vittayakorn and N. Vittayakorn "Sonochemical Synthesis of Spherical $BaTiO_3$ Nanoparticles" Ferroelectrics, 457(1): 44–52 (2013), Impact Factor = 0.415
3. P. Charoonsuk, R. Baitahe, W. Vittayakorn, N. Atiwongsangthong, R. Muanghua, P. Seeharaj and N. Vittayakorn "Synthesis of Monodispersed Perovskite Barium Zirconate ($BaZrO_3$) by the Sonochemical Method" Ferroelectrics, 453: 54–61 (2013), Impact Factor = 0.415
4. N. Chaiyo, R. Muanghlua, Y. Wongprasert, P. Seeharaj and N. Vittayakorn "Rapid Synthesis of Potassium Sodium Niobate ($K_{1/2}Na_{1/2}NbO_3$) Lead–free Piezoelectric Powder Using the Combustion Method" Integrated Ferroelectrics, 149: 128–134 (2013), Impact Factor = 0.375
5. R. Baitahe, C. Kongmark, R. Muanghlua, P. Seeharaj and N. Vittayakorn "X–ray Absorption Spectroscopy Studies of $Cu_{(2-x)}Zn_xP_2O_7$ Binary Pyrophosphates" Ferroelectrics, 453: 100–105 (2013), Impact Factor = 0.415
6. N. Chaiyo, R. Muanghlua, Y. Wongprasert, P. Seeharaj and N. Vittayakorn "Combustion Synthesis of Lead–free Piezoelectric Alkali Metal Niobate Family" Ferroelectrics, 453: 26–37 (2013), Impact Factor = 0.415
7. R. Roongtao, R. Baitahe, N. Vittayakorn, W. Klysubun and W. Vittayakorn "Structural and Magnetic Properties of Zn Doped $CoFe_2O_4$" Integrated Ferroelectrics, 148: 145–152 (2013), Impact Factor = 0.375
8. C. Nawanil, W. Vittayakorn, J. Prachayawarakorn and N. Vittayakorn "Preparation and Dielectric Properties of 3–3 Lead Zirconate/Polyvinylidene Fluoride Nanocomposite" Ferroelectrics Letters Section, 40: 94–100 (2013), Impact Factor = 0.600

9. W. Vittayakorn, N. Pulphol, R. Muanghlua and N. Vittayakorn “Fabrication and Properties of $BaTiO_3$–$CoFe_2O_4$ Nanocomposites” Integrated Ferroelectrics, 148: 153–160 (2013), Impact Factor = 0.375
10. S. Kahatta, W. Techitdheera, N. Chaiyo, W. Pecharapa and N. Vittayakorn “Synthesis and Characterization of Thermochromic $La_{0.75}Ca_{0.25}MnO_3$ Perovskite Manganites Nano–powders by Microwave–assisted Solution Combustion Synthesis” Integrated Ferroelectrics, 150: 96–106 (2014), Impact Factor = 0.375
11. U. Sukkha, N. Vittayakorn, R. Guod and A. S. Bhalla “Phase transition behavior of $Ba(Mg_{1/3}Nb_{2/3})O_3$ modified $PbZrO_3$ solid solution” Journal of Materials Chemistry C, 2: 2929–2938 (2014), Impact Factor = 5.066
12. U. Sukkha, W. Vittayakorn, R. Muanghlua, S. Niemcharoen and N. Vittayakorn “Effect of A–site and B–site ion replaced with small ions on the intermediate phase in $PbZrO_3$ ceramic” Materials Chemistry and Physics, 143: 1517–1521 (2014), Impact Factor = 2.101
13. R. Baitahe and N. Vittayakorn “Phase formation and evolution of Cu:Zn partials in binary metal pyrophosphates $Cu_{(2-x)}Zn_{(x)}P_2O_7$; x = 1” Thermochimica Acta, 596: 21–28 (2014), Impact Factor = 1.938
14. N. Chaiyo, D. P. Cann and N. Vittayakorn "Phase transitions, ferroelectric, and piezoelectric properties of lead–free piezoelectric xBaZrO3–(0.25–x)$CaTiO_3$–0.75$BaTiO_3$ ceramics” Journal of Materials Science, 50: 6171–6179 (2015), Impact Factor = 2.302
15. J. Janbua, J. Mayamae, S. Wirunchit, R. Baitahe and N. Vittayakorn “Directed synthesis, growth process and optical properties of monodispersed $CaWO_4$ microspheres via a sonochemical route” RSC Advances, 5: 19893–19899 (2015), Impact Factor = 3.289
16. S. Wirunchit, T. Charoonsuk and N. Vittayakorn “Facile sonochemical synthesis of near spherical barium zirconate titanate ($BaZr_{1-y}Ti_yO_3$; BZT); perovskite stability and formation mechanism” RSC Advances, 5: 38061–38074 (2015), Impact Factor = 3.289
17. M. Sutapun, W. Vittayakorn, R. Muanghlua and N Vittayakorn “High piezoelectric response in the new coexistent phase boundary of 0.87$BaTiO_3$–(0.13–x)$BaZrO_3$–$x$$CaTiO_3$” Materials and Design 86: 564–574 (2015), Impact Factor = 3.997
18. N. Pulphol, R. Muanghlua, S. Niemcharoen, N. Vittayakorn and W. Vittayakorn “Fine Grain $BaTiO_3$–$Co_{0.5}Ni_{0.5}Fe_2O_4$ Ceramics Prepared by the Two–Stage Sintering Technique” Ferroelectrics, 488: 170–180 (2015), Ferroelectrics, 453: 26–37 (2013), Impact Factor = 0.415

19. U. Sukkha, S. Niemcharoen, N. Vittayakorn, R. Guo and A. S. Bhalla “Effect of $BiYbO_3$ Addition with a Small Tolerance Factor on Ferroelectricity and T_C in $PbZrO_3$ Ceramics Ferroelectrics, 487: 55–67 (2015), Impact Factor = 0.415
20. R. Roongtao, N. Vittayakorn, W. Klysubun and W. Vittayakorn “Effect of Annealing Time on the Cation Distribution in Mn Doped $CoFe_2O_4$ Ferroelectrics, 492: 43–53 (2016), Impact Factor = 0.415
21. R. Baitahe and N. Vittayakorn “Dielectric Properties and Characterizations of Binary $Cu_{(2-x)}Mg_xP_2O_7$ Pyrophosphates Ferroelectrics” 490: 174–183 (2016), Impact Factor = 0.415
22. M. Sutapun, R. Muanghlua and N. Vittayakorn “Phase Transition, Dielectric and Piezoelectric Properties of Lead–Free Piezoelectric $(K_{1/2}Na_{1/2})NbO_3$–$Bi(Zn_{2/3}Nb_{1/3})O_3$ Ceramics” Ferroelectrics, 490: 1–12 (2016), Impact Factor = 0.415
23. J. Mayamae, U. Sukkha, S. Niemchareon, R. Muanghlua and N. Vittayakorn “Dielectric, Ferroelectric and Piezoelectric Properties of the Lead Free $0.9BaTiO_3$–$(0.1–x)Bi_{0.5}Na_{0.5}TiO_3$–$xBi(Mg_{0.5}Ti_{0.5})O_3$ Solid Solution” Ferroelectrics, 490: 23–35 (2016), Impact Factor = 0.415
24. J. Janbua, S. Niemchareon, R. Muanghlua and N. Vittayakorn “High Strain Response of the $(1–x)$ $(0.94Bi_{0.5}Na_{0.5}TiO_3–0.06BaTiO_3)–xBaSnO_3$ Lead Free Piezoelectric Ceramics System Ferroelectrics, 490: 13–22 (2016), Impact Factor = 0.4
25. T. Charoonsuk and N. Vittayakorn “A facile one step conversion of the sub-micrometer to uniform nanopowder in tetragonal $BaTiO_3$ *via* a surface active etching salt” Materials and Design Volume 110, page 233-244 (2016) Impact Factor = 3.997

อยู่ระหว่างขั้นตอนการพิจารณาบทความ 1 เรื่องคือ

1. Thitirat Charoonsuk, Naratip Vittayakorn and Taras V. Kolodiazhnyi “Lattice Evolution and Point Defect Chemistry in Ta-Doped Ceria” Submitted to Advanced Functional Materials; Impact Factor = 11.8

การนำเสนอผลงานในงานประชุมวิชาการระดับชาติทั้งสิ้น 5 เรื่อง

(1). Charoonsuk, P., Vittayakorn, N., Seeharaj P., Atiwongsangthong, N., Muanghlua, R., Vittayakorn W. "The synthesis of monodispersed perovskite barium zirconate ($BaZrO_3$) in an ethanol-water mixture solvent by sonochemical method" The 40th Congress on Science and Technology of Thailand (STT40),

2-4 December 2014, Khon Kaen University, Khon Kaen, Thailand (Oral Presentation)

(2). Janbua, J., Niemchareon, S., Muanghlua, R., Vittayakorn, N. “High strain response of the (1-x)($0.94Bi_{0.5}Na_{0.5}TiO_3$-$0.06BaTiO_3$)-x$BaSnO_3$ lead free piezoelectric ceramics system” The 40th Congress on Science and Technology of Thailand (STT40), 2-4 December 2014, Khon Kaen University, Khon Kaen, Thailand (Oral Presentation)

(3). Mayamae, J., Sukkha, U., Karbkaew, A., Niemchareon, S., Muanghlua, R., Vittayakorn, N. “Dielectric, ferroelectric and piezoelectric properties of the lead free $0.9BaTiO_3$- (0.1- *x*)$Bi_{0.5}Na_{0.5}TiO_3$-*x*$Bi(Mg_{0.5}Ti_{0.5})O_3$ solid solution” The 40th Congress on Science and Technology of Thailand (STT40), 2-4 December 2014, Khon Kaen University, Khon Kaen, Thailand (Oral Presentation)

(4). Charoonsuk, P., Vittayakorn, N., “Facile Molten Salt Synthesis Method of Monodispersed $BaTiO_3$ Nanoparticles” The 41st Congress on Science and Technology of Thailand (STT41), 6-8 November 2015, Suranaree University of Technology Nakhon Ratchasima, Nakhon Ratchasima, Thailand (Oral presentation)

(5). Chaiyo, N., Cann, D.P., Vittayakorn, N. “Bipolar Fatigue Behaviors, Phase Transitions, Ferroelectric, and Piezoeelctric Properties of Lead-free Piezoelectric *x*$BaZrO_3$-(0.25-*x*)$CaTiO_3$-$0.75BaTiO_3$ Ceramics” The 41st Congress on Science and Technology of Thailand (STT41), 6-8 November 2015, Suranaree University of Technology Nakhon Ratchasima, Nakhon Ratchasima, Thailand (Oral presentation)

การนำเสนอผลงานในงานประชุมวิชาการระดับนานาชาติทั้งสิ้น 6 เรื่อง

(1). Charoonsuk, P., Vittayakorn, W., Vittayakorn, N., Seeharaj P., Maensiri S. “Sonochemical synthesis of monodispersed perovskite barium zirconate ($BaZrO_3$) by using an ethanol–water mixed solvent” The Joint International Conference of the 9th Asian Meeting on Ferroelectricity (AMF-9) and the 9th Asian Meeting on Electroceramics (AMEC-9), 26-30 October 2014, Shanghai International Convention Center, Shanghai, China (Oral Presentation)

(2). Janbua, J., Niemchareon, S., Muanghlua, R., Vittayakorn, N. “High strain response of the (1-*x*)($0.94Bi_{0.5}Na_{0.5}TiO_3$-$0.06BaTiO_3$)-*x*$BaSnO_3$ lead free piezoelectric ceramics system” The Joint International Conference of the 9th

Asian Meeting on Ferroelectricity (AMF-9) and the 9th Asian Meeting on Electroceramics (AMEC-9), 26-30 October 2014, Shanghai International Convention Center, Shanghai, China (Poster Presentation)

(3). Mayamae, J., Sukkha, U., Niemchareon, S., Muanghlua, R., Vittayakorn, N. "Dielectric, ferroelectric and piezoelectric properties of the lead free $0.9BaTiO_3$-$(0.1-x)Bi_{0.5}Na_{0.5}TiO_3$-$xBi(Mg_{0.5}Ti_{0.5})O_3$ solid solution" International Conference of the 9th Asian Meeting on Ferroelectricity (AMF-9) and the 9th Asian Meeting on Electroceramics (AMEC-9), 26-30 October 2014, Shanghai International Convention Center, Shanghai, China (Poster Presentation)

(4). Sutapun, M., Muanghlua, R., Vittayakorn., N. "Phase transition, dielectric and piezoelectric properties of lead-free piezoelectric $(K_{1/2}Na_{1/2})NbO_3$ – $Bi(Zn_{2/3}Nb_{1/3})O_3$ ceramics" International Conference of the 9th Asian Meeting on Ferroelectricity (AMF-9) and the 9th Asian Meeting on Electroceramics (AMEC-9), 26-30 October 2014, Shanghai International Convention Center, Shanghai, China (Poster Presentation)

(5). Sutapun, M., Muanghlua, R., Vittayakorn., N. "The influence of $Bi(X_{2/3}Nb_{1/3})O_3$; X = Mn, Zn and Mg addition on the phase transition, microstructure and piezoelectric property of $(K_{1/2}Na_{1/2})NbO_3$ ceramic" International Conference of the 9th Asian Meeting on Ferroelectricity (AMF-9) and the 9th Asian Meeting on Electroceramics (AMEC-9), 26-30 October 2014, Shanghai International Convention Center, Shanghai, China (Poster Presentation)

(6). Chaiyo, N., Vittayakorn, N., Cann D.P. "Phase transition, ferroelectric and piezoelectric properties of lead-free piezoelectric $0.75BaTiO_3$-$xBaZrO_3$-$(0.25-x)CaTiO_3$ ceramics" Electronic Materials and Applications 2015 (EMA2016), 21-23 January 2015, Doubletree by Hilton Orlando at Sea World, Orlando, Florida, USA (Oral presentation)

(7) Nopsiri Chaiyo, David P. Cann and Naratip Vittayakorn "Enhanced Piezoelectric Properties and Fatigue-free Behavior of Lead-free Piezoelectric $xBaZrO_3$-$(0.85-x)BaTiO_3$-$0.15CaTiO_3$ Ceramics"

ผลงานได้รับรางวัลจากงานประชุมวิชาการระดับนานาชาติทั้งสิ้น 3 รางวัล

(1). **Excellent Poster Awards** "High strain response of the $(1-x)(0.94Bi_{0.5}Na_{0.5}TiO_3$-$0.06BaTiO_3)$-$xBaSnO_3$ lead free piezoelectric ceramics system" The Joint International Conference of the 9th Asian Meeting on Ferroelectricity (AMF-9)

and the 9th Asian Meeting on Electroceramics (AMEC-9), Shanghai International Convention Center, Shanghai, China, 26-30 October 2014**.** Janbua, J., Niemchareon, S., Muanghlua, R., Vittayakorn, N.

(2). **Best student award**, The Joint International Conference of the 9th Asian Meeting on Ferroelectricity (AMF-9) and the 9th Asian Meeting on Electroceramics (AMEC-9), Shanghai International Convention Center, Shanghai, China, 26-30 October 2014**.** Charoonsuk, P.

(3) **Best oral presentation** "Enhanced Piezoelectric Properties and Fatigue-free Behavior of Lead-free Piezoelectric $x$$BaZrO_3$-(0.85-$x$)$BaTiO_3-0.15CaTiO_3$ Ceramics" Nopsiri Chaiyo, David P. Cann and Naratip Vittayakorn in International Conference on Science and Technology of Emerging Materials (STEMa2016) at Holiday Inn, Pattaya, Thailand, during July 27-29, 2016**.**

OUTPUT

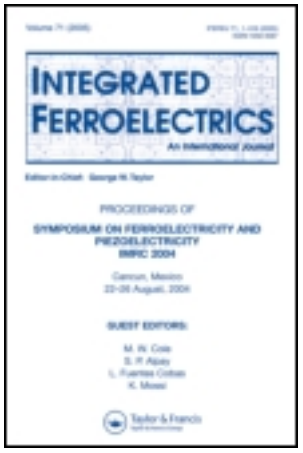

Integrated Ferroelectrics: An International Journal
Publication details, including instructions for authors and subscription information:
http://www.tandfonline.com/loi/ginf20

Synthesis and Morphology of $KNbO_3$ Powders via Hydrothermal Method

Sirajit Vuttivong [a] & Naratip Vittayakorn [a b]

[a] Electroceramic Research Laboratory, College of Nanotechnology , King Mongkut's Institute of Technology Ladkrabang , Bangkok , 10520 , Thailand

[b] Advanced Materials Research Unit, Department of Chemistry, Faculty of Science , King Mongkut's Institute of Technology Ladkrabang , Bangkok , 10520 , Thailand

Published online: 07 Dec 2013.

To cite this article: Sirajit Vuttivong & Naratip Vittayakorn (2013) Synthesis and Morphology of $KNbO_3$ Powders via Hydrothermal Method, Integrated Ferroelectrics: An International Journal, 149:1, 25-31, DOI: 10.1080/10584587.2013.852915

To link to this article: http://dx.doi.org/10.1080/10584587.2013.852915

Integrated Ferroelectrics, 149:25–31, 2013

ISSN: 1058-4587 print / 1607-8489 online
DOI: 10.1080/10584587.2013.852915

Taylor & Francis
Taylor & Francis Group

Synthesis and Morphology of $KNbO_3$ Powders via Hydrothermal Method

SIRAJIT VUTTIVONG[1] AND NARATIP VITTAYAKORN[1,2,*]

[1]Electroceramic Research Laboratory, College of Nanotechnology, King Mongkut's Institute of Technology Ladkrabang, Bangkok 10520, Thailand
[2]Advanced Materials Research Unit, Department of Chemistry, Faculty of Science, King Mongkut's Institute of Technology Ladkrabang, Bangkok 10520, Thailand

In this research, potassium niobate ($KNbO_3$) powder was synthesized successfully for 6–24 h in 15 M of KOH solutions at 120–200°C via the hydrothermal method. The effects of reaction temperatures and reaction times on the precipitation of $KNbO_3$ powders were investigated. A hydrothermal precursor yielded a pure single phase $KNbO_3$ for 18 h at 150°C. When the reaction time increased to 24 h, the morphology of $KNbO_3$ changed from an irregular shape to a rod- or bar-shape. The reaction temperature had a marked effect on both structure and phase formation, while the reaction time could affect morphology. The direct synthesis of $KNbO_3$ from Nb_2O_5 and aqueous KOH under hydrothermal conditions therefore represents an easy method for the preparation of this compound.

Keywords Potassium niobate ($KNbO_3$); hydrothermal method

1. Introduction

Potassium niobate ($KNbO_3$) is a lead-free piezoelectric material with perovskite-type structure, and considered to be a promising compound for replacing PZT-based material. Lead-contained compounds possess excellent properties and are important industrially. However, hazardous lead oxide is the origin of much environmental pollution and many medical symptoms [1]. $KNbO_3$ is a well-known ferroelectric material, in which several phase transitions occur from high to low symmetry as temperature decreases such as: cubic to tetragonal at 435°C, tetragonal to orthorhombic at 225°C and finally orthorhombic to rhombohedral at −10°C [2]. It is a frequency doubling material and holographic storage medium that act as optical waveguides in finding applications in electro-optic and non-linear optic devices. This material also is highly promising for use in surface acoustic wave devices, since its electromechanical coupling coefficient is higher than that of $LiNbO_3$, which is manufactured most for this application [3]. Conventional, solid-state synthesis of $KNbO_3$ requires prolonged heating using mixed powders at the high temperature of 820°C [4]. An aqueous solution route also has been used at 25°C to precipitate amorphous $KNbO_3$ powders that are then crystallized by heating to 600°C [5]. The modified process involving two-stage calcinations (first stage at 600°C and second stage at 1000°C) is very effective

Received December 9, 2012; in final form August 25, 2013.
*Corresponding author. E-mail: naratipcmu@yahoo.com

in obtaining $KNbO_3$ ceramics with a high density ratio >96% and a high resistivity, ρ, of $>10^{12}$ Ω·cm and that are nondeliquescent [6]. Therefore, many methods have been developed for preparing $KNbO_3$ such as the homogeneous sol-gel process, colloid chemistry and microemulsion mediated synthesis. $KNbO_3$ powder has been prepared by template crystallization of a precursor gel [7]. However, these synthesis methods demand long reaction times (6–7 days); and template crystallization of the precursor gel is a two-step route including high temperature calcinations (T > 500°C).

Recently, hydrothermal synthesis became extremely interesting because of its simple process and short reaction time at low reaction temperature, which saves energy, and several research groups have used this method to synthesize crystalline powder such as $BaTiO_3$, ZnO and $PbTiO_3$. The theoretical design of the hydrothermally synthesized pure $KNbO_3$ powder was in a K-Nb-O tri-component system, where stability yields diagrams and the optimum conditions. It is found that the experiment is in great agreement with the theoretical design [8]. Moreover, non doped $KNbO_3$ crystal powders were synthesized by ultrasonic-assisted hydrothermal method. By using the ultrasonic assist technique, the yield constant of the hydrothermally synthesized $KNbO_3$ crystal powders was 96% when the synthesis time and temperature were 3 h and 190°C, respectively [9]. So, this research reports the synthesis of $KNbO_3$ powder via the hydrothermal method using niobium oxide (Nb_2O_5) and potassium hydroxide (KOH) as starting materials. Effects on the evolution phase and morphology of $KNbO_3$ powders at different reaction temperatures and reaction times were investigated.

2. Experimental Procedure

Analytical grade niobium oxide (Nb_2O_5, 99.95 %, Aldrich, USA) and potassium hydroxide (KOH, 99 %, Sigma-Aldrich, Germany) were used as starting materials. A typical synthesis of $KNbO_3$ powders was as follows: Nb_2O_5 was added to 25 ml of 15 M KOH solution, which was stirred vigorously in air for 30 min. Thereafter, the reaction mixture was sealed in a 100 cm^3 Teflon-lined stainless steel autoclave and heated for 6–24 h at 120–200°C. After cooling to room temperature, the products were washed several times with distilled water and ethanol followed by drying for 5 h at 80°C. The product was analyzed by X-ray powder diffraction (XRD; Bruker AXS, D8 Advance, Karlsruhe Germany) using Ni-filtered CuK_α radiation to identify the phase formed and optimum condition for the formation of $KNbO_3$ powders. The room temperature FT-IR spectra were recorded in the range of 4,000–400 cm^{-1}, with eight scans on a Perkin-Elmer Spectrum GX spectrometer, and the resolution of 4 cm^{-1}. Powder morphology and grain size were imaged directly using scanning electron microscopy (LEO, LEO 1455VP, Cambridge, England).

3. Results and Discussion

Figure 1 shows the X-ray diffraction pattern of $KNbO_3$ powder, synthesized for 24 h at different reaction temperatures. From reaction time at 120°C, un-dissolved Nb_2O_5 was observed with no evidence of perovskite $KNbO_3$ in the XRD pattern. This result implies that no reaction occurred under these conditions. When the reaction temperature was increased to 150°C, the XRD pattern exhibited a single-phase perovskite structure with orthorhombic symmetry, which can be indexed according to JCPDS card no. 71-2171 ($KNbO_3$) and refined cell parameters, a = 5.697 Å, b = 3.971 Å and c = 5.721 Å. When reaction temperature in the preparation reached 200°C, it was found surprisingly that the obtained $KNbO_3$ powders exhibited structure corresponding to the cubic instead of orthorhombic phase [10]. Evidence of $K_4Nb_6O_{17}\cdot 3H_2O$ or complete dissolution of the initial niobium oxide was not observed

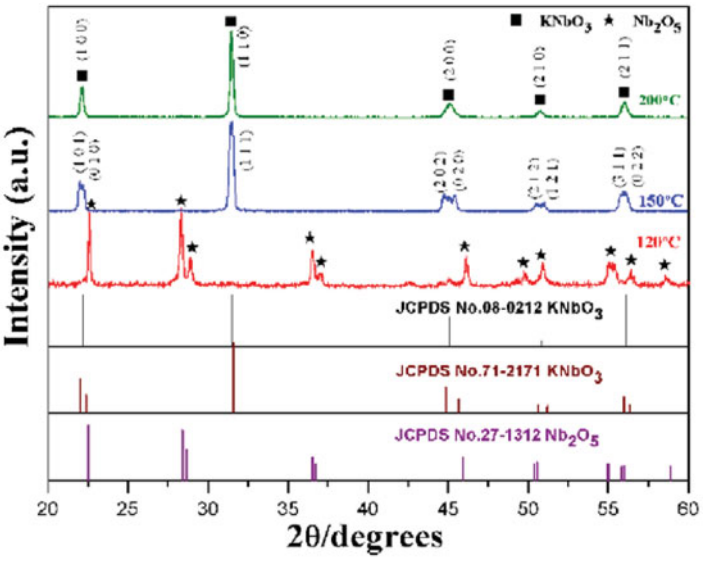

Figure 1. The XRD patterns of $KNbO_3$ powders synthesized for 24 h using different reaction temperatures via the hydrothermal method. (Color figure available online.)

in the pattern. The XRD pattern of this powder was consistent with that reported in JCPDS No. 08-0212 [10]. The above results imply that the increasing reaction temperature in the hydrothermal reaction influenced the crystalline structure of $KNbO_3$. The effect of reaction time on the crystalline structure of the final product was studied under the constant reaction temperature of 150°C. Figure 2 shows the XRD patterns of the $KNbO_3$ powders synthesized

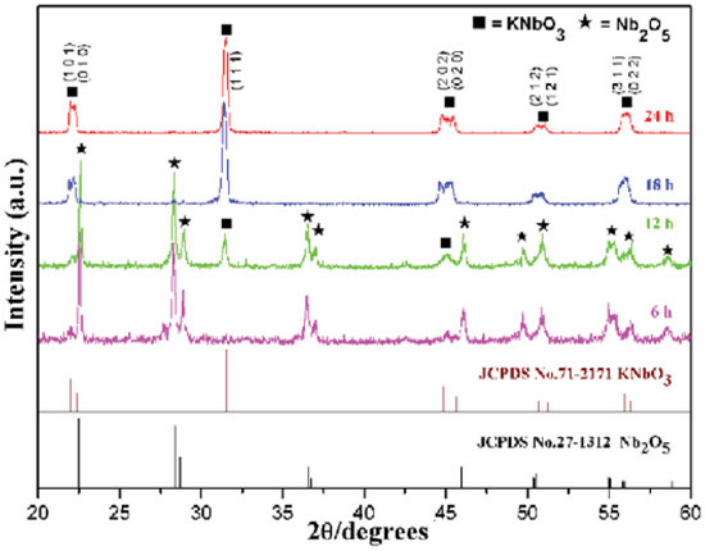

Figure 2. The XRD patterns of $KNbO_3$ powders hydrothermally synthesized for different reaction times with the reaction temperature at 150°C. (Color figure available online.)

for different reaction times at 150°C. Only Nb_2O_5 existed in the products at a reaction time of 6 h. This result implies that no reaction occurred under these conditions. When the reaction time was increased to 12 h, a small amount of $KNbO_3$ perovskite was crystallized, but when increased to 18 h, a large amount of $KNbO_3$ perovskite was generated. Formation of $KNbO_3$ in hydrothermal condition can be expressed as follows: while Nb_2O_5 is in hydrothermal condition, with the temperature above 150°C, it can be ionized, dissolved, and reacted easily with KOH. Superficial parts of the Nb_2O_5 particle were hydroxylized and dissolved into the solution, before the dissolved proportion reacted further with KOH in different alkalinity and generated $KNbO_3$ [11]. The above results reveal that the reaction time is a critical controlling factor for synthesizing $KNbO_3$ powder.

The FT-IR spectrum was used as a second tool to support the XRD results. The IR spectra of the $KNbO_3$ powders synthesized for different reaction times at 150°C are presented in Figure 3. All the spectra display bands that are characteristic of O–H stretching modes (3,437 and 1,640 cm^{-1}), and several bands are characteristic of the oxygen-metals/stretching mode at around 600 and 500 cm^{-1} [12, 13]. At 3,437 cm^{-1}, absorption of stretching vibrations for the H_2O- and OH-group was observed in $KNbO_3$ powder synthesized for 6 and 12 h at 150°C, but no absorption was seen when synthesized for 18 and 24 h. The FT-IR spectrum of the sample synthesized for 18 h showed a very strong and broad IR band centered at 614 cm^{-1} and 854cm^{-1}, which can be attributed to the amorphous Nb_2O_5 that was in line with the XRD measurement [14]. Synthesis at a longer reaction time led to a significant change in the infrared spectra, thus causing the bands to disappear at 614 and 854 cm^{-1}. At the reaction time of 18 h, and at about 635 cm^{-1}, the band was associated with the Nb–O stretching vibration of the NbO_6 octahedron in the perovskite structure [15]. Powder synthesized for 24 h showed similar spectral behavior. To investigate the morphology of hydrothermally grown crystals, this research showed scanning electron microscope (SEM) images of $KNbO_3$. Figure 4 shows the SEM image of the $KNbO_3$ powders synthesized for different reaction times at 150°C. The SEM image of $KNbO_3$ powders synthesized for 12 h at 150°C is shown in Figure 4a, in which the particles are irregular and uneven. The

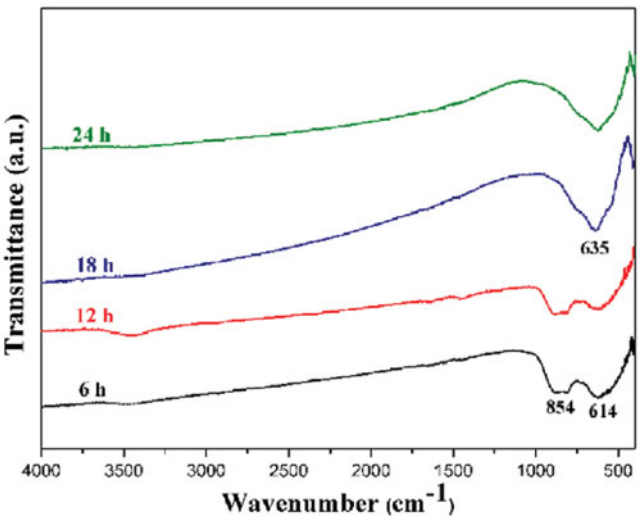

Figure 3. IR spectra of $KNbO_3$ powders prepared with the reaction temperature at 150°C. (Color figure available online.)

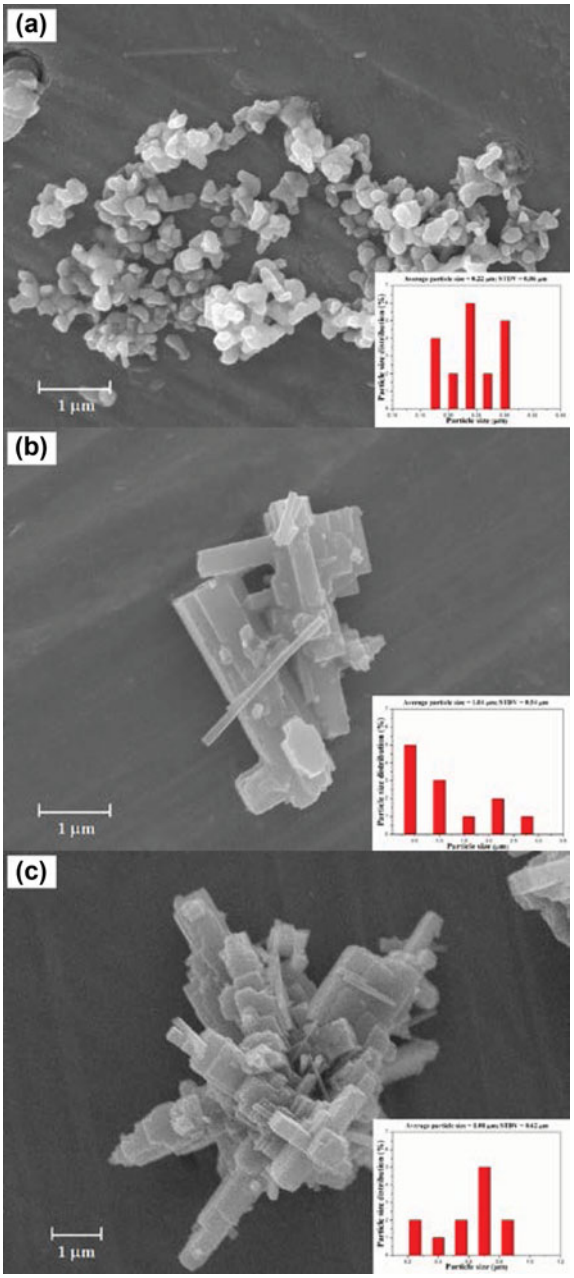

Figure 4. SEM micrographs of $KNbO_3$ powders prepared at 150°C in reaction times of (a) 12 h, (b) 18 h and (c) 24 h, consecutively. (Color figure available online.)

average particle size, which can be estimated from micrographs, was found to be 0.22 ± 0.06 μm. When the reaction time increased [Figure 4(b-c)], the morphology of $KNbO_3$ changed from an irregular shape to a rod- or bar-shape. No evidence of a different or pyrochlore phase was found, which suggested the homogeneous character of the prepared

powder. The changes in the morphology are in agreement with the results of the XRD patterns. These findings indicate that the reaction time and reaction temperature play a key role in the crystal structure of the powder and morphology of the $KNbO_3$ products. The direct synthesis of $KNbO_3$ from Nb_2O_5 and aqueous KOH under hydrothermal conditions thus represents an easy method for preparing this compound. This method eliminates the need for using high temperature reactions, calcination steps, or less accessible precursors.

4. Conclusions

$KNbO_3$ particles were synthesized successfully using niobium oxide (Nb_2O_5) and potassium hydroxide (KOH) as starting materials via the hydrothermal method. The effects of reaction temperatures (from 120°C to 200°C) and reaction times (from 6 h to 24 h) on the precipitation of $KNbO_3$ powders were investigated. When the reaction temperature in the preparation reached 200°C, it was found surprisingly that the obtained $KNbO_3$ powders exhibited a structure corresponding to the cubic instead of orthorhombic phase. Furthermore, the morphology of $KNbO_3$ changed from an irregular shape to a rod- or bar-shape. These findings indicate that the reaction time and reaction temperature play a key role in the crystal structure of the powder and morphology of the $KNbO_3$ products.

Acknowledgments

This work has been fully supported by research fund from the Thailand Research Fund (Grant No. BRG5680006).

References

1. T. Takenaka, and H. Nagata, Current status and prospects of lead-free piezoelectric ceramics. *J Eur Ceram Soc*. **25**, 2693–2700 (2005).
2. G. K. L. Goh, C. G. Levi, J. H. Choi, and F. F. Lange, Hydrothermal epitaxy of $KNbO_3$ thin films and nanostructures. *J Cryst Growth*. **286**, 457–464 (2006).
3. A. J. Paula, R. Parra, M. A. Zaghete, and J. A. Varela, Synthesis of $KNbO_3$ nanostructures by a microwave assisted hydrothermal method. *Mater Lett*. **62**, 2581–2584 (2008).
4. U. Fluckiger, and H. Arend, Synthesis of $KNbO_3$ powder. *J Am Ceram Soc*. *Bull* **56**, 575–577 (1977).
5. K. M. Jin, and M. Egon, Preparation and characterization of uniform submicrometer metal niobate particles: Part II. Magnesium niobate and potassium niobate. *J Mater Res*. **7**(4), 912–918 (1992).
6. H. Nagata, K. Matsumoto, T. Hirosue, Y. Hiruma, and T. Takenaka, Fabrication and electrical properties of potassium niobate ferroelectric ceramics. *Jpn J Appl Phys*. **46**, 7084–7088 (2007).
7. I. Pribošič, D. Makovec, and M. Drofenik, Formation of nanoneedles and nanoplatelets of $KNbO_3$ perovskite during templated crystallization of the precursor gel. *Chem Mater*. **17**(11), 2953–2958 (2005).
8. X. Han, D. Zhang, Z. Zhong, F. Yang, N. Wei, K. Zheng, Z. Li, and Y. Gao, Theoretical design and experimental study of hydrothermal synthesis of $KNbO_3$. *J Phys Chem Solids*. **69**, 193–198 (2008).
9. M. Ishikawa, Y. Kadota, N. Takiguchi, H. Hosaka, and T. Morita, Synthesis of nondoped potassium niobate ceramics by ultrasonic assisted hydrothermal method. *Jpn J Appl Phys*. **47**(9), 7673–7677 (2008).
10. M. M. Amini, and M. Mirzaee, Effect of solvent and temperature on the preparation of potassium niobate by hydrothermal-assisted sol-gel processing. *Ceram Int*. **35**, 2367–2372 (2009).

11. J. F. Liu, X. L. Li, and Y. D. Li, Synthesis and characterization of nanocrystalline niobates. *J Cryst Growth*. **247**, 419–424 (2003).
12. J. M. R. Gallo, H. O. Pastore, and U. Schuchardt, Study of the effect of the base, the silica and the niobium sources on the [Nb]-MCM-41 synthesized at room temperature. *J Non-Cryst Solids*. **354**, 1648–1653 (2008).
13. A. Chowdhury, J. Bould, M. G. S. Londesborough, and S. J. Milne, The effect of refluxing on the alkoxide-based sodium potassium niobate sol-gel system: thermal and spectroscopic studies. *J Solid State Chem*. **184**(2), 317–324 (2011).
14. F. Rubio-Marcos, J. J. Romero, M. S. Martin-Gonzalez, and J. F. Fernandez, Effect of stoichiometry and milling processes in the synthesis and the piezoelectric properties of modified KNN nanoparticles by solid state reaction. *J Eur Ceram Soc*. **30**(13), 2763–2771 (2010).
15. N. Chaiyo, A. Ruangphanit, R. Muanghlua, S. Niemcharoen, B. Boonchom, and N. Vittayakorn, Synthesis of potassium niobate ($KNbO_3$) nano-powder by a modified solid state reaction. *J Mater Sci*. **46**, 1585–1590 (2011).

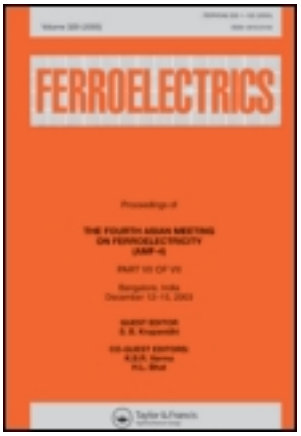

Ferroelectrics
Publication details, including instructions for authors and subscription information:
http://www.tandfonline.com/loi/gfer20

Sonochemical Synthesis of Spherical $BaTiO_3$ Nanoparticles

Sirajit Vuttivong [a d], Surasak Niemcharoen [b], Panpailin Seeharaj [c], Wanwilai C. Vittayakorn [a] & Naratip Vittayakorn [a c d]

[a] Electroceramic Research Laboratory, College of Nanotechnology, King Mongkut's Institute of Technology Ladkrabang , Bangkok , 10520 , Thailand

[b] Department of Electronics , Faculty of Engineering, King Mongkut's Institute of Technology Ladkrabang , Bangkok , 10520 , Thailand

[c] Advanced Materials Research Unit, Department of Chemistry, Faculty of Science, King Mongkut's Institute of Technology Ladkrabang , Bangkok , 10520 , Thailand

[d] Thailand Center of Excellence in Physics, CHE, Ministry of Education , Bangkok , 10400 , Thailand

Published online: 09 Dec 2013.

To cite this article: Sirajit Vuttivong , Surasak Niemcharoen , Panpailin Seeharaj , Wanwilai C. Vittayakorn & Naratip Vittayakorn (2013) Sonochemical Synthesis of Spherical $BaTiO_3$ Nanoparticles, Ferroelectrics, 457:1, 44-52, DOI: 10.1080/00150193.2013.847332

To link to this article: http://dx.doi.org/10.1080/00150193.2013.847332

Ferroelectrics, 457:44–52, 2013

ISSN: 0015-0193 print / 1563-5112 online
DOI: 10.1080/00150193.2013.847332

Taylor & Francis
Taylor & Francis Group

Sonochemical Synthesis of Spherical $BaTiO_3$ Nanoparticles

SIRAJIT VUTTIVONG,[1,4] SURASAK NIEMCHAROEN,[2] PANPAILIN SEEHARAJ,[3] WANWILAI C. VITTAYAKORN,[1] AND NARATIP VITTAYAKORN[1,3,4,*]

[1]Electroceramic Research Laboratory, College of Nanotechnology, King Mongkut's Institute of Technology Ladkrabang, Bangkok 10520, Thailand
[2]Department of Electronics, Faculty of Engineering, King Mongkut's Institute of Technology Ladkrabang, Bangkok 10520, Thailand
[3]Advanced Materials Research Unit, Department of Chemistry, Faculty of Science, King Mongkut's Institute of Technology Ladkrabang, Bangkok 10520, Thailand
[4]Thailand Center of Excellence in Physics, CHE, Ministry of Education, Bangkok 10400, Thailand

Monosized spherical barium titanate ($BaTiO_3$) nanoparticles have been synthesized successfully via sonochemical reaction. The as-synthesized $BaTiO_3$ nanoparticles were characterized using X-ray diffraction of powder, Fourier transform infrared spectroscopy, Raman spectroscopy, scanning electron microscopy and transmission electron microscopy. The XRD pattern of $BaTiO_3$ particles, which were synthesized under irradiation of ultrasonic sound for 0.5 h, showed sharp diffraction peaks that corresponded to the cubic $BaTiO_3$ phase. Only a small amount of $BaCO_3$ contamination was present in the sample. The Raman active modes of the samples in this study were similar to the cubic phase of $BaTiO_3$. The average diameter of sonochemical synthesized particles was ~99.54 ± 18.25 nm. The synthesized $BaTiO_3$ nanoparticles were almost spherical.

Keywords Barium titanate ($BaTiO_3$); sonochemical method; nanoparticles

1. Introduction

Barium titanate ($BaTiO_3$) has been one of the most widely used ceramics for electronic devices in the technological ceramic industry, such as fabrication of multilayer ceramic capacitors (MLCCs), pyroelectric elements, heaters with a positive temperature coefficient of resistivity (PTCR) and embedded capacitance in printed circuit boards (PCB). This is because it has ferroelectric, thermoelectric and piezoelectric properties when assuming a tetragonal structure [1]. The conventional method of preparing $BaTiO_3$ particles is via a solid-state reaction from the calcinations of $BaCO_3$ and TiO_2 [2, 3]. The as-prepared powder is typically coarse and highly agglomerated. $BaTiO_3$ nanoparticles have been prepared recently via solid-state reaction from nanocrystalline TiO_2 with $BaCO_3$ of different particle sizes [3]. However, solid-state reaction is time-consuming and energy-intensive. Several

Received December 11, 2012; in final form March 13, 2013.
*Corresponding author. E-mail: naratipcmu@yahoo.com

chemical techniques are available for synthesizing pure $BaTiO_3$ powders with uniform and fine particle size such as the precipitation, hydrothermal, solvothermal, sol-gel and combustion methods [4, 5]. The preparations of $BaTiO_3$ powders are required with a well-crystallized, smaller and more uniform particle size.

In 1927, Wood and Loomis conducted a preliminary survey on the chemical effects of ultrasound. Since then, various chemical effects have been reported and reviewed [6, 7]. Currently, the sonochemical method is used extensively to generate novel materials with unusual properties because it causes much smaller particle formation and higher surface area than that reported by other methods. The chemical effects of ultrasound arise from acoustic cavitations, i.e., the formation, growth, and implosive collapse of bubbles in liquid. The implosive collapse of the bubbles generates a localized hotspot through adiabatic compression or shock wave formation within the gas phase of the collapsing bubble. The conditions formed in these hotspots have been determined experimentally, with transient temperatures of ~5,000 K, pressures of 1,800 atm, and cooling rates in excess of 10^{10} K/s. Until now, only a few studies have reported the sonochemical synthesis of perovskite-type oxides with the general formula, ABO_3 [8].

This research reported the preparations of barium titanate ($BaTiO_3$) nanoparticles via the sonochemical method in a strong alkaline environment, using barium chloride dehydrate ($BaCl_2{\cdot}2H_2O$) as the barium source and titanium (IV) chloride ($TiCl_4$) as the titanium source. The effects of different reaction times on the formation of $BaTiO_3$ nanoparticles were reported as well.

2. Experimental Procedure

$BaTiO_3$ nanoparticles were prepared by sonochemical synthesis. Appropriate proportions of high-purity barium chloride dehydrate ($BaCl_2{\cdot}2H_2O$; 99%) and titanium (IV) chloride ($TiCl_4$; 99%) were used as the Ba and Ti sources. The deionized water used in this experiment was boiled for 15 min at 100°C in order to remove the CO_2 dissolved in it. Then, the dilution procedure involved 0.20 M of concentrated $TiCl_4$ being added slowly to 15 ml of deionized water at a temperature lower than ~5°C, while stirring until it turned into a homogeneous solution. The solution was brought to bubble for 15 min with Ar gas, and $BaCl_2{\cdot}2H_2O$ was added and stirred into the Ti^{4+} solution. After that, 12 M of excess NaOH was added in the chamber. The initial pH value of the suspension was controlled at 14. Ultrasound irradiation was accomplished with a high-intensity ultrasonic probe, immersed directly at 0.5 h in the reaction solution. After completion of the reaction at 0.5 h, the white precipitation was separated centrifugally and washed several times with deionized water. Next, the products were dried at 90°C for 5 h before the white products were obtained.

The product was analyzed by X-ray powder diffraction (Bruker AXD, D8 Advance, Karlsruhe Germany) using Ni-filtered Cu K_α radiation ($\lambda = 0.1546$ nm) to identify the phase formed and optimum condition for the formation of $BaTiO_3$ powders. Room temperature FT-IR spectra were recorded in the range of 4,000–400 cm^{-1} with eight scans on a Perkin-Elmer Spectrum GX spectrometer, and in the resolution of 4 cm^{-1}. A thermo scientific DXR Raman microscope was used to analyze the content of residual inorganic and organic carbon contaminations in the powders. Powder morphology and grain size were imaged directly using a scanning electron microscope (Hitachi S4700, USA) and transmission electron microscope (Philips, Tecnai 20, Holland).

3. Results and Discussion

Figure 1 shows the XRD patterns of the as-synthesized nanoparticles synthesized at different ultrasonic reaction times. Perovskite phase was detected at 0.5 h of ultrasonic reaction time,

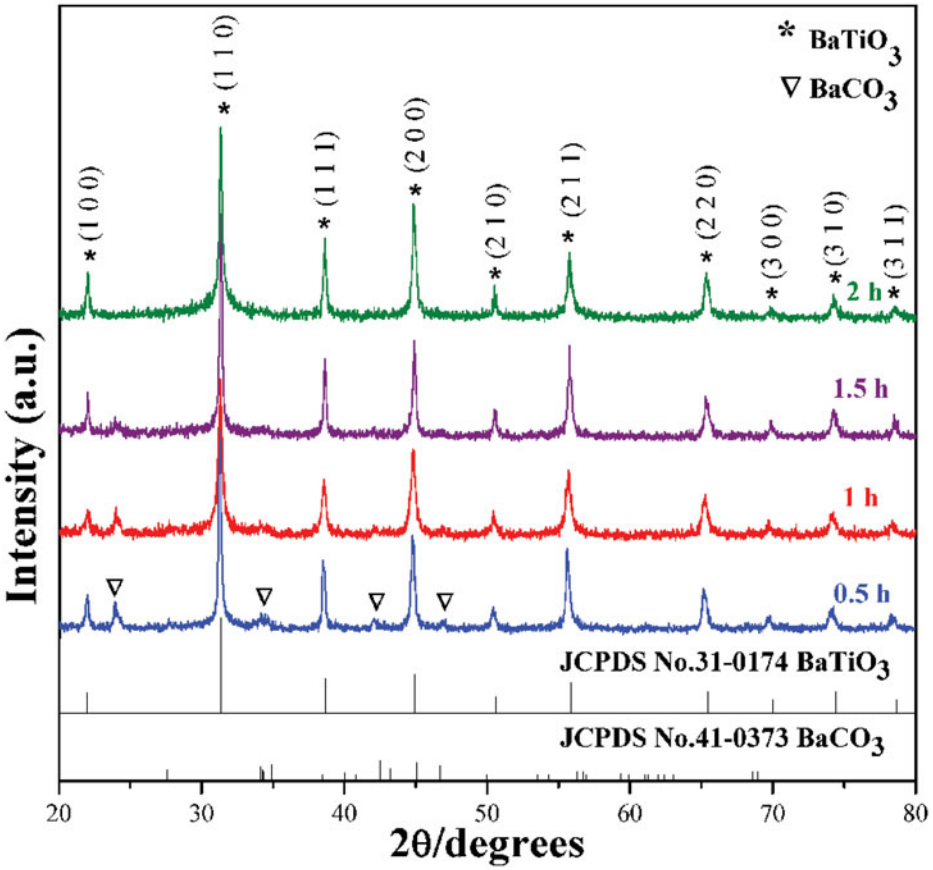

Figure 1. The XRD patterns of the $BaTiO_3$ nanoparticles synthesized at different ultrasonic reaction times. (Color figure available online.)

while the $BaCO_3$ phase also could be found. $BaCO_3$ usually coexists with the perovskite $BaTiO_3$ phase, which should be attributed to the open-air synthesis system. The $BaCO_3$ could be reduced or eliminated by using a closed system. As the reaction time increases, the peaks of $BaCO_3$ disappear. A pure perovskite phase is obtained at 2 h of reaction time. Regarding $BaTiO_3$ crystal with a 4 mm tetragonal symmetry, two peaks are seen from 44° to 46° that correspond with (0 0 2) and (2 0 0) planes. However, at 44.8° only one symmetric peak was observed in all of the samples in this study, which suggested that the particles obtained the cubic $BaTiO_3$ phase. When compared to traditional solid state synthesis, this result indicates that the $BaTiO_3$ phase was formed completely during the sonochemical synthesis without further heating or calcination. The Rietveld method was used to confirm the cubic structure of $BaTiO_3$. Structure refinement of the $BaTiO_3$ nanoparticles was performed by the REX program [9]. Figure 2 shows the refinement result for $BaTiO_3$, and the R- and S-values were $R_p = 19.00$, $R_{wp} = 24.20$, and $S = 1.50$, respectively. Table 1 presents the refinement results of $BaTiO_3$. The results in Table 1 and Fig. 2 show that the Rietveld refinement method indicates good agreement between the XRD patterns observed experimentally and those calculated theoretically. According to the literature [9], quality of the data from structural refinement is checked generally by R-values (R_p, R_{exp}, R_{wp}) as well as the quality of fit ($GoF = R_{wp}/R_{exp}$). Additionally, the difference

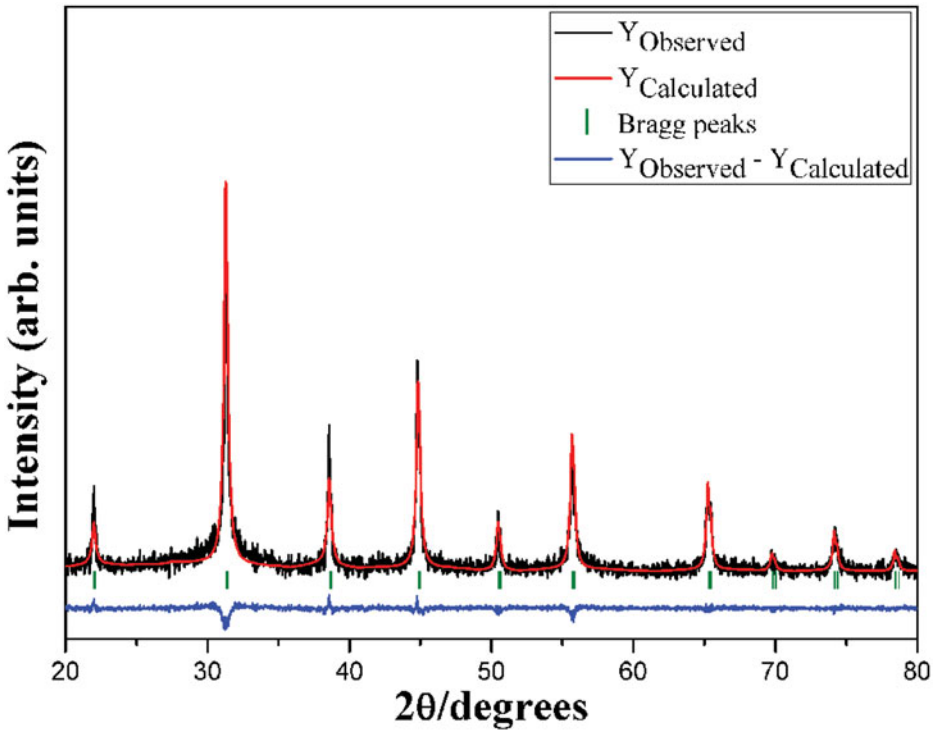

Figure 2. Rietveld refinements of the $BaTiO_3$ nanoparticles synthesized in the reaction time of 2 h. (Color figure available online.)

between experimental profiles of XRD patterns and calculated data is slightly different in the scale of intensity, as illustrated by the line, $Y_{Observed} - Y_{Calculated}$. Furthermore, the crystalline size of 29.13 nm was calculated using the Scherrer equation from the full width at half-maximum of the 110 planes in the XRD pattern.

FT-IR spectra of the as-synthesized samples were performed in order to trace possible organic substances. Figure 3 shows the FT-IR spectra of samples synthesized at different ultrasonic reaction times. The FT-IR spectrum consisted mainly of three regions: the first region shows bands at 3,440 and 1,627 cm^{-1}, which are due to the OH stretching vibration

Table 1
Lattice parameters, unit cell volume, c/a ratio and atomic position of the $BaTiO_3$ nanoparticles

Atoms	Wyckoff	Site	x	y	z	Occupancy
Ba	1a	m-3 m	0	0	0	1
Ti	1b	m-3 m	0.5	0.5	0.5	1
O	3c	4/mm. m	0	0.5	0.5	1

Pm-3 m (221), Cubic ($a = b = c = 4.0413 \pm 0.0004$ Å; $c/a = 1$; $V = 66.0$ Å^3), $\chi^2 = 1.50$

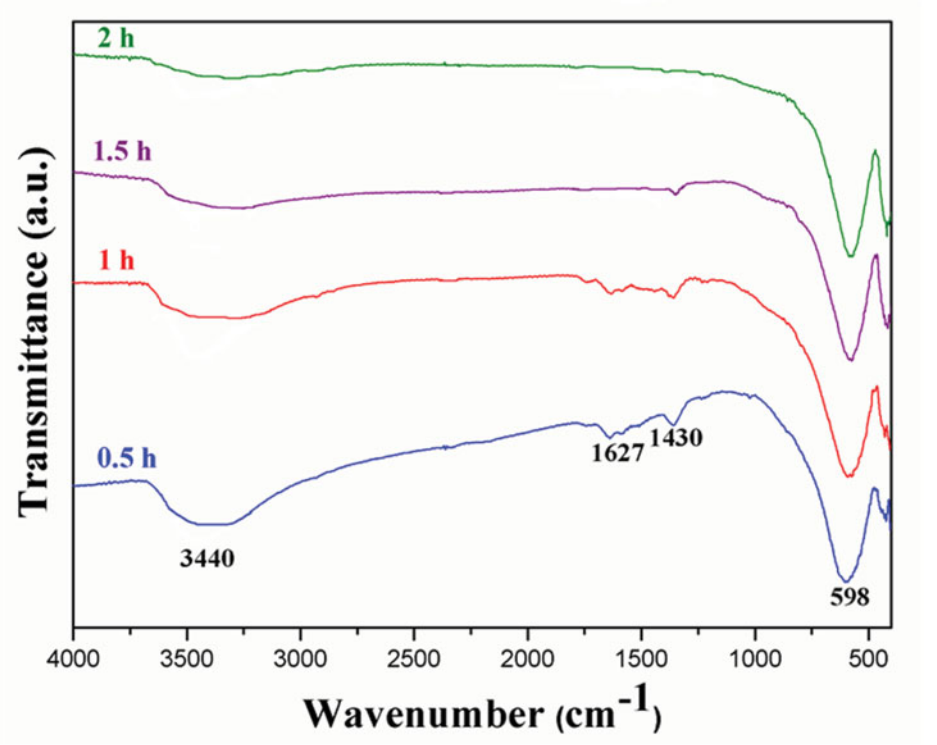

Figure 3. IR spectra of the $BaTiO_3$ nanoparticles synthesized at different ultrasonic reaction times. (Color figure available online.)

(υ) and OH deformation vibration (δ), respectively, arising from the water present in the surface of the barium titanante nanoparticle. The second region corresponds to the absorption bands at 1,430 cm^{-1}, characteristic for the asymmetric stretch vibration of the carbonate groups and Ba^{2+} ions. The third region, 600–380 cm^{-1}, represents the characteristic infrared absorptions of the Ti-O vibrations. The band situated around 598 cm^{-1} is due to TiO_6 stretching vibration connected to the barium [10]. Finally, the peak at 414 cm^{-1} can be attributed to normal TiO_{II} bending vibrations [10, 11]. By increasing the ultrasonic reaction time, the absorption bands of about 598 cm^{-1} became increasingly stronger, indicating that the $BaTiO_3$ phase was created initially at about 0.5 h of reaction. The asymmetric stretch vibration of the carbonate groups decreased significantly and disappears at reaction time of 2 h. This result indicated that, $BaTiO_3$ crystallites grew increasingly by increasing the reaction time, which was also consistent with the XRD determined previously. The peak position of TiO_6 stretching vibration mode shifted to lower wave number with the increase of the reaction time. The frequency shifts in FTIR spectra are related to the change of the bonding characteristics, such as bond angle and bond length and also the structure of the material.

Raman spectroscopy is a highly sensitive spectroscopic technique generally used for probing structure in atomic scale on the basis of vibrational symmetry [12]. Cubic $BaTiO_3$ has no inherent Raman-active modes, which are however, expected for noncentrosymmetric tetragonal structure. Raman spectra of as-synthesized powders, synthesized at different

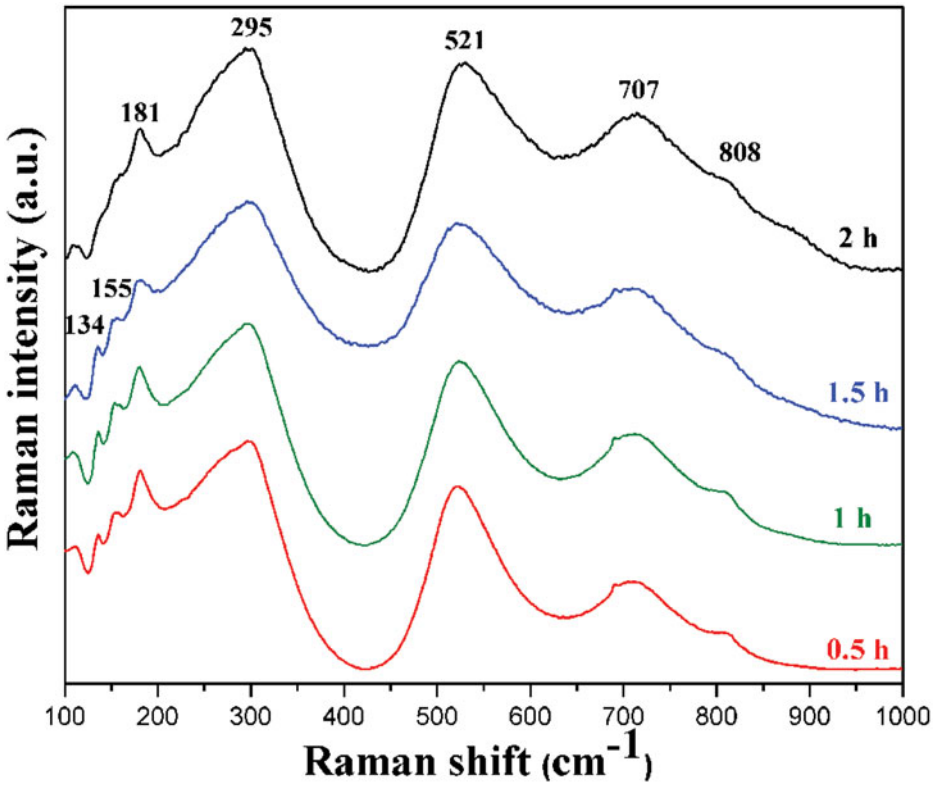

Figure 4. Raman spectra of the $BaTiO_3$ nanoparticles synthesized at different ultrasonic reaction times. (Color figure available online.)

ultrasonic reaction times, are presented in Fig. 4. It is well known that $BaTiO_3$ has five atoms, fifteen degrees of freedom per unit cell, octahedral rotational symmetry in the cubic phase, and fifteen degrees of freedom divided into the optical representations, $3F_{1u} + F_{2u}$, while another F_{1u} symmetry mode corresponds to the acoustical branch. The $BaTiO_3$ spectra revealed the presence of a tetragonal structure, mainly characterized by the A_1(1TO), A_1(2TO), E(2TO), A_1(3TO), and A_1(3LO)/E(LO) Raman modes, while no Raman-active mode is predicted for the cubic phase (*Pm3m*) [12]. When the reaction time at 0.5 h, the Raman shift peaks located at around 181, 295, 521 and 707 cm^{-1} match well with the typical Raman peaks of $BaTiO_3$ [13]. The bands around 295 and 521 cm^{-1} are assigned to the transverse optical (TO) modes of A_1 symmetry, whereas the peak at 181 cm^{-1} arises due to interference from anharmonic coupling between the three A_1(TO) phonons. The peak at 707 cm^{-1} is related to the highest frequency longitudinal optical mode (LO) with A_1 symmetry [14]. In addition, the small peaks at around 134, 155 and 808 cm^{-1} correspond to the symmetric stretching mode of C—O bond from minimal $BaCO_3$ traces. With increasing reaction time, the symmetric C—O stretching vibration becomes weaker and disappears at 2 h of reaction. The decreasing of symmetric C—O stretching vibration band in Raman is corresponded well with FT-IR spectrum. For such compound, the E(2TO) ($\sim$307 cm^{-1}) phonon mode indicates an asymmetry within the TiO_6 octahedra, suggesting the presence of a tetragonal crystalline structure. The E(2TO)($\sim$307cm^{-1}) phonon mode

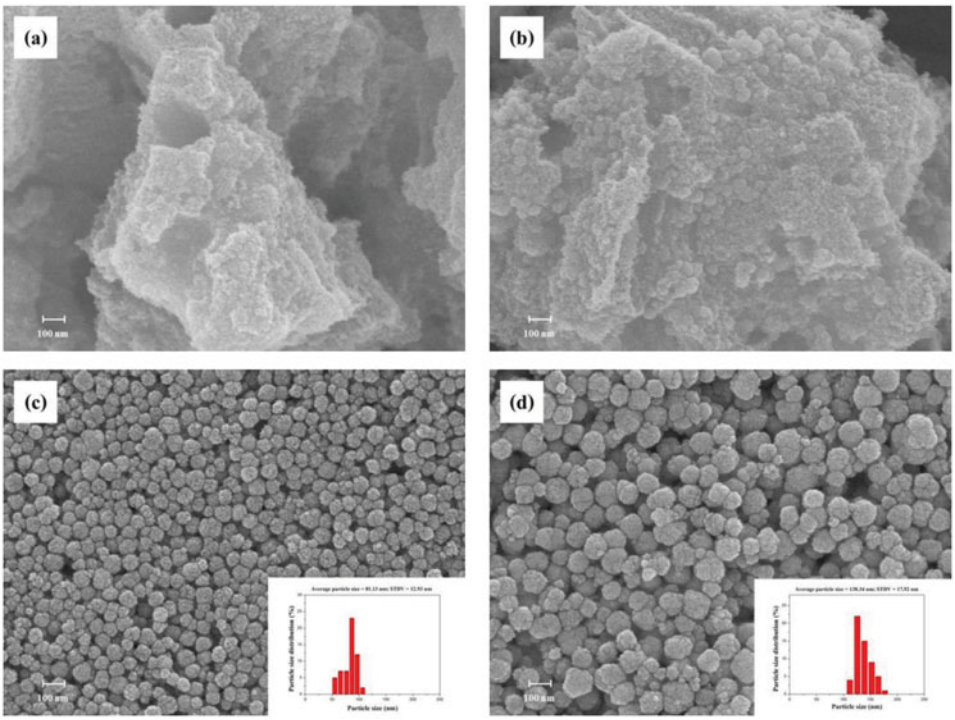

Figure 5. SEM micrographs of the $BaTiO_3$ nanoparticles prepared in the reaction times of (a) 0.5 h, (b) 1 h, (c) 1.5 h and (d) 2 h, respectively. (Color figure available online.)

was not observed at all in any compositions. Thus, these powders present a cubic structure that is in agreement with XRD and Rietveld refinement results.

Figure 5 shows formation of the $BaTiO_3$ aggregated particles sonochemically synthesized in different reaction times. As shown in Fig. 5(a), a large amount of $BaTiO_3$ nanocrystals was created initially from the Ti-based precursor under ultrasonic irradiation before aggregation of $BaTiO_3$ particles from large particles. Sphere-like particles were obtained after 0.5 h, and the particle size increased slightly after 2 h under ultrasonic irradiation. The $BaTiO_3$ particles showed a monosized spherical shape that was different from that in other preparation methods. The products had a spherical or very close to spherical morphology, and the particle size distribution was rather narrow. In addition, the average grain size was increased from 81.13 ± 12.93 nm to 138.34 ± 17.52 nm in diameter by increasing the reaction times from 1.5 h to 2 h, respectively, as seen in Fig. 5(a-d). Figure 6 shows TEM micrographs of the $BaTiO_3$ nanoparticles. The particle size calculated from Scherrer analysis was not consistent with the TEM result. In this research, the average diameter of the sonochemically synthesized particles was about 99.54 ± 18.25 nm. Figure 5 shows that the large $BaTiO_3$ particles were characterized as aggregates of 5–10 nm small nanocrystals. The difference between the XRD crystallite size and TEM primary particle size is thought to associate with the existence of hierarchical structure [15]. The XRD crystallite size may stem from the secondary mesostructure that consisted of the primary smaller particles.

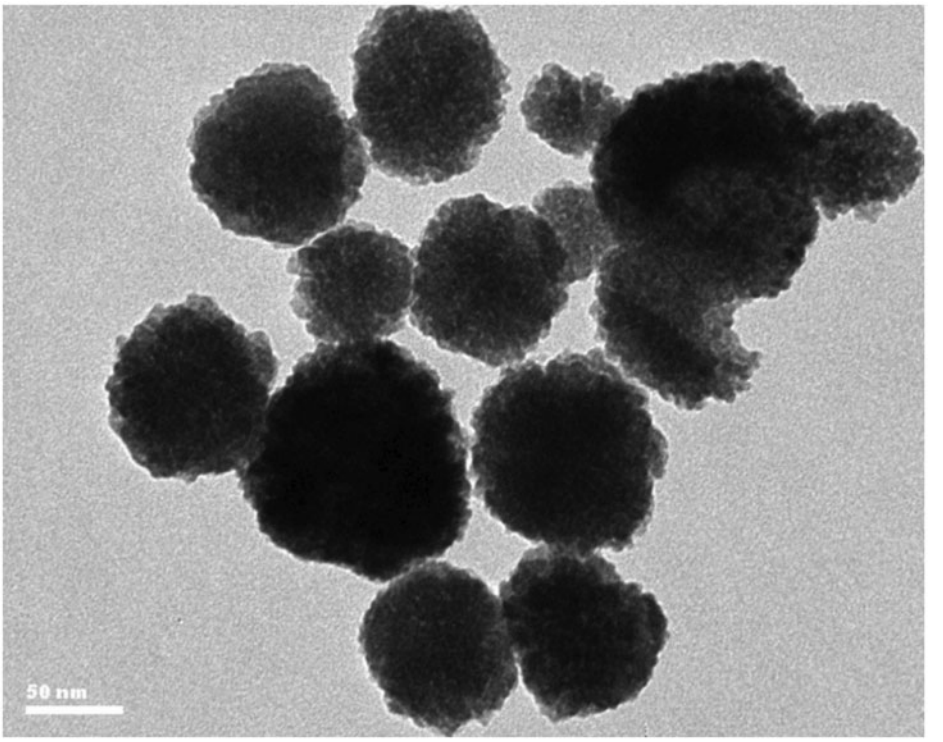

Figure 6. TEM micrographs of the $BaTiO_3$ nanoparticles.

4. Conclusion

In this research, the spherical nanoparticles of barium titanate ($BaTiO_3$) were prepared successfully by the sonochemical method in a strong alkaline environment, using $BaCl_2{\cdot}2H_2O$ and $TiCl_4$ as starting materials. The effects of reaction times on $BaTiO_3$ nanoparticles were investigated. The XRD patterns that revealed the sample at 2 h had good crystalline, and all the main diffraction peaks corresponded to peaks of the cubic $BaTiO_3$ particles. The FT-IR and Raman spectra indicated presence of the bonding vibration of Ti-O stretching within the $BaTiO_3$ structure. The $BaTiO_3$ particles from sonochemical synthesis showed a monosized spherical shape and narrow size distribution. The average diameter of the sonochemically synthesized particles was 99.54 ± 18.25 nm at 2 h of ultrasonic reaction time, as identified by TEM.

Acknowledgments

This research was supported by the KMITL Research Fund (KMITL Fund) and Thailand Research Fund (TRF) (Grant No. BRG5680006).

References

1. D. Hennings, M. Klee, and R. Waser, Advanced dielectrics: bulk ceramics and thin films. *Adv. Mater.* **3**, 334–340 (1991).

2. D. F. K. Hennings, B. S. Schrenemacher, and H. Schrenemacher, Solid-state preparation of $BaTiO_3$-based dielectrics, using ultrafine raw materials. *J. Am. Ceram. Soc.* **84**, 2777–2782 (2001).
3. M. T. Buscaglia, M. Bassoli, and V. Buscaglia, Solid-state synthesis of ultrafine $BaTiO_3$ powders from nanocrystalline $BaCO_3$ and TiO_2. *J. Am. Ceram. Soc.* **88**, 2374–2379 (2005).
4. M. Boulos, S. Guilemet-Fritsch, F. Mathieu, B. Durand, T. Lebey, and V. Bley, Hydrothermal synthesis of nanosized $BaTiO_3$ powders and dielectric properties of corresponding ceramics. *Solid State Ion.* **176**, 1301–1309 (2005).
5. N. Maso, H. Beltran, E. Cordoncillo, A. A. Flores, P. Escribano, and D. C. Sinclair, Synthesis and electrical properties of Nb-doped $BaTiO_3$. *J. Mater. Chem.* **16**, 3114–3119 (2006).
6. R. W. Wood and A. L. Loomis, The physical and biological effects of high frequency sound waves of great intensity. *Philos. Mag.* **4**, 414 (1927).
7. T. J. Mason, *Chemistry with ultrasound*. University of Michigan, New York, 1990.
8. Y. C. Yu, L. Z. Zhang, Q. Li, K. W. Xu, and J. Lin, Sonochemical preparation of nanoporous composites of titanium. *Langmuir.* **19**, 7673–7675 (2003).
9. S. Parida, S. K. Rout, and L. S. Cavalcante, Structural refinement, optical and microwave dielectric properties of $BaZrO_3$. *Ceram Int.* **38**, 2129–2138 (2011).
10. Y. Zhang, L. Wang, and D. Xue, Molten salt route of well dispersive barium titanate nanoparticles. *Powder Technol.* **217**, 629–633 (2012).
11. E. B. Slamovich and I. A. Aksay, Structure evolution in hydrothermally processed ($<100^\circ$C) $BaTiO_3$ films. **79**, 239–247 (1996).
12. Y. Shiratori, C. Pithan, J. Dornseiffer, and R. Waser, Raman scattering studies on nanocrystalline $BaTiO_3$ Part I – isolated particles and aggregates. *J. Raman. Spectrosc.* **38**, 1288–1299 (2007).
13. M. B. Smith, K. Page, T. Siegrist, P. L. Redmond, E. C. Walter, R. Seshadri, L. E. Brus, and M. L. Steigerwald, Crystal structure and the paraelectric-to-ferroelectric phase transition of nanoscale $BaTiO_3$. *J. Am. Chem. Soc.* **130**, 6955–6963 (2008).
14. Z. Deng, Y. Dai, W. Chen, X. Pei, and J. Liao, Synthesis and characterization of bowl-like single-crystalline $BaTiO_3$ nanoparticles. *Nanoscale Res. Lett.* **5**, 1217–1221 (2010).
15. A. Clauset, C. Moore, and M. E. J. Newman, Hierarchical structure and the prediction of missing links in networks. *Nature.* **453**, 98–101 (2008).

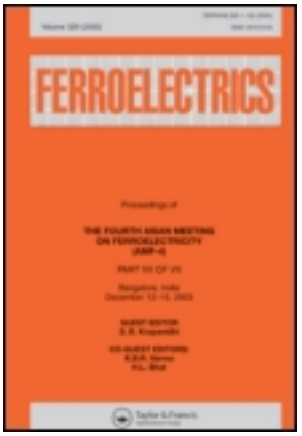

Ferroelectrics
Publication details, including instructions for authors and subscription information:
http://www.tandfonline.com/loi/gfer20

Synthesis of Monodispersed Perovskite Barium Zirconate ($BaZrO_3$) by the Sonochemical Method

Piyanut Charoonsuk [a], Rattanai Baitahe [a], Wanwilai Vittayakorn [a b], Narin Atiwongsangthong [c], Rangson Muanghua [c], Panpailin Seeharaj [d] & Naratip Vittayakorn [a b d]

[a] College of Nanotechnology, King Mongkut's Institute of Technology Ladkrabang, Bangkok, 10520, Thailand

[b] ThEp Center, CHE, 328 Si Ayutthaya Road, Bangkok, 10400, Thailand

[c] Department of Electronics, Faculty of Engineering, King Mongkut's Institute of Technology Ladkrabang, Bangkok, 10520, Thailand

[d] Advanced Materials Research Unit, Department of Chemistry, Faculty of Science, King Mongkut's Institute of Technology Ladkrabang, Bangkok, 10520, Thailand

Published online: 09 Dec 2013.

To cite this article: Piyanut Charoonsuk, Rattanai Baitahe, Wanwilai Vittayakorn, Narin Atiwongsangthong, Rangson Muanghua, Panpailin Seeharaj & Naratip Vittayakorn (2013) Synthesis of Monodispersed Perovskite Barium Zirconate ($BaZrO_3$) by the Sonochemical Method, Ferroelectrics, 453:1, 54-61, DOI: 10.1080/00150193.2013.842105

To link to this article: http://dx.doi.org/10.1080/00150193.2013.842105

Ferroelectrics, 453:54–61, 2013

ISSN: 0015-0193 print / 1563-5112 online
DOI: 10.1080/00150193.2013.842105

Taylor & Francis
Taylor & Francis Group

Synthesis of Monodispersed Perovskite Barium Zirconate ($BaZrO_3$) by the Sonochemical Method

PIYANUT CHAROONSUK,[1] RATTANAI BAITAHE,[1] WANWILAI VITTAYAKORN,[1,2] NARIN ATIWONGSANGTHONG,[3] RANGSON MUANGHUA,[3] PANPAILIN SEEHARAJ,[4] AND NARATIP VITTAYAKORN[1,2,4,*]

[1]College of Nanotechnology, King Mongkut's Institute of Technology Ladkrabang, Bangkok 10520, Thailand
[2]ThEp Center, CHE, 328 Si Ayutthaya Road, Bangkok 10400, Thailand
[3]Department of Electronics, Faculty of Engineering, King Mongkut's Institute of Technology Ladkrabang, Bangkok 10520, Thailand
[4]Advanced Materials Research Unit, Department of Chemistry, Faculty of Science, King Mongkut's Institute of Technology Ladkrabang, Bangkok 10520, Thailand

Barium zirconate ($BaZrO_3$) was synthesized successfully by the sonochemical method. The monophase of $BaZrO_3$ was formed completely in short irradiation time without the calcination process. X-ray diffraction, Fourier transform and Raman spectroscopy were used to characterize formation of the perovskite $BaZrO_3$ phase, which occurs in a 60 minute single phase with a cubic crystal structure at room temperature. Therefore, sonochemical irradiation could accelerate the formation of $BaZrO_3$ particles significantly. Furthermore, scanning electron microscopy investigated the uniform shape and size. The size distribution became narrow with increasing time, as a function of irradiation.

Keywords Barium zirconate; sonochemical method

1. Introduction

Barium zirconate ($BaZrO_3$; BZ) is one of the most studied perovskite materials, presenting a wide range of technological applications [1]. At room temperature, $BaZrO_3$ has a cubic crystal structure that does not undergo phase transitions in the range of 4–1,600 K, and it has a high dielectric constant of about 30 [2]. It is a well known refractory material with very high melting point (2,600°C), small thermal expansion coefficient, poor thermal conductivity, and excellent mechanical properties towards corrosive compound [1]. Therefore, it is a good candidate for many structural applications. $BaZrO_3$ is used in the functional utility as an inert crucible material and substrate for thin film deposition, and it demonstrates its sensor applications at high temperature in H_2 containing atmosphere [1]. The quality of powders used for producing electronic devices is a key for obtaining optimal properties. Thus,

Received December 11, 2012; in final form March 5, 2013.
*Corresponding author. E-mail: naratipcmu@yahoo.com

highly disagglomerated, submicro-size powders are interesting because of their physical properties depending on grain size. Conventionally, barium zirconate has been synthesized through solid-state reaction of barium carbonate and zirconium oxide. The solid state reaction was performed at temperatures of up to 1,300°C [3]. The powder prepared by this method has several drawbacks such as lack of reproducibility, large particle size, wide size distribution, and chemical inhomogeneity. Therefore, a number of chemical techniques have been developed. The chemical routes provide atomic level mixing of elements, thus reducing the diffusion path to nanometric scale for obtaining the desired material, and needing lower synthesis temperature than that by solid state reaction. Regarding the existing solid-state method, "soft-chemistry" techniques are increasingly important in barium zirconate synthesis such as precipitation [4], oxalate route [5] and sol-gel method [6]. However, these techniques still need the calcination process and only a few of them can control particles size, shape and size distribution. Recently, the sonochemical synthesis became an effective method for improving the properties of synthesized particles. According to Gedanken, nanomaterials were obtained in almost all sonochemical reactions leading to inorganic products. It has been proved that the ultrasound-assisted technique possesses such controllability on phase formation, stoichiometry, morphology, particle size and size distribution, and ultrasound-assisted synthesis is a potential method for synthesizing high performance ceramic particles in a short period of time [7]. In 2006, Xu et al. successfully synthesized $BaTiO_3$ particles by using the sonochemical method [8]. Grainne et al. reported that ultrasonic irradiation caused self-assembling of sonochemically synthesized $BaTiO_3$ particles [9]. Otherwise, sonochemical synthesis of $BaZrO_3$ has not been report until now.

This study reported the first synthesis of monodispersed perovskite barium zirconate ($BaZrO_3$) by the sonochemical method. $BaZrO_3$ was formed completely without the calcinations process. The single phase of $BaZrO_3$ occurred in a short period of time. The monodisperse shape and size of $BaZrO_3$ particles could be obtained under ultrasonic irradiation.

2. Experimental Procedure

All reagents were pure analytically and used without further purification. The sonochemical process was carried out in sonication glassware (total capacity, 15 ml). Stoichiometric amounts of $BaCl_2 \cdot 2H_2O$ and $ZrOCl_2 \cdot 8H_2O$ were dissolved typically in DI-water. The total concentration of cations in the mixed solution was kept at 1 mol/dm^3 with a molar ratio of Ba/Zr equal to 1.00. The mixed solution was added drop by drop to the sonication glassware, which contained 20 mol/dm^3 of NaOH solution. Then, the suspension was exposed to high-intensity ultrasound irradiation under argon gas flow for a given time. The ultrasound irradiation was carried out by employing a direct immersion of ultrasonic probe (3 mm diameter; Ti-horn, 20 kHz). The white precipitate was separated by centrifugation at 3,000 rpm, washed with DI-water and dried at 80°C overnight. The precipitates were characterized by the X-ray diffraction (XRD) technique with a Bruker D8 Advance diffractrometer (monochromatized Cu$K\alpha$ radiation) for crystallographic identification. Fourier transforms infrared (FT-IR) spectroscopy with a Perkin-Elmer, Spectrum GX FT-IR spectrometer was used to identify the IR active functional groups using the KBr pellet technique. Phase identification was supported further by Raman spectroscopy. Visible laser light was used for Raman measurements (DXR Raman microscope, Thermo Scientific). The particle sizes and morphology of the powders were studied by scanning electron microscope (SEM, Hitachi 54700).

3. Results and Discussion

XRD patterns of the as-prepared $BaZrO_3$ powders, with different times of ultrasound irradiation are presented in Fig. 1, in which the main peaks (indexed by a star) of powders for all conditions correspond to the perovskite $BaZrO_3$ phase with a cubic crystal structure. The main (110) diffraction plane relates to the periodic arrangement of the dodecahedral (BaO_{12}) and octahedral (ZrO_6) sites [2]. Peak position of the $BaZrO_3$ phase agrees well with standard data (JCPDS: 06-0399) that has a P*m3m* space group. The weak peak (indexed by a circle) is assigned to the orthorhombic $BaCO_3$ phase (JCPDS: 05-0378) with a P*mcn* space group, as seen in the powders at 5, 10 and 15 min. The $BaCO_3$ could be formed, due to dissolution of CO_2 from the air in solution. The XRD result indicated that low crystalline $BaZrO_3$ was formed for the first time at 5 min together with the reflections of $BaCO_3$, thus the crystallization process remained incomplete in this condition. By increasing the irradiation time, intensity of $BaZrO_3$ diffraction peaks increased, while that of the diffraction peaks of $BaCO_3$ gradually decreased. The mol% of $BaCO_3$ (calculated from the ReX program [10]) was founded to be 18.99, 11.17, 6.96 and 2.04% for 5, 10, 15 and 30 min of irradiation, respectively. Finally, the crystalline $BaZrO_3$ phase was observed clearly at 60 min of irradiation, and the $BaCO_3$ mol% was about 0.00%. It is interesting to note that the $BaZrO_3$ phase was formed completely during the sonochemical synthesis, without further heating or the calcination process. Structural refinement by the Rietveld method [10] was performed to confirm the $BaZrO_3$ structure, and the refinement results for $BaZrO_3$ at 60 min of irradiation are shown in Table 1. The results confirmed that $BaZrO_3$ powder has a cubic structure with a space group (P*m3m*), as established from the pattern matching analysis. The atomic coordinate positions were the same as those found from results in the literature [10]. Furthermore, the refined lattice parameter ($a = b = c =$ 4.2016(2) Å) was calculated and identified by the ReX program, which is close to (within

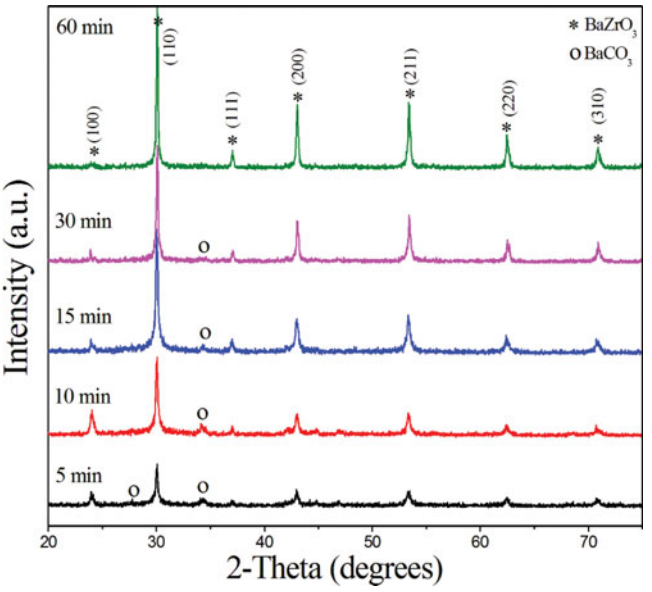

Figure 1. XRD pattern of $BaZrO_3$ powders at various irradiation times from 5 to 60 min. (Color figure available online.)

Table 1
Rietveld refinement results of the X-ray diffraction data of $BaZrO_3$ powders synthesized at 60 min of irradiation

Atom	Wyckoff	*x*	*y*	*z*	Occupancy
Ba1	1a	0.000000	0.000000	0.000000	1.000000
Zr1	1b	0.500000	0.500000	0.500000	1.000000
O1	3c	0.000000	0.500000	0.500000	1.000000

P*m*3*m* (2 2 1) – cubic ($a = b = c = 4.2016(2)$ Å; Vol = 74.174 Å^3)
$R_{exp} = 33.033$; $R_p = 18.093$; $R_{wp} = 25.088$; $R_{bragg} = 3.856$ and $x^2 = 1.68$

0.02) the lattice parameter from JCPDS No. 06–0399 ($a = b = c = 4.18$ Å). The refinement was continuous until convergence reached the value of the quality factor, x^2 approaching 1, which confirmed the quality of the refinement. The R-values were $R_{exp} = 33.033$, $R_p = 18.093$, $R_{wp} = 25.088$ and $R_{bragg} = 3.856$. In addition, the representative of a typical Rietveld refinement analysis output for the quality of fitting is shown in Fig. 2. This figure illustrates the $BaZrO_3$ phase from experimental XRD data, indicating good agreement with theoretical data.

FT-IR spectroscopy gave further support to the presence of significant amounts of $BaZrO_3$ phase in powders, as shown in Fig. 3. All conditions have shown that a very broad band at around 3,400 cm^{-1} and peak at 1,640 cm^{-1} correspond to O—H stretching and O—H bending, respectively, which is typical of hydroxyl species [11]. The presence of O-H groups could be due to adsorbed moisture or the process occurring in a strong alkaline base (pH value ~14). The band at around 1,450 cm^{-1} corresponded to the presence of CO_3^{2-} species by comparison with pure $BaCO_3$ [11]. When increasing irradiation time, intensity of the characteristic carbonate peak decreased until disappearing in the powders at 60 min. Finally, the peak at around 545 cm^{-1} can be attributed to the stretching vibration of

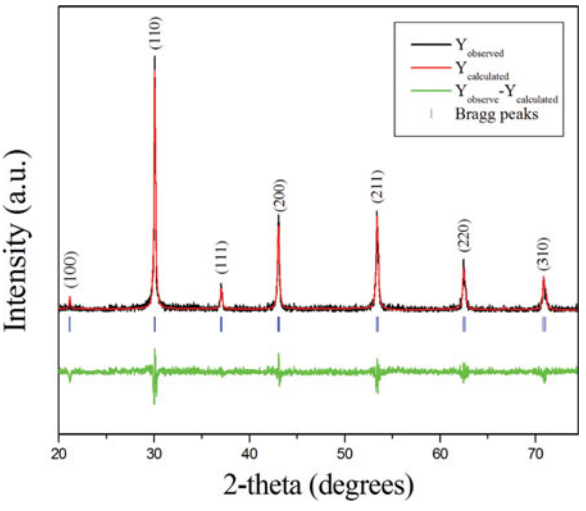

Figure 2. Rietveld refinement fits of $BaZrO_3$ powders synthesized at 60 min of irradiation. (Color figure available online.)

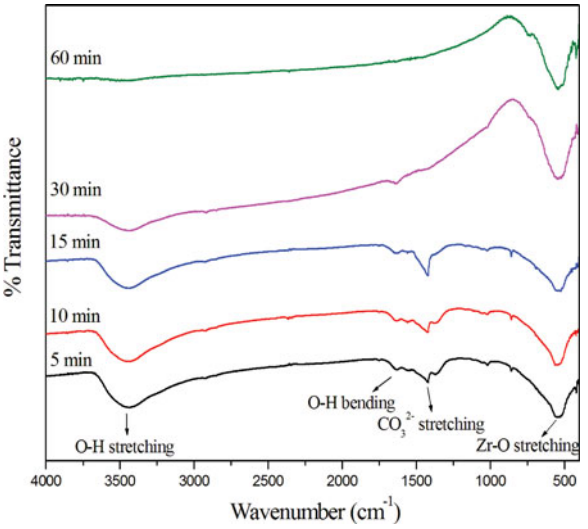

Figure 3. FT-IR spectra of $BaZrO_3$ powders at various irradiation times from 5 to 60 min. (Color figure available online.)

Zr-O octahedra in the perovskite structure [11], which is seen to sharpen and intensify after synthesis at 60 min of irradiation. These FT-IR results suggest that the perovskite $BaZrO_3$, without any other phase, can be obtained in powders at 60 min of irradiation, which agrees well with the result from XRD measurement.

The Raman scattering technique was used as a secondary tool to support the formation of $BaZrO_3$. For the first-order, cubic $BaZrO_3$ possesses 4 Raman active modes that are split into 2 longitudinal (LO) and 2 transverse (TO) modes, as well as 2 Raman active modes in a secondary order structure [2]. However, the Raman spectra of $BaZrO_3$ have showed weak bands because of the perovskite structure, in which all atoms occupy sites with inversion symmetry. Figure 4 shows the Raman spectra of the $BaZrO_3$ powders ranging from 100–1,000 cm^{-1}. Powders at 5, 10 and 15 min of irradiation showed typical Raman active modes of $BaCO_3$ at around 130, 150 and 690 cm^{-1} [12] respectively, without the Raman active mode of $BaZrO_3$. The Raman active mode of the $BaZrO_3$ phase was not observed because the vibration mode superposition of the $BaCO_3$. In addition, $BaCO_3$ phase is more sensitive than that of $BaZrO_3$ in Raman spectroscopy [2, 12]. At 30 min of irradiation, Raman active $BaZrO_3$ began to be seen in powders at around 218 and 404 cm^{-1}, which corresponded to the secondary order structure of $BaZrO_3$. Also, the peak at around 484 cm^{-1} corresponded to the $A_1(LO_2)$ Raman active mode of the $BaZrO_3$ first order. When the irradiation time was increased to 60 min, the orthorhombic $BaCO_3$ reacted completely to the cubic $BaZrO_3$ phase. New peaks were observed at around 105, 186 and 515 cm^{-1}, which can be attributed to the vibration of $A_1(TO_1)$, $A_1(TO_2)$, and $A_1(TO_4)$ modes, respectively. These vibrational groups are typical modes of $BaZrO_3$ with a cubic structure [2, 12]. The Raman result can indicate that the cubic barium zirconate phase was the main one, which became more favorable than the barium and zirconium individual phases after 60 min of synthesis. It is interesting to note that XRD, FT-IR and Raman spectroscopy are used to carry out analysis of the crystal evolution together with the synthesis process. The result could conclude that the low crystalline $BaZrO_3$ phase has initial formation at 5 min of irradiation. Then, the $BaZrO_3$ phase can be put into action after 60 min of processing, as a suitable crystalline cubic phase with a well defined spherical shape, as seen in Fig. 5.

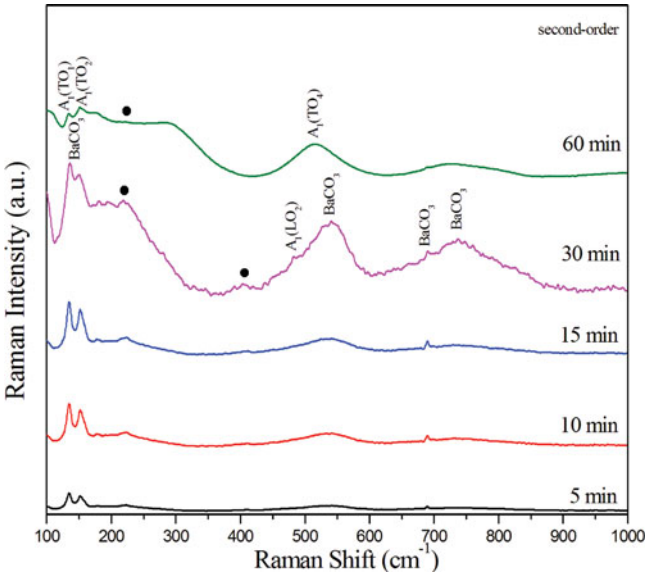

Figure 4. Raman spectra of $BaZrO_3$ powders at various irradiation times from 5 to 60 min. (Color figure available online.)

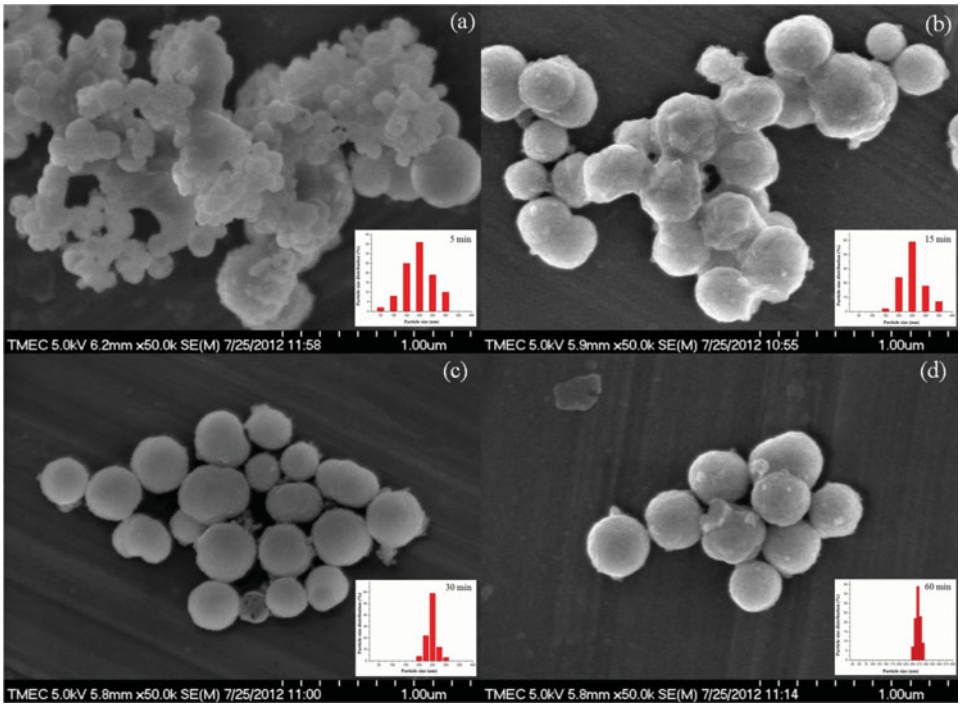

Figure 5. SEM micrograph of $BaZrO_3$ powders at 5, 15, 30 and 60 min of irradiation. (Color figure available online.)

Table 2
Comparison of different preparation methods for calculating calcination temperature, reaction time and average particle size

Method	Calcination temperature (°C)	Time	Particle size
Precipitation method [8]	1200	4 h	1.0–2.0 μm
Oxalate method [9]	900	6 h	3.0–7.0 μm
Sol-gel method [10]	1000	3 h	0.5–2.5 μm
Polymerization [11]	1100	4 h	1.0–3.0 μm
Sonochemical (this study)	Non-calcined	1h	276.3 $\pm$ 16 nm

Morphology of $BaZrO_3$ powders that were synthesized with different reaction times by the sonochemical method is shown in Fig. 5. A distorted spherical shape of $BaZrO_3$ was formed initially in 5 min of irradiation, with an average particle size of about 157.2 $\pm$ 95 nm. Then, the $BaZrO_3$ particle caused aggregation in a short period of time under ultrasonic irradiation. The mono spherical shape of the $BaZrO_3$ particles began after 15 min of irradiation, and the average particle size increased with increasing irradiation time up until 60 min, when it was found to be 276.3 $\pm$ 16 nm. Although the average particles size increased with increasing time, the size distribution narrowed. According to the mechanism, this report could propose the four step mechanisms of ultrasound on the formation of $BaZrO_3$ particles. The first step involves ultrasonic irradiation that accelerates the formation of $BaZrO_3$ particles in liquid by chemical reaction, which is used for a short period of time (about 60 min). The second step is nucleation of $BaZrO_3$ crystals, and the third crystal growth. The last step involves aggregation of the $BaZrO_3$ particles caused by ultrasonic irradiation, and the narrow size distribution obtained [13]. The same reaction was performed with precipitation [4], without sono-assisted synthesis. $BaZrO_3$ particles from precipitation were produced at the same temperature (80°C), but the particle size of about 1–2 μm [4] was much larger than that 276.3 $\pm$ 16 nm of the sonochemical synthesis. Table 2 shows comparison with other methods, which are still needed for the calcination process, but not required in this method. Reaction time of the synthesis was clearly shorter. Furthermore, the average particle size was smaller than that in other methods.

4. Conclusion

In this study, $BaZrO_3$ powders were synthesized successfully by the sonochemical method in a short period of time, without the calcination process. XRD showed that the single phase of $BaZrO_3$ can be obtained at 60 min of irradiation, with a cubic crystal structure. The monodispersed shape and size of $BaZrO_3$ could be obtained. The average particle size increased with increasing time, and was found to be about 276.3 $\pm$ 16 nm, while the size distribution became narrower when the irradiation time increased. However, the particle size of $BaZrO_3$ from the sonochemical method was smaller than that in other techniques. The main advantages of this process are its short time synthesis, and ability to obtain well-disperse $BaZrO_3$ particles under ultrasonic irradiation. $BaZrO_3$ powders were obtained in a single-step process by directly subjecting a precursor complex of the respective metal ions, with no need for a calcination process.

Acknowledgments

This research was supported by KMITL Research Fund (KMITL Fund) and The Thailand Research Fund (TRF).

References

1. A. M. Azad, S. Subramaniam, and T. W. Dung, On the development of high density barium metazirconate ($BaZrO_3$) ceramics. *J Alloys Compd*. **334**, 118–130 (2002).
2. L. R. Macario, M. L. Moreira, J. Andres, *et al*., An efficient microwave-assisted hydrothermal synthesis of $BaZrO_3$ microcrystals: growth mechanism and photoluminescence emissions. *Cryst Eng Comm*. **12**, 3612–3619 (2010).
3. S. Tao and J. T. S. Irvine, Conductivity studies of dense yttrium-doped $BaZrO_3$ sintered at 1325°C. *J Solid State Chem*. **180**, 3493–3499 (2007).
4. F. Boschini, B. Robertz, A. Rulmont, *et al*., Preparation of nanosized barium zirconate powder by thermal decomposition of urea in an aqueous solution containing barium and zirconium, and by calcination of the precipitate. *J Eur Ceram Soc*. **23**, 3035–3042 (2003).
5. B. Robertz, F. Boschini, R. Cloots, *et al*., Importance of soft solution processing for advanced $BaZrO_3$ materials. *Int J Inorg Mater.* **3**, 1185–1187 (2001).
6. S. Agusti, B. E. Montaser, and O. Philippe, Synthesis and sintering of large batches of barium zirconate nanopowders. *J Am Ceram Soc*. **85**, 1928–1932 (2002).
7. A. Gedanken, Using sonochemistry for the fabrication of nanomaterials. *Ultrason Sonochem*. **11**, 47–55 (2004).
8. M. Xu, Y. Lu, Y. Liu, *et al*., Sonochemical synthesis of monosized spherical $BaTiO_3$ particles. *Powder Technol*. **161**, 185–189 (2003).
9. F. Dang, K. Kato, H. Lmai, *et al*., Growth of $BaTiO_3$ nanoparticles in ethanol-water mixture solvent under ultrasound assisted synthesis. *Chem Eng*. **170**, 333–337 (2011).
10. S. Parida, S. K. Rout, L. S. Cavalante, *et al*., Structural refinement, optical and microwave dielectric properties of $BaZrO_3$. *Ceram Int*. **38**, 2129–2138 (2012).
11. H. P. Kumar, C. Vijayakumar, C. N. George, *et al*., Characterization and sintering of $BaZrO_3$ nanoparticles synthesized through a sing-step combustion process. *J Alloy Compd*. **458**, 528–531 (2008).
12. P. S. Dobal, A. Dixit, R. S. Katiyar, *et al*., Micro-Raman scattering and dielectric investigation of phase transition behavior in the $BaTiO_3$-$BaZrO_3$ system. *J Appl Phys*. **89**, 8085–8091 (2001).
13. K. Yasui, T. Tuziuti, and K. Kato, Numerical simulations of sonochemical production of $BaTiO_3$ nanoparticles. *Ultrason Sonochem*. **18**, 1211–1217 (2009).

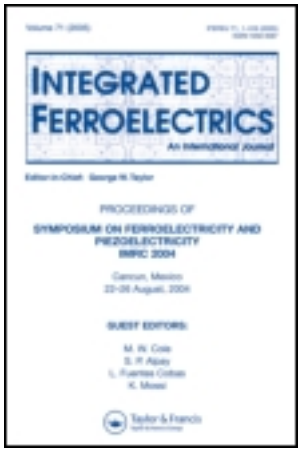

Integrated Ferroelectrics: An International Journal
Publication details, including instructions for authors and subscription information:
http://www.tandfonline.com/loi/ginf20

Rapid Synthesis of Potassium Sodium Niobate ($K_{1/2}Na_{1/2}NbO_3$) Lead-free Piezoelectric Powder Using the Combustion Method

Nopsiri Chaiyo [a] , Rangson Muanghlua [b] , Yothin Wongprasert [b] , Panpailin Seeharaj [c] & Naratip Vittayakorn [a c]

[a] Electroceramic Research Laboratory, College of Nanotechnology , King Mongkut's Institute of Technology Ladkrabang , Bangkok , 10520 , Thailand

[b] Department of Electronics Engineering, Faculty of Engineering , King Mongkut's Institute of Technology Ladkrabang , Bangkok , 10520 , Thailand

[c] Advanced Materials Research Unit Department of Chemistry, Faculty of Science , King Mongkut's Institute of Technology Ladkrabang , Bangkok , 10520 , Thailand

Published online: 07 Dec 2013.

To cite this article: Nopsiri Chaiyo , Rangson Muanghlua , Yothin Wongprasert , Panpailin Seeharaj & Naratip Vittayakorn (2013) Rapid Synthesis of Potassium Sodium Niobate ($K_{1/2}Na_{1/2}NbO_3$) Lead-free Piezoelectric Powder Using the Combustion Method, Integrated Ferroelectrics: An International Journal, 149:1, 128-134, DOI: 10.1080/10584587.2013.853591

To link to this article: http://dx.doi.org/10.1080/10584587.2013.853591

Integrated Ferroelectrics, 149:128–134, 2013

ISSN: 1058-4587 print / 1607-8489 online
DOI: 10.1080/10584587.2013.853591

Taylor & Francis
Taylor & Francis Group

Rapid Synthesis of Potassium Sodium Niobate ($K_{1/2}Na_{1/2}NbO_3$) Lead-free Piezoelectric Powder Using the Combustion Method

NOPSIRI CHAIYO,[1] RANGSON MUANGHLUA,[2] YOTHIN WONGPRASERT,[2] PANPAILIN SEEHARAJ,[3] AND NARATIP VITTAYAKORN[1,3,*]

[1]Electroceramic Research Laboratory, College of Nanotechnology, King Mongkut's Institute of Technology Ladkrabang, Bangkok 10520, Thailand
[2]Department of Electronics Engineering, Faculty of Engineering, King Mongkut's Institute of Technology Ladkrabang, Bangkok 10520, Thailand
[3]Advanced Materials Research Unit Department of Chemistry, Faculty of Science, King Mongkut's Institute of Technology Ladkrabang, Bangkok 10520, Thailand

Potassium sodium niobate ($K_{1/2}Na_{1/2}NbO_3$) powder was synthesized successfully by the combustion synthesis. The raw materials of KNO_3, $NaNO_3$ and Nb_2O_5 were used with glycine as fuel. The thermal behaviour of the precursor was determined using thermo gravimetric analysis (TGA) and derivative thermo gravimetric (DTG) analysis. The conditions for preparing perovskite phase formation, influence of the fuel-to-oxidizer molar ratio, and crystal structure were characterized by the X-ray diffraction technique (XRD) and Fourier transform infrared (FTIR) spectroscopy. The morphology and particle size were investigated through a scanning electron microscope (SEM).

Keywords Lead-free piezoelectric; potassium sodium niobate; combustion synthesis

1. Introduction

Potassium sodium niobate [(K,Na)NbO_3; KNN] is one of the best-known perovskite alkali niobate families [1]. It has been studied since the 1950s and showed promise, due to its outstanding piezoelectric and ferroelectric properties [2]. Moreover, severe restrictions were put in force by recent directives on the use of hazardous substances in electronic equipment, from which lead and other heavy metals should have been banned or phased out [3]. Therefore, development of low-lead-content and/or lead-free piezoelectric materials has been more attractive for replacing lead-based materials in commercial applications [4]. According to superior properties, KNN was proposed as alternative piezoelectric materials [5]. KNN powders have been prepared by a conventional solid-state reaction method using oxide or carbonate compound as raw materials [6]. The use of this method was found to be difficult in obtaining fine particles with stoichiometric chemical composition, which can cause problems from the moisture-sensitive nature of starting materials [7]. Furthermore,

Received December 9, 2012; in final form August 25, 2013.
*Corresponding author. E-mail: naratipcmu@yahoo.com

high calcination temperature and long heating time can lead to the evaporation of volatile compound and agglomerate particles. Thus, the manufacture of dense, homogeneous single-phase ceramics is not always released.

Combustion synthesis (CS) or self-propagating high temperature synthesis (SHS) has been reported as an effective, low-cost method for producing various industrially useful materials. It commenced as a quick, straightforward preparation process for producing homogeneous, very fine, crystalline and unagglomerated multicomponent oxide ceramic powders, without intermediate decomposition and/or calcination steps [8]. This synthesis technique uses a mixture of easily oxidized reactants (such as nitrates) and a suitable organic fuel on the basis of redox reaction. Then, a highly exothermic reaction occurs, which produces a long duration of temperature that is high enough for the synthesis to take place, even without an external heating source [9]. A large amount of gas released from the system results in ultrafine nano-sized powder with dry, fluffy, crystalline, unagglomerated features. Metal nitrate was found to be the salt preferred, due to its water solubility, and homogeneous solution could be achieved easily by melting at a low temperature [10]. Recently, this method has been applied also to synthesize lead-free alkali niobate sodium niobate ($NaNbO_3$) powders using sodium nitrate ($NaNO_3$) and Nb_2O_5. Monophasic nanocrystalline $NaNO_3$ powder was obtained after calcinations at a relatively low temperature of 400°C [11]. In this study, the combustion synthesis was used to synthesize potassium sodium niobate ($K_{1/2}Na_{1/2}NbO_3$) powder using glycine as fuel. Effects of various fuel-to-oxidizer molar ratios on the phase evolution and particle morphology were studied.

2. Experimental Procedure

Potassium sodium niobate ($K_{1/2}Na_{1/2}NbO_3$) powder was synthesized via the combustion synthesis. AR grade potassium nitrate (KNO_3 99.5%), sodium nitrate ($NaNO_3$ 99.5%) and niobium pentoxide (Nb_2O_5 99.95%) were used as the oxidizer and starting material. Glycine (NH_2CH_2COOH 99.7%) was a selected fuel. First, the appropriate amount of KNO_3, $NaNbO_3$ and Nb_2O_5 was weighed, mixed with de-ionized water in a glass beaker and stirred regularly for 30 min. The fuel (glycine) was then added and the mixture stirred for 30 min. After stirring, the precursor solution was heated using a hotplate before being boiled and evaporated. Once the solution had thickened and begun to dry, ignition took place when the temperature rapidly increased, which resulted in self-sustaining combustion. Rapid evolution of gas products in a large volume and formation of voluminous powder occurred, and potassium sodium niobate ($K_{1/2}Na_{1/2}NbO_3$) powder was obtained.

For investigation on thermal behaviour of the precursor, the mixture of starting material was determined using thermo gravimetric analysis (TGA) and derivative thermo gravimetric (DTG) analysis. The X-ray diffraction (XRD, Advance D8) technique was carried out on the combustion synthesized powder, using Ni-filtered Cu$K\alpha$ radiation for phase identification and mean crystalline size estimation. The final powder product was characterized by using the Fourier transform infrared (FT-IR) technique and scanning electron microscope (SEM, Hitachi S4700).

3. Results and Discussion

Figure 1 shows the TG/DTG plots of the stoichiometric precursor for $K_{1/2}Na_{1/2}NbO_3$ powder synthesis. From observations of the TGA curve, there appeared to be a three-staged weight loss from room temperature to 800°C, which related to DTG peak at 243, 430 and

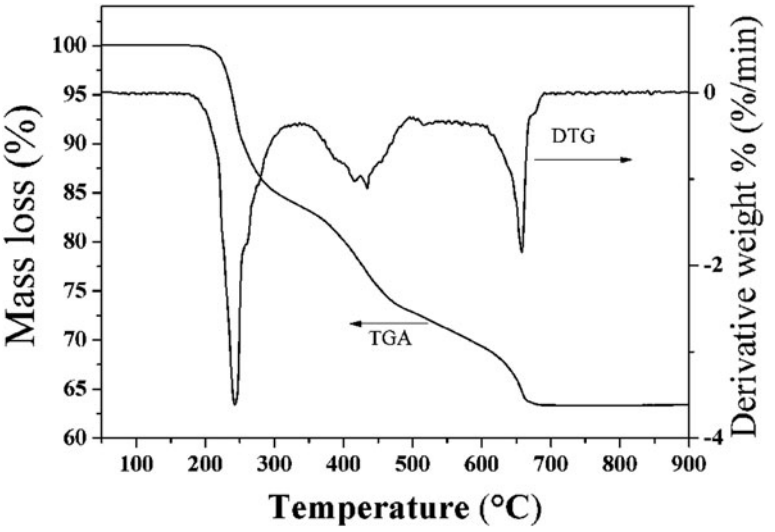

Figure 1. TG-DTG curves of the precursor mixed in the equivalent stoichiometric proportion of $K_{1/2}Na_{1/2}NbO_3$.

658°C. As suspected, the initial temperature (T_{in}) occurred when the sample weight started changing rapidly during the chemical reaction [12]. A significant weight loss was observed as the temperature increased from 200°C to 250°C, indicating that the T_{in} was around this temperature. The overall weight loss of about 36.66% was close to the theoretical value of 35.75%, which corresponded to the release of 25 mol H_2O, 14 mol N_2 and 20 mol CO_2, and related to the following reaction:

$$9KNO_3 + 9NaNO_3 + 9Nb_2O_5 + 10NH_2CH_2COOH \rightarrow$$
$$18K_{1/2}Na_{1/2}NbO_3 + 25H_2O + 14N_2 + 20CO_2 \quad (1)$$

This result supported our idea that a hotplate can be a suitable heating source, since it is capable of initiating the combustion reaction at a temperature as low as that of the T_{in}.

The X-ray diffraction (XRD) patterns of potassium sodium niobate ($K_{1/2}Na_{1/2}NbO_3$) powder, which was synthesized using different fuel-to-oxidant molar ratios, are illustrated in Fig. 2. The diffraction pattern of the powder with a fuel-to-oxidant molar ratio of 1:0.56, which is the equivalent stoichiometric ratio calculated for maximum energy release, suggests a perovskite phase. These diffraction peaks are detected for all different fuel content molar ratios (fuel-to-oxidant molar ratio ranging from 0.56 to 1.80). The well-split diffraction peak can be observed by using a fuel-to-oxidant molar ratio of 0.56 to 0.80. As the fuel-to-oxidant molar ratio increased to over 0.80, the peak split of (400)(004) and peak intensity were found to decrease, thus indicating a decrease in synthesized powder crystallinity. In addition, a fuel-rich composition resulted in less crystallinity, and a diffraction peak of un-reacted Nb_2O_5 raw material also was found (JCPDS file no. 30-0873).

The average crystalline size (D) of as-prepared $K_{1/2}Na_{1/2}NbO_3$ powders was considered from the diffraction peak as a function of fuel content by using X-ray line broadening through Scherrer's equation [13]:

$$D = k\lambda/\beta \cos\theta_B \quad (2)$$

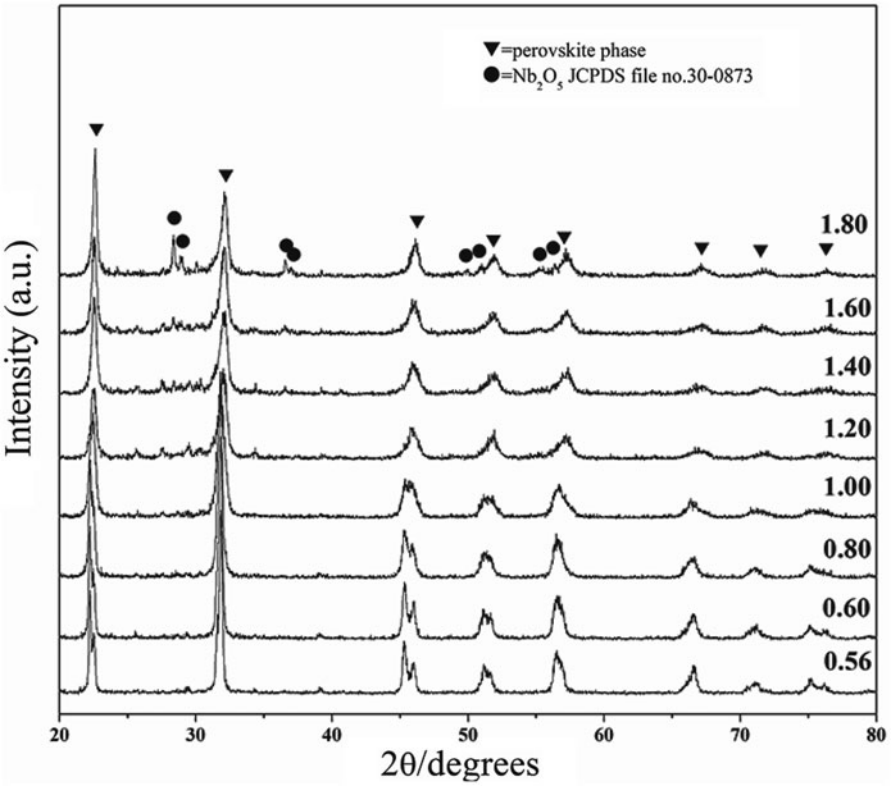

Figure 2. X-ray diffraction patterns of $K_{1/2}Na_{1/2}NbO_3$ powder obtained from various fuel-to-oxidant molar ratios.

where D is the average crystalline size, k a constant taken as 0.89; the wavelength of X-ray radiation, β the full width at half maximum (FWHM) and θ_B the diffraction angle. Figure 3 shows average crystallite sizes of $K_{1/2}Na_{1/2}NbO_3$ powder obtained from various fuel-to-oxidant molar ratios. In powder synthesized using a fuel-to-oxidant molar ratio of 0.56, the average crystallite size was found to be 29 ± 11 nm. As fuel content increased to the molar ratio of 1.0, its average crystallite size was found to decrease regularly to 14 ± 3 nm. As fuel content increased to more than that used, the average crystallite sizes were stable and increased slightly when the fuel content reached the ratio of 1.8 (16 ± 6 nm). This observation of decreased crytallite size with increasing fuel content could be caused by a larger amount of gas product produced from the combustion reaction [10–11]. This suggested that elevated fuel content could lead to the production of a smaller crystalline size (related to a small particle size) of powder.

Nevertheless, as a consequence of additional cost and more carbon residual, an extremely high fuel-to-oxidizer molar ratio (fuel-rich ratio) did not always result in the desired production of powder, as reported initially. Figure 4 shows the FT-IR spectroscopic studies of the crystalline potassium sodium niobate ($K_{1/2}Na_{1/2}NbO_3$) before and after combustion synthesis. An IR band of around 3,450 cm^{-1} assigned to O—H asymmetric stretching (ν_3) [14] was observed in the precursor mixture without heat treatment. This band related to the moisture content that could belong to KBr media. In addition, the IR spectrum indicated peaking of the characteristic band at 1,626, 1,385 and 828 cm^{-1}, which corresponded to

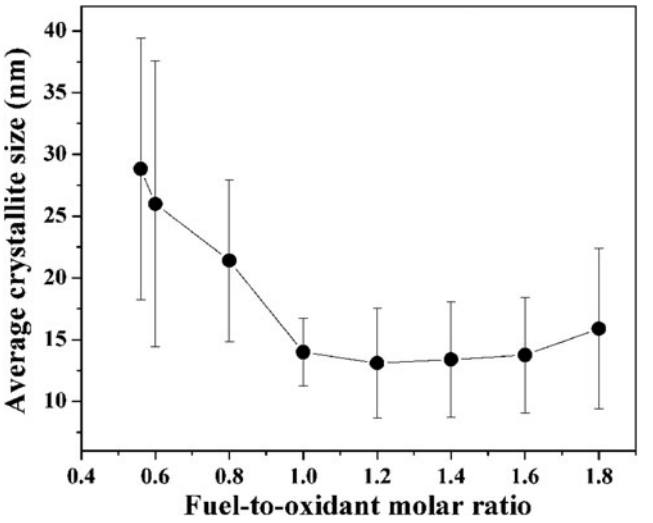

Figure 3. Average crystallite sizes of $K_{1/2}Na_{1/2}NbO_3$ powder obtained from various fuel-to-oxidant molar ratios.

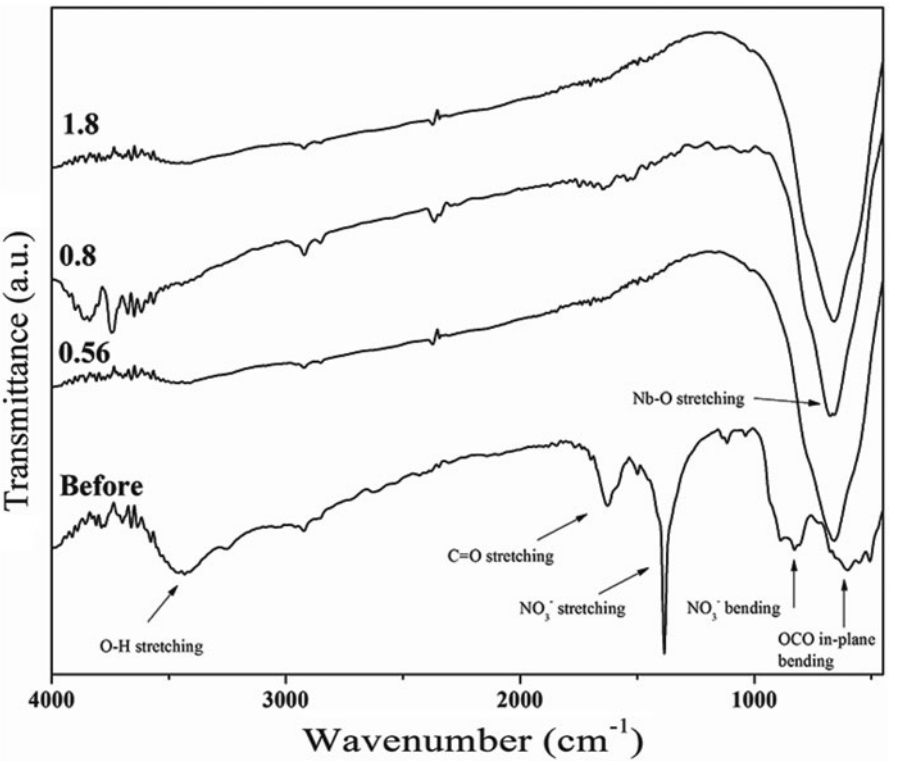

Figure 4. FT-IR spectra of the precursor mixed in the stoichiometric proportion of $K_{1/2}Na_{1/2}NbO_3$ and powder obtained from various fuel-to-oxidant molar ratios.

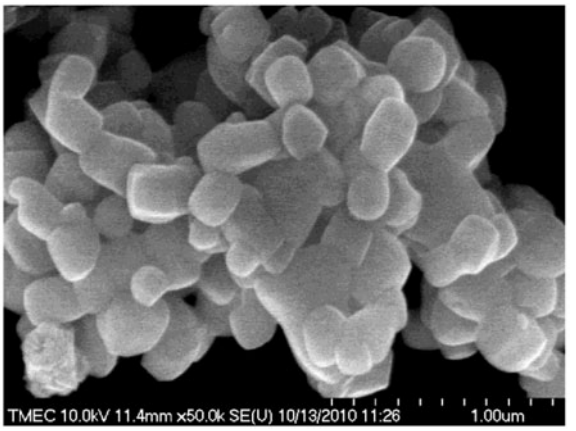

Figure 5. SEM micrographs showing $K_{1/2}Na_{1/2}NbO_3$ powder obtained from fuel-to-oxidant molar ratio of 0.6.

the anti-symmetric carboxyl group stretching vibration, anti-symmetry NO_3^{-1} stretching and bending vibration, respectively [15]. This result indicated existence of the carboxyl and NO_3^{-1} group belonging to the starting material.

After combustion reaction, an FT-IR band was detected at a low wave number of around 600 to 1,000 cm^{-1}, without others bands. This outcome suggests an Nb—O bond formation, which was believed to be the vibration (ν_3) mode in the corner-shared NbO_6 octahedron, as reported IR spectra of niobate glass ceramics [15]. Therefore, this result led to the assumption that the perovskite $K_{1/2}Na_{1/2}NbO_3$ phase was synthesized (which correlated to XRD analysis).

Figure 5 illustrates an SEM micrograph of the as-prepared $K_{1/2}Na_{1/2}NbO_3$ powder using the fuel-to-oxidant molar ratio of 0.6. The agglomerated uniform cubic-like particle, $K_{1/2}Na_{1/2}NbO_3$, was observed. No evidence of secondary phase was found. The mean particle size estimation using the linear intercept method was found to be about 229 $\pm$ 52 nm. This observation agreed well with evidence suggested from the XRD technique, in which $K_{1/2}Na_{1/2}NbO_3$ powder was synthesized via the combustion method without the calcinations step.

4. Conclusions

Crystalline $K_{1/2}Na_{1/2}NbO_3$ powder was prepared rapidly from the combustion synthesis. Glycine was used as the fuel. The final product was confirmed by XRD, FT-IR and SEM techniques. This is a facile, simple cost and time-saving method for synthesizing stoichiometric, homogeneous, and fine $K_{1/2}Na_{1/2}NbO_3$ powder. The powder obtained was found to be a uniform agglomerated particle that possesses an average crystallite size (defined by XRD) decreasing from 29 $\pm$ 11 nm (ratio of 0.56) to 16 $\pm$ 6 nm (ratio of 1.8), and a mean particle size (defined by SEM micrograph) of 229 $\pm$ 52 nm.

Acknowledgments

This work has been fully supported by research fund from the Thailand Research Fund (Grant No. BRG5680006). This research is also partly supported by grants from the National

Research Council of Thailand (NRCT), National Nanotechnology Center (NANOTEC) NSTDA, through its Center of Excellence Network, and the KMITL Research Fund. C. Chaiyo would like to acknowledge the Royal Golden Jubilee Ph.D. Program (RGJ) under Thailand Research Fund (TRF) for her Ph.D. scholarship.

References

1. Y. Shiratori, A. Magrez, C. and Pithan, Particle size effect on the crystal structure symmetry of $K_{0.5}Na_{0.5}NbO_3$. *J Eur Ceram Soc*. **25**, 2075–2079 (2005).
2. G. Shirane, R. Newnham, and R. Pepinsky, Dielectric Properties and Phase Transitions of $NaNbO_3$ and (Na, K)NbO_3. *Phys Rev.* **96**, 581–588 (1954).
3. DIRECTIVE 2002/96/EC OF THE EUROPEAN PARLIAMENT AND OF THE COUNCIL of 27 January 2003 on waste electrical and electronic equipment (WEEE), Official Journal of the European Union.
4. E. Cross, Materials science: Lead-free at last. *Nature*. **432**: 24–25 (2004).
5. Y. Saito, H. Takao, T. Tani, T. Nonoyama, K. Takatori, T. Homma, T. Nagaya, and M. Nakamura, Lead-free piezoceramics. *Nature*. **432**, 84–87 (2004).
6. K. Singh, V. Lingwal, S. C. Bhatt, N. S. Panwar, and B. S. Semwal, Dielectric properties of potassium sodium niobate mixed system. *Mater Res Bull*. **36**, 2365–2374 (2001).
7. E. Ringgard, and T. Wurlitzer, Lead-free piezoelectric based on alkali niobates. *J Eur Ceram Soc*. **25**, 2701–2706 (2005).
8. K. C. Patil, S. T. Aruna, and S. Ekambaram, Combustion synthesis. *Curr Opin Solid State Mater Sci*. **2**, 158–165 (1997).
9. K. C. Patil, S. T. Aruna, and T. Mimani, Combustion synthesis: an update. *Curr Opin Solid State Mater Sci*. **6**, 507–512 (2002).
10. D. A. Fumo, M. R. Morelli, and A. M. Segadães, Combustion synthesis of calcium aluminates. *Mater Res Bull*. **31**, 1243–1255 (1996).
11. N. Chaiyo, R. Muanghlua, S. Niemcharoen, B. Boonchom, and N. Vittayakorn, Solution combustion synthesis and characterization of lead-free piezoelectric sodium niobate ($NaNbO_3$) powders. *J Alloys Comd*. **509**, 2445–2449 (2011).
12. L. A. Chick, L. R. Pederson, G. D. Maupin, J. L. Bates, L. E. Thomas, and G. J. Exarthos, Glycine-nitrate combustion synthesis of oxide ceramic powders. *Mater Lett* **10**, 6–12.(1990).
13. H. P. Klug, and L. E. Alexander, *X-ray Diffraction Procedure of Polycrystalline and Amorphous Materials*, John Wiley & Sons, New York, 1974.
14. C. Weifan, L. Fengsheng, L. Leili, and L. Yang, One-Step Synthesis of Nanocrytalline Perovskite $LaMnO_3$ Powders via Microwave-Induced Solution Combustion Route. *J Rare Earths*. **24**, 782–787 (2006).
15. S. H. Xiao, W. F. Jiang, and L. Y. Li, Low-temperature auto-combustion synthesis and magnetic properties of cobalt ferrite nanopowder. *Mater Chem Phys*. **106**, 82–87 (2007).

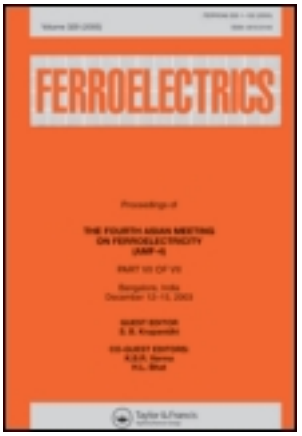

Ferroelectrics
Publication details, including instructions for authors and subscription information:
http://www.tandfonline.com/loi/gfer20

X-ray Absorption Spectroscopy Studies of $Cu_{(2-x)}Zn_xP_2O_7$ Binary Pyrophosphates

Rattanai Baitahe [a] , Chanapa Kongmark [b] , Rangson Muanghlua [c] , Panpailin Seeharaj [d] & Naratip Vittayakorn [a d]

[a] Electroceramic Research Laboratory, College of KMITL Nanotechnology, King Mongkut's Institute of Technology Ladkrabang , Bangkok , 10520 , Thailand

[b] Synchrotron Light Research Institute , 111 University Avenue , Muang , Nakhon Ratchasima , 30000 , Thailand

[c] Department of Electronics Engineering , Faculty of Engineering, King Mongkut's Institute of Technology Ladkrabang , Bangkok , 10520 , Thailand

[d] Advanced Materials Research Unit, Department of Chemistry, Faculty of Science, King Mongkut's Institute of Technology Ladkrabang , Bangkok , 10520 , Thailand

Published online: 09 Dec 2013.

To cite this article: Rattanai Baitahe , Chanapa Kongmark , Rangson Muanghlua , Panpailin Seeharaj & Naratip Vittayakorn (2013) X-ray Absorption Spectroscopy Studies of $Cu_{(2-x)}Zn_xP_2O_7$ Binary Pyrophosphates, Ferroelectrics, 453:1, 100-105, DOI: 10.1080/00150193.2013.842137

To link to this article: http://dx.doi.org/10.1080/00150193.2013.842137

Ferroelectrics, 453:100–105, 2013

ISSN: 0015-0193 print / 1563-5112 online
DOI: 10.1080/00150193.2013.842137

Taylor & Francis
Taylor & Francis Group

X-ray Absorption Spectroscopy Studies of $Cu_{(2-x)}Zn_xP_2O_7$ Binary Pyrophosphates

RATTANAI BAITAHE,[1] CHANAPA KONGMARK,[2] RANGSON MUANGHLUA,[3] PANPAILIN SEEHARAJ,[4] AND NARATIP VITTAYAKORN[1,4,*]

[1]Electroceramic Research Laboratory, College of KMITL Nanotechnology, King Mongkut's Institute of Technology Ladkrabang, Bangkok 10520, Thailand
[2]Synchrotron Light Research Institute, 111 University Avenue, Muang, Nakhon Ratchasima 30000, Thailand
[3]Department of Electronics Engineering, Faculty of Engineering, King Mongkut's Institute of Technology Ladkrabang, Bangkok 10520, Thailand
[4]Advanced Materials Research Unit, Department of Chemistry, Faculty of Science, King Mongkut's Institute of Technology Ladkrabang, Bangkok 10520, Thailand

Binary metal pyrophosphates; $Cu_{(2-x)}Zn_xP_2O_7$ (x = 0.0–2.0) compounds, were prepared via the solid solution method. The synthesize powders were characterized by X-ray diffraction (XRD). The local structure of Cu was analyzed by the mean of synchrotron X-ray absorption near the edge structure (XANES). The Cu^{2+}-O1, Cu^{2+}-O2 and Cu-Cu/Zn distances determined are extended X-ray absorption fine structure (EXAFS) measurements at the Cu K-edge, with a distance of about 1.52, 2.11, and 2.74 Å. The correlation between the structural changes and Cu content was analyzed and discussed. The analysis of the EXAFS spectra collected at the Cu K-edge indicates that the local structure around Cu atoms also is affected by the introduction of Zn atoms in the structure.

Keywords X-ray absorption spectroscopy; binary metal pyrophosphates

1. Introduction

Copper pyrophosphate ($Cu_2P_2O_7$) is one of a series of crystallographically related pyro-compounds, which have isostructural high temperature phases (called β) as a monoclinic system with space group C2/m (Base-centered). The low temperature phase (called α) is a monoclinic system with space group C2/c (Base-centered) [1]. These compounds have the generalized formula of $M_2X_2O_7$, with M as the cation and X an element showing the disposition of tetrahedral coordination with oxygen atoms. This series of compounds include the mineral, thortveitite. It has been observed that structure in which the radius of M is less than 0.97 Å (M = Mg^{2+}, Mn^{2+}, Co^{2+}, Cu^{2+}, Ni^{2+} and Zn^{2+}), in a pair of $P_2O_7^{4-}$ groups in eclipsed conformation, crystallizes at about the center of symmetry, with bridging O atoms extending towards each other. When the radius of M is greater than 0.97 Å

Received December 11, 2012; in final form March 8, 2013.
*Corresponding author. E-mail: naratipcmu@yahoo.com

($M = Ba^{2+}$, Cd^{2+}, Ca^{2+}, Sr^{2+}, and Pb^{2+}) the structure is a dichromate type in which $P_2O_7^{4-}$ exists in staggered conformation [2]. The $M_2P_2O_7$ was found to have many applications such as $Cu_2P_2O_7$, which can be used as catalysts in the cyclohexane conversion process. $Mn_2P_2O_7$ can be utilized as an additive in a lithium-ion battery [3], and $Mg_2P_2O_7$, $Ca_2P_2O_7$, and $Zn_2P_2O_7$ used for low temperature co-fired ceramics (LTCC), especially α-$Zn_2P_2O_7$ that exhibits rather low sintering temperature (875°C) [4–6]. Mix metal pyrophosphate, called binary metal pyrophosphates have the advantage of combining different materials together such as $Cu_{(2-x)}Zn_xP_2O_7$. The properties vary by crystal structure of the materials. Thus, the study of structure is necessary.

This study described the use of conversion-electron, extended X-ray absorption fine structure (EXAFS) as a tool to investigate the site distribution of metal cation (Zn^{2+}) in copper pyrophosphate. As this technique offers element specificity, as well as local structure and chemical sensitivity, it is suited ideally for such a study. In addition, this technique is applied readily to powder and thin films on thin supporting substrates, without the need for additional sample preparation.

2. Experimental Procedure

Synthesis of $Cu_{(2-x)}Zn_xP_2O_7$ ($x = 0.0, 0.5, 1.0, 1.5$, and 2.0) was conducted using traditional solid-state reaction techniques. High purity ZnO (99.9%), CuO (99.9%), and $(NH_4)_2HPO_4$ (99%) were used as raw materials. Stoichiometric mixtures of starting materials were homogenized by ball milling with ZrO_2 media in ethanol for 24 hrs and calcined at 800°C for 2 hrs. The structure and crystallite sizes of $Cu_2P_2O_7$ and $Zn_2P_2O_7$ samples were studied by X-ray powder diffraction using a D8 Advanced powder diffractometer (Bruker AXS, Karlsruhe, Germany) with Cu K_α radiation ($\lambda = 0.1546$ nm). The Scherrer method was used to evaluate the crystalline size. Experiments were conducted at room temperature on the beam line (BL8) of the National Synchrotron Research Center (Thailand), with a double crystal Ge(220) for the XANES mono-chromator. X-ray absorption (XAS) spectra at the

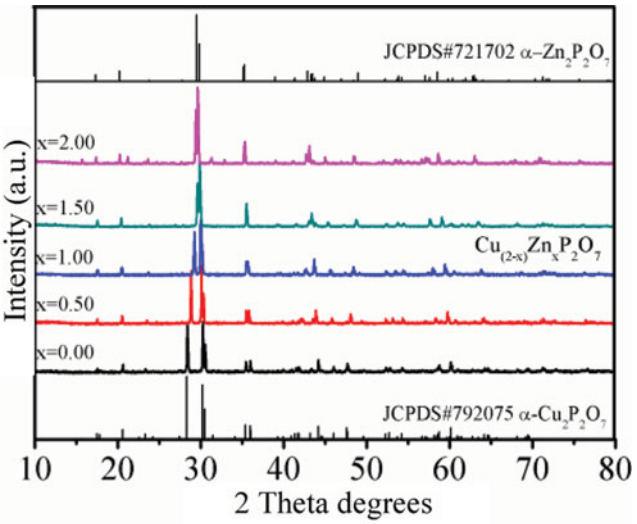

Figure 1. XRD patterns of $Cu_{(2-x)}Zn_xP_2O_7$. (Color figure available online.)

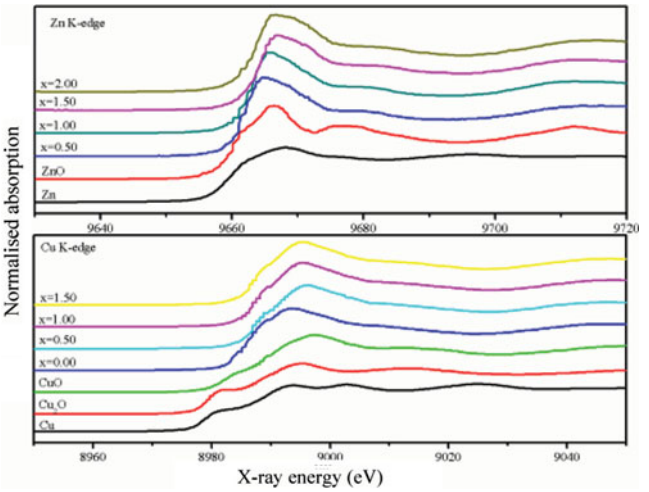

Figure 2. XANES spectra of $Cu_{(2-x)}Zn_xP_2O_7$. (Color figure available online.)

Cu/Zn K edge were obtained in transmission mode with air chambers. Reference materials used for X-ray absorption near-edge spectroscopy (XANES) measurements included Cu foil, Zn foil, Cu_2O, CuO, and ZnO. The data from XANES were analyzed by a supporting program.

3. Results and Discussion

The $Cu_{(2-x)}Zn_xP_2O_7$ ($x = 0.0$, 0.5, 1.0, 1.5, and 2.0) samples were analyzed by X-ray diffractmeter (XRD), together with the $Cu_2P_2O_7$ at x = 0.00–1.50 and $Zn_2P_2O_7$ at x = 2.00 as reference compounds, as shown in Fig. 1. The lattice parameter of each pyrophosphate was refined by pattern matching using FullProf software [7]. In the case of the composition, x = 0.00–1.50, a base centered monoclinic structure was observed, and the deduced cell parameters suitably followed Vegard's law, as seen in Table 1. The result from the case of the composition, $x = 2.00$, indicated that the $Zn_2P_2O_7$ crystal structure was a monoclinic system with space group I2/c. No compositions detected the pyrochlore phase. Obtaining the solid solutions, $Cu_{(2-x)}Zn_xP_2O_7$, was confirmed by these results.

Table 1
Average crystallite size and lattice parameter of $Cu_{(2-x)}Zn_xP_2O_7$ calculated from XRD data

	Lattice parameters			
x	a(Å)	b(Å)	c(Å)	β(°)
2.0	20.0971(6)	8.2716(2)	9.1020(3)	106.31
1.5	6.6662(4)	8.2409(5)	4.5308(3)	106.46
1.0	6.7246(4)	8.1972(4)	4.5431(3)	107.47
0.5	6.7900(2)	8.1574(3)	4.5580(2)	108.43
0.0	6.8809(4)	8.1172(4)	9.1598(6)	109.52

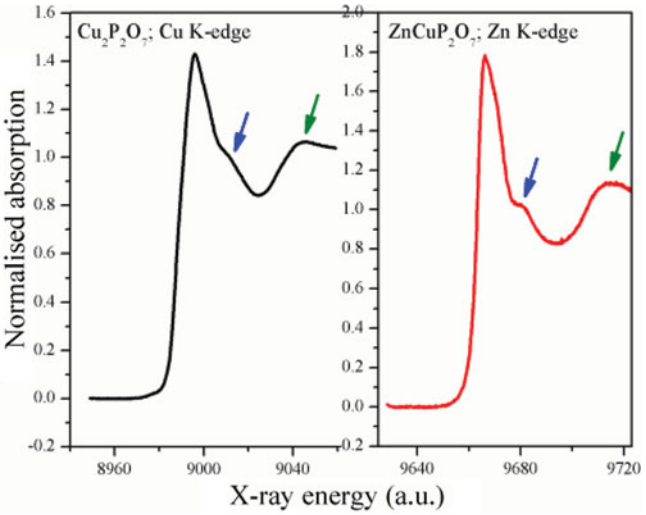

Figure 3. XANES spectra comparison of $Cu_2P_2O_7$ and $CuZnP_2O_7$.

As X-ray absorption near the edge structure (XANES) is very sensitive to both the oxidation state and change in the local geometry, spectra collected at both edges could help in understanding Fourier transform evolutions. The XANES spectra of samples, as shown at the Cu K-edge in Fig. 2, remain identical to the signal observed for Cu(II)O, whatever the Cu content,. Copper atoms thus remain Cu^{2+} in a monoclinic symmetry. XANES spectra in the Zn K-edge in the case of Zinc, remain identical to the signal observed for Zn(II)O. Zinc atoms therefore remain Zn^{2+} in the crystal structure. Fig. 3 presents the local environment of Zn atoms when they enter the $Cu_2P_2O_7$ structure. The spectrum of zinc in $CuZnP_2O_7$ and $Cu_2P_2O_7$ compound is practically identical, indicating that the Zn is divalent and the coordinated environments in the two compounds are similar [8].

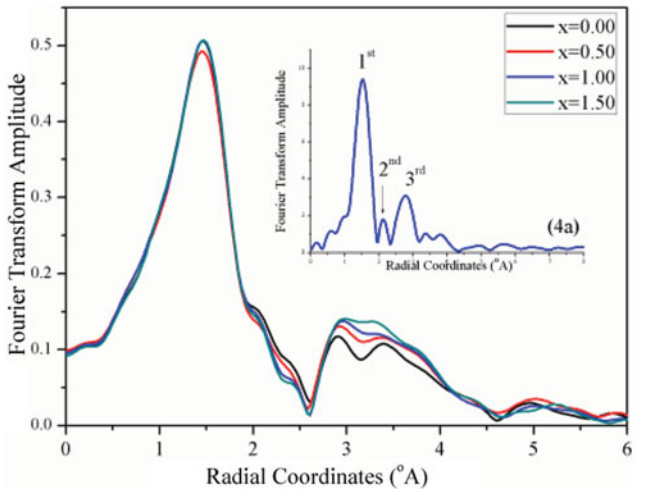

Figure 4. EXAFS patterns of $Cu_{(2-x)}Zn_xP_2O_7$.

Figure 4 shows the extended X-ray absorption fine structure (EXAFS) plot of the samples, and the spectrum distance of around 2.5–4.5 Å exhibits structure ordering. As Zn content increases, peaks have low amplitude, which indicates presence of structural disorder. Regarding k^3-weighted EXAFS, Figure 4(a) shows the separated Fourier transform (FT) peak of the first two orders for the initial, as apparent evidence of the Jahn–Teller distorted CuO_6 octahedral site. The first shell to be modeled for the $Cu_{(2-x)}Zn_xP_2O_7$ ($x = 0.0, 0.5, 1.0$, and 1.5) was the one that consisted of four equatorial oxygen atoms (Cu-O1), with bond lengths of about 1.52 Å. Then, the two axial oxygen atoms were taken into account for the second shell, thus introducing the Jahn Teller distortion effect, undergone by the copper octahedral centered site in the model (Cu-O2), with bond lengths of about 2.11 Å. A third shell was then added to the model in order to describe Cu-M (M = Cu, Zn) interaction with a distance of about 2.74 Å. An additional fourth shell did not improve the quality of analysis.

4. Conclusion

This work presented an electronic and structural characterization by XAS of the solid solution, $Cu_{(2-x)}Zn_xP_2O_7$ ($x = 0.0$, 0.5, 1.0, and 1.5), which was synthesized via solid state reaction. The pyrochlore phase was found in neither XRD patterns nor XAS spectra. XANES and EXAFS spectra (performed at the K-edge of each atom type) show that the oxidation state of zinc and copper is 2+. The Cu/Zn-O in binary metal pyrophosphate, which coordinates locally in the two compounds, is similar to $Cu_2P_2O_7$. This shows that Zn completely replaces Cu atomic position in the $Cu_2P_2O_7$ structure. Distances between Cu^{2+}-O1, Cu^{2+}-O2 (distorted) and Cu-Cu/Zn are measured at the Cu/Zn K-edge at about 1.52, 2.11, and 2.74 Å, respectively.

Acknowledgments

This work was supported by the Thailand Research Fund (TRF), KMITL research Fund, the National Nanotechnology Center (NANOTEC), NSTDA, Ministry of Science and Technology, Thailand, through its program of Center of Excellence Network and Synchrotron Light Research Institute (Public Organization), 114 Nakhon Ratchasima, Thailand.

References

1. B. E. Robertson, and C. Calvo, Crystal structure of β-$Cu_2P_2O_7$. *Canadian Journal of Chemistry.* **46**, 605–612 (1968).
2. M. Weil, and B. Stöger, Crystal chemistry of transition metal diarsenates $M_2As_2O_7$ (M = Mn, Co, Ni, Zn): Variants of the thortveitite structure. *Acta Crystallographica Section B: Structural Science*. **66**, 603–614 (2010).
3. S. Wang, X. Jiang, G. Du, Z. Guo, J. Jang, and S.-J. Kim, Solvothermal synthesis of $Mn_2P_2O_7$ and its application in lithium-ion battery. *Materials Letters*. **65**, 3265–3268 (2011).
4. J.-J. Bian, D.-W. Kim, and K. S. Hong, Microwave dielectric properties of $Ca_2P_2O_7$. *J Eur Ceram Soc*. **23**, 2589–2592 (2003).
5. J. J. Bian, D. Kim, and K. S. Hong, Microwave dielectric properties of $(Zn_{1-x}Mn_x)_{(2)}P_2O_7$. *J Mater Sci*. **40**, 1801–1803 (2005).
6. J. I. Bian, D. W. Kim, and K. S. Hong, Microwave dielectric properties of $A_{(2)}P_{(2)}O_{(7)}$ (A = Ca, Sr, Ba; Mg, Zn, Mn). *Jpn J Appl Phys*. **43**, 3521–3525 (2004).

7. M. Casas-Cabanas, Rodríguez-Carvajal, J. Canales-Vázquez, Y. Laligant, P. Lacorre, and Palacín, Microstructural characterisation of battery materials using powder diffraction data: DIFFaX, FAULTS and SH-FullProf approaches. *Journal of Power Sources*. **174**, 414–420 (2007).
8. S.-T. Myung, S. Komaba, N. Hirosaki, N. Kumagai, K. Arai, R. Kodama, Y. Terada, and I. Nakai, Emulsion drying preparation of layered $LiMn_xCr_{1-x}O_2$ solid solution and its application to Li-ion battery cathode material. *Journal of Power Sources*. **119**, 211–215 (2003).

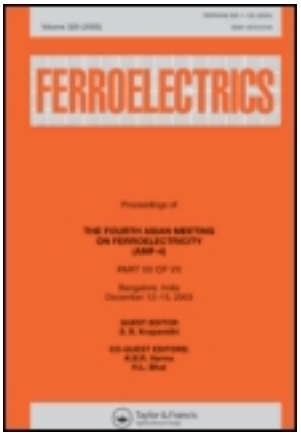

Ferroelectrics
Publication details, including instructions for authors and subscription information:
http://www.tandfonline.com/loi/gfer20

Combustion Synthesis of Lead-free Piezoelectric Alkali Metal Niobate Family

Nopsiri Chaiyo [a] , Rangson Muanghlua [b] , Yothin Wongprasert [b] , Panpailin Seeharaj [c] & Naratip Vittayakorn [a c]

[a] Electroceramic Research Laboratory, College of Nanotechnology, King Mongkut's Institute of Technology Ladkrabang , Bangkok , 10520 , Thailand

[b] Department of Electronics Engineering , Faculty of Engineering, King Mongkut's Institute of Technology Ladkrabang , Bangkok , 10520 , Thailand

[c] Advanced Materials Research Unit, Department of Chemistry, Faculty of Science, King Mongkut's Institute of Technology Ladkrabang , Bangkok , 10520 , Thailand

Published online: 09 Dec 2013.

To cite this article: Nopsiri Chaiyo , Rangson Muanghlua , Yothin Wongprasert , Panpailin Seeharaj & Naratip Vittayakorn (2013) Combustion Synthesis of Lead-free Piezoelectric Alkali Metal Niobate Family, Ferroelectrics, 453:1, 26-37, DOI: 10.1080/00150193.2013.842087

To link to this article: http://dx.doi.org/10.1080/00150193.2013.842087

Ferroelectrics, 453:26–37, 2013

ISSN: 0015-0193 print / 1563-5112 online
DOI: 10.1080/00150193.2013.842087

Taylor & Francis
Taylor & Francis Group

Combustion Synthesis of Lead-free Piezoelectric Alkali Metal Niobate Family

NOPSIRI CHAIYO,[1] RANGSON MUANGHLUA,[2] YOTHIN WONGPRASERT,[2] PANPAILIN SEEHARAJ,[3] AND NARATIP VITTAYAKORN[1,3,*]

[1]Electroceramic Research Laboratory, College of Nanotechnology, King Mongkut's Institute of Technology Ladkrabang, Bangkok 10520, Thailand
[2]Department of Electronics Engineering, Faculty of Engineering, King Mongkut's Institute of Technology Ladkrabang, Bangkok 10520, Thailand
[3]Advanced Materials Research Unit, Department of Chemistry, Faculty of Science, King Mongkut's Institute of Technology Ladkrabang, Bangkok 10520, Thailand

Nano-crystalline alkali metal niobate ($ANbO_3$; A = K and Na) powders were synthesized by the combustion of nitrate compounds and Nb_2O_5 using glycine as the fuel. The chemical reaction, nucleation mechanisms and influence of the fuel-to-oxidizer ratio to phase formation were studied. The precursor and product powders were characterized, using the thermo gravimetric analysis (TGA), Fourier transform infrared (FT-IR) spectroscopy, X-ray diffraction (XRD) technique, and scanning electron microscopy (SEM). Different fuel-to-oxidizer ratios were found to be a key factor of the process. As-prepared and calcined powders provided the perovskite structure with a nano-scale of mean crystalline size.

1. Introduction

Combustion synthesis (CS) or self-propagating high temperature synthesis (SHS) has been reported as a simple, rapid, energetically economic and low-cost method for producing various industrially useful advanced materials [1]. This process is provided, based on the fundamentals of a highly exothermic redox chemical reaction, in which an oxidation and a reduction reaction take place simultaneously. This synthesis technique begins with a mixture of easily oxidized reactants (such as nitrates) and a suitable organic fuel (as a reducing agent). The mixture is then heated until ignition, when it produces a self-sustaining combustion reaction with long duration of temperature that is high enough for the synthesis to take place, even without an external heating source [2]. A large amount of gas released during chemical reaction results in ultrafine nano-sized powder with dry, fluffy, usually crystalline and unagglomerated features [3]. Thus, combustion synthesis is known as a quick, straightforward preparation process for producing homogeneous, very fine crystalline and unagglomerated multicomponent oxide ceramic powders, without intermediate

Received December 11, 2012; in final form March 13, 2013.
*Corresponding author. E-mail: naratipcmu@yahoo.com

decomposition and/or calcination steps [4]. Metal nitrate was found to be the oxidizing salt preferred, due to its water solubility. Furthermore, it possesses a relatively low melting temperature and permits achievement of a homogeneous solution [1]. Combustion synthesis has been utilized to produce numerous industrially useful refractory, magnetic, dielectric, semiconducting, insulator, catalyst, sensor, phosphor, etc. oxide materials and carbide, boride, silicide, nitride, etc. non-oxide materials [1]. When compared with conventional ceramic processing, the most obvious advantages of combustion synthesis are primarily: (1) high reaction temperature production that can volatilize low boiling point impurities and, therefore, result in higher purity products; (2) reaction that has a simple exothermic nature, and needs inexpensive processing facilities and equipments; (3) short exothermic reaction time that results in low operating and processing costs; (4) high thermal gradients and rapid cooling rates that can produce new non-equilibrium or metastable phases; (5) inorganic materials that can be synthesized and consolidated simultaneously into a final product by utilizing the chemical energy of the reactants; and (6) formation of nearly all sizes and shapes of the products [5]. These advantages have engrossed researchers enough to become more active in researching the combustion synthesis of new and improved materials, with specialized mechanical, electrical, optical and chemical properties.

Solid state reaction is a traditional and conventional method used for synthesizing oxide ceramics [6], and has been used widely for mass production of several advanced industrial materials. It is probably one of the most fundamental and practical routine methods being used. The stoichiometric constituent of oxides and carbonate starting materials are mixed and then calcined for an appropriate duration at a high temperature in air or oxygen. Intermediate grinding is required to obtain phase-pure and homogeneous products. This method is found to be relatively simple, but time-consuming and energy intensive. As the Directives on Waste from Electrical and Electronic Equipment (WEEE), Restriction of Hazardous Substances (RoHS) and End-of-Life Vehicles (ELV) have enforced EU legislation on disposal of waste products since 2004, 2006 and 2003, respectively, non-lead piezoelectric materials need to be considered for environmental protection [7–8]. One of the main obstacles for commercial development of non-lead piezoelectric materials seems to be difficulties in processing, especially densification. Therefore, development of alternative methods, which can produce powder with high sinterability and controlled stoichiometric composition, are necessary and challenging.

The combustion synthesis was found to be a superior alternative chemical process because of its characteristics, as explained above. This work synthesized perovskite alkali metal niobate ($ANbO_3$; A = K and Na) powders via the combustion synthesis technique for the first time. The chemical reaction, nucleation mechanisms and influence of fuel content to phase formation were studied.

2. Experimental Procedure

Exothermic redox reaction could be initiated only when oxidizer and fuel were mixed intimately in a fixed proportion. The elemental stoichiometric coefficient, ϕ, could be calculated for releasing maximum energy by following the method of Jain *et al*. [9], which is based on thermochemical concepts used in propellant chemistry. The ratio between the total valencies of fuel (glycine; NH_2CH_2COOH) and that of the oxidizer (sodium nitrate and/or potassium nitrate) should be united. To satisfy the principle in the present system, the nitrate (oxidizing valency = 5−) to glycine (reducing valency = 9+) molar ratio was found to be 1:0.56. The comprehensive reaction that formed alkali niobate can be written

as:

$$36NaNO_3 + 18Nb_2O_5 + 20NH_2CH_2COOH \rightarrow 36NaNbO_3 + 50H_2O + 28N_2 + 40CO_2 \quad (1)$$

$$36KNO_3 + 18Nb_2O_5 + 20NH_2CH_2COOH \rightarrow 36KNbO_3 + 50H_2O + 28N_2 + 40CO_2 \quad (2)$$

$$18KNO_3 + 18NaNO_3 + 18Nb_2O_5 + 20NH_2CH_2COOH \rightarrow 36K_{0.5}Na_{0.5}NbO_3 + 50H_2O + 28N_2 + 40CO_2 \quad (3)$$

Various fuel-to-oxidizer ratios should be calculated for investigating and comparing the effect of fuel- rich/fuel-lean mixtures on the synthesis of alkali niobate powder. Different fuel-to-oxidizer molar ratios, such as fuel-deficient (<0.56), equivalent stoichiometric (0.56) and fuel-rich (>0.56) condition, were applied.

For the combustion synthesis, AR grade sodium nitrate ($NaNO_3$; 99.5%), potassium nitrate (KNO_3; 99.5%) and niobium pentaoxide (Nb_2O_5; 99.95%) were used as the starting materials, and glycine (NH_2CH_2COOH; 99.7%) was used as fuel. Without a purification step, the appropriate amount of starting materials was weighed, mixed with de-ionized water in a glass beaker and stirred regularly for 30 min. The fuel (glycine) was then added and the mixture was stirred for 30 min. After that, the solution precursor was boiled on a hotplate inside a fume-cupboard under ventilation and then evaporated. Once the solution had thickened and begun to dry, the ignition took place when the temperature rapidly increased, resulting in self-sustaining combustion, with a large volume of rapidly evolving gas products, and formation of voluminous powder.

To investigate thermal behavior of the precursor, the mixture of starting material was determined using thermo gravimetric analysis (TGA, Perkin Elmer). The X-ray diffraction (XRD, Advance D8) technique was performed on the combustion synthesized and calcined powders, using Ni-filtered CuK_α radiation for phase identification and mean crystalline size calculation. The volume fraction of the perovskite phase formation was considered by approximate calculation of the main X-ray peak intensity ratio of alkali niobate and/or other secondary phases [10], according to the following equation;% perovskite $= (I_{\text{perovskite}}/(I_{\text{perovskite}} + I_{\text{nd}})) \times 100$, where $I_{\text{perovskite}}$ and I_{nd} stand for intensities belonging to the strongest reflection peak of perovskite and secondary phase, respectively. Based on the X-ray powder diffraction data, Scherrer's formula [11] was used to calculate the crystallite sizes; $D = \frac{k\lambda}{\beta \cos\theta_B}$, where D is the average crystallite size, k a constant equal to 0.94, λ the wavelength of X-ray radiation, β the full width at half maximum (FWHM) and θ_B the diffraction angle. As-synthesized and final powder products were characterized by using the Fourier transform infrared (FT-IR, Perkin-Elmer Spectrum GX spectrometer) technique and scanning electron microscopy (SEM, Hitachi S4700).

3. Results and Discussion

The TG/DTG plots of the stoichiometric precursor for $NaNbO_3$, $KNbO_3$ and $K_{0.5}Na_{0.5}NbO_3$ powders are shown in Fig. 1. The combination observed on the TGA and DTG curves appeared to show three-stages of weight loss from room temperature to 900°C. The first one is of relative importance, as it is assumed to be at an initial temperature (T_{in}) when the sample weight starts to change rapidly during the chemical reaction [12]. A significant weight loss was observed as the temperature reached 200°C, demonstrating that the T_{in}

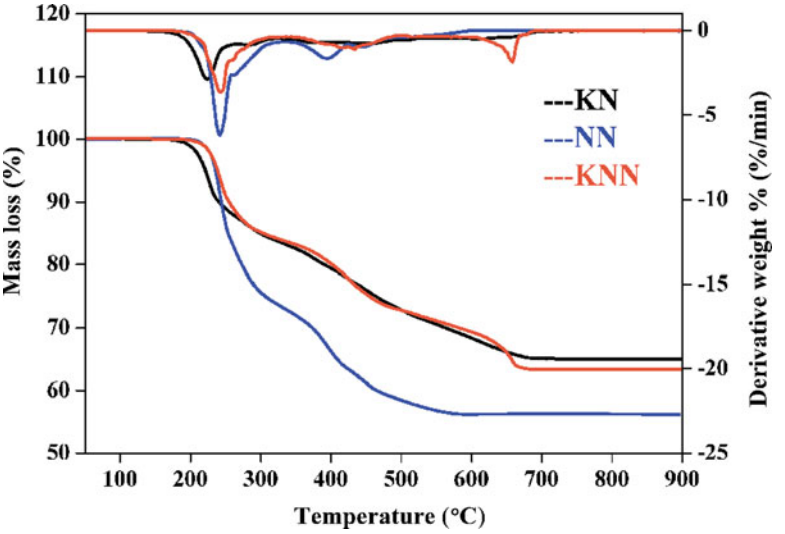

Figure 1. The TG/DTG plots of the stoichiometric precursor for $NaNbO_3$, $KNbO_3$ and $K_{0.5}Na_{0.5}NbO_3$ powders.

was at around this heat. This result supported the concept of this study in that a hotplate can be applied as a heating source to initiate the combustion reaction at a temperature as low as that of the T_{in}. As the temperature increased, weight loss proceeded continuously until residual mass finally remained. It was indicated that this reaction belongs to a multi-stage reaction. The overall weight loss was found to be about 34.99%, 40.00% and 36.66%, which is close to the theoretical value of 34.71%, 36.87% and 35.75% for $KNbO_3$, $NaNbO_3$ and $K_{0.5}Na_{0.5}NbO_3$, respectively. These overall weight losses correspond to the release of 50 mol H_2O, 28 mol N_2 and 40 mol CO_2 related to Eq. (1), (2) and (3), respectively.

To investigate the effect of fuel proportion and oxidizing agent on phase formation, the nitrate-to-glycine molar ratio of 1:0.56 (equivalent stoichiometric ratio) was used for the combustion synthesis. Figure 2 shows XRD patterns of the as-synthesized $NaNbO_3$, $KNbO_3$ and $K_{0.5}Na_{0.5}NbO_3$ powders. Regarding $K_{0.5}Na_{0.5}NbO_3$, the presence of reflection peaks ascribed to the crystalline perovskite phase of the sample could be matched with orthorhombic potassium sodium niobate JCPDS file no. 74-2025. This illustrated that the perovskite phase of $K_{0.5}Na_{0.5}NbO_3$ was produced directly after the combustion process. The XRD patterns of $KNbO_3$ and $NaNbO_3$ could be correlated to the diffraction peaks of Nb_2O_5 (•) (JCPDS file no. 30-0873) and $NaNO_3$ (■) (JCPDS file no. 85-0859) starting materials, with no evidence found of a perovskite phase. This was correlated with the experimental observation that auto-ignition did not occur in those conditions, although the equivalent stoichiometric ratio was calculated for maximum energy release. Oxygen deficiency then could be indicated in the system, and its environment might lead to combustion reaction and failure to follow the theory. Thereby, various fuel-to-oxidizer ratios were carried out for investigating and comparing the effect of fuel-rich/fuel-lean mixtures on phase formation. Figure 3 shows the XRD patterns of as-synthesized $KNbO_3$ ceramic powders obtained from various fuel-to-oxidant molar ratios. For the equivalent stoichiometric (0.56) and fuel-deficient (0.5) ratios, diffraction peaks of Nb_2O_5 (•) (JCPDS file no. 30-0873) starting materials were detected, with no evidence of perovskite phase. These results were correlated with the experimental observation of no ignition and combustion reaction in

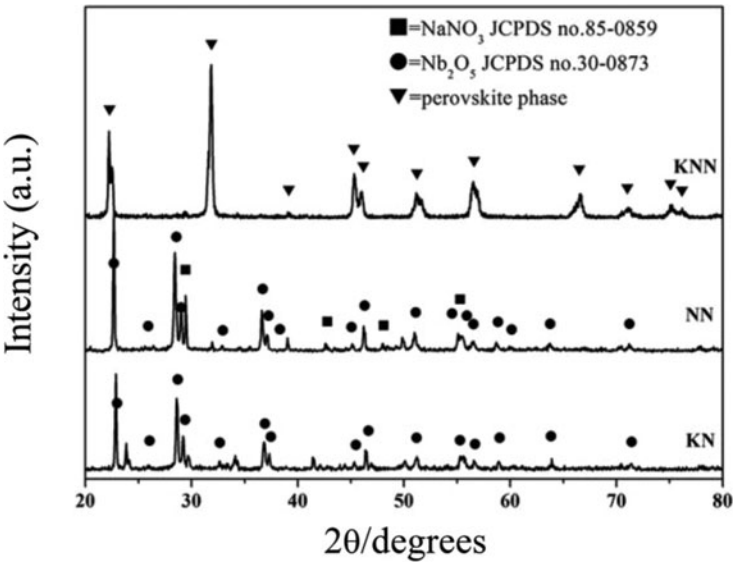

Figure 2. XRD patterns of the as-synthesized $NaNbO_3$, $KNbO_3$ and $K_{0.5}Na_{0.5}NbO_3$ powders.

those compositions. Furthermore, despite ultra-high fuel content with the fuel-to-oxidant molar ratio of 3 being studied, no diffraction peak of perovskite phase was apparent. However, the diffraction pattern correlated to the orthorhombic $KNbO_3$ perovskite phase (⧫) JCPDS file no. 32-0822, and the space group, Cm2m (38), was found when using fuel-rich

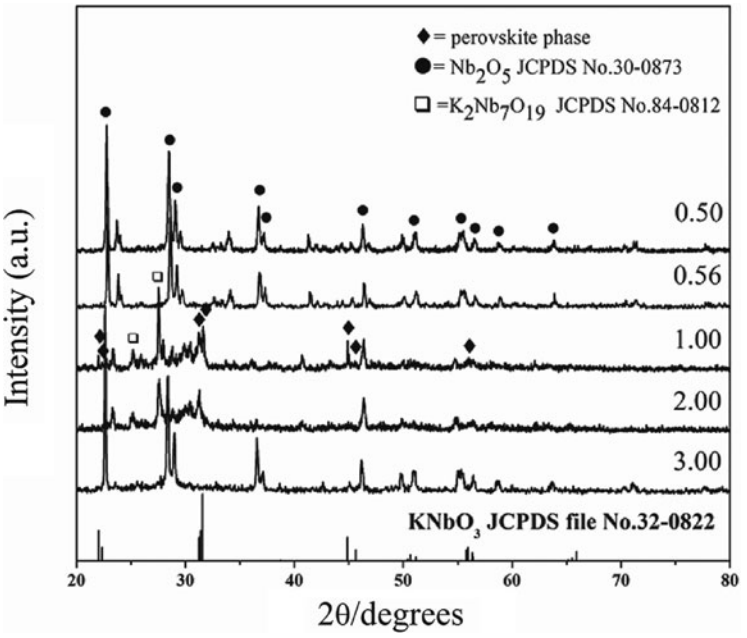

Figure 3. XRD patterns of as-synthesized $KNbO_3$ ceramic powders obtained from various fuel-to-oxidant molar ratios.

Table 1
Volume fractions of the perovskite phase formation of $KNbO_3$, $NaNbO_3$ and $K_{0.5}Na_{0.5}NbO_3$ powders obtained from various fuel-to-oxidant molar ratios

%wt perovskite	Fuel-to-oxidant molar ratios								
	0.56	0.6	0.8	1.0	1.2	1.4	1.6	1.8	
As-prepared $K_{0.5}Na_{0.5}NbO_3$	100.00	100.00	100.00	100.00	83.04	74.13	75.22	76.83	
	0.7	0.8	0.9	1.0	1.2	1.4	1.6	1.8	2.0
As-prepared $NaNbO_3$	92.87	92.48	92.53	92.91	91.33	89.49	88.89	91.35	62.77
	Calcination temperature (°C)								
	As-prepared	300°C	400°C	500°C	600°C	700°C	800°C	900°C	
$KNbO_3$	35.42	44.69	30.92	85.47	95.47	95.65	96.65	96.49	

mixture with fuel-to-oxidant molar ratios of 1.0 and 2.0. These $KNbO_3$ minor peaks were found to accompany the major peak of $K_2Nb_7O_{19}$ (□) JCPDS file no. 84-0812. Therefore, results from the fine nucleation condition of the monophasic $KNbO_3$ phase, found that the fuel-to-oxidizer molar ratio of 1.0 created the highest volume fraction of the perovskite phase formation (% perovskite), and was selected to investigate the effect of calcination temperature. The volume fraction of the perovskite phase powder formation, which resulted from the combustion method that used various fuel-to-oxidizer molar ratios, is shown in Table 1. Thus, the as-prepared powder was calcined for 4 h at different temperatures, with a heating/cooling rate of 20°C/min. The XRD patterns of those calcined $KNbO_3$ powders are illustrated in Fig. 4. With regard to the powders calcined at relatively low temperatures of 300°C and 400°C, their diffraction patterns suggested apparent un-reacted raw materials accompanied by a minor perovskite phase, similar to those in as-prepared powder. As calcination temperatures increased to 500°C, diffraction peaks that could correspond to the orthorhombic potassium niobate perovskite phase ($KNbO_3$) JCPDS no. 32-0822 (♦) were shown clearly with the minor peak of the $K_2Nb_7O_{19}$ secondary phase. The secondary phase was found to be a main problem, which was usually discovered in synthesizing $KNbO_3$, as many kinds of potassium niobate compounds with various crystal structures could occur in the K_2O-Nb_2O_5 system, such as $K_4Nb_6O_{17}$ or $K_2Nb_7O_9$ [13]. Apart from $KNbO_3$, the combustion synthesis method also was used systematically to synthesize $NaNbO_3$. In the Na_2O-Nb_2O_5 system, as shown in Fig. 2, the stoichiometric fuel-to-oxidize molar ratio of 0.56 was found to be unsuitable. No perovskite phase occurred when using the above fuel content. After trying various fuel contents, as-synthesized $NaNbO_3$ with a fuel-to-oxidize molar ratio of 1 was found to possess the highest value of 93% volume fraction of the perovskite phase, comprising a slight Nb_2O_5 (·)(JCPDS file no. 30-0873) phase, as shown in Figure 5(c). After calcination, intensity of the Nb_2O_5 phase was found to decrease with increasing calcination temperature (data not shown). The diffraction peak corresponding to the Nb_2O_5 disappeared after calcination for 4 h at 400°C, whereas the monophasic perovskite $NaNbO_3$ phase was obtained, as illustrated in Figure 5(d). This $NaNbO_3$ phase (▼) was consistent with JCPDS file no. 82-0606, which corresponded to an orthorhombic structure with the space group, $P2_1ma$ (26). When comparing with a $KNbO_3$ preparation [XRD pattern shown in Fig. 5(a) and (b)], the calcination temperature used to achieve the monophasic $NaNbO_3$ phase was lower because the perovskite phase of 35% found for as-synthesized $KNbO_3$ powder was lower than that of 93% for $NaNbO_3$. Nevertheless, these

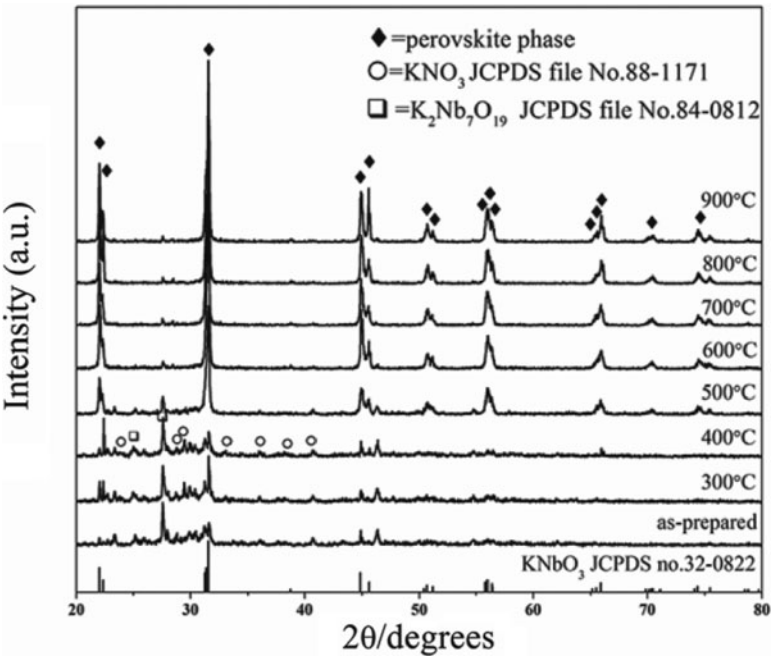

Figure 4. XRD patterns of $KNbO_3$ powders calcined at different temperatures for 4 h with a heating/cooling rate of 20°C/min.

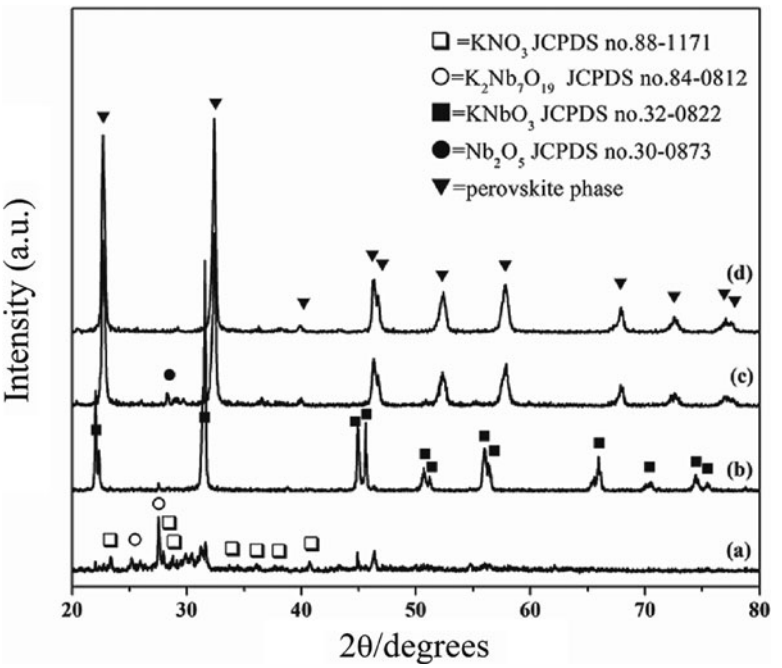

Figure 5. XRD patterns of the as-prepared powders, $KNbO_3$ (a), $KNbO_3$ calcined for 4 h at 900°C (b), as-prepared $NaNbO_3$ (c) and $NaNbO_3$ calcined for 4 h at 400°C.

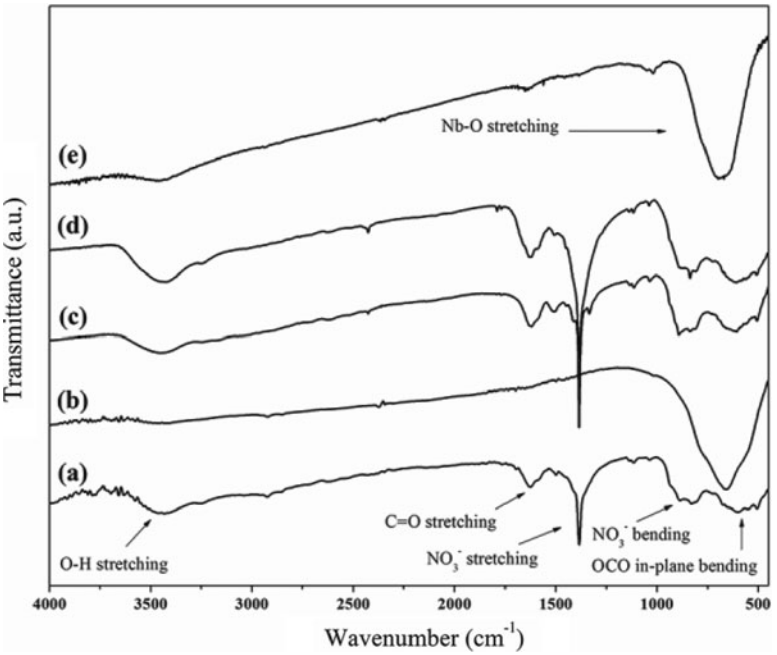

Figure 6. FT-IR spectroscopic studies of the precursor of the powders, $K_{0.5}Na_{0.5}NbO_3$ (a), as-synthesized $K_{0.5}Na_{0.5}NbO_3$ using a ratio of 0.56 (b), $NaNbO_3$ precursor (c), as-synthesized $NaNbO_3$ using a ratio of 1.0 (d) and $NaNbO_3$ calcined at 400°C (e).

results implied that the fuel content and calcination temperature play an important role in perovskite phase formation. The most suitable fuel-to-oxidize molar ratio should be used in order to produce a high perovskite phase form or monophasic phase power. In addition, corresponding average crystallite sizes, as determined from the XRD pattern in accordance with Scherrer's equation, are shown in Table 2. As $K_{0.5}Na_{0.5}NbO_3$ powder increased in fuel content, the average crystalline size (D) was found to decrease with regularity from 29 ± 11nm (ratio of 0.56) to 14 ± 3 nm (ratio of 1.0). As the fuel content increase exceeded that used, the values were stable and increased slightly when the fuel content reached the ratio of 1.8 (16 ± 6 nm). Likewise, the average crystalline size (D) of $NaNbO_3$ was found to decrease from 44.51 ± 11.99 nm (ratio of 0.7) to 23.79 ± 5.52 (ratio of 1.8), and then increase to 26.11 ± 13.69 nm (ratio of 2.0). The elevated fuel content was found to result in a smaller crystalline size (related to a small particle size) of powder, due to the larger amount of gas evolved. Nevertheless, higher fuel content that releases more energy can accelerate the crystallite growth and lead to formation of agglomerates. As a consequence of additional cost and more carbon residual, an extremely high fuel-to-oxidizer molar ratio (fuel-rich ratio) did not always provide the desired powder production.

Figure 6 shows the FT-IR spectroscopic studies of the as-synthesized and calcined alkali niobate powders. The IR band at ∼3,500 cm^{-1} was assigned to O-H asymmetric stretching (ν_3), as observed in all samples. It also was related to the moisture content of the KBr pellet, as the scissor bending mode (ν_2) of HO-H at 1,600 cm^{-1}. Regarding the precursor powders of $K_{0.5}Na_{0.5}NbO_3$ and $NaNbO_3$ without heat treatment [Figure 6(a) and (c)], the IR spectrum indicated characteristic band peaking at ∼1,612, ∼1,385 and ∼890 cm^{-1}, which corresponded to the anti-symmetric carboxyl group stretching vibration,

Table 2
Average crystalline sizes of $KNbO_3$, $NaNbO_3$ and $K_{0.5}Na_{0.5}NbO_3$ powders obtained from various fuel-to-oxidant molar ratios

	Fuel-to-oxidant molar ratios								
D	0.7	0.8	0.9	1.0	1.2	1.4	1.6	1.8	2.0
As-prepared $NaNbO_3$	44.51 ± 11.99	42.59 ± 11.54	37.31 ± 8.54	29.09 ± 5.29	27.45 ± 5.86	26.29 ± 5.97	24.40 ± 4.92	23.79 ± 5.52	26.12 ± 13.69
	Calcination temperature (°C)								
	200°C	300°C	400°C	500°C	600°C	700°C	800°C	900°C	
Calcined $NaNbO_3$	29.95 ± 4.51	31.51 ± 4.02	27.84 ± 7.12	30.82 ± 5.43	38.84 ± 8.09	60.72 ± 8.09	70.87 ± 9.22	85.27 ± 15.65	
		0.56	0.6	0.8	1.0	1.2	1.4	1.6	1.8
As-prepared $K_{0.5}Na_{0.5}NbO_3$		28.83 ± 10.58	25.99 ± 11.57	21.40 ± 6.56	13.99 ± 2.72	13.10 ± 4.43	13.39 ± 4.68	13.75 ± 4.67	15.88 ± 6.48

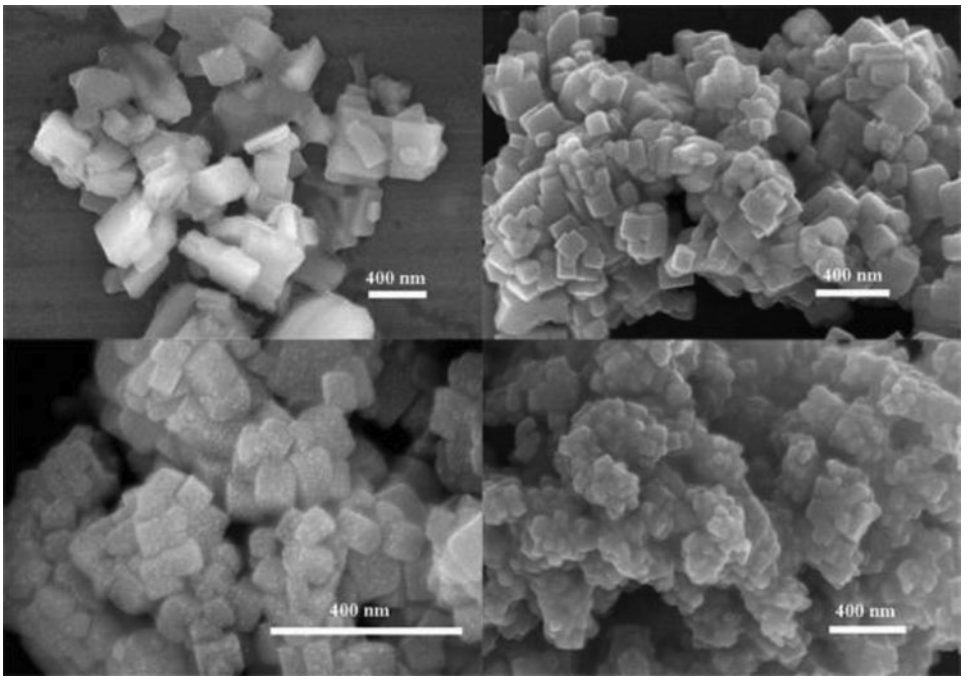

Figure 7. SEM images showing as-synthesized powders of $KNbO_3$ using a ratio of 1.0 (a), as-synthesized $K_{0.5}Na_{0.5}NbO_3$ using a ratio of 0.56 (b), as-synthesized $NaNbO_3$ using a ratio of 1.0 (c) and $NaNbO_3$ calcined at 400°C (d).

anti-symmetry $NO_3{}^{-1}$ stretching and bending vibration, respectively [14]. These spectrums also were found in as-prepared $NaNbO_3$ powder [Fig. 6(d)]. These results showed existence of the carboxyl and $NO_3{}^{-1}$ group that belonged to the starting material in samples without apparent broad absorption bands at a low wave number of $\sim$673 cm^{-1}, which was believed to be the vibration ($\nu 3$) mode of the Nb–O bond in the corner-shared NbO_6 octahedron [15]. However, this broad band of Nb–O bond was newly found in as-synthesized $K_{0.5}Na_{0.5}NbO_3$ powder and $NaNbO_3$ powder calcined for 4 h at 400°C [Figure 6(b) and (e)], without observation of any starting material band. This result led to assumption that the perovskite niobate phase was synthesized, which correlated to XRD analysis, and indicated success in synthesizing monophasic perovskite $K_{0.5}Na_{0.5}NbO_3$ and $NaNbO_3$ after the combustion process and calcination for 4 h at a temperature as low as 400°C, respectively.

SEM images of the as-prepared powders, $KNbO_3$ (a), $K_{0.5}Na_{0.5}NbO_3$ (b), $NaNbO_3$ (c) and $NaNbO_3$ calcined at 400°C (d), are presented in Fig. 7. No evidence of a different phase was found in those results. The as-prepared $KNbO_3$ SEM image [Fig. 7(a)] reveals rectangular particles with an average particle size of 230 ± 54 nm. The as-prepared powders, $K_{0.5}Na_{0.5}NbO_3$ and $NaNbO_3$ [Fig. 7(b) and (c)], are composed of aggregated polyhedral in nanoparticle shape, due to their extremely small dimensions and high surface energy of the powders obtained [16]. The average particle sizes, which can be estimated from micrographs, were found to be in the range of 229 ± 52 nm and 137 ± 52 nm for as-prepared $K_{0.5}Na_{0.5}NbO_3$ and $NaNbO_3$, respectively. However, the particle growth of calcined powder appeared to be seen in the calcined powder of $NaNbO_3$, with a relatively

higher average particle size of 226 ± 46 nm. It can be said that the firing process tends to produce agglomerated particles and grain growth.

4. Conclusion

The combustion synthesis was used successfully for synthesizing alkali metal niobate ($ANbO_3$; A = K and Na) powders. Crystalline $K_{0.5}Na_{0.5}NbO_3$ powder was synthesized directly after the combustion process. Monophasic perovskite $NaNbO_3$ and $KNbO_3$ powders were obtained following an additional calcination step. The fuel-to-oxidizer ratio was found to be the key factor for perovskite phase formation and characteristics of the powder obtained. This combustion synthesis method was studied as an alternative way to produce nano-crystalline powder alkali metal niobates ($ANbO_3$; A = K and Na), with the desired chemical composition, and reduced time and cost.

Acknowledgments

This work was supported by the Royal Golden Jubilee Ph.D. Program (RGJ), the Thailand Research Fund (TRF), KMITL research Fund, and the National Nanotechnology Center (NANOTEC) NSTDA, Ministry of Science and Technology, Thailand, through its program of Center of Excellence Network.

References

1. K. C. Patil, S. T. Aruna, and S. Ekambaram, Combustion synthesis. *Curr Opin Solid State Mater Sci*. **2**, 158–165 (1997).
2. N. P. Bansal and Z. Zhong, Combustion synthesis of $Sm_{0.5}Sr_{0.5}CoO_{3-x}$ and $La_{0.6}Sr_{0.4}CoO_{3-x}$ nanopowders for solid oxide fuel cell cathodes. *J Power Sources*. **158**, 148–153 (2006).
3. S. H. Xiao, W. F. Jiang, and L. Y. Li, Low-temperature auto-combustion synthesis and magnetic properties of cobalt ferrite nanopowder. *Mater Chem Phys*. **106**, 82–87 (2007).
4. K. C. Patil, S. T. Aruna, and T. Mimani, Combustion synthesis: an update. *Curr Opin Solid State Mater Sci*. **6**, 507–512 (2002).
5. J. J. Moore and H. J. Feng, Combustion synthesis of advanced materials: Part I. reaction parameters. *Progress in Matter Sci*. **39**, 243–273 (1995).
6. E. Ringgard and T. Wurlitzer, Lead-free piezoelectric based on alkali niobates. *J Eur Ceram Soc*. **25**, 2701–2706 (2005).
7. DIRECTIVE 2002/96/EC OF THE EUROPEAN PARLIAMENT AND OF THE COUNCIL of 27 January 2003 on waste electrical and electronic equipment (WEEE), Official Journal of the European Union.
8. DIRECTIVE 2002/95/EC OF THE EUROPEAN PARLIAMENT AND OF THE COUNCIL of 27 January 2003 on the restriction of the use of certain hazardous substances in electrical and electronic equipment, Official Journal of the European Union.
9. S. R. Jain, K. C. Adiga, and V. R. P. Verneker, A new approach to thermochemical calculations of condensed fuel-oxidizer mixtures. *Combust Flame*. **40**, 71–79 (1981).
10. G. Feng, H. Rongzi, L. Jiaji, L. Zhen, C. Lihong, and T. Changsheng, Phase formation and characterization of high temperature $xBiYbO_3$-$(1-x)PbTiO_3$ piezoelectric ceramics. *J Eur Ceram Soc*. **29**, 1687–1693 (2009).
11. H. P. Klug and L. E. Alexander, *X-ray Diffraction Procedure of Polycrystalline and Amorphous Materials*, New York: John Wiley & Sons, 1974.
12. L. A. Chick, L. R. Pederson, G. D. Maupin, J. L. Bates, L. E. Thomas, and G. J. Exarthos, Glycine-nitrate combustion synthesis of oxide ceramic powders. *Mater Lett*. **10**, 6–12 (1990).

13. Y. Saito and H. Takao, Synthesis of polycrystalline plate like $KNbO_3$ particles by the topochemical micro-crystal conversion method and fabrication of grain-oriented $(K_{0.5}Na_{0.5})NbO_3$ ceramics. *J Eur Ceram Soc*. **27**, 4085–4092 (2007).
14. S. H. Xiao, W. F. Jiang, and L. Y. Li, Low-temperature auto-combustion synthesis and magnetic properties of cobalt ferrite nanopowder. *Mater Chem Phys*. **106**, 82–87 (2007).
15. C. Weifan, L. Fengsheng, L. Leili, and L. Yang, One-step synthesis of nanocrytalline perovskite $LaMnO_3$ powders via microwave-induced solution combustion route. *J Rare Earths*. **24**, 782–787 (2006).

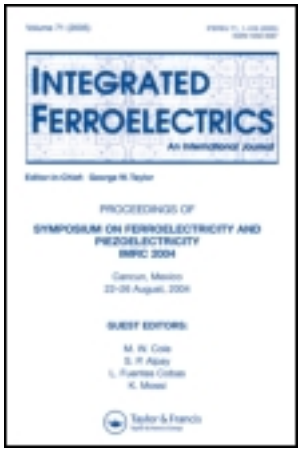

Integrated Ferroelectrics: An International Journal

Publication details, including instructions for authors and subscription information:
http://www.tandfonline.com/loi/ginf20

Structural and Magnetic Properties of Zn Doped $CoFe_2O_4$

Rachanusorn Roongtao [a b], Rattanai Baitahe [a], Naratip Vittayakorn [a c], Wantana Klysubun [b] & Wanwilai C. Vittayakorn [a]

[a] College of Nanotechnology, King Mongkut's Institute of Technology Ladkrabang, Bangkok, 10520, Thailand

[b] National Synchrotron Research Center, 111 University Avenue, Muang District, Nakhon Ratchasima, 30000, Thailand

[c] Advanced Materials Science Research Unit, Department of Chemistry, Faculty of Science, King Mongkut's Institute of Technology Ladkrabang, Bangkok, 10520, Thailand

[d] Department of Chemistry, Faculty of Science, King Mongkut's Institute of Technology Ladkrabang, Bangkok, 10520, Thailand

Published online: 07 Dec 2013.

To cite this article: Rachanusorn Roongtao, Rattanai Baitahe, Naratip Vittayakorn, Wantana Klysubun & Wanwilai C. Vittayakorn (2013) Structural and Magnetic Properties of Zn Doped $CoFe_2O_4$, Integrated Ferroelectrics: An International Journal, 148:1, 145-152, DOI: 10.1080/10584587.2013.852450

To link to this article: http://dx.doi.org/10.1080/10584587.2013.852450

Integrated Ferroelectrics, 148:145–152, 2013

ISSN: 1058-4587 print / 1607-8489 online
DOI: 10.1080/10584587.2013.852450

Taylor & Francis
Taylor & Francis Group

Structural and Magnetic Properties of Zn Doped $CoFe_2O_4$

RACHANUSORN ROONGTAO,[1,2] RATTANAI BAITAHE,[1] NARATIP VITTAYAKORN,[1,3] WANTANA KLYSUBUN,[2] AND WANWILAI C. VITTAYAKORN[1,*]

[1]College of Nanotechnology, King Mongkut's Institute of Technology Ladkrabang, Bangkok 10520, Thailand
[2]National Synchrotron Research Center, 111 University Avenue, Muang District, Nakhon Ratchasima 30000, Thailand
[3]Advanced Materials Science Research Unit, Department of Chemistry, Faculty of Science, King Mongkut's Institute of Technology Ladkrabang, Bangkok 10520, Thailand
[4]Department of Chemistry, Faculty of Science, King Mongkut's Institute of Technology Ladkrabang, Bangkok 10520, Thailand

Zinc doped cobalt ferrite powders were prepared by the solid state reaction method. The effect of zinc substitution on structure, morphology and magnetic properties was investigated. The X-ray analysis confirmed existence of the single phase cubic spinel structure, while Rietveld refinement data showed increasing of lattice parameters with zinc content. In addition, saturated magnetization increased with increasing zinc concentration and it was contained at maximum in $CoFe_{1.9}Zn_{0.1}O_4$ powders. However, the value of coercivity was decreased with zinc doped content. Furthermore, the oxidative states were characterized by X-ray absorption spectroscopy. The results confirm that the structure contained Co^{2+}, Fe^{3+} and Zn^{2+} ions.

Keywords Cobalt ferrite; zinc doping; magnetic properties; XANES spectra

Introduction

Cobalt ferrite is a ferromagnetic cubic spinel and important in many technological applications such as magnetic recording media, magnetic refrigerators, microwave devices and other high frequency appliances [1]. It is a well-known hard ferrite material that has been studied in detail, due to its very high cubic magnetocrystalline anisotropy, reasonably saturated magnetization, high wear resistance and good electrical insulation [2]. It shows various magnetic properties depending on the thermal history, composition and site preference of the cations among the tetrahedral (A) and octahedral (B) sites [1–3]. The partial substitution of transition metal in the $CoFe_2O_4$ offers an excellent opportunity for engineering specific magnetic interactions in the crystal lattice [4]. The addition of nonmagnetic zinc in cobalt ferrite raises saturated magnetization, due to zinc being the transition metal with strong

Received December 9, 2012; in final form August 25, 2013.
*Corresponding author. E-mail: w.vittayakorn@yahoo.com

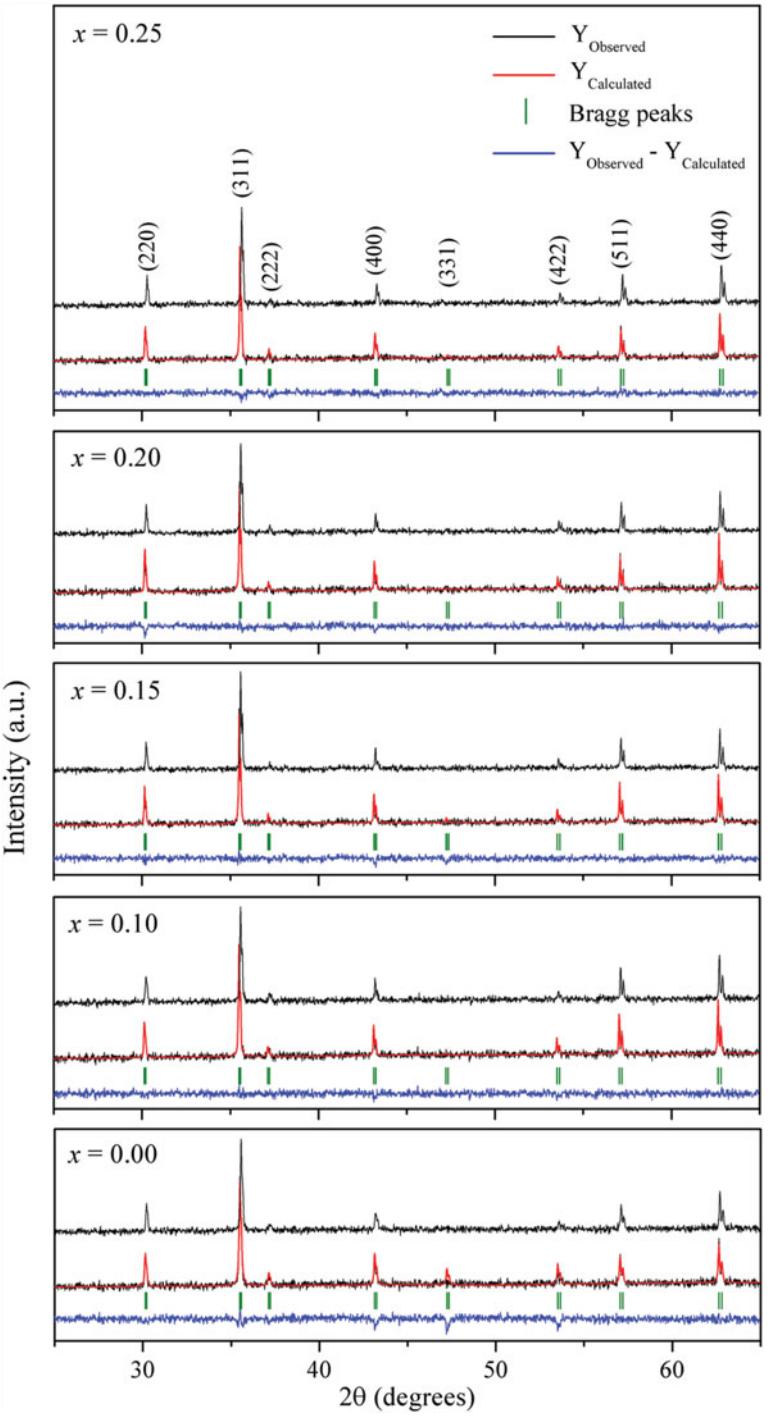

Figure 1. XRD patterns and Rietveld refinement plots of $CoFe_{2-x}Zn_xO_4$ powder calcined for 48 h at 900°C. (Color figure available online.)

A-site preference [3]. Thus, Y. Köseoğul *et al*. [2] prepared a cobalt zinc ferrite nanoparticle by using the microwave method. It was reported from the magnetic properties studied that the composition, $Co_{0.8}Zn_{0.2}Fe_2O_4$, has the highest value of saturated magnetization. However, the oxidative state of each element in the samples has yet to be investigated in any great extent. Therefore, this work aimed to study the valence state of structural elements by synthesizing $CoFe_{2-x}Zn_xO_4$ powders using solid state reaction, which is a very simple and the most economical method [5]. The samples were characterized by various techniques and then studied for their structure, magnetic behavior and oxidative state of each structural element.

Experimental Procedure

A series of $CoFe_{2-x}Zn_xO_4$ ferrites (where $x = 0.00, 0.10, 0.15, 0.20, 0.25$) were prepared by conventional ceramic processing. Raw material of Fe_2O_3 (Sigma-Aldrich, ≥99.0% purity), Co_3O_4 (Aldrich, ≥99.0% purity) and ZnO (Fluka, ≥99.0% purity) powders were weighed and mixed by the ball milling technique for 24 h in a PVC container, using an alumina ball and ethanol as the medium. The mixed powders were dried in a hot air oven and calcined at 900°C for 48 h with a heating/cooling rate of 5°C/min in air. The calcined powders were well ground using an agate mortar, and a single phase of spinel ferrite was confirmed at room temperature by X-ray diffractometer (XRD). The morphologic characterizations of the samples were performed by scanning electron microscopy (SEM). The saturated magnetization and coercivity of the powder were measured with a vibrating sample magnetometer (VSM) at a maximum applied field of 8 kOe at room temperature. The oxidative states of the element in the samples were measured using X-ray absorption spectroscopy (XAS). XANES data were collected from the Co K-edge (7709 eV) and Fe K-edge (7112 eV) in the transmission mode, and Zn K-edge (9659 eV) at room temperature in the fluorescence mode, at the XAS facility (BL-8) of the Siam Photon Laboratory, Synchrotron Light Research Institute, Nakhon Ratchasima.

Results and Discussion

Figure 1 shows the X-ray diffraction pattern and Rietveld refinement of $CoFe_{2-x}Mn_xO_4$ ($0.00 \leq x \leq 0.25$) powder, calcined at 900°C for 48 h. All peaks in the pattern correspond

Table 1
Rietveld refinement result, average particle size, and magnetic properties of $CoFe_{2-x}Zn_xO_4$ at room temperature

x	a (Å)	V (10^6pm^3)	R_w (%)	χ^2	Average particle size (μm)	M_s (emu/g)	M_r (emu/g)	H_c (Oe)
0.00	8.3843 (6)	589.385	4.823	1.408	0.40 ± 0.12	97.32	34.55	844.10
0.10	8.3851 (5)	589.554	5.304	1.525	0.52 ± 0.21	124.02	33.53	181.09
0.15	8.3820 (4)	588.897	5.124	1.470	0.57 ± 0.19	103.91	22.86	119.75
0.20	8.3776 (4)	587.982	5.228	1.432	0.59 ± 0.16	111.25	17.22	75.94
0.25	8.3720 (5)	586.799	5.028	1.418	0.60 ± 0.14	96.30	9.21	52.57

to the cubic $CoFe_2O_4$ phase, according to the standard JCPDS file no. 22-1086, with the lattice parameters, $a = 8.3910$ Å, and space group, Fd3m (no. 227) [6]. No other impurity phases with increased zinc contents were observed. This confirms the formation of a single spinel phase, and the lattice parameters were performed by the Rietveld refinement method. The lattice parameters and results of a quantitative phase analysis from the refinement are given in Table 1. The structure refinement shows the corresponding fits and confirms that the structure is a truly cubic type. Furthermore, the lattice constant and unit cell volume for each composition were seen to decrease with increasing Zn substitution. This was probably due to the ionic radius of 0.65 Å for low spin and 0.745 Å for high spin of Co^{2+} ions. Co^{2+} ions coordinated six-fold with O^{2-} ions was larger than the 0.6 Å for Zn^{2+} ions, which were coordinated four-fold with O^{2-} ions in the spinel structure [7]. Also, the unit cell

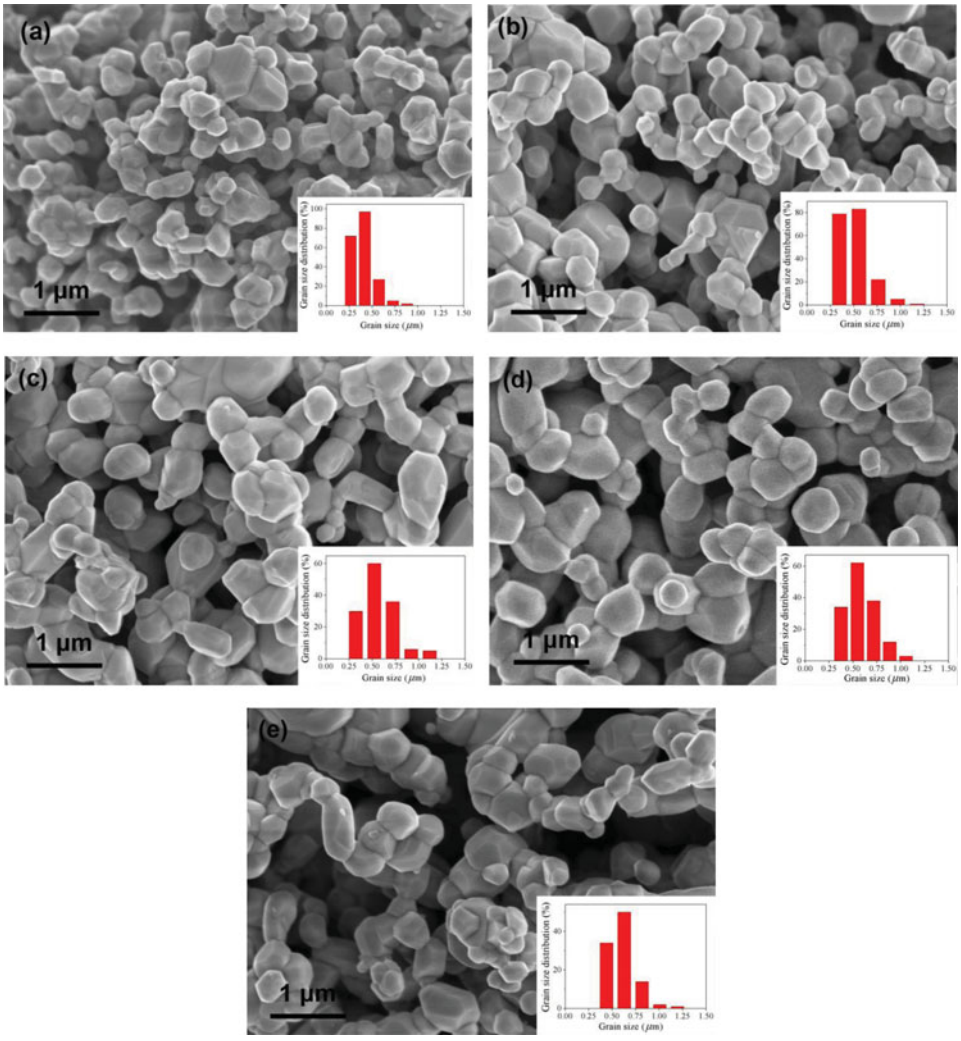

Figure 2. Morphology and particle size distribution of the $CoFe_{2-x}Zn_xO_4$ powders for (a) $x = 0.00$, (b) $x = 0.10$, (c) $x = 0.15$, (d) $x = 0.20$ and (e) $x = 0.25$. (Color figure available online.)

parameters varied linearly with the composition for continuous substitution, in which ions that substitute each other are distributed randomly according to Vegard's law [6].

Figure 2(a)–(e) shows SEM micrographs and particle size distribution measurement of the $CoFe_{2-x}Zn_xO_4$ powders, with different Zn doped content, calcined at 900°C for 48 h. From the morphology, all powders are agglomerated and basically irregular in shape, with a substantial variation in particle sizes. Heating resulted in calcinations for the well-faceted particle to form solid bodies [2]. Results of the average particle sizes are shown in Table 1, in which they increase with increasing amount of dopant, due to any Zn content having corresponding effect on the resulting particle size. In addition, the particle size distribution observed from the SEM image had narrow range distribution and increased with increasing Zn doping.

Figure 3 shows the magnetic hysteresis loop of $CoFe_{2-x}Zn_xO_4$ powders at room temperature, with a maximum applied field of up to 8 kOe. The saturated magnetization, remanence and coercivity are summarized in Table 1. The magnetization value of doped samples increases sharply with the external magnetic field strength at the low field region. The highest saturated magnetization can be obtained in $x = 0.1$ of Zn doped cobalt ferrites. Increases in saturated magnetization can be attributed to influence of the cationic stoichiometry and its occupancy in specific sites. The magnetic order in the cubic system of ferromagnetic spinels is due to occurrence of the super-exchange interaction mechanism between metal ions in the tetrahedral A-site and octahedral B-site [2]. When the nonmagnetic zinc ion is substituted by the cobalt ferrite lattice, due to the zinc ferrite being a normal spinel, it has a stronger preference for the tetrahedral site and thus reduces the amount of

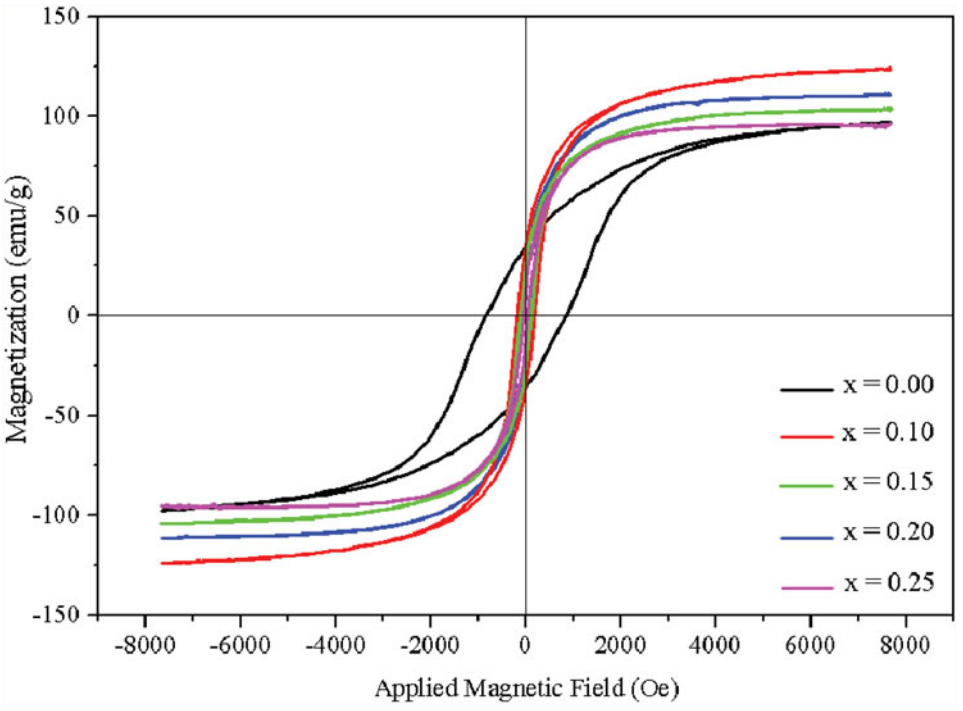

Figure 3. Magnetic hysteresis loops of $CoFe_{2-x}Zn_xO_4$ powders at room temperature. (Color figure available online.)

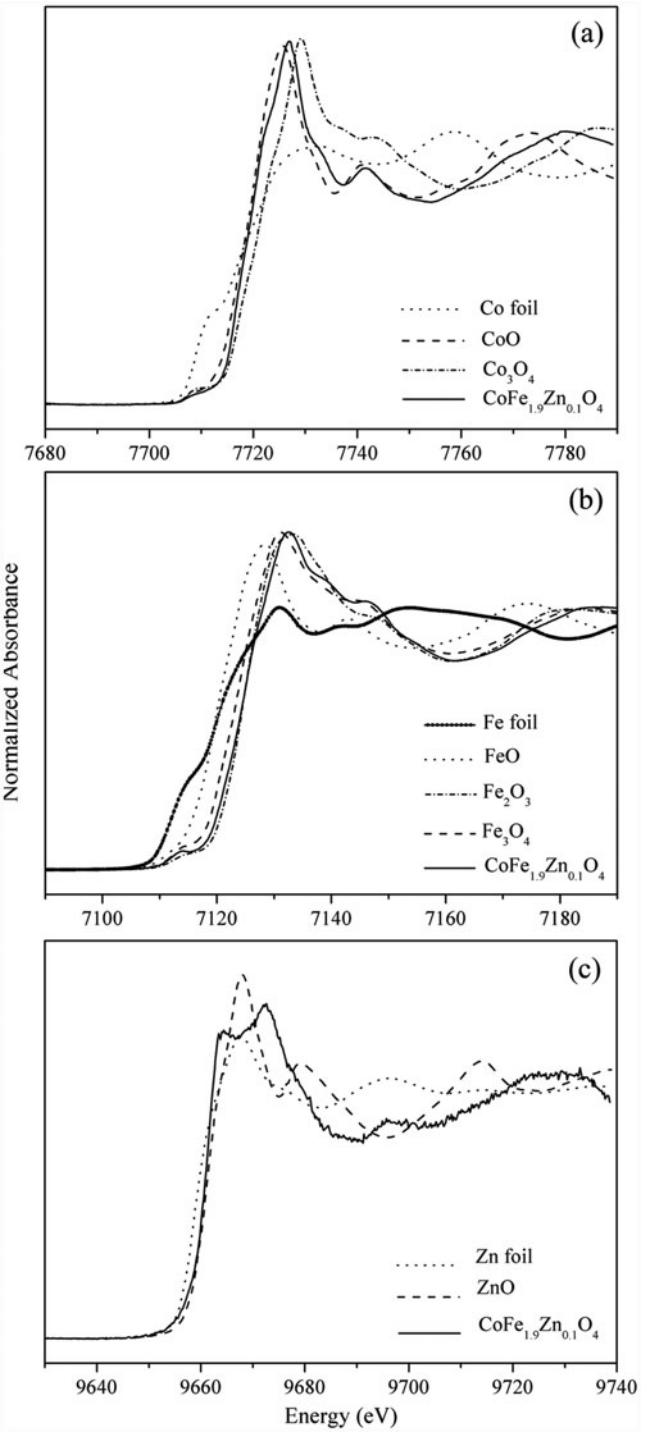

Figure 4. XANES spectra of $CoFe_{1.9}Mn_{0.1}O_4$ samples and the standards obtained at (a) Co K-edge, (b) Fe K-edge and (c) Zn K-edge.

Fe^{3+} in the A site. The net result, due to antiferromagnetic coupling, is an increase in magnetic moment on the B lattice and an increase in saturated magnetization. However, at high levels of zinc substitution in $x > 0.1$, the A-site magnetic ion becomes so diluted that coupling between the two lattices is lost, and the saturated magnetization drops [3]. Furthermore, the changes in remanence and coercivity of the samples by increasing the Zn content can be attributed to the magnetic character and anisotropic nature of cobalt. As more Zn ions are replaced with Co ions by increasing the "*x*", the remanence and coercivity decreases [8].

The XANES regions of the absorption spectrum are important because they contain electronic information on the immediate environment of the absorbing atom, which in principle can be translated into spatial, geometrical information. The first derivative of the XANES spectra is useful because it highlights the features around the absorption edge and facilitates determination of the oxidative state [9–10]. Figure 4(a) shows the XANES spectra of $CoFe_{1.9}Zn_{0.1}O_4$ samples and varied cobalt standards obtained at the Co K- edge. The valence state of Co in the ferrite samples was determined from energy of the main maxima in the spectra [11]. The curves of samples in the threshold region are close to that of CoO, suggesting existence of a divalent state. The E_0 values of $CoFe_{1.9}Zn_{0.1}O_4$ samples, Co foil, CoO and Co_3O_4 are 7718.408, 7708.960, 7718.750 and 7721.194, respectively. As observed, the spectra for the samples are similar to those obtained for the CoO standard, in which Co^{2+} is coordinated six-fold with O^{2-} ions, suggesting that Co ions exist in a divalent state in six coordinated oxygen atoms [12]. Figure 4 (b) shows XANES spectra of $CoFe_{1.9}Zn_{0.1}O_4$, Fe foil, FeO, Fe_3O_4 and Fe_2O_3 in the vicinity of the Fe K-edge, with their E_0 of 7125.540, 7112.061, 7121.192, 7124.186 and 7125.525, respectively, which leads to existence of Fe^{3+} in the samples. Fig. 4 (c) shows that the threshold energy of $CoFe_{1.9}Zn_{0.1}O_4$ samples is higher than that of Zn foil, but close to the energy of ZnO. The E_0 values of $CoFe_{1.9}Zn_{0.1}O_4$, Zn foil and ZnO are 9661.148, 9658.964 and 9661.104, respectively, suggesting existence of a divalent state of Zn in the samples.

Conclusion

In summary, zinc doped $CoFe_2O_4$ powders were synthesized successfully by the mixed-oxide method. The structural characteristics revealed that all samples have a single spinel structure, and Rietveld refinement showed that the lattice parameters were decreased by Zn content, whereas the size of particles increased. VSM measurements showed that saturated magnetization of the samples increased with increasing Zn content. The coercivity and remnant magnetization of the samples decreased with increasing Zn content, which attributed to the anisotropic nature of Co ions. Furthermore, Co^{2+}, Fe^{3+} and Zn^{2+} ions are the valence states of element in the structure.

Acknowledgments

This work has been fully supported by research fund from KMITL research Fund. This research is also partly supported by grants from the National Research Council of Thailand (NRCT), National Nanotechnology Center (NANOTEC) NSTDA, through its Center of Excellence Network, and the Thailand Research Fund (Grant No. BRG5680006). R. Roongtao would like to acknowledge the Ph.D. scholarship provided by Synchrotron Light Research Institute (Public Organization). The authors would like to thank Department of Physics, Kasetsart University (KU) for VSM measurement.

References

1. L. Zhao, H. Yang, X. Zhao, L. Yu, Y. Cui, and S. Feng, Magnetic properties of $CoFe_2O_4$ ferrite doped with rare earth ion. *Materials Letter.* **60**, 1–6 (2006).
2. Y. Köseoğlu, A. Baykal, F. Gözüak, and H. Kavas, Structural and magnetic properties of $Co_xZn_{1-x}Fe_2O_4$ nanocrystals synthesized by microwave method. *Polyhedron*. **28**, 2887–2892 (2009).
3. R. C. Buchanan, *Ceramic Materials for Electronics*. USA: Marcel Dekker, 2004.
4. A. Goldman, *Modern Ferrite Technology*. USA: Pittsburgh, 2006.
5. G. H. Haertling, Ferroelectric ceramics: history and technology. *J Am Ceram Soc*. **82**, 797–818 (1999).
6. Y. Köseoğlu, F. Alan, M. Tan, R. Yilgin, and M. Öztürk, *Low temperature hydrothermal synthesis and characterization of Mn doped cobalt ferrite nanoparticles*. Ceram Int. 2012 (in press).
7. R. D. Shannon, Revised Effective Ionic Radii and Systematic Studies of Interatomic Distances in Halides and Chalcogenides. *Acta Crystallogr.* **A32**, 751–767 (1976).
8. A. J. Moulson and J. M. Herbert, *Electroceramics*. England: John Wiley & Sons, 2003.
9. M. H. Nilsen, C. Nordhei, A. L. Ramstad, D. G. Nicholson, M. Poliakoff, and A. Cabañas, XAS (XANES and EXAFS) Investigations of nanoparticulate ferrites synthesized continuously in near critical and supercritical water. *J Phys Chem C*. **111**, 6252–6262 (2007).
10. M. F. F. Lelis, A. O. Portob, C. M. Gonçalvesb, and J. D. Fabris, Cation occupancy sites in synthetic Co-doped magnetites as determined with X-ray absorption (XAS) and Mössbauer Spectroscopies. *J Magn Magn Mater.* **278**, 263–269 (2004).
11. G. Bonsdorf, M. A. Deneckeb, K. Schäfer, S. Christen, H. Langbein, and W. Gunßer, X-ray absorption spectroscopic and Mössbauer studies of redox and cation-ordering processes in manganese ferrite. *Solid State Ionics*. **101–103**, 351–357 (1997).
12. M. F. F. Lelis, A. O. Portob, C. M. Gonçalvesb, and J. D. Fabris, Cation occupancy sites in synthetic Co-doped magnetites as determined with X-ray absorption (XAS) and Mössbauer Spectroscopies. *J Magn Magn Mater.* **278**, 263–269 (2004).

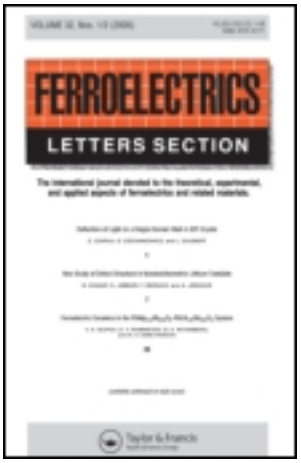

Ferroelectrics Letters Section
Publication details, including instructions for authors and subscription information:
http://www.tandfonline.com/loi/gfel20

Preparation and Dielectric Properties of 3-3 Lead Zirconate/Polyvinylidene Fluoride Nanocomposite

Chanisa Nawanil [a b], Wanwilai Vittayakorn [a b], Jutarat Prachayawarakorn [b c] & Naratip Vittayakorn [a b c]

[a] Electroceramic Research Laboratory, College of Nanotechnology, King Mongkut's Institute of Technology Ladkrabang, Bangkok, 10520, Thailand

[b] Advanced Material Research Unit, Faculty of Science, King Mongkut's Institute of Technology Ladkrabang, Bangkok, 10520, Thailand

[c] Department of Chemistry, Faculty of Science, King Mongkut's Institute of Technology Ladkrabang, Bangkok, 10520, Thailand

To cite this article: Chanisa Nawanil, Wanwilai Vittayakorn, Jutarat Prachayawarakorn & Naratip Vittayakorn (2013) Preparation and Dielectric Properties of 3-3 Lead Zirconate/Polyvinylidene Fluoride Nanocomposite, Ferroelectrics Letters Section, 40:4-6, 94-100, DOI: 10.1080/07315171.2007.830060

To link to this article: http://dx.doi.org/10.1080/07315171.2007.830060

Ferroelectrics Letters Section, 40:94–100, 2013

ISSN: 0731-5171 print / 1563-5228 online
DOI: 10.1080/07315171.2007.830060

Preparation and Dielectric Properties of 3-3 Lead Zirconate/Polyvinylidene Fluoride Nanocomposite

CHANISA NAWANIL,[1,2] WANWILAI VITTAYAKORN,[1,2]
JUTARAT PRACHAYAWARAKORN,[2,3]
AND NARATIP VITTAYAKORN[1,2,3,*]

[1]Electroceramic Research Laboratory, College of Nanotechnology, King Mongkut's Institute of Technology Ladkrabang, Bangkok 10520, Thailand
[2]Advanced Material Research Unit, Faculty of Science, King Mongkut's Institute of Technology Ladkrabang, Bangkok, 10520, Thailand
[3]Department of Chemistry, Faculty of Science, King Mongkut's Institute of Technology Ladkrabang, Bangkok 10520, Thailand

Communicated by Professor Amar S. Bhalla
(*Received in final form February 10, 2013*)

Composites made of electroactive ceramics and a ferroelectric polymer are very attractive for applications since they exhibit good piezoelectric and pyroelectric properties, low densities and their properties can be tailored to various requirements. Here, we reported the preparation and dielectric properties of 3-3 PZ/PVDF nanocomposites by infusion of polyvinylidenedifluoride (PVDF) into the PZ nanofiber mat followed by heating of the composite at 80°C. The 3-3 PZ/PVDF composites were characterized by X-ray diffraction, FT-IR, SEM and LCR meter. The dielectric constant of the PZ/PVDF nanocomposite are relatively stable in the range of 21.98–18.21 within the measurement frequencies from 100 Hz to 2 MHz. This value is higher than the dielectric constant of the polyvinylidene fluoride. Moreover, the dielectric loss of the composite is below 0.09 at low frequencies.

Keywords PZ; PVDF; composite; dielectric

1. Introduction

Piezoelectric ceramic-polymer composites were intensively studied within the last decades because of their considerable potential for applications such as pyroelectric sensors, ultrasonic transducers, and hydrophones [1]. Piezoelectric ceramics have high piezoelectric strain coefficient and high electromechanical coupling coefficient [2]. However, the relatively high density, high acoustic impedance and mechanical stiffness limit their applications. On the other hand, piezoelectric polymers have acoustic impedance well matched to water and biological issues, but their piezoelectric strain coefficient and electromechanical coupling coefficient, are lower than those of piezoelectric ceramics [3]. Thus, in many applications, one might optimize conflicting requirements by combining the most useful properties of two or more phases that do not ordinarily appear together in nature. Therefore,

*Corresponding author. E-mail: naratipcmu@yahoo.com

different kinds of composites such as porous ceramics and ceramic-polymer composites are typically developed.

Antiferroelectric materials have attracted much research interest due to their potential applications in microactuators and energy conversion devices [4]. Lead zirconate, $PbZrO_3$ (PZ), is a well known antiferroelectric materials. This material can be processed into various forms such as bulk ceramics, thin films, and fibers, depending on the application area. The hysteresis characteristics of Antiferroelectric $PbZrO_3$ regions are well suited for either power-storage or actuator applications. Moreover, the extremely large charge which is released from the FE state to the AFE state may be useful as alternate capacitor materials in DRAMs [5]. In recent years, researchers have focused on synthesizing nanosized PZ fibers to improve desired properties. Fibrous PZ have potential for utilization in high performance electric-mechanical application such as actuators, sensors, high energy storage capacitors and microelectromechanical systems (MEMS). Due to the high surface-to-volume ratio and their novel properties that are significantly different from their bulk, such as mechanical [6] and electrical property [7]. Nanoscale PZ fibers incorporated into a piezoelectric polymer are expected to obtain smart piezocomposite structures and to find wide applications, particularly in nanoelectronics, photonics, sensors, and actuators. Both kinds of materials show different piezoelectric properties, such as resonance frequencies and electromechanical coupling coefficients because of differences in their microscopic structures, their elastic properties and their typical transducer geometries [8]. Due to such special qualities, piezoelectric polymers have been increasingly used in a rapidly expanding range of applications such as electromechanical transducers, position sensors and vibration control actuators [9]. Often piezo- and pyroelectric polymers such as nylon [10], polyvinyl chloride (PVC) [3] and polyvinylidene fluoride (PVDF) [11] were used as matrix. Based on our knowledge, there has been no previous report on the fabrication of PZ fibers/PVDF composite.

Polyvinylidene fluoride (PVDF) is a piezoelectric polymer that has been used in many applications including microphones, transducers, sensors and actuators, due to its high piezo-, pyro- and ferroelectric properties [12]. The PVDF has low permittivity, low thermal conductivity and is flexible and relatively low in cost [13]. In addition, it is exceptionally sensitive, for example, sensors based on PVDF film have been applied even in erosive media to detect pressure, in biological environments to aid minimally invasive surgery, test and characterize fabrics, and monitor human health [12].

Therefore this study fabricated 3-3 PZ/PVDF nanocomposite using PZ fibers embedded in PVDF matrix. The crystal structure and morphology were investigated. Moreover, the dielectric properties of the resultant 3-3 PZ/PVDF nanocomposite was characterized.

2. Experimental Procedure

PZ nanofibers were synthesized by an electrospinning method utilizing a solution which contained poly(ethylene oxide) (PEO, $M_w \sim 300{,}000$; Aldrich), and sol-gel precursor solution of PZ [14]. After obtaining the PZ fiber mats, PZ/PVDF nanocomposite samples were prepared. Firstly, Polyvinylidene fluoride (PVDF; $M_w \sim 534{,}000$; Aldrich) powder was dissolved in DMF solvent to obtain the polymer matrix of the composite. This solution was poured on to the calcined PZ fiber mat and this sample was kept under vacuum for 10 min to eliminate trapped air. Then, the sample was dried 24 h at 80°C. X-ray diffraction (XRD; Bruker-D8 Advance) using CuK_α radiation was used to determine the phases formed. The room-temperature FTIR spectrum ranging 4,000–370 cm^{-1} was recorded by a Perkin Elmer Spectrum GX FTIR/FT-Raman spectrometer, with 8 scans and a resolution of

$4\ cm^{-1}$ using KBr pellets. A scanning electron microscope (SEM, JEOL JSM5910LV) was used to observe the microstructures of the PZ/PVDF nanocomposite. Finally, dielectric properties of the PZ/PVDF nanocomposites were measured from 100 Hz to 2 MHz using a precision LCR meter HP-4284A (Hewlett-Packard, Palo Alto, CA). The samples were prepared into thin, rectangular, parallel plates, and the dielectric measurements were taken by placing the samples between two parallel metal plates of the sample holder.

3. Results and Discussion

PZ/PVDF nanocomposite achieved from embedded PZ nanofibers in PVDF polymer has a smooth surface, with no buckling or folding over, thus indicating that the solvent evaporated uniformly. The morphology of the PZ/PVDF composite was revealed by scanning electron microscopy (SEM). Figure 1 shows SEM photographs of the composite. From Figure 1(a), it is shown that the polymer matrix phase was infiltrated thoroughly into the fiber network, and an intimate mixture of two phases was obtained. Figure 1(b) shows the backscattering electrons SEM image of the composite section, in which the PZ phase is visible with a bright-white contrast, and the PVDF phase is identifiable as the darker-gray region. The microgeometry of the inclusion and the interface between the filler and the matrix could be important. The mixing rules of a given property are controlled by the connectivity of the individual phases [13]. From the Figure, it reveal that the composite has 3-3 connectivity by using Newnham's convention on connectivity of piezocomposites, in which the active PZ and polymer matrix phases are both connected in three dimensions in the micrometer scale [7].

The crystalline phases of 3-3 PZ/PVDF composite was revealed by X-ray diffraction spectra. Figure 2 shows the XRD patterns of the 3-3 PZ/PVDF composite compared with PZ fibers and PVDF powder. From the Figure, it is revealed that crystalline PZ/PVDF composite were obtained. According to JCPDS card no.75-1607, the diffraction peaks can be indexed as an orthorhombic perovskite structure of lead zirconate. Moreover, peaks of polyvinylidene fluoride (PVDF) could be observed in the XRD patterns of the composite, because of PVDF is a semi-crystalline polymer with typical crystallinity of 50%. The spectra of the PVDF polymer are also seen to have well defined peaks at $2\theta = 20.3^{\circ}$, referent to the sum of the diffractions in plane (110) and (200) characteristic of the β phase. Peak at $2\theta = 26.64^{\circ}$ referent to the diffractions in planes (021), which characteristic of α phase [15].

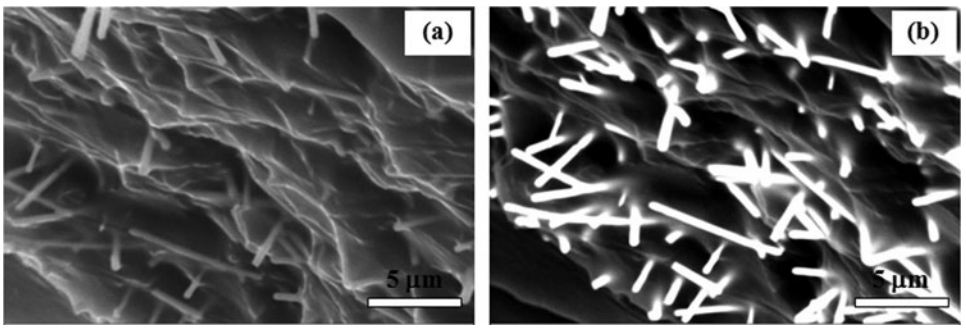

Figure 1. SEM micrograph of the composite structure of 3-3 PZ/PVDF nanocomposite.

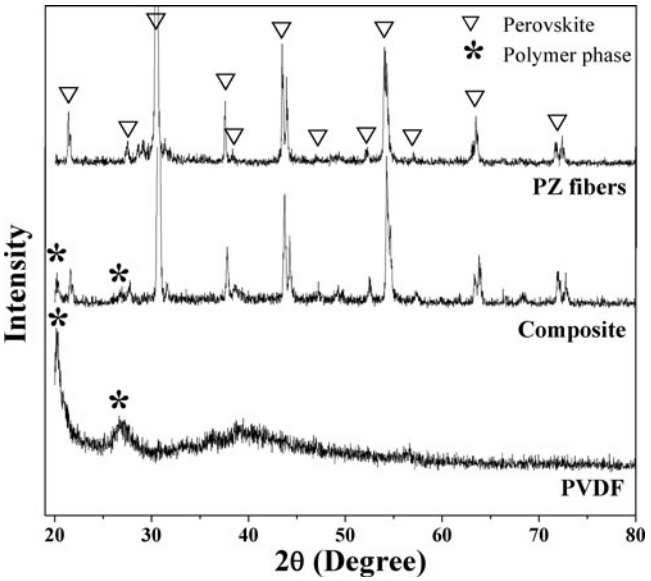

Figure 2. XRD patterns of 3-3 PZ/PVDF nanocomposite compared with PZ fibers and PVDF powder.

Formation of the 3-3 PZ/PVDF composite was confirmed further by the FTIR spectra, as shown in Figure 3. The spectrum of the 3-3 PZ/PVDF composite shows multiple absorption bands in the region of 400 to 4,000 cm^{-1}, which corresponds to the stretching and bending vibrations of ceramic, polymers and moisture. Peaks of around 1,450 cm^{-1} correspond to the aliphatic CH group vibrations of the CH_2 mode of PVDF polymer [9]. The wave number at ~1,600 cm^{-1} and broad peak at around 3,400 cm^{-1} both correspond

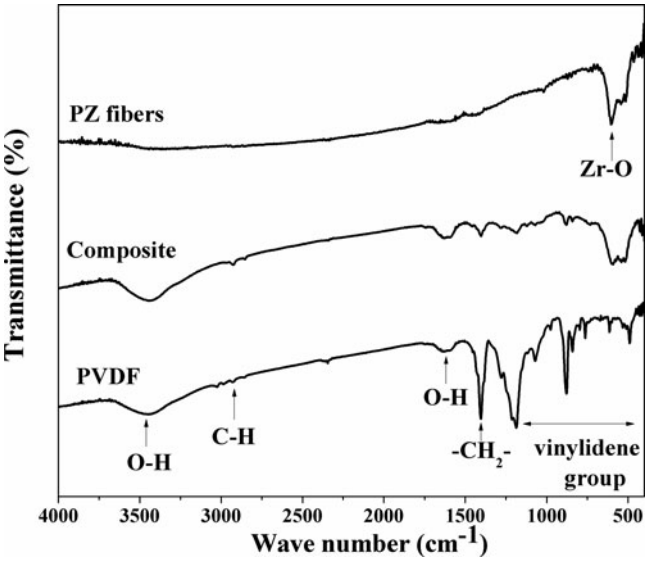

Figure 3. FT-IR spectra of 3-3 PZ/PVDF nanocomposite.

to the O—H stretching vibration of moisture [10]. The symmetric and asymmetric CH stretching vibration of PVDF is observed at 2900 cm^{-1} [16]. The absorbtion band at 480, 530, 612,764, 797, 855, 976 and 1410 cm^{-1} correspond to large amount of α crystal phase, whereas peak at 1226 cm^{-1} indicates β phase of vinylidene group of polymer [15, 17]. In addition, the absorption peak at ~548 cm^{-1} is attributed to Zr—O stretching vibration [11], which corresponds to the polycrystalline PZ fiber. This study can guarantee that its sample consists of two phases, including ceramic and polymer phases.

Dielectric properties of the resultant 3-3 PZ/PVDF nanocomposite was characterized by LCR meter. The dielectric constant of the 3-3 composite was found to be relatively stable in the range of 21.98–18.21 within the measurement frequencies from 100 Hz to 2 MHz (Figure 4). This value is higher than the dielectric constant of the polyvinylidene fluoride, which was measured as 13.14 (at 2 MHz) in this study. This is due to the increasing contribution of PZ to the dielectric properties of the composites, because PZ has a substantially higher dielectric constant ($\varepsilon_r = 116$ at room temperature [18]) than the polymer. This result demonstrated that, a particular response of a composite to an external field may depend either on the corresponding response of individual phases or may result in a property not existent in the phases composing the material. In addition, a particular property of the composite may depend on several properties of the individual phase [19]. The polymer phase in the composite was burnt out at 600°C, and the weight of the sample was recorded. From the theoretical density of PZ (8.085 g/cm^3) and PVDF (0.6 g/cm^3), the volume fraction of the PZ fibers in this composite structure was determined to be about 10%. Using the rule of mixtures according to equation (1) and dielectric constants of the constituent phases, polyvinylidene fluoride and PZ, the calculated dielectric constant of the composite was 23.43. [20]

$$\varepsilon'_{composite} = \varepsilon'_{polymer}\, V_{polymer} + \varepsilon'_{ceramic}\, V_{ceramic} \tag{1}$$

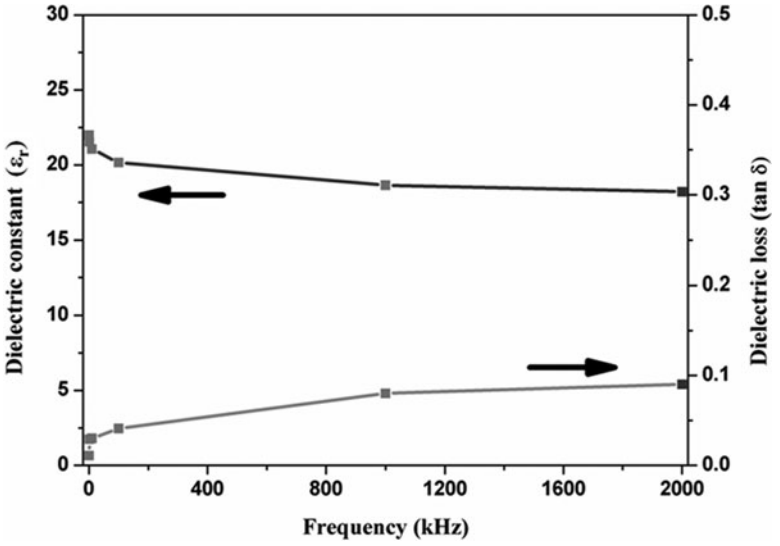

Figure 4. Dielectric properties of 3-3 PZ/PVDF nanocomposite within the measurement frequencies from 100 Hz to 2 MHz.

The calculated value is higher than the measured value, this may be due to the porosity and its contribution to the dielectric constant of the composite. The dielectric loss of the composite is below 0.09 at low frequencies.

4. Conclusions

In summary, this study prepared 3-3 PZ/PVDF nanocomposite successfully by infiltrating a polyvinylidene fluoride (PVDF) polymer into the PZ nanofiber mat. The composite has relatively smooth surface. The PZ/PVDF composite consists of two phases, including ceramic phase with orthorhombic perovskite structure and polymer phases. The dielectric constant of the composite measured at room temperature is higher than the polymer matrix and reasonably agrees with the prediction from the rule of mixtures.

Acknowledgments

This research has supported by The Royal Golden Jubilee Ph.D. Program (RGJ) under The Thailand Research Fund (TRF), the KMITL research fund and The Thailand Research Fund (TRF).

References

1. A. Petchsuk, W. Supmak, and A. Thanaboonsombut, *Journal of Applied Polymer Science*. **114**, 1048 (2009).
2. M. Wu, H. Huang, W. Chu, L. Guo, L. Qiao, and J. Xu, T.-Y. Zhang, *J. Phys. Chem. C*. **114**, 9955 (2010).
3. L. Xiaofang, X. Chuanxi, S. Huajun, D. Lijie, L. Rui, and L. Yang, *Journal of Wuhan University of Technology-Mater. Sci. Ed.* **20**, 4 (2005), 60.
4. X. J. Lou, and J. Wang, *Applied Physics Letters*. **96**, 102906. (2010).
5. I. Kim, S. Bae, K. Kim, H. Kim, J. S. Lee, J. Jeong, and K. Yamakawa, *Journal of the Korean Physical Society.* **33**, 2, 180 (1998).
6. L. R. Xu, L. Li, C. M. Lukehart, and H. Kuai, *Journal of Nanoscience and Nanotechnology.* **7**, 1 (2007).
7. A. Safari, *Journal of Physics III France*. **4**, l129 (1994).
8. K. Arlt and M. Wegener, *IEEE*. **1178** (2010).
9. A. M. Vinogradov, V. H. Schmidt, G. F. Tuthill, and G. W. Bohannan, *Mechanics of Materials*. **36**, 1007 (2004).
10. A. Petchsuk, and W. Supmak, A. Thanaboonsombut, *Journal of Applied Polymer Science*. **114**, 1048 (2009).
11. H. L. W. Chan, W. K. Chan, Y. Zhang, and C. L. Choy, *IEEE Transactions on Dielectrics and Electrical Insulation*. **5**, 4 (1998).
12. Y. R. Wang, J. M. Zheng, G. Y. Ren, P. H. Zhang, and C. Xu, *Smart Materials Structure*. **20**, 7 (2011).
13. S. Hajeesaeh, and S. Muensit, *Journal of Science and Technology.* **29** (2007).
14. C. Nawanil, B. Boomchom, J. Prachayawarakorn, W. C. Vittayakorn, and N. Vittayakorn, *Materials Science and Engineering B*. **177**, 1009 (2012).
15. V. Ostasevicius, I. Milasauskaite, R. Dauksevicius, V. Baltrusaitis, and V. Grigaliunas, I. Prosycevas, ISSN 1392-1207, **6**(86) (2010).
16. K. Kitaoka, H. Kozuka, and T. Yoko, *Journal of American Ceramics Society.* **81**, [5] 1189 (1998).
17. A. Kumar, and M. Deka, ISBN 978-953-7619-86-2, **438** (2010).

18. N. Vittayakorn, P. Charoonsuk, P. Kasiansin, S. Wirunchit, and B. Boonchom, *Journal of Applied Physics*. **106**, 064104 (2009).
19. B. Hilczer, J. Kułek, E. Markiewicz, M. Kosec, and B. Mali, *Journal of Non-Crystalline Solids*. **305**, 167 (2002).
20. E. M. Alkoy, C. Dagdeviren, and M. Papila, *Journal of American Ceramics Society.* **92** [11], 2566 (2009).

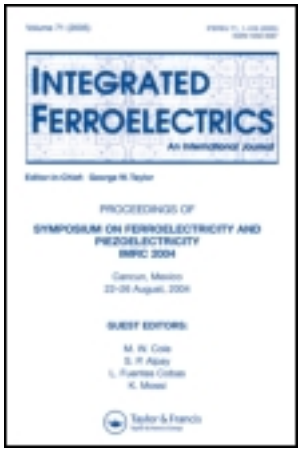

Integrated Ferroelectrics: An International Journal
Publication details, including instructions for authors and subscription information:
http://www.tandfonline.com/loi/ginf20

Fabrication and Properties of $BaTiO_3$-$CoFe_2O_4$ Nanocomposites

Wanwilai C. Vittayakorn [a b], Nattakarn Pulphol [a], Rangson Muanghlua [c] & Naratip Vittayakorn [a d]

[a] College of Nanotechnology, King Mongkut's Institute of Technology Ladkrabang, Bangkok, 10520, Thailand

[b] Thailand Center of Excellence in Physics (ThEP), Commission on Higher Education, Bangkok, 10400, Thailand

[c] Department of Electronics Engineering, Faculty of Engineering, King Mongkut's Institute of Technology Ladkrabang, Bangkok, 10520, Thailand

[d] Advanced Materials Science Research Unit, Department of Chemistry, Faculty of Science, King Mongkut's Institute of Technology Ladkrabang, Bangkok, 10520, Thailand

Published online: 07 Dec 2013.

To cite this article: Wanwilai C. Vittayakorn, Nattakarn Pulphol, Rangson Muanghlua & Naratip Vittayakorn (2013) Fabrication and Properties of $BaTiO_3$-$CoFe_2O_4$ Nanocomposites, Integrated Ferroelectrics: An International Journal, 148:1, 153-160, DOI: 10.1080/10584587.2013.852454

To link to this article: http://dx.doi.org/10.1080/10584587.2013.852454

Integrated Ferroelectrics, 148:153–160, 2013

ISSN: 1058-4587 print / 1607-8489 online
DOI: 10.1080/10584587.2013.852454

Taylor & Francis
Taylor & Francis Group

Fabrication and Properties of $BaTiO_3$-$CoFe_2O_4$ Nanocomposites

WANWILAI C. VITTAYAKORN,[1,2,*] NATTAKARN PULPHOL,[1] RANGSON MUANGHLUA,[3] AND NARATIP VITTAYAKORN[1,4]

[1]College of Nanotechnology, King Mongkut's Institute of Technology Ladkrabang, Bangkok 10520, Thailand
[2]Thailand Center of Excellence in Physics (ThEP), Commission on Higher Education, Bangkok 10400, Thailand
[3]Department of Electronics Engineering, Faculty of Engineering, King Mongkut's Institute of Technology Ladkrabang, Bangkok 10520, Thailand
[4]Advanced Materials Science Research Unit, Department of Chemistry, Faculty of Science, King Mongkut's Institute of Technology Ladkrabang, Bangkok 10520, Thailand

In this work, $BaTiO_3$-x$CoFe_2O_4$, where x = *0, 0.1, 0.2, 0.3, 0.4 and 0.5, nanocomposites were prepared by conventional mixing method and followed by normal sintering in air. The effect of processing condition on phase formation, microstructure, magnetic and electrical properties of the $BaTiO_3$-$CoFe_2O_4$ nanocomposites was investigated. The phase development and microstructural evolution of this system have been determined via X-ray diffractometer and scanning electron microscope. From the results, it concludes that phase formation, microstructure, electrical and magnetic properties of the $BaTiO_3$-x$CoFe_2O_4$ nanocomposites strongly depend on chemical composition.*

Keywords $BaTiO_3$; $CoFe_2O_4$; nanocomposite

1. Introduction

Multiferroic material is a material which can simultaneously exhibit ferroelectricity and ferromagnetism. Magnetization (or polarization) of this material can be induced by applying electric (or magnetic) field. So, this phenomenon will offer new opportunities to this kind of material such as the possible of modifying magnetic properties by applying an electric field and vice versa. The coexistence of magnetic and electric subsystem in multiferroic material can produce new materials with the product property, for example, the composite exhibits response that are not available in each individual phase, thus allowing an additional degree of freedom in the design of electronic components. Moreover, the interaction of the magnetic and electric subsystem can manifest itself as the giant magnetoelectric effect and the effect of mutual influence of the magnetization and polarization. These phenomena are of practical interest for many kinds of electronic applications such as microelectronics, magnetic memory, spintronics and sensors. Barium titanate-cobalt ferrite ($BaTiO_3$-$CoFe_2O_4$)

Received December 9, 2012; in final form August 25, 2013.
*Corresponding author. E-mail: w.vittayakorn@yahoo.com

nanocomposite is one of the most interested multiferroic composites due to its outstanding properties, high chemical stability and low particle size. The magnetic, electrical and mechanical properties including magnetoelectrism of $BaTiO_3$-$CoFe_2O_4$ nanocomposite can be varied by modifying the chemical stoichiometry, processing parameter and microstructural architecture. Variety of $BaTiO_3$-$CoFe_2O_4$ nanostructures are proposed such as multilayer structure, self-assembled nanostructured thin film and core-shell structure [1, 2]. Various techniques are used to fabricate $BaTiO_3$-$CoFe_2O_4$ nanocomposites such as sputtering, pulse laser deposition, sol-gel method and co-precipitation [3, 4]. Effect of processing parameters on structure and property is also studied by many researchers [5, 6]. However, the main problems of nanocomposite fabrications are still nanometer-scale preservation and highly densification of final body. As well known, microstructure and density of ceramics can be engineered through processing condition, therefore, this research will take this opportunity to reveal the relationship between processing parameters, compositions, microstructure and properties of $BaTiO_3$-$CoFe_2O_4$ nanocomposites, which would help to understand more clearly in basic principle of this system. The preparation technique in this work will mainly base on conventional milling followed by conventional sintering in order to reduce cost and complexity. The effect of processing parameters on phase development, microstructural evolution, electrical and magnetic properties of $BaTiO_3$-$CoFe_2O_4$ nanocomposites will be investigated. Finally, the relationships among these experimental results will be discussed.

2. Experimental

High purity grade of $BaTiO_3$ ($\sim$50 nm) and $CoFe_2O_4$ (20–50 nm) nanopowders (Inframat, $>$99.9% purity) were mixed together in the compositions of $BaTiO_3$-$x$$CoFe_2O_4$, where $x = 0$, 0.1, 0.2, 0.3, 0.4 and 0.5 mol%, and ball-milled with alumina media in ethanol for 24 h. Then, the slurry were dried, ground and pressed into pellets with 10 mm diameter. Green bodies were placed in high-purity alumina crucible and sintered at 1050, 1100, 1150 and 1200°C for 2 h in air with heating/cooling rates of 5°C/min. The crystallinity and phase formation of the sintered ceramics were examined by X-ray diffractometer (XRD). Densities of all ceramics were measured using Archimedes method. After that, grain morphology and size were directly imaged using scanning electron microscopy (SEM). The saturated magnetization and coercivity of the ceramics were measured with a vibrating sample magnetometer (VSM) at a maximum applied field of 8 kOe at room temperature. For dielectric measurement, silver paste was painted on both sides of samples. Dielectric properties of all sintered ceramics were studied as a function of both temperature and frequency. The capacitance was measured by LCR meter controlled by a computer system and the testing temperature was varied from room temperature to 200°C. Dielectric permittivity (ε_r) was then calculated using the geometric area and thickness of discs. Finally, the Curie temperature (T_C) was determined by the temperature dependence of the dielectric constant at 1 kHz.

3. Results and Discussion

The phase formation of $BaTiO_3$-$x$$CoFe_2O_4$ nanocomposites, where $x = 0$, 0.1, 0.2, 0.3, 0.4 and 0.5, is revealed by XRD as shown in Fig. 1. It is seen that both $BaTiO_3$ and $CoFe_2O_4$ form in every composites after sintering process which suggests that both constituents behave almost as single phases in composites prepared by mixture of precursors. For $x = 0$ (pure $BaTiO_3$), typical tetragonal perovskite structure (JCPDS file no. 5-0626) was

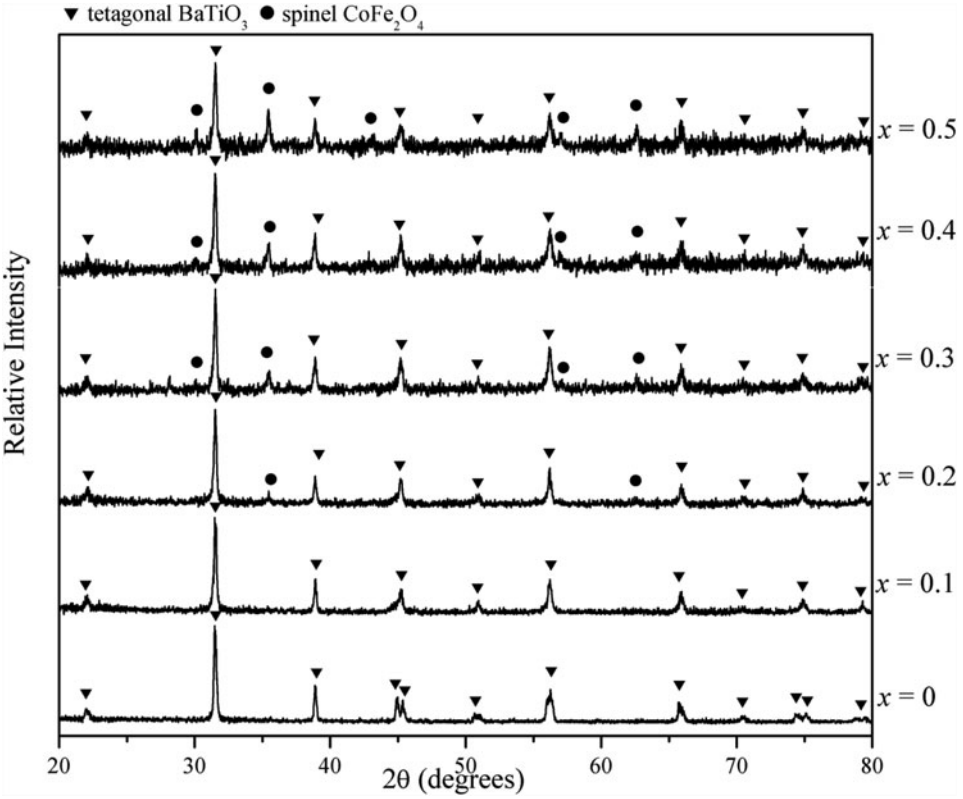

Figure 1. XRD patterns of $BaTiO_3$-$x CoFe_2O_4$ nanocomposites.

formed in this composition with the lattice parameters $a = 4.001$ Å and $c = 4.027$ Å. The tetragonality (c/a) of this $BaTiO_3$ is 1.006. After added $CoFe_2O_4$ into system, XRD graph still shows no evidence of any phase other than that of tetragonal $BaTiO_3$, this was due possibly to the amount of $CoFe_2O_4$ additive being at a very small level and less than the XRD detection limit. With increasing $CoFe_2O_4$ content to $x = 0.2$, XRD peaks show the existence of both cubic spinel $CoFe_2O_4$ (JCPDS file no. 22–1086) and tetragonal perovskite $BaTiO_3$ (JCPDS file no. 5-0626) and the intensity of $CoFe_2O_4$ peaks increase with increasing of x. However, it is well known that $BaTiO_3$ shows different polymorphs depend on their thermodynamic stability. For this system, XRD patterns of ceramics after added $CoFe_2O_4$ additive did not clearly show the splitting of (002)/(200) peaks, which are characteristic of tetragonal $BaTiO_3$. Therefore, these compositions might attribute to the symmetric cubic $BaTiO_3$ (JCPDS file no. 31–0174). The lattice parameters of all samples calculated from XRD data exhibit in Table 1. From the results, it suggests that, after added $CoFe_2O_4$ into system, the lattice parameters slightly change but the c/a value remains constant at 1.007. With increasing $CoFe_2O_4$ content to $x = 0.4$ and 0.5, the c/a value significantly decreases and converges to 1, which confirms the appearance of cubic phase and support assumption about the cubic phase formation in above line. On the other hand, the lattice parameter of $CoFe_2O_4$ phase shows almost constant value. For the crystallite size (D) of samples which also calculated from XRD data (Table 1), after added $CoFe_2O_4$ into system, the crystallite size of $BaTiO_3$ suddenly drops and continuously decreases with increasing of x, whereas

Table 1
Lattice parameters and crystallite size (D) of $BaTiO_3$-$x CoFe_2O_4$ nanocomposites

	$BaTiO_3$				$CoFe_2O_4$	
x	a (Å)	c (Å)	c/a	D (nm)	a (Å)	D (nm)
0	4.001	4.027	1.006	62.5	—	—
0.1	4.005	4.034	1.007	60.8	—	—
0.2	4.006	4.035	1.007	60.2	—	30.4
0.3	4.005	4.034	1.007	60.4	8.39	49.9
0.4	4.007	4.029	1.005	58.7	8.39	58.6
0.5	4.007	4.025	1.004	58.4	8.38	64.0

the crystallite size of $CoFe_2O_4$ increases with increasing of $CoFe_2O_4$ content. Therefore, all results here can suggest that firing process of $BaTiO_3$-$x CoFe_2O_4$ ceramics may affect their microstructures, resulting in different polymorphs in this system. Moreover, the stability of tetragonal structure in ferroelectric-ferrimagnetic composite strongly depends on mechanical boundary conditions of each ceramics because the cubic-tetragonal transition relates to interphase stress which means that firing temperature and microstructural characteristics play an important role in stability of tetragonal cell in composite structure [5, 7].

After sintered all pellets in the temperature range of 1050–1200°C, it is found that the optimum sintering temperature of all compositions is 1150°C. The average value of relative density for all composites is about 95% with 17% of shrinkage and 8% of weight loss. Microstructure development of $BaTiO_3$-$CoFe_2O_4$ nanocomposites is revealed by scanning electron microscope (SEM) and shows in Fig. 2. Pure $BaTiO_3$ ceramic shows highly dense of irregular-shape grains with the maximum grain size of 4.0 μm, minimum grain size of 0.5 μm and the average grain size of about 1.35 μm (Fig. 2(a)). After added $CoFe_2O_4$ into $BaTiO_3$ ceramic ($x = 0.1$), the microstructure is similar to pure $BaTiO_3$ with slightly smaller grains ($\sim$1.30 μm) as seen in Fig. 2(b). Furthermore, with carefully observation, whisker-like shape structure ($\sim$10 nm in width) is clearly seen to distribute and coat over every grains in this composition. With increasing $CoFe_2O_4$ amount, the average grain size of ceramics swings in the same value and the whiskers still appear all over the grains. However, it can noticeably observe that grain morphology of these compositions is more equiaxed than that of pure $BaTiO_3$ (Fig. 2(c) and (d)). Even though exact mechanism of the microstructure observed here is not well established, but it should be noted that the various features of microstructure in $BaTiO_3$-based ceramics are dependent on the grain growth rate in the different planes [8]. However, the sintering process and growth environment also play an important role in the formation [9].

The magnetic measurements for all samples sintered at 1150°C are showed in Fig. 3 and summarized in Table 2. The maximum magnetization (M_{max}) determines from the magnitude of the maximum possible magnetization of a sample, the remanent magnetization (M_r) is the magnitude of the magnetization of a sample when the applied magnetic field is zero and the coercive field (H_C) is the applied field where the overall magnetization of a sample is zero. For pure $BaTiO_3$ ($x = 0$), VSM graph shows linear line which means $BaTiO_3$ exhibits no magnetic property. After added $CoFe_2O_4$ into system, M_{max} and M_r increase with increasing of x due to presence of ferrite phase in the system which can induce magnetic characteristic to the ceramics. When the amount of ferrite increases, the

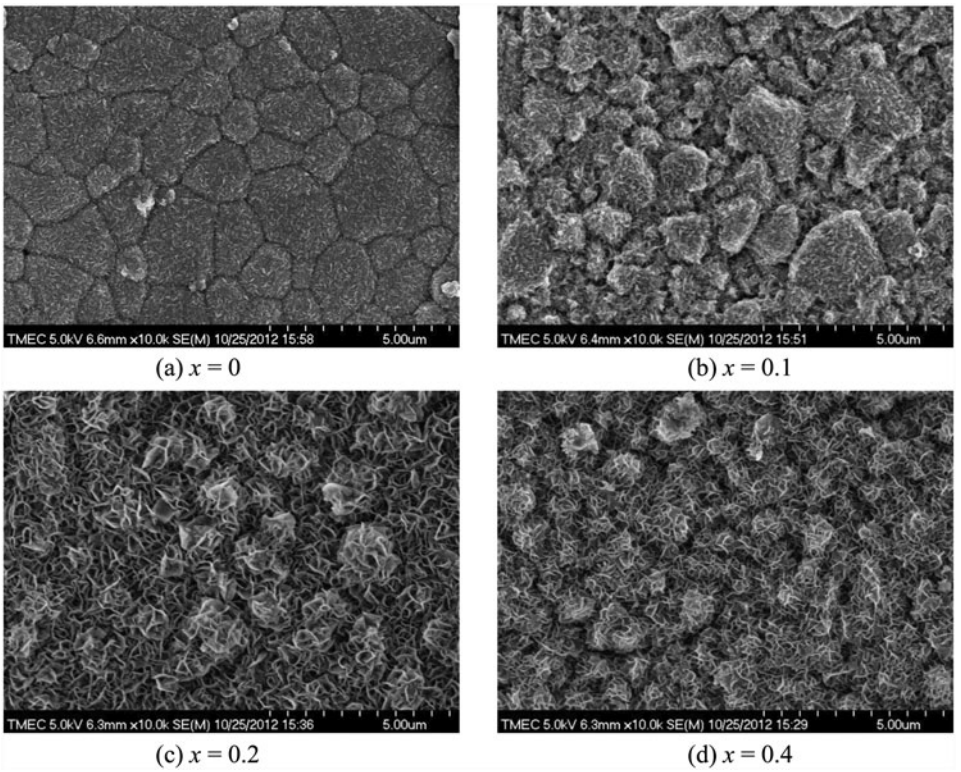

Figure 2. SEM images of $BaTiO_3$-$x CoFe_2O_4$ nanocomposites where $x =$ (a) 0, (b) 0.1, (c) 0.3 and (d) 0.4.

magnetic contacts between grains also increases which leads to higher value of composite magnetization. However, the H_C value does not vary significantly when the amount of $CoFe_2O_4$ increases which can be explained that the agglomeration of ferrite particle may hinder the motion of magnetic domains.

Table 2
Magnetic and dielectric properties of $BaTiO_3$-$x CoFe_2O_4$ nanocomposites

	Magnetic properties			Dielectric properties		
x	M_{max} (emu/g)	M_r (emu/g)	H_C (Oe)	ε_r at 30°C	ε_r at T_C or T_{max}	T_C or T_{max} (°C)
0	—	—	—	3000	3360	129
0.1	3.9	1.4	315	2210	2230	40
0.2	11.3	4.7	408	2860	4020	50
0.3	20.4	9.7	481	1565	—	—
0.4	27.6	13.8	497	1110	—	—
0.5	35.7	18.3	547	830	—	—

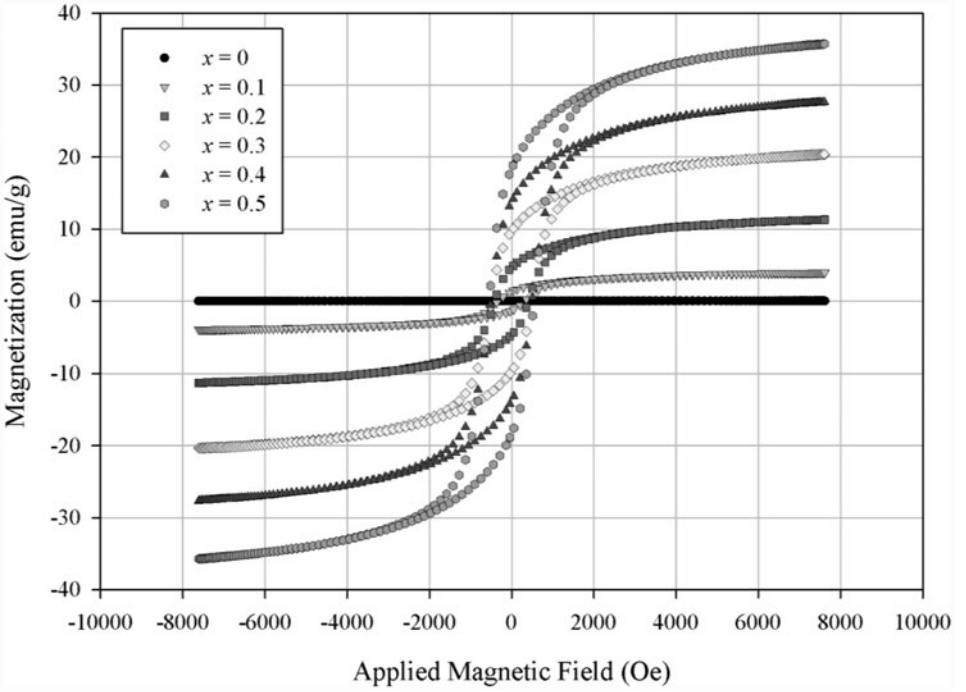

Figure 3. Magnetic hysteresis loops of $BaTiO_3$-$x CoFe_2O_4$ nanocomposites.

Temperature dependence of dielectric constant for $BaTiO_3$-$x CoFe_2O_4$ nanocomposites is revealed in Fig. 4 and dielectric properties are tabulated in Table 2. For $x = 0.0$ (pure $BaTO_3$), the ε_r peak is sharp and approaches 3360 at $T_C \sim 129^\circ$C. Curie point corresponds to transition between ferroelectric and paraelectric phases which lead structure to change from tetragonal to cubic. After added $CoFe_2O_4$ into system, it is seen that ε_r curve becomes broad peak with maximum temperature (T_{max}) at 40°C for $x = 0.1$ and 50°C for $x = 0.2$, respectively. With increase more $CoFe_2O_4$ contents ($x = 0.3$, 0.4 and 0.5), dielectric curves become flat with positive slope, which means that there are no phase transition between ferroelectric and paraelectric here. The dielectric behavior of this system can be explained that since $BaTiO_3$ is high dielectric constant material, while $CoFe_2O_4$ ferrite has a low dielectric constant, thus it affects the ε_r value of composites to decrease in the compositions with higher $CoFe_2O_4$ amount. Moreover, if referred with XRD results above, cubic $BaTiO_3$ is about to occur around these compositions, therefore it is possible that flat curve of dielectric constant may also result from this cubic phase. The ε_r value at room temperature (30°C) also decreases with increasing of x due to reducing of ferroelectric $BaTiO_3$ phase in the composites. For the dielectric loss, the tanδ value hasn't showed significantly change in all compositions, however it should be noted that the dielectric loss of all ceramics increases rapidly at high temperature as a result of thermally activated space charge conduction. From all dielectric data, it can be concluded that the ferroelectricity of $BaTiO_3$-$x CoFe_2O_4$ nanocomposites decreases with increasing of x which effect from magnetism and conductivity of $CoFe_2O_4$ phase.

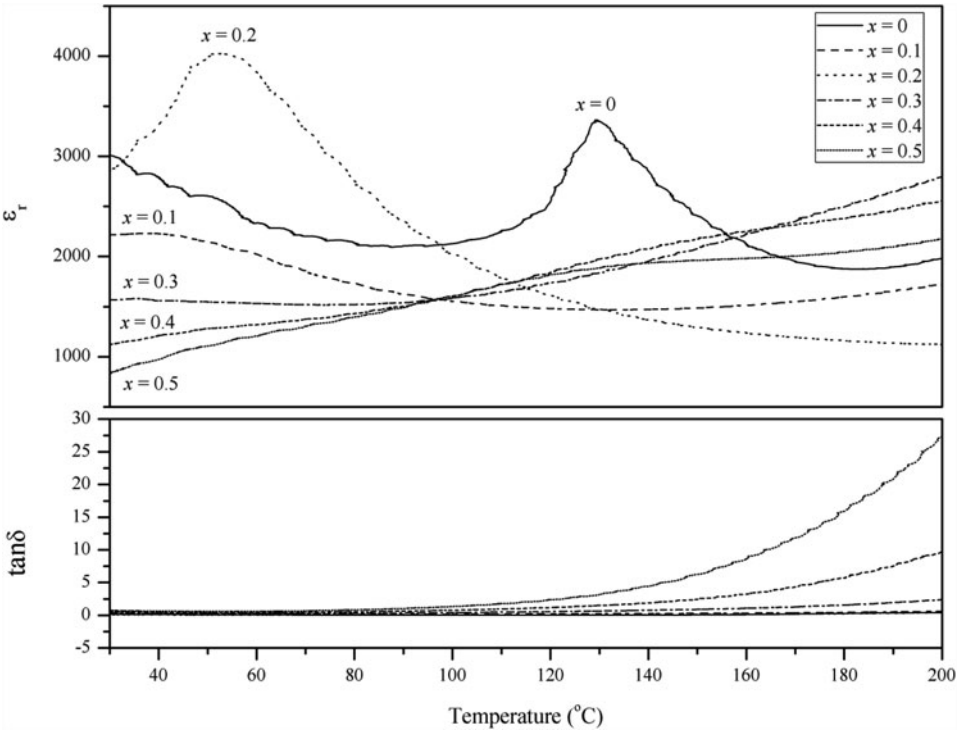

Figure 4. Variation of dielectric constant (ε_r) and dielectric loss ($tan\delta$) with temperature of $BaTiO_3$-$x CoFe_2O_4$ nanocomposites measured at 1 kHz.

4. Conclusions

This work mainly studies on fabrication and properties of $BaTiO_3$-$x CoFe_2O_4$, where x = 0, 0.1, 0.2, 0.3, 0.4 and 0.5, nanocomposites prepared by conventional milling method and followed by normal sintering in air. Phase formation, microstructural development, magnetic and dielectric properties for all ceramics were investigated. The results show that both $BaTiO_3$ and $CoFe_2O_4$ phases form in all nanocomposites after sintering. Highly dense microstructures present in all compositions and whisker-like structure is found to cover all over the grains in $BaTiO_3$-$CoFe_2O_4$ nanocomposites which can explain by various grain growth mechanisms in $BaTiO_3$-based ceramics. Maximum and remanent magnetizations of nanocomposites increase with increasing of x due to presence of ferrite phase in the system. From dielectric results, ferroelectric-paraelectric phase transition is exhibited only at compositions $x = 0$, 0.1 and 0.2.

Acknowledgments

This work has been fully supported by research fund from KMITL research Fund. This research is also partly supported by grants from the National Research Council of Thailand (NRCT) and National Nanotechnology Center (NANOTEC) NSTDA, through its "Center of Excellence Network" Program and the Thailand Research Fund (TRF) under grant number BRG5680006.

References

1. H. Zheng, J. Wang, S. E. Lofland, Z. Ma, L. Mohaddes-Ardabili, T. Zhao, L. Salamanca-Riba, S. R. Shinde, S. B. Ogale, F. Bai, D. Viehland, Y. Jia, D. G. Schlom, M. Wuttig, A. Roytburd, and R. Ramesh, Multiferroic $BaTiO_3$-$CoFe_2O_4$ nanostructures. *Science*. **303**, 661–663 (2004).
2. K. Raidongia, A. Nag, A. Sundaresan, and C. N. R Rao, Multiferroic and magnetoelectric properties of core-shell $CoFe_2O_4$@$BaTiO_3$ nanocomposites. *Appl. Phys. Lett*. **97**, 062904–062903 (2010).
3. N. Dix, V. Skumryev, V. Laukhin, L. Fàbrega, F. Sánchez, J. Fontcuberta, Sputtering growth and characterization of $CoFe_2O_4$-$BaTiO_3$ nanostructures. *Mater. Sci. Eng., B*. **144**, 127–131 (2007).
4. I. Fina, N. Dix, L. Fàbrega, F. Sánchez, J. Fontcuberta, Magnetocapacitance in $BaTiO_3$-$CoFe_2O_4$ nanocomposites. *Thin Solid Films*. **518**, 4634–4636 (2010).
5. L. V Leonel, J. B Silva, A. S Albuquerque, J. D Ardisson, W. A. A. Macedo, N. D. S Mohallem, Structural and Mössbauer investigation on barium titanate–cobalt ferrite composites. *J. Phys. Chem. Solids*. **73**, 1362–1371 (2012).
6. L. M Hrib and O. F Caltun, Effects of the chemical composition of the magnetostrictive phase on the dielectric and magnetoelectric properties of cobalt ferrite–barium titanate composites. *J. Alloys Compd*. **509**, 6644–6648 (2011).
7. L. Mitoseriu and V. Buscaglia, Intrinsic/extrinsic interplay contributions to the functional properties of ferroelectric-magnetic composites. *Phase Transitions*. **79**, 1095–1121 (2006).
8. W. Chaisan, R. Yimnirun, and S. Ananta, Two-stage sintering of barium titanate ceramic and resulting characteristics. *Ferroelectrics*. **346**, 84–92 (2007).
9. R. M German, *Sintering Theory and Practice Place*, Wiley, 1996.

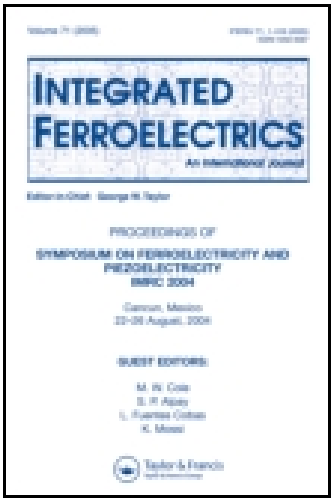

Integrated Ferroelectrics: An International Journal
Publication details, including instructions for authors and subscription information:
http://www.tandfonline.com/loi/ginf20

Synthesis and Characterization of Thermochromic $La_{0.75}Ca_{0.25}MnO_3$ Perovskite Manganites Nano-powders by Microwave-assisted Solution Combustion Synthesis

Sagulthai Kahatta [a], Wicharn Techitdheera [a], Nopsiri Chaiyo [b], Wisanu Pecharapa [b] & Naratip Vittayakorn [b c d]

[a] School of Applied Physics, King Mongkut's Institute of Technology Ladkrabang, Bangkok, 10520, Thailand

[b] College of Nanotechnology, King Mongkut's Institute of Technology Ladkrabang, Bangkok, 10520, Thailand

[c] Advanced Materials Research Unit, Faculty of Science, King Mongkut's Institute of Technology Ladkrabang, Bangkok, 10520, Thailand

[d] Department of Chemistry, Faculty of Science, King Mongkut's Institute of Technology Ladkrabang, Bangkok, 10520, Thailand

Published online: 25 Feb 2014.

To cite this article: Sagulthai Kahatta, Wicharn Techitdheera, Nopsiri Chaiyo, Wisanu Pecharapa & Naratip Vittayakorn (2014) Synthesis and Characterization of Thermochromic $La_{0.75}Ca_{0.25}MnO_3$ Perovskite Manganites Nano-powders by Microwave-assisted Solution Combustion Synthesis, Integrated Ferroelectrics: An International Journal, 150:1, 96-106, DOI: 10.1080/10584587.2014.874821

To link to this article: http://dx.doi.org/10.1080/10584587.2014.874821

Integrated Ferroelectrics, 150:96–106, 2014

ISSN: 1058-4587 print / 1607-8489 online
DOI: 10.1080/10584587.2014.874821

Synthesis and Characterization of Thermochromic $La_{0.75}Ca_{0.25}MnO_3$ Perovskite Manganites Nano-powders by Microwave-assisted Solution Combustion Synthesis

SAGULTHAI KAHATTA,[1] WICHARN TECHITDHEERA,[1] NOPSIRI CHAIYO,[2] WISANU PECHARAPA,[2] AND NARATIP VITTAYAKORN[2,3,4,*]

[1]School of Applied Physics, King Mongkut's Institute of Technology Ladkrabang, Bangkok 10520, Thailand
[2]College of Nanotechnology, King Mongkut's Institute of Technology Ladkrabang, Bangkok 10520, Thailand
[3]Advanced Materials Research Unit, Faculty of Science, King Mongkut's Institute of Technology Ladkrabang, Bangkok 10520, Thailand
[4]Department of Chemistry, Faculty of Science, King Mongkut's Institute of Technology Ladkrabang, Bangkok 10520, Thailand

The microwave-assisted solution combustion synthesis was developed for application with initially synthesized thermochromic perovskite manganese oxide $La_{0.75}Ca_{0.25}MnO_3$ nano-powders. Dry and very fine powders were obtained after one-step combustion reaction for less than 10 min in a modified domestic microwave oven. The thermal behavior, phase formation and purity of the precursor, and as-synthesized and calcined powders, were investigated by TGA/DTA, X-ray diffraction (XRD) and FT-IR techniques. The morphology of the powder obtained was characterized using a scanning electron microscope (SEM). The XRD pattern and FT-IR results showed that as-synthesized $La_{0.75}Ca_{0.25}MnO_3$ powders were crystalline, and the monophasic perovskite phase occurred with an average crystallite size of 30.46 ± 5.54 nm for 6 h at a relatively low calcination temperature of 900°C. The small particle size obtained by SEM suggested a high specific surface area and high sinterability. This method was found to be simple, rapid and cheap, and an effective way to prepare nano-size perovskite powders.

Keywords $La_{0.75}Ca_{0.25}MnO_3$; combustion synthesis; perovskite; manganites

1. Introduction

Combustion synthesis (CS) is an innovative approach to synthetic strategies of solid synthesis. It also is called 'self-propagation high-temperature synthesis' (SHS) and fire or furnace-less synthesis and has been reported as the high-temperature, fast heating rate and short reaction time method [1–2]. It has been used successfully in the preparation of

Received in final form August 10, 2013.
*Corresponding author. E-mail: naratipcmu@yahoo.com

more than 500 oxide and nonoxide compounds with high-purity, metastable phases, and variable sizes and shapes [1–2]. Extensive research, carried out recently, emphasized the capabilities of CS in improving material, saving energy and protecting the environment. CS makes use of highly exothermic redox chemical reactions between metals and nonmetals or reaction involving redox compounds/mixtures [3–4]. Various types of CS reactions that depend on the nature of reactant, i.e. elements or compounds (solid, liquid or gas) and exothermicity (adiabatic temperature, T_{ad}) have been discussed. CS can be described as SHS; low-temperature combustion synthesis (LCS); solution combustion synthesis (SCS); gel-combustion, sol-gel combustion, emulsion combustion, volume combustion (thermal combustion), etc. [1, 5].

SCS is an alternative method (compared to others) recently developed for using redox mixtures (oxidizer-fuel). It was discovered after α–Al_2O_3 foam had been prepared by rapidly heating a solution of aluminum nitrate-urea mixture. Hundreds of oxide materials have been prepared by aqueous solution containing stoichiometric amounts of respective metal nitrate (oxidizer) and fuels like urea, glycine, hydrazide, carbohydrazide, citric acid, oxalyl dihydrazide (ODH), malonic acid dihydrazide (MDH), ethylene diamine tetraacetic acid (EDTA), etc. [1, 6]. A major drawback of ceramic procedure or the conventional solid state method is the diffusion control problem that requires repeated grinding and calcinations for a long duration at high temperatures, which results in large particle sizes, non-homogeneity and presence of impurity [1, 4, 7]. Furthermore, most developed chemical methods, i.e. sol-gel, hydrothermal and citrate-gel techniques, also require high purity, expensive reagents, complicated equipment and a great deal of time [8]. On the other hand, the SCS method prepared oxide materials fast and simply with fine, crystalline, homogeneous, dispersive nano-sized powder and the desired composition/structure [9]. It is already known that microwave heating can be used to prepare crystalline powders [10]. Recently, microwave-assisted CS has been used with high-efficiency to synthesize a variety of narrowly distributed nano-sized inorganic powders in a relatively short period of time when compared to conventional combustion [11–12]. As microwave energy heats whole sample volume at the molecular level, a thermal gradient during processing can be avoided, thus providing a uniform environment for chemical reaction, whereas, conventional heating heats from the outer surface to interior, thus causing thermal gradient and heterogeneous heating [8, 15].

$La_{0.75}Ca_{0.25}MnO_3$ (LCM) is a perovskite-type phase of lanthanum manganese, with the general formula, $La_{1-x}A_xMnO_3$ (a representative divalent cation such as Ca, Sr, Ba, Pb). This manganite family has been attractive material for decades because of its temperature-dependent metal-insulator (MI) phase transitions and colossal magnetoresistance effect (CRM) near phase transition temperature (T_{MI}). This is based on its ability to undergo a reversible structural distortion as a function of temperature. Both electrical conduction and ferromagnetic coupling in these compounds are found to arise from a double exchange process, in which Mn^{3+} and Mn^{4+} ions are coupled by electron exchange via oxygen ions. Recently, thermochromic properties of $La_{1-x}A_xMnO_3$ (A = Ca, Ba) were studied by investigating their temperature-dependent hemispherical emittance [13]. These thermochromic materials are of considerable interest, due to their application in optical switching devices, smart windows, thermal sensors, field-effect transistors, etc. Since novel physical and chemical properties were found to be caused by size scaling; processing and production of nanoparticles have been important scientific challenges and a major research objective over the last few years [9]. Additionally, nanoparticle production, with homogeneous component mixing, was believed to be a precursor available for lower calcination temperature, shorter duration and higher sinterability, and a cost and time saving method

for commercial preparation [14–15]. Generally, these manganite samples are prepared by ceramic techniques actually using oxide, carbonates or hydroxide as sources of La, Ca and Mn ions. These methods possess disadvantages, as mentioned above, and the powder has to be calcined several times [13]. With reference to our previous work, it was found that SCS can synthesize perovskite-type materials successfully in rapid time by using simple laboratory equipment, which results in homogeneous, soft agglomerate nano-size powder through a relatively low calcination temperature [16]. This unique process can prepare a homogeneous reaction product, due to all starting material being mixed in a solution at the molecular level. However, in this study, attention was paid to the composition, $x = 0.25$, since it usually shows both antiferromagnetic (AF) and ferromagnetic (FM) behavior [14]. The perovskite-type compound, $La_{0.75}Ca_{0.25}MnO_3$, was prepared via microwave-assisted SCS, using glycine as a fuel for the first time. Effect of the molar ratio; oxidizer to fuel, and calcination temperature on the formation, size and morphology of LCM particles has been reported.

2. Experimental Procedure

$La_{0.75}Ca_{0.25}MnO_3$ was synthesized via a solution combustion synthesis (SCS). Analytical-grade powders of $La(NO_3)_3{\cdot}6H_2O$, $Ca(NO_3)_2{\cdot}4H_2O$, $MnCO_3$ and glycine (NH_2CH_2COOH 99.7%) were used as starting materials and fuel. On the basis of combustion synthesis, which comes from the thermochemical concept used in the field of propellants and explosives, calculation of the reducing oxidization ratio in the mixture for releasing maximum energy could be performed simply [3, 5]. Since CO_2, H_2O and N_2 were found to be usual products; C and H were considered as reducing elements with the corresponding valencies, +4 and +1. O was deemed to be an oxidizing element with the valency, –2, and N to have a valency of zero. Metals also were considered as a reducing element with the valencies they possessed in the corresponding compound [3, 6, 8]. The total valencies in $La(NO_3)_3{\cdot}6H_2O$, $Ca(NO_3)_2{\cdot}4H_2O$, $MnCO_3$ and glycine were –15, –9, 0 and +9, respectively. Based on the concept of propellant chemistry, the ratio of total oxidizing valencies to reducing valencies should be unified. To satisfy the equivalent stoichiometric ratio, the oxidizer-to-glycine molar ratio was found to be 1:2.7. The combustion reaction can be represented as follows:

$$0.75La(NO_3)_3 \times 6H_2O + 0.25Ca(NO_3)_2 \times 4H_2O + MnCO_3 + 2.78NH_2CH_2COOH + 3.12O_2 \rightarrow La_{0.75}Ca_{0.25}MnO_3 + 12.44H_2O + 2.76N_2 + 6.56CO_2 \quad (1)$$

In this study, the powder characteristics were studied in detail by varying the molar ratio on either side of the stoichiometric ratio, i.e. fuel-deficient ratio (1:2.5) and fuel-rich ratio (1:3.0). It should be noted that this calculation is based on a theoretical reaction equation that neglects all secondary phenomena such as urea hydrolysis and thermal decomposition, as well as nitrate decomposition, which would alter the initial oxidizer-to-glycine molar ratio.

All cation source compounds were dissolved in de-ionized water and stirred by magnetic stirrer. Glycine was then added into the nitrate solution under continuous stirring. The precursor solution was heated using a modified domestic microwave oven inside a fume-cupboard under ventilation. Evaporation then occurred and the solution became dry. While the exothermic redox reaction was taking place, the temperature reached a point when ignition could arise. The temperature rapidly increased and resulted in self-sustaining

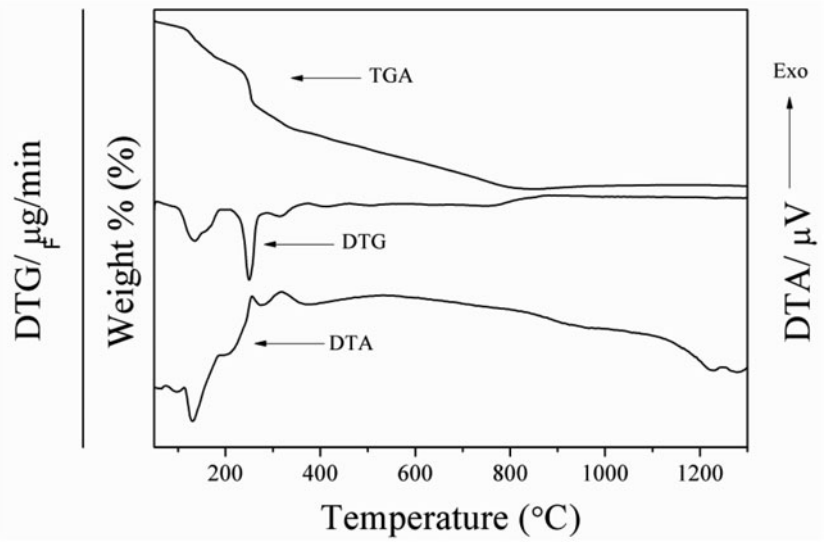

Figure 1. TGA/DTG/DTA curves of the precursor mixed in the stoichiometric proportion of $La_{0.75}Ca_{0.25}MnO_3$.

combustion, with rapid evolution of a large volume of gas products and voluminous powder. For investigating thermal behaviour of the precursor, the mixture of starting material was determined using thermo gravimetric analysis (TGA) and differential thermal analysis (DTA). The X-ray diffraction (XRD, Advance D8) technique was carried out on the combustion synthesized powder, using Ni-filtered CuK_α radiation for phase identification and mean crystalline size estimation. The final powder product was characterized by using the Fourier transform infrared (FTIR, Perkin-Elmer Spectrum GX spectrometer) technique and scanning electron microscope (SEM, JEOL JSM-6335F).

3. Results and Discussion

Figure 1 shows the TGA/DTG/DTA curves of the stoichiometric precursor for $La_{0.75}Ca_{0.25}MnO_3$ powder preparation. From observations of the TGA curve, there appeared to be multi-stages of weight loss from room temperature to 1,300°C. A 20% weight loss was observed as the temperature rose to 200°C, which corresponded to the first endothermic peak of the DTA and DTG curve, centered at about 130°C. This range of mass loss could indicate the release of water molecules that are lost from starting hydrated reagent. When raising the temperature to over 200°C, a significant weight loss was observed. This drastic weight loss was matched to the exothermic peak of the DTA and DTG curve, centered at about 250°C. As the heat increased, weight loss continued until the temperature reached 800°C. The overall weight loss was found to be about 78%, which is close to the theoretical value of 73% that corresponds to the release of H_2O, N_2 and CO_2 related to Eq. (1). The initial temperature (T_{in}) of the reaction was reported as the point when the sample weight begins to change quickly during the chemical reaction [6]. Hence, T_{in} of this reaction could be expected at around the temperature of 200°C. This result supported our idea that a microwave oven can be used as a heating source, which is capable of initiating combustion reaction.

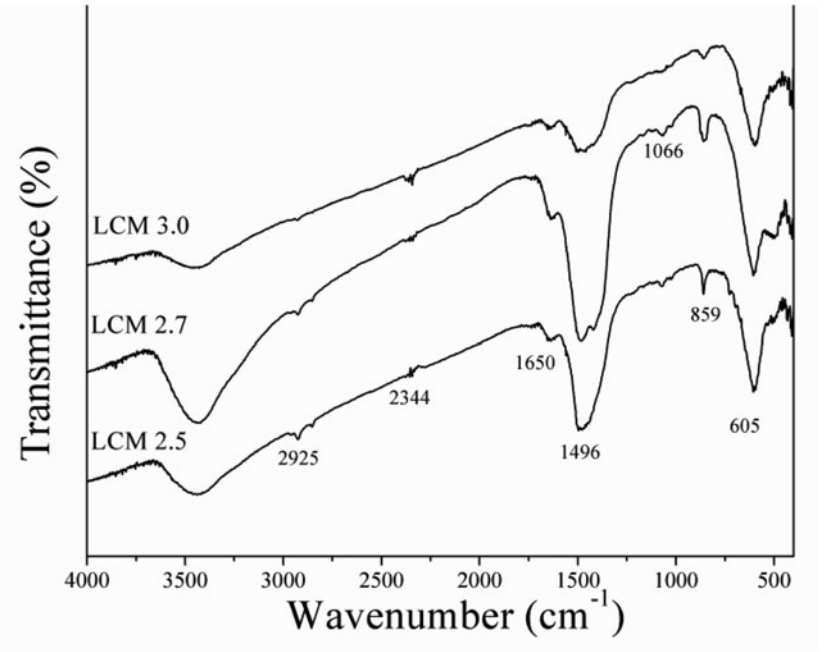

Figure 2. FT-IR spectra of the as-synthesized $La_{0.75}Ca_{0.25}MnO_3$ powders prepared using different oxidizer-to-glycine molar ratios.

Figure 2 illustrates the FTIR spectra of the as-synthesized $La_{0.75}Ca_{0.25}MnO_3$ powders with a different oxidizer-to-glycine molar ratio. A broad peak at ~3,450 cm^{-1} and small peak at ~2,340 cm^{-1} and ~1,650 cm^{-1} correspond with anti-symmetric stretching (ν_{OH}), symmetric stretching (ν_{OH}), and bending (δ_{OH}) vibrations of the surface-adsorbed water and oxygen species [17]. The shoulder bands at ~2,925 cm^{-1} and ~2,850 cm^{-1} are attributed to the stretching vibrations of C—H bond. The characteristic band at ~1,500 cm^{-1} is matched with the anti-symmetric stretching COO^- group [18]. Glycine, which was used as fuel in solution combustion synthesis (SCS), is the simplest amino acid and has a carboxyl, methylene and an amino group ($H_2N—CH_2—COOH$). It was reported that dissolved glycine can reveal the changes in covalent bond strength with rising temperature, for instance, when the N—H bonds of NH_3^+ become stronger; structure of the COO^- group becomes asymmetric; and strength of the C—C and C—N bond becomes weaker, resulting in three sections being divided according to their functional group, i.e. $—NH_3^+$, $—COO^-$ and $>CH_2$. Since FT-IR bands belonging to $—COO^-$ and $>CH_2$ were observed, as mentioned above, the $—NH_3^+$ band also could be detected. However, when considering FTIR spectra, the $–NH_3^+$ stretching vibration band and asymmetric deformation could not be found at ~3,050 cm^{-1} and ~1,500 cm^{-1}, due to these bands being very weak and strongly overlapped with an anti-symmetric stretching band of water molecule and COO^- asymmetric stretching band, respectively. Weak band peaking at ~1,066 cm^{-1} and ~860 cm^{-1} corresponded to stretching of the C—O bond and anti-symmetric NO_3^{-1} bending vibration, respectively. When considering the NO_3^{-1} functional group, which possesses anti-symmetry stretching vibration at ~1,385 cm^{-1}, this spectral band could not be observed clearly, due to the COO^- asymmetric stretching band being overlapped. Therefore, all functional groups

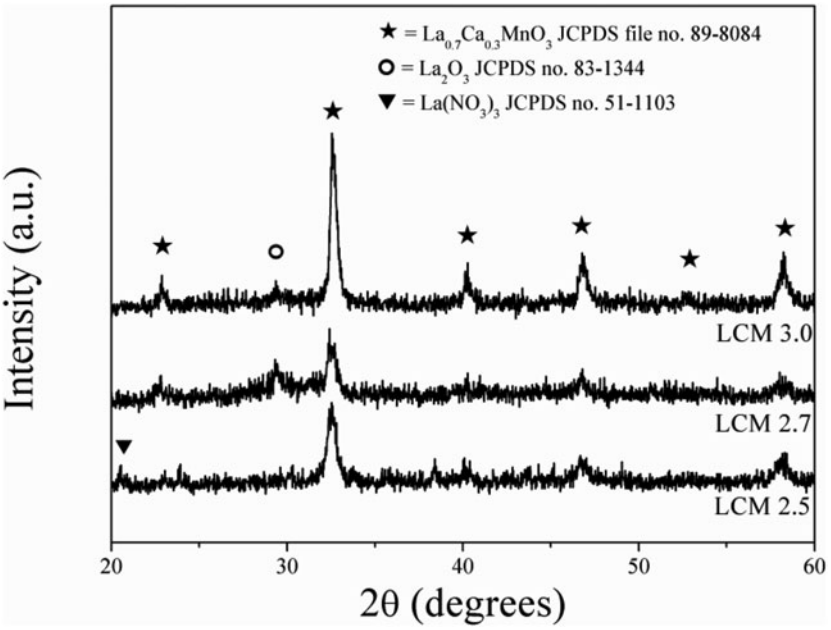

Figure 3. X-ray diffraction patterns of as-synthesized $La_{0.75}Ca_{0.25}MnO_3$ powders with different oxidizer-to-glycine molar ratios.

apparently indicated traces of starting compound in as-synthesized products. Nonetheless, the IR spectra band centred at ~600 cm^{-1} was identified as the characteristic band of M-O (M = Mn) and believed to be the vibration (ν_3) mode in the corner-shared MO_6 (M = metal) octahedron. This observation might suggest perovskite phase formation of $La_{0.75}Ca_{0.25}MnO_3$.

Figure 3 shows the XRD patterns of as-synthesized $La_{0.75}Ca_{0.25}MnO_3$ powders prepared through a different oxidizer-to-glycine molar ratio. The XRD patterns clearly indicate that the perovskite $La_{0.75}Ca_{0.25}MnO_3$ phase was formed for all oxidizer-to-glycine molar ratio conditions. These patterns corresponded to the standard JCPDS file no. 89-8084, with orthorhombic crystal structure, space group Pnma(62), and peaks that were indexed (★). Thus, it can be suggested that this single-step microwave-assisted SCS is capable of producing $La_{0.75}Ca_{0.25}MnO_3$ powder. Regarding the fuel-deficient ratio (1:2.5), a small peak corresponding to $La(NO_3)_3$ JCPDS file no. 52-1103 was observed at 2θ~20° (▼). This could indicate that the trace of starting material remaining in the powder product was due to incomplete reaction caused by the lack of fuel. This XRD result was found to match an FT-IR spectroscopic study, in which an anti-symmetric NO_3^{-1} bending vibration band was detected at ~860 cm^{-1}, as mentioned above. Regarding a higher fuel ratio (1:2.7 and 1:3.0), an $La(NO_3)_3$ peak was found to disappear, while a small peak that could be matched with La_2O_3 JCPDS file no. 83-1344 was observed at 2θ~29° (○). Formation of the La_2O_3 phase might occur from the result of energy released from exothermic redox reaction [19]. Nevertheless, when considering the crystallinity of a product from XRD patterns, using a fuel-rich ratio (1:3.0), the result in a well crystalline peak can be compared to the equivalent stoichiometric ratio (1:2.7), which shows higher intensity and sharper peaks. Furthermore, a relatively low amount of pyrochlore La_2O_3 phase also was detected in the fuel-rich ratio (1:3.0) powder product. Therefore, to optimize the fine nucleation condition of the

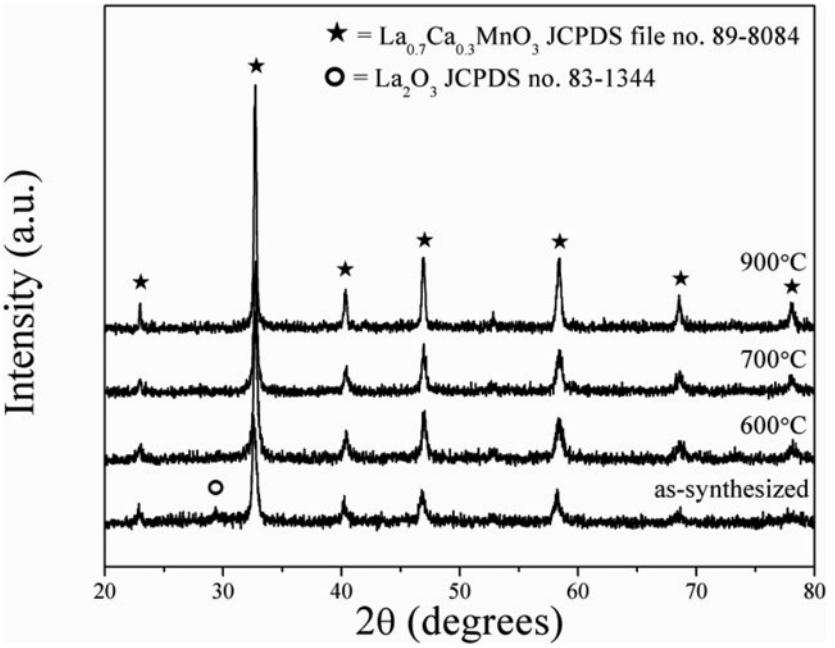

Figure 4. X-ray diffraction patterns of $La_{0.75}Ca_{0.25}MnO_3$ powder (using an oxidizer-to-glycine molar ratios of 3.0) calcined at various temperatures for 6 h with a heating/cooling rate of 20°C /min.

monophasic $La_{0.75}Ca_{0.25}MnO_3$ phase, the fuel-to-oxidizer molar ratio of 3.0 was selected to investigate the effect of calcination temperature on evolution of the perovskite phase.

Thus, the as-prepared powder was calcined at different temperatures for 6 h with a heating/cooling rate of 20°C/min. The X-ray diffraction (XRD) patterns of $La_{0.75}Ca_{0.25}MnO_3$ powder, calcined for 6 h at different temperatures, are illustrated in Fig. 4. Perovskite $La_{0.75}Ca_{0.25}MnO_3$ phase was seen to occur in all samples. The diffraction peak corresponded to the pyrochlore La_2O_3 phase, which was detected in as-prepared powder and seen to disappear after 6 h of calcination in at least 600°C, whereas monophasic perovskite $La_{0.75}Ca_{0.25}MnO_3$ phase was obtained (100% yield within the limitations of the XRD technique). Nonetheless, the powders calcined from 600°C to 900°C showed diffraction peaks that could correspond to the orthorhombic $La_{0.75}Ca_{0.25}MnO_3$ perovskite phase JCPDS file no. 89-8084 (★). Amplified peak intensities can be seen after calcinations at increased temperatures, which could refer to a relatively high crystallinity of the powder obtained. This is confirmed by the calculation of crystalline size (D), as described below.

The above results suggested that the perovskite $La_{0.75}Ca_{0.25}MnO_3$ powder could be synthesized by using the microwave-assisted SCS process, which was discovered as a simple, time-saving, energy-intensive and cost-effective method when compared with the traditional solid-state reaction that requires repeated grinding, more time and higher temperature [1, 6– 8]. However, for confirmation of the synthesized monophasic perovskite $La_{0.75}Ca_{0.25}MnO_3$ phase, all calcined powders were investigated using FT-IR spectroscopic studies. Figure 5 shows the FT-IR spectra of the crystalline $La_{0.75}Ca_{0.25}MnO_3$ obtained after combustion synthesis, and powder calcined at different temperatures for 6 h. As mentioned above, the FT-IR spectra band of the $-COO^-$, $>CH_2$ and NO_3^{-1} functional groups, which belong to starting reagents and fuel, was shown in as-prepared $La_{0.75}Ca_{0.25}MnO_3$ powders

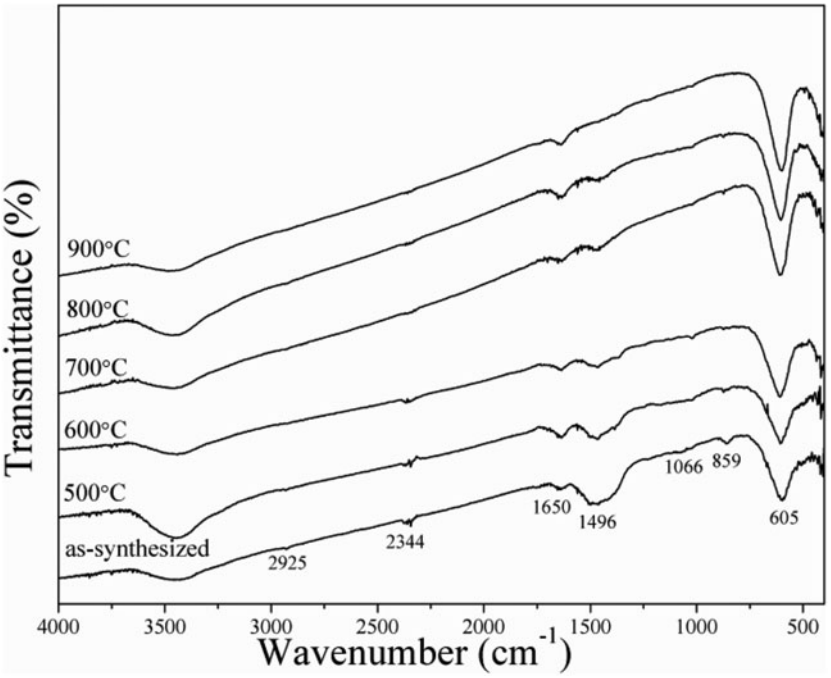

Figure 5. FT-IR spectra of the $La_{0.75}Ca_{0.25}MnO_3$ powders (using an oxidizer-to-glycine molar ratio of 3.0) calcined at various temperatures for 6 h with a heating/cooling rate of 20°C /min.

for all fuel-to-oxidizer molar ratios. After calcination in the range of 600°C to 800°C, IR bands were found also in $La_{0.75}Ca_{0.25}MnO_3$ powders. This notification demonstrated that powder calcined at 600°C was not a monophasic perovskite $La_{0.75}Ca_{0.25}MnO_3$ phase. Nevertheless, the XRD pattern (Fig. 4) showed that powder calcined at 600°C corresponded to the monophasic perovskite $La_{0.75}Ca_{0.25}MnO_3$ phase. The contrast could occur due to limitations of the XRD technique, from which only the crystalline phase can be detected. Thereby, the combination of XRD and FT-IR results can demonstrate that the monophasic perovskite $La_{0.75}Ca_{0.25}MnO_3$ phase was obtained after 6 h of calcination at 900°C. This calcination temperature was found to be lower than that when using conventional solid-state reaction. In addition, this microwave-assisted SCS was a novel single-step method, which required no re-ground or re-calcination step [13].

Since the XRD investigation of $La_{0.75}Ca_{0.25}MnO_3$ powder suggested an orthorhombic crystal structure, the calculation of lattice parameters could be performed by means of the Unit Cell program package [20]. The consequent cell parameters, which are close to those reported in JCPDS file No. 89-8084 ($a = 5.465$ Å, $b = 7.726$ Å and $c = 5.482$ Å), are given in Table 1. The suggested orthorhombic crystal structure, obtained from matching with the JCPDS file, could be supported by this correlation of lattice parameters. Nonetheless, from the reflection peak, the average crystalline size (D) of $La_{0.75}Ca_{0.25}MnO_3$ powders was considered as a function of fuel content and calcination temperature by using X-ray line broadening through Scherrer's equation [21].

$$D = \frac{k\lambda}{\beta \cos\theta_B} \tag{2}$$

Table 1

Lattice parameters of the $La_{0.75}Ca_{0.25}MnO_3$ powder prepared using different oxidizer-to-glycine molar ratios and calcined at various temperatures for 6 h with a heating/cooling rate of 20°C /min

Compound	Method	*a* (Å)	*b* (Å)	*c* (Å)
$La_{0.7}Ca_{0.3}MnO_3$	JCPDS # 83–1344	5.465	7.726	5.482
$La_{0.75}Ca_{0.25}MnO_3$ in this work				
As-prepared	Fuel-to-oxidant molar ratios			
	2.5	5.486 ± 0.018	7.802 ± 0.061	5.566 ± 0.088
	2.7	5.517 ± 0.010	7.784 ± 0.109	5.616 ± 0.164
	3.0	5.496 ± 0.031	7.771 ± 0.023	5.516 ± 0.033
Calcined powders (3.0)	Calcination temperature (°C)			
	600°C	5.431 ± 0.045	7.731 ± 0.003	5.471 ± 0.004
	700°C	5.462 ± 0.025	7.731 ± 0.001	5.473 ± 0.002
	900°C	5.465 ± 0.008	7.736 ± 0.001	5.471 ± 0.002

where D is the average crystalline size, k a constant taken as 0.89, λ the wavelength of X-ray radiation, β the full width at half maximum (FWHM) and θ_B the diffraction angle. However, when powder samples were used, the XRD peak broadened, due to mechanical strain, instrument error and other sources that were ignored in this calculation. The consequent values are reported in Table 2. As the fuel content increased, the average crystalline size (D) was found to increase from 12.14 ± 1.45 nm (ratio of 2.5) to 17.53 ± 2.19 nm (ratio of 3.0). This suggested that elevated fuel content could lead to the production of a higher crystalline size of powder. In addition, as the calcination temperature increased, a higher crystalline size from 20.21 ± 0.82 to 30.46 ± 5.54 also was found. This can imply that calcination temperature also plays an important role in developing the pure phase creation [15] as commonly observed from the amplified XRD peak intensities, which can be seen after calcinations at increased temperatures.

Table 2

Average crystalline sizes, D, of the $La_{0.75}Ca_{0.25}MnO_3$ powder using different oxidizer-to-glycine molar ratios and calcined at various temperatures for 6 h with a heating/cooling rate of 20°C /min

D (nm)	Fuel-to-oxidant molar ratios		
As-prepared	2.5	2.7	3.0
	12.14 ± 1.45	14.51 ± 0.53	17.53 ± 2.19
	Calcination temperature (°C)		
Calcined powders (3.0)	600°C	700°C	900°C
	20.21 ± 0.82	21.37 ± 1.38	30.46 ± 5.54

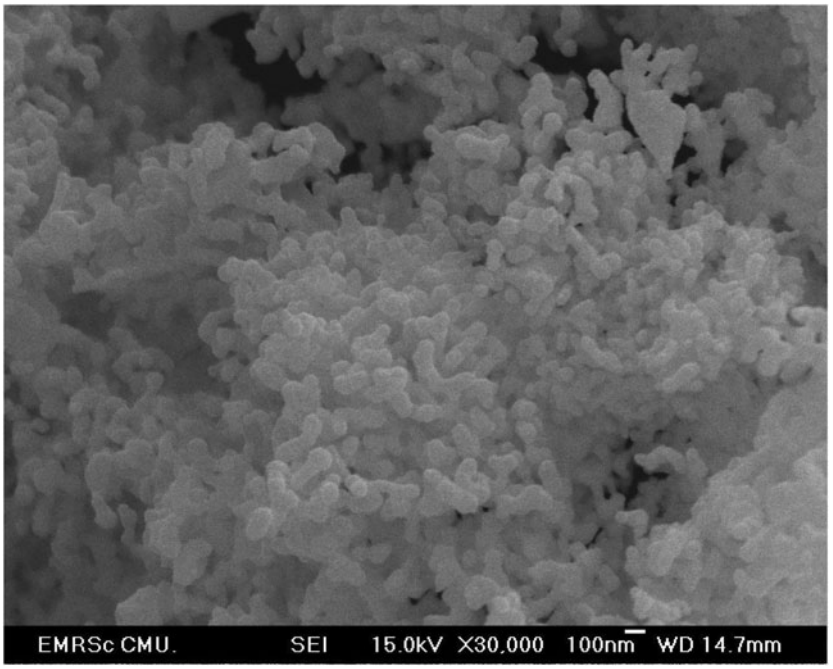

Figure 6. SEM micrograph of $La_{0.75}Ca_{0.25}MnO_3$ powders synthesized using an oxidizer-to-glycine molar ratio of 3.0.

Figure 6 shows a scanning electron microscope (SEM) micrograph of crystalline $La_{0.75}Ca_{0.25}MnO_3$ powder prepared by using the fuel-to-oxidizer molar ratio of 3.0, and calcined at 800°C for 6 h. The SEM micrograph shows powder with a spongy-like structure and uniform features. No evidence of a different or pyrochlore phase was found, which suggested the homogeneous character of the prepared powder. This spongy-like structure could result from a combination of small individual particles of average particle size, estimated from micrographs of around 100 nm. These particle size values are greater than the average crystalline size calculated from X-ray line broadening, because a particle can be formed generally from many crystallites.

4. Conclusion

A microwave-assisted solution combustion synthesis (SCS) using metal nitrates and glycine was found to enable synthesis of thermochromic perovskite manganese oxide $La_{0.75}Ca_{0.25}MnO_3$ nano-powders, with an average crystalline size (D) of 12.14 ± 1.45 nm to 30.46 ± 5.54 nm. Higher crystalline size was found to be influenced by increasing fuel content and calcination temperature. This method proved production of a nano-sized, homogeneous and stoichiometric controllable product, with a rapid, simple and an energetically economic process. Monophasic perovskite $La_{0.75}Ca_{0.25}MnO_3$ phase was obtained after 6 h of calcination at the relatively low temperature of 900°C, when compared to the conventional solid-state reaction method. A scanning electron microscope (SEM) image showed a spongy-like powder rising from a small individual particle that possessed a size of around 100 nm.

Funding

This work has been fully supported by the Thailand Research Fund (Grant No. BRG5680006).

References

1. K. C. Patil, S. T. Aruna, and S. Ekambaram, Combustion synthesis. *Curr Opin Solid State Mater Sci*. **2**, 158–165 (1997).
2. S. T. Aruna, and A. S. Mukasyan, Combustion synthesis and nanomaterials. *Curr Opin Solid State Mater Sci*. **12**, 44–50 (2008).
3. A. Civera, M. Pavese, G. Saracco, and V. Specchia, Combustion synthesis of perovskite-type catalysts for natural gas combustion. *Catal Today.* **83**, 199–211 (2003).
4. V. C. Sousa, A. M. Segadães, M. R. Morelli, and R. H. G. A. Kiminami, Combustion synthesized ZnO powders for varistor ceramics. *Int J Inorg Mater.* **1**, 235–241 (1999).
5. K. C. Patil, S. T. Aruna, and T. Mimani, Combustion synthesis: an update. *Curr Opin Solid State Mater Sci*. **6**, 507–512 (2002).
6. C. C. Hwang, T. Y. Wu, J. Wan, and J. S. Tsai, Development of a novel combustion synthesis method for synthesizing of ceramic oxide powders. *Mater Sci Eng*. **B 111**, 49–56 (2004).
7. X. H. Zuo, X. Y. Deng, Y. Chen, M. Ruan, W. Li, B. Liu, Y. Qu, and B. Xu, A novel method for preparation of barium strontium titanate nanopowders. *Mater Lett*. **64**, 1150–1153 (2010).
8. I. Ganesh, R. Johnson, G. V. N. Rao, Y. R. Mahajan, S. S. Madavendra, and B. M. Reddy, Microwave-assisted combustion synthesis of nanocrystalline $MgAl_2O_4$ spinel powder. *Ceram Int*. **31**, 67–74 (2005).
9. S. V. Chavan, P. U. M. Sastry, and A. K. Tyagi, Combustion synthesis of nano-crystalline Nd-doped ceria and Nd_2O_3 and their fractal behavior as studied by small angle X-ray scattering. *J Alloys Compd*. **456**, 51–56 (2008)
10. P. D. Pamesh, B. Vaidhyanathan, M. Ganguli, and K. J. Rao, Synthesis of SiC powder by use of microwave radiation. *J Mater Res*. **9**, 3025–3027 (1994)
11. R. H. G. A. Kiminami, M. R. Morelli, D. C. Folz, and D. E. Clark, Microwave synthesis of alumina powders. *Bull Am Ceram Soc*. **79**, 63–67 (2000).
12. H. Mohebbi, T. Ebadzadeh, and F. A. Hesari, Synthesis of nano-crystalline NiO-YSZ by microwave-assisted combustion synthesis. *Powder Tech*. **188**, 183–186 (2009)
13. G. Tang, Y. Yu, W. Chen, and Y. Cao, Thermochromic properties of manganese oxides $La_{1-x}A_xMnO_3$ (A = Ca, Ba). *Mater Lett*. **62**, 2914–2916 (2008)
14. T. Yi, S. Gao, X. Qi, Y. Zhu, F. Cheng, B. Ma, Y. Huang, C. Liao, and C. Yan, Low temperature synthesis and magnetism of $La_{0.75}Ca_{0.25}MnO_3$ nanoparticles. *J Phys Chem Solids*. **61**, 1407–1413 (2000).
15. N. Chaiyo, B. Boonchom, and N. Vittayakorn, Solid-state reaction synthesis of sodium niobate ($NaNbO_3$) powder at low temperature. *J Mater Sci*. **45**, 1443–1447 (2010).
16. N. Chaiyo, R. Muanghlua, S. Niemcharoen, B. Boonchom, and N. Vittayakorn, Solution combustion synthesis and characterization of lead-free piezoelectric sodium niobate ($NaNbO_3$) powders. *J Alloys Compd*. **509**, 2304–2310 (2011).
17. B. Boonchom, and N. Vittayakorn, Dehydration Behavior of Synthetic $Al_{0.5}Fe_{0.5}PO_4{\cdot}2.5H_2O$. *J Chem Eng Data*. **55**, 3307–3311 (2010).
18. C. Weifan, L. Fengsheng, L. Leili, and L. Yang, One- Step Synthesis of Nanocrytalline Perovskite $LaMnO_3$ Powders via Microwave-Induced Solution Combustion Route. *J Rare Earths*. **24**, 782–787 (2006).
19. D. Jiawen, W. Yanli, S. Weili, and L. Yongxiu, Preparation of $La(OH)_3$ and La_2O_3 with Rod Morphology by Simple Hydration of La_2O_3. *J Rare Earths*. **24**, 440–442 (2006).
20. ftp://rock.esc.cam.ac.uk/pub/minp/UnitCell/
21. H. P. Klug, and L. E. Alexander, *X-ray Diffraction Procedure of Polycrystalline and Amorphous Materials*, Jonh Wciley & Sons, New York. 1974.

Journal of Materials Chemistry C

PAPER

Phase transition behavior of $Ba(Mg_{1/3}Nb_{2/3})O_3$ modified $PbZrO_3$ solid solution

Cite this: J. Mater. Chem. C, 2014, 2, 2929

Usa Sukkha,[ac] Naratip Vittayakorn,*[abc] Ruyan Guo[d] and Amar S. Bhalla[d]

Received 28th November 2013
Accepted 30th January 2014

DOI: 10.1039/c3tc32353f

www.rsc.org/MaterialsC

Different compositions of $(1-x)PbZrO_3$–$xBa(Mg_{1/3}Nb_{2/3})O_3$ (PZ–BMN) system, with $x = 0.00$–0.50, were synthesized using the columbite precursor method. The effects of BMN content on phase transition, electrical and thermal properties of $PbZrO_3$ ceramic were investigated. The composition range and stability of the ferroelectric phase in perovskite PZ–BMN system can be improved by optimizing BMN substitution. Phase transition behavior of various solid solutions of PZ compositions can be predicted by a phase diagram established from the average electronegativity difference *versus* tolerance factor of the end members.

1. Introduction

Antiferroelectric (AFE) materials are interesting because of their properties, which include giant electrocaloric effects[1] or high electrostriction.[2] AFE materials can be used in a wide range of applications such as high energy storage capacitors, electrocaloric refrigerators and high strain actuators and transducers. Extensive investigations concerning AFE materials, both experimental and theoretical, have been reported.[3] Lead zirconate ($PbZrO_3$, PZ) was the first compound to be identified as an AFE material.[3,4] Both pure and compositionally modified PZ have been studied. PZ is orthorhombic at room temperature[5] and has an orthorhombic AFE to cubic paraelectric (PE) phase transition at 236 °C, and a sandwiched rhombohedral ferroelectric phase (FE) exists over a very narrow temperature range (233–236 °C).[3–6] It is well known that at room temperature the AFE to FE phase transition in PZ ceramic requires a strong electric field; otherwise dielectric breakdown occurs. In order to modify the critical field and control physical and electrical properties, many research groups have investigated the substitution of metal oxides into the PZ structure.[3,6–8] They have reported that the stability of the FE phase in PZ can also be altered by various substitutions at the A-site or B-site of the perovskite structure (ABO_3). For example, the FE phase of PZ can be stabilized by adding Ba^{2+}, Sr^{2+} and La^{3+} at the A-site, and $Ti^{4+}$and Sn^{4+} at the B-site.[7] Tan *et al.* proposed that the FE phase can be stabilized by substitution with larger ions at the A-site, or smaller ones at the B-site, whereas, the AFE phase can be stabilized by substitution with smaller ions at the A-site, or larger ones at the B-site.[9] Recently, the present group was able to control the FE phase in PZ by substitution of the perovskite structure at the B-site by combining PZ and relaxor ferroelectric (RFE) compositions to get PZ–PNN, PZ–PZN and PZ–PCoN;[10–12] and order–disorder ferroelectric compositions to obtain PZ–PIN and PZ–PYbN;[13,14] and antiferroelectric compositions to synthesize PZ–PMW and PZ–PYN.[15,16] Also, an alternative FE phase was synthesized with replacement of ions at both the A-site and B-site in the PZ structure by combining PZ with $BiAlO_3$ and $Ba(Al_{1/2}Nb_{1/2})O_3$.[17,18] Furthermore, it was found that if the tolerance factor, t, of the solid solution is higher than pure PZ, the FE phase can be induced, while the AFE phase is stabilized when the t value of the solid solution is lower than that of pure PZ.[18] However, it cannot explain why PNW and NN, which tend to have t values higher than that of pure PZ, fail to induce the FE intermediate phase of PZ.[19,20] Thus, tolerance factor is perhaps not the only aspect to be considered for the prediction of phase transitions in the PZ system. Although the ferroelectricity of materials cannot be predicted by the average electronegativity difference ($\bar{\chi}$) alone, it has been reported that ferroic behavior in both pure and complex perovskites can be separated when plotted as t value *versus* $\bar{\chi}$.[21] It was found that many unstable complex perovskites, which had low t and $\bar{\chi}$, exhibited relaxor ferroelectric behavior. Thus, the average electronegativity difference of each end member may be another factor for considering prediction of phase transitions in $PbZrO_3$:mixed oxide based ceramics.

Barium magnesium niobate [$Ba(Mg_{1/3}Nb_{2/3})O_3$; BMN] is a lead-free complex perovskite, which has been of interest as a candidate microwave dielectric material, because BMN has a high dielectric permittivity of 32 and very low dielectric loss tangent ($Q = 5600$, where $Q = 1/\tan\delta$) at room temperature.[22–24]

[a]*Electroceramic Research Laboratory, College of Nanotechnology, King Mongkut's Institute of Technology Ladkrabang, Bangkok 10520, Thailand*

[b]*Department of Chemistry, Faculty of Science, King Mongkut's Institute of Technology Ladkrabang, Bangkok 10520, Thailand. E-mail: naratipcmu@yahoo.com; Fax: +66-2-326-4415*

[c]*Advanced Materials Research Unit, Faculty of Science, King Mongkut's Institute of Technology Ladkrabang, Bangkok 10520, Thailand*

[d]*Department of Electrical and Computer Engineering, College of Engineering, University of Texas at San Antonio (UTSA), San Antonio, Texas 78256, USA*

In the solid solution, $(1-x)Ba(Mg_{1/3}Nb_{2/3})O_3$–$xPbTiO_3$, it is found that at room temperature the morphotropic phase boundary is located in the composition range from $x = 0.71$ to 0.74. Additionally, relaxor ferroelectric behavior has been shown in the composition 0.4BMN–0.6PT and a high dielectric permittivity of ~4000 at T_{max} close to room temperature was observed.[25,26] There are no reports on the solid solution of AFE PZ and microwave dielectric BMN. This work deals with the binary system of $(1-x)PbZrO_3$–$xBa(Mg_{1/3}Nb_{2/3})O_3$, where substitution is considered at both A-site and B-site, in order to obtain more information concerning the combination of AFE PZ and microwave dielectric material. In addition, the lead content is also reduced when compared with the PZ–PMN, PZ–PZN, PZ–PCoN and PZ–PNN solid solution compositions. The influences of BMN on crystal structure, phase transition behavior and thermal, dielectric and ferroelectric properties of PZ–BMN solid solution are investigated. Furthermore, the average electronegativity difference of the end members in relation to the tolerance factor is discussed for predicting the phase transition of PZ:mixed oxide based ceramics.

2. Experimental procedure

Ceramics of the $(1-x)PbZrO_3$–$xBa(Mg_{1/3}Nb_{2/3})O_3$ system, where $x = 0.00$, 0.02, 0.04, 0.06, 0.08, 0.10, 0.20, 0.30, 0.40 and 0.50, were prepared *via* the columbite precursor method. High purity (>99.0%) PbO, ZrO_2, $BaCO_3$, MgO and Nb_2O_5 were used as the starting materials. The columbite precursor, $MgNb_2O_6$, was synthesized first by mixing MgO and Nb_2O_5 in ethanol and ball milling for 18 h, then mixed powders were calcined at 1100 °C for 2 h at a heating/cooling rate of 5 °C min^{-1}. The columbite precursor was then mixed with PbO, ZrO_2 and $BaCO_3$ by ball milling and calcined at 850–900 °C for 4 h at a heating/cooling rate of 5 °C min^{-1} in order to obtain the desired composition of $(1-x)$PZ–xBMN. All compositions of $(1-x)$PZ–xBMN powders were ball milled again for 18 h and subsequently ground and sieved to reduce the particle size. The calcined powders were pressed into a pellet using 5 wt% polyvinyl alcohol (PVA) binder to facilitate pressing. After binder decomposition at 500 °C for 2 h, the pellets were sintered at temperatures between 1200 and 1250 °C, depending on the composition, for 4 h. In order to reduce lead loss in the ceramics during sintering, the pellets were submerged in $PbZrO_3$ powder. All crystal structure compositions of sintered ceramics were characterized using an X-ray diffractometer (XRD; Bruker-AXS D8, CuK_α radiation). The effect of BMN on the phase transition of $(1-x)$PZ–xBMN was investigated using a differential scanning calorimeter (DSC 2920, TA Instrument) between room temperature and 350 °C, with a heating rate of 10 °C min^{-1}. Samples for electrical measurements were prepared by polishing both their sides and coating them with silver (C1000, Heraeus) to serve as electrodes. An LCR meter (HP4284A, Hewlett-Packard, Palo Alto, CA) was used to measure the dielectric properties, and the temperature was varied between 50 and 250 °C at a heating rate of 2 °C min^{-1}. The polarization–electric field (P–E) hysteresis loops were obtained at room temperature using a standardized ferroelectric tester system (RT66A) at a frequency of 4 Hz. The peak field was maintained at 35 kV cm^{-1} during measurement.

3. Results and discussion

Fig. 1 shows the XRD patterns of the sintered $(1-x)$PZ–xBMN ceramics for $0.00 \le x \le 0.50$. All compositions showed a pure perovskite structure, which matched with JCPDS file no. 75-1607. No secondary phase was observed in the patterns, which indicated that all compositions in the series of $(1-x)$PZ–xBMN form solid solutions with a perovskite structure. The 1/4 (*hkl*) superlattice reflection peaks were seen clearly in all compositions, and those peaks are marked with a "*". As is well known, $PbZrO_3$ displays an orthorhombic perovskite structure with lattice parameter $a = 5.889$ Å, $b = 11.784$ Å and $c = 8.226$ Å.[27,28] The orthorhombic unit cell, which contains eight formula units, is a pseudocubic perovskite. According to previous works, this superstructure is due to the antiparallel shifts of Pb^{2+} ions along the pseudocubic ⟨110⟩ direction, which leads to the AFE behavior.[27,29] Kittel described an antiferroelectric state in which lines of ions in the crystal are spontaneously polarized, but with neighboring lines polarized in an antiparallel direction.[30] So, the crystal does not show spontaneous polarization.

The 1/4 (*hkl*) superlattice reflections (*), (111), and (200), were chosen to identify phase evolution of the samples, as shown in Fig. 2. In compositions of $0.00 \le x \le 0.04$, the 1/4 (*hkl*) superlattice reflections and a splitting (200) peak at around 43° were observed, indicating that those ceramics possessed an orthorhombic symmetry. XRD patterns for the compositions, $0.06 \le x \le 0.10$, showed a single (200) peak and splitting (111) reflections, indicating that their crystal structure was of rhombohedral symmetry. At the higher BMN content of $0.20 \le x \le 0.50$, the XRD patterns still exhibited a single (200) peak, but the splitting (111) peak became a single one. These results indicated that the crystal structure of the composition $x = 0.20$ was

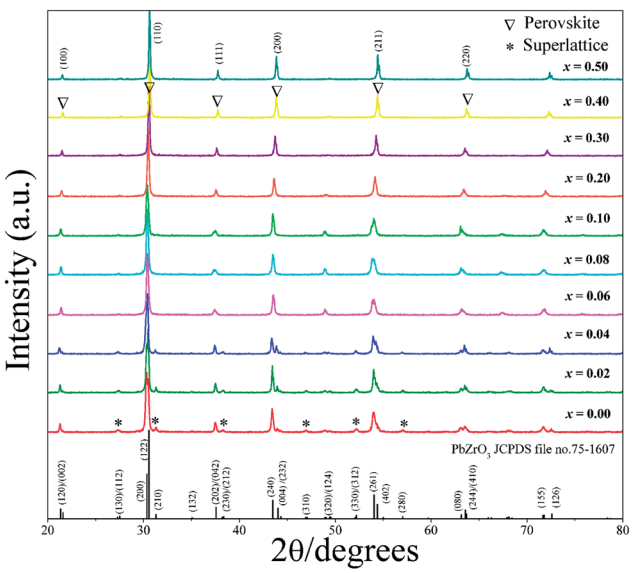

Fig. 1 XRD patterns of sintered ceramics for various compositions of $(1-x)PbZrO_3$–$xBa(Mg_{1/3}Nb_{2/3})O_3$, where $x = 0.0$–0.5.

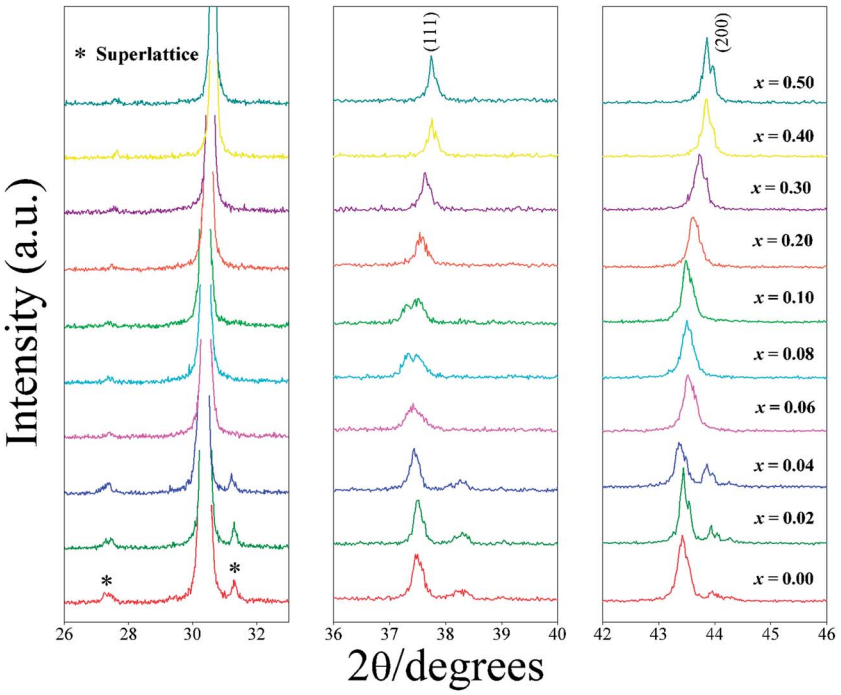

Fig. 2 XRD patterns of the 1/4 (*hkl*)-type superlattice reflections, and the (111) and (200) peaks of $(1-x)$PZ–xBMN ceramics, with $x = 0.0$–0.5.

of pseudocubic symmetry and it transformed into cubic symmetry for compositions of $0.30 \leq x \leq 0.50$. As mention above the 1/4 (*hkl*) superlattice reflection is observed in all compositions, indicating that these compositions, $0.06 \leq x \leq 0.50$, have a mixed phase with the coexistence of orthorhombic structure, as listed in Table 1. Later, description of the *P*–*E* hysteresis result supported this assumption.

Concerning the 1/4 (*hkl*) superlattice reflections, the intensity of these reflections tends to decrease with increasing BMN content and it drastically decreased at the composition of $x = 0.06$. The 1/4 (*hkl*) superlattice reflections are observed only in orthorhombic AFE phase, but not in the rhombohedral FE phase.[30] As mentioned before, the crystal structure changed from orthorhombic to rhombohedral when BMN was increased. Thus, the formation of orthorhombic AFE phase is inhibited during the cooling process, which results in the decrease of intensity of the 1/4 (*hkl*) superlattice reflections.[31] In other words, the substitution of the Pb^{2+} ions by Ba^{2+} ions, and Zr^{4+} ions by Mg^{2+}/Nb^{5+} ions, decreases the driving force for an antiparallel shift of Pb^{2+} ions. Moreover, it has been reported that the presence of polarization in the [111] direction for rhombohedral structure,[30] ensuing on the improvement of a net polarization for PZ–BMN system.

The A-site of the ABO_3 perovskite structure in the BMN system is occupied by Pb^{2+} and Ba^{2+} ions, while the B-site is occupied by Zr^{4+}, Mg^{2+} and Nb^{5+} ions. The average ionic radius of A-site and B-site ions in the $(1-x)$PZ–xBMN can be calculated from the following equations:

Table 1 Physical properties of $(1-x)$PZ–xBMN ceramics[a]

		Lattice parameter (Å)			
Composition (x)	Crystal structure	a	b	c	Unit cell volume (Å^3)
0.00	O	5.8396 ± 0.0097	11.9257 ± 0.0183	8.3976 ± 0.0478	584.8199
0.02	O	5.8446 ± 0.0122	11.8888 ± 0.0393	8.3686 ± 0.0365	581.4945
0.04	O	5.8546 ± 0.0130	11.8626 ± 0.0194	8.3352 ± 0.0236	578.8861
0.06	O + R	4.1602 ± 0.0042	—	—	72.0017
0.08	O + R	4.1571 ± 0.0058	—	—	71.8408
0.10	O + R	4.1530 ± 0.0046	—	—	71.6285
0.20	O + PC	4.1482 ± 0.0039	—	—	71.3804
0.30	O + C	4.1416 ± 0.0274	—	—	71.0402
0.40	O + C	4.1298 ± 0.0175	—	—	70.4348
0.50	O + C	4.1230 ± 0.0184	—	—	70.0874

[a] (R, rhombohedral; O, orthorhombic; PC, pseudocubic; C, cubic).

$$r_{\text{A-site}} = (1 - x)r_{Pb^{2+}} + xr_{Ba^{2+}} \quad (1)$$

$$r_{\text{B-site}} = (1 - x)r_{Zr^{4+}} + x\left(\frac{1}{3}r_{Mg^{2+}} + \frac{2}{3}r_{Nb^{5+}}\right) \quad (2)$$

where ionic radii of Pb^{2+} and Ba^{2+} in 12 coordinate environment were 1.49 Å and 1.61 Å, and Zr^{4+}, Mg^{2+} and Nb^{5+} in 6 coordinate environment were 0.72 Å, 0.72 Å and 0.64 Å of the perovskite structure, respectively.[32] The average ionic radius of A-site and B-site ions in the $(1 - x)$PZ–xBMN system are listed in Table 2. It can be seen that the increasing average radii rate of the A-site (0.120 Å mol^{-1}) is higher than the decreasing average radii rate of the B-site (0.053 Å mol^{-1}). Therefore, substitution of Ba^{2+} at the A-site and Mg^{2+} and Nb^{5+} at the B-site should produce a decrease in the lattice parameters and unit cell volume of PZ–BMN ceramics. However, as presented in Table 1, the calculated lattice parameters and unit cell volume of $(1 - x)$PZ–xBMN; $x = 0.00$–0.50, tend to decrease with increasing BMN content. This result may be due to the large size of Ba^{2+}, which prevents a proportion of Ba^{2+} ions from entering the A-site of the perovskite structure to substitute Pb^{2+} ions. In addition, BMN has a hexagonal structure that is different from the crystal structure of PZ.[24] PZ and BMN cannot form a solid solution completely due to different ionic sizes and crystal structures, when mixed phases occur in this system. However, a secondary phase in this system was not observed in the XRD patterns for all compositions; perhaps the detection limit of the equipment could not detect the existence of a secondary phase of a nanometer size scale.

The tolerance factor (t) for an ABO_3 perovskite structure can be expressed by the general formula: $t = (R_A + R_O)/(\sqrt{2})(R_B + R_O)$, where R_A and R_B are the radii of A (CN = 12) and B (CN = 6), respectively, and R_O is the radius of oxygen (CN = 6). The tolerance factor values in $(1 - x)$PZ–xBMN ceramics are presented in Table 2. It can be seen that the t values here tend to be higher than that of pure PZ. As mentioned above, if the t value of a solid solution is higher than that of pure PZ, the FE phase can be induced, while the AFE phase is stabilized when the t value of a solid solution is lower than that of pure PZ. Therefore, the FE phase is expected to be observable at room temperature. Later, ferroelectric data provide support for this assumption.

Table 2 Average ionic radius of the A-site and B-site and tolerance factor of $(1 - x)PbZrO_3$–$xBa(Mg_{1/3}Nb_{2/3})O_3$ ceramics

	Average ionic radius (Å)		
Composition (x)	A-site	B-site	Tolerance factor (t)
0.00	1.490	0.72	0.964
0.02	1.492	0.719	0.965
0.04	1.495	0.718	0.967
0.06	1.497	0.717	0.968
0.08	1.500	0.716	0.969
0.10	1.502	0.715	0.970
0.20	1.514	0.709	0.977
0.30	1.526	0.704	0.983
0.40	1.538	0.699	0.990
0.50	1.550	0.693	0.996

Fig. 3 shows the temperature dependence of relative permittivity and dielectric loss (tan δ), while heating $(1 - x)$PZ–xBMN ceramics at various frequencies between 1 and 100 kHz. The relative permittivity curves of pure PZ show a sharp peak at around 234 °C, which is characteristic of the first order phase transition of orthorhombic AFE to cubic PE phase transition.[3] Furthermore, the relative permittivity of pure PZ above the Curie temperature obeyed the Curie–Weiss law, $1/\varepsilon_r = (T - T_0)/C$, with $C \sim 2.65 \times 10^5$ K and $T_0 \sim 190$ °C. PZ underwent only one phase transition due to temperature dependence of the relative permittivity, and no further anomaly was found to correspond to the transient FE phase. The absence of an AFE to FE transition might be due to the existence of impurities from starting materials, which stabilize the AFE phase.[33,34] Regarding the compositions of $0.02 \leq x \leq 0.04$, the relative permittivity curves and dielectric loss exhibited two distinct dielectric peaks, which corresponded to the phase transitions. A lower temperature was linked with the orthorhombic AFE to rhombohedral FE phase transition, while a higher one corresponded with the rhombohedral FE to cubic PE phase transition. Later, the P–E hysteresis loop description further supported this assumption. The AFE to FE and FE to PE phase transition temperatures of $(1 - x)$PZ–xBMN ceramics are summarized in Table 3. It is interesting to note that when BMN was introduced into PZ, both AFE to FE and FE to PE phase transition temperatures of $(1 - x)$PZ–xBMN ceramics decreased to room temperature. Additionally, the temperature range width of the rhombohedral FE phase also increases continuously when BMN concentration is increased. The relative permittivity curves for the compositions of $0.06 \leq x \leq 0.10$ showed a phase transition arising from only that of rhombohedral FE to cubic PE, due to the AFE to FE phase transition temperature shifting to below room temperature. Regarding the composition $x = 0.20$, FE to PE phase transition may occur at around room temperature, due to this composition having high relative permittivity at room temperature, as listed in Table 3. Both AFE to FE and FE to PE phase transitions shifted to below room temperature for the higher BMN concentrations. Thus, no dielectric peak corresponding to a phase transition was observed in the composition range $0.30 \leq x \leq 0.50$, and the relative permittivity tended to decrease with increasing temperature. These results indicated that the compositions of $0.30 \leq x \leq 0.50$ have a paraelectric phase at room temperature, which corresponds well with XRD data, showing these compositions have a cubic phase. In addition, 0.8PZ–0.2BMN was selected to study dielectric properties at low temperature (−100 °C to 150 °C). Fig. 4 shows the temperature dependence of relative permittivity (ε_r) and dielectric loss (tan δ), while cooling 0.8PZ–0.2BMN ceramic at various frequencies between 100 Hz and 1 MHz. It is clearly seen that the temperature dependent relative permittivity of 0.8PZ–0.2BMN ceramic exhibited the characteristic of relaxor ferroelectric (RFE). The relative permittivity (ε_r) and dielectric loss (tan δ) as a function of temperature show broad and strong frequency dispersive peaks of phase transition attributed to the dispersion of polar nanoregions (typically 10–100 nm).[35–38] The maximum temperature is dependent on the frequency and increases with increasing frequency.[36] Moreover, the maximum relative permittivity ($\varepsilon_{r,max}$) did not correspond to

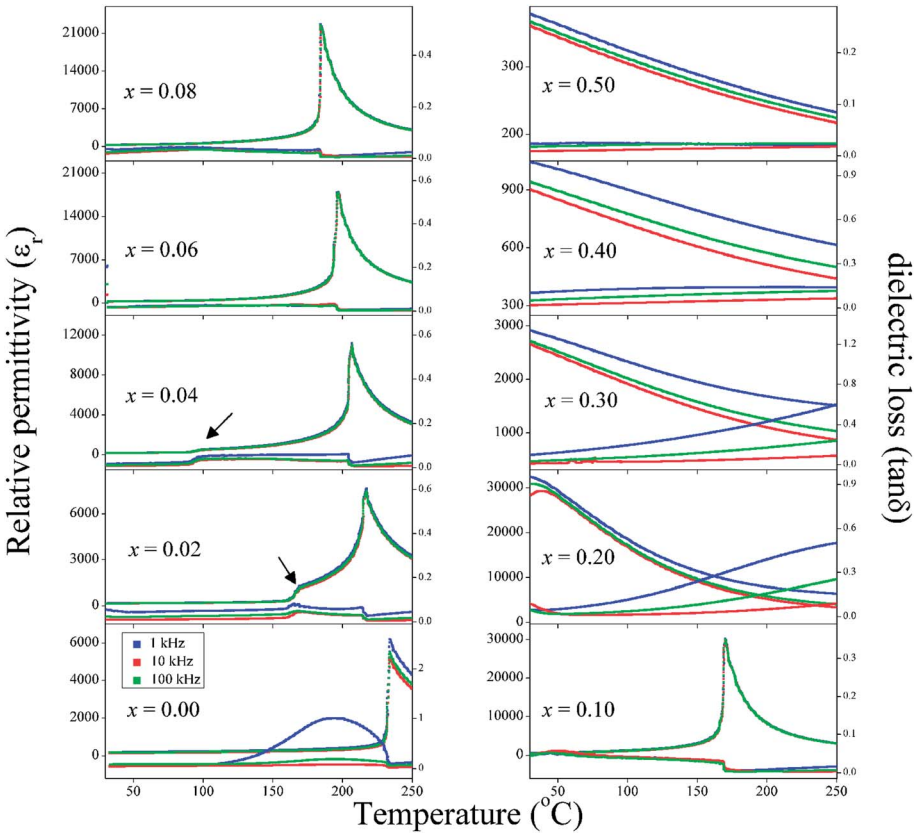

Fig. 3 Temperature dependence of the dielectric properties of (1 − *x*)PZ–*x*BMN ceramics. Arrows indicate the AFE to FE phase transition.

Table 3 Phase transition temperatures of (1 − *x*)$PbZrO_3$–*x*$Ba(Mg_{1/3}Nb_{2/3})O_3$ ceramics[a]

	Phase transition temperature (°C)			
	Relative permittivity		DSC	
Composition (*x*)	T_{AFE-FE}	T_{FE-PE}	T_{AFE-FE}	T_{FE-PE}
$x = 0.00$	—	234.0[a]	—	233.5[a]
$x = 0.02$	168.0	217	168.5	216
$x = 0.04$	96.0	207	95.0	206
$x = 0.06$	—	197	—	197
$x = 0.08$	—	184	—	186
$x = 0.10$	—	170	—	171.5
$x = 0.20$	—	—	—	—
$x = 0.30$	—	—	—	—
$x = 0.40$	—	—	—	—
$x = 0.50$	—	—	—	—

[a] Indicates antiferroelectric to ferroelectric phase transition temperature.

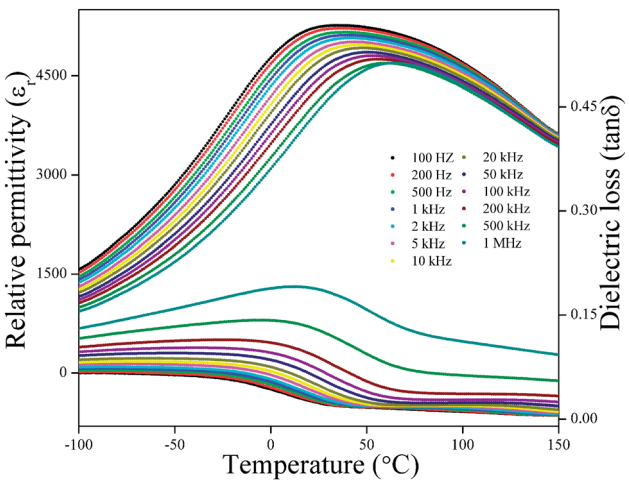

Fig. 4 Temperature dependence of the dielectric properties of 0.8PZ–0.2BMN ceramics at low temperature.

the maximum dielectric loss (tan δ_{max}).[38] Based on the dielectric data, it could be said that 0.8PZ–0.2BMN ceramic is relaxor ferroelectric. As is well known, a relaxor ferroelectric displays a slim *P*–*E* hysteresis loop with low remanent polarization (P_r) and coercive field (E_c) due to the dynamic nature and small size of spontaneous polarization regions.[37] Moreover, the transition maxima temperature, T_m, is around room temperature. Thus, even a slimmer *P*–*E* hysteresis loop in 0.8PZ–0.2BMN ceramic is expected to be obtained at room temperature.

The relative permittivity ($\varepsilon_{r,room}$) and dielectric loss (tan δ) at room temperature, and maximum relative permittivity ($\varepsilon_{r,max}$) at 1 kHz of all compositions, are shown in Table 4. It was found that $\varepsilon_{r,room}$ for the compositions $0.02 \leq x \leq 0.20$ tends to increase with increasing BMN content, due to the decrease of FE to PE phase transition temperature. Regarding the composition

$x = 0.20$, $\varepsilon_{r,room}$ increases abruptly, due to the FE to PE phase transition temperature being around room temperature. With regard to the compositions $0.30 \leq x \leq 0.50$, $\varepsilon_{r,room}$ decreases with increasing BMN content, since the FE to PE phase transition temperature is below room temperature. However, PZ–BMN solid solution showed $\varepsilon_{r,room}$ values for all compositions that were higher than its value of pure PZ. Furthermore, the maximum relative permittivity of the compositions $0.02 \leq x \leq 0.10$ is also higher than the value of pure PZ. Therefore, it could be assumed that BMN substitution can enhance the dielectric properties of pure PZ ceramic.

The differential scanning calorimetry (DSC) technique was used for confirming the effect of added BMN on the phase transition of PZ–BMN ceramics, and detecting the heat capacity of phase transformations recorded in the absence of an external electric field. The thermograms of PZ–BMN ceramics at a heating rate of 10 °C min^{-1} between room temperature and 350 °C are shown in Fig. 5. It was found that the DSC results corresponded well with the dielectric data. Pure PZ exhibited only a sharp exothermic peak, arising from the phase transition at the Curie temperature of ~233.5 °C, which corresponded to sharp changes in the relative permittivity curve of PZ. The DSC curves clearly showed two exothermic peaks for the compositions $0.02 \leq x \leq 0.10$. The lower and higher temperature were linked to the transition temperatures of the AFE to FE and FE to PE phase transitions, respectively. No exothermic peak was observed at a higher BMN content. Table 3 provides the transition temperatures, including AFE to FE and FE to PE transitions for all compositions. It is clearly seen that AFE to FE and FE to PE phase transition temperatures shift to a lower temperature with an increase of x in the composition.

Thermodynamic parameters, enthalpy change (ΔH^*/J g^{-1}), heat capacity (C_p/J g^{-1} K^{-1}), entropy change (ΔS^*/J g^{-1} K^{-1}), and Gibbs energy change (ΔG^*/J g^{-1}), can be calculated from the DSC data. The heat change involved in each step per unit mass of the specimen was used directly to calculate the enthalpy change value. The ΔH^* thus determined was employed to calculate the specific heat capacity (C_p) using the following equation:[39,40]

$$C_p = \frac{\Delta H}{\Delta T} \quad (3)$$

where $\Delta T = T_2 - T_1$; T_1 is the temperature at which the DSC peak begins to depart from the baseline, and T_2 is the temperature at which the peak lands. Subsequently, the entropy change (ΔS^*), and Gibbs energy change (ΔG^*) were calculated using the following equations:[39,40]

$$\Delta S^* = 2.303 C_p \log \frac{T_2}{T_1} \quad (4)$$

$$\Delta G^* = \Delta H^* - T_p \Delta S^* \quad (5)$$

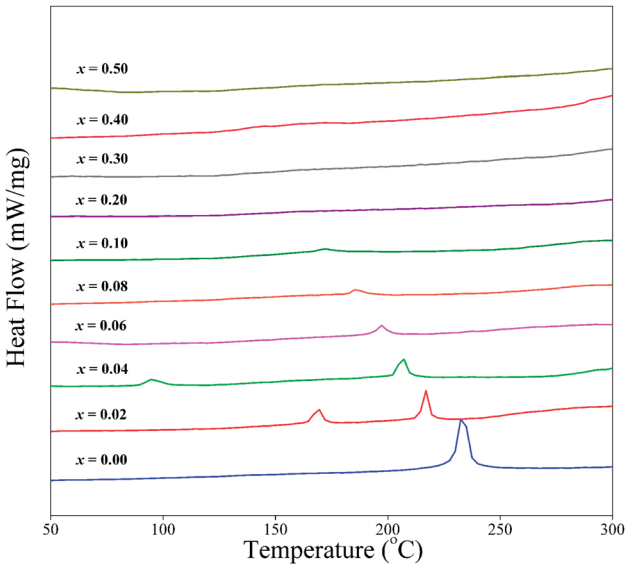

Fig. 5 Typical differential scanning calorimetry (DSC) curves for $(1 - x)$ PZ–xBMN ceramics, with $x = 0.00$–0.50.

Table 5 provides the calculated values of ΔH^*, ΔS^*, C_p and ΔG^* for the phase transitions of the ceramics. The positive values of ΔH^* indicated that the AFE to FE and FE to PE phase transitions are exothermic processes.[41] Regarding ΔG^* of both phase transitions, the positive values indicated that these phase transitions are non-spontaneous. Furthermore, the values of ΔS^* for the AFE to FE and FE to PE phase transitions are positive for all compositions. Based on the activated complexes theory (transition theory),[42–46] a positive value of ΔS^* points to the degree of randomness and disorder of the transition stage, when compared with the initial stage. The ΔS^* values of FE to PE phase transitions for each composition are higher than those of AFE to FE phase transitions. This means that the

Table 4 Electrical properties of $(1 - x)PbZrO_3$–$xBa(Mg_{1/3}Nb_{2/3})O_3$ ceramics

Composition (x)	T_C (°C) at 1 kHz	$\varepsilon_{r,max}$ at 1 kHz	$\varepsilon_{r,room}$ at 1 kHz	tan δ_{room} at 1 kHz	P_r (μC cm^{-2})	P_s (μC cm^{-2})	E_c (kV cm^{-1})
0.00	234.0	6200	185	0.04	—	—	—
0.02	217.0	7664	186	0.05	—	—	—
0.04	207.0	11203	188	0.02	—	—	—
0.06	197.0	17925	263	0.02	29.3	32.0	11.0
0.08	184.0	22302	296	0.03	29.5	33.0	7.9
0.10	170.0	30232	504	0.05	2.3	23.6	0.8
0.20	—	—	32501	0.05	2.4	24.0	1.1
0.30	—	—	2928	0.10	—	—	—
0.40	—	—	1045	0.10	—	—	—
0.50	—	—	381	0.02	—	—	—

Table 5 Thermodynamic parameters for phase transition of $(1-x)PbZrO_3$–$xBa(Mg_{1/3}Nb_{2/3})O_3$ ceramics calculated from DSC data

	AFE to FE phase transition				FE to PE phase transition			
(x)	ΔH^* (J g^{-1})	C_p (J g^{-1} K^{-1})	ΔS^* (J g^{-1} K^{-1})	ΔG^* (J g^{-1})	ΔH^* (J g^{-1})	C_p (J g^{-1} K^{-1})	ΔS^* (J g^{-1} K^{-1})	ΔG^* (J g^{-1})
0.00	—	—	—	—	4.96	93×10^{-2}	9.8×10^{-3}	219×10^{-5}
0.02	0.98	18×10^{-2}	2.2×10^{-3}	65×10^{-5}	1.74	46×10^{-2}	3.6×10^{-3}	94×10^{-5}
0.04	0.63	17×10^{-2}	1.7×10^{-3}	55×10^{-5}	1.38	31×10^{-2}	2.9×10^{-3}	91×10^{-5}
0.06	—	—	—	—	0.85	12×10^{-2}	1.8×10^{-3}	62×10^{-5}
0.08	—	—	—	—	0.46	7×10^{-2}	1.0×10^{-3}	60×10^{-5}
0.10	—	—	—	—	0.32	4×10^{-2}	0.7×10^{-3}	1×10^{-5}
0.20	—	—	—	—	—	—	—	—
0.30	—	—	—	—	—	—	—	—
0.40	—	—	—	—	—	—	—	—
0.50	—	—	—	—	—	—	—	—

degree of randomness and disorder in the corresponding activated complex for FE to PE phase transition is higher than that in the AFE to FE phase transition, meaning the FE to PE phase transition is harder to achieve than the AFE to FE phase transition. Also ΔS^* values of the FE to PE phase transitions tend to decrease with increasing BMN concentration. As higher concentrations of BMN were introduced in the PZ–BMN ceramics, the FE to PE phase transition, with decreasing phase transition temperature, is found to be easier.

The ferroelectric hysteresis loop measurements were used to demonstrate the existence of FE phase in PZ–BMN ceramics. At room temperature, the electrical polarization (P–E) hysteresis loops were carried out at 35 kV cm^{-1} electric field strength with a frequency of 4 Hz. The P–E hysteresis loops for $(1-x)$PZ–xBMN ceramics are shown in Fig. 6. Compositions of $0.00 \leq x \leq 0.04$ exhibit a linear field dependence of polarization, which is characteristic of an AFE material. As AFE has a net remanent polarization (P_r) of zero, and also the existence of antiparallel dipole moments, the AFE to FE phase transition requires an intense electric field. However, it is well known that the electric field required for inducing the AFE to FE phase transition in PZ ceramics at room temperature is higher than the breakdown strength of the ceramics. This result indicated that the AFE phase persists in PZ–BMN ceramics for $0.0 \leq x \leq 0.04$ at room temperature. The hysteresis loops were obtained for the composition $0.06 \leq x \leq 0.20$ at 35 kV cm^{-1} electric field strength. Based on dielectric and DSC results, for the compositions of $0.06 \leq x \leq 0.20$, the AFE–FE transition temperature of PZ–BMN ceramics is lower than room temperature, whereas the FE–PE transition temperature is higher than that temperature. From the XRD results, orthorhombic AFE phase also exists in these compositions but the applied electric field is not enough to switch the AFE domains. Thus, only P–E hysteresis loops resulting from FE phase were observed at room temperature. In addition, the shape of the hysteresis loops clearly shows that the compositions $0.06 \leq x \leq 0.20$ can be separated into two groups. Firstly, the P–E hysteresis loops show a symmetric shape and square loops for the compositions $0.06 \leq x \leq 0.08$, resulting in domain switching in an electric field. In addition, these compositions have high values of P_r, P_s and E_c, due to them containing long range interaction between dipoles in the ferroelectric micro-domain. The remanent polarization (P_r), saturation polarization (P_s) and coercive field (E_c) are summarized in Table 4. When BMN is increased to $x = 0.10$ and 0.20, the P–E hysteresis loops show a slim loop which is a characteristic of a RFE. Furthermore, these compositions have low values of P_r, P_s and E_c, suggestive of the presence of local spontaneous polarization regions (with a nanometer size scale).[35,47] Combining the ferroelectric, dielectric and XRD results of 0.9PZ–0.1BMN ceramic, the sharp phase transition in the dielectric measurement might be due to a phase transition from cubic to the orthorhombic AFE phase, whereas, the slim hysteresis loop which is characteristic of RFE is attributable to the rhombohedral phase. These results indicated that PZ–BMN ceramics at room temperature are FE or RFE in nature. In addition, the composition $x = 0.20$ did not lose ferroelectric properties, thus supporting the supposition that the crystal structure of this ceramic is pseudo-cubic type at room temperature. Behavior of phase transition from normal FE to relaxor FE in the PZ–BMN system is similar to that in $PbZrO_3$–$Pb(Ni_{1/3}Nb_{2/3})O_3$.[10] When the BMN content increased further to $0.30 \leq x \leq 0.50$, a linear curve was detected, which means that the ceramic was in the cubic PE phase at room temperature. This result corresponds with the dielectric and DSC results that the FE–PE transition temperature of PZ–BMN ceramics with $0.30 \leq x \leq 0.50$ is lower than room temperature. Also, the orthorhombic AFE phase which coexists with the cubic PE phase cannot switch by the applied electric field (35 kV cm^{-1}). Thus only the linear curve which is a characteristic of a PE phase is observed in the compositions $0.30 \leq x \leq 0.50$ at room temperature. P–E hysteresis loop measurements indicated that BMN can induce the FE phase in PZ-based ceramics, as expected.

Based on the results, the effect of BMN substitution can induce the FE phase in perovskite PZ. This behavior followed the previous assumption of this study; that if the tolerance factor value of a solid solution is higher than that of pure PZ, the FE phase can be induced, while the AFE phase is stabilized when the t value of the solid solution is lower than that of pure PZ.[18] These results confirm that the tolerance factor can be used for predicting ferroelectricity and antiferroelectricity in a $PbZrO_3$:mixed oxide based system. Recently, this research group found that PNW and NN can induce another AFE intermediate

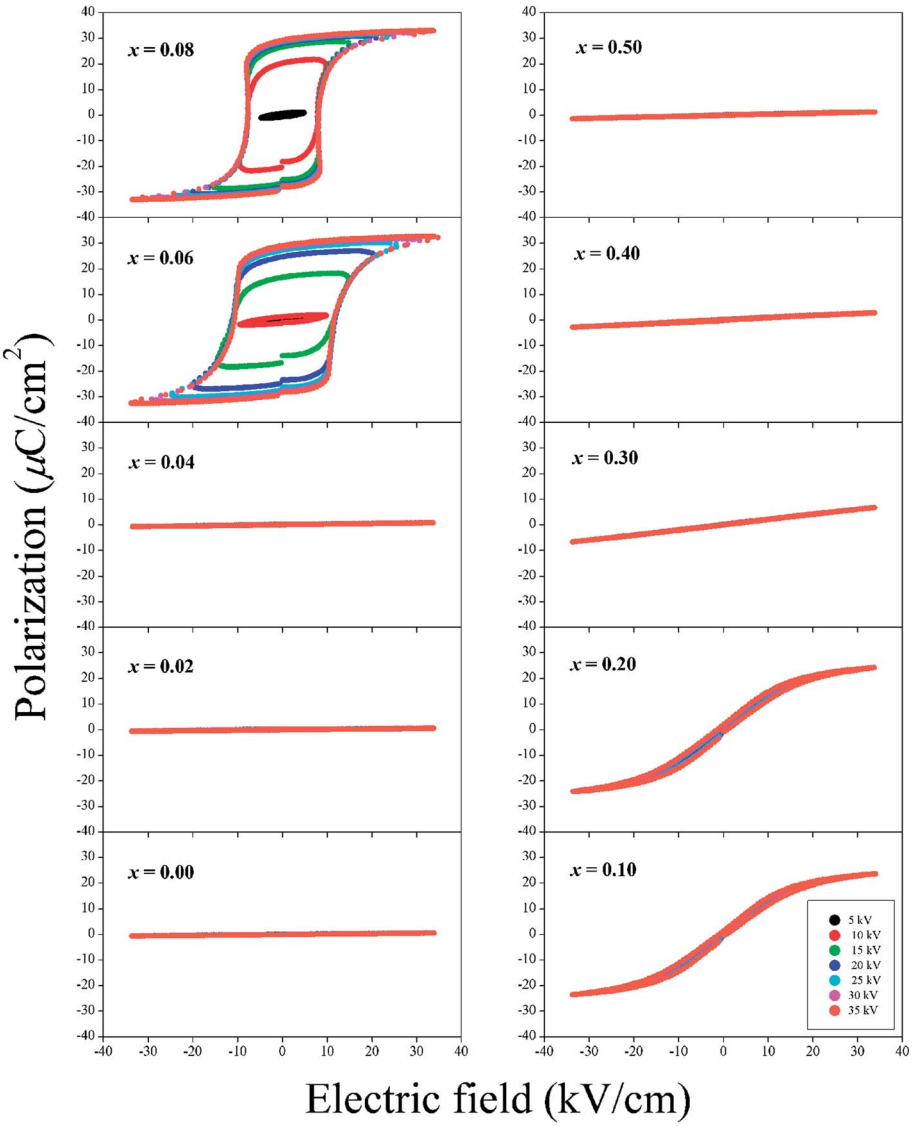

Fig. 6 Polarization–electric field hysteresis loops of (1 − *x*)PZ–*x*BMN ceramics.

phase in the PZ intermediate phase, but not in a ferroelectric phase, although the tendency of t in PZ–PNW and PZ–NN solid solutions is higher than that of pure PZ.[19,20] Thus, it could be said that the tolerance factor is a good indicator, but not the only aspect to be considered for predicting phase transitions in $PbZrO_3$:mixed oxide based ceramics.

It is well known that the stability of a perovskite compound can be expressed by the tolerance factor (t) and average electronegativity difference ($\bar{\chi}$). These factors reflect structural distortion, rotation and tilt of the BO_6 octahedra and chemical bonds, which have an effect on the properties of the perovskite structure, such as transition temperature, dielectric properties, *etc.*[48] Thus, the average electronegativity differences of the end members should also be considered for predicting phase transitions in the $PbZrO_3$:mixed oxide based ceramics.

The average electronegativity difference ($\bar{\chi}$) is expressed by:[21]

$$\bar{\chi} = (\chi_{AO} + \chi_{BO})/2 \quad (6)$$

where χ_{AO} = electronegativity difference between A-site cation and oxygen and χ_{BO} = electronegativity difference between B-site cation and oxygen.

The electronegativity difference of the A-site cation and oxygen and B-site cation and oxygen was calculated using Pauling's electronegativity scale.[49] For complex perovskite, a weighted average value was used for calculating the average electronegativity difference. Fig. 7 shows the plot of tolerance factor *versus* average electronegativity difference of the end member in PZ-based solid solutions. The perovskite compounds, which induced FE intermediate phase in PZ-based ceramics, are marked by a filled symbol, while perovskite compounds that stabilized the AFE phase are marked by a half opened symbol. It was found that the average electronegativity difference for most non-lead perovskites is higher than that of lead-based perovskites. A close analysis of the relationship between t and $\bar{\chi}$ of PZ:mixed oxide based ceramics (marked by filled and half opened circles) found that this phase diagram

consists of three regions. Firstly, the ferroelectric phase region has a high tolerance factor. It is noticeable that end members that have a t value higher than 0.98 can induce an FE phase except for $BiAlO_3$ (BA). However, PIN, which has the same tolerance factor value as its PZ value, $t = 0.946$, can induce a ferroelectric phase. Thus, it could be said that the lower limit of tolerance factor for inducing the FE phase in PZ:mixed oxide based ceramics was 0.964, or t of PZ. Secondly, the AFE phase region has a low tolerance factor. End members that have a t value lower than 0.964 can stabilize the AFE phase. Furthermore, a higher limit in tolerance factor is noticeable for the AFE phase. Thirdly, the overlap zone is the region of the AFE and FE phase. The tolerance factor of this region ranges from the lower limit of t value for the FE phase to the higher limit of t value for the AFE phase; 0.964 to 0.98. The FE intermediate phase and AFE phase in this region can be stabilized, as found in PZ–PIN or PNW and PZ–NN systems, respectively. Therefore, it could be said that if the end members form a relationship between t and $\bar{\chi}$ in this area, the FE and AFE phases may be stabilized in PZ:mixed oxide based solid solutions. Concerning the PZ–BA system, as shown in Fig. 7, BA could not induce a FE phase although t of BA is higher than the upper limit of the tolerance factor for the AFE phase. It is noticeable that BA has a very low $\bar{\chi}$ when compared with other non-lead compounds, which develops a relationship between t and $\bar{\chi}$ in the FE phase area. Thus, it is possible that the very low $\bar{\chi}$ of BA causes the stabilization of AFE phase in PZ–BA system. From this result, the relationship between t and $\bar{\chi}$ of the end members diagram (Fig. 7) perhaps has a higher/lower limit for the AFE/FE phases also. Therefore, more details about the effect of $\bar{\chi}$ on such phase transitions will be studied in the near future.

To prove that the relationship between t and $\bar{\chi}$ of the end member can be used for predicting phase transitions in PZ-based solid solutions we used this factor with PZ:metal oxide based solid solutions which have been studied in several previous works. The $\bar{\chi}$–t relationship of the end members in PZ:metal oxide based solid solutions are shown in Fig. 7. Perovskite compounds that stabilized the AFE phase are marked by a half opened diamond, while perovskite compounds which can induce the FE phase in PZ are marked by the filled diamond. Guided by our proposed $\bar{\chi}$–t relationship, the stabilized phase regions for FE phase, AFE phase and AFE–FE regions are shown in Fig. 7. It was found that the stabilized phase in each system corresponds well with our proposed hypothesis. Thus, it could be said that the $\bar{\chi}$–t relationship diagram can be highly useful for predicting the ferroelectricity and antiferroelectricity in the $PbZrO_3$-based solid solution systems.

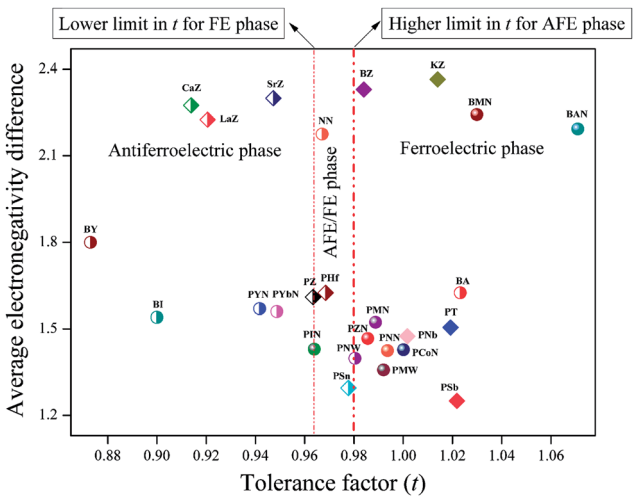

Fig. 7 Tolerance factor *versus* average electronegativity difference of the end members for PZ-based solid solutions: where PSb = $PbSbO_3$, PT = $PbTiO_3$, PNb = $PbNbO_3$, PSn = $PbSnO_3$, PHf = $PbHfO_3$, KZ = $KZrO_3$, BZ = $BaZrO_3$, SrZ = $SrZrO_3$, LaZ = $LaZrO_3$, CaZ = $CaZrO_3$, PNN = $Pb(Ni_{1/3}Nb_{2/3})O_3$, PCoN = $Pb(Co_{1/3}Nb_{2/3})O_3$, PMN = $Pb(Mg_{1/3}Nb_{2/3})O_3$, PZN = $Pb(Zn_{1/3}Nb_{2/3})O_3$, PIN = $Pb(In_{1/2}Nb_{1/2})O_3$, PYN = $Pb(Y_{1/2}Nb_{1/2})O_3$, PYbN = $Pb(Yb_{1/2}Nb_{1/2})O_3$, PNW = $Pb(Ni_{1/2}W_{1/2})O_3$, PMW = $Pb(Mg_{1/2}W_{1/2})O_3$, BY = $BiYbO_3$, BAN = $Ba(Al_{1/2}Nb_{1/2})O_3$ and BMN = $Ba(Mg_{1/3}Nb_{2/3})O_3$. Solid and half filled symbols are used for perovskite compounds that induced FE intermediate phase and stabilized the AFE in PZ-based solid solutions, respectively.

4. Conclusion

The perovskite structure $(1 - x)PbZrO_3$–$xBa(Mg_{1/3}Nb_{2/3})O_3$ ceramics were prepared successfully by the columbite precursor method. Added BMN has been found to strongly influence crystal structure, electrical and thermal properties of PZ ceramics. The sequence of phase transitions in PZ–BMN ceramics at room temperature changed from orthorhombic AFE to rhombohedral FE to pseudo-cubic RFE and to cubic PE when the amount of BMN increased. The dielectric properties of PZ–BMN exhibited significant improvement with BMN loading. The relationship between $\bar{\chi}$ and t of the end members is used for predicting phase transition behavior of PZ:mixed oxide based ceramics.

Acknowledgements

This research was supported by a grant from the program for Strategic Scholarships for Frontier Research Network for the Joint Ph.D. Program Thai Doctoral degree of the Commission on Higher Education (CHE), KMITL Research Fund (KMITL Fund), the Thailand Research Fund under Grant #BRG5680006 and the National Nanotechnology Center (NANOTEC) NSTDA, Ministry of Science and Technology, Thailand, through its "Center of Excellence Network" program. Authors also acknowledge the support of INAMM/NSF at UTSA under the grant #0844081.

References

1 A. S. Mischenko, Q. Zhang, J. F. Scott, R. W. Whatmore and N. D. Mathur, *Science*, 2006, **311**, 1270–1271.
2 S. T. Zhang, A. B. Kounga, W. Jo, C. Jamin, K. Seifert, T. Granzow, J. Rodel and D. Damjanovic, *Adv. Mater.*, 2009, **21**, 4716–4720.
3 B. Jaffe and W. R. Cook, *Piezoelectric Ceramic*, R.A.N. Publishers, 1971.
4 E. Sawaguchi, H. Maniwa and S. Hoshino, *Phys. Rev.*, 1951, **83**, 1078.

5 F. Jona, G. Shirane, F. Mazzi and R. Pepinsky, *Phys. Rev.*, 1957, **105**, 849–856.
6 B. P. Pokharel and D. Pandey, *Phys. Rev. B: Condens. Matter Mater. Phys.*, 2002, **65**, 214108.
7 Y. Xu, *Ferroelectric Materials and Their Application*, Elsevier, Amsterdam, 1991.
8 G. Shirane, *Phys. Rev.*, 1952, **86**, 219–227.
9 Q. Tan, Z. Xu and D. Viehland, *J. Mater. Res.*, 1999, **14**, 4251–4258.
10 S. Wirunchit, P. Laoratanakul and N. Vittayakorn, *J. Phys. D: Appl. Phys.*, 2008, **41**, 125406.
11 W. Banlue and N. Vittayakorn, *Appl. Phys. A*, 2008, **93**, 565–569.
12 U. Sukkha, R. Muanghlua, S. Niemcharoen, B. Boonchom and N. Vittayakorn, *Appl. Phys. A*, 2010, **100**, 551–559.
13 U. Sukkha, R. Muanghlua, S. Niemcharoen, B. Boonchom and N. Vittayakorn, *J. Am. Ceram. Soc.*, 2011, **94**, 3397–3404.
14 U. Sukkha, R. Muanghlua, S. Niemcharoen, B. Boonchom, W. Vittayakorn and N. Vittayakorn, *J. Mater. Sci.*, 2012, **47**, 1452–1459.
15 N. Vittayakorn, P. Charoonsuk, P. Kasiansin, S. Wirunchit and B. Boonchom, *J. Appl. Phys.*, 2009, **106**, 064104.
16 U. Sukkha, R. Muanghlua, S. Niemcharoen, B. Boonchom and N. Vittayakorn, *Ferroelectrics*, 2011, **416**, 8–15.
17 N. Vittayakorn and B. Boonchom, *J. Alloys Compd.*, 2011, **509**, 2304–2310.
18 U. Sukkha, W. Vittayakorn, R. Muanghlua, S. Niemcharoen, B. Boonchom and N. Vittayakorn, *J. Am. Ceram. Soc.*, 2012, **95**, 3151–3157.
19 U. Sukkha, W. Vittayakorn, R. Muanghlua, S. Niemcharoen, A. Karbkaew, P. Seeharaj and N. Vittayakorn, *Ferroelectrics*, 2013, **451**, 30–40.
20 U. Sukkha, W. Vittayakorn, R. Muanghlua, S. Niemcharoen and N. Vittayakorn, *Mater. Chem. Phys.*, 2014, **143**, 1517–1521.
21 A. Halliyal, T. R. Gururaja, U. Kumar and A. Safari, *IEEE Trans. Ultrason. Ferroelectrics Freq. Contr.*, 1986, **33**, 437–441.
22 S. M. Gupta, E. Furman, E. Colla, Z. Xu and D. Viehland, *J. Appl. Phys.*, 2000, **88**, 2836–2842.
23 M. A. Akbas and P. K. Davies, *J. Am. Ceram. Soc.*, 1998, **81**, 670–676.
24 Z. Q. Tian, H. Wang, W. J. Huang and C. Y. Zhang, *J. Mater. Sci.: Mater. Electron.*, 2008, **19**, 227–232.
25 X. Long and Z. G. Ye, *Chem. Mater.*, 2007, **19**, 1285–1289.
26 X. Long and Z. G. Ye, *16th IEEE International Symposium on Applications of Ferroelectrics.*, 2007, 493, (ISAF2007).
27 F. Jona, G. Shirane, F. Mazzi and R. Pepinsky, *Phys. Rev.*, 1957, **105**, 849–856.
28 A. M. Glazer, K. Roleder and J. Dec, *Acta Crystallogr.*, 1993, **49**, 846–852.
29 G. Shirane and S. Hoshino, *Acta Crystallogr.*, 1954, **7**, 203–210.
30 C. Kittel, *Phys. Rev.*, 1951, **82**, 729–732.
31 B. P. Pokharel and D. Pandey, *J. Appl. Phys.*, 1999, **86**, 3327–3332.
32 R. D. Shannon, *Acta Crystallogr., Sect. A: Cryst. Phys., Diffr., Theor. Gen. Crystallogr.*, 1976, **32**, 751–767.
33 V. J. Tennery, *J. Electrochem. Soc.*, 1965, **112**, 1117–1120.
34 V. J. Tennery, *J. Am. Ceram. Soc.*, 1966, **49**, 483–486.
35 L. E. Cross, *Ferroelectrics*, 1987, **76**, 241–267.
36 D. Viehland, S. J. Jang and L. E. Cross, *J. Appl. Phys.*, 1990, **68**, 2916–2921.
37 C. A. Randall, A. S. Bhalla, T. R. Shrout and L. E. Cross, *J. Mater. Res.*, 1990, **5**, 829–834.
38 C. A. Randall and A. S. Bhalla, *Jpn. J. Appl. Phys.*, 1990, **29**, 327–333.
39 S. A. Halawy, N. E. Fouad, M. A. Mohamed and M. I. Zaki, *J. Therm. Anal. Calorim.*, 2005, **82**, 671–675.
40 R. H. Abu-Eittah, N. G. Zaki, M. M. A. Mohamed and L. Kamel, *J. Anal. Appl. Pyrolysis*, 2006, **77**, 1–11.
41 P. Richet, *The Physical Basis of Thermodynamics with Applications to Chemistry*, Kluwer Academic/Plenum, New York, 2001.
42 H. X. Ma, J. R. Song, F. Q. Zhao, R. Z. Hu and H. M. Xiao, *J. Phys. Chem. A*, 2007, **111**, 8642–8649.
43 C. Head and A. C. K. Smith, *Applied Physical Chemistry*, McMilan Press, London, 1982.
44 J. J. Sestak, *Thermodynamical properties of solids*, Academia, Prague, 1984.
45 D. Young, *Decomposition of solids*, Pergamon Press, Oxford, 1966.
46 S. Ch. Turmanova, S. D. Genieva, A. S. Dimitrova and L. T. Vlaev, *eXPRESS Polym. Lett.*, 2008, **2**, 133–146.
47 K. Uchino, *Ferroelectrics*, 1994, **151**, 321–330.
48 A. S. Bhalla, R. Guo and R. Roy, *Mater. Res. Innovations*, 2000, **4**, 3–26.
49 A. Pauling, *The nature of chemical bonds*, Cornell University Press, New York, 1960.

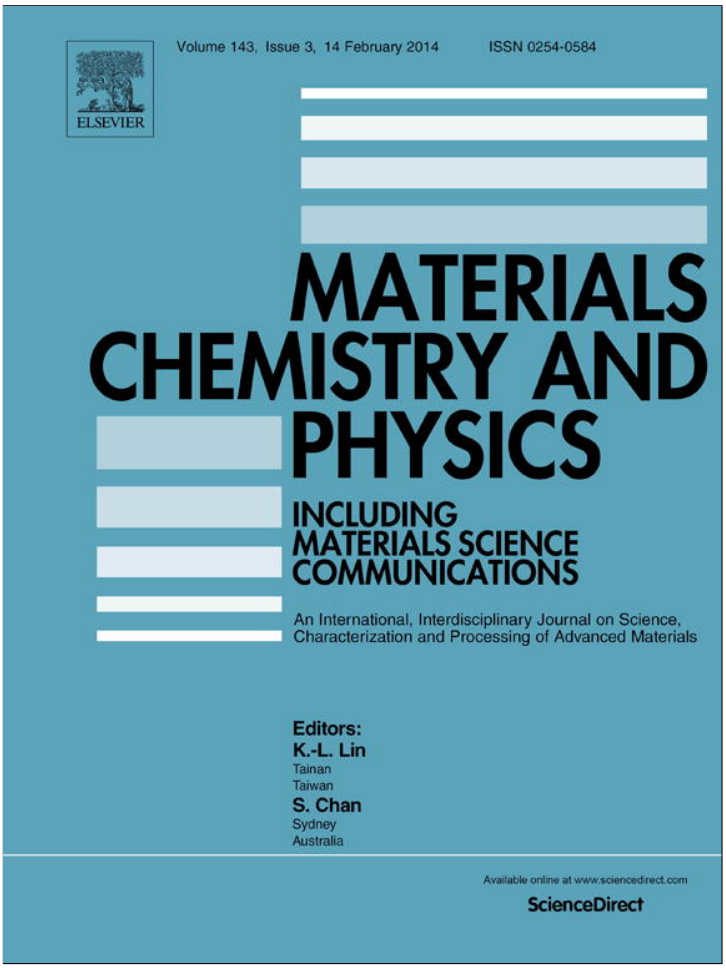

Materials Chemistry and Physics 143 (2014) 1517–1521

Contents lists available at ScienceDirect

Materials Chemistry and Physics

journal homepage: www.elsevier.com/locate/matchemphys

Effect of A-site and B-site ion replaced with small ions on the intermediate phase in $PbZrO_3$ ceramic

Usa Sukkha [a], Wanwilai Vittayakorn [a], Rangson Muanghlua [b], Surasak Niemcharoen [b], Naratip Vittayakorn [a,c,d,*]

[a] Electroceramic Research Laboratory, College of Nanotechnology, King Mongkut's Institite of Technology Ladkrabang, Bangkok 10520, Thailand
[b] Department of Electronics, Faculty of Engineering, King Mongkut's Institute of Technology Ladkrabang, Bangkok 10520, Thailand
[c] Advance Materials Research Unit, Faculty of Science, King Mongkut's Institute of Technology Ladkrabang, Bangkok 10520, Thailand
[d] Department of Chemistry, Faculty of Science, King Mongkut's Institute of Technology Ladkrabang, Bangkok 10520, Thailand

HIGHLIGHTS

- The relative permittivity curves for the composition, $0.02 \leq x \leq 0.06$, showed two anomalous peaks.
- The intermediate phase in PZ–NN system is antiferroelectric-like structure.
- The ferroelectric phase diagram of PZ–NN was established in this work.

ARTICLE INFO

Article history:
Received 14 August 2013
Received in revised form
20 November 2013
Accepted 8 December 2013

Keywords:
Phase transitions
Ferroelectricity
Electronic characterisation
Dielectric properties

ABSTRACT

The solid solution of $(1-x)PbZrO_3$–$xNaNbO_3$ ceramics, where $x = 0.0$–0.08, was synthesized by solid state reaction. The basic characterizations were performed using X-ray diffraction (XRD), dielectric spectroscopy, hysteresis measurement and differential scanning calorimetry (DSC) techniques. The results indicated that the crystal structure of the solid solution, $(1-x)$PZ–xNN, where $x = 0.00$–0.08, is of orthorhombic symmetry. It was found that the effect of NN being replaced with small ions at the A-site and B-site can induce an AFE-like phase in PZ. The FE intermediate phase of PZ cannot be induced, although Zr^{4+} ions were substituted by small Nb^{5+} ions. This is due to the decreasing average rate of radii in the A-site (0.1 Å mol^{-1}) being higher than that in the B-site (0.08 Å mol^{-1}).

1. Introduction

Lead zirconate ($PbZrO_3$, PZ) is a prototype of antiferroelectric ceramics. PZ is interesting material, as it can be used extensively for many different electronic devices such as high charge storage capacitors and large strain actuators, due to the behavior of electric field-induced antiferroelectric to ferroelectric phase transformation [1,2]. The crystal structure of PZ changes from orthorhombic antiferroelectric phase (AFE) to cubic paraelectric phase (PE) at 236 °C, and a rhombohedral ferroelectric phase (FE) exists over a very narrow temperature range (233–236 °C) [3]. Sometimes, this FE phase is called the FE intermediate phase. The FE phase of PZ can be alternated by adding small amounts of ions at the A-site and/or B-site. Q. Tan et al. reported that substitution with larger ions at the A-site, or smaller ones at the B-site, can stabilize the FE phase, whereas, substitution with smaller ions at the A-site, or larger ones at the B-site, can stabilize the AFE phase [4]. Recently, this study researched the effect of $BiAlO_3$ substitution on $PbZrO_3$ by replacing ions at the A-site and B-site with smaller ones, and found that the AFE phase stabilized, due to the average rate of radii in the A-site decreasing more than that in the B-site [5]. Also, Z. Ujma et al. reported that the substitution of Nb^{5+} in PZ can induce an FE phase of PZ [6]. Therefore, this work dealt with the binary system of $(1-x)PbZrO_3$–$xNaNbO_3$ (PZ–NN), in which the decreasing average rate of radii in both the A-site and B-site were close. This study reports the effect of NN content on the crystal structure of $(1-x)PbZrO_3$–$xNaNbO_3$ ceramic, phase transition of PZ–NN ceramics and the intermediate phase in $PbZrO_3$ ceramic.

* Corresponding author. Department of Chemistry, Faculty of Science, King Mongkut's Institute of Technology Ladkrabang, Bangkok 10520, Thailand. Fax: +66 2 326 4415.
E-mail address: naratipcmu@yahoo.com (N. Vittayakorn).

0254-0584/$ – see front matter © 2013 Elsevier B.V. All rights reserved.
http://dx.doi.org/10.1016/j.matchemphys.2013.12.010

2. Experiment

The $(1-x)$PZ–xNN ceramics, with $x = 0.00$, 0.02, 0.04, 0.06 and 0.08, were synthesized using the solid state method. The PbO (≥99.0% purity), ZrO_2 (99.0% purity), Na_2CO_3 (99.0% purity), and Nb_2O_5 (99.5% purity) powders were used as raw materials. PZ and NN powders were prepared separately. For preparation of PZ powder, PbO and ZrO_2 powders were mixed for 18 h by ball-milling. After drying, the mixed powder was calcined as PZ powder for 4 h at 750 °C. A similar process was used to prepare NN powder, which was obtained by calcining for 5 h at 800 °C. Both PZ and NN powders were weighed according to the stoichiometric formula and re-milled. The mixed powders were calcined as PZ–NN powders for 4 h at 850 °C. After pressing into pellet form, the pellets were sintered for 4 h at 1250 °C inside a covered alumina crucible. Phase-purity check and structure analysis were performed using the X-ray diffraction technique (XRD, Bruker-AXS D8). Phase transition of PZ–NN ceramics was investigated by a differential scanning calorimeter (DSC 2920, TA Instrument). The sample surfaces were polished and electroded with silver (C1000, Heraeus) as electrodes in order to measure electrical properties. The dielectric constant (ε_r) was measured by an HP4284A LCR meter The polarization–electric field (P–E) hysteresis loops were observed using a standardized ferroelectric tester system (RT66B, Radiant Technologies) at a frequency of 4 Hz. The peak field was maintained at 35 kV cm^{-1} during measurement.

3. Results and discussion

Room temperature XRD patterns of $(1-x)$PZ–xNN sintered ceramics are shown in Fig. 1. For all compositions of $(1-x)$PZ–xNN ceramics, all of the diffraction peaks that correspond to the perovskite structure can be assigned and matched well with JCPDS No. 75-1607. The crystal structure of ceramics is an orthorhombic symmetry at the composition, $0.00 \leq x \leq 0.08$. Furthermore, diffractions from the secondary phases were not observed in the patterns, which indicate pure perovskite structure within the detection limit of the equipment. The ¼ (hkl) superlattice reflection peaks, marked by "*", which arise from antiparallel displacement of Pb^{2+} cations, were observed in all compositions. However, their

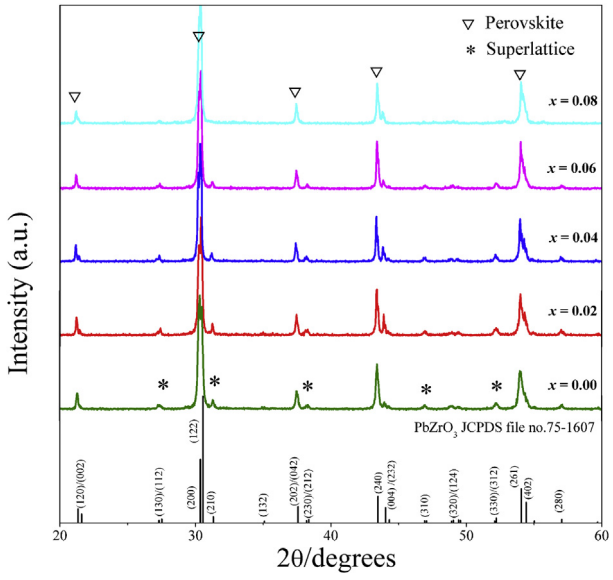

Fig. 1. XRD patterns of sintered ceramics for various compositions of $(1-x)PbZrO_3$–$xNaNbO_3$, where $x = 0.02$–0.08.

Table 1
Lattice parameters and unit cell volume of PZ–NN ceramics.

Composition (x)	Lattice parameters (Å)			Unite cell volume (Å^3)
	a	b	c	
0.00	5.884 ± 0.02	11.780 ± 0.03	8.309 ± 0.01	575.93
0.02	5.877 ± 0.04	11.775 ± 0.05	8.304 ± 0.09	574.65
0.04	5.886 ± 0.07	11.778 ± 0.03	8.312 ± 0.09	576.23
0.06	5.878 ± 0.06	11.735 ± 0.02	8.316 ± 0.03	573.62
0.08	5.879 ± 0.06	11.759 ± 0.03	8.185 ± 0.02	565.84

intensity tended to decrease with increasing NN concentration, which indicated that replacements of the Pb^{2+} ions by Na^+ ions, and Zr^{4+} ions with Nb^{5+} ions, decrease the driving force for an antiparallel shift of Pb^{2+} ions. The calculated lattice parameters and unit cell volume of $(1-x)$PZ–xNN ceramics are shown in Table 1. These values decrease with increased NN content by replacing Pb^{2+}-site (1.49 Å) and Zr^{4+}-site (0.72 Å) ions with small Na^+ (1.39 Å) and Nb^{5+} (0.64Å) ions, respectively [7].

Tolerance factor (t) for the perovskite structure is given by the general formula: $t = (R_A + R_O)/(\sqrt{2})(R_B + R_O)$, where R_A and R_B are the radius of A (CN = 12) and B (CN = 6), respectively, and R_O is the radius of oxygen (CN = 6). When t is <1, the antiferroelectric (AFE) phase is stabilized, whereas when t is >1, the ferroelectric (FE) phase is stabilized [8]. The average ionic radius of A-site and B-site ions in the $(1-x)$PZ–xNN can be calculated from the following equations: $r_{A\text{-site}} = (1-x)r_{Pb} + xr_{Na}$, and $r_{B\text{-site}} = (1-x)r_{Zr} + xr_{Nb}$. The average ionic radius of A-site and B-site ions, and tolerance factor in the $(1-x)$PZ–xNN ceramics, are presented in Table 2. It can be seen that the tolerance factor of PZ–NN ceramics is in the range from 0.9639 to 0.9642. This result indicated that the AFE phase is expected to be found at room temperature. Later, the ferroelectric property provided support for this assumption.

Fig. 2 shows the temperature dependence of relative permittivity, while heating $(1-x)$PZ–xNN ceramics at frequencies of 1, 10 and 100 kHz. The relative permittivity curve of pure PZ shows only one sharp maximum at 231 °C, which is characteristic of the first order phase transition. It is well known that PZ has a ferroelectric intermediate phase between the AFE phase and PE phase. However, the AFE to FE phase transition of PZ was not observed, due to the impurities from raw materials. The relative permittivity and dielectric loss curves for the composition, $0.02 \leq x \leq 0.06$, showed two anomalous peaks. A higher temperature was linked with the Curie temperature, while a lower temperature suggested the existance of another phase transition. The values of dielectric loss in the intermediate phase are not significantly different from those of the AFE phase. It is known that the FE phase has significantly higher dielectric loss than the AFE phase because of domain wall motion [9,10]. The small Na^+ ions were added at the A-site of PZ and the tolerance factor of the ceramics was lower than 1. Then, the intermediate phase is possibly another AFE phase. However, the ferroelectric intermediate phase of PZ may be induced by adding Nb^{5+} ions at the B-site because partial substitution of Nb^{5+} has been

Table 2
The average ionic radius of A-site and B-site ions and the tolerance factor of $(1-x)$ PZ–xNN ceramics.

Composition (x)	Ionic radii (Å)		Tolerance factor (t)
	A-site	B-site	
0.00	1.4900	0.7200	0.96394
0.02	1.4880	0.7184	0.96400
0.04	1.4860	0.7168	0.96406
0.06	1.4840	0.7152	0.96412
0.08	1.4820	0.7136	0.96418

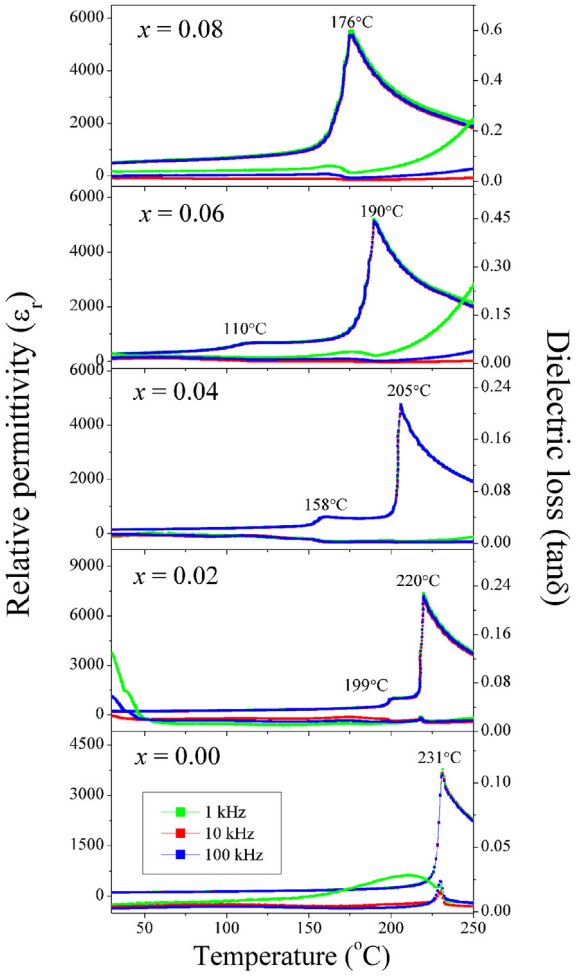

Fig. 2. Temperature dependence of dielectric properties of $(1-x)PbZrO_3$–$xNaNbO_3$ ceramics.

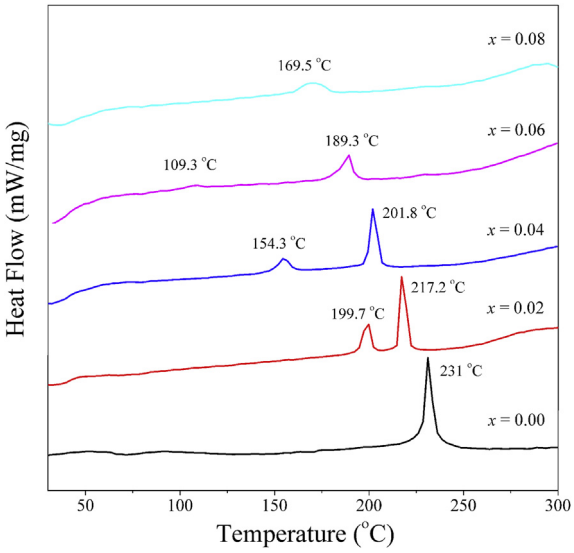

Fig. 3. Typical differential scanning calorimetry (DSC) curves for $(1-x)PbZrO_3$–$xNaNbO_3$ ceramics.

reported as an excess-valency, and a small sized Zr^{4+} brings about a ferroelectric intermediate phase [4,11,12]. Therefore, the lower transition temperature should be interpreted carefully because the intermediate phase may be FE or another AFE. To clarify this point, the *P*–*E* hysteresis loop of the sample was measured as a function of temperature. If the intermediate phase is FE, the hysteresis loops should be seen. In addition, the phase transition temperature of ceramics shifts towards room temperature when NN is added to PZ. The temperature range width of the intermediate phase also increases continuously. No anomalous peak corresponding to the AFE to intermediate phase transition was observed in the composition, $x = 0.08$, because decreasing transition temperature possibly loses to room temperature.

The DSC technique was used as a secondary tool to confirm the phase transitions of ceramics, since it was operated in the absence of an external electric field. The results of DSC analysis on heating ceramics are shown in Fig. 3. As expected, the DSC curves for PZ showed a sharp exothermic peak at a Curie temperature of 231 °C, which is in accordance with abrupt changes in the relative permittivity curve of PZ. Two phase transitions in $(1-x)$PZ–xNN ceramics in the composition, $0.02 \leq x \leq 0.04$, were obtained with dielectric measurement and clearly confirmed by DSC measurement. The peak positions shifted to a lower temperature with a higher composition of *x*. The temperature range width of the intermediate phase increased with increasing amounts of NN content.

In order to clarify the intermediate phase in $(1-x)$PZ–xNN ceramics, the *P*–*E* hysteresis loop of each composition was measured as a function of temperature at 35 kV cm^{-1} electric field strength. At room temperature, no ferroelectric loop was observed in any composition because the electric fields were insufficient for switching antiferroelectric domains. Generally, AFE has a zero net dipole moment, owing to existence of the antiparallel alignment of dipole moments in the unit cell. When the external electric field is weak, the polarization is proportional to the electric field, and macroscopic polarization of hysteresis is not shown [13]. Meanwhile, when the electric field exceeds the critical field, the AFE becomes FE and the polarization shows hysteresis with respect to the field. Furthermore, the hysteresis loop also forms in the negative field, in which a double-loop is linked with antiparallel dipole moments in adjacent unit cell sublattices. However, it is well known that the electric field required for inducing the AFE to FE phase transition in PZ ceramics is higher at room temperature than the breakdown strength of the ceramics. This could indicate that all compositions of $0.00 \leq x \leq 0.08$ have AFE behavior at room temperature. The $0.98PbZrO_3$–$0.02NaNbO_3$ ceramic was selected for investigating polarization behavior sequence while heating to 240 °C. The *P*–*E* hysteresis loops on heating for 0.98PZ–0.02NN ceramic are shown in Fig. 4. A linear behavior of polarization remains from room temperature to 210 °C. When the temperature was increased to 215 °C, the ceramic exhibited AFE-like behavior, in which the *P*–*E* loop became a double-loop type. Such double-loop behavior remains at temperatures of up to 230 °C. However, the critical field tends to reduce continuously with increasing temperature. This result is caused by a higher temperature, which reduces the ferroelectric interaction among the dipoles. A linear curve could be observed in this composition when above the transition temperature of 230 °C, which implied that the ceramic was in the PE phase. It is clear that the intermediate phase in this system is not a ferroelectric phase. However, the intermediate phase that reveals a *P*–*E* double loop may or may not be another AFE phase because incommensurate ordering in PZ-based solid solution is still able to exhibit AFE behavior [14–16].

It is well known that the structure of PZ at low temperature (<230 °C) is orthorhombic with the lattice parameters of $a = 5.884$ Å, $b = 11.768$ Å, and $c = 8.22$ Å [17]. The orthorhombic unit cell consists of eight formula units and eight primitive cells,

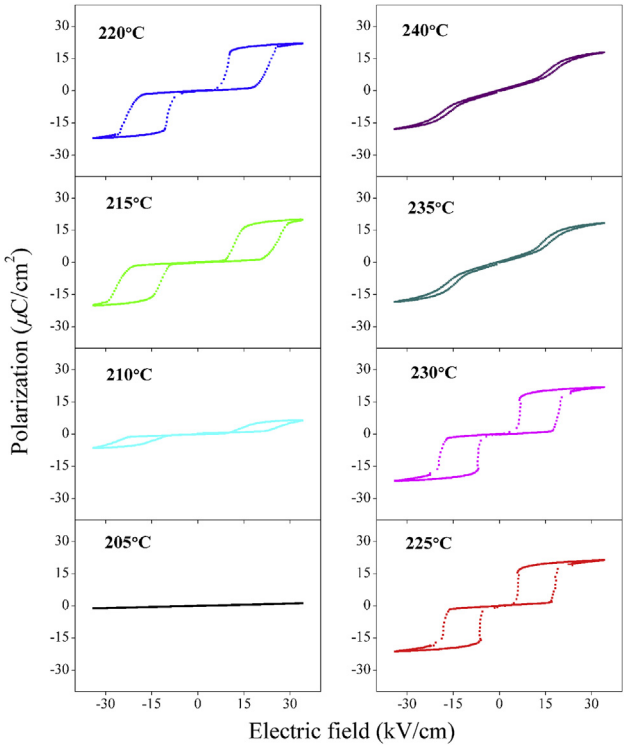

Fig. 4. Polarization–electric field hysteresis loops of $0.98PbZrO_3$–$0.02NaNbO_3$ ceramic at 4 Hz during heating.

with a pseudocubic structure [3]. PZ is the AFE ordering, which manifests by itself as the antiparallel shift of Pb^{2+} ion along the pseudocubic <110> direction, resulting in antiferroelectricity [3,17–20]. Sawaguchi et al. reported that the strips of commensurate ordering of Pb^{2+} shifts had periodicity of four pseudocubic (110) planes, which are characterized by the presence of a ¼ (110) superlattice reflection [3,14,17,21,22]. Many research groups concerned used transition electron microscopy (TEM) for investigating commensurate ordering in PZ and PZ-based solid solutions with a Zr-rich side [14,15,18,21–25]. Dwight Viehland et al. observed $1/x$ (110) incommensurate superlattice reflections in a narrow temperature range between intermediate FE and orthorhombic AFE phases in PZ [18]. Also, PZ-based solid solutions on the Zr-rich side, including PZT [18], PZST [23], PLZT [21,23,25,26] and PNZST [16,22,27], have been studied in this area. It was reported that PZ-based solid solutions have shown $1/x$ (110) incommensurate superlattice reflections. The incommensurate phases in modified PZ comprise strips of commensurate ordering with a periodicity of 6–8 (110) spacings [21,27,28]. Furthermore, Tan et al. studied the phase transition of PNZST ceramics using Raman spectroscopy, and found that Raman spectroscopy can be used to distinguish the two AFE phases, one with commensurate ordering AFE and the other with incommensurate ordering AFE [15]. Based on previous work, it could be said that the commensurate ordering in PZ can be disrupted by adding impurities or working on solid solutions. Regarding $(1 - x)$PZ–xNN where $0.02 \leq x \leq 0.06$, a possible interpretation of lower phase transition might be commensurate AFE to incommensurate AFE phase transition when FE data combined with the XRD result show ¼ (110) superlattice reflections at room temperature and the dielectric result shows insignificant change of tan δ between AFE, and the intermediate phase and these compositions are on the Zr-rich side of solid solution. The intensities of ¼ superlattice reflections for the composition, $x = 0.08$, are very weak, thus indicating the destabilization of commensurate

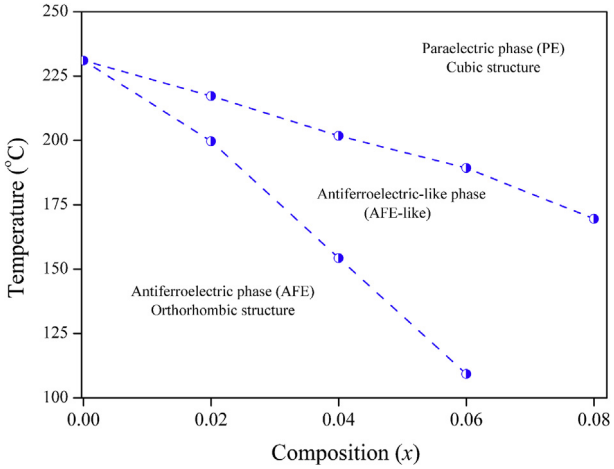

Fig. 5. Ferroelectric phase diagram of the $(1 - x)$PZr–xNN system.

ordering in PZ. In addition, 0.92PZ–0.08NN has the highest tolerance factor among the studied range of $0.02 \leq x \leq 0.08$. It is accepted that the tolerance factor of perovskite reflects the distortion and controls octahedral rotation [26]. Generally, the AFE phase is stabilized if t is low, whereas, the FE phase is stabilized if t is high. Therefore, it is possible that the tolerance factor of the composition, $x = 0.08$, is critical due to the possible occurrence of competition between AFE and FE phases, as found in the PLZT system [26]. Furthermore, Xu et al. reported that the incommensurate ordering phase is attributed to the competition of AFE and FE phases [18]. Then, the mixture phases of commensurate ordering AFE, and incommensurate ordering AFE and FE, may be observed at room temperature by using a high resolution technique such as TEM, Raman, neutron diffraction, etc. Further details about phase transition in this composition will be published later.

After accumulating all data, the ferroelectric phase diagram of $(1 - x)$ PZ–xNN was established, as shown in Fig. 5. The phase diagram consists of three regions in this system; high temperature cubic PE, AFE-like, and orthorhombic AFE. In the PZ–NN system, the FE intermediate phase of PZ cannot be induced, although Zr^{4+} ions were substituted by small Nb^{5+} ions. This is due to the decreasing average rate of radii in the A-site (0.1 Å mol^{-1}) being higher than that in the B-site (0.08 Å mol^{-1}), which is similar to other systems [5]. Additionally, when the tolerance factor of all compositions is lower than 1, the AFE phase remains stabilized. Fesenko et al. previously studied the relationship between composition, structure and properties in solid solutions of $Pb(Zr,Ti)O_3$–$PbB'B''O_3$ and $PbTiO_3$–$NaNbO_3$ [29]. They established phase diagrams and discovered the morphotropic phase transition in various solid solutions. Furthermore, from that information they were able to use the fundamental theory, which relates electrophysical and structural parameters of solid solutions for predicting the composition of piezoelectric materials, with suitable properties given for different applications. In the same way, this work may be useful for theoretical and experimental data for AFE–AFE solid solution.

4. Conclusion

The $(1 - x)PbZrO_3$–$xNaNbO_3$ ceramics were prepared by the solid state method. The XRD results indicate that the $(1 - x)$PZ–xNN solid solutions exhibited a single phase perovskite structure for all compositions. The crystal structure of the solid solution, $(1 - x)$PZ– xNN, where $x = 0.00$–0.08, is orthorhombic symmetry.

Adding $NaNbO_3$ cannot induced FE intermediate phase of PZ. The phase transition sequence of $(1-x)$PZ–xNN ceramics changes on heating from orthorhombic AFE into AFE-like into PE phase. The temperature range width of AFE-like intermediate phase increases with the amount of increasing $NaNbO_3$

Acknowledgments

This research was supported by a grant from the program for Strategic Scholarships for Frontier Research Network for the Joint Ph.D. Program Thai Doctoral degree of the Commission on Higher Education (CHE), KMITL Research Fund (KMITL Fund) and the Thailand Research Fund (TRF).

References

[1] K. Uchino, Ferroelectric Devices, Marcel Dekker Inc., New York, 2000.
[2] B. Jaffe, W.R. Cook, Piezoelectric Ceramics, R.A.N. Publishers, India, 1971.
[3] E. Sawaguchi, G. Shirane, S. Hoshino, Phys. Rev. 83 (1951) 1078.
[4] X. Tan, Z. Xu, D. Viehland, J. Mater. Res. 14 (1999) 4251–4258.
[5] N. Vittayakorn, B. Boonchom, J. Alloys Compd. 509 (2011) 2304–2310.
[6] Z. Ujma, D. Dmytrow, M. Pawelczyk, Ferroelectrics 120 (1991) 211–224.
[7] R.D. Shannon, Theor. Gen. Crystallogr. A 32 (1976) 751–767.
[8] K.J. Rao, C.N.R. Rao, Phase Transitions in Solids, McGraw-Hill, New York, 1978.
[9] K.H. Hardtl, Ceram. Int. 8 (1982) 121–127.
[10] G. Arlt, H. Denderichs, Ferroelectrics 29 (1980) 47–50.
[11] D. Berlincourt, H.H.A. Krueger, B. Jaffe, J. Phys. Chem. Solids 25 (1964) 659–674.
[12] D. Berlincourt, H. Jaffe, H.H.A. Krueger, H. Jaffe, Appl. Phys. Lett. 3 (1963) 90–92.
[13] F. Moura, A.Z. Simões, L.S. Cavalcante, M.A. Zaghete, J.A. Varela, E. Longoa, J. Alloys Compd. 466 (2008) L15–L18.
[14] Z. Xu, X. Dai, D. Viehland, Phys. Rev. B 81 (1995) 6261–6271.
[15] H. He, X. Tan, J. Phys.:Condens. Matter 19 (2007) 136003.
[16] H. He, X. Tan, J. Am. Ceram. Soc. 90 (2007) 2090–2094.
[17] F. Jona, G. Shirane, F. Mazzi, R. Pepinsky, Phys. Rev. 105 (1957) 849–856.
[18] Z. Xu, X. Dai, D. Viehland, D.A. Payne, J. Am. Ceram. Soc. 78 (1995) 2220–2224.
[19] F. Jona, G. Shirane, F. Mazzi, R. Pepinsky, Phys. Rev. 97 (1955) 1584–1590.
[20] G. Shirane, E. Sawaguchi, Y. Takagi, Phys. Rev. 84 (1951) 476–481.
[21] I. MacLaren, R. Villaurrutia, B. Schaffer, L. Houben, A. Peláiz-Barranco, Adv. Funct. Mater. 22 (2012) 261–266.
[22] X. Tan, C. Ma, J. Frederick, S. Beckman, K.G. Webber, J. Am. Ceram. Soc. 94 (2011) 4091–4107.
[23] D. Viehland, D. Forst, Z. Xu, J.F. Li, J. Am. Ceram. Soc. 78 (1995) 2101–2112.
[24] D. Viehland, X.H. Dai, J.F. Li, Z. Xu, J. Appl. Phys. 84 (1998) 458–471.
[25] X. Dai, D. Viehland, J. Appl. Phys. 76 (1994) 3701–3709.
[26] J. Knudsen, D.I. Woodward, I.M. Reaney, J. Mater. Res. 18 (2003) 262–271.
[27] H. He, X. Tan, Phys. Rev. B 72 (2005) 024102.
[28] Y. Cai, F. Phillipp, A. Zimmermann, L. Zhou, F. Aldinger, M. Ruhle, Acta Mater. 51 (2003) 6429–6436.
[29] E.G. Fesenko, A.Ya. Dantsiger, L.A. Resnitchenko, M.F. Kupriyanov, Ferroelectrics 41 (1982) 137–142.

Thermochimica Acta 596 (2014) 21–28

Contents lists available at ScienceDirect

Thermochimica Acta

journal homepage: www.elsevier.com/locate/tca

Phase formation and evolution of Cu:Zn partials in binary metal pyrophosphates $Cu_{(2-x)}Zn_{(x)}P_2O_7$; $x \approx 1$

Rattanai Baitahe [a], Naratip Vittayakorn [a,b,*]

[a] Electroceramic Research Laboratory, College of KMITL Nanotechnology, King Mongkut's Institute of Technology Ladkrabang, Bangkok 10520, Thailand
[b] Advanced Materials Science Research Unit, Department of Chemistry, Faculty of Science, King Mongkut's Institute of Technology Ladkrabang, Bangkok 10520, Thailand

ARTICLE INFO

Article history:
Received 12 May 2014
Received in revised form 13 August 2014
Accepted 13 August 2014
Available online 28 September 2014

Keywords:
Phase formation
Metal pyrophosphates
X-ray absorption spectroscopy

ABSTRACT

Binary metal pyrophosphate powders were prepared by the solid state reaction method and subsequently calcined at 400, 500, 600, 700, and 800 °C in order to study Cu:Zn partial evolution to the final $CuZnP_2O_7$ product. Synchrotron X-ray absorption, X-ray diffraction, Raman, FT-IR spectroscopy, and thermogravimetric analysis were used in this investigation. Phase evolution of the reaction products was investigated systemically. The results showed that complicated mixtures contributed to the reaction of synthesis temperature. The reaction comprised $3CuO{\cdot}2P_2O_5{\cdot}0.3NH_3{\cdot}0.2H_2O$, $Cu_2P_2O_7$, $Zn_2P_2O_7$, and $Zn_2P_2O_7{\cdot}3H_2O$ intermediates. Decreasing percentage of $3CuO{\cdot}2P_2O_5{\cdot}0.3NH_3{\cdot}0.2H_2O$ intermediates was related directly to an increasing final product. Cu:Zn contents changed in $Cu_{(2-x)}Zn_{(x)}P_2O_7$ in the temperature range of 400–600 °C, when $x \approx 1$ clearly was related linearly to the reaction temperature. The final product was confirmed by EXAFS fitting spectra as solid solution between the Cu and Zn atom in the $CuZnP_2O_7$ structure, and it indicated environment around metal atoms.

1. Introduction

Metal pyrophosphates have had a wide range of applications such as microwave dielectric materials, chelating agents, corrosion-resistant coatings, glass ceramics, biomedical cements, and high-quality fertilizers [1–3]. The metal pyrophosphate, $M_2P_2O_7$, has been reported as various phase types [4]. An M radius structure greater than 0.97 Å has been observed as a dichromate type ($M = Ba^{2+}$, Cd^{2+}, Ca^{2+}, Sr^{2+}, and Pb^{2+}), in which a pair of $P_2O_7^{4-}$ groups crystallize in eclipsed conformation around the center of symmetry, with bridging O atoms extending towards each other. When the M radius is less than 0.97 Å ($M = Mg^{2+}$, Mn^{2+}, Co^{2+}, Cu^{2+}, Ni^{2+}, and Zn^{2+}), the structure is a thortveitite type, in which $P_2O_7^{4-}$ exists in staggered conformation. Furthermore, metal pyrophosphates were classified into two groups by stable phase temperatures [5]. They included alpha-phases, which are stable at low temperatures and beta-phases at high temperatures. Alpha and beta phases can be alternated at a critical temperature. In addition, different syntheses exhibited many phases such as glass → X → Y → β ←→ α phases [6]. Binary copper zinc pyrophosphate ceramic has different physicochemical, mechanical and biological properties because of different processes.

Most studies of metal phosphate focused on the synthesis and characterizations of both bulk [7,8] and nano particles [9], kinetics and the thermodynamics of reaction [10,11], and their properties [12,13]. However, the study of phase formation and atomic evolution of the final product, and intermediate substance relating phase, is not widely understood, and is therefore of interest. The objective of this study was to investigate Cu:Zn evolution of possible binary copper zinc pyrophosphate formation in a solid state reaction at different temperatures. In order to investigate the ideality of a fully solid solution, the probe needs to be more local. X-ray absorption spectroscopy (XAS), using synchrotron radiation, is an extremely suitable technique for studying local atomic and electronic structures of mixed metal phosphates, such as $CuZnP_2O_7$, and using extended X-ray absorption fine structure (EXAFS) measurements for probing structure of the final product.

2. Experimental procedure

Synthesis of $CuZnP_2O_7$ was conducted using traditional solid-state reaction techniques. High purity ZnO (99.9%), CuO (99.9%), and $(NH_4)_2HPO_4$ (99%) were used as raw materials. Stoichiometric mixtures of starting materials were homogenized by ball milling

* Corresponding author at: Advanced Materials Science Research Unit, Department of Chemistry, Faculty of Science, King Mongkut's Institute of Technology Ladkrabang, Bangkok 10520, Thailand. Fax: +66 2 326 4415.
E-mail address: naratipcmu@yahoo.com (N. Vittayakorn).

http://dx.doi.org/10.1016/j.tca.2014.08.038
0040-6031/

with ZrO_2 media in ethanol for 24 h, and batching was calcined for 2 h at 400, 500, 600, 700, and 800 °C. The phase content of the prepared samples was studied by X-ray powder diffraction using a Bruker D8 Advance X-ray Diffractometer (Bruker AXS, Karlsruhe, Germany) with Cu Kα radiation (λ = 0.1546 nm). Room temperature Fourier transform infrared (FT-IR) spectra were recorded in the range of 4000–400 cm^{-1} with eight scans on a PerkinElmer Spectrum GX spectrometer with the resolution of 4 cm^{-1}. Raman spectra were recorded in the range of 1300–100 cm^{-1} with eight scans on a thermo scientific DXR Raman microscope. Thermal analysis measurements (thermogravimetry, TG; derivative thermogravimetry, DTG) were taken using a PerkinElmer, Pyris 1 TGA. Experiments were conducted at room temperature on the beam line (BL8) of the National Synchrotron Research Center (Thailand), with a double crystal Ge(220) for the EXAFS mono-chromator. X-ray absorption (XAS) spectra at the Cu and Zn K-edge were obtained in transmission mode with air chambers. In addition, complete substitutional solid solutions, in accordance with the Hume–Rothery rules, may form if the solute and solvent have: similar atomic radii; $R_{Cu(II)}$ = 0.73 Å and $R_{Zn(II)}$ = 0.74 Å [14], similar electronegativities; Cu = 1.90 and Zn = 1.65, similar valency; Cu = 2+ and Zn = 2+ and same crystal structure; β-$Cu_2P_2O_7$ = monoclinic, C_2/m and β-$Zn_2P_2O_7$ = monoclinic, C_2/m. These data show high possibility of substitutional solid solution between Cu and Zn ions in pyrophosphate compound.

3. Results and discussion

Infrared and Raman spectroscopy are two powerful methods used to analyze compound bonding. These popular techniques are used to observe vibrational, rotational, and other low-frequency modes in the phosphates system. Fig. 1 shows Raman shift spectra when $x \approx 1$. Powders were calcined at different batch temperatures (400, 500, 600, 700, and 800 °C) using the solid state reaction method. Raman spectra were assigned as relating to the vibration unit; PO_4^{3-}, $P_2O_7^{4-}$, P_2O_5 clusters and metal oxide (M—O) bond. The samples were calcined at 600, 700, and 800 °C. The peak bands were similar. It is noticeably clear that the studied compounds exhibit more splitting and sharpness, especially in the low-frequency region (1400–100 cm^{-1}), indicating polymerization of

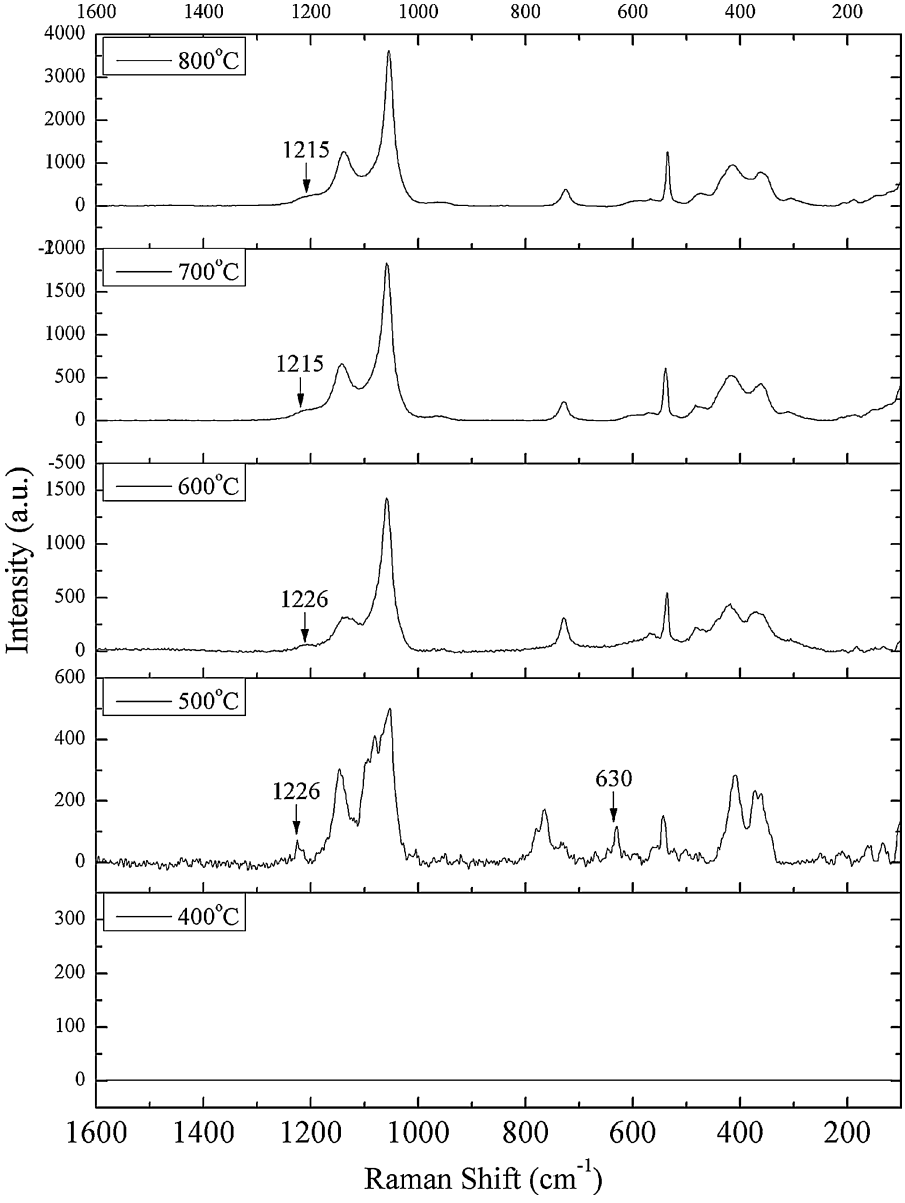

Fig. 1. Raman spectra of $Cu_{(2-x)}Zn_xP_2O_7$; $x \approx 1.00$, subsequently calcined at 400, 500, 600, 700, and 800 °C.

$[PO_4^{3-}]$ to $[P_2O_7]^{4-}$ [15,16]. The strong vibration bands around 1000–1100 cm^{-1} are attributed to stretching of the PO_4^{3-} unit. The bending vibration of the PO_4^{3-} unit is observed at about 450–650 cm^{-1}. These vibration bands were shown to remain in the phosphates group. The asymmetric and symmetric stretch of the P—O—P bridge in the $[P_2O_7]^{4-}$ unit for this sample were observed at around 930–970 and 680–760 cm^{-1} respectively, while P—O—P bending vibration is expected in the area 600–500 cm^{-1} (PO_2^{2-} radical) and 500–370 cm^{-1} (P—O—P bridge). These peaks were confirmed as characteristic of pyrophosphate compounds. In addition, the PO_3 deformation and rocking modes, P—O—P deformations, and torsional and external mode were found in the 430–180 cm^{-1} region. Metal—O stretching usually appears in the bending mode region, as the bending modes of the P—O—P bridge and absorption bands associated with these vibrations are usually very weak [17]. The weak band of approximately 1220 cm^{-1} exhibits a high temperature phase in pyrophosphate groups. These binary metal phosphates closely resemble those of the β-$Zn_2P_2O_7$ with a monoclinic structure and space group C_2/m [18]. A wave number of 630 cm^{-1} for sample powders was calcined at 500 °C, and assigned to asymmetric stretching of P—O in the P_2O_5 cluster [19]. The sample was calcined at 400 °C, which unable to be observed any peak. Generally, Raman spectroscopy only detect crystalline of compounds [20]. The very low crystallinity of sample was calcined at 400 °C caused Raman to be inactive. While, calcination temperature increases due to growing crystallinity of the sample. Intensity of Raman spectra shows high intensities following calcination temperature. This phenomena is similar to those observed by Zhang et al. [21], Liu et al. [22], and Fairbrother et al. [23]. However, Raman spectroscopy results did not clarify H_2O and NH_3 molecules, and this signifies the limitation of the Raman instrument. Therefore, H_2O and NH_3 molecules were analyzed by FT-IR spectroscopy techniques. The FT-IR spectra of samples are shown in Fig. 2. All strong vibration bands were attributed to the phosphates group according to Raman results. However, medium peaks in the range of 1630–1640 cm^{-1} were referred to as the bending vibration of water for samples calcined at 400, 500, and 600 °C. In addition, FT-IR spectra show a weak band at about 1430 cm^{-1}, particularly when calcined at 400 and 500 °C, and there is asymmetric bending

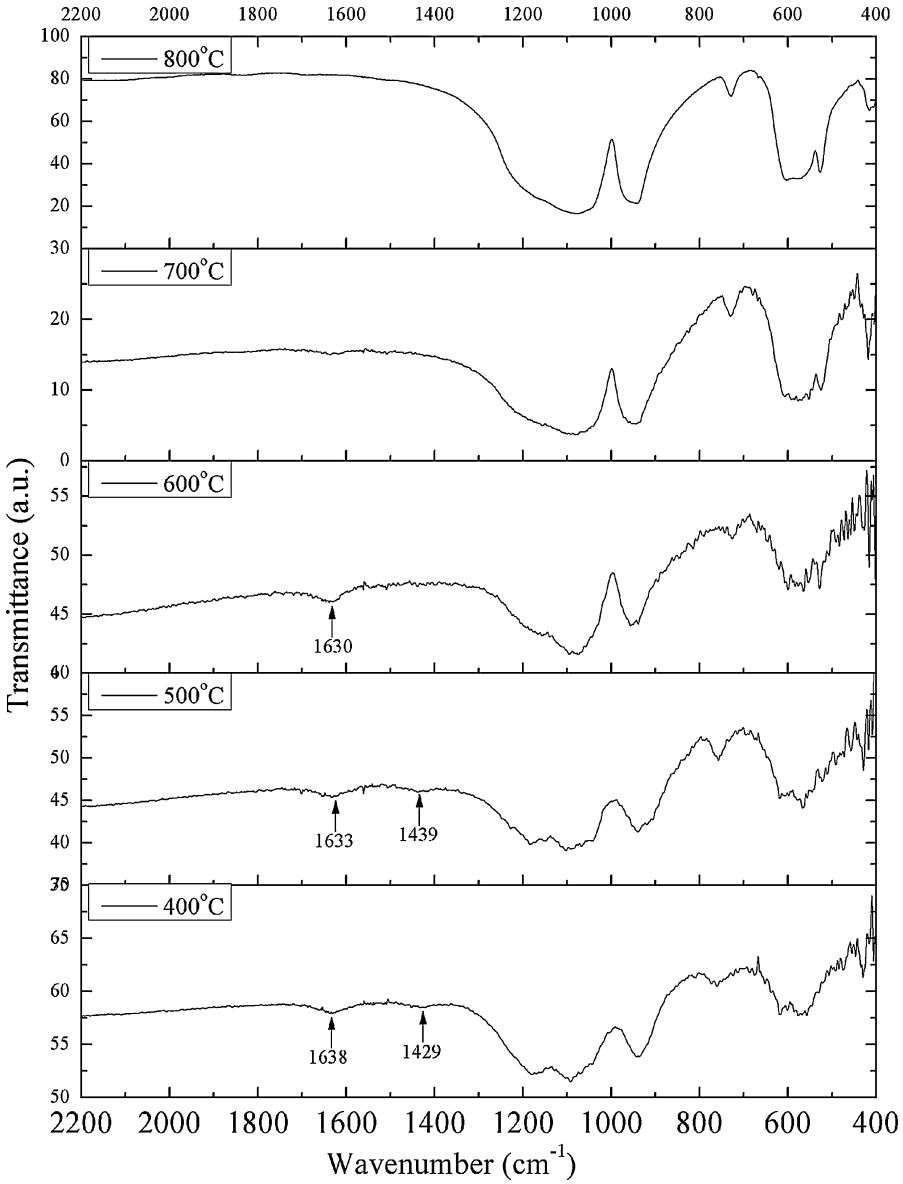

Fig. 2. FT-IR spectra of $Cu_{(2-x)}Zn_xP_2O_7$; $x \approx 1.00$, subsequently calcined at 400, 500, 600, 700, and 800 °C.

vibration of ammonia molecules in $3CuO{\cdot}2P_2O_5{\cdot}0.3NH_3{\cdot}0.2H_2O$ compound [24].

The XRD patterns of samples are shown in Fig. 3. This technique can be investigated by both qualitative and quantitative analysis. X-ray diffraction is used often to semi-quantitatively determine the weight fraction of constituents, which can be identified by comparing the integrated intensities of the diffraction peaks from each of the known phases. In addition, complex mixtures containing more than two phases also can be quantified. Even if one phase is amorphous, diffraction can still yield a relative amount of each phase. The diffraction pattern includes information of peak positions and intensity. The peak positions are indicative of the crystal structure and symmetry of the contributing phase. The peak intensities reflect total scattering from each plane in the crystal structure of the phase, and are dependent directly on the distribution of particular atoms in the structure [25]. Thus, intensities are ultimately related to both the structure and composition of the phase. The diffraction intensity equation has been studied many times [26–29], and is summarized below;

$$I_{(hkl)\alpha} = \frac{I_0\lambda^3}{64\pi r}\left(\frac{e^2}{m_e c^2}\right)^2 \frac{M_{(hkl)}}{V_\alpha^2}|F_{(hkl)\alpha}|^2 \left(\frac{1+\cos^2(2\theta)\cos^2(2\theta_m)}{\sin^2\theta\psi o\sigma\theta}\right)_{hkl} \frac{\nu_\alpha}{\mu_s} \quad (1)$$

where:

$I_{(hkl)\alpha}$: intensity of reflection of *hkl* in phase α.
I_0: incident beam intensity.
r: distance from specimen to detector.
λ: X-ray wavelength.
$(e^2/m_e c^2)^2$: square of classical electron radius.
μ_s: linear absorption coefficient of the specimen.
ν_α: volume fraction of phase α.
$M_{(hkl)}$: multiplicity of reflection *hkl* of phase α.
0: Lorentz-polarization (and monochromator) correction $\left(\frac{1+\cos^2(2\theta)\cos^2(2\theta_m)}{\sin^2\theta\cos\theta}\right)$.
V_α: volume of the unit cell of phase α.
$2\theta_m$: diffraction angle of the monochromator.

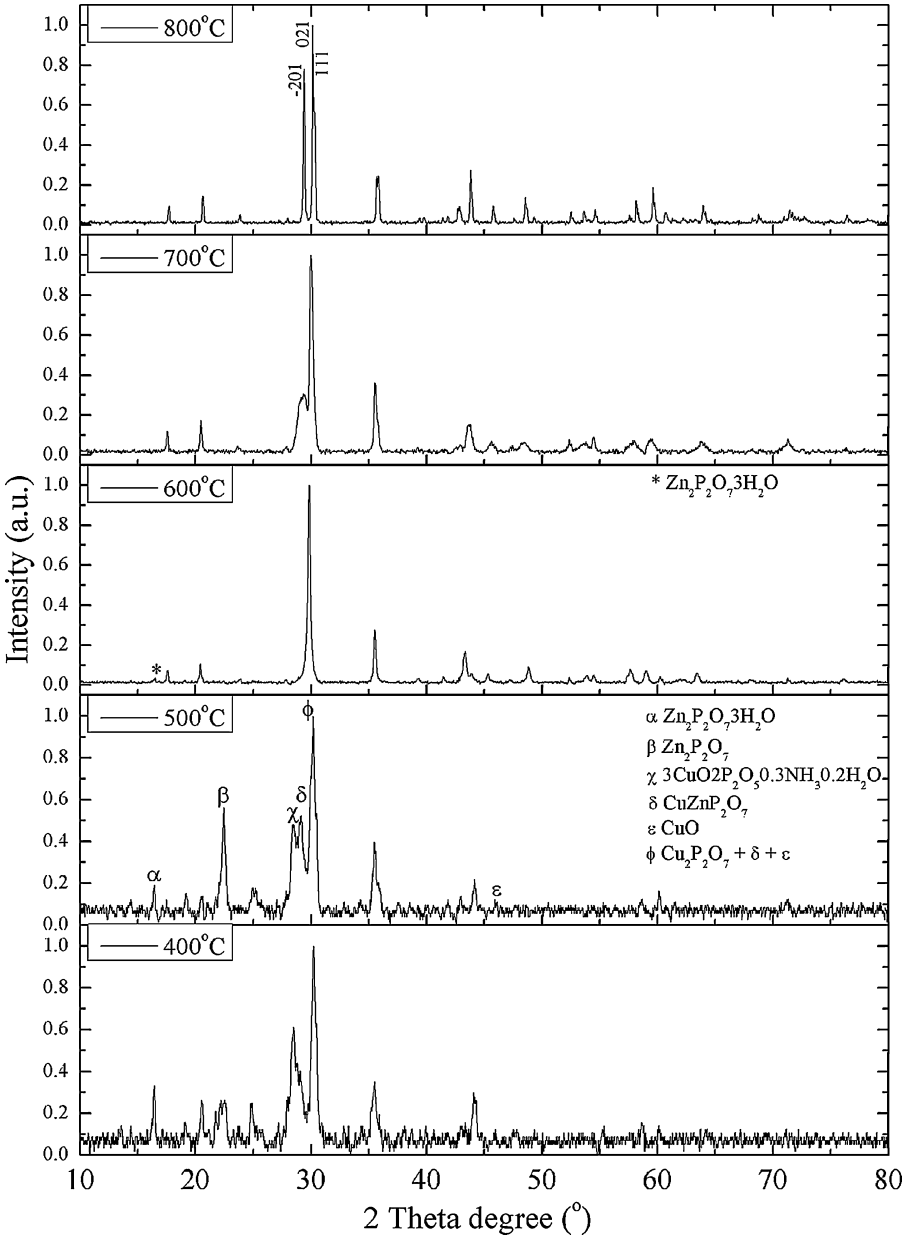

Fig. 3. XRD patterns of $Cu_{(2-x)}Zn_xP_2O_7$; $x \approx 1.00$, subsequently calcined at 400, 500, 600, 700, and 800 °C.

$F_{(hkl)\alpha}$: structure factor for reflection *hkl* of phase α (i.e., the vector sum of scattering intensities of all atoms contributing to that reflection).

In recognizing that many of these terms are consistent for a particular experimental setup, the experimental constant, K_e, can be defined. The constant, $K_{(hkl)\alpha}$, can be defined for a given phase that is in effect equal to the structure factor term for phase α. In substituting the weight fraction (X_α) for the volume fraction, the density of the phase (ρ_α) for the volume, and the mass absorption coefficient of the specimen $(\mu/\rho)_s$ for the linear absorption coefficient, yields the following equation:

$$I_{(hkl)\alpha} = \frac{K_e K_{(hkl)\alpha} X_\alpha}{\rho_\alpha (\mu/\rho)_s} \quad (2)$$

This equation describes the intensity for peak *hkl* in phase α in similar terms. The weight fraction, f_1, could be described as follows:

$$f_1 = \frac{(I_1^{mix}/I_1^{pure})A_2}{A_1 - (I_1^{mix}/I_1^{pure})(A_1 - A_2)} \quad (3)$$

where $I_1{}^{mix}$ and $I_1{}^{pure}$ are the phase 1 intensities in the mixture and pure material, respectively, and A_1 and A_2 are the mass absorption coefficients. Based on probability analysis, it is believed that the formation path of the $CuZnP_2O_7$ phase could be described as follows:

$$3CuO_{(s)} + 4NH_4H_2PO_{4(s)} \rightarrow 3CuO{\cdot}2P_2O_5{\cdot}0.3NH_3{\cdot}0.2H_2O_{(s)} + 3.7NH_{3(g)} + 5.8H_2O_{(g)} \quad (4)$$

$$2CuO_{(s)} + 2NH_4H_2PO_{4(s)} \rightarrow Cu_2P_2O_{7(s)} + 2NH_{3(g)} + 3H_2O_{(g)} \quad (5)$$

$$3CuO{\cdot}2P_2O_5{\cdot}0.3NH_3{\cdot}0.2H_2O_{(s)} + CuO_{(s)} \rightarrow 2Cu_2P_2O_{7(s)} + 0.3NH_{3(g)} + 0.2H_2O_{(g)} \quad (6)$$

$$2ZnO_{(s)} + 2NH_4H_2PO_{4(s)} \rightarrow Zn_2P_2O_7{\cdot}3H_2O_{(s)} + 2NH_{3(g)} \quad (7)$$

$$Zn_2P_2O_7{\cdot}3H_2O_{(s)} \rightarrow Zn_2P_2O_{7(s)} + 3H_2O_{(g)} \quad (8)$$

$$Cu_2P_2O_{7(s)} + Zn_2P_2O_{7(s)} \rightarrow 2CuZnP_2O_{7(s)} \quad (9)$$

It is highly probable that all reactions proceeded together. In Eqs. (4) and (5) reaction was competitive to reactions as follows:

$$5CuO_{(s)} + 6NH_4H_2PO_{4(s)} \rightarrow Cu_2P_2O_{7(s)} + 3CuO{\cdot}2P_2O_5{\cdot}0.3NH_3{\cdot}0.2H_2O_{(s)} + 5.7NH_{3(g)} + 8.8H_2O_{(g)} \quad (10)$$

Part of $Zn_2P_2O_7{\cdot}3H_2O$ was decomposed to $Zn_2P_2O_7$ and H_2O molecules, as in Eq. (8), while the $Cu_2P_2O_7$ and $Zn_2P_2O_7$ molecules were forced somewhat to fuse together by heating, as in Eq. (9). Products calcined at 400 °C represented the reaction at about 400 °C. The result exhibited the complication of mixed phases, which included CuO (JCPDS no. 80-1917), α-$Cu_2P_2O_7$ (JCPDS no. 44-0182), $3CuO{\cdot}2P_2O_5{\cdot}0.3NH_3{\cdot}0.2H_2O$ (JCPDS no. 49-1004), α-$Zn_2P_2O_7$ (JCPDS no. 49-1240), $Zn_2P_2O_7{\cdot}3H_2O$ (JCPDS no. 51-0201), and $Cu_{(2-x)}Zn_{(x)}P_2O_7$ when $x \approx 1$. All product contents (%wt) are shown in Table 1. The chemical reaction process is proposed in Eq. (11).

$$CuO_{(s)} + ZnO_{(s)} + 2NH_4H_2PO_{4(s)} \rightarrow 0.7358Cu_{(0.8695)}Zn_{(1.1305)}P_2O_{7(s)} + 0.0782Cu_2P_2O_{7(s)} + 0.0509(CuO)_3{\cdot}(P_2O_5)_2{\cdot}0.3NH_3{\cdot}0.2H_2O_{(s)} + 0.0389Zn_2P_2O_7{\cdot}3H_2O_{(s)} + 0.0452Zn_2P_2O_{7(s)} + 0.0509CuO_{(s)} + 1.9847NH_{3(g)} + 2.8732H_2O_{(g)} \quad (11)$$

Since starting reaction at room temperature until 400 °C, the total mass loss was 21.89% of NH_3 and H_2O (gas phases). The sample calcined at 500 °C, represented the reaction moment. This stage clearly shows decreasing content of $3CuO{\cdot}2P_2O_5{\cdot}0.3NH_3{\cdot}0.2H_2O$ and CuO compounds because the rate of reaction between CuO and $3CuO{\cdot}2P_2O_5{\cdot}0.3NH_3{\cdot}0.2H_2O$ to $Cu_2P_2O_7$ was increasing, while $Cu_2P_2O_7$ reacted with $Zn_2P_2O_7$ to $Cu_{(2-x)}Zn_{(x)}P_2O_7$; $x \approx 1$ to bring increasing $Cu_{(2-x)}Zn_{(x)}P_2O_7$ and decreasing $Cu_2P_2O_7$. This stage is the proposed reaction in Eq. (12) as follows.

$$CuO_{(s)} + ZnO_{(s)} + 2NH_4H_2PO_{4(s)} \rightarrow 0.7422Cu_{(0.9369)}Zn_{(1.0631)}P_2O_{7(s)} + 0.0776Cu_2P_2O_{7(s)} + 0.0373(CuO)_3{\cdot}(P_2O_5)_2{\cdot}0.3NH_3{\cdot}0.2H_2O_{(s)} + 0.0177Zn_2P_2O_7{\cdot}3H_2O_{(s)} + 0.0878Zn_2P_2O_{7(s)} + 0.0373CuO_{(s)} + 1.9888NH_{3(g)} + 2.9393H_2O_{(g)} \quad (12)$$

Total mass loss in NH_3 and H_2O gas phases at this stage was 22.21%, when the calcination temperature reached 600 °C. The result detected only $Cu_{(2-x)}Zn_{(x)}P_2O_7$; $x \approx 1$ and the trace quantity of $Zn_2P_2O_7{\cdot}3H_2O$ phases. This effect exhibited temperatures below 600 °C, and CuO and $3CuO{\cdot}2P_2O_5{\cdot}0.3NH_3{\cdot}0.2H_2O$ were a complete reaction. A majority of $Zn_2P_2O_7{\cdot}3H_2O$ was decomposed to $Zn_2P_2O_7$ and reacted with $Cu_2P_2O_7$ to $Cu_{(2-x)}Zn_{(x)}P_2O_7$; $x \approx 1$. This stage proposed the following reaction in Eqs. (8) and (9), the total mass loss was 22.52%.

$$CuO_{(s)} + ZnO_{(s)} + 2NH_4H_2PO_{4(s)} \rightarrow Cu_{(1.0009)}Zn_{(0.9991)}P_2O_{7(s)} + 0.0009Zn_2P_2O_7{\cdot}3H_2O_{(s)} + 2NH_{3(g)} + 2.9972H_2O_{(g)} \quad (13)$$

According to IR results, no peak was detectable at around 1430 cm^{-1} of asymmetric bending vibration of ammonia ($\delta_{as}NH_4$) clusters. However, IR observed a weak band at about 1630 cm^{-1}, which indicated bending vibration of a water molecule for $Zn_2P_2O_7{\cdot}3H_2O$. The $CuZnP_2O_7$ sample was a complete reaction at a temperature of about 700 °C. XRD results showed a single phase of $Cu_{(2-x)}Zn_{(x)}P_2O_7$; $x = 1$. Diffraction patterns of the sample were similar to those obtained from individual β-$M_2P_2O_7$ [5,30]. At the 700 °C, The XRD pattern showed only a single phase of $CuZnP_2O_7$, and peak (−2 0 1), (0 2 1), and (1 1 1) clearly were separated. These affects caused atomic arrangement that brought long ordering in the crystal structure. In this state, the total mass loss was equal to that in the previous state. The reaction could be concluded as follows:

$$CuO_{(s)} + ZnO_{(s)} + 2NH_4H_2PO_{4(s)} \rightarrow Cu_{(1.0000)}Zn_{(1.0000)}P_2O_{7(s)} + 2NH_{3(g)} + 3H_2O_{(s)} \quad (14)$$

Intermediates of all of states included α-$Cu_2P_2O_7$, $3CuO{\cdot}2P_2O_5{\cdot}0.3NH_3{\cdot}0.2H_2O$, α-$Zn_2P_2O_7$, and $Zn_2P_2O_7{\cdot}3H_2O$, of

Table 1
Approximation of percentage by weigh from XRD results.

Temperature (°C)	Percentage of compounds (%wt)					
	CuO	$3CuO{-}2P_2O_5 0.3NH_3 0.2H_2O$	$Cu_2P_2O_7$	$Zn_2P_2O_7$	$Zn_2P_2O_7 3H_2O$	$Cu_{(2-x)}Zn_{(x)}P_2O_7$
800	–	–	–	–	–	100.00
700	–	–	–	–	–	100.00
600	–	–	–	–	2.03	97.97
500	2.97	19.83	23.37	26.74	6.36	20.71
400	4.05	27.08	23.54	13.78	13.95	17.61

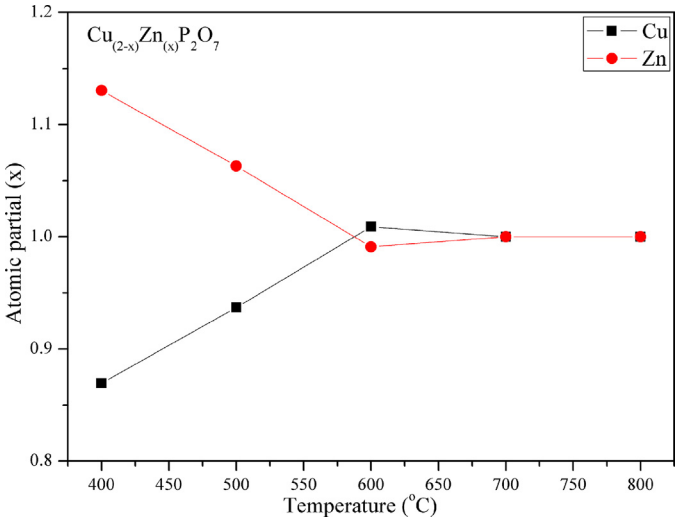

Fig. 4. Plots of the relationship of the atomic partial, Cu:Zn, versus reaction temperature.

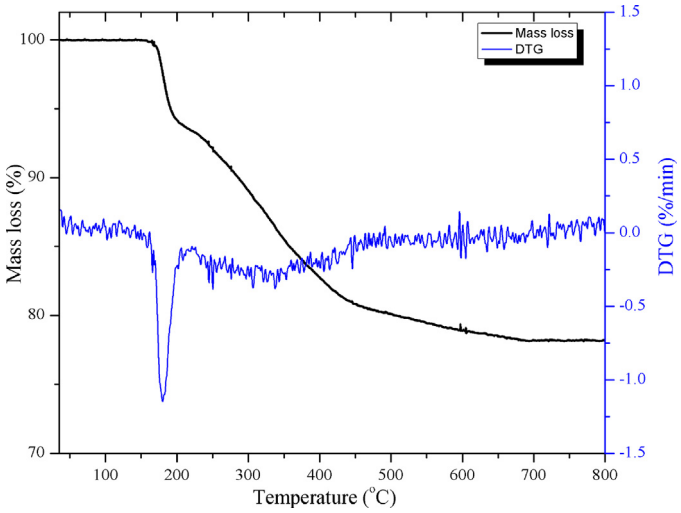

Fig. 5. TG/DTG of $CuZnP_2O_7$ precursor powder.

which $Zn_2P_2O_7{\cdot}3H_2O$ was the strongest intermediate substance, because the heating energy it requires to reach temperatures higher than 600 °C breaks all bonds in $Zn_2P_2O_7{\cdot}3H_2O$ molecules.

When evaluation of Zn and Cu atoms to $CuZnP_2O_7$ structure is considered, the relationship of the atomic partial, Cu:Zn, versus reaction temperature is shown in Fig. 4. This result was classified into two parts. Firstly, a reaction temperature of below 600 °C was included, and secondly a reaction temperature above 600 °C. In the former, the increasing relationship of Cu or decreasing Zn clearly occupied a linear relationship with:

$$b = 0.0003a + 0.2949 \quad (15) \qquad (15)$$

and strong linear regression of $R^2 = 0.9996$, when b is the atomic partial, and a the reaction temperature (°C). These relationships predict occupancies between Cu and Zn atoms in $Cu_{(2-x)}Zn_{(x)}P_2O_7$; $x \approx 1$ structure at different temperatures. In the latter, atomic occupancy was close to 1. This range of temperature was close to a complete reaction. The other phases were fused to β-$Cu_2P_2O_7$ and β-$Zn_2P_2O_7$ (high temperature phases) before being assembled into one structure. A similar crystal structure with a monoclinic system, and C_2/m space group, was above two compounds. Normally, low temperature is called alpha phases, α-$Cu_2P_2O_7$ is a crystal structure with a monoclinic system and C_2/c space group, $Z = 4$, and α-$Zn_2P_2O_7$ is a crystal structure with a monoclinic system and I2/c space group, $Z = 12$. Meanwhile, β-$Cu_2P_2O_7$ and β-$Zn_2P_2O_7$ phases are finally intermediate and easily phased for formation of $CuZnP_2O_7$ compound. In addition, the mechanisms of the proposed $CuZnP_2O_7$ phase formation were supported by the result of Thermogravimetric analysis (TGA).

The thermal property of the studied compound was investigated on a TG-DTG (Thermogravimetry, TG; Derivative Thermogravimetry, DTG). The TG curve in Fig. 5 shows the mass loss of between 30 and 800 °C, which is a related multi-stage decomposition. On the basis of TG data, the final decomposed product seemed to occur at a temperature above 700 °C and the water and ammonia content were determined. The first mass loss was 18.24% in the range of 50–400 °C. The second to fifth mass loss was 19.88, 21.09, 21.79, and 21.79%, in the range of 400–500, 500–600, 600–700 and 700–800 °C, respectively. All stages corresponded in continuum with the elimination of three molecules of crystallized water and two molecules of crystallized ammonia. The total mass loss of 21.81% was close to the XRD values. The retained mass of about 78% was comparable with the value expected for the formation of $CuZnP_2O_7$, thus verified by XRD, Raman, and FT-IR measurements. Comparison values between the proposed TGA and XRD mass loss, which are close, are shown in Table 2.

As extended X-ray absorption fine structure (EXAFS) is very sensitive to change in local geometry, spectra collected at both edges could help in understanding Fourier transform evolutions. The EXAFS results were used for support XRD results of substitutional solid solution between Cu and Zn ions in the binary metal pyrophosphate compound. Therefore, EXAFS data were supported. The data set were then analyzed by 'data processing' with ATHENA software [31]. Accurate details of EXAFS such as interatomic distances and coordination numbers were obtained by 'curve fitting' (Fig. 6) through ARTHEMIS software [31]. The details of shell which were presented in Table 3. Cu K-edge and Zn K-edge were considered. In the case of Cu K-edge, the primitive EXAFS model was taken from parameters obtained from Robertson et al. [30]. The results of fitting were demonstrated the asymmetry of CuO_6 octahedral. The first shell to be modeled was the one consisting of four equatorial oxygen atoms, ($Cu—O_{eq}$) with interatomic distances of 1.96081 Å. Then the two axial oxygen atoms were taken into account ($Cu—O_{ax}$) with interatomic distances of 2.26967 Å, introducing the Jahn–Teller distortion effect undergone by the copper octahedral centered site into the model. The next shell was then added to the model to describe the combination of Cu–M (M = Cu/Zn), and Cu–P interaction. Addition of fourth shell did not improve the quality of the fitting. Zn K-edge were similar to the Cu K-edge fitting, the initial EXAFS model was taken from parameters obtained from Calvo [5]. Zn K-edge EXAFS spectrum was identified, as in the case of Cu, with interatomic distances of 2.03230 and 2.35242 Å for first and second shell, respectively. The peak shifted to a high radial distance, due to a larger atomic radius. These results clearly confirmed that the

Table 2
Comparison values between the proposed TGA and XRD mass loss.

Temperature (°C)	Mass loss (%)	
	XRD	TGA
400	21.89	18.24
500	22.21	19.88
600	22.52	21.09
700	22.54	21.78
800	22.54	21.81

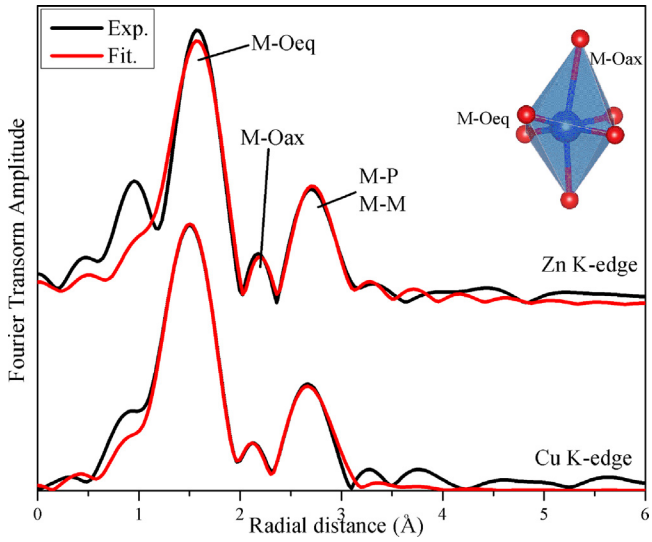

Fig. 6. Experiment (Black line) and fitted EXAFS data (Red line) at Cu and Zn K-edge of $CuZnP_2O_7$. (For interpretation of the references to color in this figure legend, the reader is referred to the web version of this article.)

Table 3
Results obtained by EXAFS fitting analysis.

Sample	Path	Shell	CN	R(Å)	σ^2(Å^2)	R-factor
$CuZnP_2O_7$	Cu-Oeq	1	4	1.96081	0.00704	0.0061
	Cu-Oax	2	2	2.26967	0.01537	
	Cu-Cu	3	1	3.01409	0.00738	
	Cu-P1	3	2	3.07768	0.05747	
	Cu-P2	3	2	3.11544	0.04976	
	Zn-Oeq	1	4	2.03230	0.00796	0.0123
	Zn-Oax	2	2	2.35242	0.07798	
	Zn-Zn	3	1	3.12398	0.01144	
	Zn-P1	3	2	3.18988	0.04815	
	Zn-P2	3	2	3.22903	0.00469	

$Zn_2P_2O_7$ is a completely solid solution with $Cu_2P_2O_7$ being brought to a $CuZnP_2O_7$ compound.

4. Conclusion

Phase formation of the binary metal pyrophosphate, $CuZnP_2O_7$, was studied at different temperatures in the range of 400–800 °C. Samples were obtained by solid state reaction using stoichiometry of CuO, ZnO and $NH_4H_2PO_4$ at ambient temperature to 800 °C. Intermediate substances of reaction were observed by FT-IR, Raman, and XRD measurements that included α-$Cu_2P_2O_7$, α-$Zn_2P_2O_7$, $3CuO{\cdot}2P_2O_5{\cdot}0.3NH_3{\cdot}0.2H_2O$, and $Zn_2P_2O_7{\cdot}3H_2O$, of which $Zn_2P_2O_7{\cdot}3H_2O$ was the strongest intermediate substance. The $CuZnP_2O_7$ sample completely reacted at a temperature of about 700 °C, with low crystallinity. When the temperature increased to about 800 °C, the structure had an ordering atomic arrangement, which was brought to long range order and increased crystallinity. Cu:Zn evolution in the structure was separated into two parts with increasing temperature that started below 600 °C. Thus, increasing Cu and decreasing Zn contents had clear linear relationships. When the temperature rose above 600 °C, the range of reaction was close to completion. The calcination temperature has been found to have a pronounced effect on phase formation and chemical composition of the calcined $CuZnP_2O_7$ powders. The complete solid solution was clearly confirmed by EXAFS fitting spectra.

Acknowledgements

This work has partially been supported by the National Nanotechnology Center (NANOTEC), NSTDA, Ministry of Science and Technology, Thailand, through its program of Center of Excellence Network, the Synchrotron Light Research Institute (Public Organization) for EXAFS measurement and the Thailand Research Fund (TRF) under Grant No. BRG5680006.

References

[1] J.J. Bian, D.W. Kim, K.S. Hong, Microwave dielectric properties of $A_2P_2O_7$ (A = Ca, Sr Ba; Mg, Zn, Mn), Jpn. J. Appl. Phys. 1 43 (2004) 3521–3525.
[2] J.J. Bian, D.W. Kim, K.S. Hong, Microwave dielectric properties of $(Ca_{1-x}Zn_x)_2P_2O_7$, Mater. Lett. 59 (2005) 257–260.
[3] W. Wenwei, F. Yanjin, W. Xuehang, L. Sen, L. Shushu, Preparation via solid-state reaction at room temperature and characterization of layered nanocrystalline $NH_4MnPO_4{\cdot}H_2O$, J. Phys. Chem. Solids 70 (2009) 584–587.
[4] M. Weil, B. Stöger, Crystal chemistry of transition metal diarsenates $M_2As_2O_7$ (M = Mn, Co, Ni, Zn): variants of the thortveitite structure, Acta Crystallogr. B 66 (2010) 603–614.
[5] C. Calvo, The crastal structure and phase transition of β-$Zn_2P_2O_7$, Can. J. Chem. 43 (1965) 1147–1153.
[6] M.A. Petrova, V.I. Shitova, G.A. Mikirticheva, V.F. Popova, A.E. Malshikov, New data on $Zn_2P_2O_7$ phase transformations, J. Solid State Chem. 119 (1995) 219–223.
[7] Z.W. Xiao, G.R. Hu, Z.D. Peng, K. Du, X.G. Gao, Solid state synthesis and characterization of iron(II) pyrophosphate $Fe_2P_2O_7$, Chin. Chem. Lett. 18 (2007) 1525–1527.
[8] A. Bensalem, M. Ahluwalia, T.V. Vijayaraghavan, Y.H. Ko, Synthesis of amorphous $MgHPO_4{\cdot}x(R)$ [R = ethanol; ethylene glycol] in anhydrous media, Mater. Res. Bull. 32 (1997) 1473–1483.
[9] C. Díaz, M.L. Valenzuela, V. Lavayen, K. Mendoza, D.O. Peña, C. O'Dwyer, Nanostructured copper oxides and phosphates from a new solid-state route, Inorg. Chim. Acta 377 (2011) 5–13.
[10] D. Brandová, M. Trojan, M. Arnold, F. Paulik, J. Paulik, Mechanism of dehydration and condensation of $CuHPO_4{\cdot}H_2O$, J. Therm. Anal. 34 (1988) 1449–1454.
[11] D. Brandová, M. Trojan, F. Paulik, J. Paulik, Mechanism of dehydration of $ZnHPO_4{\cdot}H_2O$, J. Therm. Anal. 32 (1987) 1923–1928.
[12] A. Jouini, J.C. Gâcon, M. Ferid, M. Trabelsi-Ayadi, Luminescence and scintillation properties of praseodymium poly and diphosphates, Opt. Mater. 24 (2003) 175–180.
[13] T. Yang, J. Lin, Hydrothermal syntheses and low temperature magnetic behaviors of $ACo_3(P_2O_7)_2$ (A = Ca, Sr Ba, Pb), J. Solid State Chem. 198 (2013) 1–5.
[14] R. Shannon, Revised effective ionic radii and systematic studies of interatomic distances in halides and chalcogenides, Acta Crystallogr. A 32 (1976) 751–767.
[15] E. Steger, B. Käßner, Die infrarotspektren von wasserfreien schwermetall-diphosphaten, Spectrochim. Acta A M 24 (1968) 447–456.
[16] B. Boonchom, R. Baitahe, Synthesis and characterization of nanocrystalline manganese pyrophosphate $Mn_2P_2O_7$, Mater. Lett. 63 (2009) 2218–2220.
[17] B. Boonchom, M. Thongkam, S. Kongtaweelert, N. Vittayakorn, Flower-like microparticles and novel superparamagnetic properties of new binary $Co_{1/2}Fe_{1/2}(H_2PO_4)_22H_2O$ obtained by a rapid solid state route at ambient temperature, Mater. Res. Bull. 44 (2009) 2206–2210.
[18] K. Pogorzelec-Glaser, A. Pietraszko, B. Hilczer, M. Polomska, Structure and phase transitions in $Cu_2P_2O_7$, Phase Transit. 79 (2006) 535–544.
[19] K. Meyer, Characterization of the structure of binary zinc ultraphosphate glasses by infrared and Raman spectroscopy, J. Non-Cryst. Solids 209 (1997) 227–239.
[20] L. Jin-bing, J. Zhi-quan, Q. Kun, H. Wei-xin, Effect of calcination temperature on surface oxygen vacancies and catalytic performance towards CO oxidation of Co_3O_4 nanoparticles supported on SiO_2, Chin. J. Chem. Phys. 25 (2012) 103.
[21] S. Zhang, C. Zhang, H. Yang, Y. Zhu, Formation and performances of porous $InVO_4$ films, J. Solid State Chem. 179 (2006) 873–882.
[22] F.M. Liu, J.H. Ye, B. Ren, Z.L. Yang, Y.Y. Liao, A. See, L. Chan, Z.Q. Tian, Raman spectroscopic studies of the formation processes of cobalt silicide thin films, Thin Solid Films 471 (2005) 257–263.
[23] A. Fairbrother, X. Fontané, V. Izquierdo-Roca, M. Espíndola-Rodríguez, S. López-Marino, M. Placidi, L. Calvo-Barrio, A. Pérez-Rodríguez, E. Saucedo, On the formation mechanisms of Zn-rich Cu_2ZnSnS_4 films prepared by sulfurization of metallic stacks, Sol. Energ. Mat. Sol. C 112 (2013) 97–105.
[24] G. Berhault, P. Afanasiev, H. Loboue, C. Geantet, T. Cseri, C. Pichon, C. Guillot-Deudon, A. Lafond, In Situ XRD XAS, and magnetic susceptibility study of the reduction of ammonium nickel phosphate $NiNH_4PO_4H_2O$ into nickel phosphide, Inorg. Chem. 48 (2009) 2985–2992.
[25] P.Y.Z.K. Vitalij Pecharsky, Fundamentals of Powder Diffraction and Structural Characterization of Materials, 2nd ed., Springer, 2009, 2014.
[26] H.P. Klug, L.E. Alexander, X-ray Diffraction Procedures for Polycrystalline and Amorphous Materials, 2nd ed., Wiley, New York, 1974.
[27] J.I. Langford, A.J.C. Wilson, Scherrer after sixty years: a survey and some new results in the determination of crystallite size, J. Appl. Crystallogr. 11 (1978) 102–113.

[28] S. Calvin, S.X. Luo, C. Caragianis-Broadbridge, J.K. McGuinness, E. Anderson, A. Lehman, K.H. Wee, S.A. Morrison, L.K. Kurihara, Comparison of extended X-ray absorption fine structure and Scherrer analysis of X-ray diffraction as methods for determining mean sizes of polydisperse nanoparticles, Appl. Phys. Lett. 87 (2005) .
[29] D.-M. Smilgies, Scherrer grain-size analysis adapted to grazing-incidence scattering with area detectors, J. Appl. Crystallogr. 42 (2009) 1030–1034.
[30] B.E. Robertson, C. Calvo, Crystal structure of β-$Cu_2P_2O_7$, Can. J. Chem. 46 (1968) 605–612.
[31] B. Ravel, M. Newville, Athena, Artemis, Hephaestus, data analysis for X-ray absorption spectroscopy using IFEFFIT, J. Synchrotron Radiat. 12 (2005) 537–541.

Phase transitions, ferroelectric, and piezoelectric properties of lead-free piezoelectric x$BaZrO_3$–(0.25–x)$CaTiO_3$–0.75$BaTiO_3$ ceramics

Nopsiri Chaiyo, David P. Cann & Naratip Vittayakorn

Journal of Materials Science
Full Set - Includes `Journal of Materials Science Letters'

ISSN 0022-2461
Volume 50
Number 18

J Mater Sci (2015) 50:6171-6179
DOI 10.1007/s10853-015-9174-y

Springer

J Mater Sci (2015) 50:6171–6179
DOI 10.1007/s10853-015-9174-y

Phase transitions, ferroelectric, and piezoelectric properties of lead-free piezoelectric xBaZrO$_3$–(0.25−x)CaTiO$_3$–0.75BaTiO$_3$ ceramics

Nopsiri Chaiyo[1,2] · David P. Cann[2] · Naratip Vittayakorn[3,4]

Received: 27 April 2015 / Accepted: 10 June 2015 / Published online: 17 June 2015

Abstract Lead-free xBaZrO$_3$–(0.25−x)CaTiO$_3$–0.75BaTiO$_3$; x = 0.00–0.25 ceramics were successfully prepared using the conventional solid-state reaction method. Analysis of the sintered ceramics showed that all compositions exhibited a pure phase perovskite. The effects of composition on the phase transition, ferroelectric properties, and piezoelectric properties were studied. With the increasing BaZrO$_3$ content, the phase transition temperature (T_C) decreased and the coercive field E_c decreased. The phase diagram featuring a cubic–rhombohedral–tetragonal triple point ($x \sim 0.125$) was derived from X-ray diffraction data and dielectric data as a function of temperature. Compositions near the convergence region exhibited the maximum peak in permittivity of ~11,400 at T_C. In addition, the morphotropic phase boundary compositions showed an enhancement in ferroelectric and piezoelectric properties. The composition 0.125BaZrO$_3$–0.125CaTiO$_3$–0.75BaTiO$_3$ exhibited the highest strain values of 0.14 % and a d^*_{33} of 474 pm/V.

✉ Nopsiri Chaiyo
azino_noise@hotmail.com; chaiyon@onid.oregonstate.edu

[1] Electroceramic Research Laboratory, College of Nanotechnology, King Mongkut's Institute of Technology Ladkrabang, Bangkok 10520, Thailand

[2] Materials Science, School of Mechanical, Industrial, and Manufacturing Engineering, Oregon State University, Corvallis, OR 97331, USA

[3] Department of Chemistry, Faculty of Science, King Mongkut's Institute of Technology Ladkrabang, Bangkok 10520, Thailand

[4] Advanced Materials Research Unit, Faculty of Science, King Mongkut's Institute of Technology Ladkrabang, Bangkok 10520, Thailand

Introduction

Lead-free piezoelectric materials have been an important research topic in the drive to find alternative materials to replace PZT-based ceramics according to global restrictions concerning the toxicity of lead and its derivatives [1–3]. Barium titanate (BaTiO$_3$; BT) is a well-known ferroelectric perovskite oxide which possesses high piezoelectric coefficients (e.g. d_{33} = 190 pC/N) [4]. To modify its piezoelectric properties, complex perovskite materials with A- and/or B-site substituted systems have been studied. Perovskites that feature a composition-induced phase transition between two ferroelectric phases or morphotropic phase boundary (MPB) have been reported to possess superior properties, and materials which exploit this approach are promising candidates for next-generation environmentally benign piezoelectric materials [5–7]. In 2009, the pseudo-binary lead-free Ba(Zr$_{0.2}$Ti$_{0.8}$)O$_3$–x(Ba$_{0.7}$Ca$_{0.3}$)TiO$_3$ system was reported by Liu and Ren [8] with excellent piezoelectric properties that were claimed to be due to the existence of cubic–rhombohedral–tetragonal (C–R–T) triple point similar to that observed in PZT and PMN-PT [8, 9]. The composition 50Ba(Zr$_{0.2}$Ti$_{0.8}$)O$_3$–50(Ba$_{0.7}$Ca$_{0.3}$)TiO$_3$ exhibited a surprisingly high piezoelectric coefficient d_{33} value of 560–620 pC/N which exceeds that of soft PZT compositions. The value of dS/dE equal to 1140 pm/V is higher than that of all PZT ceramics, which are typically around 360–900 pm/V [8]. The origin of the high dielectric constant and excellent piezoelectric properties was proposed to be due to the anisotropic flattening of the free energy function for compositions at the MPB composition. The very weak polarization anisotropy yields a low barrier between ⟨001⟩T and ⟨111⟩R polarization states which allows the polarization to rotate easily [8]. This is similar to the mechanism in PZT-based ceramics [8, 9]. Recently, there are many attempts to

study and explain the superior properties of the system via composition–structure–property relationships. The terms "convergence region" [10] and "diffusion phase transition" [11] were proposed rather than the tricritical point (TCP) due to ambiguity in the transition region.

Considering the coexistence of the R and T phases, since the symmetries of these phases are not group–subgroup related and the parent phase $BaTiO_3$ has an intermediate orthorhombic phase (O) between the two, high-resolution synchrotron X-ray diffraction (XRD) [10, 12], Raman spectroscopy, [13–15] and convergent beam electron diffraction (CBED) [16] techniques have been utilized to analyze ceramics near the MPB compositions. These findings revealed the existence of an intermediate O phase between the T and R phases in the MPB region [10, 11, 13, 14]. In contrast, several literature reports have claimed that there is no evidence of an orthorhombic intermediate phase [12, 15, 16]. The coexistence of two different phases in different ratios was proposed and as part of a so-called two-phase mixture model [12, 14, 15]. Furthermore, a microstructure study of MPB compositions showed that high piezoelectric coefficient also coincides with a miniaturized nanodomain structure with a domain hierarchy [17, 18]. The low polarization anisotropy, polarization extension, and elastic softening at MPB were reported to be the mechanisms for the superior piezoelectric properties [19–22]. Nevertheless, in contrast to the nearly vertical MPB separating the R and T phases in PZT, the boundary in the $Ba(Zr_{0.2}Ti_{0.8})O_3$–$(Ba_{0.7}Ca_{0.3})TiO_3$ system is strongly temperature and composition dependent.

To study the composition-induced transition, a range of compositions was designed around the known MPB composition. The present study examines ceramics in the ternary system of $x BaZrO_3$–$(0.25-x)CaTiO_3$–$0.75BaTiO_3$; $x = 0.00$–0.25 (xBZ–CT–0.75BT) which has not been investigated elsewhere. Ceramics were prepared and examined to determine the dielectric, ferroelectric, and piezoelectric properties. These results will enable a more complete ternary phase diagram to be developed which will aid in the development of new improved environmentally benign piezoelectric materials.

Experimental procedure

Synthesis and fabrication

The $x BaZrO_3$–$(0.25-x)CaTiO_3$–$0.75BaTiO_3$; $x = 0.00$–0.25 (xBZ–CT–0.75BT) ceramics were synthesized using a conventional solid-state reaction method. $BaCO_3$ (≥98.5 %, Sigma-Aldrich), ZrO_2 (99.0 %, Riedel-deHaën), $CaCO_3$ (99.5 %, BDH Chemicals), and TiO_2 (99.0–100.5 %, Riedel-deHaën) were used as the raw materials. Each starting material was weighed according to the stoichiometric formula and ball milled for 18 h in polyethylene bottle with yttria-stabilized zirconia balls using ethyl alcohol as medium. After drying, the precursor was calcined in an alumina crucible at 1200 °C for 4 h followed by grinding using mortar and pestle, 2nd-milling and sieving. Then, the powder was mixed with 5 wt% polyvinyl alcohol (PVA) solution and uniaxially pressed into green disk with a diameter of 10 mm. The pellets were sintered at 1400 °C for 4 h in a covered alumina crucible.

Characterizations

Densities of sintered ceramics disks were determined by the Archimedes' method. The phase and crystal structure determination of crashed sintered pellets were characterized using an X-ray diffractometer (XRD, Bruker AXS D8 Discover, Madison, WI, USA) in the range of 2θ between 20° and 80°. The surface of ceramics was examined using scanning electron microscope (SEM, FEI Quanta 600 FE-SEM, Hillsboro, OR, USA). In order to prepare electrodes for electrical properties measurements, silver paste was applied on both surfaces of the polished disk and then fired at 700 °C for 30 min. The temperature-dependent dielectric constant ε_r and dielectric loss tan δ measurements over a temperature range of −150–200 °C were performed in the frequency range from 1 to 100 kHz using a custom sample holder placed in a Delta Design 9023 Environmental Test Chamber (Delta design, INC., Poway, CA, USA) coupled with an LCR meter (Agilent 4284A, Santa Clara, CA, USA). Polarization hysteresis was measured at room temperature and 1 Hz using a Radiant Technology ferroelectric test system (RT66A, Albuquerque, New Mexico) utilizing Vision software. Strain hysteresis measurements were acquired at room temperature using this system coupled with an interferometric sensor (MTI Instruments 2100 Fotonic Sensor, Albany, New York). Low-field piezoelectric coefficient d_{33} was determined at room temperature on pooled samples by a YE2730A d_{33} test meter (SINOCERA, Yangzhou, China). The samples were pooled in silicone oil bath by applying a DC electric field of 40 kV/cm for 30 min at room temperature. The planar electromechanical coupling factor k_p and quality factor Q_m were determined by a resonance–antiresonance method with an impedance analyzer (Solartron SI1260A equipped with Solartron 1296A dielectric interface, Farnborough, UK) in the frequency range of 100–600 kHz by applying the SMaRT impedance measurement software program.

Results and discussion

The sintered density values for ceramic disks of the compositions $x BaZrO_3$–$(0.25-x)CaTiO_3$–$0.75BaTiO_3$; $x = 0.00$–0.25 (xBZ–CT–0.75BT) were determined by the Archimedes'

method [23] and the relative theoretical densities (%TD) are reported in Table 1. In general, the ceramics achieved relatively high densities in the range of 93–98 % of theoretical density. The approximate average grain size values extracted from SEM micrographs of the surface of BT–BZ–CT ceramics using the linear intercept method [24] were found to be in the range of 4–17 μm for all compositions. There were no apparent trends in the relationship between grain size and composition.

The XRD patterns of crushed sintered ceramics are shown in Fig. 1a. Figure 1b shows the enlarged reflections. It can be clearly seen that all specimens possess a single-phase perovskite without any secondary phases. With the increasing BZ content, the diffraction peaks shifted significantly to lower angles which correlates well with the expectations due to an increase in average cation radii due to the substitution of the larger Ba^{2+} (1.64 Å) for Ca^{2+} (1.34 Å) on the A-site and the substitution of the larger Zr^{4+} (0.72 Å) for Ti^{4+} (0.605 Å) on the B-site. This also resulted in an increased volume of the unit cell. The corresponding lattice parameters calculated using Cohen's method [25] and unit cell volumes for all compositions in this study are shown in Table 1. For the compositions with $x = 0.00$–0.10, the splitting of the {200} reflection is characteristic of tetragonal symmetry (Fig. 1b). The degree of splitting diminished as the BZ content increased and eventually became negligible for $x > 0.10$. This suggests that the solid solution undergoes a transformation from tetragonal symmetry to another phase with higher symmetry.

Figure 2 shows temperature dependence of dielectric constant ε_r (a) and dielectric loss tan δ (b) of the xBZ–CT–0.75BT ceramics measured at 1 kHz upon cooling from 200 to −150 °C. The ε_r data show a dielectric maxima along with an abrupt change in dielectric loss tan δ which are linked to a ferroelectric tetragonal to paraelectric cubic phase transition. This indicates that, for the composition $x > 0.175$, the ceramic possess a cubic structure due to a shift in phase transition temperature to below room temperature. With the increasing BZ content, the temperature at which ε_r is maximum (T_{max}), which corresponds to the tetragonal–cubic (T_{C-T}) transition, tended to decrease from 98 °C (for $x = 0.00$) to −14 °C (for $x = 0.25$). This is consistent with the results reported for $Ba(Ti_{1-x}Zr_x)O_3$ [26] and BZT–xBCT ceramics [13, 27]. The decrease in the phase transition temperature might be due to the chemical stability of Zr^{4+} [15].

The phase transition became increasingly diffuse in compositions with higher BZ content. This is likely related to the substitution of Zr^{4+} which enhances cation disorder on the B-site which perturbs the long-range dipole order [11, 22, 27, 28]. For the compositions with $x = 0.05$–0.10, two obvious phase transitions are observed which correspond to the rhombohedral–tetragonal (T_{T-R}) and tetragonal-cubic (T_{C-T}) transitions, respectively. The T_{T-R} transition peak shifts toward higher temperatures with the increasing BZ content. At the composition around $x = 0.125$, the two phase transitions seem to merge together and only one transition peak was observed for compositions with higher BZ content. Thus, a pseudobinary phase diagram with the convergence region around the compositions of $x = 0.10$–0.15 can be created using the temperature-dependent dielectric results along with the XRD data as shown in Fig. 3. The maximum dielectric constant ε_{max} and the room temperature dielectric constant

Table 1 The relative theoretical densities (%TD), lattice parameters, ferroelectric, and piezoelectric properties of xBaZrO$_3$–(0.25−x)CaTiO$_3$–0.75BaTiO$_3$ ceramics

Composition (x)	Properties								
	%TD	Lattice parameter		P_{max} (μC/cm^3)	E_C (kV/cm)	d^*_{33} (pm/V)	d_{33} (pC/N)	Q_m	k_p
		a	c						
$x = 0.000$	93.1	3.9617	4.0010	15.0	10.0	173	95	732	0.19
$x = 0.025$	95.1	3.9747	4.0080	14.0	8.2	204	111	628	0.24
$x = 0.050$	94.7	3.9845	4.0139	14.8	6.8	284	150	314	0.28
$x = 0.075$	95.5	3.9956	4.0155	16.3	5.2	429	225	227	0.36
$x = 0.100$	96.4	4.0020	4.0157	18.4	3.7	464	264	205	0.42
$x = 0.125$	93.4	4.0135	–	16.3	2.8	474	222	82	0.33
$x = 0.150$	94.1	4.0240	–	15.7	2.2	312	141	140	0.19
$x = 0.175$	96.0	4.0340	–	15.1	2.0	250	69	165	0.09
$x = 0.200$	97.4	4.0384	–	14.0	1.7	317	–	–	–
$x = 0.225$	97.8	4.0499	–	12.4	1.7	226	–	–	–
$x = 0.250$	97.9	4.0503	–	11.1	1.5	173	–	–	–

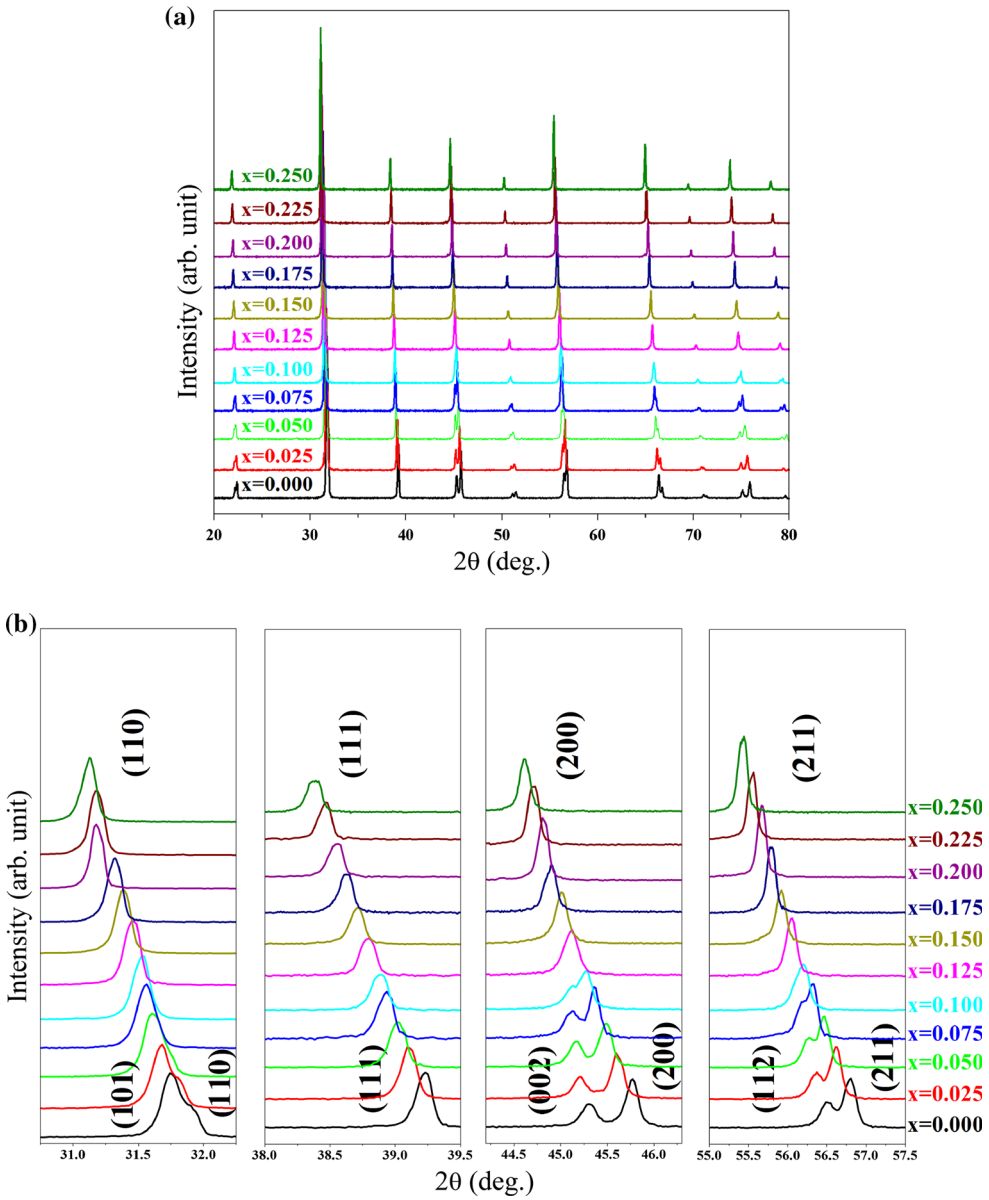

Fig. 1 **a** X-ray diffraction data on crushed sintered ceramics of xBZ–CT–0.75BT where $x = 0.00$–0.25, and **b** the enlarged reflection peaks of (110), (111), (200), and (211) planes

ε_r of all compositions are shown in Fig. 4. The maximum dielectric constant (ε_{max}) first increased to a maximum value of 11,400 for $x = 0.15$ and then decreased slightly to 9110 for $x = 0.25$. Likewise, the values for ε_r at room temperature increased with the BZ content from 315 for $x = 0.00$ up to 4990 for $x = 0.125$ which is about 2.5 times higher than that of pure $BaTiO_3$ [4]. As x increased to 0.15, the values for ε_r drastically increased up to a value of 10,200. As it is well known that the dielectric constant sharply increased in the vicinity of a phase transition, the large values associated with the $x = 0.15$ compositions are likely due to the fact that the phase transition point was shifted close to room temperature. In addition, the pseudocubic phase appears to possess higher dielectric constants than the tetragonal phase due to the effects of the phase transition [8].

Figure 5a shows the ferroelectric hysteresis data at room temperature for xBZ–CT–0.75BT ceramics as a function of composition (xBZ) under an applied field of 50 kV/cm. The maximum polarization P_{max} and remnant polarization P_r and coercive field E_c values obtained from this data are shown in Fig. 5b and tabulated in Table 1. In general, fully saturated hysteresis loops were observed in ceramics with low BZ content with a tetragonal crystal structure. With the increasing BZ content, the P_{max} values first enlarged to a maximum value of 18 μC/cm^2 at $x = 0.10$ and then decreased. The increase in polarization is likely due to the enhanced coupling of the TiO_6 octahedra [29]. Slim hysteresis loops with negligible P_r were observed for compositions with the increased BZ content as expected from the phase evolution to the paraelectric pseudocubic phase from the XRD and dielectric data shown previously. It was also

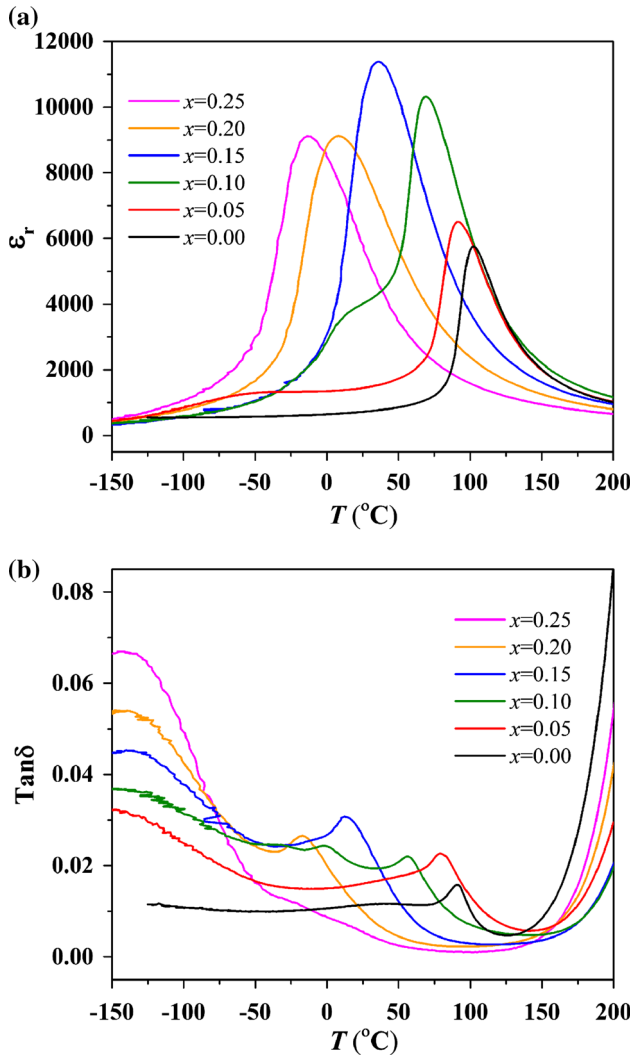

Fig. 2 **a** Temperature dependence of the dielectric constant ε_r, and **b** the dielectric loss (tan δ) of xBZ–CT–0.75BT ceramics measured at 1 kHz over the temperature range of −150–200 °C

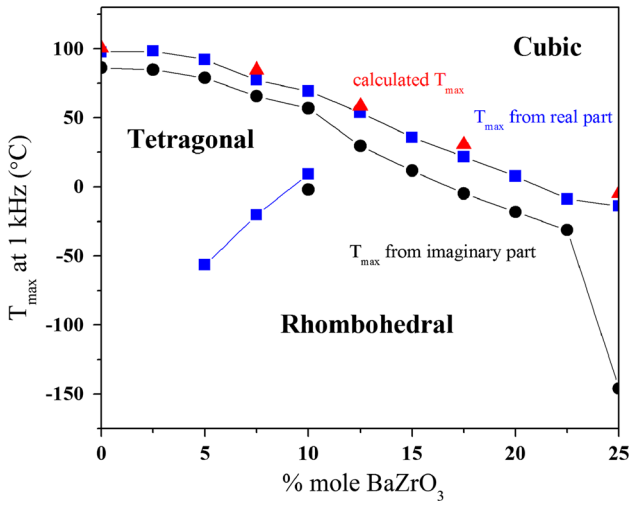

Fig. 3 The phase diagram of xBZ–CT–0.75BT system, where $x = 0.00$–0.25 determined from XRD analysis, and temperature-dependent dielectric spectra (T_{max} values identified from peak values of the real and imaginary component of the dielectric constant)

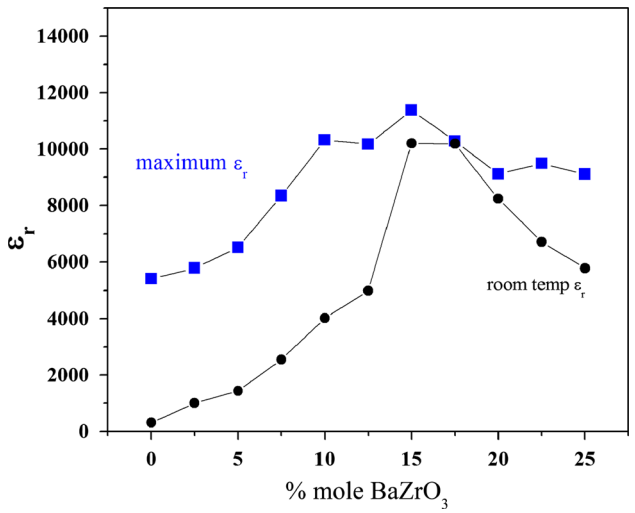

Fig. 4 The maximum dielectric constant ε_{max} and dielectric constant at room temperature extracted from data measured at 1 kHz for xBZ–CT–0.75BT ceramics, where $x = 0.00$–0.25

observed that E_c gradually decreased to values as small as 2 kV/cm. Thus, it can be seen that solid solutions "softened" due to the free energy profile expected from polarization rotation with negligible anisotropy in compositions near the MPB as reported elsewhere [13–15].

Figure 6a displays the bipolar electromechanical strain data for the xBZ–CT–0.75BT ceramics. Typical butterfly-shaped loops with negative strain were observed for compositions with $x = 0.00$–0.10. This is expected as these features are characteristic of ferroelectric materials with a tetragonal crystal structure. At higher BZ content, the strain data take on a parabolic shape with no negative strain which is consistent with electrostriction associated with a paraelectric pseudocubic structure. The normalized strain d^*_{33} which corresponds to the inverse piezoelectric effect, is defined as

$$d^*_{33} = \frac{S_{max}(\%)}{E_{max}(\text{kV/cm})} \times 10^5, \quad (1)$$

where S_{max} is the maximum strain and E_{max} is the maximum applied electric field. The d^*_{33} values for the materials in this study are listed in Table 1. The compositions around the convergence region exhibited higher normalized piezoelectric coefficients as shown in Fig. 6b. When comparing d^*_{33} values obtained using electric fields of 30 and 60 kV/cm, due to the curvature of the loop, the magnitude of the strain values at lower electric fields showed higher d^*_{33} values. The composition 0.125BZ–0.125CT–

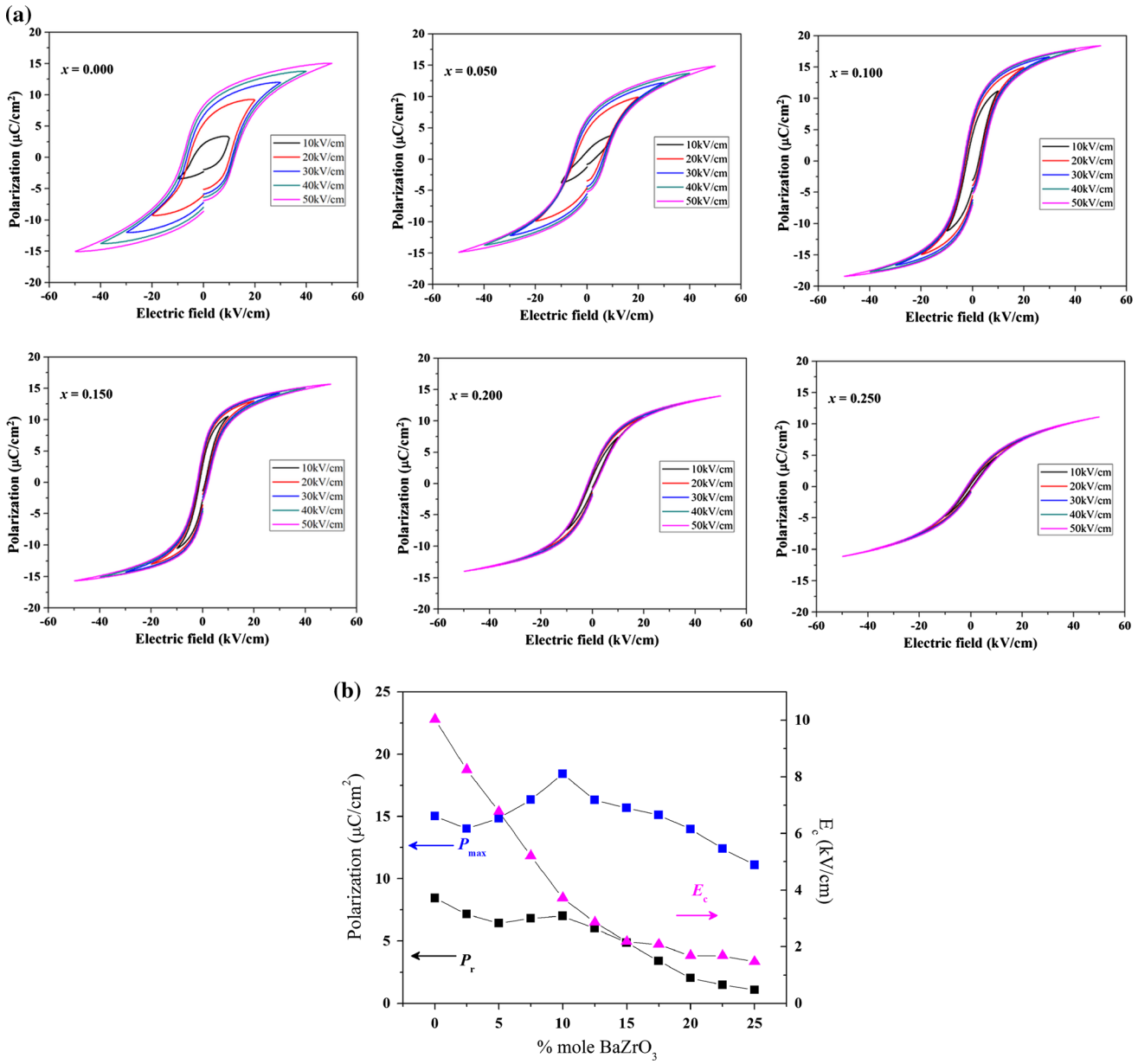

Fig. 5 **a** Room temperature ferroelectric hysteresis data (measured at 1 Hz) for xBZ–CT–0.75BT ceramics, where $x = 0.00$–0.25 at applied fields ranging from 10 to 50 kV/cm, and **b** the maximum polarization P_{max}, remnant polarization P_r, and the coercive field E_c as a function of BZ content

0.75BT exhibited the highest strain values of 0.14 % with $d^*_{33} = 474$ pm/V at an applied electric field of 30 kV/cm. The large electromechanical strains in this composition is further evidence that the crystal lattice is elastically "soft" which is consistent with the low coercive field [14].

Figure 7 shows the low-field piezoelectric coefficient d_{33} (a), mechanical quality factor Q_m, and planar electromechanical coupling factor k_p (b) as a function of BZ content. The d_{33}, Q_m, and k_p values obtained from ceramics in this study are provided in Table 1. The Q_m values were calculated following IEEE standards where Q_m is assumed to be equal for both resonance and antiresonance modes [30]. It can be observed that both d_{33} and k_p exhibit a maximum value with the composition of $x = 0.10$ with $d_{33} = 264$ pC/N with the mechanical coupling factor k_p of 0.42. The Q_m value decreases with the increasing BZ content as is consistent with a gradual decrease in E_c.

These results show that for compositions in the vicinity of the MPB composition, there is a significant enhancement in dielectric, piezoelectric, and ferroelectric properties. The excellent piezoelectric properties originate from the vanishing polarization anisotropy and lattice distortion in a TCP-type MPB model as evidenced by the enhanced ε_r [31, 32].

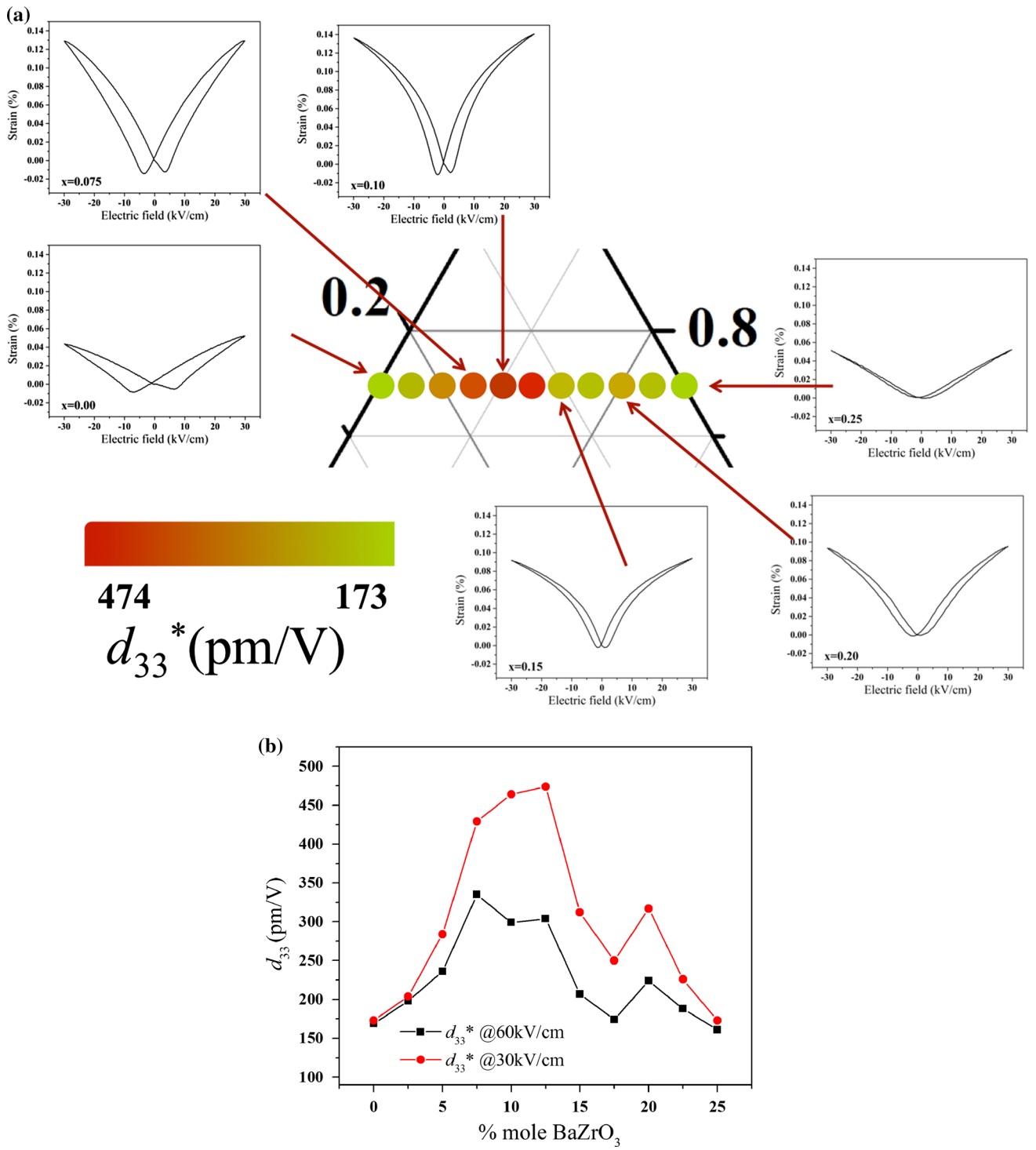

Fig. 6 **a** Bipolar strain versus electric field (S–E) hysteresis data and normalized strain d^*_{33} under an applied field of 30 kV/cm for xBZ–CT–0.75BT ceramics as a function of x, and **b** normalized strain d^*_{33} at applied electric fields of 30 and 60 kV/cm

Conclusions

Pb-free piezoelectric ceramics within the solid solution $x\mathrm{BaZrO_3}$–$(0.25-x)\mathrm{CaTiO_3}$–$0.75\mathrm{BaTiO_3}$ were prepared by the solid-state reaction technique. Analysis by XRD and temperature-dependent dielectric measurements indicated a composition-induced phase transition from tetragonal symmetry to cubic symmetry. Increasing BZ content influenced both the temperature of the phase transition and the character of the dielectric spectra. With the increasing

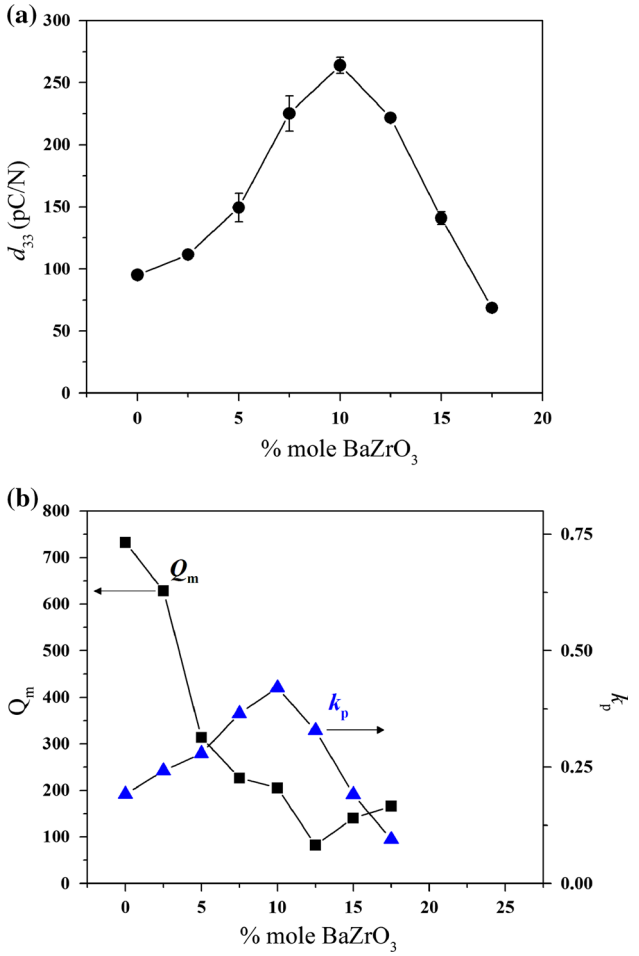

Fig. 7 **a** The room temperature low-field piezoelectric coefficient d_{33}, and **b** quality factor Q_m and planar electromechanical coupling factor k_p determined by a resonance–antiresonance method as a function of BZ content for poled xBZ–CT–0.75BT ceramics where $x = 0.00$–0.175

BZ content, the T_{C-T} shifted to lower temperatures, while the T_{T-R} transition shifted toward higher temperatures resulting in a pseudobinary phase diagram with a convergence region located around $x = 0.10$–0.15. Compositions near the convergence region exhibited high dielectric properties with an ε_{max} of $\sim$11,400, a significant enhancement in ferroelectric and piezoelectric properties with a low field $d_{33} = 264$ pC/N, and a high field $d^*_{33} = 474$ pm/V. These results are in agreement with the TCP-type MPB model proposed for the $BaZrO_3$–$CaTiO_3$–$BaTiO_3$ system that explains the superior piezoelectric coefficients above other lead-free ceramics. Based on these excellent properties, these environmentally benign piezoelectric ceramics are potential candidates for actuator applications.

Acknowledgements This work was supported by the Thailand Research Fund (TRF) under Grant Number BRG5680006. N. Chaiyo would like to thank The Royal Golden Jubilee (RGJ-Ph.D. Program) Scholarship program for financial support.

References

1. Takenaka T, Nagata H, Hiruma Y, Yoshii Y, Matumoto K (2007) Lead-free piezoelectric ceramics based on perovskite structures. J Electroceram 19:259–265
2. Takenaka T, Nagata H, Hiruma Y (2008) Current developments and prospective of lead-free piezoelectric ceramics. Jpn J Appl Phys 47(5):3787–3801
3. Rödel J, Jo W, Seifert KTP, Anton EM, Granzow T, Damjanovic D (2009) Perspective on the development of lead-free piezoceramics. J Am Ceram Soc 92(6):1153–1177
4. Haertling GH (1999) Ferroelectric ceramics: history and technology. J Am Ceram Soc 82(4):797–818
5. Hiruma Y, Nagata H, Takenaka T (2008) Phase transition temperatures and piezoelectric properties of $(Bi_{1/2}Na_{1/2})TiO_3$–$(Bi_{1/2}K_{1/2})TiO_3$–$BaTiO_3$ lead-free piezoelectric ceramics. J Appl Phys 104:124106
6. Takenaka T, Maruyama K, Sakata K (1991) $(Bi_{1/2}Na_{1/2})TiO_3$–$BaTiO_3$ system for lead-free piezoelectric ceramics. Jpn J Appl Phys 30(9B):2236
7. Jaffe B (1971) Piezoelectric ceramics. Academic Press, London
8. Liu W, Ren X (2009) Large piezoelectric effect in Pb-free ceramics. Phys Rev Lett 103:257602
9. Cox DE, Noheda B, Shirane G, Uesu Y, Fujishiro K, Yamada Y (2001) Universal phase diagram for high-piezoelectric perovskite systems. Appl Phys Lett 79:400
10. Keeble DS, Benabdallah F, Thomas PA, Maglione M, Kreisel J (2013) Revised structural phase diagram of $(Ba_{0.7}Ca_{0.3}TiO_3)$–$(BaZr_{0.2}Ti_{0.8}O_3)$. Appl Phys Lett 102:092903
11. Tian Y, Wei L, Chao X, Liu Z, Yang Z (2013) Phase transition behavior and large piezoelectricity near the morphotropic phase boundary of lead-free $(Ba_{0.85}Ca_{0.15})(Zr_{0.1}Ti_{0.9})O_3$ Ceramics. J Am Ceram Soc 96(2):496–502
12. Haugen AB, Forrester JS, Damjanovic D, Li B, Bowman KJ, Jones JL (2013) Structure and phase transitions in $0.5(Ba_{0.7}Ca_{0.3}TiO_3)$–$0.5(BaZr_{0.2}Ti_{0.8}O_3)$ from −100 °C to 150 °C. J Appl Phys 113:014103
13. Zhang L, Zhang M, Wang L, Zhou C, Zhang Z, Yao Y, Zhang L, Xue D, Lou X, Ren X (2014) Phase transitions and the piezoelectricity around morphotropic phase boundary in $Ba(Zr_{0.2}Ti_{0.8})O_3$–$x(Ba_{0.7}Ca_{0.3})TiO_3$ lead-free solid solution. Appl Phys Lett 105:162908
14. Cordero F, Craciun F, Dinescu M, Scarisoreanu N, Galassi C, Schranz W, Soprunyuk V (2014) Elastic response of $(1-x)$Ba(Ti0.8Zr0.2)O3–x(Ba0.7Ca0.3)TiO3 ($x = 0.45$–0.55) and the role of the intermediate orthorhombic phase in enhancing the piezoelectric coupling. Appl Phys Lett 105:232904
15. Puli VS, Pradhan DK, Pérez W, Katiyar RS (2013) Structure, dielectric tunability, thermal stability and diffuse phase transition behavior of lead free BZT–BCT ceramic capacitors. J Phys Chem Solids 74(3):466–475
16. Gao J, Zhang L, Xue D, Kimoto T, Song M, Zhong L, Ren X (2014) Symmetry determination on Pb-free piezoceramic $0.5Ba(Zr_{0.2}Ti_{0.8})O_3$–$0.5(Ba_{0.7}Ca_{0.3})TiO_3$ using convergent beam electron diffraction method. J Appl Phys 115:054108
17. Lu S, Xu Z, Su S, Zuo R (2014) Temperature driven nano-domain evolution in lead-free $Ba(Zr_{0.2}Ti_{0.8})O_3$–$50(Ba_{0.7}Ca_{0.3})TiO_3$ piezoceramics. Appl Phys Lett 105:032903
18. Gao J, Xue D, Wang Y, Wang D, Zhang L, Wu H, Guo S, Bao H, Zhou C, Liu W, Hou S, Xiao G, Ren X (2011) Microstructure

basis for strong piezoelectricity in Pb-free $Ba(Zr_{0.2}Ti_{0.8})O_3$–$(Ba_{0.7}Ca_{0.3})TiO_3$ ceramics. Appl Phys Lett 99:092901
19. Damjanovic D (2010) A morphotropic phase boundary system based on polarization rotation and polarization extension. Appl Phys Lett 97:062906
20. Damjanovic D (2009) Comments on origins of enhanced piezoelectric properties in ferroelectrics. IEEE Trans Ultrason Ferroelectr Freq Control 56(8):1574–1585
21. Budmir M, Damjanovic D, Setter N (2003) Piezoelectric anisotropic-phase transition relations in perovskite single crystals. J Appl Phys 94(10):6753–6761
22. Xue D, Zhou Y, Bao H, Zhou C, Gao J, Ren X (2011) Elastic, piezoelectric, and dielectric properties of $Ba(Zr_{0.2}Ti_{0.8})O_3$–$50(Ba_{0.7}Ca_{0.3})TiO_3$ Pb-free ceramic at the morphotropic phase boundary. J Appl Phys 109:054110
23. ASTM Standard test method for water absorption, bulk density, apparent porosity, and apparent specific gravity of fired whiteware products, ceramic tiles, and glass tiles. C373-14
24. Callister WD (2007) Materials science, engineering: an introduction. Wiley, New York
25. Cullity BD, Stock SR (2001) Elements of X-ray diffraction. Prentice Hall, Upper Saddle River
26. Tang XG, Chew KH, Chan HLW (2004) Diffuse phase transition and dielectric tenability of $Ba(Zr_yTi_{1-y})O_3$ relaxor ferroelctric ceramics. Acta Mater 52(17):5177–5183
27. Coondoo I, Panwar N, Amorín H, Alguero M, Kholkin AL (2013) Synthesis and characterization of lead-free $0.5Ba(Zr_{0.2}Ti_{0.8})O_3$–$0.5(Ba_{0.7}Ca_{0.3})TiO_3$ ceramic. J Appl Phys 113:214107
28. Tian Y, Chao X, Wei L, Liang P, Yang Z (2013) Phase transition behavior and electrical properties of lead-free $(Ba_{1-x}Ca_x)(Zr_{0.1}Ti_{0.9})O_3$ piezoelectric ceramics. J Appl Phys 113:184107
29. Jeong IK, Ahn JS (2012) The atomic structure of lead-free $Ba(Zr_{0.2}Ti_{0.8})O_3$–$(Ba_{0.7}Ca_{0.3})TiO_3$ by using neutron total scattering analysis. Appl Phys Lett 101:242901
30. ANSI/IEEE 176-1987 (1987)
31. Bao H, Zhou C, Xue D, Gao I, Ren X (2010) A modified lead-free piezoelectric BZT–*x*BCT system with higher T_C. J Phys D 43:465401
32. Damjanovic D (2005) Contributions to the piezoelectric effect in ferroelectric single crystals and ceramics. J Am Ceram Soc 88(10):2663–2676

RSC Advances

PAPER

Cite this: *RSC Adv.*, 2015, **5**, 19893

Directed synthesis, growth process and optical properties of monodispersed $CaWO_4$ microspheres *via* a sonochemical route

Jira Janbua,[a] Jitkasem Mayamae,[a] Supamas Wirunchit,[a] Rattanai Baitahe[a] and Naratip Vittayakorn*[abc]

Received 23rd November 2014
Accepted 12th February 2015

DOI: 10.1039/c4ra15064c

www.rsc.org/advances

Monodispersed calcium tungstate ($CaWO_4$) microspheres were synthesized successfully *via* a sonochemical process in deionized (DI) water. The functional group and phase formation analyses were carried out using Fourier transform infrared (FT-IR) and X-ray diffraction (XRD), respectively. XRD revealed that all samples were of pure tetragonal scheelite structure. FT-IR and Raman analysis exhibited a W–O stretching peak of molecular $[WO_4]^{2-}$, which related to the scheelite structure. The effect of ultrasonic irradiation times in the sonochemical process was investigated briefly for 1, 5, 15 and 30 min. The shape of the particles was revealed as spherically monodispersed with narrow size distribution and uniform features at the ultrasonic time of 5 min. This study also found that the spherical surface was composed of tightly packed nanosphere subunits. A possible mechanism for the formation of $CaWO_4$ powders with a different ultrasonic time was discussed in detail. Optical properties showed blue light emission at a wavelength of around 420 nm and an optical energy gap (E_g) value of 3.32–3.36 eV.

Introduction

The tetragonal scheelite structure and space group $I4_1/a$ of calcium tungstate ($CaWO_4$) has a Ca^{2+} and W^{6+} ion in 8-fold, and tetrahedral site of oxygen coordination, respectively.[1] It is well known that $CaWO_4$ with a scheelite structure is a commercially important material with luminescence properties.[1–3] It has been used as blue phosphor (433 nm) in laser host materials,[4–6,7] quantum electronics, scintillators in medical devices,[1,3–5] and oscilloscopes.[1,3–5] Phosphors made up from monodispersed and microsized spherical morphology are known to be suitable for application because they have higher packing density, scattering and re-absorption of light than small spherical particles.[8–10] As a result, their high resolution, screen brightness and efficiency provide better luminescence performance.

However, an ideal morphology of phosphor particles demands a perfect spherical shape, narrow size distribution and non-agglomeration. Therefore, various preparation methods have been developed actively for controlling morphology, size and distribution. For instance, Pan *et al.*[8] synthesized quasi-monodispersed AWO_4 (A = Ca, Sr, and Ba) microspheres with a diameter of about 3 μm by a hydrothermal route at a temperature of 180 °C for 8 h in the presence of citric acid. Although this method uses a low reaction temperature, it has a long holding time in the synthesis process. Furthermore, monosized $CaWO_4$ microspheres were obtained by Zhang *et al.*[9] *via* a large scale solvothermal method (4.4 to 6.8 μm) with a surfactant-assisted solution route, in which either sodium dodecylbenzenesulfonate (SDS) or cetyltrimethyl ammonium bromide (CTAB) was used. Their method needed surfactant-assisted solution, which is an expensive reagent and not environmentally friendly, and surfactants must be removed completely to obtain a pure product. This makes the synthetic step more complicated. Over the past few years, the sonochemical process has been applied to applications for synthesizing and customizing micro- and nano-structured inorganic and organic materials. The mechanism in this process occurred from acoustic cavitation (the formation, growth, and implosive collapse of bubbles in a liquid). This process has advantages such as uncomplicated steps, low energy consumption, time saving and high purity.

This study reports the fast synthesis of $CaWO_4$ microspheres almost monodispersed *via* the sonochemical route by using deionized (DI) water as intermediate solvent, which is environmentally friendly and has no assistance from surfactant or a template. The influence of different ultrasonic irradiation times, crystal structure, optical properties, and microstructure was investigated.

[a]*Electroceramic Research Laboratory, College of Nanotechnology, King Mongkut's Institute of Technology Ladkrabang, Bangkok 10520, Thailand. E-mail: naratipcmu@yahoo.com*

[b]*Department of Chemistry, Faculty of Science, King Mongkut's Institute of Technology Ladkrabang, Bangkok 10520, Thailand*

[c]*Advanced Materials Science Research Unit, Faculty of Science, King Mongkut's Institute of Technology Ladkrabang, Bangkok 10520, Thailand*

Experimental procedure

Calcium nitrate tetrahydrate (99% $Ca(NO_3)_2 \cdot 4H_2O$) and sodium tungstate dihydrate (99% $Na_2WO_4 \cdot 2H_2O$) were purchased from Sigma–Aldrich Reagents Co., Ltd. and used without further purification. In a typical procedure, each 0.0167 mole of $Ca(NO_3)_2 \cdot 4H_2O$ and $NaWO_4 \cdot 2H_2O$ was dissolved separately in 50.00 ml of deionized (DI) water by stirring continuously until dissolved completely (transparent solution), without using an adjusted pH value of starting materials. After that, two solutions were added into the chamber and the ultrasonic probe (3 mm diameter; Ti-horn) was immersed with the frequency of pulsed ultrasound waves (conducted in the 2s mode; and a pause in 1s mode) at 20 kHz and 70 W cm^{-2}. The influence of different ultrasonic irradiation times was applied in the chamber containing mixed substrate solution for 1, 5, 15, and 30 min by the following reaction:

$$Na_2WO_4 \cdot 2H_2O + Ca(NO_3)_2 \cdot 4H_2O \xrightarrow{\text{sono}} CaWO_4 + 2NaNO_3 + 6H_2O \quad (1)$$

The white precipitate particles were washed with distilled water several times and then absolute ethanol before drying at 90 °C for 24 h. The X-ray diffraction (XRD) patterns of products were characterized by an X-ray diffractometer (D8 Advance). The morphology of products was obtained by scanning electron microscope (SEM). The vibration mode of the bond in molecules was obtained from Fourier transform infrared (FT-IR spectrum Gx, Perkin Elmer, America) spectra. The sample was recorded in a wavelength range of between 400 and 4000 cm^{-1}, and a Raman spectrophotometer (DXR smart Raman, thermo scientific) with argon (Ar) laser recorded its wavelength range of between 200 and 1000 cm^{-1}. The optical properties were investigated, and a portion of emission property was measured by a fluorescence spectrophotometer (Cary Eclipse model; Agilent Technologies, Varian, USA) with Xe lamp at room temperature, using an excitation wavelength (λ_{ex}) of 235 nm. A solid sample holder was used as a coated sample. The optical absorbance spectrum was examined by a UV-Vis spectrophotometer (T60, PG Instruments Limited) in the wavelength range of between 200 and 900 nm. The solution samples were prepared *via* mixing the powder samples in hydrogen peroxide to form a concentrated solution of 2 mM.

Results and discussion

a) Crystal structure

All the diffraction peaks in XRD patterns of the as-prepared $CaWO_4$ powders were synthesized by the sonochemical method at different ultrasonic irradiation times of 1, 5, 15 and 30 min, and could be indexed to a pure tetragonal scheelite structure ($a = b \neq c$, $\alpha = \beta = \gamma = 90°$) with space group $I4_1/a$, when compare to the Joint Committee on Powder Diffraction Standards (JCPDSs) card no. 41-1431. Diffraction peaks corresponding to the secondary phase were undetected, and not a shift peak at different sonication times. In addition, peak intensities could be found to increase when ultrasound treatment time increases, as compared to the curves of four products that indicate better crystallization.[11] The percentage yield of the products obtained by this method was about 95%.

The Rietveld refinement method of XRD patterns was performed for $CaWO_4$ powders using the Fullprof program, as shown in Fig. 1. This technique is based on the least-squares method,[12] where the theoretical peak patterns are adjusted upwards to converge with the result of measured patterns. It displays various advantages of typical quantitative analysis techniques, which comprise the use of pattern-fitting algorithms, and all lines of each crystallographic phase are considered explicitly. From structural refinement analysis, which provides various data on factors generally checked by quality algorithms of *R*-factors or chi-squared (χ^2), the difference between the measured and theoretical simulation patterns is considered a way to verify success of the refinement. The χ^2 value is the quality of fit, as the value distinguishes between theoretical simulations and the XRD pattern data result, which is more or less consistent, and this value should approach 1.

Upon inspection of the data, the tetragonal $I4_1/a$ space group and parameters (a, b, c, α, β, and γ) acquired from JCPDS Card no. 41-1431 were chosen for the initial refinement of the model. The fit of the XRD pattern data gave an χ^2 value of 1.27, 1.63, 2.11 and 2.34 for ultrasonic irradiation times of 1, 5, 15 and 30 min, respectively, which agreed well with acceptance for fitting the data. A large match of model intensities in peak variety, position and shape was assumed as correct from resulting refinement. This revealed that the selected space group and parameters were correct, and not that a completely pure phase of $CaWO_4$ was obtained at a 1 min sonication time, thus suggesting this method be used for a very short time and utilized practically for synthesis of monodispersed $CaWO_4$ microspheres in field applications. The lattice parameters were calculated by using the Fullprof program, and those obtained were seen as a tetragonal unit cell type with a and c parameter values, as shown in Table 1. When comparing these lattice

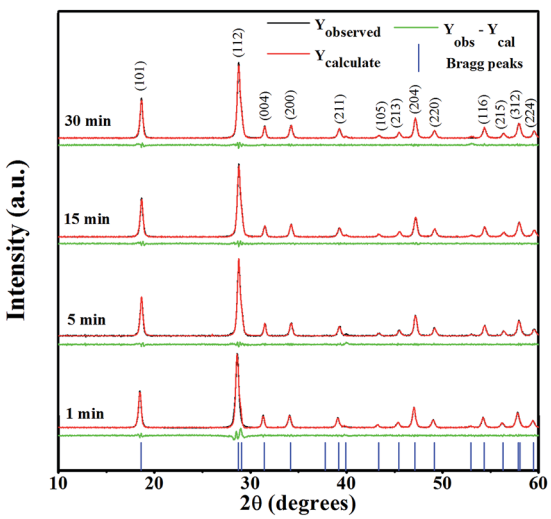

Fig. 1 Rietveld analysis of XRD patterns of $CaWO_4$ powders synthesized by the sonochemical method at different ultrasonic irradiation times.

Table 1 The refinement values of $CaWO_4$ powders and comparison with the lattice parameters from other methods

Methods	Time	Lattice parameters (Å)		χ^2	Ref.
		a	c		
Sonochemical	1 min	5.238 ± 0.002	11.389 ± 0.003	1.27	This work
Sonochemical	5 min	5.243 ± 0.001	11.370 ± 0.004	1.63	This work
Sonochemical	15 min	5.235 ± 0.001	11.369 ± 0.003	2.11	This work
Sonochemical	30 min	5.240 ± 0.001	11.379 ± 0.005	2.34	This work
Hydrothermal	8 h	5.252	11.388	—	8
Solvothermal	12 h	5.46	12.04	—	9

parameter values with JCPDS Card no. 41-1431, and lattice values from other various methods,[3,4,6,13] good and acceptable agreement is found. However, the method in this study has more precise cell parameters than in other techniques, with the least deviation observed.

The Fourier transform infrared (FT-IR) and Raman spectra were used to characterize the molecular structure of metal tungstate in order to verify the product structure. Typical $CaWO_4$ had a primitive cell of scheelite structure, which was characterized in its molecule consisting of $[WO_4]^{2-}$ molecular ionic groups (W metal in the tetrahedral site of O), with a strongly covalent W–O bond. The bonding between the $[WO_4]^{2-}$ molecular ionic groups and Ca^{2+} cations indicated loosely coupled bonds that were isolated from each other, while the Ca^{2+} was surrounded by eight oxygen ions. $CaWO_4$ presented a tetragonal structure of the symmetry, C_{4h}^6, at room temperature. The group theory calculation presented 26 different lattice vibrations for the $CaWO_4$ in a unit cell, where a zero wave vector can be described by the following equation.[3,13–15]

$$\Gamma = 3A_g + 5A_u + 5B_g + 3B_u + 5E_g + 5E_u \quad (2)$$

while only infrared (IR), and Raman active modes are determined by the following equation.[3,13,14]

$$\Gamma = 3A_g + 5B_g + 5E_g + 4A_u + 4E_u \quad (3)$$

All even vibrations (A_g, B_g and E_g) are Raman-active modes, while the odd modes (A_u and E_u) are active only in the infrared frequency range. Therefore, a 13 zone-center was expected in the Raman-active modes of $CaWO_4$, as presented in the following equation.[3,15]

$$\Gamma = 3A_g + 5B_g + 5E_g \quad (4)$$

From the literature, the vibrational modes found in the Raman spectra of $CaWO_4$ can be classified into two groups consisting of internal and external modes. Internal vibrations correspond to vibrations inside the $[WO_4]^{2-}$ molecular ionic group, which is considered as a stationary mass center. The lattice phonons or external vibrations are related to motion of the Ca^{2+} cations and rigidly molecular ionic $[WO_4]^{2-}$. In free space, $[WO_4]^{2-}$ tetrahedrons have a cubic point symmetry T_d,[3,14,15] in which their vibrations are composed of four internal modes, $\nu_1(A_1)$, $\nu_2(E_1)$, $\nu_3(F_2)$ and $\nu_4(F_2)$, with one free rotation mode, $\nu_{f.r.}(F_1)$, and one translation mode (F_2).[3,14,15]

Raman spectra of $CaWO_4$ powders were obtained at different ultrasonic irradiation times (1, 5, 15 and 30 min), and operated in the wavenumber range of 200–1000 cm^{-1} by using Ar laser as an excitation source, as shown in Fig. 2. The graph shows six different modes of $\nu_1(A_g)$, $\nu_3(B_g)$, $\nu_3(E_g)$, $\nu_4(B_g)$, $\nu_2(A_g)$, and the free rotation of the z axis $[\nu_{f.r.}(A_g)]$, occurring at about 914, 842, 798, 404, 333 and 212 cm^{-1}, respectively. The vibration modes in the Raman spectrum are A_g, B_g and E_g with peaks found mainly in internal modes, with W–O symmetric stretching vibration in molecular ionic $[WO_4]^{2-}$.[3]

FT-IR spectra of $CaWO_4$ powders obtained at different ultrasonic irradiation times (1, 5, 15 and 30 min), and operated at the wavenumber range of 400–4000 cm^{-1} are shown in Fig. 3. The FT-IR spectrum demonstrated a strong peak at about 802–803 cm^{-1}, which is in accordance with W–O asymmetric stretching vibration in molecular ionic $[WO_4]^{2-}$,[3] and weak W–O bending at about 430–460 cm^{-1}. Furthermore, O–H stretching and O–H bending vibration of residual water were detected in powder products at 3070–3690 cm^{-1} and 1620 cm^{-1},[3,16] respectively.

b) Optical properties

The optical energy gap (E_g) of $CaWO_4$ powders was obtained from the calculation of their absorbance spectrum in UV-visible

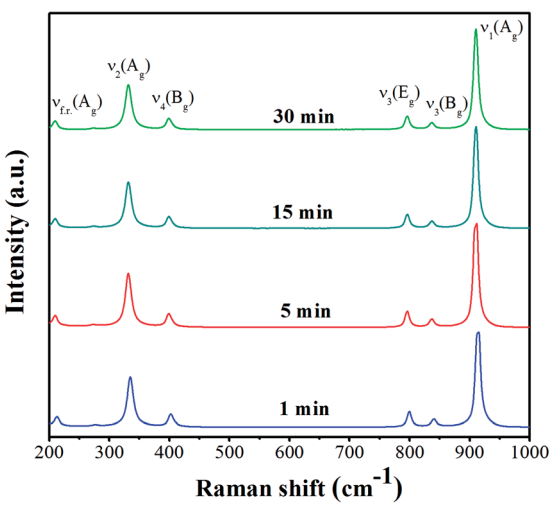

Fig. 2 Raman spectra of $CaWO_4$ powders obtained at different ultrasonic irradiation times.

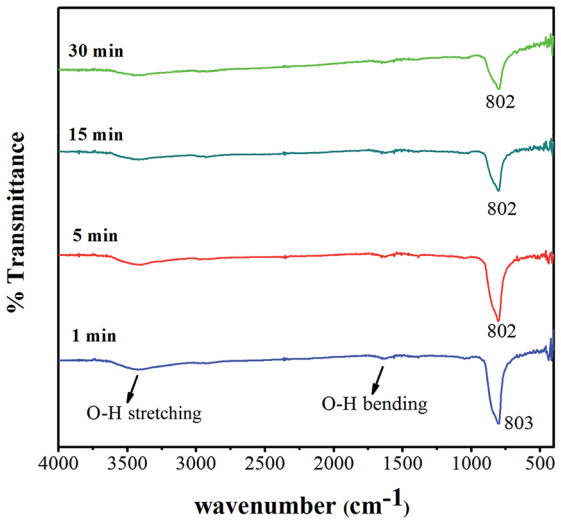

Fig. 3 FT-IR spectra of $CaWO_4$ powders obtained at different ultrasonic irradiation times.

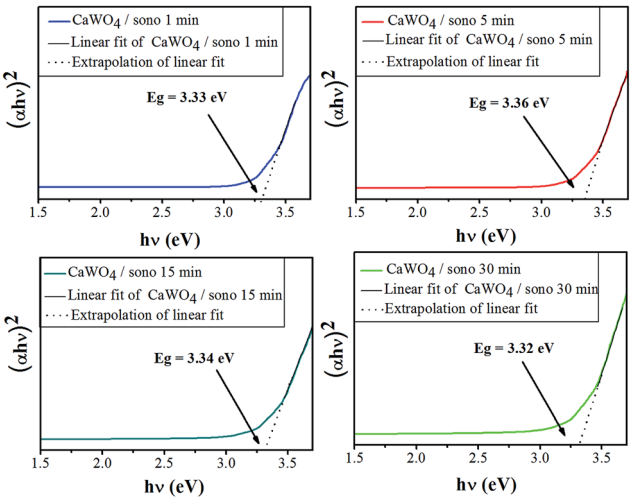

Fig. 4 Relative graph of the $(\alpha h\nu)^2$ with $h\nu$ (eV) of $CaWO_4$ powders.

range by using Wood and Tauc's equation,[3,16] which proposed the following:

$$\alpha h\nu = (h\nu - E_g)^n \quad (5)$$

where α is the optical absorption coefficient, h is the Planck constant, ν is the frequency of photon, E_g is the optical energy gap, and n is a constant that corresponds to the nature of an electronic transition. Transitions allowed directly, forbidden directly, allowed indirectly and forbidden indirectly are $n = 1/2$, 3/2, 2 and 3, respectively. According to the literature, metal tungstate with a tetragonal scheelite structure has $n = 1/2$ because its electronic transition is allowed directly.[3,13,17] The optical absorption coefficient, α, is calculated by using the following equation[13]

$$\alpha = -\ln T/d \quad (6)$$

where T is the optical transmittance and d is the optical path length through the cuvette. The E_g value was determined by extrapolating the straight linear portion of the relative graph between $(\alpha h\nu)^2$ and photon energy $(h\nu)$ at an $h\nu$ value of 0. The $(\alpha h\nu)^2$ graph relative to the $h\nu$ value of $CaWO_4$ powders shows the E_g values at different ultrasonic irradiation times in Fig. 4. Increased time makes an E_g value of 3.33, 3.36, 3.34 and 3.32 eV for different ultrasonic irradiation times of 1, 5, 15 and 30 min, respectively. It is noticeable that the E_g values differ slightly, due to the range of particle size varying insignificantly.

A fluorescence spectrophotometer was used to confirm the light emission spectrum of $CaWO_4$ powders. Fig. 5 shows the fluorescence spectra of $CaWO_4$ microsphere powder samples obtained at different sonication times by using an excitation wavelength (λ_{ex}) of 235 nm. The broad peak emission positioned at a wavelength of around 420 nm indicates the direct transition gap of $CaWO_4$ microparticles. The blue light emission occurred from the $^1T_2 \rightarrow {}^1A_1$ transition intrinsic molecular anion $[WO_4]^{2-}$group cluster.[3] The fluorescence spectrum discovered different intensities that could be the result of various particle sizes and crystallinity.[11] When comparing with the peak position of emission in bulk $CaWO_4$, the tetragonal (scheelite) structure has a wavelength of 433 nm (2.87 eV),[18] where good acceptable agreement is found.

c) Microstructure

Fig. 6(a) shows the products prepared from mixing substance solution, then leaving it until precipitation occurs (without ultrasonic irradiation). The morphology obtained varied greatly, with broad size distribution. The particle sizes were difficult to measure, due to the random aggregation of mixed powder that appeared between spherical particles and spread nanoparticles. Fig. 6(b)–(h) show $CaWO_4$ powders synthesized under different ultrasonic irradiations. Near spherical shape and narrow particle size distribution, with a micron size of the powders, were observed clearly at a radiation time of 1 min [Fig. 6(b)]. The average size of the microsphere was about 7.59 ± 1.20 μm. When enlarging the image of only one particle [Fig. 6(c)], the

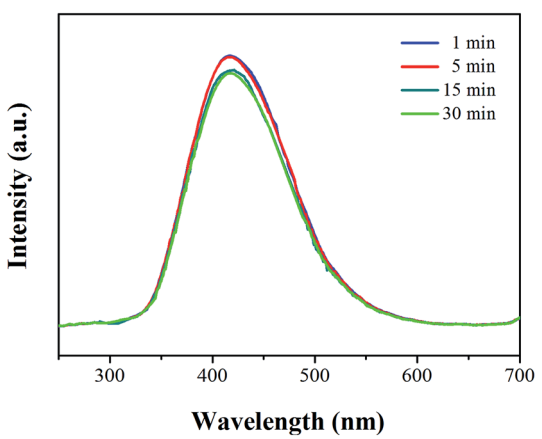

Fig. 5 Fluorescence spectrum of $CaWO_4$ powders obtained at different ultrasonic irradiation times.

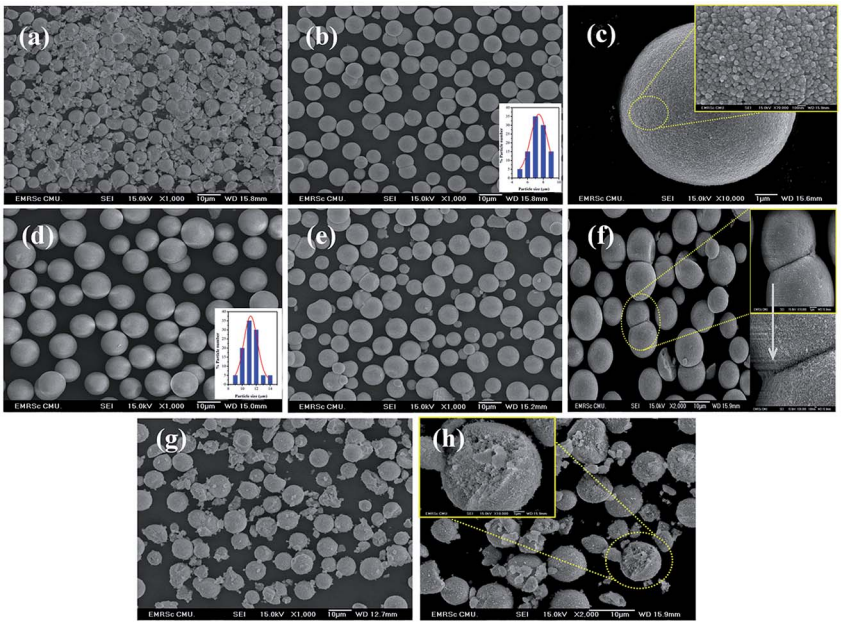

Fig. 6 SEM images of $CaWO_4$ powder obtained, (a) without ultrasonic irradiation, and produced from ultrasonic irradiation, (b) at 1 min, (c) with only one enlarged microspherical particle showing a surface with aggregated primary nanoparticles (inset image), (d) at 5 min, (e) at 15 min, (f) with the neck between microsphere particles at 15 min, (g) at 30 min, and (h) microspherical breaking at 30 min.

texture of microspheres was composed of aggregated small nanoparticles, with an average particle size of 52.87 ± 1.39 nm. The mono size with spherical shape was observed clearly at a sonication time of 5 min [Fig. 6(d)]. The average diameter of the spheres increased to about 11.20 ± 1.07 μm. Furthermore, the morphology obtained at the sonication time of 15 min was a mixture of small and large microsphere particles and rarely spherical-shaped ones [Fig. 6(e)]. Evidently, the neck between the microsphere particles was observed from this condition. Fig. 6(f) shows expansion of the neck with melted nanoparticles on the surface area. When the reaction time increased to 30 min, a very rough surface of microparticles was obtained, as shown in Fig. 6(g). Furthermore, neck point breaking is shown between microspheres, with small clusters of particles that had broken off [Fig. 6(h)].

Possible growth process and effect of ultrasonic irradiation time

Fig. 7 shows a schematic illustration of the growth process of monodispersed $CaWO_4$ microspheres *via* the sonochemical process by ultrasonic time-dependent experiments. The precursor solid (as the calcium and tungstate ion source) was hydrolyzed immediately in DI water as solvent in order to create Ca^{2+} and WO_4^{2-} ions. Additionally, Ca^{2+} and WO_4^{2-} species were attracted at the initial formation stage by electrostatic interaction, and formed numerous $CaWO_4$ nuclei. Subsequently, the mixed solution was irradiated with high-intensity ultrasound (70 W cm^{-2}, 20 kHz). Precipitation in the liquid–solid heterogeneous system was accelerated completely by ultrasonic irradiation, which resulted from the acoustic cavitation process (the formation, growth, and implosive collapse of bubbles in a liquid). At the initial state (0 min), primary nanoparticles appeared and tended to aggregate into soft nanoparticle clusters in order to reduce each other's surface energy. With the ultrasonic time at 1 min, $CaWO_4$ microspheres were assembled by unstable nanoparticle cluster orientation. As seen, each microsphere consisted of numerous tightly packed nanospheres resulting in rough surfaces. It is known that collapsing bubbles create $OH^{\bullet}$ and $H^{\bullet}$ radical species *via* the sonolysis of water in an aqueous solution, and preferably yield formation of H_2O_2, H_2O *etc.* From previous observation,[19] hydroxyl groups (–OH) were produced from radical species that prefer to react with oxygen ions, and also, H_2O_2 was likely to decompose on the surface of metal oxide particles. These hydroxyl groups on the surface of $CaWO_4$ nanoparticles promote self-attachment between unstable nanoparticles, thus resulting in aggregation of single microspheres on a surface consisting of nanospheres. This study considered that high-intensity ultrasound irradiation also plays an important role in the formation of products leading to the microspherization process.[20,21] The result of this study is similar to that of Xu *et al.*,[21,23] in which prepared polysaccharide-based and chitosan microspheres used the single-step sonochemical method. However, the morphology of $CaWO_4$ in this work was quite different from that reported by Yang *et al.*[22] The difference in morphology might be attributed to varied synthesis parameters such as ultrasonic frequency, pH value and ultrasonication mode.[22] At 5 min sonication time, stable monodispersed microspheres would steadily aggregate in mostly narrow particle size distribution. The diameter of these particles became larger simultaneously to an unsurpassable critical size limit, of which the microsphere particles in this work were about 11.20 ± 1.07 μm. The critical size limit of these particles

strongly depends on many factors such as ultrasonic frequency, velocity of interparticle collisions and shock waves generated by cavitation in liquids irradiated with ultrasound.[24] These shock waves can induce physical effect, especially by increasing mass transport. Shock waves through the microsphere particles can expedite and drive microparticles suspended in liquid into one another, and the impact velocity of these collisions between particles can be estimated at around one hundred meters per second.[23] This physical effect causes changes in surface composition, distribution of particle size and particle morphology.[23] Additionally, a short-lived localized hot-spot that produces enormous volumes of temperature at ~5000 K, pressure of ~1000 atm and heating and cooling rates of $>10^{10}$ K s^{-1} can be generated during cavitations.[24,25] As a result, necking occurred at 15 min between microsphere particles, which was similar to the initial stage of the solid-state sintering process. It is believed that this heat energy occurrence can make surface diffusion, as the melting point started from the surface area of nanoparticles on the microsphere particles. Surface diffusion is a typical mass transport in the sintering mechanism that produces surface smoothing, particle joining, grain boundary formation, neck growth, and pore rounding.[26,27] However, volume shrinkage and densification was not found, due to the sonochemical method generating local thermal energy, which is different from thermal energy of the sintering process. When increasing the sonication time to 30 min, the necking and unsmooth surface broke into a large number of particle scraps, with no single monodispered microspheres. As a result, impact from high speed microjets on the surface led to the phenomena of morphological transformations, including particles breaking and erosion of material.[23,28] Furthermore, the average particle sizes, as a function of ultrasonic irradiation time, are plotted in Fig. 8. Increasing time gradually increases microsphere particles to an average size of 11.20 ± 1.07 μm and narrow standard deviation at 5 min, which is suitable for producing uniformed spherical morphology. A broad size deviation was observed as the time increased to 15 and 30 min, due to difficulty in finding

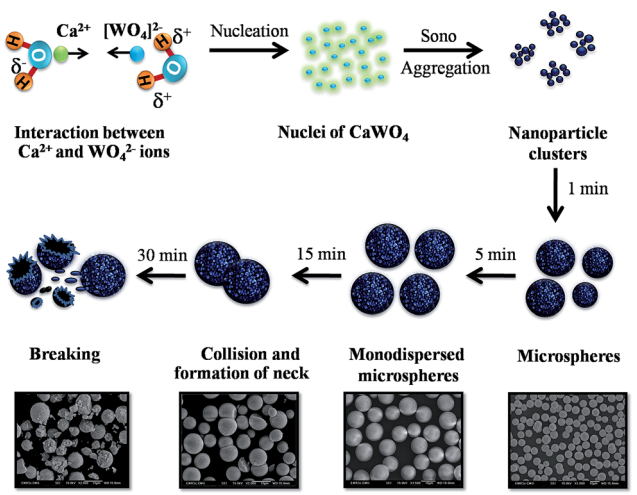

Fig. 7 Schematic illustration of the growth process of monodispersed $CaWO_4$ microspheres *via* the sonochemical process of ultrasonic irradiation time-dependent experiments.

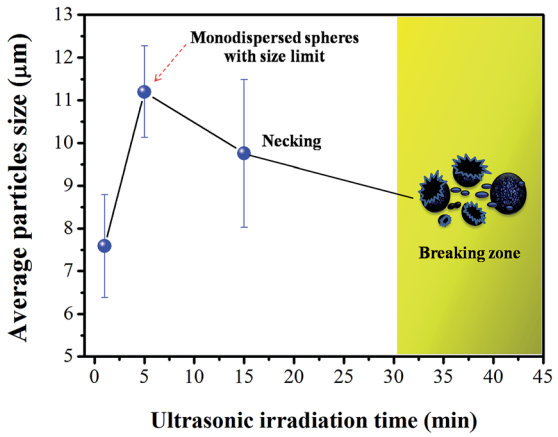

Fig. 8 Plotting of average particle sizes with ultrasonic irradiation time.

the particle sizes after necking and microsphere breakage. Based on the results obtained at different ultrasonic times, formation of the monodispersed $CaWO_4$ microsphere can be controlled easily by only one single parameter in a simple sonochemical process.

Conclusion

Nearly monodispersed $CaWO_4$ microspheres were accomplished *via* the sonochemical process by using deionized (DI) water as intermediate solvent at an ultrasonic irradiation time of 5 min. XRD results exhibited $CaWO_4$ powders as a tetragonal scheelite structure. SEM images showed the morphology as monodispersed $CaWO_4$ microspheres of 11.20 ± 1.07 μm. The growth mechanism was performed carefully by brief ultrasonic time-dependence. The fluorescence spectra of $CaWO_4$ microspheres obtained a blue light that was emitted at a wavelength of around 420 nm. The E_g values obtained results of the absorbance spectrum at 3.32–3.36 eV. This synthesized method for monodispersed $CaWO_4$ microspheres presents advantages such as uncomplicated steps, low energy consumption, high purity, time-saving and suitable application.

Acknowledgements

This work was supported by the Thailand Research Fund (TRF) under Grant no. BRG5680006. The authors would like to thank Dr. Jakrapong Kaewkhao for the support of Photoluminescence measurement.

References

1 L. Sun, M. Cao, Y. Wang, G. Sun and C. Hu, *J. Cryst. Growth*, 2006, **289**, 231–235.
2 J. Liu, Q. Wu and Y. Ding, *J. Cryst. Growth*, 2005, **279**, 410–414.
3 T. Thongtem, S. Kungwankunakorn, B. Kuntalue, A. Phuruangrat and S. Thongtem, *J. Alloys Compd.*, 2010, **506**, 475–481.

4 Y. Tian, Y. Liu, R. Hua, L. Na and B. Chen, *Mater. Res. Bull.*, 2012, **47**, 59–62.
5 Y. Wang, J. Ma, J. Tao, X. Zhu, J. Zhou, Z. Zhao, L. Xie and H. Tian, *Mater. Lett.*, 2006, **60**, 291–293.
6 S. J. Chen, J. Li, X. T. Chen, J.-M. Hong, Z. Xue and X.-Z. You, *J. Cryst. Growth*, 2003, **253**, 361–365.
7 P. Parhi, T. N. Karthik and V. Manivannan, *J. Alloys Compd.*, 2008, **465**, 380–386.
8 H. Pan, M. Hojamberdiev and G. Zhu, *J. Mater. Sci.*, 2012, **47**, 746–753.
9 Q. Zhang, W. T. Yao, X. Chen, L. Zhu, Y. Fu, G. Zhang, L. Sheng and S. H. Yu, *Cryst. Growth Des.*, 2007, **7**, 1423–1431.
10 G. Jia, D. Dong, C. Song, L. Li, C. Huang and C. Zhang, *Mater. Lett.*, 2014, **120**, 251–254.
11 J. Geng, J. J. Zhu and H. Y. Chen, *Cryst. Growth Des.*, 2006, **6**, 321–326.
12 J. E. Post and D. L. Bish, *Am. Mineral.*, 1993, **78**, 932–940.
13 S. Vidya, S. Solomon and J. K. Thomas, *J. Electron. Mater.*, 2013, **42**, 129–137.
14 J. C. Sczancoski, L. S. Cavalcante, M. R. Joya, J. W. M. Espinosa, P. S. Pizani, J. A. Varela and E. Longo, *J. Colloid Interface Sci.*, 2009, **330**, 227–236.
15 L. S. Cavalcante, J. C. Sczancoski, J. W. M. Espinosa, J. A. Varela, P. S. Pizani and E. Longo, *J. Alloys Compd.*, 2009, **474**, 195–200.
16 J. Liao, B. Qiu, H. Wen and W. You, *Opt. Mater.*, 2009, **31**, 1513–1516.
17 J. C. Sezancoski, M. D. R. Bomio, L. S. Cavalcante, M. R. Joya, P. S. Pizani, J. A. Varela, E. Longo, M. S. Li and J. A. Andrés, *J. Phys. Chem. C*, 2009, **113**, 5812–5822.
18 M. J. Weber and W. M. Yen, *Inorganic phosphors: Compositions, Preparation, and Optical Properties*, 1932, p 194.
19 S. J. Chang, W. S. Liao, C. J. Ciou, J. T. Lee and C. C. Li, *J. Colloid Interface Sci.*, 2009, **329**, 300–305.
20 N. Skirtenko, T. Tzanov, A. Gedanken and S. Rahimipour, *Chem.–Eur. J.*, 2010, **16**, 562–567.
21 R. Silva, H. Ferreira and A. Cavaco-Paulo, *Biomacromolecules*, 2011, **12**, 3353–3368.
22 L. Yang, Y. Wang, Y. Wang, X. Wang and G. Han, *Adv. Powder Technol.*, 2013, **24**, 721–726.
23 X. Hangxun, B. W. Zeiger and K. S. Suslick, *Chem. Soc. Rev.*, 2013, **42**, 2555–2567.
24 K. S. Suslick and S. J. Docktycz, *Adv. Sonochem.*, 1990, **1**, 197–230.
25 K. S. Suslick, *Sci. Am.*, 1989, 80–86.
26 J. S. Reed, *Principles of ceramics processing*, A Wiley-Interscience Publication, 1995, pp. 594–606.
27 S.-J. L. Kang, *Sintering: Densification, Grain Growth, and Microstructure*, 2005.
28 L. Zhang, V. Belova, H. Wang, W. Dong and H. Möhwald, *Chem. Mater.*, 2014, **26**, 2244–2248.

RSC Advances

PAPER

Cite this: *RSC Adv.*, 2015, **5**, 38061

Facile sonochemical synthesis of near spherical barium zirconate titanate ($BaZr_{1-y}Ti_yO_3$; BZT); perovskite stability and formation mechanism

Supamas Wirunchit,[ac] Thitirat Charoonsuk[ac] and Naratip Vittayakorn*[abc]

Received 10th March 2015
Accepted 21st April 2015

DOI: 10.1039/c5ra04267d

www.rsc.org/advances

The multicationic oxides of perovskite $Ba(Zr,Ti)O_3$ were synthesized successfully by the sonochemical method without a calcination step. Detailed exploration considering the role of sodium hydroxide (NaOH) concentration, synthesis atmosphere, ultrasonic reaction time and precursor concentration on the perovskite phase formation and particle size was presented. It was found that nanocrystals were formed directly before being oriented and aggregated into large particles in aqueous solution under ultrasonic irradiation. The nucleation in the sonocrystallization process was accelerated by the implosive collapse of bubbles, while the crystal growth process was inhibited or delayed by shock waves and turbulent flow created by ultrasonic radiation. A pure complex perovskite phase of spherical shape was formed completely in a short irradiation time without the calcination process. Sonochemical irradiation could accelerate spherical shape formation of the particles significantly. These results provide new insights into the development and design of better nanomaterial synthesis methods.

1. Introduction

Barium zirconate titanate ($BaZr_yTi_{1-y}O_3$) and/or $BaZr_yTi_{1-y}O_3$ – based ceramics have become among the most researched lead free piezoelectric materials, due to their excellent piezoelectric properties.[1–4] The conventional solid state method is a traditional way of preparing $BaZr_yTi_{1-y}O_3$ ceramics. However, this fabrication method has several drawbacks such as a long processing time,[5,6] multiple calcinations,[7,8] low purity,[9,10] submicrometer size crystals[5,6,11] and a frequent need for grinding steps,[10] and this technique is not suitable for obtaining narrow particle size distribution.[5,7,11] J. Bera *et al.*[5] investigated the formation of $BaZr_yTi_{1-y}O_3$ solid solution by using solid state reaction between $BaCO_3$, ZrO_2 and TiO_2. They reported that at a temperature of lower than 1300 °C, raw materials did not form $BaZr_yTi_{1-y}O_3$ solid solutin directly because it had a higher formation of energy (133 kcal mol^{-1}) than $BaTiO_3$ (34.3 kcal mol^{-1}) and $BaZrO_3$ (48.4 kcal mol^{-1}). The formation mechanism can be explained by multistep reactions as follows: at the initial stage, $BaTiO_3$ and $BaZrO_3$ are formed separately at a temperature ranging from 700 to 800 °C. Subsequently, the $BaTiO_3$ diffuses into the $BaZrO_3$ to form a single perovskite phase of $BaZr_yTi_{1-y}O_3$ at a temperature as high as 1600 °C. In order to obtain perovskite $BaZr_yTi_{1-y}O_3$ nanoparticles with high quality, many new wet-chemical synthesizing methods have been developed to replace conventional solid state reaction, including the combustion method,[12] sol–gel method,[13,14] direct synthesis from solution (DSS),[15] and aqueous co-precipitation method.[16] Nanosized $BaZr_yTi_{1-y}O_3$ particles are synthesized by wet-chemical methods, which make the $BaZr_yTi_{1-y}O_3$ system very attractive for developing new electronic nanodevices.[17,18] P. Julphunthong *et al.*[12] synthesized barium zirconate titanate (BZT) powder *via* the combustion technique by using urea $(NH_2)_2CO$ as a fuel to reduce the reaction temperature. Unfortunately, the powder needed to be calcined at 1000 °C for 5 h after the combustion process in order to obtain a pure perovskite structure. Generally, submicron sizes with irregular morphology of the powder are observed always after the calcination process.[11,19] It is very difficult to obtain nanoparticles of uniform size under the calcination process,[11,19] which would therefore be an undesirable step during the fabrication process of nanopowder. M. Veith *et al.*[14] reported the synthesis of homogeneous $BaZr_{0.5}Ti_{0.5}O_3$ nanopowders that derived from a alkoxide sol–gel route. The hetero-trimetallic Ba–Ti–Zr framework was synthesized from $[TiZr(OPr^i)_8 \cdot Pr^iOH]_2$ and $[Ba(OPr^i_2)]$ and used as a precursor. The processing was performed under CO_2–free argon (Ar) or nitrogen atmosphere. The most advantageous characteristics of this method are the high purity and outstanding control of the composition of resulting powders. Nevertheless, the hydrolyzed dried gel needs to be calcined at temperatures above 400 °C in order to crystallize $BaZr_yTi_{1-y}O_3$. J. Q. Qi *et al.*[15] developed a new method called direct synthesis

[a]*Electroceramics Research Laboratory, College of Nanotechnology, King Mongkut's Institute of Technology Ladkrabang, Bangkok 10520, Thailand. E-mail: naratipcmu@yahoo.com*

[b]*Department of Chemistry, Faculty of Science, King Mongkut's Institute of Technology Ladkrabang, Bangkok 10520, Thailand*

[c]*Advanced Materials Research Unit, Faculty of Science, King Mongkut's Institute of Technology Ladkrabang, Bangkok 10520, Thailand*

from solution (DSS) to prepare $BaZr_yTi_{1-y}O_3$ nanoscaled powders near room temperature under ambient pressure. By dissolving barium hydroxide into warm water as a base solution, nanocrystalline $BaZr_yTi_{1-y}O_3$ powders can be obtained by mixing isopropanal solution of zirconium isopropoxide–isopropanol and tetrabutyl titanate with hot base solution. When doing this, the particle size of the nanoparticles fell within the range of 25 to 120 nm. Recently, single phase nanocrystalline powder of $BaZr_yTi_{1-y}O_3$ was obtained successfully by the aqueous co-precipitation method at a temperature <100 °C.[16] The process was as follows: a mixed chloride solution of Ba, Ti and Zr ions was dripped slowly into a heated strong base solution (pH > 12.0). The nanocrystalline $BaZr_yTi_{1-y}O_3$ favored forming a strongly based concentration at a temperature of about 80 °C. The as-prepared powders showed an average particle size of 30 nm. The precipitant concentration and synthesis temperature play an important role as a parameter for increasing product purity.[16] However, the particles have various shapes such as spherical, acicular, elliptical, and cubic with truncated edges.[16] The particle size and shape are not controlled by this method. The different morphologic shape and wide range of particle size distribution have been the key problem to create the abnormal grain growth in the sintering process.[11]

In order to eliminate abnormal grain growth during the sintering process, $BaZr_yTi_{1-y}O_3$ nanoparticles are expected to have spherical morphology with a narrow particle size distribution.[11] Among the wet-chemical methods developed so far,[14–16,20,21] sonochemical synthesis at ambient temperature seems to be a new technique that fulfills the requirements for synthesizing extremely fine particles with spherical morphology and a narrow size distribution.[22,23] The sonochemical method uses an acoustic cavitation phenomenon from ultrasonic irradiation to generate or accelerate the chemical reaction. Acoustic cavitation is the formation, growth, and implosive collapse of bubbles in a liquid, which generates a localized hot spot, with a temperature of approximately 5000 K, pressure of 20 MPa, and heating and cooling rates that exceed 10^{10} K s^{-1}.[22,24] These transient, localized hot spots can drive many chemical reactions, such as decomposition, dissolution, oxidation, reduction, and promotion of polymerization.[22,24] By using these transient extreme conditions, various kinds of organic, inorganic and novel materials, with unusual properties such as metals,[25,26] precious metals,[27,28] simple metal oxides,[29–35] nitrides,[29] carbides,[36] sulfides[29,37] and core/shell nanocomposites[37,38] were synthesized successfully. Up until now, few studies on the sonochemical synthesis of multicationic oxides based on a complex perovskite structure $[A(B'B'')O_3]$ have been reported, and to the best of the authors' knowledge, there is no previous report on the direct sonochemical synthesis of $(BaZr_yTi_{1-y}O_3)$; y = 0.0–0.6 powders.

This study used high-intensity ultrasound irradiation to synthesize nanosized complex ternary metal oxide ($BaZr_yTi_{1-y}O_3$); y = 0.0–0.6. Various key synthesis parameters such as synthesis atmosphere, concentration of precipitating agent, concentration of the starting solution, sonication time and Zr/Ti molar ratio were investigated carefully in order to understand their effect on the perovskite phase formation and morphology of the powders. The procedure of the sonochemical formation of nanosized BZT powders also was examined.

2. Experimental procedure

2.1 Solution preparation

In this study, all the reagents used in experiments were of analytical purity and used without further purification. The barium chloride dihydrate ($BaCl_2 \cdot 2H_2O$, 99.8% Merck), zirconium oxychloride octahydrate ($ZrOCl_2 \cdot 8H_2O$, 99.5% Advance material) and titanium tetrachloride ($TiCl_4$, 99.9% Wako) were used as the starting materials. Sodium hydroxide (Fisher Scientific 97.7%) was used as the precipitating agent. In order to obtain the stock of Ti-solution, $TiCl_4$ was dripped very slowly into deionized water at a temperature lower than 5 °C and stirred vigorously until the solution was clear. Then, the separate stoichiometric amounts of $BaCl_2 \cdot 2H_2O$ and $ZrOCl_2 \cdot 8H_2O$ were dissolved typically in de-ionized water in order to obtain the barium (Ba^{2+}) and zirconium (Zr^{4+}) solution, respectively. These stocks of starting solution were prepared freshly for each set of experiments.

2.2 Synthesis of $Ba(Zr_yTi_{1-y})O_3$ powders

The barium zirconate titanate ($Ba(Zr_yTi_{1-y})O_3$; BZT) powder products, with the composition (y) = 0.00, 0.05, 0.20, 0.04 and 0.60, were synthesized by the sonochemical method without the calcination process, which was in accordance with the reaction (1):

$$\begin{aligned} BaCl_2 \cdot 2H_2O_{(aq)} + (1-y)TiCl_{4(aq)} + yZrOCl_2 \cdot 8H_2O_{(aq)} \\ + (6-2y)NaOH_{(aq)} \rightarrow Ba(Zr_yTi_{1-y})O_{3(s)} \\ + (6-2y)NaCl_{(aq)} + (13-y)H_2O_{(aq)} \end{aligned} \quad (1)$$

Firstly, the appropriate proportions of titanium and zirconium (withdrawn from the stock solution using a pipette) were mixed together to form a solution to which the barium solution was then added, with continuous stirring in order to obtain a homogeneous mixed solution. The concentrations of barium and titanium solution were varied from 0.01 mol L^{-1} to 1.5 mol L^{-1} in order to study the effect of Ba and Ti ion concentration on the perovskite phase formation. The Ba and Ti ion ratio in the mixed solution was targeted constantly at 1 : 1. After that, sonication equipment was set up for the sonochemical process. Regarding the synthesis system, the effect of synthesis atmosphere on the phase formation was studied. The powder synthesized in open air was compared with that in a closed system with Ar gas. After setting up the equipment, the sodium hydroxide (NaOH) solution was loaded into a sonication vessel for use as the precipitating agent. The concentration of NaOH solution was varied from 5 to 20 mol L^{-1} in order to study its effect. Then, the mixed starting solution was added into the sonication vessel, which contained the NaOH solution, drop by drop at a rate of about 25 ml min^{-1}. Therefore, a high pH value reached 14 during the process. In order to obtain nanoparticles of better quality, pulse ultrasonication (Sonics VCX-750, 20 kHz, 750 W) was conducted in the 2 s mode; and a pause in 1 s mode was performed in the experiments that followed. It has been

reported that synthesized powder in pulse ultrasonic mode gives a narrower particle size distribution than that in continuous ultrasonic mode.[39] This may be related to the uneven distribution of ultrasonic energy in the ultrasonic vessel.[39] During the process of adding mixed solution, white precipitation was formed instantaneously. After the irradiation time was over, the sonication vessel that contained the precipitate was cooled to room temperature by immersing in tap water. Then, the recovered precipitate was filtered out by centrifugal filtration, and washed with de-ionized water until the pH value reduced to 7. The supernatant was checked with 0.1 mol L^{-1} of $AgNO_3$ solution until no white sediment remained, which confirmed that the chloride ion was not retained. Finally, the washed precipitates were dried at 80 °C in an oven overnight in order to obtain the powder products.

2.3 Characterization

The perovskite phase formation, structure and crystallite size of the products were carried out by X-ray powder diffraction using an X-ray diffractometer (Philips PW3040, The Netherlands) with Cu Kα radiation ($\lambda = 0.15406$ nm). The acceleration voltage was 35 kV with a 150 mA current flux. X-ray diffraction (XRD) was taken of the powders attached to a glass slide, and data were collected in the 2θ range from 20° to 60°, with a scanning rate of 4° per min and sample interval of 0.02°. Crystallite size and microstrain were calculated by the X-ray line broadening method using Scherrer[40] and Hall–Williamson methods.[41] The Scherrer equation relies on utilizing the following equation:

$$D = K\lambda/\beta \cos\theta, \quad (2)$$

where λ is the CuK_α radiation of wavelength (1.5406 Å), β is the full width at haft-maximum (FWHM) in radian and θ is the scattering angle. Also, K is the shape factor (a constant equal to 0.94) and D is the crystallite size normalized to the reflecting planes. The Hall–Williamson method provides a technique for finding an average size of coherently diffracting domains and microstrain. Strain-induced peak broadening arises due to imperfect crystal and distortion, which is calculated by using the following formula:

$$\varepsilon = \frac{\beta_{hkl}}{4\tan\theta} \quad (3)$$

To estimate microstrain from the XRD pattern, Hall and Williamson proposed a formula as follows:

$$\beta_{hkl}\cos\theta = \frac{\kappa\lambda}{D} + 4\varepsilon\sin\theta \quad (4)$$

where ε is the elastic strain. When $\beta_{hkl}\cos\theta$ is plotted *versus* different diffraction planes, a linear fit is expected. Lattice strains were obtained from the slope of this line. Raman spectra were recorded in the 100–1000 cm^{-1} wave number ranges in order to support the crystal structure identification of synthesized powders with a Thermo Scientific DXR Raman microscope (532 nm excitation of the laser). The vibration mode of the bond in molecules was obtained from Fourier transform infrared (FT-IR spectrum Gx, Perkin Elmer, America) spectra. The morphology and particle size of the resulting as-prepared products were characterized initially by using a scanning electron microscope (SEM, Hitachi 54 700), equipped with energy-dispersive X-ray spectroscopy (EDX) capabilities. These samples were then coated conductively with gold by sputtering for 15 s in order to minimize charging effects under SEM imaging conditions. Regarding the study of phase transition, a differential scanning calorimeter (DSC 2920, TA Instrument) was used, and DSC curves were recorded in a temperature range from 30 °C to 200 °C with a scanning rate of 10°C min^{-1}.

3. Results and discussion

3.1 The effect of NaOH concentration on the perovskite phase formation

Changing the synthetic parameters greatly affected the perovskite phase formation. This study exposed the concentration of NaOH that had a notable effect on the perovskite phase formation. Fig. 1 shows the XRD patterns of $BaZr_yTi_{1-y}O_3$; $y = 0.0$ powders that evolved after sonication for 60 min in different NaOH concentrations in the open air system. As shown in Fig. 1, only X-ray peaks of whiterite-$BaCO_3$ and $Ba(OH)_2(H_2O)_3$ are present in powder synthesized with 5 mol L^{-1} NaOH. These kinds of unwanted phase correspond well with the literature.[21]

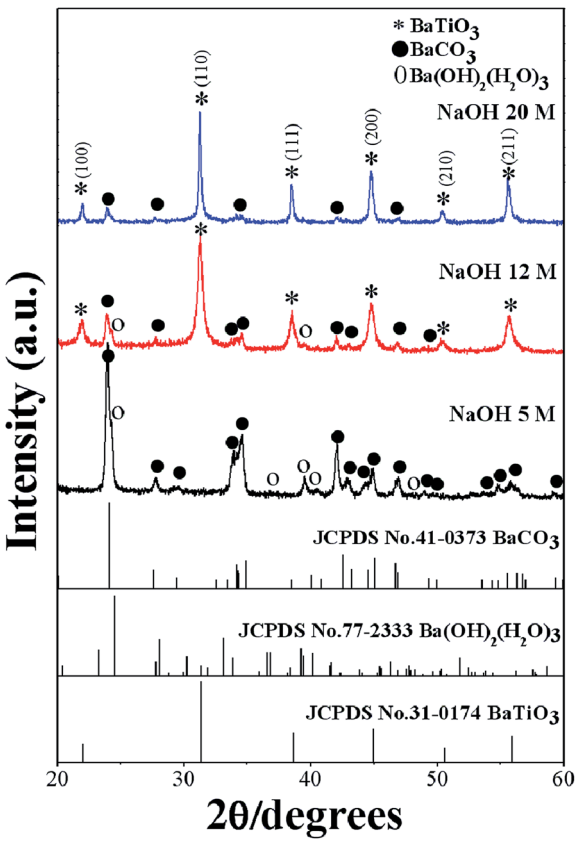

Fig. 1 XRD patterns of $BaZr_yTi_{1-y}O_3$; $y = 0.0$ powders evolved for 60 min at various NaOH concentrations in the open air system.

No perovskite structure was characteristic of diffraction peaks, thus indicating no reaction had yet been triggered for synthesis with 5 mol L^{-1} of NaOH concentration. Interestingly, the XRD pattern presented no evidence of a Ti-precursor phase, indicating that an amorphous phase might be formed.[42] When the perovskite phase started to form with increasing NaOH concentration, the $BaCO_3$ and $Ba(OH)_2(H_2O)_3$ phase decreased dramatically. Diffraction peaks of the perovskite phase are indexed with the $BaTiO_3$ cubic structure in the *Pm3m* space group from JCPDS card no. 31-0174. Intensity of the perovskite pattern increased significantly with increasing NaOH concentration. The increase in perovskite phase at high hydroxide concentration might be due to increasing formation of the complex polymeric chain network of bimetallic Ba–Ti hydroxides.[43] Nevertheless, in the open air system, a peak of $BaCO_3$ with low intensity was still present in products synthesized in 20 mol L^{-1} of NaOH concentration. The problem of forming $BaCO_3$ at a high NaOH concentration should be attributed to use of the open air synthesis system, in which the Ba-hydroxide in the solution can react easily with CO_2 in air or carbonate species in the solution.

3.2 Effect of synthesis atmosphere on the perovskite phase formation

In order to study the influence of synthesis atmosphere on the perovskite phase formation, the powder was synthesized in open-air and Ar atmosphere. Fig. 2 shows XRD patterns of $BaZr_yTi_{1-y}O_3$; $y = 0.0$ powders that evolved after sonication for 5 to 60 min in 20 mol L^{-1} of NaOH concentrations in the (a) open air system and (b) closed system with Ar gas. The XRD pattern in the open-air system showed a mixed phase of perovskite, $BaCO_3$ and $Ba(OH)_2(H_2O)_3$ phases. The $BaCO_3$ and $Ba(OH)_2(H_2O)_3$ phase remained in the pattern with increasing sonication time, indicating that the formation of $BaCO_3$ and $Ba(OH)_2(H_2O)_3$ phase are not related directly with the sonication irradiation time. Regarding powder synthesized in Ar atmosphere, the $BaCO_3$ phase disappeared after only five minutes sonication time. The relatively small XRD pattern agreed well with the perovskite structure. However, intensity of the perovskite phase was quite low, indicating that the product has low crystallinity. The crystallinity of the product was improved significantly by increasing the sonication period, and a sharp XRD pattern was observed clearly at 60 min sonication time. The observations clearly show that the $BaZr_yTi_{1-y}O_3$; $y = 0.0$ phase formation was completed during the sonochemical process itself, without the need of further calcination or a heating process. The XRD pattern indicated that the synthesized powder agreed well with the cubic $BaTiO_3$ structure in the *Pm3m* space group (JCPDS data no. 31-0174). Based on XRD results, Rietveld refinement analysis gave lattice parameters of $a = 4.0415 \pm 0.0004$ Å, which were slightly larger than those reported to value $a = 4.031$ Å (JCPDS data no. 31-0174). This slight expansion of lattice parameters (a) might be due to the presence of a trace amount of the OH group trapped in the crystal lattice, which can be confirmed by solvothermal treatment with dimethylformamide (DMF). The intensities and positions of the peaks match very well with those data reported in the literature.[15,16] No peaks in any other phase were detected, thus indicating high purity of the product. These results indicate that impurity of the $BaCO_3$ phase can be reduced or eliminated when the product is synthesized with a high concentration of precipitating agent (NaOH) and in the closed system with Ar atmosphere.

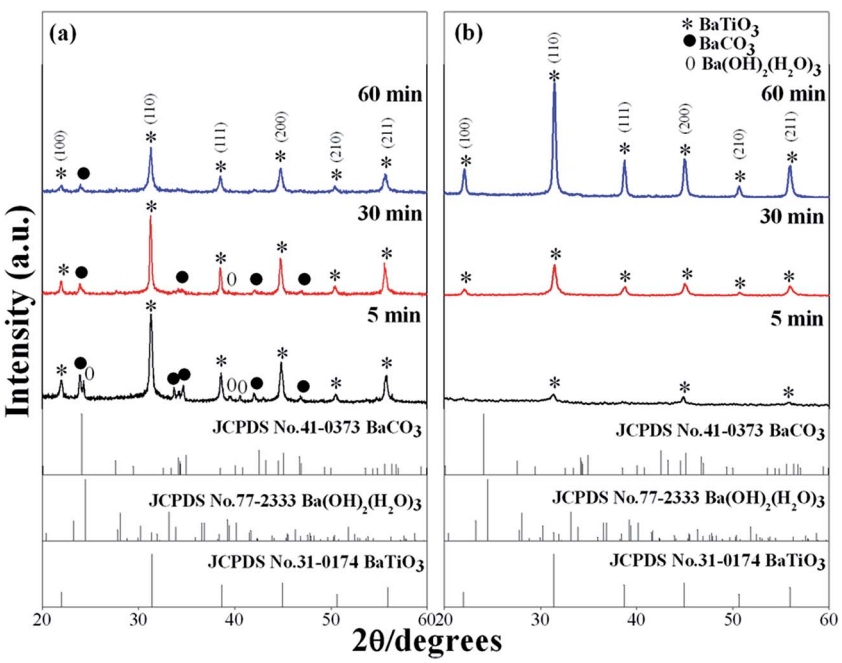

Fig. 2 XRD patterns of $BaZr_yTi_{1-y}O_3$; $y = 0.0$ powders obtained after sonication for 5 to 60 min in 20 mol L^{-1} of NaOH concentrations in the (a) open air system and (b) closed system with Ar gas.

3.3 Effect of precursor concentration on the perovskite phase formation

The effect of Ba and Ti ion concentration in the starting solution on the perovskite phase formation was observed. The Ba ion to Ti ion ratio in the solution was kept constant at 1 : 1. The precursor concentration varied from 0.01 to 1.5 mol L^{-1}. Fig. 3(a) illustrates the XRD pattern of $BaZr_yTi_{1-y}O_3$; $y = 0.0$ powders at different precursor concentrations synthesized for 60 min with 20 mol L^{-1} of NaOH in Ar atmosphere. The XRD pattern displayed the $BaCO_3$ and $Ba(OH)_2(H_2O)_3$ phase at a low precursor concentration ($\leq$0.1 mol L^{-1}), the perovskite phase was not observed. The perovskite phase started to form at 0.1 mol L^{-1}. When the concentration increased to 0.5 mol L^{-1}, the $BaCO_3$ peak disappeared, and the pure perovskite phase was obtained. Fig. 3(b)–(d) display the morphology of the product synthesized with different precursor concentrations. Two types of morphological particles were observed clearly at a low precursor concentration (0.01 mol L^{-1}); *i.e.* a large particle with irregular morphology and small one with agglomerated form. The energy dispersive X-ray (EDX) analysis [Fig. 3(b)] indicated that the large particle was the $BaCO_3$ phase, while the agglomerated cluster was the Ti-amorphous phase. The results corresponded well with the XRD pattern. The morphology of the particle changed significantly with increased precursor concentration to a more spherical shape, and a narrow size distribution was observed clearly. The histogram of particle size distribution in Fig. 3(d) illustrates nanoparticles with a narrow size distribution that ranges within the average particle dispersity (D_{SEM99}/D_{SEM50}) of 1.54. The average particle size decreased significantly with increasing precursor concentration, and when measured by SEM was found to be 123.2 $\pm$ 42.8 nm and 49.6 $\pm$ 11.2 nm for powder synthesized in 0.5 mol L^{-1} and 1.5 mol L^{-1} of precursor concentration, respectively. The intensity of the XRD pattern decreased when the precursor concentration increased to 1.5 mol L^{-1}, while the FWHM value was increased, thus indicating that nanocrystals tend to become smaller. The Hall–Williamson plot of $\beta_{hkl}\cos(\theta)/\lambda$ *versus* 4 sin θ gives the value of strain from the slop of the fit, as shown in Fig. 4(a)–(f). The crystalline size calculated from the Scherrer and Hall–Williamson methods is summarized in Table 1, where this assumption has been confirmed. The crystallite size of powder was found to be 36.61 $\pm$ 13.96 nm and 16.40 $\pm$ 01.46 nm when synthesized in 0.5 mol L^{-1} and 1.5 mol L^{-1} of precursor concentration, respectively. It is interesting to note that the particle size becomes close to the crystallite size with increasing precursor concentration, which indicates that particles synthesized at a high precursor concentration are composed of fewer crystallites. Generally, particle sizes that precipitate from solution are influenced by the relative rates of nuclei formation and crystallite growth, and a high nucleation

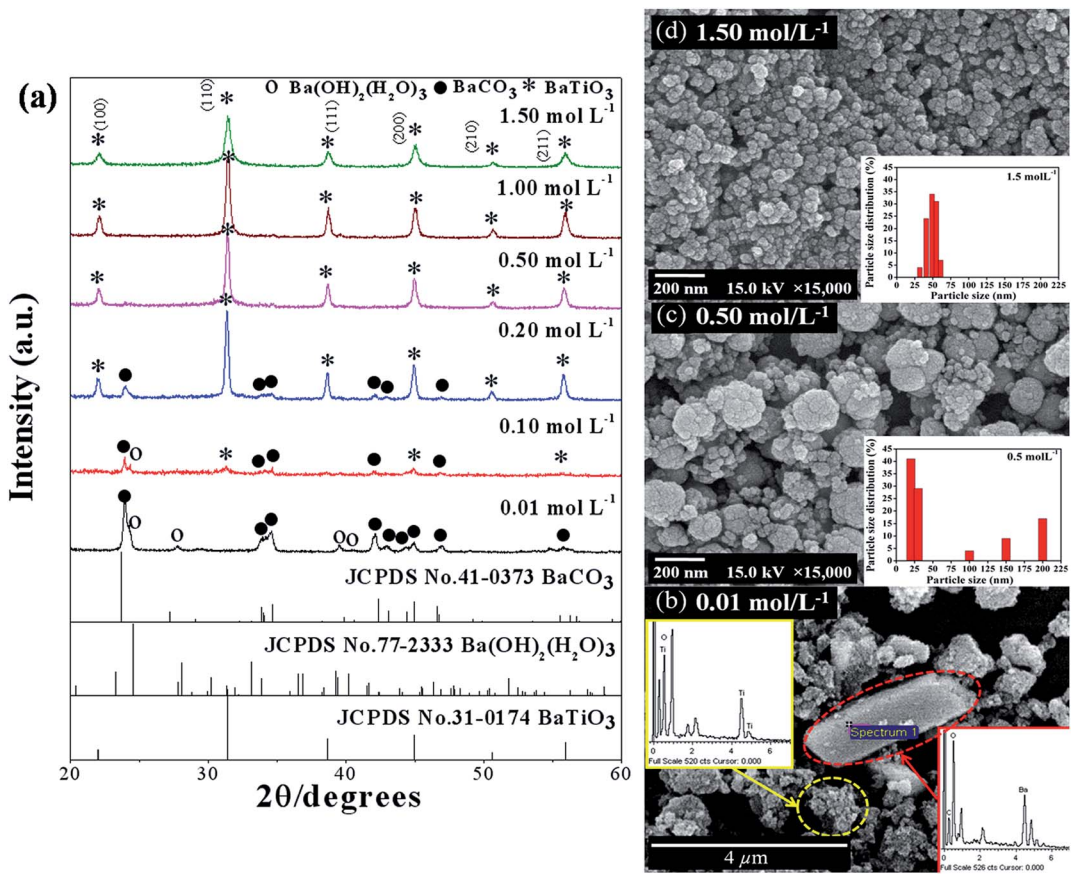

Fig. 3 XRD pattern (a) and SEM images (b) to (d) of $BaZr_yTi_{1-y}O_3$; $y = 0.0$ powders synthesized for 60 min at various precursor concentrations in 20 mol L^{-1} of NaOH in Ar atmosphere.

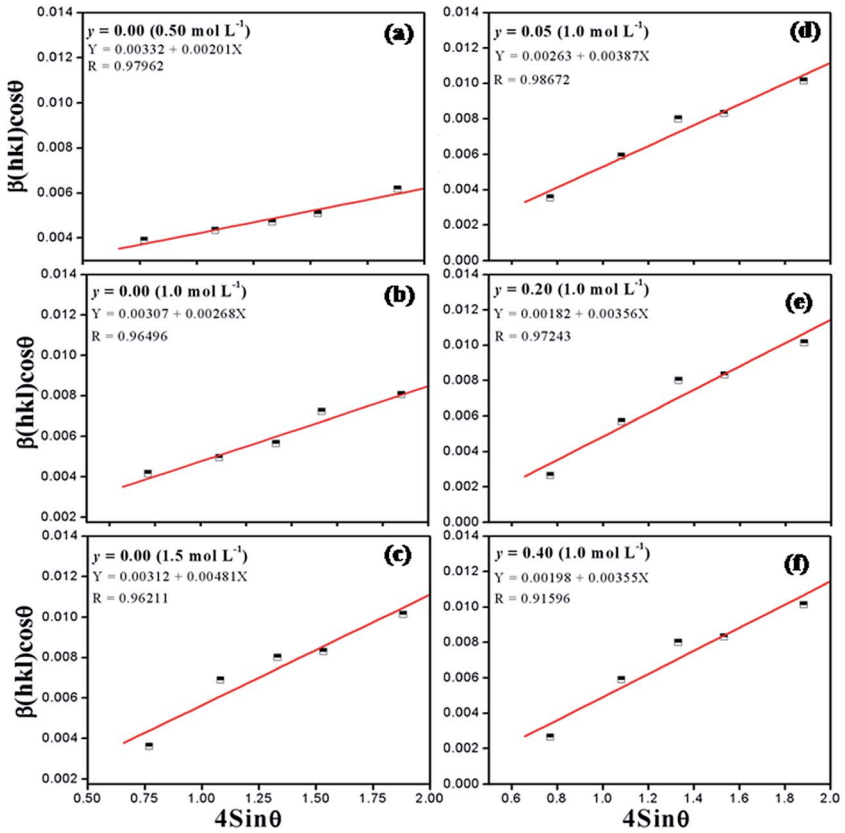

Fig. 4 Hall–Williamson plot (a) $y = 0.0$ at 0.5 mol L^{-1} of precursor concentration, (b) $y = 0.0$ at 1 mol L^{-1} of precursor concentration, (c) $y = 0.0$ at 1.5 mol L^{-1} of precursor concentration, (d) $y = 0.05$, (e) $y = 0.2$ and (f) $y = 0.4$.

Table 1 Crystalline size (D) and lattice strain calculations of the $BaZr_yTi_{1-y}O_3$; y = 0.0, 0.05, 0.2 and 0.4 powders as determined by X-ray diffraction

Sample		Scherrer method	Hall–Williamson method		SEM
y	Conc. (mol L^{-1})	Crystalline size (nm)	Crystalline size (nm)	ε ($\times 10^{-3}$)	Particle size (nm)
0.00	0.50	36.6 ± 13.9	28.5	2.01 ± 0.002	123.2 ± 42.8
0.00	1.00	28.8 ± 09.4	26.4	2.68 ± 0.001	93.0 ± 28.2
0.00	1.50	16.4 ± 01.4	15.0	1.53 ± 0.003	49.6 ± 11.2
0.05	1.00	29.8 ± 07.4	18.6	3.87 ± 0.002	96.3 ± 14.0
0.20	1.00	33.2 ± 12.7	19.1	3.56 ± 0.003	108.1 ± 19.3
0.40	1.00	33.5 ± 12.3	19.4	3.55 ± 0.002	115.5 ± 11.0

rate can produce a large number of small crystallites.[19,44] A larger number of cations at higher values of precursor concentration diffuse in solution, thus leading to a higher degree of supersaturation and higher nucleation rate.[11,29] As a result, the size of the final particles decreased with increasing precursor concentration, while a large number of small crystallites were formed. The structural and morphological characterizations converged when demonstrating that the sonochemical synthesis process leads to forming the cubic $BaTiO_3$ phase, with 100 nm grade nanopowders and a narrow size distribution.

3.4 Effect of sonication time on the morphology and particle size distribution

To investigate the details of sonochemical conversion from precursor to the final perovskite phase, a series of experiments employed different sonication times, without changing the conditions of other preparations. Fig. 5(a) shows the XRD pattern of as-prepared $BaZr_yTi_{1-y}O_3$; $y = 0.0$ powders synthesized by 1 mol L^{-1} of precursor concentration with 20 mol L^{-1} of NaOH in Ar atmosphere at different sonication times. The pure perovskite structure was observed clearly at 5 min sonication time by using a strong base solution (20 mol L^{-1} NaOH) and

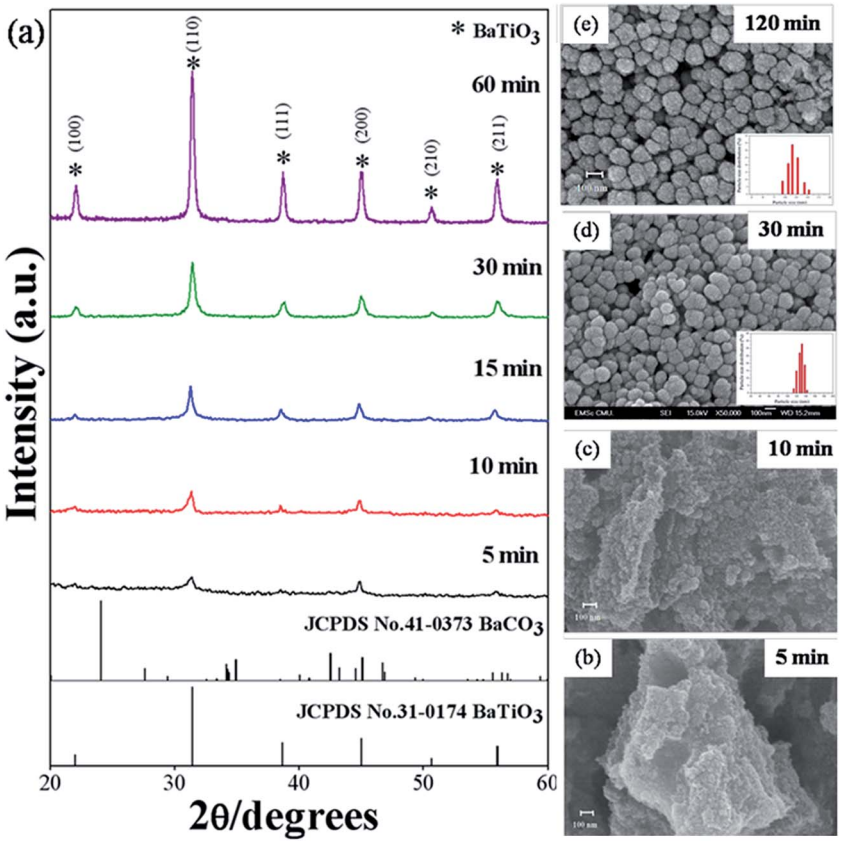

Fig. 5 XRD pattern (a) and SEM images (b) to (e) of $BaZr_yTi_{1-y}O_3$; $y = 0.0$ powders synthesized at various reaction durations in 20 mol L^{-1} of NaOH in Ar atmosphere.

high precursor concentration (≥0.5 mol L^{-1}), with the powder synthesized in a closed system with Ar gas. No $BaCO_3$ phase or unwanted phase was found, but intensity of the perovskite phase was quite low. This indicated that the product had low crystallinity, which improved significantly with increasing ultrasonic irradiation time. A sharp XRD pattern was observed clearly at 60 min sonication time. Fig. 5(b)–(d) illustrate the secondary electron images of $BaZr_yTi_{1-y}O_3$; $y = 0.0$ synthesized at different sonication times. Fig. 5(b) and (c) show that nanocrystals of $BaZr_yTi_{1-y}O_3$; $y = 0.0$ were formed firstly under ultrasonic irradiation, and then readily agglomerated into aggregated particles in a short period of time, in order to minimize high surface energy. The particle size and shape of the cluster are difficult to identify. However, the spherical shape and uniformity of the particle were observed clearly with increased sonication time [Fig. 5(d)–(f)]. Sphere-like particles were achieved, evidently after 20 min sonication time, and the particle size increased slightly after 2 h under ultrasonic irradiation. The particles showed a monosized spherical shape that was different from that in other wet chemical synthesizing methods.[12,14–16] The products had a slightly spherical morphology, and the particle size distribution was rather narrow. Furthermore, by increasing the sonication time further, the formation of neck between the particles was observed, which is caused by high velocity interparticle collision generated by ultrasonic irradiation [Fig. 5(d)]. The high velocity of interparticle collision can make surface diffusion, as the melting point starts from the surface area of nanoparticles.[24] Surface diffusion is transportation of a typical mass in the sintering mechanism that produces surface smoothing,[29] particle joining,[23,45] grain boundary formation[24,45] and neck growth.[45] Nevertheless, densification and volume shrinkage did not originate, as the sonochemical method generated local thermal energy that differed from thermal energy of the sintering process.[22]

3.5 Effect of the Zr/Ti molar ratio on the perovskite phase formation

The evolution of XRD patterns of $BaZr_yTi_{1-y}O_3$; $y = 0.0$, 0.2, 0.4 and 0.6 powders synthesized in different sonication times is shown in Fig. 6(a)–(d). Strong influence of the Zr/Ti ratio was observed clearly on perovskite phase formation, which started for the composition, $y = 0.0$, at 5 minutes sonication time [Fig. 6(a)]. Otherwise, formation of the perovskite phase started to form at 10 and 15 minutes sonication time for the composition, $y = 0.2$ and 0.4, respectively [Fig. 6(b) and (c)]. However, as shown in Fig. 6(d), no strong crystal phases can be found from the XRD pattern for the composition, $y = 0.6$, meaning that the samples were composed of an amorphous phase, of which its formation might be related to different regions of sonochemical activity. Two regions of sonochemical activity are known to exist, as postulated by Suslick and co-workers.[22,46] One

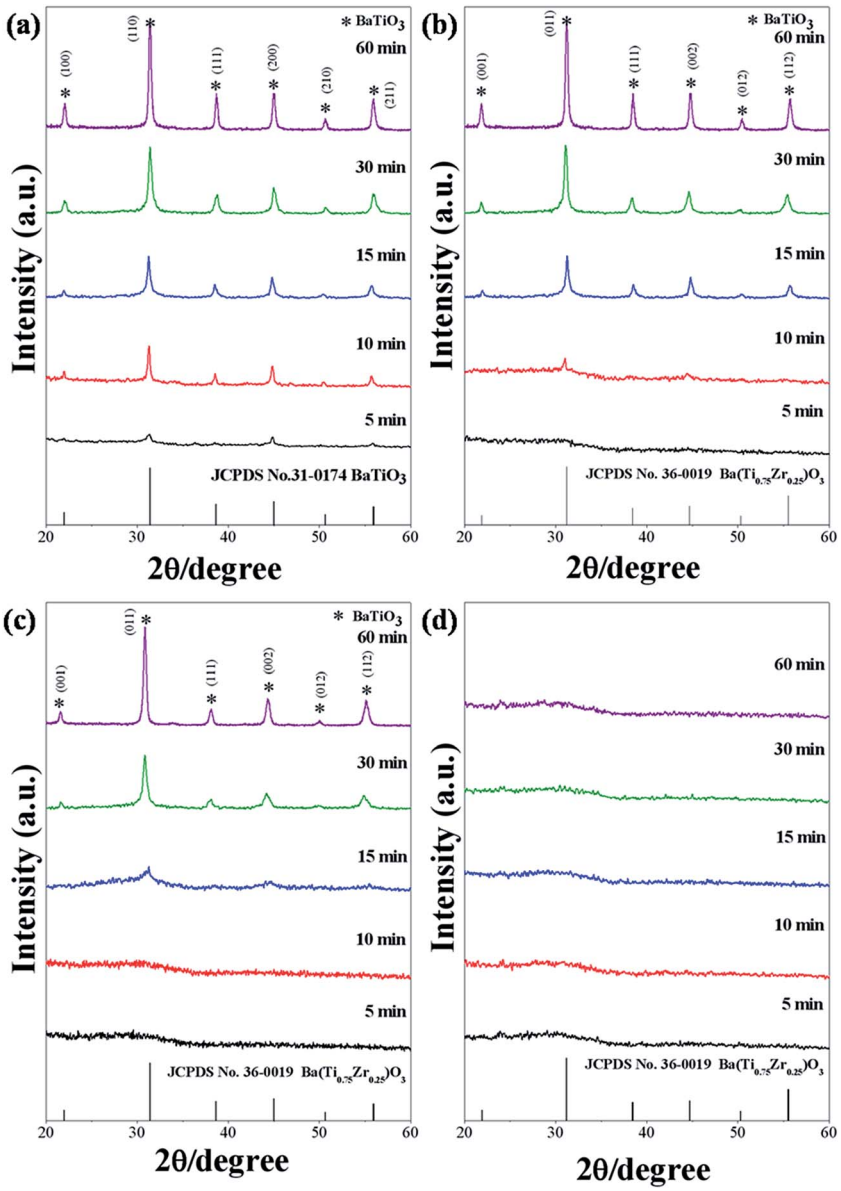

Fig. 6 XRD patterns of $BaZr_yTi_{1-y}O_3$; $y = 0.0$, 0.2, 0.4 and 0.6 powders synthesized at various sonication times in 20 mol L^{-1} of NaOH solutions (a) $y = 0.0$, (b) $y = 0.2$, (c) $y = 0.4$ and (d) $y = 0.6$.

is the inside of collapsing bubbles and the other the interfacial region between the cavitation bubbles and surrounding solution. The inside of collapsing bubbles generates extremely high temperature (>5000 K), pressure (>20 MPa) and very high cooling rates (excess of 10^{10} K s^{-1}), whereas the interfacial region generates a much lower temperature, which is still high enough to rupture chemical bonds and induce a variety of reactions.[45] When a reaction takes place inside collapsing bubbles, the final product is amorphous, as a result of the extremely rapid cooling rate (>10^{10} K s^{-1}) that occurs during the collapse. Conversely, if a reaction occurs within the interfacial region, nanocrystalline products are expected to materialize. Since amorphous powders were obtained in this study at a high Zr/Ti ratio, the authors postulate that the formation of $Ba(Zr/Ti)O_3$ at a high and low Zr/Ti ratio probably occurs inside and at the interfacial region of collapsing bubbles, respectively. Similar behavior was observed in stibnite (Sb_2S_3) nanorod that was synthesized by the sonochemical method.[47] Besides, another factor might relate to the difference in formation constant of the complex metallic hydroxide network. At a high Zr concentration, heterotrimetallic Ba–Ti–Zr-hydroxide may have difficulty in forming a network.[44] All compositions of powders synthesized at 60 min sonication time were selected in order to investigated the solid solution and identify the crystal structure. The XRD pattern of $BaZr_yTi_{1-y}O_3$; $y = 0.0$, 0.2, and 0.4 nanoparticles, synthesized for 60 min sonication time are presented in Fig. 7(a). All powders exhibit a pure perovskite structure without a trace of impurity, indicating that Zr^{4+} has diffused into the host lattice to form a solid solution. One symmetric peak observed at 2θ ~44° to 46° in all of the samples confirmed that all

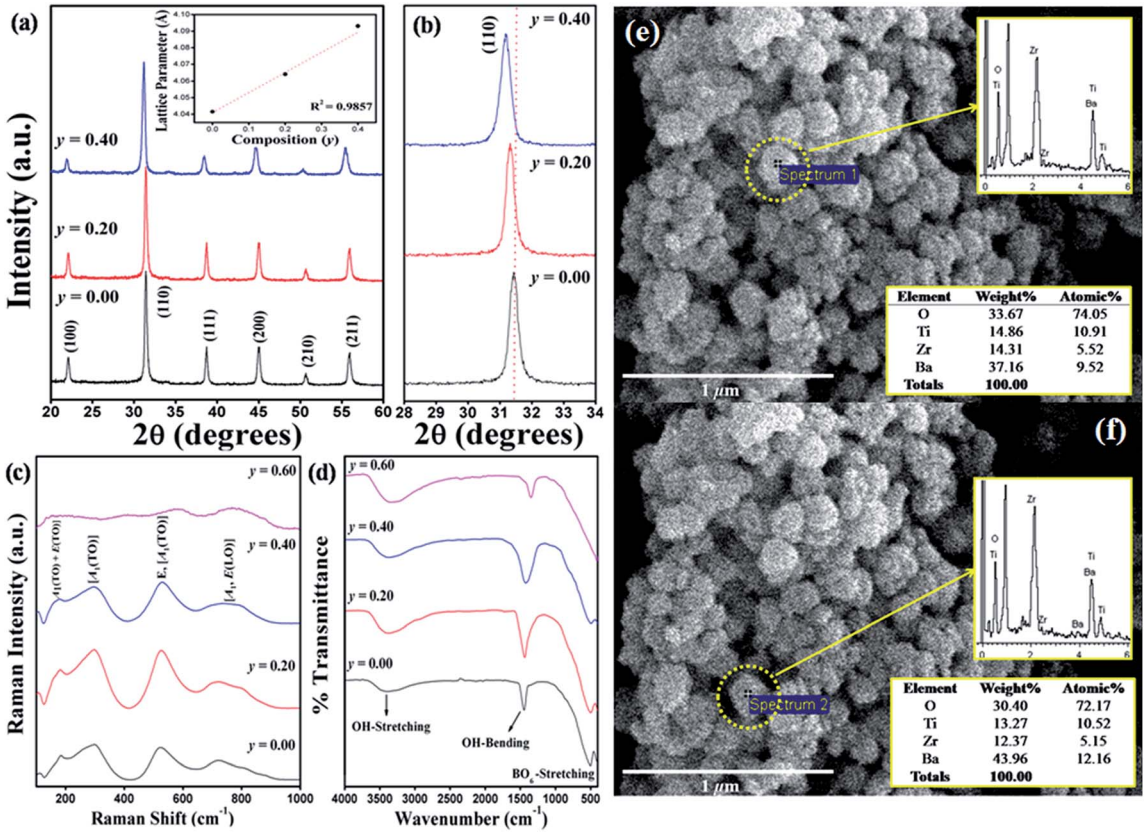

Fig. 7 XRD patterns of $BaZr_yTi_{1-y}O_3$; $y = 0.0$, 0.2 and 0.4 powders synthesized at 60 min sonication time (a) enlarged ranges of 28–34°, (b) Raman spectrum (c) and FT-IR spectrum (d) SEM/EDX results of the composition $y = 0.4$ powders (e and f).

Table 2 Lattice parameter (a), and unit cell volume (v) of the $BaZr_yTi_{1-y}O_3$; $y = 0.0$, 0.2 and 0.4 powders as determined by X-ray diffraction

Sample		Lattice parameters (a)/(Å)	Unit cell volume (v)/(Å)^3
y	Conc. (mol L^{-1})		
0.00	1.00	4.0415 ± 0.0004	65.42
0.20	1.00	4.0641 ± 0.0004	67.12
0.40	1.00	4.0931 ± 0.0011	68.57

compositions had a cubic symmetry. This agreed well with previous reports that used the co-precipitation method.[16] Additionally, the XRD pattern demonstrated a progressive peak shift toward the lower diffraction angle with increased Zr^{4+} [Fig. 7(b)]. This phenomenon can be explained qualitatively with respect to the unit cell volume caused by the substitution of Zr^{4+} at the Ti-site. According to Shannon's effective ionic radii, with a coordination number of 6, the ionic radius of B-site ions (Zr^{4+}) is 0.86 Å, which is close to the radius of Ti^{4+} (0.745 Å).[48] The calculated lattice parameters (a) and unit cell volume (v) of $BaZr_yTi_{1-y}O_3$; $y = 0.0$, 0.2, and 0.4 powders are reported in Table 2. These values increase with increased Zr content by replacing Ti^{4+}-site (0.745 Å) with large Zr^{4+} (0.86 Å) ions. The Raman spectra are shown clearly in Fig. 7(c). All Raman peaks of the composition $y = 0.00$, 0.20 and 0.40 were observed similarly. The 4 broadening peaks at around 186, 303, 522 and 715 cm^{-1} are assigned to the [A_1(TO) + E(LO)], [A_1(TO)], [E, A_1(TO)] and [A_1, E(LO)] Raman-active modes of tetragonal ($P4mm$) symmetry.[49] It is noteworthy that despite the XRD data [Fig. 7(a)] showing the cubic ($Pm3m$) symmetry, the Raman spectra show the tetragonal ($P4mm$) crystal structure. This is because of the hydroxyl defect from a high basic environment. The –OH groups can substitute the sub-lattice to form a metastable cubic phase. However, the hydroxyl defect existed as interstitial defects in many unit cells, but not all. Therefore, some unit cells can stabilize in a tetragonal structure. Nevertheless, characterization by XRD gives results in a static and average symmetry, while the result in a dynamic and local symmetry could be characterized by Raman spectroscopy.[49] Therefore, the results from Raman did not correlate with those from XRD data in this situation. In fact, the crystal structure of powder products may exhibit a mixture between the tetragonal and cubic crystal structure. However, the hydroxyl defects could be removed by chemical treatment with DMF, which is discussed later. Furthermore, Fig. 7(c) also reveals that all of the Raman peaks disappeared when the composition (y) of the Zr/Ti ratio was increased to 0.60. The presence of a very broad hump demonstrated a predominantly amorphous phase characteristic. This result confirms that the condition of powder products was stabilized in the amorphous phase. Furthermore, the FT-IR spectrum of powder products at various Zr/Ti ratios was studied

and reported in Fig. 7(d). The band appearing for all compositions at around 3600 and 1600 cm^{-1} is attributed to O–H stretching and O–H bending vibration, respectively. In corresponding with previous results, it could be said that the OH vibration bands in the 0.00–0.40 compositions of the Zr/Ti ratios come from the OH-defects, that existed on the surface particles and in the sub-lattice. On the other hand, the O–H vibration band in the 0.60 composition of the Zr/Ti ratio may come from the mixture between OH^- species defects and –OH groups from the amorphous phase. In addition, the absorption peak at around 520 cm^{-1} was used to indicate the difference of trimetallic Ba–Ti–Zr hydroxides amorphous and crystalline BZT phases. This peak is assigned mainly to the characteristic peak of the perovskite structure, while associating with the absorption vibration of Ti–O and Zr–O asymmetric stretching in BO_6 octahedra.[14,50] The 0.00–0.40 compositions showed the strong of asymmetric stretching in BO_6 octahedra, thus confirming that the powder products in these conditions were formed as BZT solid solution without the impurity or the other phases. Interestingly, the BO_6 vibration band disappeared at the 0.60 composition of the Zr/Ti ratio, while the OH absorption band exhibited large intensity, thus suggesting that the BZT solid-solution phase was not found at this condition. Therefore, it can be confirmed that the product powder may stabilize in the form of trimetallic Ba–Ti–Zr hydroxides in the amorphous phase. The SEM/EDX analysis at different points on the surface of individual particles was performed in order to confirm the homogeneity of the powder products. Fig. 5(e) and (f) display the EDX spectra at different points on the surface of individual particles. It can be seen from these figures that the concentrations of various elements (Ba, Ti, Zr and O) involved in the individual particle are very close to each other indicating to the homogeneity of the powder products. The result from SEM/EDX spectra showed good correspondence with the result from XRD [Fig. 7(a)]. This observation clearly demonstrates that the multicationic perovskite $BaZr_yTi_{1-y}O_3$; $y = 0.0$–0.4 solid solution was formed completely during the sonochemical process itself, without the need for further calcination or a heating process.

3.6 Effect of chemical treatment on the crystal structure by using dimethyl formamide (DMF)

Ordinarily, hydroxyl (–OH) groups play an important role in the synthesis of perovskite nanopowders *via* wet-chemical processes, especially in a very high OH concentration (pH > 12).[20,49–53] The powder products can contain much chemical bonding with the two types of OH species. Weakly bonded OH^- species are adsorbed on particle surfaces, while strongly bonded OH^- species are entrapped in the crystal lattice, to form lattice OH^- defects.[20] These defects can affect the stability of lattice vibration and decrease tetragonality to form a metastable cubic phase, which leads to the absence of phase transition.[20] From the literature, the OH^- species on particle surfaces could be eliminated by thermal heat treatment above 300 °C, and above 1100 °C for eliminating the lattice OH^- species.[20,52,53] This work investigated sonochemical $Ba(Zr_yTi_{1-y})O_3$ powder products and found hydroxyl defects similar to those in the $BaTiO_3$ reported in the literature.[20,53] Nevertheless, in this work, lattice hydroxyl defects could be removed completely by solvothermal treatment with DMF solution at only 170 °C. In studying the effect of DMF on the crystal structure, a selected region of XRD patterns in $2\theta = 42°$ to 48° of $Ba(Zr_yTi_{1-y})O_3$ ($y = 0.00$) powder products was compared between before and after treatment, as shown in Fig. 8(a). The results clearly show the difference of tetragonal *versus* cubic crystal structure. Before treatment, the powder products showed a single peak of (200) reflection, which agreed well with the characteristic of a cubic crystal structure. When the powder products were treated with DMF solution at 170 °C for 24 h, splitting of (200) reflected at a higher region, with a (002) shoulder at the lower region, and this corresponded to the characteristics of a tetragonal crystal structure. In accordance with a large amount of lattice OH^-, a high amount of protons (H^+) can link and exist in an oxygen sub-lattice. Therefore, the unit cell volume was enlarged with close correlation, and distortion of the tetragonal crystal structure was observed. Consequently, a cubic crystal structure was presented;[20] then, when the lattice OH^- was removed, the tetragonal structure returned to stabilize it. FT-IR spectroscopy was used to investigate the functional group of $Ba(Zr_yTi_{1-y})O_3$ ($y = 0.00$) powders. The spectrum is shown in Fig. 8(b). O–H stretching vibration of the hydroxyl group and Ti–O_6 stretching vibration of in BO_6 octahedra of $BaTiO_3$ were detected on $Ba(Zr_yTi_{1-y})O_3$ ($y = 0.00$) powders before treatment. Then, the band of O–H stretching disappeared, while TiO_6-stretching was still present after the treatment process. It could be seen that the hydroxyl species were desorbed more effectively after the treatment process. However, it is difficult to distinguish between the surfaced-adsorbed and lattice hydroxyl groups because the peak position of two OH^- species is very similar.[52,53] Furthermore, Raman scattering spectroscopy also was studied for further investigation. The Raman spectra of $Ba(Zr_yTi_{1-y})O_3$ ($y = 0.00$) compared before and after chemical treatment are shown in Fig. 8(c). All Raman-active modes in the powder products after chemical treatment clearly correspond to those in the $4E(TO + LO) + 3A_1(TO + LO) + B_1(TO + LO)$ of a tetragonal (*P*4*mm*) crystal structure.[49] However, there are 3 broadening peaks at around 303, 522 and 715 cm^{-1} in powder products before treatment, which are assigned to the Raman-active modes of tetragonal (*P*4*mm*) symmetry, indicating that the crystal structure of powder products before treatment may exhibit a mixture between tetragonal and cubic crystal structure. However, when the chemical treatment was preceded by DMF, the cubic crystal structure changed completely to be tetragonal. In addition, it is well known that the existence of OH^- defects leads to loss of phase transition in ferroelectric materials.[49,50] Therefore, DSC measurement was used for further investigation of $Ba(Zr_yTi_{1-y})O_3$ ($y = 0.00$) phase transition. The DSC data are shown in Fig. 8(d). The powder products before treatment show only the baseline, without the change of enthalpy (ΔH), while those after treatment clearly show the exothermic transition on cooling at temperatures of about 127.1 °C, which correlates to the phase transition temperature of tetragonal to cubic crystal structure. The relating change in

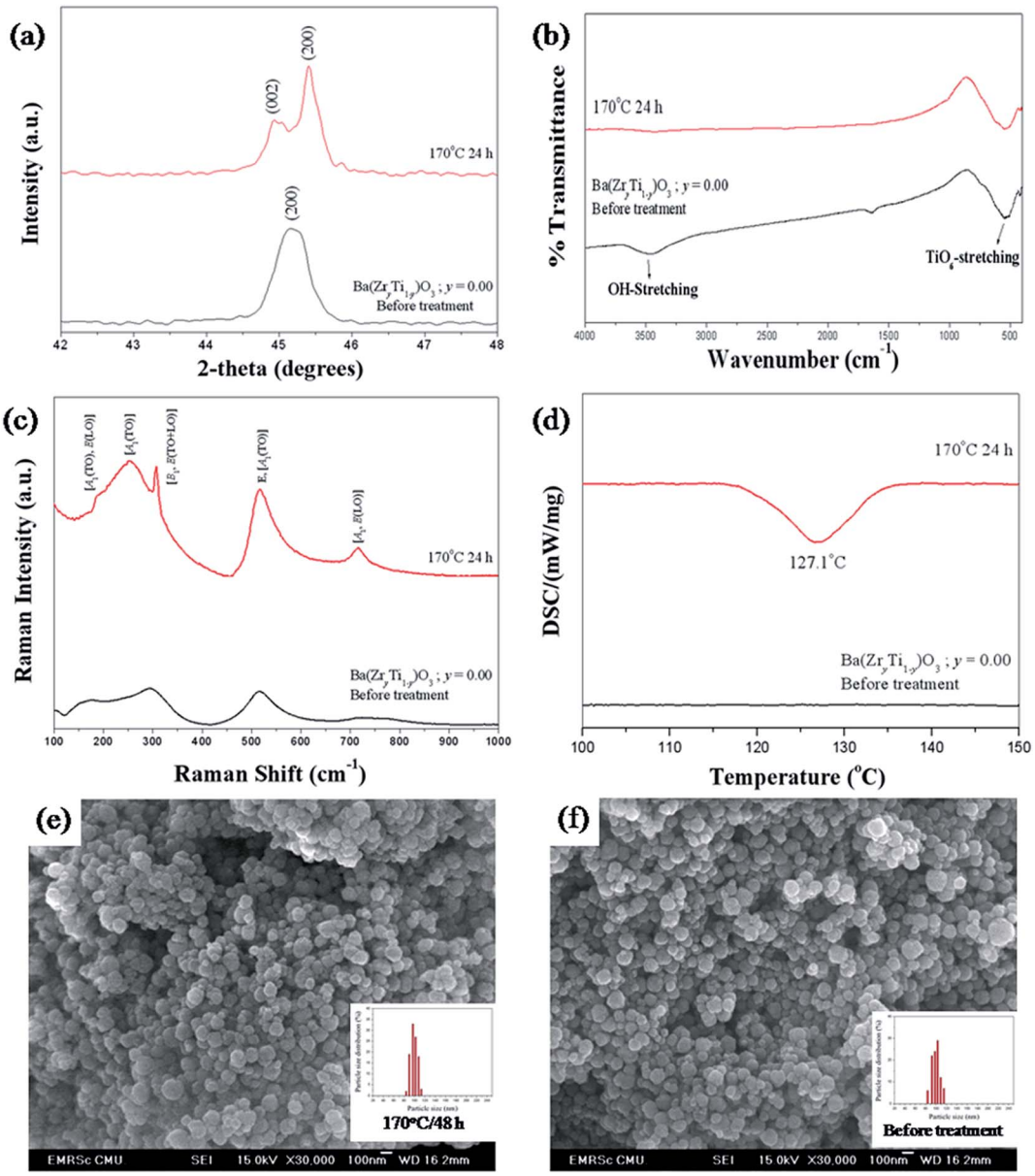

Fig. 8 XRD pattern (a), FT-IR (b), Raman (c), DSC (d) and SEM image of $BaZr_yTi_{1-y}O_3$; $y = 0.0$ untreated powders (e) and chemically treated powders with DMF (f).

enthalpy (ΔH) value of this transformation is 593 mJ g^{-1}, which corresponds to 650 mJ g^{-1} of the commercial $BaTiO_3$ tetragonal structure. On the other hand, the Curie temperature observed from DSC data can be used to confirm the 1 : 1 stoichiometry Ba/Ti ratio in $Ba(Zr_yTi_{1-y})O_3$ ($y = 0.00$) powder products, which is similar to reports from F. Baeten.[51] Finally, all the results from this part of this study indicate that the use of chemical treatment with DMF solution possibly eliminates OH^- defects from the oxygen sub-lattice. The tetragonal crystal structure was improved, and the phase transition observed at 127 °C. In addition, the chemical treatment with DMF had no significant effect on the particle shape, size or size distribution. The particle size changed slightly from 97.4 ± 19.2 nm to 103.5 ± 13.3 nm with a narrow size distribution. The SEM micrographs of powder products before and after chemical treatment are shown in Fig. 8(e) and (f), respectively.

3.7 Mechanism of crystal growth formation

Based on the results achieved with different synthetic parameters, perovskite phase formation of the $BaZrTiO_3$ spheres involved the crystallization process and was similar to mechanical stirring.[54] A plausible mechanism that explains all these data is shown in Fig. 9. The first stage of the synthesis is forming a complex network of the amorphous phase, which is assumed to be flows: *i.e.* barium cations that form $Ba(OH)^+$ species in the NaOH concentration. Furthermore, titanium and zirconium cations were hydrolyzed readily in NaOH solutions to form soluble $[Ti(OH)_6]^{2-}$ and $[Zr(OH)_5]^-$ anions. The formation

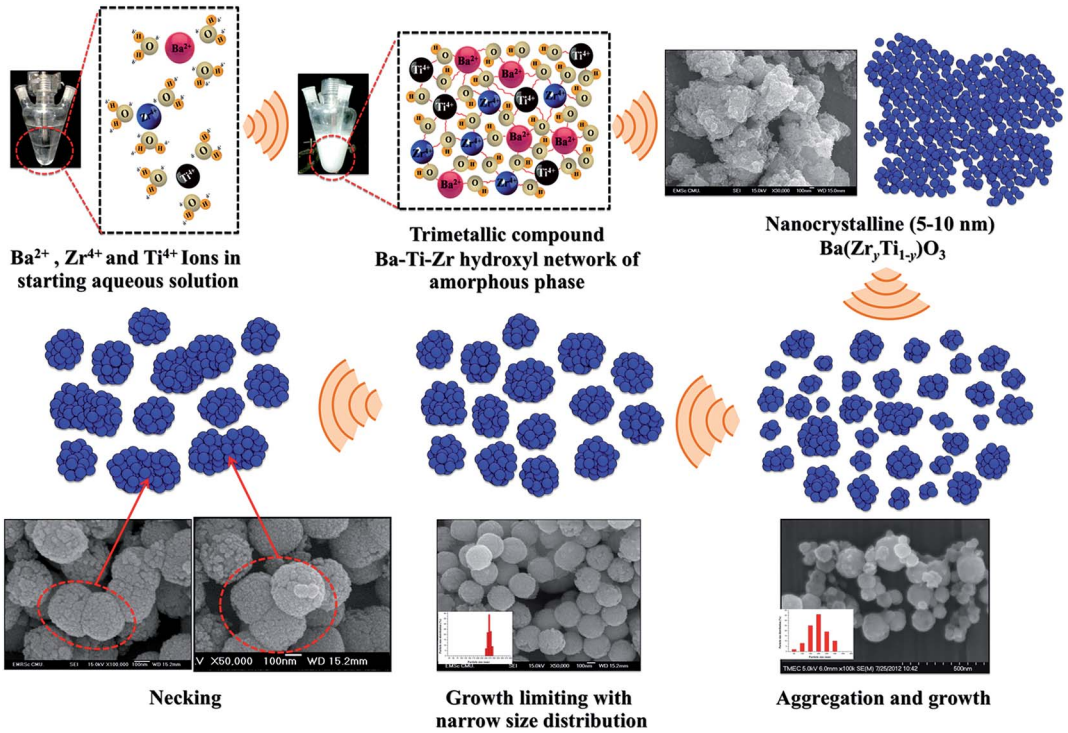

Fig. 9 Schematic diagrams illustrating formation of the crystal growth mechanism.

of hexahydroxy titanate(IV) and pentahydroxy zirconate(IV) $[Zr(OH)_5]^-$ in the presence of strong alkaline condition were described also by N. C Pramanik *et al.*[42] and Boschini *et al.*[55] respectively. The reaction between $Ba(OH)^+$, $[Ti(OH)_6]^{2-}$ and $[Zr(OH)_5]^-$ initiated the formation of gels comprising an entangled complex network of polymeric chains of trimetallic Ba–Ti–Zr hydroxides. The skeleton of the polymer corresponds to the Ba, Ti and Zr atom linked by bridging O atoms. The second stage of the synthesis is accelerating the formation of tiny primary BZT particulates (crystallization) by ultrasonic irradiation. The results presented in a previous section of this study strongly indicate that formation of BZT is dominated by a nucleation and growth mechanism. When the complex network of amorphous phases was irradiated ultrasonically, the formation, growth, and implosive collapse of bubbles (microjet effect) in liquid medium generated extreme synthesis conditions (localized hot spot with high temperature of *ca.* 5000 K, pressure of *ca.* 20 MPa, and a very high cooling rate of *ca.* 10^{10} K S^{-1}). Also, due to vaporization of the solvent into bubbles, solubility of the reactants was enhanced, thus elevating supersaturation of the reactant solutions. In the conventional crystallization process from a solution, two steps are involved; nucleation and crystal growth, of which both have supersaturation as a common driving force. Crystals in the supersaturated solution can neither form nor grow. The nucleation rate in the crystallization process is small and only few nuclei can be generated at the initial time of growth. Then, nuclei grow in spatial orientations fixed by solute crystallized structures. However, nucleation in the sonocrystallization process was accelerated by the implosive collapse of bubbles, while the crystal growth process was inhibited or delayed by shock waves and turbulent flow created by ultrasonic radiation.[22,29] This effect promoted nucleation over grain growth to form tiny primary particulates (crystalline), which tended to aggregate into large particles due to tremendous surface energy; and stability of the particles can be expressed as:[56,57]

$$S = (R_a + R_b)\int_{R_a - R_b}^{\infty} \exp\left[\frac{V(C)}{k_B T}\right] \frac{dC}{C^2} \quad (5)$$

where S is the stability factor of the particles, R_a and R_b are the radius of the two particles, respectively, $V(C)$ is the function of potential energy interaction, C is the distance between the two particles, k_B is Boltzmann's constant (1.3806×10^{-23} J K^{-1}) and T is the temperature (K). When the distance between particles is decreased to a certain extent, short-range reactions (van der Waal's forces and existence of an electrostatic barrier) lead to strong attraction between particles.[56,57] The third stage of synthesis is forming spherical particles with a narrow size distribution. The turbulent flow and mechanical effects, such as microjet impact and shock waves that generate from the implosive collapse of bubbles under ultrasonication,[24,46] can create a relatively uniform reaction in fluid medium,[24,46] which improves the spherical shape of monodispersed BZT particles. Microjets with a high velocity of over 400 km h^{-1} crush the aggregated cluster in all directions,[21,43] and nanocrystalline particles are driven together at extremely high speeds, thus inducing effective melting at the point of impact.[22,45] These phenomena generate relatively monodispersed particles with a narrow size distribution. Furthermore, when increasing the sonication time further, neck formation was observed between

the particles, caused by high velocity of the interparticle collision generated by ultrasonic irradiation.[45] Suslick *et.al.*[45,46] proposed that the effects of cavitation in the phenomenon of interparticle collisions come from the shock waves released into liquid and not from the temperature of the localized hot-spot formed within the collapsing bubble. It is interesting to note that volume shrinkage and densification did not originate, due to the sonochemical method that generated local thermal energy, which differed from thermal energy of the sintering process.

4. Conclusion

Multicationic oxides based on the complex perovskite structure of $Ba(Zr_yTi_{1-y})O_3$; $y = 0.0$–0.4 nanoparticles were synthesized directly under ultrasonic irradiation in the sonochemical synthesis process, without a calcination step. The concentration of NaOH, the precursor and synthesized atmosphere play a key role in forming the perovskite structure. Strong and high concentration of NaOH and the precursor, respectively, not only initiate nucleation, but also eliminate the formation of $BaCO_3$. Nanocrystalline was formed in a short period of time and then aggregated to form large particles. Narrow size distribution was acquired for the aggregated particles under ultrasonic irradiation. However, the synthesized powder had some of the OH group trapped in the crystal lattice, which was caused by strong OH concentration during the synthesis process. A plausible crystal growth mechanism was proposed by this study.

Acknowledgements

This work was supported by the Thailand Research Fund (TRF) under grant no. BRG5680006 and S. Wirunchit would like to thank The Royal Golden Jubilee (RGJ-Ph.D program) Scholarship program for financial support.

References

1 X. G. Tang, K. H. Chew and H. L. W. Chan, *Acta Mater.*, 2004, **52**, 5177–5183.
2 W. Liu and X. Ren, *Phys. Rev. Lett.*, 2009, **103**, 257602.
3 L. Zhang, M. Zhang, L. Wang, C. Zhou, Z. Zhang, Y. Yao, L. Zhang, D. Xue, X. Lou and X. Ren, *Appl. Phys. Lett.*, 2014, **105**, 162908.
4 H. Guo, B. K. Voas, S. Zhang, C. Zhou, X. Ren, S. P. Beckman and X. Tan, *Phys. Rev. B: Condens. Matter Mater. Phys.*, 2014, **90**, 014103.
5 J. Bera and S. K. Rout, *Mater. Lett.*, 2005, **59**, 135–138.
6 A. J. Moulson and J. M. Herbert, *Electroceramics: Materials, Properties, Applications*, Wiley, 2003.
7 M. Sopicka-Lizer, *High-Energy Ball Milling: Mechanochemical Processing of Nanopowders*, Elsevier Science, 2010.
8 X. Hou and J. Yu, *J. Am. Ceram. Soc.*, 2013, **96**, 2218–2224.
9 A. S. Bhalla, R. Guo and R. Roy, *Mater. Res. Innovations*, 2000, **4**, 3.
10 G. H. Haertling, *J. Am. Ceram. Soc.*, 1999, **82**, 797–818.
11 J. S. Reed, *Principles of Ceramics Processing*, Wiley, 1995.
12 P. Julphunthong and T. Bongkarn, *Curr. Appl. Phys.*, 2011, **11**, S60–S65.
13 N. Binhayeeniyi, P. Sukvisut, C. Thanachayanont and S. Muensit, *Mater. Lett.*, 2010, **64**, 305–308.
14 M. Veith, S. Mathur, N. Lecerf, V. Huch, T. Decker, H. P. Beck, W. Eiser and R. Haberkorn, *J. Sol-Gel Sci. Technol.*, 2000, **17**, 145–158.
15 J. Q. Qi, Y. Wang, W. P. Chen, L. T. Li and H. L. W. Chan, *J. Nanopart. Res.*, 2006, **8**, 959–963.
16 S. B. Reddy, K. P. Rao and M. S. R. Rao, *Scr. Mater.*, 2007, **57**, 591–594.
17 Z. L. Wang and J. Song, *Science*, 2006, **312**, 242–246.
18 X. Wang, J. Song, J. Liu and L. W. Zhong, *Science*, 2007, **316**, 102–105.
19 D. Segal, *Chemical Synthesis of Advanced Ceramic Materials*, Cambridge University Press, 1991.
20 P. K. Dutta, R. Asiaie, S. A. Akbar and W. Zhu, *Chem. Mater.*, 1994, **6**, 1542–1548.
21 K. J. Leonard, S. Sathyamurthy and M. P. Paranthaman, *Chem. Mater.*, 2005, **17**, 4010–4017.
22 J. H. Bang and K. S. Suslick, *Adv. Mater.*, 2010, **22**, 1039–1059.
23 J. Janbua, J. Mayamae, S. Wirunchit, R. Baitahe and N. Vittayakorn, *RSC Adv.*, 2015, **5**, 19893–19899.
24 K. S. Suslick, *Science*, 1990, **247**, 1439–1445.
25 B. Zhou, B. Liu, L.-P. Jiang and J.-J. Zhu, *Ultrason. Sonochem.*, 2007, **14**, 229–234.
26 I. Haas, S. Shanmugam and A. Gedanken, *J. Phys. Chem. B*, 2006, **110**, 16947–16952.
27 C. Wu, B. P. Mosher and T. Zeng, *Chem. Mater.*, 2006, **18**, 2925–2928.
28 L.-P. Jiang, S. Xu, J.-M. Zhu, J.-R. Zhang, J.-J. Zhu and H.-Y. Chen, *Inorg. Chem.*, 2004, **43**, 5877–5883.
29 H. Xu, B. W. Zeiger and K. S. Suslick, *Chem. Soc. Rev.*, 2013, **42**, 2555–2567.
30 D. Ghanbari, M. Salavati-Niasari and M. Ghasemi-Kooch, *J. Ind. Eng. Chem.*, 2014, **20**, 3970–3974.
31 F. Dang, K. Kato, H. Imai, S. Wada, H. Haneda and M. Kuwabara, *Ultrason. Sonochem.*, 2010, **17**, 310–314.
32 S. Vuttivong, S. Niemcharoen, P. Seeharaj, W. C. Vittayakorn and N. Vittayakorn, *Ferroelectrics*, 2013, **457**, 44–52.
33 M. Xu, Y. N. Lu, Y. F. Liu, S. Z. Shi, T. S. Qian and D. Y. Lu, *Powder Technol.*, 2006, **161**, 185–189.
34 K. Yasui, T. Tuziuti and K. Kato, *Ultrason. Sonochem.*, 2011, **18**, 1211–1217.
35 P. Charoonsuk, R. Baitahe, W. Vittayakorn, N. Atiwongsangthong, R. Muanghua, P. Seeharaj and N. Vittayakorn, *Ferroelectrics*, 2013, **453**, 54–61.
36 T. Hyeon, M. Fang and K. S. Suslick, *J. Am. Chem. Soc.*, 1996, **118**, 5492–5493.
37 J. Geng, L. Jiang and J. Zhu, *Sci. China: Chem.*, 2012, **55**, 2292–2310.
38 S. Singh, N. Kumar, R. Bhargava, M. Sahni, K. D. Sung and J. H. Jung, *J. Alloys Compd.*, 2014, **587**, 437–441.
39 Y. Han, D. Radziuk, D. Shchukin and H. Moehwald, *J. Mater. Chem.*, 2008, **18**, 5162–5166.

40 Y. Waseda, E. Matsubara and K. Shinoda, *X-Ray Diffraction Crystallography: Introduction, Examples and Solved Problems*, Springer, 2011.
41 C. Suryanarayana and G. Norton, *X-Ray Diffraction: A Practical Approach*, Springer, 1998.
42 N. C. Pramanik, S. I. Seok and B. Y. Ahn, *J. Colloid Interface Sci.*, 2006, **300**, 569–576.
43 M. M. Lencka and R. E. Riman, *Ferroelectrics*, 1994, **151**, 159–164.
44 Pankaj, in *Theoretical and Experimental Sonochemistry Involving Inorganic Systems*, ed. M. Ashokkumar, Springer, Netherlands, 2011, pp. 213–271.
45 T. Prozorov, R. Prozorov and K. S. Suslick, *J. Am. Chem. Soc.*, 2004, **126**, 13890–13891.
46 W. B. McNamara, Y. T. Didenko and K. S. Suslick, *Nature*, 1999, **401**, 772–775.
47 H. Wang, Y.-N. Lu, J.-J. Zhu and H.-Y. Chen, *Inorg. Chem.*, 2003, **42**, 6404–6411.
48 R. D. Shannon, *Acta Crystallogr., Sect. A: Cryst. Phys., Diffr., Theor. Gen. Crystallogr.*, 1976, **32**, 751.
49 T. Noma, S. Wada, M. Yano and T. Suzuki, *J. Appl. Phys.*, 1996, **80**, 5223–5233.
50 S. Wada, T. Tsurumi, H. Chikamori, T. Noma and T. Suzuki, *J. Cryst. Growth*, 2001, **229**, 433–439.
51 F. Baeten, B. Derks, W. Coppens and E. Van Kleef, *J. Eur. Ceram. Soc.*, 2006, **26**, 589–592.
52 M. H. Frey and D. A. Payne, *Phys. Rev. B: Condens. Matter Mater. Phys.*, 1996, **54**, 3158–3168.
53 R. Kota and B. Lee, *J. Mater. Sci.: Mater. Electron.*, 2007, **18**, 1221–1227.
54 A. Testino, M. T. Buscaglia, V. Buscaglia, M. Viviani, C. Bottino and P. Nanni, *Chem. Mater.*, 2004, **16**, 1536–1543.
55 F. Boschini, A. Rulmont, R. Cloots and B. Vertruyen, *J. Eur. Ceram. Soc.*, 2009, **29**, 1457–1462.
56 K. S. Birdi, *Handbook of Surface and Colloid Chemistry*, CRC Press, 3rd edn, 2008.
57 W. B. Russel, D. A. Saville and W. R. Schowalter, *Colloidal Dispersions*, Cambridge University Press, 1992.

Materials and Design 86 (2015) 564–574

Contents lists available at ScienceDirect

Materials and Design

journal homepage: www.elsevier.com/locate/jmad

High piezoelectric response in the new coexistent phase boundary of $0.87BaTiO_3$–$(0.13\text{-}x)BaZrO_3$–$xCaTiO_3$

Manoon Sutapun [a], Wanwilai Vittayakorn [a], Rangson Muanghlua [b], Naratip Vittayakorn [a,c,*]

[a] College of Nanotechnology, King Mongkut's Institute of Technology Ladkrabang, Bangkok 10520, Thailand
[b] Department of Electronics, Faculty of Engineering, King Mongkut's Institute of Technology Ladkrabang, Bangkok 10520, Thailand
[c] Advanced Materials Research Unit, Department of Chemistry, Faculty of Science, King Mongkut's Institute of Technology Ladkrabang, Bangkok 10520, Thailand

ARTICLE INFO

Article history:
Received 1 July 2015
Received in revised form 27 July 2015
Accepted 30 July 2015
Available online 31 July 2015

Keywords:
Lead-free piezoelectric
Phase transition
$BaTiO_3$
$BaZrO_3$
$CaTiO_3$

ABSTRACT

An investigation of the coexistent ferroelectric phase was carried out on the ternary system of $0.87BaTiO_3$–$(0.13\text{-}x)BaZrO_3$–$xCaTiO_3$ [abbreviated as BT–BZ–xCT (where $0.00 \le x \le 0.13$)]. Temperature-, frequency-dependent dielectric data, electric field-dependent strain and polarization as a function of composition are presented in order to understand the relationships of structure-properties and find the high piezoelectric response in this system. Results showed that ceramics in the composition range of $0.00 \le x < 0.04$ were of a rhombohedral structure and transformed into a tetragonal structure at $x > 0.06$. The multiphase coexistence of the rhombohedral and tetragonal phase in this system was identified at $x = 0.06$. A large, virtually hysteresis-free electric field induced strain of 0.23% was achieved with the composition, $x = 0.06$, at 40 kV/cm on the boundary between rhombohedral and tetragonal phase. This relates to an extraordinarily high and normalized piezoelectric coefficient (S_{max}/E_{max}) of 1280 pm/V, which was reached at a low electric field applied at 10 kV/mm. These results indicated that a high piezoelectric response may stem primarily from the rhombohedral-tetragonal phase boundary, due to greater lattice softening and reduced energy barriers for polarized rotation.

1. Introduction

Lead-based piezoelectric ceramics, e.g. lead zirconate titanate ($PbZr_xTi_{1-x}O_3$)-based or Pb-based relaxor ferroelectic are used widely for various electronic applications, such as buzzers, actuators, transducers, sensors, transformers and piezoelectric energy harvesting, as these materials exhibit excellent piezoelectric and ferroelectric properties at the morphotropic phase boundary (MPB) [1]. Nevertheless, lead-based piezoelectric ceramics contain more than 65 wt.% of highly toxic lead oxide, which is a serious threat to the environment, due to its volatility at high temperature (above 880 °C) during the fabrication process (calcination and sintering at high temperature) [2–4]. Thus, development of lead-free piezoelectric materials, with comparable electrical properties to lead-based piezoelectric materials, is an urgent task for researchers [2,5]. A series of typical lead-free systems based on a perovskite structure such as $(K_{1/2}Na_{1/2})NbO_3$ (KNN), $BaTiO_3$ (BT), and $(Bi_{1/2}Na_{1/2})TiO_3$ (BNT) have been investigated extensively in pure and modified form, in order to replace materials containing lead [2,6–8]. Much attention regarding lead-free piezoelectric materials has focused recently on $BaTiO_3$ (BT)-based ceramics because they exhibit excellent piezoelectric properties [9–12]. Recent work by Liu and Ren [10] reported excellent piezoelectric properties (d_{33} ~ 500–600 pC/N) in $Ba(Zr_{0.2}Ti_{0.8})O_3$–$(Ba_{0.7}Ca_{0.3})TiO_3$ ceramics, which are close to critical triple points of ferroelectric tetragonal, rhombohedral and paraelectric cubic phases. It is known that enhanced piezoelectric properties, accompanied by the occurrence of a morphotropic phase boundary (MPB) or polymorphic phase transition (PPT), are associated with the coexistence of multiple ferroelectric phases [2,5,10,13]. This phenomenon can cause polarized rotation of the ferroelectric domain easily by electric field or external stress, leading to enhancement of dielectric, piezoelectric and ferroelectric properties. Recently, Li et al. [14] observed excellent piezoelectric properties in the $(Ba_{(1-x)}Ca_x)(Ti_{0.95}Zr_{0.05})O_3$ system. A polymorphic phase transition that coexisted with the orthorhombic–tetragonal phase was observed in a composition of around $x = 0.07$ and $d_{33} =$ 387 pC/N and $k_p = 44.2\%$. These ceramic processes have orthorhombic symmetry in the composition, $x \le 0.06$, which transforms into tetragonal symmetry in the composition, $x \ge 0.12$. Zhang et al. [15] published results of the $(Ba_{0.95}Ca_{0.05})(Ti_{(1-x)}Zr_x)O_3$ system, and reported a polymorphic phase transition, with coexisting rhombohedral–tetragonal phase, in a composition of around $0.5 \le x \le 0.7$. Based on results from the literature [14–19], the ferroelectric phase diagram of the $BaTiO_3$–$BaZrO_3$–$CaTiO_3$ ternary system was established, as shown in Fig. 1. Many compositions in the "white region" of the ferroelectric phase diagram are expected to have a multiphase coexistence, and these compositions have not been investigated according to the authors' knowledge. Furthermore, it is interesting to note that the multiphase coexistence

* Corresponding author at: Department of Chemistry, Faculty of Science, King Mongkut's Institute of Technology Ladkrabang, Bangkok 10520, Thailand.
E-mail address: naratipcmu@yahoo.com (N. Vittayakorn).

http://dx.doi.org/10.1016/j.matdes.2015.07.172
0264-1275/

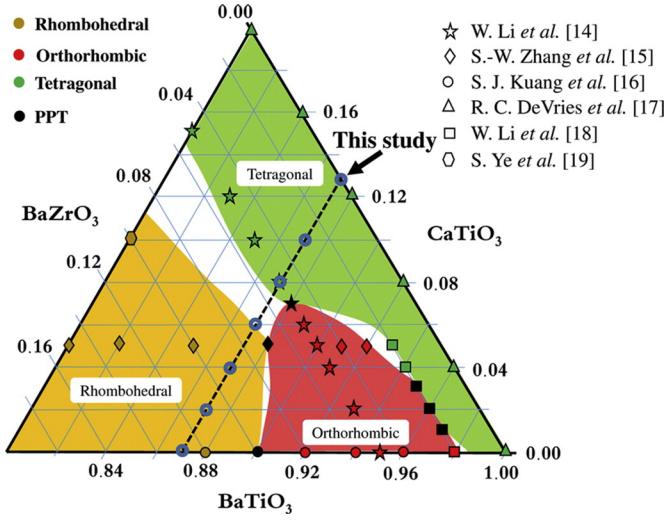

Fig. 1. Composition phase diagram and composition studied in the BT–BZ–CT ternary system.

boundary line needs to be complete in order to achieve high performance lead-free piezoelectric ceramics in the $BaTiO_3$–$BaZrO_3$–$CaTiO_3$ ternary system. In order to complete the multiphase coexistence boundary line in $BaTiO_3$–$BaZrO_3$–$CaTiO_3$ ternary systems, this study examined the composition groups, as indicated by a "circular dot", by increasing the CT content and systemically investigating its effects on the crystal structure and phase transition of ferroelectric and piezoelectric properties. Meanwhile, the origin of large piezoelectrics near the PPT also was discussed. The research results will be of benefit for the design of a polymorphic phase boundary (PPB) line, with high performance in $BaTiO_3$–$BaZrO_3$–$CaTiO_3$ ternary systems.

2. Experimental procedure

The ternary system of $0.87BaTiO_3$–$(0.13\text{-}x)BaZrO_3$–$xCaTiO_3$ [abbreviated as BT–BZ–(xCT)], with $0.00 \le x \le 0.13$, was prepared by the conventional mixed oxide method and normal sintering. Analytical-grade $BaCO_3$ (99.0%, Fluka), TiO_2 (99.0%, Riedel-de Haen), ZrO_2 (99.9%, Inframat Advanced Materials: USA) and $CaCO_3$ (99.5%, Riedel-de Haen) were used as raw materials. All powders were dried in an oven at 120 °C for 24 h in order to remove residual moisture before use. All of the raw materials were weighed according to the chemical formula and vibro-ball milled for 4 h, using yttrium-stabilized zirconia balls as grinding media. After drying, the mixed powders were calcined at 1300 °C for 4 h in an alumina crucible, and then sieved and uniaxially pressed into pellets of 11 mm in diameter at 150 MPa, using 3 wt.% polyvinyl alcohol (PVA) as a binder. The samples were sintered at 1350–1450 °C for 4 h in air, with a heating/cooling rate of 5 °C/min. The density of the sintered samples was determined using a water immersion technique based on Archimedes' principle [20]. Ceramics with more than 94% theoretical density were selected for investigating electrical properties. The phase analysis of the samples was carried out with an X-ray diffractometer (XRD; Bruker — AXS D8 Advance) using C_uK_α radiation with $\lambda = 1.5418$ Å. Room temperature XRD data were collected in the 2θ scan range of 20–80° with a step size of 0.02°. Raman spectra were measured in the 100–1000 cm^{-1} wave number range with a Thermo Scientific DXR Raman microscope, using the 532 nm exciting line of a He–Ne laser, in order to support the crystal structure identification of ceramics. The samples were polished to obtain smooth and parallel surfaces prior to making electrical measurements. After polishing, the samples were painted with a silver paste (Heraeus, C1000) on both sides to form an electrode before they were fired at 750 °C for 30 min, with a heating/cooling rate of 5 °C/min. The dielectric property measurement allowed determination of the phase transition temperature, permittivity value and dielectric loss. Dielectric properties of the ceramics, as a function of temperature, were performed using an LCR analyzer (HP4284A, Hewlett-Packard, Palo Alto, CA), and the temperature varied between 25–160 °C, with a heating/cooling rate of 2 °C/min. The ferroelectric properties of the ceramics were characterized using the standard ferroelectric tester system (RT66B; Radient Technologies, Inc., Albuquerque, NM), which performs measurement of polarization as a function of electric field (P–E loop) at room temperature. The electrical strains were obtained at room temperature by using an optical displacement sensor (MTI-2100) combined with the radiant ferroelectric test system. The normalized piezoelectric coefficient, d_{33}^*, which relates to the piezoelectric constant of inverse piezoelectric effects, was determined by evaluating the ratio of maximum strain (S_{max}) to maximum electric field (E_{max}), S_{max}/E_{max}, from unipolar strain measurements. For piezoelectric measurement, samples were poled first at room temperature by stirring in silicone oil at 35–40 kV/cm for 30 min, using a DC power supply. The piezoelectric constant (d_{33}) was measured using a quasistatic d_{33} meter (YE2730A, APC International Ltd.).

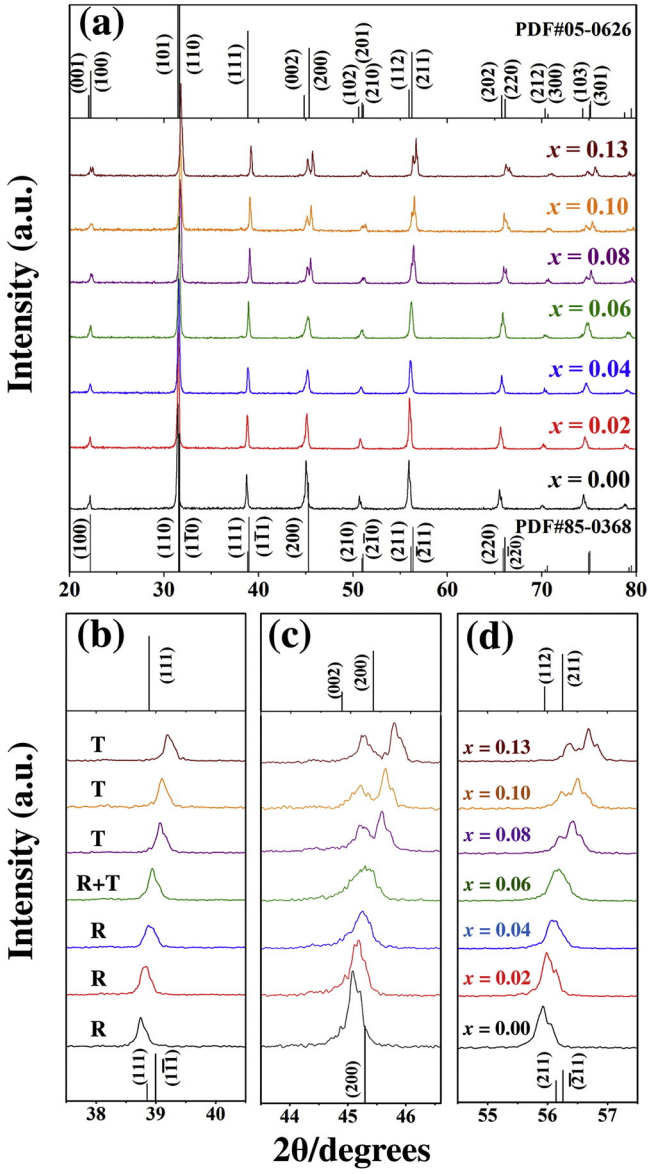

Fig. 2. (a) XRD patterns of sintered BT–BZ–xCT ceramics at room temperature with $x = 0.0$–0.13, (b) position of the (111) peaks at 2θ ~ 38.5, (c) position of the (200) peaks at 2θ ~ 45, and (d) position of the (211) peaks at 2θ ~ 56.

3. Results and discussion

The XRD patterns of BT–BZ–*x*CT; $x = 0.00$–0.13 ceramics at room temperature are shown in Fig. 2(a). All of the specimens have a pure perovskite structure without a secondary phase formation. The result indicates that the solid solution between BT, BZ and CT was developed well in order to complete solid solution in all the compositions studied, with Ca^{2+} entering the Ba^{2+} site of the A-site; and Zr^{4+} entering the Ti^{4+} site of the B-site in the ABO_3-type perovskite structure. Furthermore, most diffraction peak positions of these ceramics shifted to a higher angle with increased CT content, which correlated to a decrease in cell parameters. In order to determine the dependence of phase structure on the composition, enlarged XRD patterns for all compositions in the 2θ of 37.5°–40.5°, 43.5°–46.5° and 54.5°–57.5° are presented in Fig. 2(b), (c) and (d), respectively. Regarding the composition, $0.00 \le x < 0.04$, there was no evidence of splitting of (200) and (211) peaks at around the 2θ of 45.2° and 56°. Although splitting of the (111) peak was not observed clearly, it could be seen to broaden in the composition, $x = 0.04$ [Fig. 2(b)]. This observation corresponds to the rhombohedral symmetry characteristic, and agrees well with previous literature [21] and the established ferroelectric phase diagram in Fig. 1. With increasing CT content ($x > 0.04$), separation in the (200) peak begins to appear and it eventually splits into (002) and (200) peaks at the composition, $x = 0.08$. The same behavior was evident in the (211) peak as well [Fig. 2(c)]. The peak intensity of (200) is higher than that of (002), which represents the characteristic of the tetragonal phase. The results indicate that the phase structure transformed into a tetragonal one. Interestingly, a broadening (111) peak was observed clearly in the composition, $x = 0.06$, which indicates that the sample also consists of a rhombohedral phase. Splitting of the (200) peaks are presented clearly with increasing *x*. A wide range of splitting was observed clearly with increasing compositions of *x*, indicating increasing tetragonality of the structure. By using the XRD data, the lattice parameter, unit cell volume and tetragonality (c/a) are calculated and plotted in Fig. 3. The lattice parameters and unit cell volume actually decrease linearly, with increasing *x*. The tetragonality increased significantly with increasing composition of *x*, which indicates that stabilization of the ferroelectric phase occurred when CT was incorporated in BT–BZ. Decrease in the cell parameter and unit cell volume is attributed to substitution of the Ba^{2+} ions (1.61 Å; coordination number = 12) and Zr^{4+} ions (0.72 Å coordination number = 6) by the smaller cation ions; Ca^{2+} (r = 1.34 Å; coordination number = 12) and Ti^{4+} (r = 0.605 Å: coordination number = 6) in the A- and B-site of the ABO_3 perovskite structure, respectively. In relation to Bragg's equation ($2d\sin\theta = n\lambda$), the decrease of lattice parameters moves the peak toward high diffraction angles.

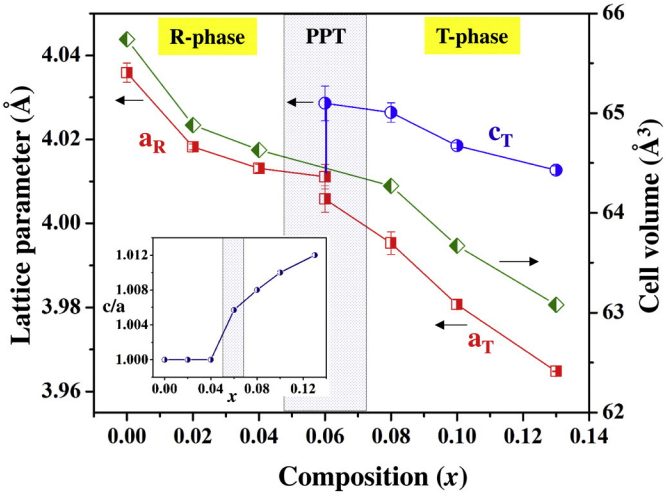

Fig. 3. Relationship between the Lattice parameter (Å), cell volume (Å^3) and composition *x* in the BT–BZ–*x*CT ternary system.

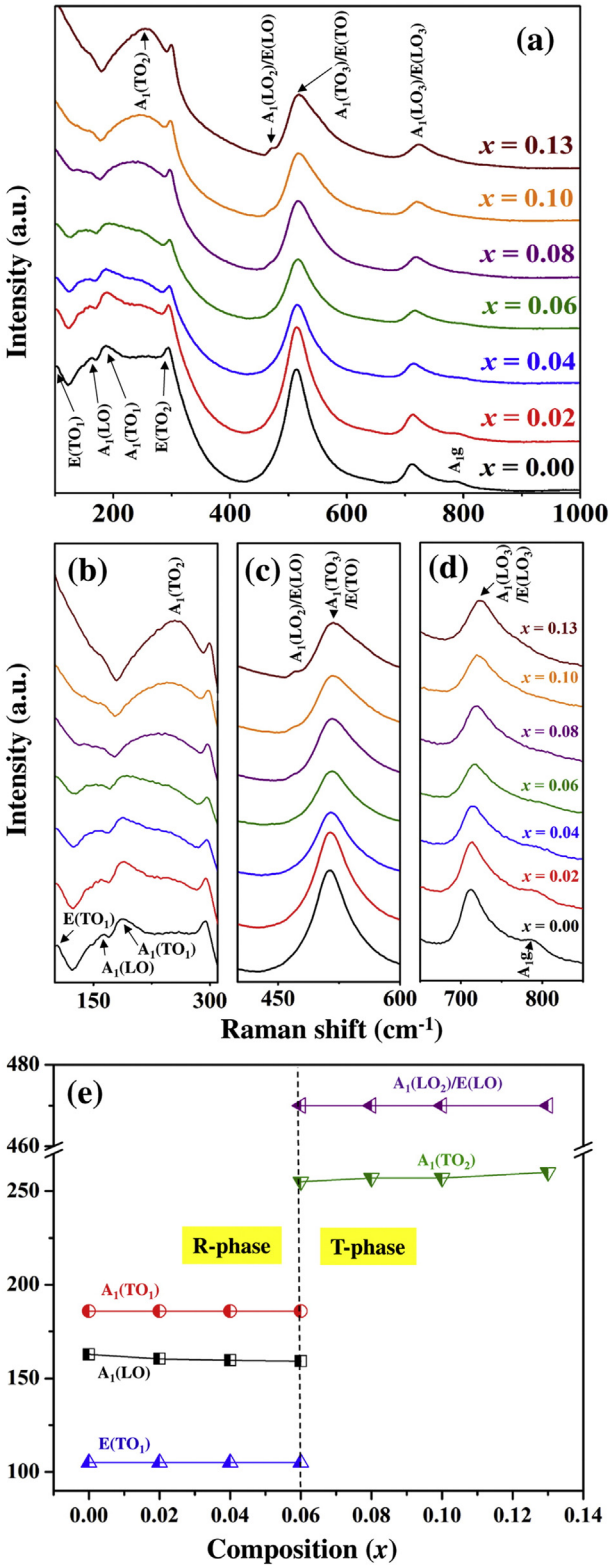

Fig. 4. (a) Raman spectra of sintered BT–BZ–*x*CT ceramics at room temperature with $x = 0.0$–0.13, (b) magnified Raman spectra in the wave number range from 100 to 300 cm^{-1}, (c) those in the wave number range from 400 to 600 cm^{-1}, (d) those in the wave number range from 650 to 850 cm^{-1}, and (e) Position of the Raman active modes observed, with the dot line indicating the ferroelectric phase transition between rhombohedral and tetragonal phases.

Since Raman spectroscopy is a well-known versatile technique used to investigate the vibration modes and sensitivity of local structure in inorganic materials, the Raman scattering technique was used together with X-ray diffraction to confirm the crystal structure of BT–BZ–*x*CT ceramics. Raman spectra were measured in a range of between 100 and 1000 cm^{-1} at room temperature for reconfirming the phase structure of BT–BZ–*x*CT ceramics, as shown in Figs. 4 (a–e). Based on group theory analysis, the perovskite structure for an ideal cubic paraelectric phase of ABO_3 does not permit any Raman-active modes in its vibrational spectra. In the tetragonal ferroelectric phase, each F_{1u} mode transforms into A_1 and E mode, whereas the F_{2u} mode gives rise to B_1 and D mode. The Raman spectrum in Fig. 4(a) shows all Raman-active modes of the ferroelectric phase; a broad band centered at 257 cm^{-1} corresponding to the $A_1(TO_2)$ phonon mode, a sharp peak near 295 cm^{-1} corresponding to the $E(TO_2)$ phonon mode, a broad band at 515 cm^{-1} attributed to E(TO) and $A_1(TO_3)$ modes, a broad band centered at 712 cm^{-1} corresponding to the mixed $A_1(LO_3)$ and $E(LO_3)$ phonon mode, and an interference dip at 172 cm^{-1}. The vibration modes in the Raman spectrum are found mainly at 515 cm^{-1} in internal modes, with B–O symmetric bending and stretching vibration in molecular ionic $[BO_6]^{2-}$. Furthermore, the characteristic signatures in the Raman active mode of the rhombohedral phase were presented evidently in the composition, $x \le 0.06$. Presence of the rhombohedral phase is indicated by coexistence of the triple Raman active peaks at 104, 163 and 186 cm^{-1} and sharpening of the Raman active mode at 515 cm^{-1} [Fig. 4(b) and (c)]. Two sharp interference dips are evident at 123 and 172 cm^{-1} in the composition, $x \le 0.06$, and they are caused by the antiresonance effect between narrow $A_1(TO_1)$ and broad $A_2(TO_2)$ modes and narrow $A_1(TO_1)$ and broad $A_1(TO_2)$ modes. It is important to note that the Raman spectra of the composition, $x \le 0.06$, revealed a well-defined octahedral breathing mode (A_{1g}) peak at 793 cm^{-1} [Fig. 4(d)], whereas this mode was absent from single cation spectra occupying the

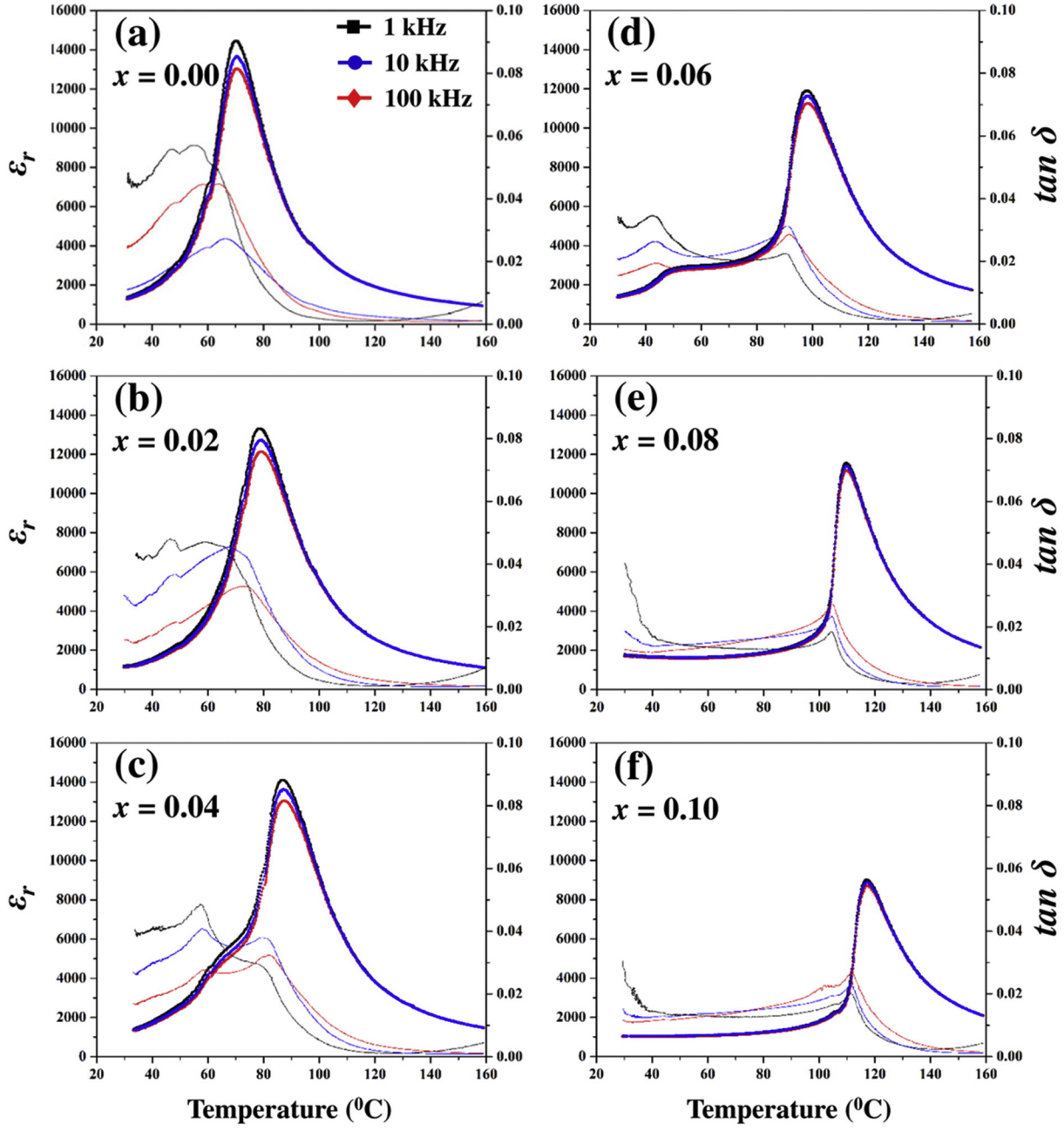

Fig. 5. Temperature dependence of the dielectric constant and dielectric loss measured between 25 and 140 °C for BT–BZ–*x*CT ceramics; (a) $x = 0.0$, (b) $x = 0.02$, (c) $x = 0.04$, (d) $x = 0.06$, (e) $x = 0.08$, and (f) $x = 0.13$.

octahedral BO_6 of the perovskite structure. Generally, the A_{1g} octahedral breathing mode in pure BT is symmetrical and, therefore, Raman becomes inactive. However, with two or more different cation species occupying the B-site (Zr and Ti), the A_{1g} becomes Raman active, since the presence of different ions in the center of the octahedra makes asymmetry in the breathing mode. Besides, this mode is sensitive only to modification of B-site occupancy and does not result in substitution on the A-site [22,23]. The Raman active mode connects to vibrations of the polar BO_6 octahedra, which changes significantly with increasing CT content, especially in a low-frequency region (100–300 cm^{-1}). The Raman active mode characteristic of the rhombohedral phase transforms smoothly into a tetragonal phase. The sharpness of the dip weakens reasonably at 123 cm^{-1}. Weakening interference of the dip at 123 cm^{-1} is an indication of reduced coupling between A(TO) modes. The coexistence phase of rhombohedral and tetragonal ferroelectric phases was detected in the compositions, $x = 0.06$ and 0.08. This transition point is consistent with XRD measurements. The intensity of triple Raman active peaks disappears progressively with increasing CT content at 104, 163 and 186 cm^{-1}, together with disappearing interference dipping at 123 cm^{-1}, when a broadening peak of $A_1(TO_3)$ is clearly in evidence at 515 cm^{-1} [Fig. 4(b) and (c)]. This suggests that the rhombohedral symmetry is lost gradually. The characteristic signature of the tetragonal phase is clearly in evidence in the compositions, $x = 0.08$, 0.10 and 0.13; when the interference dips at 172 cm^{-1}, the Raman-active mode becomes sharp at 295 cm^{-1}, a broad $A_1(TO_2)$ peak appears at 257 and swelling $A_1(LO_2)$/E(LO) weakens at 470 cm^{-1}. The appearance of interference dips at 123 cm^{-1}, which results from the presence of

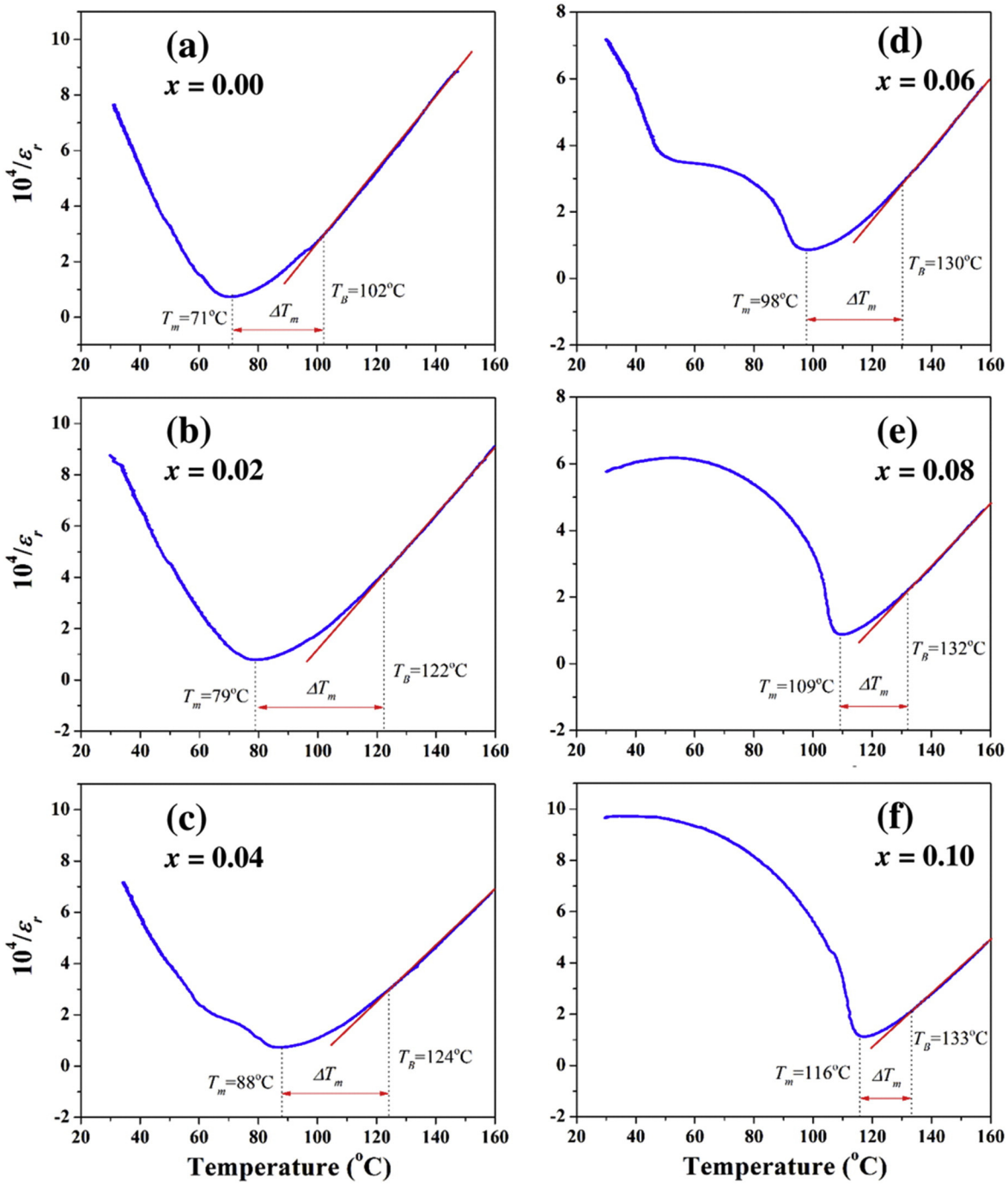

Fig. 6. Temperature dependence of the inverse dielectric constant, $1/\varepsilon_r$ at 10 kHz, for BT–BZ–*x*CT ceramics; (a) $x = 0.0$, (b) $x = 0.02$, (c) $x = 0.04$, (d) $x = 0.06$, (e) $x = 0.08$, and (f) $x = 0.13$.

nanosized ordered Zr-rich clusters [24]. The A_{1g} octahedral breathing mode peaks at 793 cm^{-1}, resulting from the presence of two different cation species that occupy the B-site (Ti^{4+} and Zr^{4+}ion), decrease slightly with increasing CT content and disappear when the composition reaches $x = 0.10$. Zhang et al. [25] reported that when substituting the $BaTiO_3$ structure with the Ca^{2+} ion, the latter can substitute both the Ba- and Ti-site with solubility limits of 25 and 4 mol%, respectively. When an inactive A_{1g} octahedral breathing mode peaks at 793 cm^{-1}, it clearly confirms that Ca^{2+} ions reside in the A-site, and octahedral BO_6 occupy only Ti^{4+} ions. Furthermore, by increasing the CT content, the Raman-active band shifts to a higher frequency at 515 and 712 cm^{-1}, which involves an increase of force constant resulting from the presence of higher amounts of Ca^{2+} and Ti^{4+} occupying the Ba-sites and Zr-sites, respectively [26]. The structure observed by Raman spectra agrees well with the powder in Raman spectra reported by Maiti et al. [27] and Farhi et al. [24] and corresponds well with the XRD data.

Fig. 5 displays the dependence of relative permittivity (ε_r) and dielectric loss, ($tan\ \delta$), on the temperature of BT–BZ–*x*CT; $x = 0.00$–0.13 ceramics at 1, 10 and 100 kHz. The permittivity and dielectric loss exhibit different anomalies depending on the composition of *x*. Regarding the composition, $x < 0.04$, relative permittivity exhibits only one broad dielectric maximum, which corresponds to the phase transitions of rhombohedral ferroelectric phase to cubic paraelectric phase. The peak of dielectric constant is in accordance with dielectric loss data, with only one peak anomaly observed clearly. It is interesting to note that relative permittivity shows a frequency-dependent response near the transition temperature attributed to the characteristic of diffuse phase transition behavior, which is represented by frequency dependence of the permittivity versus temperature curve in the ferroelectric phase. Also, a greater shift in transition temperature has been found in many lead-based [28] and lead-free piezoelectric ceramics, such as $(BiNa)TiO_3$-based ceramic [2,29]. Regarding the composition, $0.04 \le x \le 0.06$, two polymorphic phase transitions, together with lost tangent peaks, are in evidence, which corresponds to the phase transitions of rhombohedral–tetragonal (T_{RT}) and tetragonal–cubic (T_m) phases. The polymorphic phase transition temperatures of T_{RT} are about 64 °C and 40 °C, which corresponds to BT–BZ–*x*CT ceramics at $x = 0.04$ and 0.06, respectively. The T_{RT} transition displays a declining trend with increasing *x* and disappears when the concentration, *x*, reaches 0.08. The tetragonal phase can be stabilized at room temperature when *x* is > 0.08. Frequency dispersion of relative permittivity and variation of T_m at a frequency near maximum permittivity were not observed with increased composition of $x \ge 0.08$. This indicated a normal ferroelectric phase transition at T_m, which increased linearly at the increasing rate of 4.80 °C/mol% and increasing composition of *x*. The increasing trend of T_m and tetragonality (c/a) could be attributed to a strong bonding force interaction and off-centering of the BO_6 octahedral unit, which is believed to arise from partial substitution of Ca^{2+} for Ba^{2+} and Ti^{4+} for Zr^{4+} in the BCZT lattice. Generally, cations with a smaller ionic radius tend to produce stronger covalent bonds with the oxygen ligands. Replacement of the Zr^{4+} ion (0.72 Å), with a comparatively undersized and strong ferroelectric active Ti^{4+} ion, forms polar clusters of $BaTiO_3$ that lead to off-centering of the Ti^{4+} (r = 0.605 Å) cations within the octahedral cage, via hybridization between Ti *3d* and O *2p* orbitals. This forms a strong long-range Coulomb field and its effect leads directly to increasing transition temperature. It is interesting to note that the enhancement of tetragonality does not occur because of larger off centering of the B-site in the perovskite unit, but due instead to the effect of decreased oxygen octahedral volume that also raises tetragonality effectively.

It is known that the relative permittivity of normal ferroelectrics with first order phase transition above T_c can follow the Curie–Weiss law [30]:

$$\frac{1}{\varepsilon_r} = \frac{T - T_o}{C},\ (T > T_c) \tag{1}$$

Table 1
The temperature of maximum dielectric permittivity (T_m), maximum dielectric permittivity (ε_m), temperature above which the dielectric constant follows the Curie–Weiss law (T_{cw}), deviation (ΔT_m), Curie–Weiss temperature (T_0), Curie–Weiss constant (C), and diffuseness (γ) of BT–BZ–*x*CT ceramics.

Compositions (x)	T_m (°C)	ε_m	T_{cw} (°C)	ΔT_m (°C)	T_0 (°C)	C ($\times 10^5$°C)	Γ
0.00	71	13,680	102	31	80	0.77	1.67
0.02	79	12,750	122	43	91	0.76	1.70
0.04	88	13,600	124	36	97	0.92	1.68
0.06	98	11,620	130	32	104	0.93	1.63
0.08	109	11,400	132	23	108	1.08	1.48
0.10	116	8880	133	17	113	0.96	1.46
0.13	121	7010	135	14	114	0.85	1.31

where ε_r is the relative permittivity, T is the Cure–Weiss temperature and C is the Curie–Weiss constant. Fig. 6 illustrates a plot of inverse relative permittivity as a function of temperature. The fitting parameter results are summarized in Table 1. Results show that the Curie–Weiss law fails to describe permittivity behavior in the Curie point vicinity. The deviation from the Curie–Weiss law is defined as [31]:

$$\Delta T_m = T_{cw} - T_m, \tag{2}$$

where T_{cw} corresponds to the temperature at which the relative permittivity starts to deviate from the Curie–Weiss law, and T_m represents the temperature of relative permittivity when it reaches the maximum value. The decreasing ΔT_m values for $x = 0.02$, 0.06, 0.08 and 0.13 are 43, 32, 23, and 14 °C, respectively, indicating a transformation from relaxor-like ferroelectric to a normal ferroelectric phase for higher CT content. The diffuseness of ferroelectric phase transition can be proposed by the following empirical equation [30]:

$$\frac{1}{\varepsilon} - \frac{1}{\varepsilon_m} = \frac{(T - T_m)^\gamma}{C}, \tag{3}$$

where the γ parameter represents information on the characteristic of phase transition: the phase transition for $\gamma = 1$ follows the Curie–Weiss law, which indicates the first-order phase transition; and complete diffuse phase transition for $\gamma = 2$ is observed. It is assumed that γ and C are constant. Based on the temperature plots of ε' at 10 kHz,

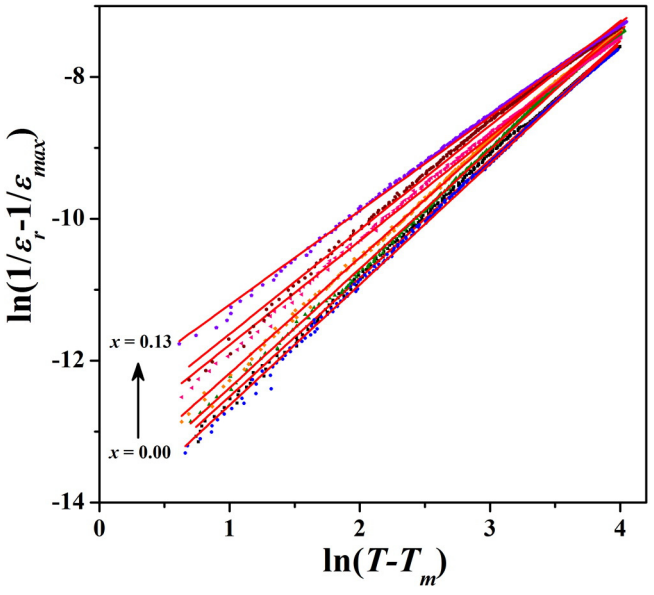

Fig. 7. The ln [$1/\varepsilon_r - 1/\varepsilon_{max}$] as a function of ln [$T - T_m$] at 10 kH for BT–BZ–*x*CT ceramics, with $x = 0.0$–0.13.

the plots of $\ln(1/\varepsilon' - 1/\varepsilon'_m)$ as a function of $\ln(T - T_m)$ for BT–BZ–xCT; x = 0.00–0.13 ceramics are shown in Fig. 7. The values of diffuse constant γ are reported in Table 1, and a linear relationship is observed for CT-substituted BZT ceramics. The values of diffuse constant γ were determined by least-squared fitting experimental data to the equation, and they varied from 1.70 to 1.31. As the CT content increased from 0.01 to 0.05, the diffuse constant γ decreased from 1.70 to 1.31. The results clearly imply that BT–BZ–xCT ceramics exhibit a strong normal ferroelectric phase transition for higher CT content. The diffuse phase transition or relaxor ferroelectric behavior in the solid solution of $Ba(Zr_yTi_{1-y})O_3$ can be controlled by varying the Zr/Ti ratio [32]. The pair distribution function (PDF) technique suggested that the diffusion phase transition/relaxor ferroelectric behavior in $Ba(Zr_yTi_{1-y})O_3$ solid solution is caused by formation of nonpolar $BaZrO_3$ clusters in the polar $BaTiO_3$ matrix [33,34]. Ti^{4+} and Zr^{4+} are bonded with oxygen ligands in $Ba(Zr_yTi_{1-y})O_3$ solid solution, thus forming distorted polar [TiO_6] and non-polar [ZrO_6] clusters. The inhomogeneous distribution of non-polar [ZrO_6] clusters creates a randomly distributed electrical or strain field in the $BaTiO_3$ matrix, leading to diffusion phase transition behavior. The evidence of dynamic disorder, due to incorporating non-polar [ZrO_6] clusters, is supported also by extended X-ray absorption of fine structure (EXAFS) analysis [34,35]. However, when $CaTiO_3$ was substituted in the BZT structure, the Ca^{2+} ions generally substituted Ba^{2+} ions at the A-site of the structure, whereas Ti^{4+} ions substituted Zr^{4+} ions at the B-site of the perovskite structure. The B-site was occupied by only Ti^{4+} ions at the composition, $x = 0.13$, whereas the A-site was occupied by two cations (Ca^{2+} and Ba^{2+} ions). However, diffuse phase transition was not observed. The results indicated that the diffuse

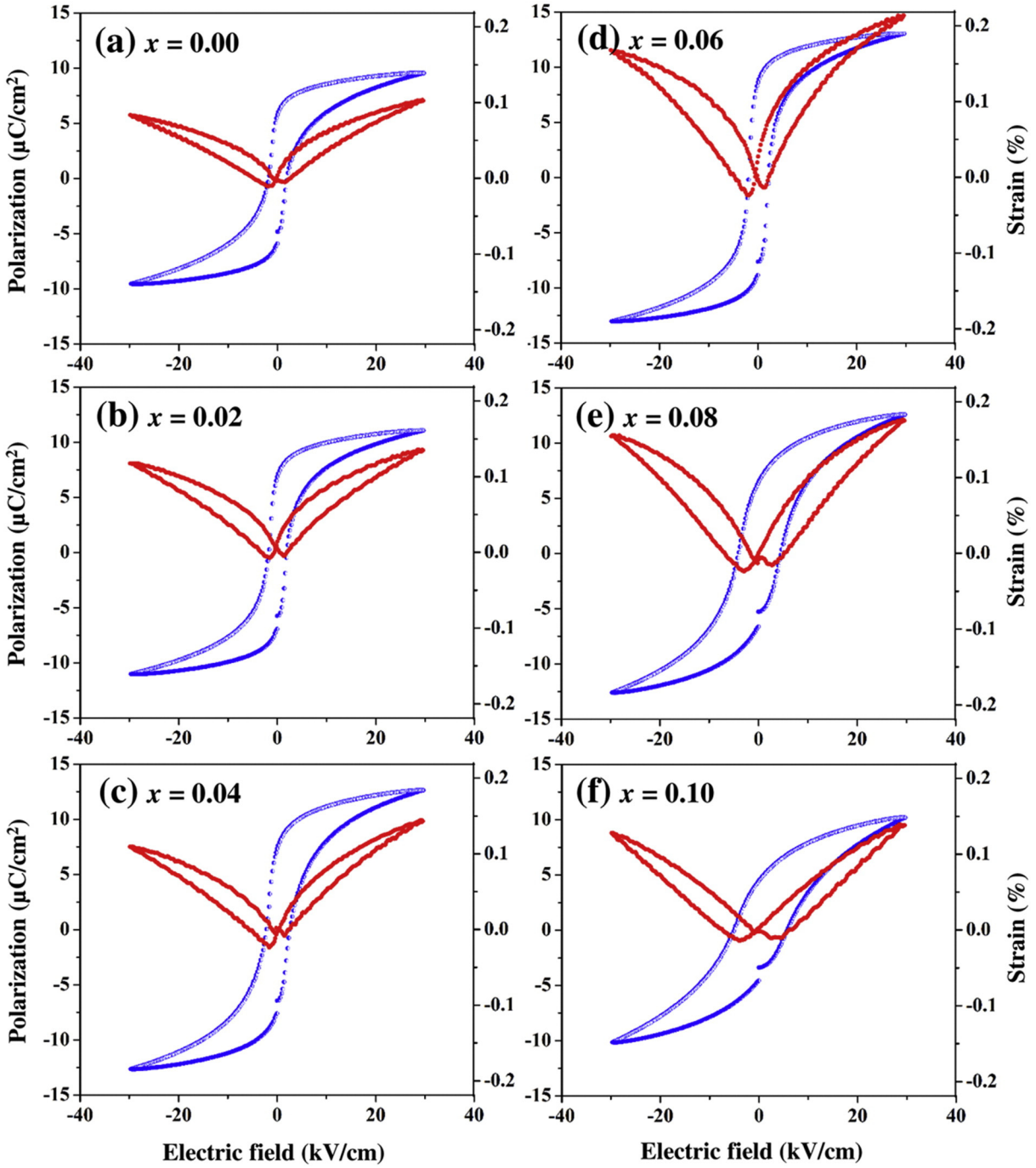

Fig. 8. Bipolar strain and ferroelectric hysteresis loop of BT–BZ–xCT ceramics at room temperature with (a) $x = 0.0$, (b) $x = 0.02$, (c) $x = 0.04$, (d) $x = 0.06$, (e) $x = 0.08$, and (f) $x = 0.01$.

phase transition in the BT–BZ–CT system would be influenced by disordered arrangement of cations at the B-site of the structure, rather than the A-site, which was consistent with recent results reported by Y. Tian et al. [21]. It has been reported that diffuse phase transition behavior was suppressed when a small amount of Ba^{2+} had been substituted by a Ca^{2+} ion at the A-site in $(Ba_{1-x}Ca_x)(Zr_{0.1}Ti_{0.9})O_3$ ceramic.

Fig. 8(a–f) exhibit polarization–electric field (P–E) hysteresis loops and bipolar field-induced strains at room temperature for samples with $x = 0.0$–0.10. All ceramic samples displayed well-saturated *P–E* loops at room temperature, which confirmed that all ceramic samples are of typical forms characterizing ferroelectric materials. An electric field-induced strain loop with a typical sprout-shaped curve was obtained in all compositions. This type of bipolar strain shape is different from soft PZT [1,36] and lead-free BNT-based ceramic [2,37]. The negative strain in all compositions is close to zero, which can be attributed to the difference in the domain reorientation process [36]. The electric field-induced strain behavior corresponds well with results of ferroelectric hysteresis.

In order to evaluate the optimized piezoelectric response of the BT–BZ–*x*CT system, all compositions were examined under different electric fields (10 kV/cm and 40 kV/cm). Fig. 9(a–f) show the unipolar strain curve for various compositions of $x = 0.0$–0.10, measured at 10 kV/cm and 40 kV/cm. The unipolar strain initially increases at electric field loading of under 10 kV/cm, with increasing *x* of up to 0.06, and reaches a maximum value of 0.128% for the composition, $x = 0.06$. When increasing *x* further to 0.10, the unipolar strain decreases to 0.028%. The calculated $d_{33}{}^*$ value of the BT–BZ–*x*CT ceramics for all compositions is summarized in Table 2. The d_{33}^* exhibits a similar tendency for strain and reaches the maximum value of 1280 pm/V as *x* increases to 0.06. Generally, outstanding piezoelectric properties are related basically to

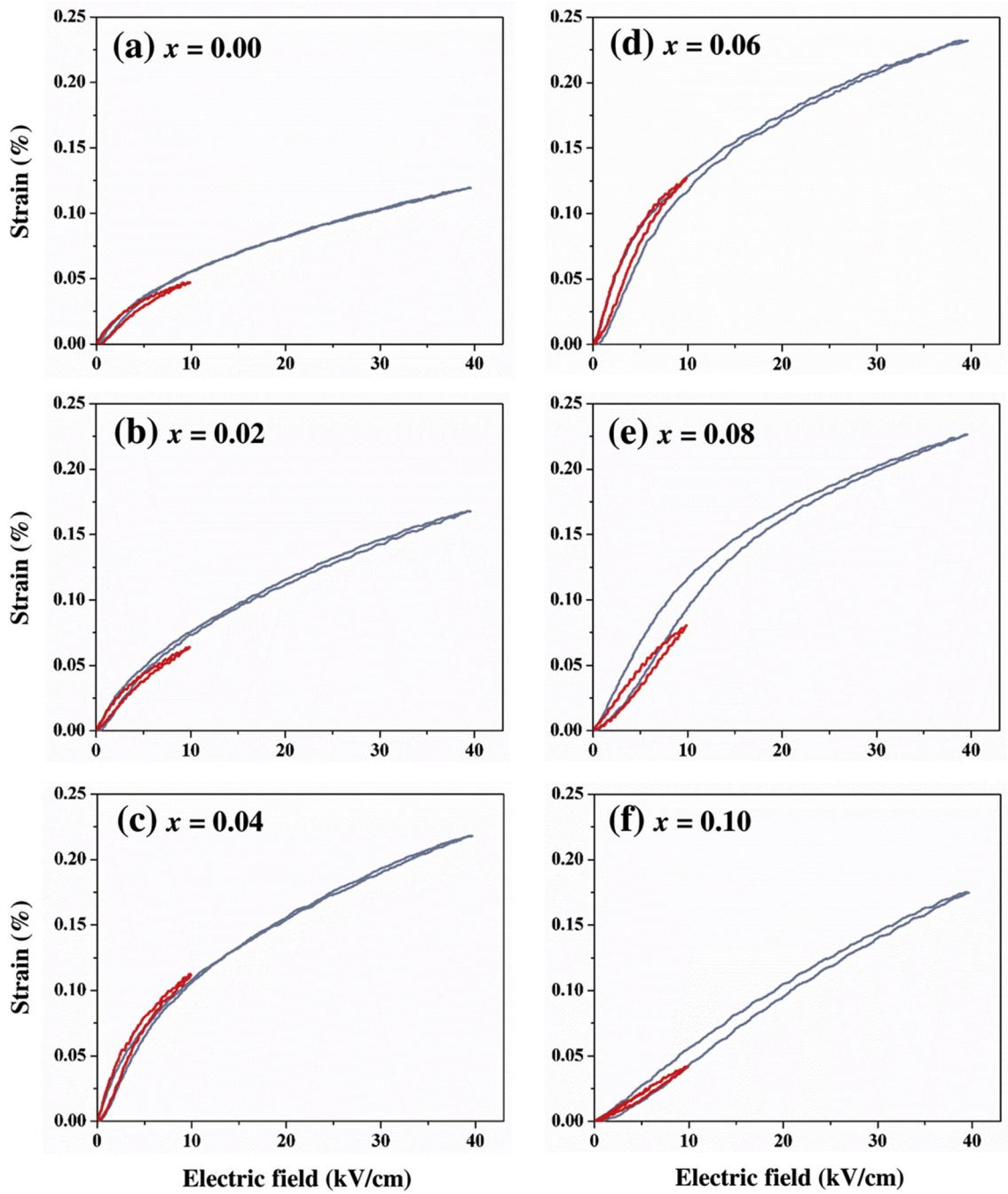

Fig. 9. Unipolar strain of BT–BZ–*x*CT ceramics with (a) $x = 0.0$, (b) $x = 0.02$, (c) $x = 0.04$, (d) $x = 0.06$, (e) $x = 0.08$, and (f) $x = 0.01$ under 10 and 40 kV/cm of the electric field applied.

Table 2
Ferroelectric and piezoelectric properties of BT–BZ–*x*CT ceramics.

Composition (x)	Ec (kV/cm)	P_r (μC/cm^2)	R_{sq}	S_m (%)		d_{33}^* (pm/V)		d_{33} (μC/N)
				10 kV/cm	40 kV/cm	10 kV/cm	40 kV/cm	
0.00	1.9	5.8	0.76	0.047	0.120	473	299	232
0.02	2.0	6.9	0.78	0.070	0.168	700	420	286
0.04	2.3	7.5	0.79	0.113	0.218	1128	546	329
0.06	2.5	8.8	0.92	0.128	0.233	1280	582	439
0.08	4.5	6.6	0.65	0.080	0.227	800	568	354
0.10	5.7	4.6	0.57	0.041	0.175	410	438	210
0.13	6.5	2.4	0.45	0.028	0.110	280	276	140

both intrinsic and extrinsic contributions. Intrinsic contribution refers mainly to variation in lattice distortion, which can be enhanced by adjusting chemical compositions within a coexistence zone of multiphase. Extrinsic contribution is attributed to the strains that form mainly the domain reorientation (switching and rotation) process. Each type of ferroelectric domain has different dynamic orientation processes along the electric field applied. In this work, the extraordinary d_{33}^* value of BT–BZ–*x*CT ceramics, at the composition, $x = 0.06$, correlates to the intrinsic contribution caused by multiphase coexistence of rhombohedral and tetragonal phases, and the extrinsic contribution caused by a low coercive field (E_c), and corresponds to ease the domain reorientation process. BT–BZ–*x*CT ceramic, under high electric field loading (40 kV/cm), exhibited increased maximum strain (S_{max}) values of up to 0.23% at the coexistence phase composition, $x = 0.06$, which is nearly double the value obtained from pure BT, before it decreased to 0.17% at $x = 0.10$. Furthermore, the electric field induced strain curve for the composition close to that of the coexistence phase ($x = 0.06$ and 0.08) consists of two distinguishable regions. Region I (low electric field region < 20 kV/cm), shows a nonlinear and hysteretic strain curve that can be ascribed to the domain switching process. In Region II (high electric field region > 20 kV/cm), most of the domain is clamped by the electric field, leading to minimal contribution from the domain wall motion or domain switching to piezoelectric activity. The piezoelectric responses are induced by lattice deformation and reversible motion of internal interfaces. It is interesting to note that the compositions, $x = 0.06$ and 0.08 which comprise unipolar strain curves that are almost hysteresis-free, and a desired feature for high precision actuator application, were observed at a high electric field. The appearance of a hysteresis-free large strain is found commonly in the Pb-based relaxor ferroelectrics, PZN–PT and PMN–PT [1], but is not very common generally among lead free piezoelectric ceramics [37,38]. The giant strain of 0.45% under both unipolar field loadings in the $K_{1/2}Na_{1/2}NbO_3$ modified $Na_{1/2}Bi_{1/2}TiO_3$–$BaTiO_3$ system was reported by S–T Zhang et al. [38]. Nevertheless, it was accompanied by an undesirably large hysteresis, which limited its practical utility. From this viewpoint, the hysteresis-free giant strain of 0.34% in CT-substituted BZT makes this ceramic a strong candidate for lead-free precision actuator applications. Fig. 10 displays the varied composition of remnant polarization (P_r), coercive field (E_c), (P_{sat}–P_r) value, longitudinal piezoelectric coefficient (d_{33}) and normalized piezoelectric coefficients (d_{33}^*) of BT–BZ–*x*CT ceramics. The remnant polarization of the ceramics increases with increasing composition, x, and reaches a maximum value of 8.8 μC/cm^2 at $x = 0.06$. Then, P_r decreases with x increasing further, until reaching a minimum value of 2.4 μC/cm^2 at $x = 0.13$, while E_c is between 6.5 kV/cm and 1.9 kV/cm. Such a low coercive field indicates that the BT–BZ–*x*CT ceramic is "*soft*" with respect to the electric field. The "soft" sample indicates that the free energy profile for electrically polarized rotation is anisotropically flattened at the multiphase coexistence. This low energy barrier can facilitate the rotation of polarization greatly and also improve the piezoelectric properties effectively. The observed E_c in the rhombohedral side increases slightly, with x increasing until $x = 0.06$, and then it increases significantly in the tetragonal side, with increasing x, and reaches a maximum value of 6.5 kV/cm at $x = 0.06$.

The P_r on the rhombohedral side is higher than that on the tetragonal side, while E_c on the tetragonal side is higher than that on the rhombohedral side. This behavior is ascribed mainly to the domain structure and motion of the domain walls. It is known that the rhombohedral phase has three types of domains: 71°, 109°, and 180°, while the tetragonal phase has only 180° and 90° domains. Non-90° domain switching needs a lower electric field than 90° domain switching, and the ferroelectric domain in rhombohedral ceramic is easier to switch than that in tetragonal ceramic. The value of (P_{sat}–P_r) shows the same trend as that of E_c. Lower (P_{sat}–P_r) values are observed evidently in the rhombohedral side ($0.0 \le x < 0.06$) of the system, and then they increase significantly at the coexistence phase composition, $x = 0.06$. The significantly enhanced P_{sat}–P_r value is related to the phase transition from rhombohedral to tetragonal phase near room temperature. This phenomenon can be attributed to the lower free energy barrier, where the ferroelectric domains switch back easily when electric fields decrease to zero.

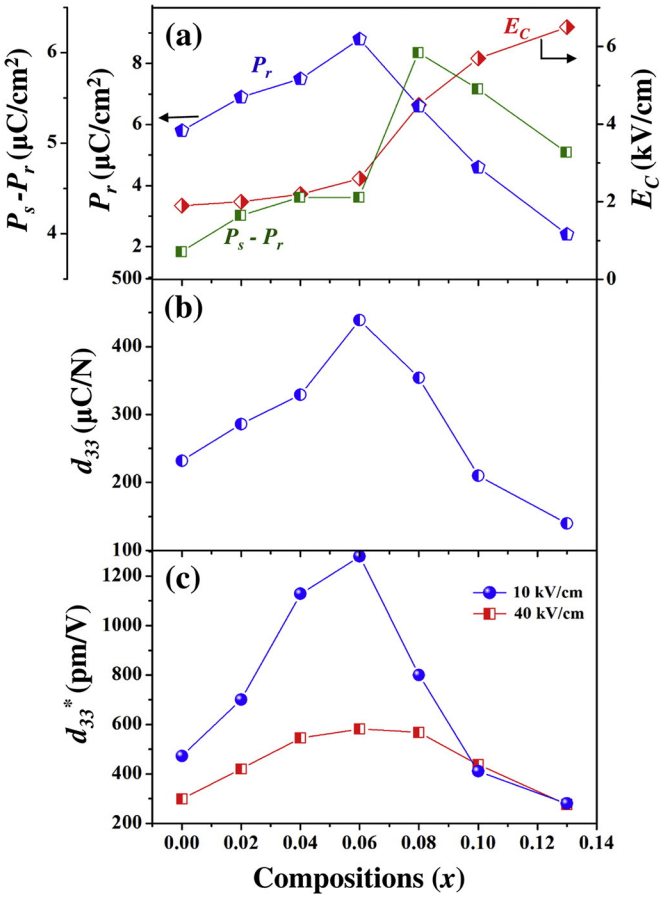

Fig. 10. (a) Ferroelectric properties; P_r, E_c, and P_s–P_r as a function of composition, and piezoelectric coefficient (d_{33}) and normalized strain (S_{max}/E_{max}) value measured at (b) 10 kV/cm and (c) 40 kV/cm of the electric field applied.

The longitudinal piezoelectric coefficient (d_{33}) also shows a similar trend as a function of composition. The d_{33} increases from 232 pC/N for the composition, $x = 0.0$ (rhombohedral side), to 439 pC/N at $x = 0.06$ (PPB composition). It then falls continuously after $x = 0.06$, with $d_{33} = 354$ pC/N at $x = 0.08$ and 140 pC/N at $x = 0.13$ (tetragonal side). This trend is similar to remnant polarization results. In order to quantify the change in the P–E hysteresis loop, the empirical relationship between P_s, P_r and polarization at fields above E_c were used to calculate squareness of the hysteresis loop, as proposed by Haertling and Zimmer [39] with:

$$R_{sq} = \frac{P_r}{P_s} + \frac{P_{1.1E_c}}{P_r} \tag{4}$$

where, R_{sq} is the squareness of the hysteresis loop and P_s and P_r are saturated and remanent polarization, respectively. $P_{1.1Ec}$ is polarization at an increasing electric field of 1.1 times the coercive field (E_c). The squareness parameter has been used to investigate the quantification of changes in P–E hysteresis loops in many lead-based/lead-free ferroelectric ceramics. For an ideal P–E hysteresis loop, the R_{sq} should be equal to 2. The calculated R_{sq} value is also summarized in Table 2. It was found clearly that the R_{sq} parameter of the ceramics increases with increasing composition x, and reaches a maximum value of 0.92 at $x = 0.06$. Then it decreases with x increasing further, until reaching a minimum value of 0.45 at $x = 0.13$, indicating that the P–E hysteresis loop becomes more slanted.

Based on XRD, Raman and Dielectric data, the composition–temperature ferroelectric phase diagram of BT–BZ–xCT ceramics was established, as shown in Fig. 11. The ferroelectric phase diagram in this system consists of three distinct crystallographic phases; high temperature paraelectric cubic, rhombohedral, and ferroelectric tetragonal. With increased CT content, the transition temperature increase is approximately linear with x, from $T_m = 71$ °C for $x = 0.0$ to 121 °C for $x = 0.13$. The rhombohedral ferroelectric to tetragonal ferroelectric phase transition temperatures decrease with increasing CT content. The ceramics undergo a phase transition from rhombohedral to tetragonal near $x = 0.06$ at room temperature.

4. Conclusion

The ternary system, $0.87BaTiO_3$–$(0.13\text{-}x)BaZrO_3$–$xCaTiO_3$ ($0.00 \le x \le 0.13$), fabricated via the solid state reaction method, exhibits excellent piezoelectric properties in proximity of the R–T phase in the coexistence zone. Substitution of $CaTiO_3$ changes the symmetry from tetragonal phase for ceramics with $0.0 \le x < 0.06$ to phase for ceramics with $0.08 \le x \le 0.13$. Substitution of CT also improves the transition temperature of the ceramics, and an extraordinarily "soft" character has been achieved in $x = 0.06$. The enhancement of piezoelectric properties in the system is attributed mainly to multiphase coexistence of the

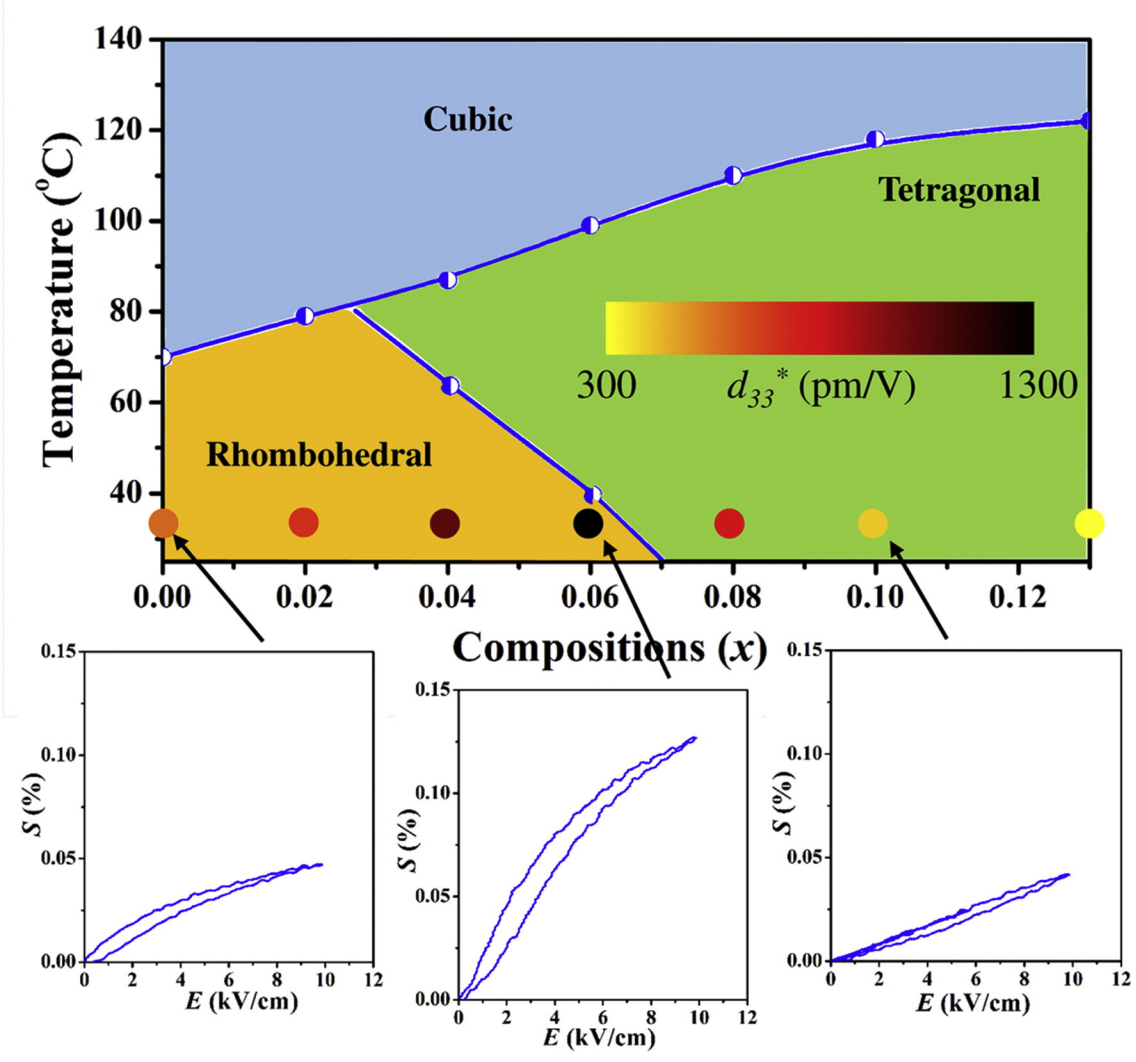

Fig. 11. Composition–temperature ferroelectric phase diagram of BT–BZ–xCT ceramics.

rhombohedral and tetragonal phase, and reduction of energy barriers for polarized rotation. A composition–temperature ferroelectric phase diagram was proposed, in which an R–T phase boundary is formed near room temperature. This work provides a new coexistence phase composition for designing high-performance piezoelectric materials.

Acknowledgements

This work was supported by the Thailand Research Fund (TRF) under grant. No BRG5680006.

References

[1] E. Sun, W. Cao, Relaxor-based ferroelectric single crystals: growth, domain engineering, characterization and applications, Prog. Mater. Sci. 65 (2014) 124–210.
[2] T. Takenaka, H. Nagata, Current status and prospects of lead-free piezoelectric ceramics, J. Eur. Ceram. Soc. 25 (2005) 2693–2700.
[3] T.R. Shrout, S.J. Zhang, Lead-free piezoelectric ceramics: alternatives for PZT? J. Electroceram. 19 (2007) 111–124.
[4] K. Uchino, Ferroelectric Devices, Marcel Dekker, Inc., New York, 2000.
[5] T. Takenaka, H. Nagata, Y. Hiruma, Current developments and prospective of lead-free piezoelectric ceramics, Jpn. J. Appl. Phys. 47 (2008) 3787–3801.
[6] N. Chaiyo, D. Cann, N. Vittayakorn, Phase transitions, ferroelectric, and piezoelectric properties of lead-free piezoelectric $xBaZrO_3$–$(0.25\text{-}x)CaTiO_3$–$0.75BaTiO_3$ ceramics, J. Mater. Sci. 50 (2015) 6171–6179.
[7] X. Wang, J. Wu, D. Xiao, J. Zhu, X. Cheng, T. Zheng, et al., Giant piezoelectricity in potassium-sodium niobate lead-free ceramics, J. Am. Chem. Soc. 136 (2014) 2905–2910.
[8] H.I. Humburg, M. Acosta, W. Jo, K.G. Webber, J. Rödel, Stress-dependent electromechanical properties of doped $(Ba_{1-x}Ca_x)(Zr_yTi_{1-y})O_3$, J. Eur. Ceram. Soc. 35 (2015) 1209–1217.
[9] S. Wirunchit, T. Charoonsuk, N. Vittayakorn, Facile sonochemical synthesis of near spherical barium zirconate titanate ($BaZr_{1-y}Ti_yO_3$; BZT); perovskite stability and formation mechanism, RSC Adv. 5 (2015) 38061–38074.
[10] W. Liu, X. Ren, Large piezoelectric effect in Pb-Free ceramics, Phys. Rev. Lett. 103 (2009) 257602.
[11] M. Acosta, N. Novak, W. Jo, J. Rödel, Relationship between electromechanical properties and phase diagram in the $Ba(Zr_{0.2}Ti_{0.8})O_3$–$x(Ba_{0.7}Ca_{0.3})TiO_3$ lead-free piezoceramic, Acta Mater. 80 (2014) 48–55.
[12] N. Kumar, A. Ionin, T. Ansell, S. Kwon, W. Hackenberger, D. Cann, Multilayer ceramic capacitors based on relaxor $BaTiO_3$–$Bi(Zn_{1/2}Ti_{1/2})O_3$ for temperature stable and high energy density capacitor applications, Appl. Phys. Lett. 106 (2015) 252901.
[13] W. Jo, J.E. Daniels, J.L. Jones, X. Tan, P.A. Thomas, D. Damjanovic, et al., Evolving morphotropic phase boundary in lead-free $(Bi_{1/2}Na_{1/2})TiO_3$–$BaTiO_3$ piezoceramics, J. Appl. Phys. 109 (2011) 014110.
[14] W. Li, Z. Xu, R. Chu, P. Fu, G. Zang, Piezoelectric and dielectric properties of $(Ba_{1-x}Ca_x)(Ti_{0.95}Zr_{0.05})O_3$ lead-free ceramics, J. Am. Ceram. Soc. 93 (2010) 2942–2944.
[15] S.-W. Zhang, H. Zhang, B.-P. Zhang, S. Yang, Phase-transition behavior and piezoelectric properties of lead-free $(Ba_{0.95}Ca_{0.05})(Ti_{1-x}Zr_x)O_3$ ceramics, J. Alloys Compd. 506 (2010) 131–135.
[16] S.J. Kuang, X.G. Tang, L.Y. Li, Y.P. Jiang, Q.X. Liu, Influence of Zr dopant on the dielectric properties and Curie temperatures of $Ba(Zr_xTi_{1-x})O_3$ ($0 \le x \le 0.12$) ceramics, Scr. Mater. 61 (2009) 68–71.
[17] R.C. DeVries, R. Roy, Phase equilibria in the system $BaTiO_3$—$CaTiO_3$, J. Am. Ceram. Soc. 38 (1955) 142–146.
[18] W. Li, Z. Xu, R. Chu, P. Fu, G. Zang, High piezoelectric d_{33} coefficient in $(Ba_{1-x}Ca_x)(Ti_{0.98}Zr_{0.02})O_3$ lead-free ceramics with relative high Curie temperature, Mater. Lett. 64 (2010) 2325–2327.
[19] S. Ye, J. Fuh, L. Lu, Effects of Ca substitution on structure, piezoelectric properties, and relaxor behavior of lead-free $Ba(Ti_{0.9}Zr_{0.1})O_3$ piezoelectric ceramics, J. Alloys Compd. 541 (2012) 396–402.
[20] C.B. Carter, G. Norton, Ceramic Materials: Science and Engineering, Springer, 2013.
[21] Y. Tian, X. Chao, L. Wei, P. Liang, Z. Yang, Phase transition behavior and electrical properties of lead-free $(Ba_{1-x}Ca_x)(Zr_{0.1}Ti_{0.9})O_3$ piezoelectric ceramics, J. Appl. Phys. 113 (2013) 184107.
[22] J. Pokorný, U.M. Pasha, L. Ben, O.P. Thakur, D.C. Sinclair, I.M. Reaney, Use of Raman spectroscopy to determine the site occupancy of dopants in $BaTiO_3$, J. Appl. Phys. 109 (2011) 114110.
[23] U.M. Pasha, H. Zheng, O.P. Thakur, A. Feteira, K.R. Whittle, D.C. Sinclair, et al., In situ Raman spectroscopy of A-site doped barium titanate, Appl. Phys. Lett. 91 (2007) 062908.
[24] R. Farhi, M. El Marssi, A. Simon, J. Ravez, A Raman and dielectric study of ferroelectric ceramics, Eur. Phys. J. B 9 (1999) 599–604.
[25] L. Zhang, O.P. Thakur, A. Feteira, G.M. Keith, A.G. Mould, D.C. Sinclair, et al., Comment on the use of calcium as a dopant in X8R $BaTiO_3$-based ceramics, Appl. Phys. Lett. 90 (2007) 142914.
[26] S.-Y. Kuo, W.-Y. Liao, W.-F. Hsieh, Structural ordering transition and repulsion of the giant LO–TO splitting in polycrystalline BST, Phys. Rev. B 64 (2001) 224103.
[27] T. Maiti, R. Guo, A.S. Bhalla, Evaluation of experimental resume of $BaZr_xTi_{1-x}O_3$ with perspective to ferroelectric relaxor Family: an overview, Ferroelectrics 425 (2011) 4–26.
[28] U. Sukkha, N. Vittayakorn, R. Guo, A.S. Bhalla, Phase transition behavior of $Ba(Mg_{1/3}Nb_{2/3})O_3$ modified $PbZrO_3$ solid solution, J. Mater. Chem. C 2 (2014) 2929–2938.
[29] H. Nagata, T. Takenaka, Additive effects on electrical properties of $(Bi_{1/2}Na_{1/2})TiO_3$ ferroelectric ceramics, J. Eur. Ceram. Soc. 21 (2001) 1299–1302.
[30] C. Chen, H. Zhuang, X. Zhu, K. Zhou, D. Zhang, Enhancement of relaxor properties by Nb doping in $Ba_{0.8}Sr_{0.12}Ca_{0.08}TiO_3$ lead-free ferroelectric ceramics, Ceram. Int. 41 (2015) 9893–9898.
[31] A. Paterson, H.T. Wong, Z. Liu, W. Ren, Z.-G. Ye, Synthesis, structure and electric properties of a new lead-free ferroelectric solid solution of (1 — x)BaTiO3–xBi (Zn2/3Nb1/3)O3, Ceram. Int. 41 (Suppl. 1) (2015) S57–S62.
[32] L. Zhang, M. Zhang, L. Wang, C. Zhou, Z. Zhang, Y. Yao, et al., Phase transitions and the piezoelectricity around morphotropic phase boundary in $Ba(Zr_{0.2}Ti_{0.8})O_3$-$x(Ba_{0.7}Ca_{0.3})TiO_3$ lead-free solid solution, Appl. Phys. Lett. 105 (2014).
[33] C. Laulhé, F. Hippert, R. Bellissent, A. Simon, G.J. Cuello, Local structure in BZT relaxors from neutron pair distribution function analysis, Phys. Rev. B 79 (2009) 064104.
[34] A. Bootchanont, J. Jutimoosik, S. Chandarak, M. Unruan, P. Kidkhunthod, W. Klysubun, et al., Synchrotron X-ray absorption spectroscopy study of local structure transformation behavior in perovskite Ba(Ti, Zr)O3 system, J. Alloys Compd. 616 (2014) 430–435.
[35] C. Laulhé, F. Hippert, J. Kreisel, M. Maglione, A. Simon, J.L. Hazemann, et al., EXAFS study of lead-free relaxor ferroelectric $BaTi_{1-x}Zr_xO_3$ at the Zr K edge, Phys. Rev. B 74 (2006) 014106.
[36] G. Bertotti, I.D. Mayergoyz, The Science of Hysteresis: 3-volume Set, Elsevier Science, 2005.
[37] C. Ma, H. Guo, X. Tan, A new phase boundary in $(Bi_{1/2}Na_{1/2})TiO_3$–$BaTiO_3$ revealed via a novel method of electron diffraction analysis, Adv. Funct. Mater. 23 (2013) 5261–5266.
[38] S.-T. Zhang, A.B. Kounga, E. Aulbach, H. Ehrenberg, J. Rödel, Giant strain in lead-free piezoceramics $Bi_{0.5}Na_{0.5}TiO_3$–$BaTiO_3$–$K_{0.5}Na_{0.5}NbO_3$ system, Appl. Phys. Lett. 91 (2007) 112906.
[39] G.H. Haertling, W.J. Zimmer, Analysis of hot-pressing parameters for lead zirconate-lead titanate ceramics containing two atom percent bismuth, Am. Ceram. Soc. Bull. 45 (1966) 1084–1089.

Ferroelectrics

ISSN: 0015-0193 (Print) 1563-5112 (Online) Journal homepage: http://www.tandfonline.com/loi/gfer20

Fine Grain $BaTiO_3$-$Co_{0.5}Ni_{0.5}Fe_2O_4$ Ceramics Prepared by the Two-Stage Sintering Technique

Nattakarn Pulphol, Rangson Muanghlua, Surasak Niemcharoen, Naratip Vittayakorn & Wanwilai Vittayakorn

To cite this article: Nattakarn Pulphol, Rangson Muanghlua, Surasak Niemcharoen, Naratip Vittayakorn & Wanwilai Vittayakorn (2015) Fine Grain $BaTiO_3$-$Co_{0.5}Ni_{0.5}Fe_2O_4$ Ceramics Prepared by the Two-Stage Sintering Technique, Ferroelectrics, 488:1, 170-180, DOI: 10.1080/00150193.2015.1070639

To link to this article: http://dx.doi.org/10.1080/00150193.2015.1070639

Published online: 23 Dec 2015.

Ferroelectrics, 488: 170–180, 2015

ISSN: 0015-0193 print / 1563-5112 online
DOI: 10.1080/00150193.2015.1070639

Fine Grain $BaTiO_3$-$Co_{0.5}Ni_{0.5}Fe_2O_4$ Ceramics Prepared by the Two-Stage Sintering Technique

NATTAKARN PULPHOL,[1] RANGSON MUANGHLUA,[2] SURASAK NIEMCHAROEN,[2] NARATIP VITTAYAKORN,[1,3,4,*] AND WANWILAI VITTAYAKORN[1,4]

[1]College of Nanotechnology, King Mongkut's Institute of Technology Ladkrabang, Bangkok 10520, Thailand
[2]Department of Electronics Engineering, Faculty of Engineering, King Mongkut's Institute of Technology Ladkrabang, Bangkok 10520, Thailand
[3]Advanced Materials Research Unit, Department of Chemistry, Faculty of Science, King Mongkut's Institute of Technology Ladkrabang, Bangkok 1520, Thailand
[4]Nano-KMITL Center of Excellence on Nanoelectronic Devices, KMITL, Ladkrabang, Bangkok, 10520,Thailand

This work investigated the improvement of density and controllable grain size of multiferroic ceramics by using the system of $(0.8)BaTiO_3$-$(0.2)Co_{0.5}Ni_{0.5}Fe_2O_4$ nanocomposites via the two-stage sintering technique. The sintering process was divided into two steps. Firstly, samples were fired at the optimized temperature of T_1 to activate grain boundary migration in order to obtain an initial high density. Secondly, the samples were cooled immediately to the temperature of T_2 and soaked at various times to enable dense ceramics without grain growth. All of the samples were characterized by an X-ray diffractometer, and the results confirmed that all samples were composite ceramics. Scanning electron microscopy showed the grain size of all the samples and proved that the two-stage sintering technique achieved fine grain ceramics when compared with traditional sintering. Electrical properties of all the samples were investigated using an LCR meter at room temperature to 200°C with various frequencies, and magnetic properties were characterized by a vibrating sample magnetometer.

Keywords Multiferroics ceramics; two-stage sintering; traditional sintering

1. Introduction

Nowadays, electronics technology has been developed for smaller devices with multiple functions. The reduction of particle or grain size to nanoscale enables electronic devices to be smaller with improved properties, resulting in better mechanical properties such as

Received in final form January 15, 2015.
*Corresponding author. E-mail: naratipcmu@yahoo.com
Color versions of one or more of the figures in this article can be found online at www.tandfonline.com/gfer.

hardness, strength and toughness in ceramics. It is interesting that ceramics with nano-grains have increased since the remarkable improvement in their properties when compared with coarse grain ceramics. The sintering technique has been reported to reach nanostructure bulk materials. Weibel et al. [1] studied the microstructure of nanocrystalline TiO_2 prepared by the hot pressing technique, resulting in the motivation of nanostructure ceramic production.

Diphankar Khosh et al. [2] later studied the effect of the sintering technique to obtain grain size, and the spark plasma sintering technique for acquiring dense composite and comparing with pressure less sintering. Composite samples were fired rapidly with the pressure factor during the spark plasma sintering process, and the results yielded a nano grain ceramic with high density. Although hot pressing and spark plasma sintering are good methods for ceramic preparation, based on production of nanoparticles and fine grain ceramics in nano-scale, the production cost and complex shape are limitations for these techniques.

Recently, a new sintering technique called two-stage sintering was developed by Chen and Wang [3], in which nano-grain Y_2O_3 ceramics reached full density. This technique divided the sintering process into two steps. Firstly, green bodies were fired at an optimum T_1 temperature to achieve a critical density, and then cooled immediately to a lower T_2 temperature. In the second step, the green bodies were sintered in air without pressure during the process. The rapidly cooling temperature in the second step caused the grain boundary migration to freeze while being maintained [4]. This led to a fine grain nano-size of the final product. Chen and Wang also applied two-step sintering to other materials such as, $BaTiO_3$ [5–6], Ni-Cu-Zn ferrite [5], ZnO [7], ZrO_2 [8–9], Al_2O_3 [10] and SiC [11].

Two-stage sintering is a successful technique for decreasing grain size to nano-scale in not only ferroelectric materials, but also ferrites, and it has never been applied for composite like multiferroic materials, despite its unique properties that may be adaptable for future development. Many studies have deemed compound materials corresponding to biferroic properties, non-lead ferroelectric materials, like barium titanate, and ferrite materials such as cobalt ferrite as being the most popular systems. Previous work [12] studied cobalt nickel ferrite concentration in the barium titanate system, which was prepared by the conventional solid state method. The results showed better electrical properties such as higher dielectric permittivity and lower dielectric loss, and when composite nickel substituted cobalt ferrite with barium titanate, electrical properties of the ferrite system improved by 20%.

In this study, the magnetostrictive-piezoelectric nanocomposites of $(0.8)BaTiO_3$-$(0.2)Co_{0.5}Ni_{0.5}Fe_2O_4$ were prepared by standard solid-state ceramic processing and sintered by the two-stage sintering method. The phase formation, morphology, and electrical and magnetic properties of the samples were investigated.

2. Experimental Procedure

2.1. Green Body Preparation

Multiferroic ceramics were prepared by the conventional mixed oxide method. Firstly, barium titanate and cobalt nickel ferrite nanoparticles were mixed together, using the $(0.8)BaTiO_3$-$(0.2)Co_{0.5}Ni_{0.5}Fe_2O_4$ formula. The mixed powders were ball-milled in ethanol media for 24 hours, dried, ground and then sieved to avoid agglomeration of the composite powders before pressing into disk shape.

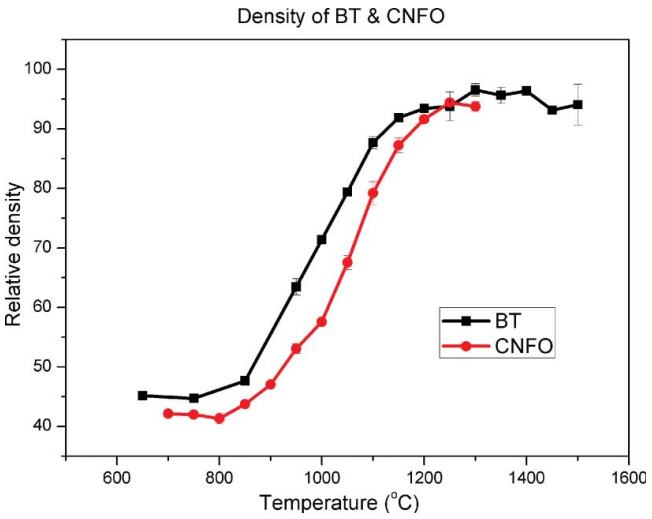

Figure 1. Temperature for two-stage sintering collected from barium titanate and cobalt nickel ferrite density.

2.2. Sintering Process

Pure barium titanate and pure cobalt ferrite were fired by normal sintering to obtain a density curve that leads to finding the optimum temperature for two-stage sintering. Figure 1 exhibits the density curve of pure barium titanate and cobalt nickel ferrite samples sintered by normal sintering. Barium titanate and cobalt nickel ferrite samples were fired in a temperature range from 650–1,500°C and 700–1,300°C, respectively, with a heating-cooling rate of 5°C/min. Densities below 850°C did not change promptly in either material. After all the samples had been heated to 850°C or more, densities increased significantly and became constant at 1,250°C. The immediate change of density after 850°C indicated that grain boundary migration is active at this and higher temperatures, which leads to decreasing porosity. Furthermore, Figure 1 shows that the highest value of density was given when both materials became constant at 1,250°C. Temperature T_1 in two-stage sintering must be high enough for grain activation and use for the diffusion of atom at T_2. Therefore, T_1 in this work was set at 1,250°C and T_2 at 850°C.

Figure 2 shows the process of two-stage sintering. Firstly, samples were heated to temperature T_1 with a heating-cooling rate of 5°C/min in order to activate grain boundary

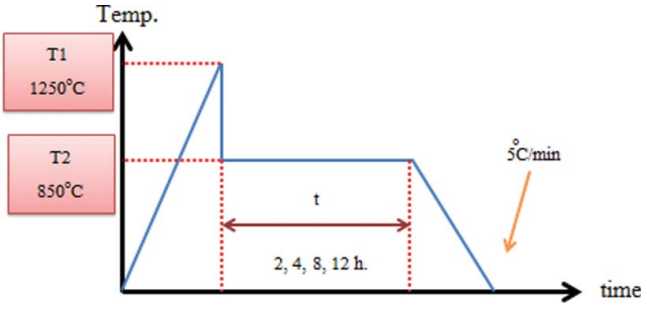

Figure 2. Two-stage sintering process.

migration, and then they were cooled immediately to temperature T_2 and held there for various periods of time (2, 4, 8 and 12 hours, consecutively). The grain size should remain constant at this stage, while density continues to increase. After holding the sintered samples for various periods of time, and cooling them to room temperature with a heating-cooling rate of 5°C/min, their density was measured by Archimedes' method and the following equation:

$$\rho_C = \left[\frac{W_1}{W_2 - W_3}\right] \times \rho_{water} \tag{1}$$

where ρ_c and ρ_{water} are density of the sample and water, respectively. W_1, W_2 and W_3 are weight of the sample when measured in air, wet and water, respectively. After the firing process, every sample was characterized and all results are discussed in the next part of this paper.

3. Results and Discussion

3.1. X-ray Diffractometer

Figure 3 shows the phase formation of $(0.8)BaTiO_3$-$(0.2)Co_{0.5}Ni_{0.5}Fe_2O_4$ composite samples sintered by two-stage sintering at various holding times (2, 4, 8 and 12 hours, consecutively). This figure illustrates the X-ray patterns of both the ferroelectric and ferrite phases, in which no pyrochlore or unknown phase was detected. When the holding time for two-step sintering is increased, it does not affect the structure of composite samples. Normally, X-ray diffraction patterns of tetragonal barium titanate, which was used as starting material in this research, exhibit splitting of the (002)/(200) peaks at 45°, but when barium titanate was mixed with cubic spinel structured ferrite, this characteristic changed. This effect was observed clearly in previous work [12], when the variation in ferrite concentration, which was added

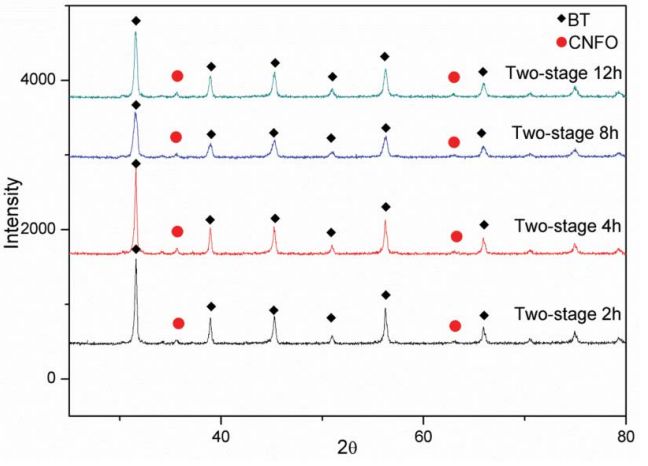

Figure 3. X-ray diffraction pattern of $(0.8)BaTiO_3$-$(0.2)Co_{0.5}Ni_{0.5}Fe_2O_4$ sintered by two-stage sintering at various holding times.

into the composite system, is capable of changing the tetragonality in barium titanate. When the amount of ferrite increased, the split (002)/(200) peaks merged slightly into one peak. The absence of (002)/(200) peaks might attribute to the symmetry of cubic barium titanate, which matched JCPDS file no. 31-0174 [12]. The important factor for the phase transition in barium titanate is its size and influence that determines the height of temperature. Composite materials must consist of two or more components that have different physical or chemical properties, and when they combine, each one clearly should remain separate. In this study, X-ray patterns apparently exhibit both the barium titanate and cobalt nickel ferrite phase in each holding time, which confirms that they coexisted to form composite materials. Nevertheless, when considering the (002)/(200) peaks of barium titanate, their separation merges slightly into one peak, which is characteristic of the cubic structure of barium titanate. This result is not consistent with the composite characteristic in a previous line. Generally, the barium titanate unit cell in a perovskite structure is a form of oxygen octahedra cage, with Ti^{4+} ions occupying sites (B sites) inside, while the Ba^{2+} ions occupy A sites [13]. The cobalt nickel ferrite, with a spinel structure, consists of Ni^{2+} ions that occupy B sites, while Fe^{3+} and Co^{2+} ions occupy both A and B sites in the unit cell [14]. To obtain bulk ceramics, composite materials require the sintering technique, which is a high temperature process that may apply more than 1,000°C with ion replacement of two different materials occurring during the firing process. The ability of ion replacement can be considered from the ionic radius of each material, which must be similar. When focusing on the ionic radius of 0.605 for titanium, and 0.745, 0.69, 0.645 for cobalt, nickel and iron, respectively [15], it is possible that nickel or iron is capable of substituting titanium at the B-site, which aids the temperature in the sintering process. Therefore, the transition of barium titanate from tetragonal to cubic structure may be caused in some regions by substitutional solid solution between tetragonal perovskite barium titanate and cubic spinel cobalt nickel ferrite during the sintering process, which leads to lower ferrite intensity in the X-ray pattern.

3.2. Scanning Electron Microscope

The morphology of $BaTiO_3$-$Co_{0.5}Ni_{0.5}Fe_2O_4$ ceramics, sintered by two-stage sintering, had a first and second temperature of 1,250°C and 850°C, respectively, at various holding times with the same magnification of 50k, as shown in Fig. 4. This figure exhibits the diffusion of large and small grains along the surface. After measuring the average grain size, as shown in Table 1 and Fig. 5, large and small grains were found to have an average size of around 200 ± 0.13 nm and 90 ± 0.02 nm, respectively. Despite soaking at various times, the grain size did not increase. Normally, in composites like multiferroic ceramics, there are two different ferroic orders, which require a different sintering temperature for grain growth. It is well known that increasing sintering temperature can produce high density ceramics, but sintering at high temperature may cause some effects such as solid solution between two different phases and/or heterogeneous microstructure that consists of large and small grains. To clarify these assumptions, all samples were analyzed using energy dispersive spectroscopy (EDS), and the results shown in Fig. 6 relate to previous assumptions that coexistence of different grain size is possibly due to high temperature in the sintering process, which causes the agglomeration or merging of small grains. In addition, solid solution was formed in some regions. These results

Table 1
The average grain size of samples sintered by two-stage sintering at various holding times

	Average grain size (μm)	
Soaking time (h)	Large grain	Small grain
2	0.26 ± 0.13	0.09 ± 0.02
4	0.21 ± 0.05	0.09 ± 0.02
8	0.23 ± 0.07	0.09 ± 0.02
12	0.24 ± 0.09	0.09 ± 0.02

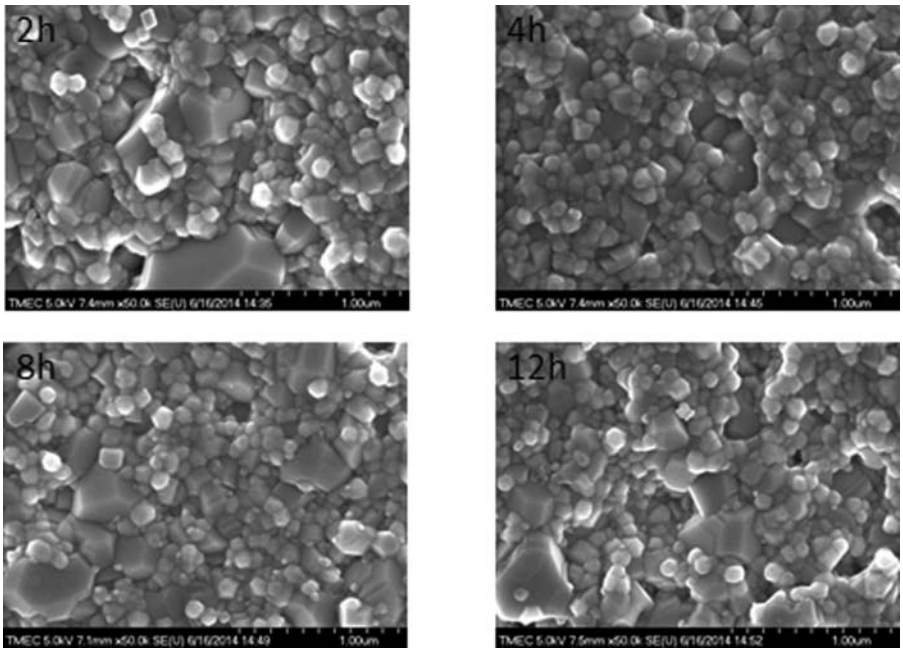

Figure 4. SEM micrographs of sintered ceramics at various holding times with the same magnification of 50 k.

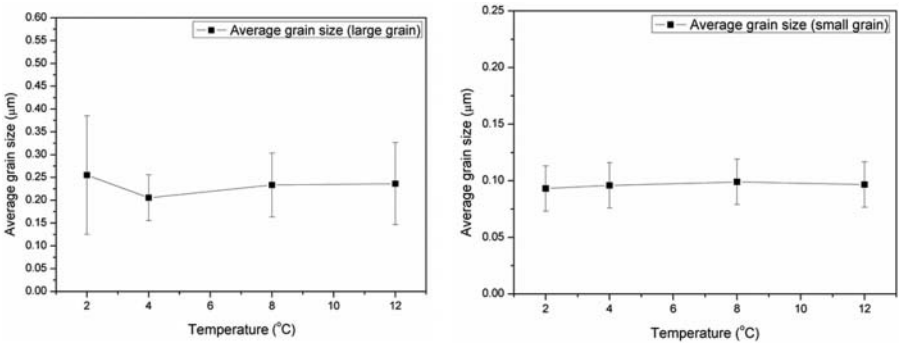

Figure 5. The average grain size of samples sintered by two-stage sintering at various holding times.

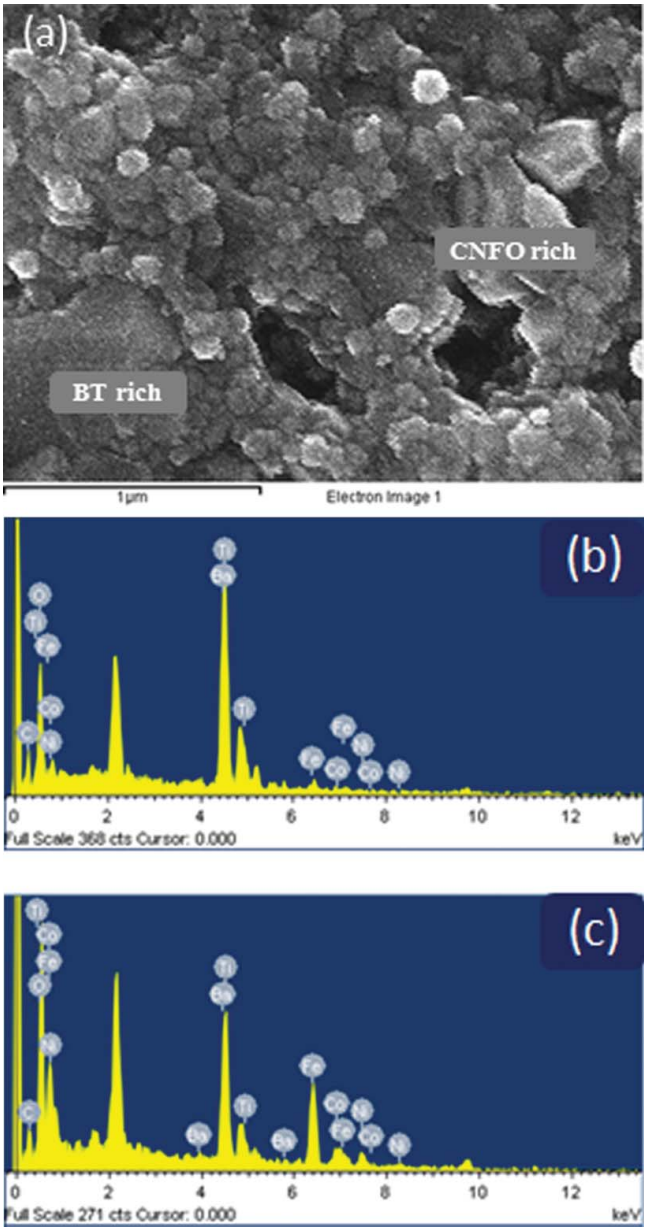

Figure 6. EDS analysis of samples sintered by two-stage sintering (a) SEM image of the BT-CNFO surface sintered by two-stage sintering (b) EDS for the BT-rich area (c) EDS for the CNFO-rich area.

corresponded to those from the X-ray diffractometer, in that merging of (002)/(200) peaks is caused by solid solution in the ceramics. During successful two-step sintering, the grain size should remain constant in the second step, unlike in conventional sintering, in which final stage densification is invariably accompanied by rapid grain

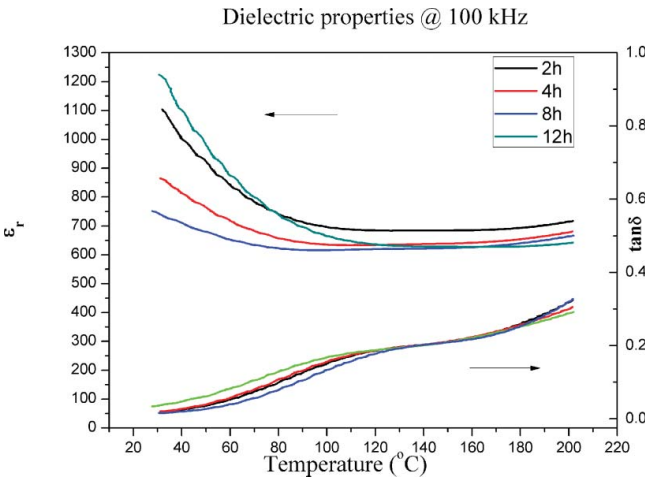

Figure 7. Electrical properties of all samples at a frequency of 100 kHz.

growth. Therefore, the two-step technique was successful in reducing grain size in this research.

3.3. Dielectric Properties

The density of dielectric properties in all samples sintered by two-stage sintering techniques is shown in Fig. 7 and Table 2. The value of dielectric permittivity at various holding times was plotted with the function of temperature. When the holding time was changed, the dielectric permittivity did not change significantly or was not proportional to the change of time. This may be caused by the effect of density. In general, the sample with high density gives a high value of dielectric permittivity. In contrast, if the sample has low density, there is much porosity that can cause a decrease of dielectric permittivity. Therefore, these results can give the assumption that porosity in ceramics is the factor which affects the dielectric properties of samples. The improvement of barium titanate has been reported in many researches in order to obtain good electrical properties such as high dielectric permittivity with low dielectric loss. Barium titanate with a tetragonal structure has been studied widely, due to its ferroelectric and piezoelectric properties. Normally, the phase transition in barium titanate occurs at the temperature of 130°C. Then, the barium titanate changes from tetragonal to cubic structure, which leads to a change from ferroelectric to paraelectric property. Also, barium titanate with a cubic

Table 2
Densities of all samples sintered by two-stage sintering

Soaking time (h)	Relative density
2	89.19 ± 0.03
4	86.86 ± 2.47
8	83.39 ± 1.72
12	89.09±1.81

structure can be found in very fine particles at room temperature [16]. Furthermore, the properties of barium titanate can be improved by the volume fraction of the dopant or composite materials [17]. When the Curie temperature (T_C) of dielectric permittivity results was considered, T_C shifted from 130°C to a temperature of around 20°C. The shift of T_C can be caused by many reasons. As mentioned in previous results, each composite material should exhibit its characteristic. In this case, due to the composite system being between two different materials, the sintering process was used at high temperature in order to obtain the final products. It is possible that some of the ferrites were diffused into barium titanate, which caused the solid solution in this system and led the shift of T_C in dielectric results to a lower temperature. For this reason, dielectric results can confirm the occurrence of solid solution in the barium titanate-cobalt nickel ferrite system, which was caused by the phase shift of Curie temperature from 130°C to 20°C in barium titanate, and this finding supports the X-ray results.

3.4. Magnetic Properties

Multiferroic materials not only have electrical properties, but also magnetic ones. Magnetic properties of composite samples were characterized by a vibrating sample magnetometer, and magnetic hysteresis loops are illustrated in Fig. 8. When the holding time was changed, the maximum magnetization or M_{max} did not change significantly. Magnetic properties of cobalt nickel ferrite nanopowders have been reported in other researches, which observed that the value of coercivity is around 5,000 A/m and 30 Am^2kg^{-1} for saturate magnetization [18]. In this study, the coercivity value of saturate magnetization decreased from 5,000 A/m to around 2,000 A/m and from 30 Am^2kg^{-1} to around 8 Am^2kg^{-1}. The decrease in magnetic properties was caused by the proportion of ferrite concentration in the composite. In this system, 20% of ferrite was added into the barium titanate system, which caused less magnetic contact between grains. When considering the difference between sintering times in this study, the magnetization of every one changed, but not for the coercive field. It is known that in ferrite materials with a spinel structure, the ions that occupy the tetrahedral (A site) and octahedral (B site) depend

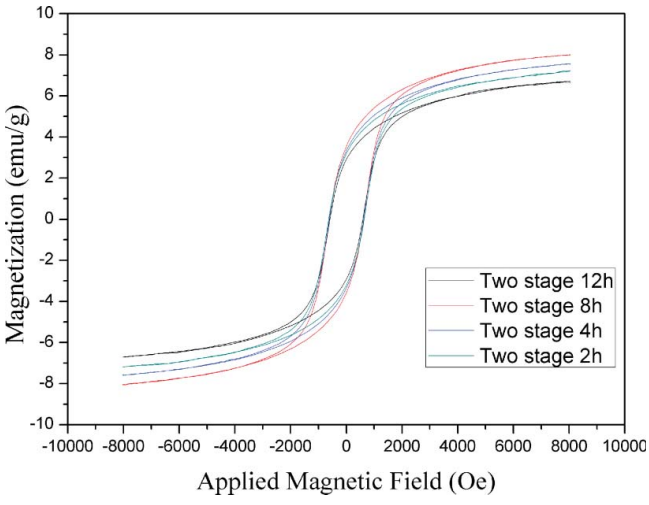

Figure 8. Magnetic hysteresis loop of composite samples sintered by two-stage sintering.

on 4 factors; 1) the ionic radii of specific ions, 2) the size of the interstices, 3) temperature, and 4) the orbital preference for specific coordination, which leads to the change of magnetic properties. Cobalt nickel ferrite consists of Ni^{2+}, Co^{2+} and Fe^{3+} ions, and the former occupies B sites, while the latter occupies both A and B sites. As seen in the X-ray results, the possibility of ion exchange in octahedral B sites is that of the ionic radius of two ions. The ionic radius of Ni^{2+} and Fe^{3+} ions are similar to Ti^{4+}ions, which means that Ni^{2+} and Fe^{3+} can be substituted by Ti^{4+} at the octahedral B sites. From this result, the Co^{2+} ions concentrated at tetrahedral B sites are decreased, which leads to a change in saturate magnetization. When the saturate magnetization in this work is considered, the values did not change as a trend. This may be caused by the migration of some Co^{2+} ions in A and B sites, which had temperature and sintering time as an aid.

4. Conclusion

This work studied the fabrication of multiferroic composite prepared by the two-stage sintering technique, using the system of $(0.8)BaTiO_3$-$(0.2)Co_{0.5}Ni_{0.5}Fe_2O_4$. The phase formation, microstructure, and electric and magnetic properties were characterized. Results from the X-ray diffractometer confirmed that all samples were composite and had some solid solution, as observed by the merging of (002)/(200) peaks. A scanning electron microscope (SEM) illustrated grain morphology, and the result from EDS supports the assumptions that solid solution was formed. Both electric and magnetic properties are shown, which confirms that they are a multiferroic composite.

Funding

This work was supported partially by the Thailand Research Fund (TRF) Grant No. BRG5680006, National Research Council of Thailand (NRCT) under Grant No 2558A11802071, and the National Nanotechnology Center (NANOTEC), NSTDA, Ministry of Science and Technology, Thailand, through its program of Center of Excellence Network.

References

1. A. Weibel, R. Bouchet, R. Denoyel, and P. Knauth, Hot pressing of nanocrystalline TiO_2 (anatase) ceramics with controlled microstructure. *J Eur Ceram Soc.* **27**, 2641–2646 (2007).
2. G. Dipankar, H. Hyuksu, C. N. Juan, S. Ghatu, and L. J. Jacob, Synthesis of $BaTiO_3$-20%wt$CoFe_2O_4$ nanocomposites via spark plasma sintering. *J Am Ceram Soc.* **95**, 2504–2509 (2012).
3. X. H. Wang, P. L. Chen, and I. W. Chen, Two-step sintering of ceramics with constant grain-size, I. Y_2O_3. *J Am Ceram Soc.* **89**, 431–437 (2006).
4. C. J. Wang, C. Y. Huang, and Y. C. Wu, Two-step sintering of fine alumina-zirconia ceramics. *Ceram Int.* **35**, 1467–1472 (2009).
5. X. H. Wang, X. Y. Deng, H. L. Bai, H. Zhou, W. G. Qu, L. T. Li, and I. W. Chen, Two-step sintering of ceramics with constant grain-size. II. $BaTiO_3$ and Ni-Cu-Zn ferrite. *J Am Ceram Soc.* **89**, 438–443 (2006).
6. A. Polotai, K. Breece, E. Dickey, C. Randall, and A. Ragulya, A novel approach to sintering nanocrystalline barium titanate ceramics. *J Am Ceram Soc.* **88**, 3008–3012 (2005).
7. P. Duran, F. Capel, J. Tartaj, and C. Moure, A strategic two-stage low-temperature thermal processing leading to fully dense and fine-grained doped-ZnO varistor. *Adv Mater.* **14**, 137–141 (2002).

8. P. C. Yu, Q. F. Li, and L. Lu, Two-stage sintering of nano-sized yttria stabilized zirconia process by powder injection moulding. *J Mater Process Tech.* **192–193**, 312–318 (2007).
9 J. Binner, K. Annapoorani, A. Pual, I. Santacruz, and B. Vaidhyanathan, Dense nanostructured zirconia by two-stage conventional/hybrid microwave sintering. *J Eur Ceram Soc.* **28**, 973–977 (2007).
10. K. Bodišová, P. Šalgalík, D. Galusek, and P. Švancárek, Two-stage sintering of alumina with submicrometer grain size. *J Am Ceram Soc.* **90**, 330–332 (2007).
11. Y. I. Lee, Y. W. Kim, and M. Mitomo, Effect of processing on densification of nanostructured SiC ceramics fabricated by two-step sintering. *J Mater Sci.* **39**, 3801–3803 (2004).
12. N. Pulphol, R. Muanglua, S. Niemcharoen, W. Pecharapa, W. Vittayakorn, and N. Vittayakorn, Magnetoelectric properties of $BaTiO_3$ – $Co_{0.5}Ni_{0.5}Fe_2O_4$ composites prepared by the conventional mixed oxide method. *Adv Mater Res.* **802**, 22–26 (2013).
13. G. H. Haertling, Ferroelectric ceramics: history and technology. *J Am Ceram Soc.* **82**, 797–818 (1999).
14. I. H. Gul, F. Amin, A. Z. Abbasi, M. Anis-ur-Rehman, and A. Maqsood, Physical and magnetic characterization of co-percipitated nanosize Co-Ni ferrites. *Scripta Mater.* **56**, 497–500 (2007).
15. R. D. Shannon, Revised effective ionic radii and systematic studies of interatomic distances in halides and chalcogenides. *Acta Crystallogr.*, **32**, 751–767 (1976).
16. L. V. Leonel, A. Righi, W. N. Mussel, J. B. Silva, and N. D. S. Mohallem, Structural characterization of barium titanate-cobalt ferrite composite powders. *Ceram Int.* **37**, 1259–1264 (2011).
17. H. C. Pant, M. K. Patra, A. Verma, S. R. Vadera, and N. Kumar, Study of the dielectric properties of barium titanate-polymer composites *Acta Mater.* **54**, 3163–3169 (2006).
18. K. Maaz, S. Karim, A. Mashiatullah, J. Liu, M. D. Hou, Y. M. Sun, J. L. Duan, H. J. Yao, and D. Mo, Y. F. Chen, Structural analysis of nickel doped cobalt ferrite nanoparticles prepared by coprecipitation route. *Phys B.* **404**, 3947–3951 (2009).

Ferroelectrics

ISSN: 0015-0193 (Print) 1563-5112 (Online) Journal homepage: http://www.tandfonline.com/loi/gfer20

Effect of $BiYbO_3$ Addition with a Small Tolerance Factor on Ferroelectricity and T_C in $PbZrO_3$ Ceramics

Usa Sukkha, Surasak Niemcharoen, Naratip Vittayakorn, Ruyan Guo & Amar S. Bhalla

To cite this article: Usa Sukkha, Surasak Niemcharoen, Naratip Vittayakorn, Ruyan Guo & Amar S. Bhalla (2015) Effect of $BiYbO_3$ Addition with a Small Tolerance Factor on Ferroelectricity and T_C in $PbZrO_3$ Ceramics, Ferroelectrics, 487:1, 55-67, DOI: 10.1080/00150193.2015.1070246

To link to this article: http://dx.doi.org/10.1080/00150193.2015.1070246

Ferroelectrics, 487: 55–67, 2015

ISSN: 0015-0193 print / 1563-5112 online
DOI: 10.1080/00150193.2015.1070246

Effect of $BiYbO_3$ Addition with a Small Tolerance Factor on Ferroelectricity and T_C in $PbZrO_3$ Ceramics

USA SUKKHA,[1] SURASAK NIEMCHAROEN,[2] NARATIP VITTAYAKORN,[3,4,5,*] RUYAN GUO,[6] AND AMAR S. BHALLA[6]

[1]Synchrotron Light Research Institute, Public Organization, Nakhon Ratchasima 3000, Thailand
[2]Department of Electronics, Faculty of Engineering, King Mongkut's Institute of Technology Ladkrabang, Bangkok 10520, Thailand
[3]Electroceramic Research Laboratory, College of Nanotechnology, King Mongkut's Institute of Technology Ladkrabang, Bangkok 10520, Thailand
[4]Advanced Material Research Unit, Faculty of Science, King Mongkut's Institute of Technology Ladkrabang, Bangkok 10520, Thailand
[5]Department of Chemistry, Faculty of Science, King Mongkut's Institute of Technology Ladkrabang, Bangkok 10520, Thailand
[6]Department of Electrical and Computer Engineering, College of Engineering, University of Texas at San Antonio (UTSA), San Antonio, Texas, 78256, USA

Perovskite $(Pb_{(1-3x/2)}Bi_x)(Zr_{(1-3x/4)}Yb_x)O_3$ (PZ-BY) ceramics, where x = 0.01–0.10, *were synthesized by conventional solid state reaction. The effect of $BiYbO_3$ on crystal structure, phase transitions and electrical properties was studied as a function of composition. The X-ray diffraction (XRD) result indicated that the perovskite structure with orthorhombic symmetry was a major phase for all samples. The pyrochlore phase, identified as $Yb_{0.2}Zr_{0.8}O_{1.9}$, coexists in PZ-BY ceramics. The influence of instability and a small tolerance factor (*t*) and the average electronegativity difference ($\overline{\chi}$) of pure BY on phase formation of PZ-BY ceramic has been discussed. Furthermore, it was found that adding small tolerance factor $BiYbO_3$ compound can stabilize the antiferroelectric (AFE) phase of PZ solid solutions and decreasing* t *of solid solution can enhance Curie temperature of PZ.*

Keywords Antiferroelectric; tolerance factor; phase transition; lead zirconate

1. Introduction

Currently, antiferroelectrics (AFE) are of interest due to their excellence properties including electrocaloric effects [1] or electrostriction [2]. They also are important in a extensive range of technical applications for example high energy density

Received October 26, 2014; in final form February 15, 2015.
*Corresponding author. E-mail:naratipcmu@yahoo.com
Color versions of one or more figures in this article can be found online at www.tandfonline.com/gfer.

capacitors, high strain actuators and transducers. The first compound to be identified as an antiferroelectric was lead zirconate ($PbZrO_3$; PZ). At room temperature, PZ has an orthorhombic symmetry with the lattice parameters; $a = 5.884$ Å, $b = 11.768$ Å, and $c = 8.22$ Å [3]. Phase transition of PZ has progressively changed from orthorhombic AFE phase to rhombohedral ferroelectric (FE) phase (233–236°C) to cubic paraelectric (PE) phase at 236°C. Sometimes, the FE phase between AFE and PE phases is called as a FE intermediate phase. As well known, phase transition of AFE to FE in PZ requires a strong electric field then dielectric breakdown will be occured. In the past, many research groups focused on adjusting this critical field and optimizing electrical and physical properties of PZ by doping some metal oxides at the A-site or B-site of a perovskite structure. It was found that FE phase of PZ can be induced by loading Sr^{2+}, Ba^{2+} and La^{3+} at A-site, and Ti^{4+} and Sn^{4+} at B-site [4]. Recently, this research group observed that the AFE and FE phases of PZ can be controlled by adding hybrid-dopants such as Ni^{2+}/Nb^{5+}, Zn^{2+}/Nb^{5+}, Mg^{2+}/W^{6+} and Y^{3+}/Nb^{5+} at the Zr^{4+}-site of the PZ structure [5–8]. However, Curie temperature (T_C) of most PZ-based solid solutions tends to decrease with increasing metal oxide content. This phenomenon limits PZ-based compounds for applications that require high operating temperature.

Recent studies have been carried out on a variety of $BiMeO_3$-$PbTiO_3$ systems, with the aim of enhancing high T_C solid solutions. Eitel et al. [11] pointed out that the smaller tolerance factor of $BiMeO_3$ can increase the transition temperature further when do solid solution with $PbTiO_3$. Crystal structure of $BiYbO_3$ has a triclinic symmetry, with the lattice parameters, $a = 8.487$ Å, $b = 8.419$ Å, and $c = 9.928$ Å [9]. The tolerance factor of 0.857 for $BiYbO_3$ is lower than that for $BiScO_3$, $BiInO_3$, etc. In 2009, G. Feng et al. studied phase transition of $x$$BiYbO_3$-(1-$x$)$PbTiO_3$ ceramics[10]. Novel perovskite $x$$BiYbO_3$-(1-$x$)$PbTiO_3$ solid solution has a high Curie temperature (up to 550°C), which is higher than the T_C of $x$$BiScO_3$-(1-$x$)$PbTiO_3$ [11]. Although the solid solutions of $BiMeO_3$-$PbTiO_3$ have been investigated widely, few reports on $BiMeO_3$ with lead zirconate (PZ) are available. Therefore, in this work PZ was used as the end member with $BiYbO_3$ to help stabilize a perovskite structure of $PbZrO_3$-$BiYbO_3$ ceramic. The influence of $BiYbO_3$ on crystal structure, phase transition and electrical properties of $PbZrO_3$ are reported. Guided by the tolerance factor, relationship with the T_C, $PbZrO_3$-$BiYbO_3$ system is expected to have a high Curie temperature.

2. Experimental Procedure

Conventional solid state reaction was used for the preparation of $(Pb_{(1-3x/2)}Bi_x)(Zr_{(1-3x/4)}Yb_x)O_3$ ceramics, where $x = 0.00$, 0.02, 0.04, 0.06 and 0.10. High purity metal oxide powders of PbO (99%), ZrO_2 (99%), Yb_2O_3 (99.9%) and Bi_2O_3 (≥99.9%) were batched in stoichiometric amounts and ball-milled with yttrium-stabilized zirconia balls and ethanol for 18 h. After drying the mixture for 24 h in an oven, the mixed powder was calcined at 900°C in air for 4 h, with a heating/cooling rate of 5°C/min. The calcined powder was ground and sieved to obtain fine particles prior to making a pellet. In order to get a green body, the fine powder of each composition was pressed into a disk shape using 5 wt% PVA as a binder and then sintered at 1,250°C for 4 h. The green bodies were fired in a sealed alumina crucible in PbO-rich atmosphere to prevent PbO volatilization. The content of perovskite phase was measured using an X-ray diffractometer (XRD; Bruker-AXS D8) with CuKα radiation.The relative amount of perovskite structure and pyrochlore phase was determined by using their major peak intensities. The percentage of perovskite

structure was calculated via the follow equation:

$$\text{Content of perovskite phase } (\%) = \frac{I_{perov}}{I_{perov} + I_{pyroc}} \times 100\ \%$$

where I_{perov} and I_{pyroc} refer to intensity of the major peak for perovskite and pyrochlore phases, respectively. The differential scanning calorimeter (DSC 2920, TA Instrument) was used to investigate the phase transition of samples in the temperature range of room temperature to 300°C at a heating rate of 10°C/min. Flat and polished samples were prepared before electrode coating with silver paste (C1000, Heraeus) on both surfaces. Capacitance and tan δ were measured as a function of temperature between 30–300°C, with a heating rate of 2°C/min using an LCR meter (HP4284A, Hewlett-Packard, Palo Alto, CA). The polarization was measured as a function of electric field using a standardized ferroelectric tester system (RT-66A, Radiant Technologies, Albuquerque, NM) at a frequency of 4 Hz. The peak field was maintained at 35 kV/cm during measurement.

3. Results and Discussion

Figure 1 shows XRD patterns of $(Pb_{(1-3x/2)}Bi_x)(Zr_{(1-3x/4)}Yb_x)O_3$ ceramics for the compositions, $0.00 \leq x \leq 0.10$, at room temperature. At the composition, $x \leq 0.01$, a phase-pure perovskite structure was obtained. All diffraction peaks are able to match well with JCPDS No. 75–1607, indicating that the crystalline structure of ceramic is an orthorhombic symmetry. In the compositions, $0.02 \leq x \leq 0.10$, the major phase was observed as a perovskite phase. The cubic pyrochlore phase, $Yb_{0.2}Zr_{0.8}O_{1.9}$ (JCPDS No. 78–1309), marked by "○", started to develop and increased in intensity with increase content of $BiYbO_3$ (BY). Under the detection limit of equipment, percentage of the perovskite phase at various compositions

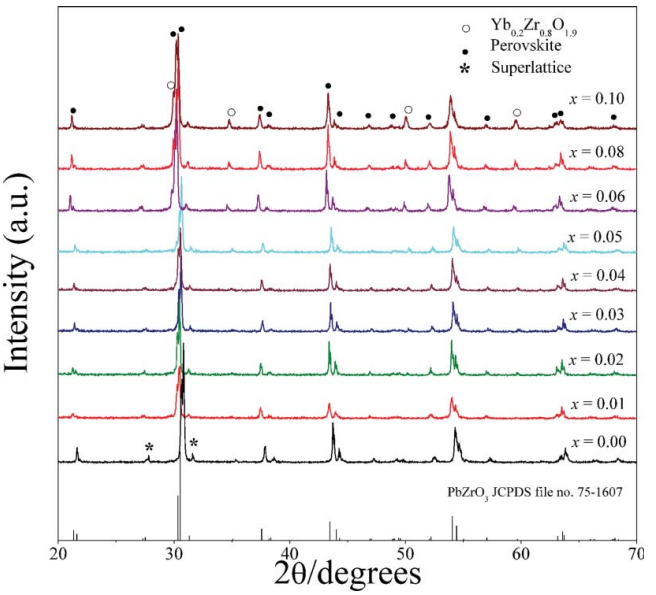

Figure 1 XRD patterns of sintered ceramics for various compositions of $(1\text{-}x)PbZrO_3 - xBiYbO_3$, where $x = 0.0$–0.1.

Table 1
Crystal structure, lattice parameters and percentage of perovskite of (1-x)$PbZrO_3$–$xBiYbO_3$ ceramics (O, orthorhombic; Py, pyrochlore)

Composition (x)	Crystal structure	Lattice parameters (Å)			Volume (Å^3)	% Perovskite
		a	b	c		
0.00	O	5.800 ± 0.040	11.691 ± 0.028	8.346 ± 0.174	565.939	100.0
0.01	O	5.894 ± 0.010	11.770 ± 0.015	8.185 ± 0.044	567.811	100.0
0.02	O + Py	5.899 ± 0.012	11.773 ± 0.012	8.171 ± 0.059	567.411	92.5
0.03	O + Py	5.856 ± 0.010	11.742 ± 0.014	8.244 ± 0.036	566.823	89.7
0.04	O + Py	5.869 ± 0.005	11.752 ± 0.006	8.221 ± 0.008	567.044	87.0
0.05	O + Py	5.844 ± 0.018	11.727 ± 0.009	8.260 ± 0.062	566.054	85.2
0.06	O + Py	5.955 ± 0.041	11.833 ± 0.021	8.130 ± 0.139	572.791	85.4
0.08	O + Py	5.924 ± 0.027	11.796 ± 0.019	8.148 ± 0.097	569.378	83.9
0.10	O + Py	5.919 ± 0.024	11.796 ± 0.022	8.158 ± 0.089	569.658	76.8

is calculated and listed in Table 1. These results point out that the solubility limit of $(Pb_{(1-3x/2)}Bi_x)(Zr_{(1-3x/4)}Yb_x)O_3$ ceramics is the composition, $x = 0.01$. Also, the existence of BY in a solid solution drops off the stability of PZ perovskite phase owing to the instability and small tolerance factor (t) and average electronegativity difference ($\overline{\chi}$) of pure BY; $t = 0.857$ and $\overline{\chi} = 1.786$. The tolerance factor (t) and average electronegativity difference ($\overline{\chi}$) are important factors used to consider the stability of perovskite structure [12].

The tolerance factor can be calculated by the general equation for perovskite structure: [4]

$$t = \frac{(R_A + R_O)}{\sqrt{2}(R_B + R_O)} \tag{1}$$

where R_A, R_B and R_O are the ionic radius of the ions occupying the A(CN = 12), B(CN = 6) and O(CN = 6) sites, respectively. BY compound has a relatively small ionic size of Bi^{3+} (1.40Å, 12 coordinate) on the A-site and a relatively large ionic size of Yb^{3+} (0.868Å, 6 coordinate) in the B-site [13], resulting in a small tolerance factor. Thus, perovskite BY compound is thermodynamically less stable, and difficult to synthesize, and the pyrochlore phase often appears. For the second factor, average electronegativity difference $\overline{\chi}$ is exhibited by [12]:

$$(\overline{\chi}) = (\chi_{AO} + \chi_{BO})/2 \tag{2}$$

where χ_{AO} and χ_{BO} are electronegativity difference between oxygen and cations occupying at the A-site and B-site. The average electronegativity difference reflects the ionic character of the chemical bonds in a perovskite structure. The percentage of ionic character is proportional to the electronegativity difference between anions and cations. For a stable perovskite, the cations and anions should form a strong ionic bond [12]. Bi-based compounds have a small $\overline{\chi}$ value when compared with other lead-free perovskites such as $BaZrO_3$ ($\overline{\chi} = 2.33$), $NaNbO_3$ ($\overline{\chi} = 2.175$), $KNbO_3$ ($\overline{\chi} = 2.23$). Then Bi-based compounds may not form a perovskite structure easily.

In addition, the PbO has a low melting point, about 890°C, which volatilizes during the sintering process, as shown in equations (3) and (4) [10].

$$PbO(s) \overset{890^oC}{\leftrightarrow} PbO(g) \overset{890^oC}{\leftrightarrow} Pb(g) + \frac{1}{2}O_2(g) \tag{3}$$

$$PbZrO_3 \overset{890^oC}{\leftrightarrow} ZrO_2 + PbO \tag{4}$$

Also, Bi_2O_3 has a low melting point of about 820°C. Then $BiYbO_3$ will decompose and bismuth compound will volatilize during the sintering process by the following equations [10]:

$$Bi_2O_3(s) \overset{820^oC}{\leftrightarrow} Bi_2O_3(g) \overset{820^oC}{\leftrightarrow} Bi(g) + \frac{3}{2}O_2(g) \tag{5}$$

$$BiYbO_3 \overset{820^oC}{\leftrightarrow} Yb_2O_3 + Bi_2O_3 \tag{6}$$

The evaporation of PbO and Bi_2O_3 leads to excessive ZrO_2 and Yb_2O_3, and then these oxides form a stable $Yb_{0.2}Zr_{0.8}O_{1.9}$ pyrochlore phase. Furthermore, this pyrochlore

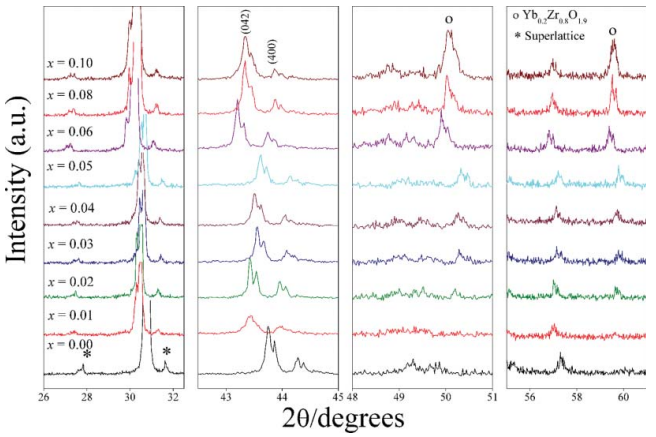

Figure 2 XRD patterns of the ¼ (h k l) reflections and the (042) and (400) peaks of perovskite phase, and extra peaks of the $Yb_{0.2}Zr_{0.8}O_{1.9}$ pyroclore phase in $(1-x)$PZ–xBY ceramics, with $x = 0.0$–0.1.

phase tends to increase with $BiYbO_3$ content increase, as found by the increasing of intensity of extra peaks of around 50° and 60° in Figure 2. A similar phenomenon has also been found in other solid solution systems [10]. Figure 2 shows enlarged profiles of the ¼ (h k l) superlattice reflections and (042) and (400) peaks of the perovskite phase, and extra peaks of the $Yb_{0.2}Zr_{0.8}O_{1.9}$ pyroclore phase in $(1-x)$PZ–xBY ceramics. The ¼ (h k l) superlattice peaks (*) and (042)/(400) of the perovskite phase were chosen for determining the crystal structure of PZ-BY ceramics. It was found that the superlattice reflections and splitting of the (2 4 0) peak were noticed at around 43° in all compositions. This result indicated that the crystal structure is an orthorhombic perovskite and the effect of adding BY does not change the symmetry of PZ throughout the studied composition range. Furthermore, instability of the PZ-BY perovskite structure, which has a small tolerance factor, prevented the MPB compositions from being synthesized. The calculated lattice parameters and unit cell volume of PZ-BY ceramics are listed in Table 1. It was found that the unit cell volume of PZ-BY ceramics at all compositions is higher than that of pure PZ, although the decreasing rate of average ionic radius at the A-site is higher than the increasing rate of average ionic radius at the B-site. An average ionic radii at the A-site and B-site ions in the $(Pb_{(1-3x/2)}Bi_x)(Zr_{(1-3x/4)}Yb_x)O_3$ can be determined by the equations:

$$r_{\text{A-site}} = \left(1 - \frac{3x}{2}\right) r_{pb^{2+}} + x r_{Bi^{3+}} \tag{7}$$

$$r_{\text{B-site}} = \left(1 - \frac{3x}{4}\right) r_{Zr^{4+}} + x r_{Yb^{3+}} \tag{8}$$

where the ionic radii of Pb^{2+} and Bi^{3+} in 12 coordinates and Zr^{4+} and Yb^{3+} in 6 coordinates of the perovskite were 1.49Å, 1.40Å, 0.72Å and 0.868Å, respectively [13]. The average ionic radii of the A-site and B-site ions for PZ –BY ceramics are listed in Table 2. It is found that the decreasing rate of average ionic radius at the A-site and increasing rate of average ionic radius at the B-site was 0.83 Å/mol and 0.33Å/mol, respectively. Thus the increase of unit cell volume may be described due to the

Table 2
Average ionic radius at the A-site and B-site and tolerance factor for $(1-x)$PZ–xBY ceramics

Composition (x)	Average ionic radius at A-site	Average ionic radius at B-site	Tolerance factor (t)
0.00	1.490	0.720	0.9639
0.01	1.482	0.723	0.9597
0.02	1.473	0.727	0.9554
0.03	1.465	0.730	0.9427
0.04	1.457	0.733	0.9469
0.05	1.448	0.736	0.9427
0.06	1.440	0.740	0.9385
0.08	1.423	0.746	0.9302
0.10	1.407	0.753	0.9218

evaporation of Bi_2O_3, resulting in change of the substitution ratio at the A-site and B-site. Furthermore, the large ionic radius of Yb^{3+} ions which is in excess in the system, can be expected to come into the $PbZrO_3$ perovskite structure in order to replace the Zr^{4+} ions. Therefore, the unit cell volume of PZ-BY ceramics is higher than its PZ. However, the swing of those values, as a function of composition, was observed over the composition range. This phenomenon could be described by the existence of pyrochlore phases and a change in the ratio of the substitution at the A-site and B-site. Regarding solid solutions, the average ionic radii of the A-site and B-site ions were used for tolerance factor calculation. For the ferroelectric perovskite; when $t < 1$, the antiferroelectric (AFE) phase stabilizes, but while $t > 1$, the ferroelectric (FE) phase stabilizes [14]. The current research group has recently found that if the t value of $PbZrO_3$-based perovskite is higher than that of pure PZ, the FE phase stabilizes. In contrast, an AFE phase is stabilized when the t value of $PbZrO_3$-based perovskite is lower than that of pure PZ [15]. The tolerance factor of $(Pb_{(1-3x/2)}Bi_x)(Zr_{(1-3x/4)}Yb_x)O_3$ ceramics decreases with increasing BY content as shown in Table 2. It is clearly seen that the t of all compositions is lower than 1 and lower than pure PZ. This result indicated that at room temperature the AFE phase is expected to be found. Furthermore, as expected, the transition temperature of PZ-BY ceramics is higher than that in pure PZ, due to the small tolerance factor of $BiYbO_3$. Subsequently, explanation of dielectric and ferroelectric properties supported these assumptions.

Figure 3 shows the temperature dependence of relative permittivity (ε_r) and loss ($\tan\delta$) of $(Pb_{(1-3x/2)}Bi_x)(Zr_{(1-3x/4)}Yb_x)O_3$ ceramics using measurement frequencies of 1–100 kHz. The relative permittivity curve of $(Pb_{(1-3x/2)}Bi_x)(Zr_{(1-3x/4)}Yb_x)O_3$ ceramics, where $0.00 \leq x \leq 0.10$ showed a sharp dielectric permittivity peak, was interpreted from the phase transition. This transition occurred from the orthorhombic AFE phase to the cubic PE phase at Curie temperature, and a later explanation of ferroelectric data supported this assumption. A frequency dependence of dielectric response was not observed at phase transition, which represent no evidence of occurrence of diffused of relaxor-like behavior. However, the dielectric data revealed a large dielectric loss at high temperature for all compositions, because space charge polarization and conductivity of insulating ceramics increased. The variations of Curie temperature (T_C), maximum relative permittivity ($\varepsilon_{r\ max}$) and maximum dielectric loss ($\tan\delta_{max}$) of each composition are shown in

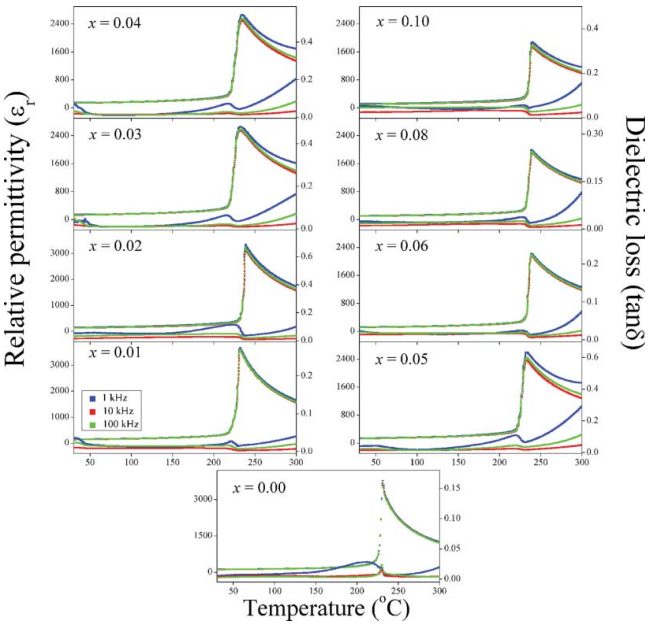

Figure 3 Temperature dependence on dielectric properties of (1-x)$PbZrO_3$ – $x$$BiYbO_3$ ceramics.

Table 3. The Curie temperature of PZ-BY for all the compositions was found to be higher than its value of pure PZ. Notably, this phenomenon was not observed in PZ-PYN and PZ-PYbN systems, although PYN and PYbN also could stabilize the AFE phase of pure PZ [8, 16]. The higher Curie temperature in PZ-BY ceramics may be attributed to the small tolerance factor of $BiYbO_3$, as found in $BiMeO_3$-$PbTiO_3$ solid solution [11]. However, the swing of Curie temperature, as a function of composition, was found throughout the composition range. This phenomenon may be due to appearance of the pyrochlore phase and change in the composition of PZ-BY after the evaporation of some Bi_2O_3. The $\varepsilon_{r\ max}$ of PZ-BY was seen to decrease with increasing BY content. Regarding lead-based perovskite, the presence of pyrochlore or secondary phase could deteriorate dielectric properties seriously. The amount of $Yb_{0.2}Zr_{0.8}O_{1.9}$ pyrochlore phase in the PZ-BY system increases with increasing BY content.

The differential scanning calorimetry (DSC) was used as a secondary technique to study and confirm the effect of $BiYbO_3$ on phase transition of the PZ-BY system. Figure 4 shows DSC curves of PZ-BY ceramics obtained when heating samples with a heating rate 10°C/min. As expected, a single exothermic peak was detected for all compositions of the PZ-BY system. This transition of energy attributed to the Curie temperature of the AFE - PE phase transition. The Curie temperature of PZ-BY ceramics is higher than its value of PZ, as shown in Table 3. As expected, there is no significant change in the Curie temperature throughout the composition range. The results of the DSC analysis are consistent with those of the dielectric measurements.

Based on DSC data, thermodynamic parameters including heat capacity (C_p), enthalpy change (ΔH^*), Gibbs energy change (ΔG^*) and entropy change (ΔS^*) were achieved and listed in Table 2. The enthalpy change was determined directly from the quantity of heat change in each step per unit mass of the sample. Thus, the ΔH^* was used

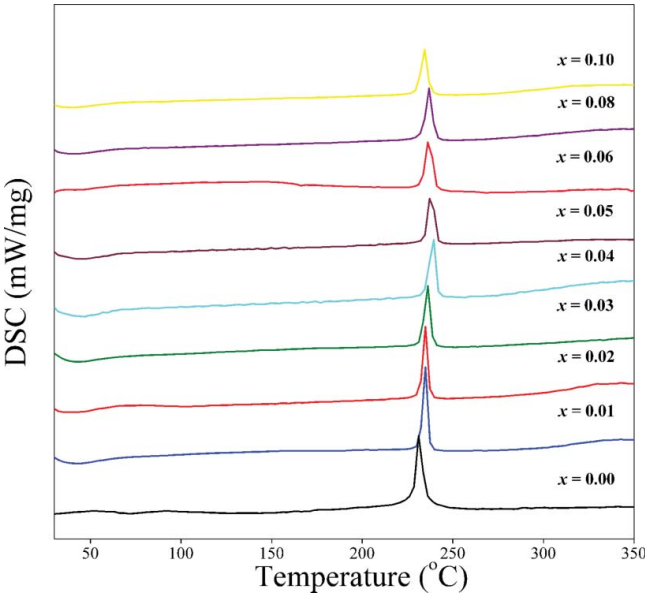

Figure 4 Typical differential scanning calorimetry (DSC) curves for (1−*x*)PZ–*x*BY ceramics, with $x = 0.00$–0.10.

to determine a specific heat capacity (C_p) by the following [17, 18]:

$$C_p = \frac{\Delta H}{\Delta T} \tag{9}$$

where $\Delta T = T_2 - T_1$; T_1 is the temperature at which point the DSC peak starts to depart from the baseline; and T_2 is the temperature at which point the peak lands. Then, the ΔG^* and the ΔS^* were calculated by the following equations [17, 18]:

$$\Delta S^* = 2.303 C_p \log \frac{T_2}{T_1} \tag{10}$$

$$\Delta G^* = \Delta H^* - T_p \Delta S^* \tag{11}$$

Table 3 clearly shows that the values of ΔH^* in all compositions are positive which indicated that AFE to PE phase transition is an exothermic process [19]. Furthermore, the values of ΔH^*, ΔS^*, C_P and ΔG^* change slightly when compared with those of pure PZ. These phenomena may be owing to the result of orthorhombic AFE to cubic PE transition throughout the composition range. However, those values are not a significant change or swing. This result is difficult to describe because the appearance of the pyrochlore phase and non-stochiometric quantities in the composition. Also, thermodynamic parameters of ferroelectric material have various variables as shown by the following equations [20]:

$$\Delta H^* = T_p \Delta S - x_i \Delta X_i - D_i \Delta E_i \tag{12}$$

$$\Delta G^* = S \Delta T - x_i \Delta X_i - D_i \Delta E_i \tag{13}$$

Table 3
Curie temperature (*T*c), maximum relative permittivity ($\varepsilon_{r\,max}$) and dielectric loss (tan δ_{max}) for $(1-x)$PZ–xBY ceramics

	Dielectric constant			DSC				
Composition (x)	T_C (°C)	$\varepsilon_{r\,max}$ at 1 kHz	tan δ_{max} at 1 kHz	T_C (°C)	ΔH *(Jg^{-1})	C_p ($Jg^{-1}K^{-1}$)	ΔS *($Jg^{-1}K^{-1}$)	ΔG *($J\,g^{-1}$)
0.00	231.0	3800	0.03	231.0	4.96	0.93	9.7×10^{-3}	0.0335
0.01	232.0	3700	0.02	235.0	4.72	1.10	9.3×10^{-3}	−0.0069
0.02	238.0	3350	0.04	235.5	4.53	0.92	8.9×10^{-3}	−0.0093
0.03	232.0	2650	0.03	236.0	4.50	0.74	8.8×10^{-3}	−0.0048
0.04	234.0	2660	0.04	239.0	4.62	0.74	9.0×10^{-3}	−0.0081
0.05	233.0	2580	0.07	238.5	4.34	0.99	8.5×10^{-3}	−0.0017
0.06	238.5	2230	0.01	237.0	4.51	0.68	8.9×10^{-3}	−0.0027
0.08	239.0	1990	0.02	237.5	4.46	0.67	8.7×10^{-3}	−0.0066
0.10	239.5	1900	0.04	234.5	4.72	1.10	9.3×10^{-3}	−0.0069

where six variables including S is entropy change, T is the temperature, X is stress, x is strain, E is electric field and D is displacement. For DSC measurement, when temperature is changed, entropy which point to the disorder of system also changes. There are many ways to introduce the disorder into a sample such as vibration of atoms, disordered electric dipoles, vacancies and other defects [21].

The P-E hysteresis loop was measured to clarify the dielectric behaviour of the AFE phase in the PZ−BY system. Measurements of the P-E hysteresis loop for all compositions were measured at 35 kV/cm of electric field strength. All compositions of the ceramics had a linear relationship between electric field and polarization at room temperature, since the electric fields were not enough for switching AFE domains. Generally, an AFE phase has a zero net dipole moment because the spontaneous polarizations of component sublattices are antiparallel to each other. As the external electric field is weak, the polarization is proportional to the external electric field, and macroscopic polarization hysteresis is not observed [22]. At room temperature, the electric field which required for inducing the FE phase in PZ ceramics is higher than the dielectric breakdown strength of the ceramics [4]. This result indicated that these $(Pb_{(1-3x/2)}Bi_x)(Zr_{(1-3x/4)}Yb_x)O_3$ ceramics, where $0.01 \leq x \leq 0.10$, have AFE behaviour at room temperature. Furthermore, P-E hysteresis loop measurements of PZ-BY ceramics, where $x = 0.01$ and $x = 0.03$, were operated at 35 kV/cm of electric field strength in a series of temperatures to clarify further how the phase transition occurs with temperature. The P-E hysteresis loops measured after the temperature had stabilized for at least 5 min are shown in Figure 5. For the composition, $x = 0.01$, when temperature is increased to 170°C, the P-E hysteresis loop shows a small polarization. The higher the temperature, the higher is the polarization observed. These results indicated that the FE phase can be induced more easily at high temperature than that at low temperature. However, the polarization is obtained by measurement the P-E hysteresis loop includes contributions from ferroelectric domain switching, dielectric displacement and electric conductivity [4, 23]. In this system, PbO and Bi_2O_3 evaporate during the sintering process, then defects such as bismuth, lead and oxygen vacancies are created which resulting in high electric conductivity. With rising temperature, the vacancies are much mobiles, thus the electric conductivity increases [24]. So, it is possible that a small polarization observed in the composition, $x = 0.01$, is attributed from the electric

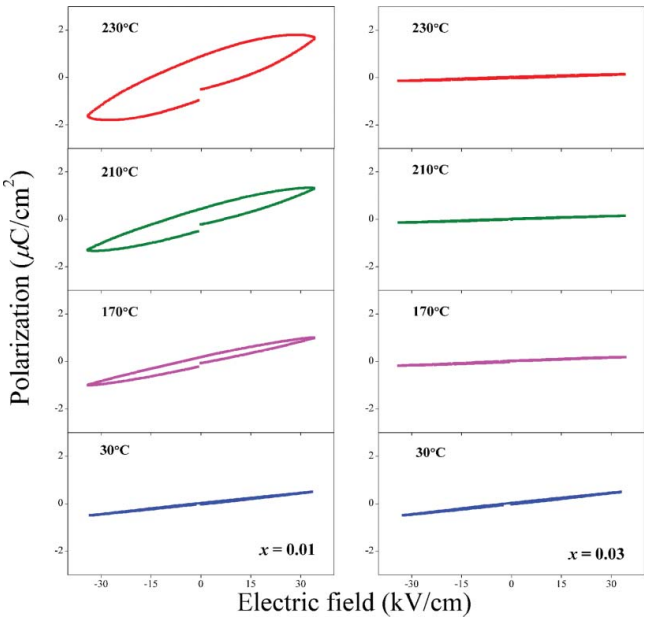

Figure 5 Polarization-electric field hysteresis loops of $PbZrO_3$ – $BiYbO_3$ ceramic at 4 Hz while heating at various temperatures.

conductivity. Unfortunately, the P-E hysteresis loop of the composition, $x = 0.03$, showed a linear relationship between polarization and electric field until the temperature was increased to 230°C, due to insufficient of electric field for switching AFE domains. As indicated in FE data, that the AFE phase existed below the temperature of maximum relative permittivity. The FE data support the assumption in dielectric results in that the AFE phase exists in PZ-BY ceramic at room temperature, and AFE changes to PE phase at Curie temperature.

4. Conclusion

The study of $(Pb_{(1-3x/2)}Bi_x)(Zr_{(1-3x/4)}Yb_x)O_3$, where $x = 0.01$–0.10, indicated that the perovskite structure with orthorhombic symmetry was a major phase for all compositions. The cubic pyrochlore phase, $Yb_{0.2}Zr_{0.8}O_{1.9}$, started to develop and increased in a intensity with increase content of $BiYbO_3$. From dielectric properties, DSC and P-E hysteresis results it is confirmed that the AFE phase of PZ can be stabilized by adding $BiYbO_3$, are result of the t value of PZ-BY being lower than that of pure PZ. In addition, the substitution of $BiYbO_3$ in the PZ perovskite also can enhance the Curie temperature of PZ-BY ceramics.

Funding

This work was supported by The Thailand Research Fund (TRF) grant No. BRG5680006. S. Niemcharoen acknowledges the support of National Research Council of Thailand (NRCT) (2557A11802281). U. Sukkha acknowledges the program for Strategic Scholarships for Frontier Research Network for the Join Ph.D. Program Thai Doctoral degree of the Commission on Higher 290 Education (CHE). RYG & AB acknowledge the support of INNAM/NSF (#0844081).

References

1. A. S. Mischenko, Q. Zhang, J. F. Scott, R. W. Whatmore, N. D. Mathur: Giant electrocaloric effect in thin-film $PbZr_{0.95}Ti_{0.05}O_3$. *Science*. **311**: 1270–1271 (2006).
2. S-T Zhang, A. B. Kounga, W. Jo, C. Jamin, K. Seifert, T. Granzow, J Rodel, D Damjanovic: High-strain lead-free antiferroelectric electrostrictors. *Adv Mater.* **21**: 4716–4720 (2009).
3. F. Jona, G. Shirane, F. Mazzi, R. Pepinsky: X-ray and neutron diffraction study of antiferroelectric lead zirconate, $PbZrO_3$. *Phys Rev.* **105**: 849–856 (1957).
4. B. Jaffe, W. R. Cook, H. Jaffe: *Piezoelectric Ceramics*. New York: Academic Press; 1971.
5. S. Wirunchit, P. Laoratanakul, N. Vittayakorn: Physical properties and phase transitions in perovskite $Pb[Zr_{1-x}(Ni_{1/3}Nb_{2/3})_x]O_3$ ($0.0 \leq x \leq 0.5$) ceramics. *J Phys D: Appl Phys.* **41**: 125406 (2008).
6. U. Sukkha, R. Muanghlua, S. Niemcharoen, B. Boonchom, N. Vittayakorn: Antiferroelectric-ferroelectric phase transition in lead zinc niobate modified lead zirconate ceramics: Crystal studies, microstructure, thermal and electrical properties. *Appl Phys A.* **100**: 551–559 (2010).
7. N. Vittayakorn, P. Charoonsuk, P. Kasiansin, S. Wirunchit, B. Boonchom: Dielectric properties and phase transition behaviors in (1-*x*) $PbZrO_3$ -*x*Pb ($Mg_{1/2}$ $W_{1/2}$) O_3 ceramics. *J Appl Phys.* **106**: 064104 (2009).
8. U. Sukkha, R Muanghlua, S. Niemcharoen, B. Boonchom, N. Vittayakorn: Effect of $Pb(Y_{1/2}Nb_{1/2})O_3$ additions on thermal and electrical properties of $PbZrO_3$ ceramics. Ferroelectrics. **416**: 8–15 (2011).
9. M. Drache, P Roussel, J. P. Wignacourt, P. Conflant: $Bi_{17}Yb_7O_{36}$ and $BiYbO_3$: Two new compounds from the Bi_2O_3-Yb_2O_3 equilibrium phase diagram determination. *Mater Res Bull.* **39**: 1393–1405 (2004).
10. G. Feng, H. Rongzi, L. Jiaji, L. Zhen, C Lihong, T. Changsheng: Phase formation and characterization of high Curie temperature *x*$BiYbO_3$-(1-*x*)$PbTiO_3$ piezoelectric ceramics. *J Eur Ceram Soc.* **29**: 1687–1693 (2009).
11. R. E. Eitel, C. A. Randall, T. R. Shrout, P. W. Rehrig, W. Hackenberger, S-E Park: New high temperature morphotropic phase boundary piezoelectrics based on $Bi(Me)O_3$-$PbTiO_3$ ceramics. *Jpn J Appl Phys.* **40**: 5999–6002 (2001).
12. A. Halliyal, T. R. Gururaja, U. Kumar, A. Safari: Stability of perovskite phase in $Pb(Zn_{1/3}Nb_{2/3})O_3$ and other A(B'B")O_3 perovskites. IEEE Trans. Ultrason. Ferroelectr & Freq Control. **33**: 437–441 (1986).
13. Y. Yamashita, Y. Hosono, K. Harada, N. Ichinose: Effect of molecular mass of B-site ions on electromechanical coupling factors of lead-based Perovskite piezoelectric materials. *Jpn J Appl Phys.* **39**: 5593–5596 (2000).
14. K. J. Rao, C. N. R. Rao: *Phase Transitions in Solid: An Approach to the Study of the Chemistry and Physics of Solids*. New York: McGraw-Hill; (1978).
15. U. Sukkha, W. Vittayakorn, R. Muanghlua, S. Niemcharoen, B. Boonchom, N. Vittayakorn: Phase transition behavior of the (1-*x*) $PbZrO_3$-*x* Ba ($Al_{1/2}$ $Nb_{1/2}$) O_3 solid solution. *J Am Ceram Soc.* **95**: 3151–3157 (2012).
16. U. Sukkha, R. Muanghlua, S. Niemcharoen, B. Boonchom, W. Vittayakorn, N. Vittayakorn: Effect of Pb ($Yb_{1/2}Nb_{1/2}$)O_3 on phase transition and thermal and electrical properties of PZ-PYbN solid solution on PZ-rich side. *J Mater Sci.* **47**: 1452–1459 (2012).
17. S. A. Halawy, N. E. Fouad, M. A. Mohamed, M. I. Zaki: Kinetic and thermodynamic parameters of the decomposition of chromium chromate in different gas atmospheres. *J Therm Anal Calorim.* **82**: 671–675 (2005).
18. R. H. Abu-Eittah, N. G. Zaki, M. M. A. Mohamed and L Kamel: Kinetics and thermodynamic parameters of the thermal decomposition of bis(imipraminium) tetrachlorocuprate, bis(imipraminium) tetrachloromercurate and imipraminium reineckate. *J. Anal. Appl. Pyrol.* **77**: 1–11 (2006).
19. P. Richet: *The physical basis of thermodynamics with applications to chemistry*. New York: Kluwer Academic/Plenum; (2001).

20. M. E. Lines, A. M. Glass: Principles and applications of ferroelectric and related materials. Clarendon: Oxford; (1977).
21. R. E. Newnham: Properties of materials: anisotropy, symmetry, structure. New York: Oxford; (2005).
22. F. Moura, A. Z. Simões, L. S. Cavalcante, M. A. Zaghete, J. A. Varela, E. Longoa: Ferroelectric and dielectric properties of vanadium-doped $Ba(Ti_{0.90}Zr_{0.10})O_3$ ceramics. *J Alloys Compd.* **466**: L15–L18 (2008).
23. H. Yan, F. Inam, G. Viola, H. Ning, H. Zhang, Q. Jiang, T. Zeng, Z. Gao, M. J. Reece: The contribution of electrical conductivity, dielectric permittivity and domain swiiching in ferroelectric hysteresis loops. *J Adv Dielectrics.* **1**: 107–118 (2011).
24 J. S. Kim, B. C. Choi, J. H. Jeong: Dielectric anormaly and electric conductivity of Nd-doped and Nd/V Co-doped $Bi_4Ti_3O_{12}$ ferroelectric ceramics. *J Korean Phys. Soc.* **55**:874–878 (2009).

Ferroelectrics

ISSN: 0015-0193 (Print) 1563-5112 (Online) Journal homepage: http://www.tandfonline.com/loi/gfer20

Effect of Annealing Time on the Cation Distribution in Mn Doped $CoFe_2O_4$

Rachanusorn Roongtao, Naratip Vittayakorn, Wantana Klysubun & Wanwilai C. Vittayakorn

To cite this article: Rachanusorn Roongtao, Naratip Vittayakorn, Wantana Klysubun & Wanwilai C. Vittayakorn (2016) Effect of Annealing Time on the Cation Distribution in Mn Doped $CoFe_2O_4$, Ferroelectrics, 492:1, 43-53, DOI: 10.1080/00150193.2015.1069924

To link to this article: http://dx.doi.org/10.1080/00150193.2015.1069924

Published online: 17 Feb 2016.

Ferroelectrics, 492: 43–53, 2016

ISSN: 0015-0193 print / 1563-5112 online
DOI: 10.1080/00150193.2015.1069924

Taylor & Francis
Taylor & Francis Group

Effect of Annealing Time on the Cation Distribution in Mn Doped $CoFe_2O_4$

RACHANUSORN ROONGTAO,[1,2] NARATIP VITTAYAKORN,[1,3] WANTANA KLYSUBUN,[2] AND WANWILAI C. VITTAYAKORN[1]

[1]Electroceramic Research Laboratory, College of Nanotechnology, King Mongkut's Institute of Technology Ladkrabang, Bangkok 10520, Thailand
[2]National Synchrotron Research Center, 111 University Avenue, Muang District, Nakhon Ratchasima 30000, Thailand
[3]Advanced Materials Science Research Unit, Department of Chemistry, Faculty of Science, King Mongkut's Institute of Technology Ladkrabang, Bangkok 10520, Thailand

In this work, the series of $CoFe_{2-x}Mn_xO_4$ powders were synthesized using the solid state method. The structure and lattice parameter of the samples were determined by the X-ray diffraction (XRD) and Rietveld refinement method. The morphology was confirmed without annealing and with annealing at 500°C for 4 and 100 h, with the samples examined by scanning electron microscopy (SEM). Then, the distribution of migrating cations was analyzed using X-ray absorption spectroscopy (XAS). Also, magnetic properties were examined by a vibrating sample magnetometer (VSM). It can be confirmed from the morphology that the average particle size before and after annealing remained unchanged, and ranged from 0.66 ± 0.20 μm to 0.79 ± 0.26 μm. Furthermore, the distribution of cations was no different after annealing Mn ions at 500°C for 100 h. However, the distribution of cations migrated to their site of preference after annealing Co and Fe ions in the structure. The result of migrations induced a saturated magnetization increase to 42.24 emu/g.

Keywords Cation distribution; X-ray absorption; EXAFS; cobalt ferrite; annealing

1. Introduction

Cobalt ferrite is an inverse spinel and important technological material, which exhibits moderate saturated magnetization (about 80 emu/g) and high coercivity (5400 Oe) as well as high resistance to wear and significant mechanical hardness [1–2]. In addition, the partial substitutions of Mn were found to be appropriate for magnetomechanical, embedded high magnetostriction applications and stress-sensing [3–4], since magnetic, electronic, and catalytic physical and chemical properties depend on cation distribution among the octahedral (B) and tetrahedral (A) sites. Thus, deciding on cation distribution between octahedral and tetrahedral sites in spinel ferrites plays an important role in determining the use of these materials, and has been the subject of many studies [5–7]. It is

Received October 26, 2014; in final form February 15, 2015.
Corresponding author: E-mail: wvittayakorn@yahoo.com
Color versions of one or more figures in this article can be found online at www.tandfonline.com/gfer.

acknowledged that causes of cation distribution over the spinel structure are composed of [8] particle size [9–10], synthetic methods [11], annealing temperature [12], octahedral site preference energy [13], size of interstices and ionic radii of ions, and annealing time [14].

V. G. Harris *et al.* [8] studied cation distribution in NiZn ferrite films, where Zinc concentration varied. The results showed that the Zinc cations occupied the A site only. The Fe cations were found to occupy both the B and A site, as did Nikel ions, but with a preference for the B site. Harris *et al.* believed that a large portion of the A site Nikel ions was natural to the thin film structure. Then, J. A. Gomes *et al.* [11] investigated cation distribution on the A and B site of copper ferrite nanoparticles that were prepared by coprecipitation and compared with copper ferrite by using the standard method. As a result, the nanoparticle sample presented dissimilar cation redistribution from the theory of copper ferrite, as it performed different cation distribution over A and B sites in ferrite, which was related to the different particle sizes obtained with various synthetic routes. Also, Z. J. Zhang *et al.* [12] determined the cation distribution in Mn ferrite spinel nanoparticles, using neutron diffraction at various temperatures. The Rietiveld method was used for fitting in order to obtain the cation distribution. The results of refinement suggest portions of Mn and Fe are on both the B and A site. Furthermore, the cation distribution can be modified by heat treatment in a vacuum. The literature reviews did not contain information about the effect of annealing time on the cation distribution of spinel ferrites. Thermal annealing was efficient noticeably on dielectric properties, ferroelectric properties, and crystal structure similar to PZT–PZN ceramic. A research by N. Vittayakorn *et al.* [15] prepared PZT–10PZN powders using the columbite precursor method. Thermal annealing was efficient noticeably when improving piezoelectric responses and dielectric PZT based ferroelectric ceramics. It also proved that annealing time has an influence on the electrical properties in 0.9PZT-0.1PZN ceramics.

Therefore, this work aimed to study the influence of annealing time on cation distribution in cobalt ferrite synthesized by a conventional mixed-oxide method. The samples were prepared by excess Mn doped cobalt ferrite, and the single phase ferrite composition was used to investigated the cation distribution in the structure. This composition made the cation sites apparent when the structure was restricted. Furthermore, transference of the cation to the preferred site was expected when the samples were annealed for a very long time. Also, control of the same average particle site of the samples was desirable for eliminating other effects of cation distribution. Thus, the samples were annealed at 500°C, due to the annealing temperature being controlled at their same average particle site, even if the annealing time took a long time. In addition, the annealing time was used for up to 100 h, due to expectation that a long annealing time would be suitable for cations changing between A and B sites.

A variety of probes can be considered for information on cation distribution; for instance, X-ray diffraction, Mössbauer spectroscopy and neutron diffraction. However, the neutron diffraction and X-ray diffraction used were limited by the low percentage of composition in the samples. Mössbauer spectroscopy was effective in deciding the surroundings of Fe ions, but did not provide information on the Mn cations and Co cation because the main purpose of this research was to emphasize cation site distribution for the structural study of spinel ferrite. Hence, extended X-Ray absorption fine structure (EXAFS) spectroscopy was chosen to detail information on the effect of annealing temperatures on manganese-doped cobalt ferrite, since EXAFS is seen as a powerful technique for presenting element specificity, chemical sensitivity and local structure. In

addition, EXAFS has been found recently as a useful method for investigating the cation distribution in spinel ferrites [7–8].

Consequently, this research focused on studying the effect of annealing time on cation distribution in Mn doped cobalt ferrite by using the X-ray absorption spectroscopy (XAS) technique. The crystal structures of $CoFe_{2-x}Mn_xO_4$ powders and confirmation of average particle size by scanning electron microscope (SEM) were reported. Furthermore, the magnetic properties between before and after annealing were discussed.

2. Experimental Procedure

Samples of the $CoFe_{2-x}Mn_xO_4$ system, where $x = 0.00$, 0.10, 0.20, 1.00, 1.10, and 1.15, were prepared by a mixed-oxide method. The reagent grades of Fe_2O_3 (Sigma-Aldrich, $\geq$ 99.0% purity), Co_3O_4 and Mn_2O_3 (Aldrich, $\geq$99.0% purity) were used as starting materials. The raw materials were weighed and mixed by the ball milling technique for 24 h in a PVC container using an alumina ball and ethanol as the medium. The mixed powders were dried in a hot oven and calcined at 900°C for 48 h with a heating/cooling rate of 5°C/min in an alumina crucible in air. The calcined powders were well ground using an agate mortar, and an X-ray diffractometer (XRD), Philips-XPert MPD, was employed at room temperature to identify the phase formation for all samples. Cu K_α radiation was applied with a step size of 0.02° and a scan rate of 3 s per step. Lattice parameters of the materials were determined from XRD patterns by the Rietveld refinement method using the FullProf program. The influence of thermal annealing was identified by the $CoFe_{0.90}Mn_{1.10}O_4$ powders being annealed at 500°C for 4 and 100 h with a heating/cooling rate of 5°C/min. The unchanging average particle sizes were confirmed by scanning electron microscopy (SEM), Hitachi S4700, with an accelerating voltage of 5 kV. The cation distribution without annealing and with annealing at 500°C for 4 and 100 h was characterized using EXAFS data from the Co K-edge (7709 eV), Fe K-edge (7112 eV), and Mn K-edge (6539 eV) in the transmission mode at room temperature, in the Siam Photon Laboratory at the XAS facility (BL-8), Synchrotron Light Research Institute. Also, magnetization measurements before and after annealing the samples were measured by a vibrating sample magnetometer (VSM) under a maximum applied magnetic field of 8 kOe at room temperature.

3. Results and Discussion

Figure 1 displays the X-ray diffraction of $CoFe_{2-x}Mn_xO_4$ powders at various compositions and calcined at 900°C for 48 h. The XRD patterns showed that peaks (when $x =$ 0.00–1.10) were of a single phase cubic structure and corresponded to JCPDS file no. 22–1086 and space group Fd3m (no. 227) [16]. However, the XRD pattern of the $CoFe_{0.85}Mn_{1.15}O_4$ powder detected secondary phases, which were Fe_3O_4, Fe_2O_3 and (Co, Mn)(Mn, Co)$_2O_4$ that corresponded to JCPDS file no. 28–0491, 25–1402 and 18–0409, respectively. Therefore, only single phase samples were used to investigate the lattice parameters, which were analyzed from XRD data by the Rietveld refinement method using the FullProf program, and the variation of lattice constants and results of a quantitative phase analysis from the refinement with Mn^{2+} doping are presented in Table 1. The structure refinement showed the corresponding fits and confirmed that the structure was cubic type. Data quality of structural refinement was checked basically by R-values (Rw) and a good fit (χ2). In addition, the distinction between XRD patterns, calculated data and experimental profiles displayed small value in the intensity scale, as

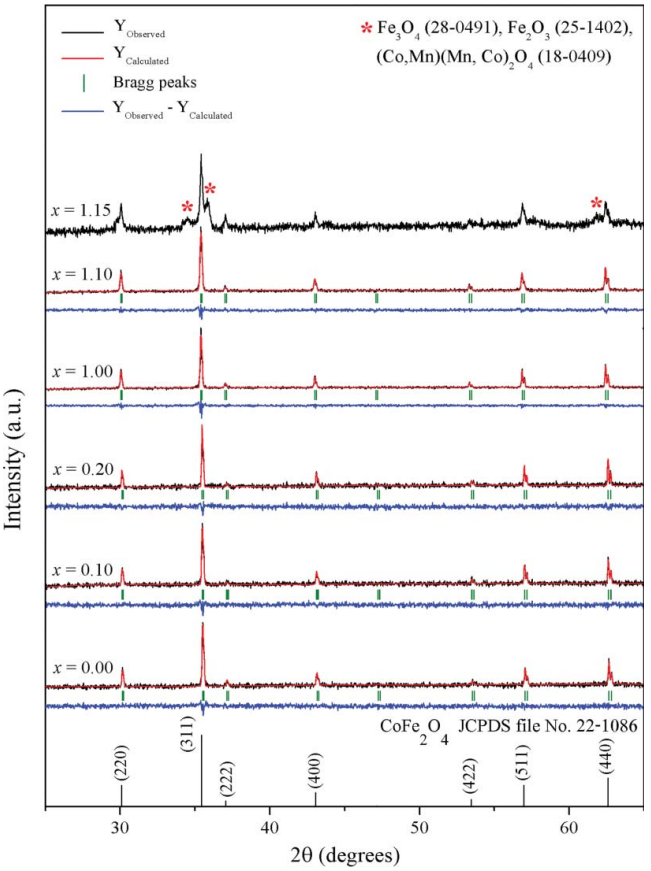

Figure 1. X-ray diffraction patterns of $CoFe_{2-x}Mn_xO_4$ powders calcined at 900°C for 48 h.

illustrated by the line, YObserved – YCalculated [17]. Furthermore, the results showed that the lattice constant and unit cell volume for each composition increased with increasing Mn ion, and gradually exhibited an almost linear dependence and linear regression with $R^2 = 0.9940$, which is in accordance with Vegard's law [16]. This showed that powders in the system are completed for continuous substitution, where atoms or ions existed [16]. The lattice parameter increased with doping, due to the ionic

Table 1
Lattice constant (a) and Rietveld refinement result of $CoFe_{2-x}Mn_xO_4$ powders calcined at 900°C for 48 h

X	a (Å)	V (10^6 pm^3)	R_w (%)	$\chi 2$
0.00	8.3843 (6)	589.010	4.01	1.11
0.10	8.3884 (6)	589.879	4.19	1.13
0.20	8.3904 (5)	590.401	4.45	1.19
1.00	8.4094 (3)	594.687	2.81	1.56
1.10	8.4103 (4)	594.893	2.62	1.33

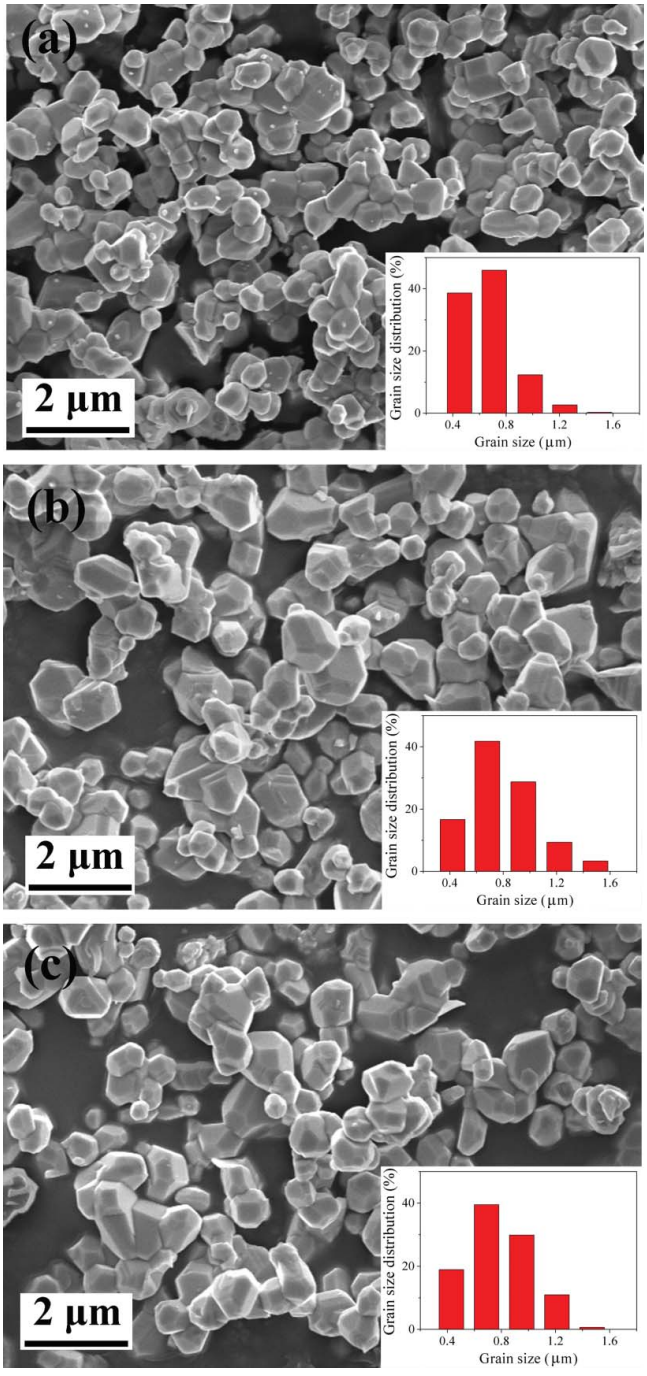

Figure 2. SEM micrographs of $CoFe_{0.90}Mn_{1.10}O_4$ powders with **(a)** no annealing, **(b)** annealing at 500°C for 4 h and **(c)** annealing at 500°C for 100 h.

Table 2
Average particle size, saturated magnetization, and coercivity of $CoFe_{0.9}Mn_{1.1}O_4$ powders as a function of annealing time.

Annealing time (h)	Average particle size (μm)	M_s (emu/g)	H_c (Oe)
no annealing	0.66 ± 0.20	37.67	130.43
4	0.79 ± 0.25	36.21	161.58
100	0.79 ± 0.23	42.24	169.37

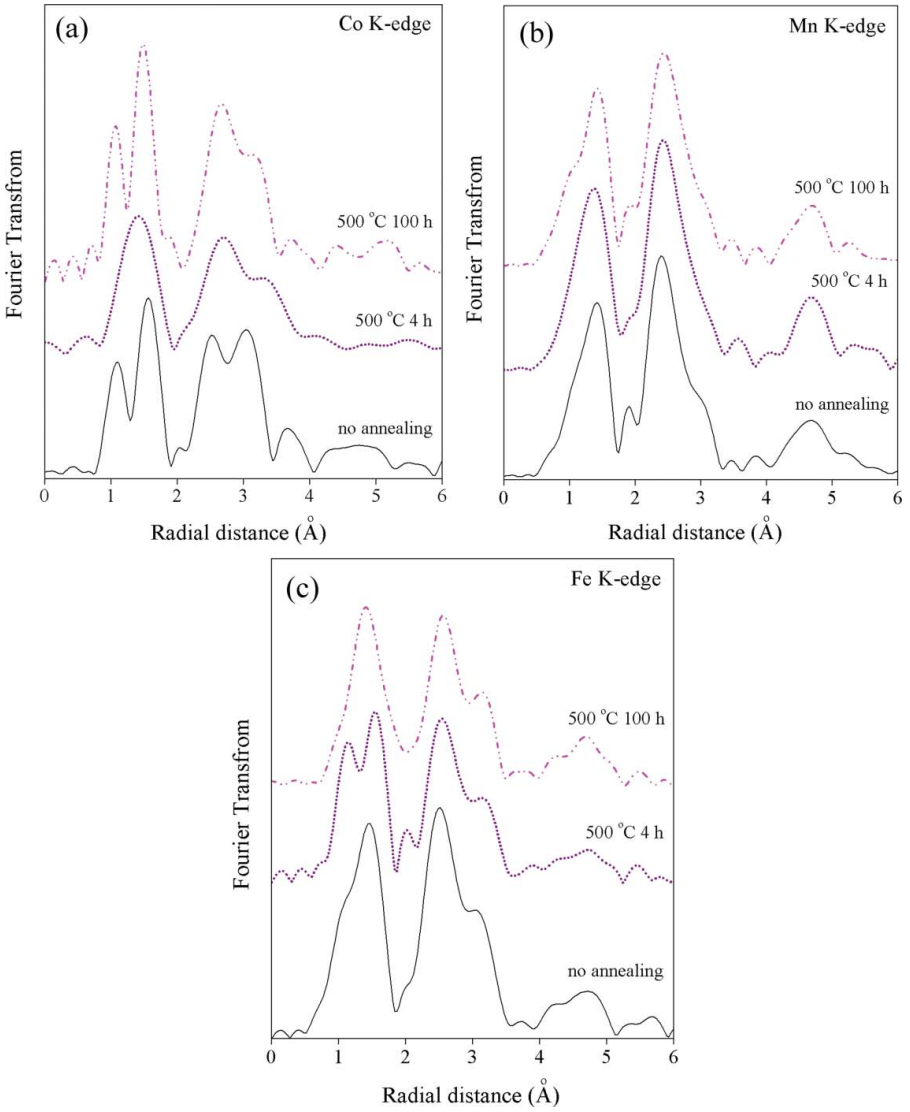

Figure 3. Fourier transformation of **(a)** Co, **(b)** Mn and **(c)** Fe EXAFS data for $CoFe_{0.90}Mn_{1.10}O_4$ powders.

radius of Mn coordinating six-fold with O^{2-} ions, which were larger than the ionic radius of Fe coordinating six-fold with O^{2-} ions in the structure [18].

The XRD results indicated that the $CoFe_{0.90}Mn_{1.10}O_4$ powders would be annealed, due to their composition having excess Mn dope in the structure. As expected, the cations in this composition were migrated easily to a preferred cation site when taking enough annealing time. Then, the $CoFe_{0.90}Mn_{1.10}O_4$ powders were annealed at 500°C for 4 and 100 h, with the average particle sizes confirmed by scanning electron microscope (SEM).

Figures 2 (a)–(c) show the morphology and particle size distribution of $CoFe_{0.90}Mn_{1.10}O_4$ powders as a function without annealing, and with annealing at 500°C for 4 and 100 h. Basically, the particles were of irregular shape and generally agglomerated. The average particle sizes of the powder were estimated from SEM micrographs and are presented in Table 2. The results showed that the average particle sizes did not change with annealing time, and they ranged from 0.66 ± 0.20 μm to 0.79 ± 0.23 μm. Furthermore, all samples showed small particle size distribution, as observed in the figures. The size distribution of powders without annealing mainly ranged from 0.57 to 0.83 μm, and slightly increased with annealing time. However, general size distribution still ranged from 0.57 to 0.83 μm. This minor increase in size distribution certainly would not have significant effect on cation distribution. These observations revealed that annealing time has no effect on average particle sizes, which affect cation distribution.

Then, the annealed and non-annealed samples were examined by X-ray absorption spectroscopy (XAS). EXAFS investigation determined the local bonding surrounding the Co, Fe and Mn. Spectra that encompassed the Co (7709 eV), Fe (7112 eV) and Mn (6539 eV) K-edges over an energy range from 100 eV below the energy edge to 800 eV above it. The information was examined by following standard EXAFS processing, which led to the Fourier transformation (FT) of information to radial coordinates. In this form, peak amplitudes reflected the occupancy of atomic shells, and the radial coordinate of the peak reflected the distance of atom shells from the absorber, which was not corrected for natural electron phase shift to XAS. [9]. Figure 3 shows the FT of Co, Fe, and Mn EXAFS data for the $CoFe_{0.90}Mn_{1.10}O_4$ powders without annealing and with annealing at 500°C for 4 and 100 h. The FT from a ΔK range of between 2 and 10 $Å^{-1}$, with k^2 weighting of the non-annealed Co EXAFS spectra, is shown as a function of distance in Figure 3 (a). This fact could be seen better when noticing the two maximum intense peaks. The first one centered near 1.5 Å presented the first shell with oxygen around the Co atoms. The second one centered near 2.8 Å, which corresponded to the next shell neighboring the Co atoms. The first peak showed splitting; the nearest metal Co-O bond neighbor appeared at r about 1.4 Å, according to the tetrahedral coordination absorbing cation, whereas the oxygen bond near 1.9 Å corresponded to the octahedral coordinating cation. The second peak also showed splitting; the peak centered near r about 2.6 Å corresponded to the Co-Co distance. This unique fingerprint identified the absorbing ion occupying the octahedral (B) sites, due to both scattering and absorbing atom occupancy on octahedral site contributions. The peak centered near 3.1 Å absorbed the tetrahedral (A) sublattice, including contributions from Co_A-M_A, Co_A-O, Co_A-M_B, and Co_B-O correlations (M is metal), but the identification was not unique. Therefore, related amplitudes of these peaks indicate qualitative distribution of the absorption cation at the B and A site [8–9, 14]. The non-annealed sample [Figure 3 (a)] shows splitting in the first and second peak, with the ratio between the second peak being approximately equal. Then, after annealing at 500°C for 4 and 100 h [Figure 3 (a)], the trend of amplitude in the second peak split associated only with the increased B site contribution at about 2.6 Å [Figure 4 (a)]. This can be explained by the increment of Co ions surrounding the octahedral site

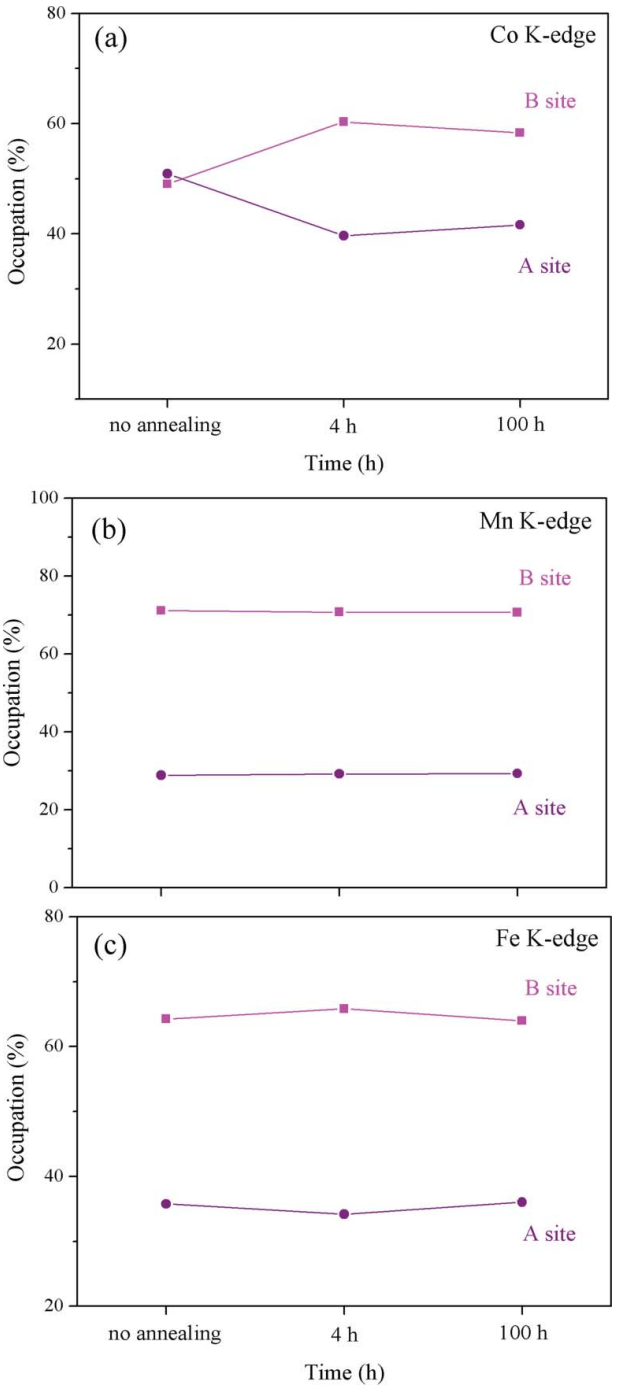

Figure 4. Trends in site occupation determined from amplitude as a function of annealing time for **(a)** Co, **(b)** Mn and **(c)** Fe K-edge.

that affects the annealing time for cation distribution. After annealing, the migration of Co ions to the B site was observed clearly in the EXAFS spectra because the cation distribution was determined by the preferred cation site, which related to the octahedral site preference energy (OSPE). The OSPE was estimated from a variety of thermodynamic data, in which the OSPE of Co ions exhibited a preference for B sites [11].

Also, interpretation of the Mn EXAFS spectra was related to the previous investigation carried out on the Co EXAFS. Examination of Figure 3 (b) and 4 (b) indicated that the Mn EXAFS spectra without an annealed sample showed the amplitude of a large peak centered near 2.6 Å of non-annealed powders that were relative to the B site contribution only. After annealing at 500°C for 4 and 100 h, the migration of Mn cations did not change, which can be explained by the annealing time having no effect on Mn ion distribution in the structure. Due to OSPE, Mn ions preferred the A or B site when taking a long annealing time, and the cation distribution trend did not change.

Then, Fe EXAFS data were shown in Figure 3 (c) and 4 (c) as a function of the radial coordinate. The Fe EXAFS spectra of the sample showed splitting in the second peak before annealing. This peak was not perfectly symmetric, and enlargement of the region between 2.6 Å indicated that Fe ions were localized at the B site. The amplitude trend of Fe ion distribution, which was relative to the B-site contribution only, decreased slightly after annealing at 500°C for 4 and 100 h. This indicated that annealing times influenced Fe ion distribution, and Fe ion OSPE was shown to prefer the A or B site [11]. Furthermore, the state of oxidation caused Fe ion migration. Basically, the chemical formula in spinel ferrite Fe ion was trivalent ions, which are generally smaller than divalent ones because the larger charge produces greater electrostatic attraction and therefore pulls the outer orbits inward [13, 19]. Also, the ionic radius of Fe ions was smaller than that of Mn ones [18]. Therefore, Fe ions were transferred to the tetrahedral (A) site more easily than Mn ions.

Figure 5 shows the magnetic hysteresis loop of $CoFe_{0.90}Mn_{1.10}O_4$ powders as a function without annealing, and with annealing at 500°C for 4 h and 100 h, and a maximum applied field of up to 8 kOe at room temperature. Basically, the magnetization curves of all samples were normal S-shaped and typically ferrimagnetic materials [19]. The variations of saturated magnetization (M_s) and coercivities (H_c) for $CoFe_{0.90}Mn_{1.10}O_4$ powder

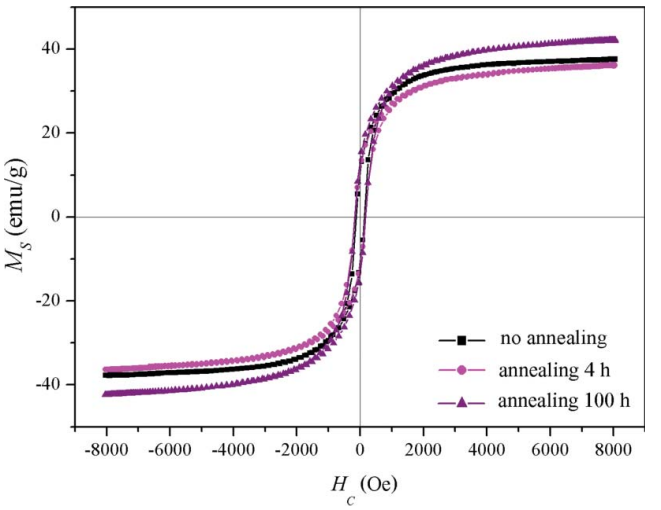

Figure 5. Magnetic hysteresis loops of $CoFe_{0.90}Mn_{1.10}O_4$ powders without annealing, and with annealing at 500°C for 4 and 100 h.

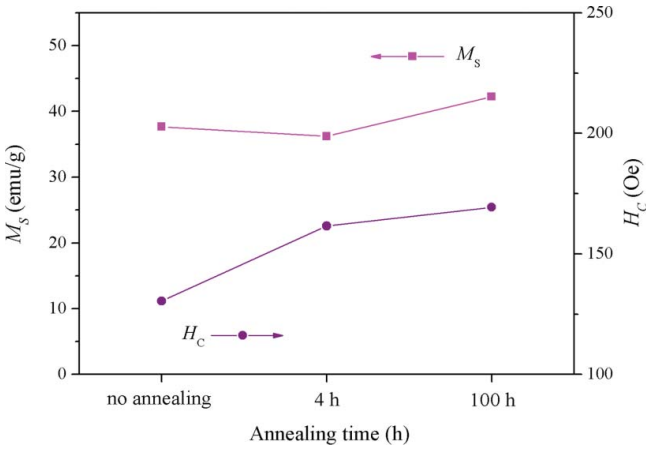

Figure 6. Variations of saturated magnetization and coercivities for $CoFe_{0.90}Mn_{1.10}O_4$ powders as a function of annealing time.

as a function of annealing time are exhibited in Figure 6 and Table 2. The results pointed out that saturated magnetization before annealing was 37.67 emu/g, but when the trend increased with increasing annealing time to 100 h, saturated magnetization read 42.24 emu/g. This confirmed that, as a result of increased saturated magnetization, the annealing time affected cation migration to the preferred site. The cation distribution results can explain the magnetic properties that determine the increase of saturated magnetization in $CoFe_{0.90}Mn_{1.10}O_4$ powders after annealing Co and Fe ions. Since net magnetic properties resulted from super exchange interaction of metal ions in the A and B site [6], increasing Co ions in the octahedral site with 3 μ_B, and decreasing Fe ions very slightly in the octahedral site with 5 μ_B, resulted in a net uncompensated moment of magnetization, and increasing saturated magnetization. Furthermore, the changing coercivity of the samples, when increasing the annealing time, can be attributed to annealing time having impact on structural distortion. Changing coercivity also increased the anisotropy of the Co ion, which was in accordance with large coercivities that were noticeable in the annealed samples [9].

4. Conclusion

In summary, Mn doped $CoFe_2O_4$ powders were synthesized successfully by the conventional mixed-oxide method. The structural characteristics revealed that samples had a single phase spinel structure. The unchanged average particle sizes of non-annealed and annealed samples were confirmed. Furthermore, annealing of $CoFe_{0.90}Mn_{1.10}O_4$ powders at 500°C for 100 h influenced cation distribution and increased magnetic properties to 42.24 emu/g.

Acknowledgment

The authors would like to thank the Department of Physics, Kasetsart University (KU) for its VSM measurement.

Funding

This research was supported by the KMITL Research Fund, and partly supported by grants from the National Research Council of Thailand (NRCT), National Nanotechnology

Center (NANOTEC) NSTDA, through its Center of Excellence Network, and the Thailand Research Fund (Grant No. BRG5680006). R. Roongtao would like to acknowledge the Ph.D. scholarship provided by Synchrotron Light Research Institute (Public Organization).

References

1. C. S. Kim, Y. S. Yi, K. T. Park, H. Namgung, J. G. Lee, Growth of ultrafine Co–Mn ferrite and magnetic properties by a sol–gel Method. *J Appl Phys.* **85**, 5223 (1999).
2. P. C. R. Varma, R. S. Manna, D. Banerjee, M. R. Varma, K. G. Suresh, A. K. Nigamc, Magnetic properties of $CoFe_2O_4$ synthesized by solid state, citrate precursor and polymerized complex methods: A comparative study. *J Alloy Compd.* **453**, 298–303 (2008).
3. H. M. I. Abdallah, T. Moyo, J. Z. Maomi, J. Supercond, The effect of annealing temperature on the magnetic properties of $Mn_xCo_{1-x}Fe_2O_4$ Ferrites Nanoparticles. Nov Magn. 2011; doi:10.1007/s10948-011-1231-4.
4. R. Roongtao, R. Baitahe, N. Vittayakorn, P. Seeharaj, W. C. Vittayakorn, Influence of Mn Doping on the Magnetic Properties of $CoFe_2O_4$. *Ferroelectrics*. **459**, 119–127 (2014).
5. S. S. More, R. H. Kadam, A. B. Kadam, A. R. Shite, D. R. Mane, K. M. Jadhav, Cation distribution in nanocrystalline Al^{3+} and Cr^{3+} co-substituted $CoFe_2O_4$. J Alloy Compd. **502**, 477–479 (2010).
6. Y. Köseoğlu, A. Baykal, F. Gözüak, H. Kavas, Structural and magnetic properties of $Co_xZn_{1-x}Fe_2O_4$ nanocrystals synthesized by microwave method. *Polyhedron*. **28**, 2887–2892 (2009).
7. D. Carta, G. Mountjoy, G. Navarra, et al. "X-ray Absorption Investigation of the Formation of Cobalt Ferrite Nanoparticles in an Aerogel Silica Matrix." *J Phys Chem C.* **111**, 6308–6317 (2007).
8. V. G. Harris, N. C. Koon, C. M. Williams, Q. Zhang, M. Abe, J. P. Kirkland, Cation distribution in NiZn-ferrite films via extended X-ray absorption fine structure. *Appl Phys Lett.* **68**, 15 (1996).
9. A. K. Giri, E. M. Kirkpatrick, P. Moongkhamklang, S. A. Majetich. "Photomagnetism and structure in cobalt ferrite nanoparticles. *Appl Phys Lett.* **80**, 13 (2002).
10. M. H. Nilsen, C. Nordhei, A. L. Ramstad, D. G. Nicholson, M. Poliakoff, A. Cabanas, XAS (XANES and EXAFS) Investigations of Nanoparticulate Ferrites Synthesized Continuously in Near Critical and Supercritical Water. *J Phys Chem C.* **111**, 6252–6262 (2007).
11. J. A. Gomes, M. H. Sousa, G. J. Silva, et al. "Cation distribution in copper ferrite nanoparticles of ferrofluids: A synchrotron XRD and EXAFS investigation. *J Magn Magn Mater.* **300**, e213–e216 (2006).
12. Z. J. Zhang, Z. L. Wang, B. C. Chakoumakos, J. S. Yin, Temperature Dependence of Cation Distribution and Oxidation State in Magnetic Mn-Fe Ferrite Nanocrystals. *J Am Chem Soc.* **120**, 1800–1804 (1998).
13. R. C. Buchanan. Ceramic Materials for Electronics, USA, Marcel Dekker, 2004.
14. A. Goldman. Modern Ferrite Technology. USA: Pittsburgh; 2006.
15. N. Vittayakorn, G. Rujijanagul, D. P. Cann, Investigation of the influence of thermal treatment on the morphologies, dielectric and ferroelectric properties of PZT-based ceramics. *J Alloy Compd.* **440**, 259–264 (2007).
16. Y. Köseoğlu, F. Alan, M. Tan, R. Yilgin, M. Öztürk, Low temperature hydrothermal synthesis and characterization of Mn doped cobalt ferrite nanoparticles. *Ceram Int.* 2012; in press.
17. S. Parida, S. K. Rout, L. S. Cavalcante, et al. Structural refinement, optical and microwave dielectric properties of $BaZrO_3$. *Ceram Int.* 2012; **38**, 2129–2138.
18. R. D. Shannon, Revised Effective Ionic Radii and Systematic Studies of Interatomic Distances in Halides and Chalcogenides. *Acta Crystallogr.* **A32**, 751–767 (1976).
19. A. J. Moulson, J. M. Herbert. Electroceramics. England: John Wiley & Sons; 2003.

Ferroelectrics

ISSN: 0015-0193 (Print) 1563-5112 (Online) Journal homepage: http://www.tandfonline.com/loi/gfer20

Dielectric Properties and Characterizations of Binary $Cu_{(2-x)}Mg_xP_2O_7$ Pyrophosphates

Rattanai Baitahe & Naratip Vittayakorn

To cite this article: Rattanai Baitahe & Naratip Vittayakorn (2016) Dielectric Properties and Characterizations of Binary $Cu_{(2-x)}Mg_xP_2O_7$ Pyrophosphates, Ferroelectrics, 490:1, 174-183, DOI: 10.1080/00150193.2015.1069923

To link to this article: http://dx.doi.org/10.1080/00150193.2015.1069923

Published online: 29 Jan 2016.

Ferroelectrics, 490: 174–183, 2016

ISSN: 0015-0193 print / 1563-5112 online
DOI: 10.1080/00150193.2015.1069923

Taylor & Francis
Taylor & Francis Group

Dielectric Properties and Characterizations of Binary $Cu_{(2-x)}Mg_xP_2O_7$ Pyrophosphates

RATTANAI BAITAHE[1] AND NARATIP VITTAYAKORN[1,2,3,4,*]

[1]Electroceramics Research Laboratory, College of Nanotechnology, King Mongkut's Institute of Technology Ladkrabang, Bangkok 10520, Thailand
[2]Advanced Materials Research Unit, Faculty of Science, King Mongkut's Institute of Technology Ladkrabang, Bangkok 10520, Thailand
[3]Department of Chemistry, Faculty of Science, King Mongkut's Institute of Technology Ladkrabang, Bangkok 10520, Thailand
[4]Nano-KMITL Center of Excellence on Nanoelectronic Devices, KMITL, Ladkrabang, Bangkok 10520, Thailand

Samples of the binary metal pyrophosphate, $Cu_{(2-x)}Mg_{(x)}P_2O_7$ ($x = 0.00 – 2.00$), were prepared via solid state reaction. Vibrational bands of $[P_2O_7]^{4-}$ anion which contains the O–P–O radical ($[PO_2]^-$) and the P–O–P bride ($[OPO]^-$) and approximate M–O stretching were identified by Raman scattering. A strong P–O–P band was observed clearly in Raman spectra, which indicated the formation of solid solution.The purity of synthetic powders were characterized by X-ray diffraction (XRD).The XRD patterns indicated that all the samples exhibited a single monoclinic phase structure. The complete solid solutions in the $Cu_{(2-x)}Mg_{(x)}P_2O_7$ ($x = 0.00 – 2.00$) system were obtained. The unit cell volume changed, due to the difference between the final product structure and $Cu_2P_2O_7$.X-ray absorption near the edge structure (XANES) technique was used to confirm oxidation state of copper in the $Cu_{(2-x)}Mg_xP_2O_7$.The relative permittivity and dielectric loss of the samples were measured. The bond length and bond angle were analyzed by EXAFS and Raman techniques. The relative permittivity was seen to maintain temperature by substituting Mg^{2+} with $Cu_2P_2O_7$. These results were used to explain the crystal structure of materials in order to change the bond which affects dielectric phenomena.

Keywords Binary metal pyrophosphates; relative permittivity; EXAFS analysis

1. Introduction

Metal phosphate ($M_x(PO_4^{3-})_y$ species) materials show interesting properties nowadays because of their wide applications in microwave dielectric materials, corrosion-resistant coatings, biomedical cements, chelating agents, glass ceramics, and high-quality fertilizers [1–3].The pyrophosphate $M_2P_2O_7$compounds have been reported to possess good dielectric loss properties as well as a relatively low sintering temperature [1]. It has been observed that an M radius structure greater than 0.97 Å [4] is a dichromate type (M =

Received October 26, 2014; in final form February 15, 2015.
*Corresponding author. E-mail: naratipcmu@yahoo.com
Color versions of one or more figures in this article can be found online at www.tandfonline.com/gfer.

Ca^{2+}, Sr^{2+}, Ba^{2+},Pb^{2+}, and Cd^{2+}), in which a pair of $P_2O_7{}^{4-}$ groups in eclipsed conformation crystallize at about the center of symmetry, with bridging O atoms spreading towards each other. When the M radius is less than 0.97 Å (M = Ni^{2+}, Mg^{2+}, Zn^{2+}, Co^{2+}, Cu^{2+}, and Mn^{2+}), the structure is a thortveitite type, in which $P_2O_7{}^{4-}$occurs in staggered conformation, and thortveitite-type pyrophosphate α-$Cu_2P_2O_7$or α-$Mg_2P_2O_7$exhibits a rather low sintering temperature when compared with metal oxides. However, single pyrophosphates groups (such as $Cu_2P_2O_7$, $Mg_2P_2O_7$, $Zn_2P_2O_7$, and $Co_2P_2O_7$) still show phase transition when changing temperature. Therefore, this primary research aimed to modify the structure of these materials in order to decrease dielectric loss and manipulate the relative permittivity to constant variations with temperature.

Most studies of metal phosphate focused on the synthesis and characterizations of both bulk [5, 6] and nano particles [7], kinetics and the thermodynamics of reaction [8, 9], and their properties [10, 11]. Nevertheless, the study of the relationship between dielectric properties and crystal structure is not widely understood, and is therefore of interest. The secondary aim of this study was to probe the crystal structure which influence dielectric phenomena of binary metal pyrophosphate compounds. Dielectric properties of the metal pyrophosphate group are due to two effects that comprise movement of M^{2+} ions in the octahedral MO_6 and shift of O atoms in the collinear P–O–P bridge. If the collinear P–O–P bond of the pyrophosphate ion is distorted, some distortion of octahedral MO_6 also can occur, which would improve the dielectric property of the molecule by producing polarization [12]. It is well known that the highly relative permittivity of tetragonal perovskite $BaTiO_3$ comes from off-centred Ti^{4+} ions in octahedral TiO_6. Putting a solid solution of Mg^{2+} into $Cu_2P_2O_7$ structure may bring about distortion of MO_6 and the collinear P–O–P bond and improve the dielectric properties of $Cu_2P_2O_7$ with a low sintering temperature. This research synthesized $Cu_{(2-x)}Mg_xP_2O_7$ (x = 0.0 – 2.0) before Raman, and XRD techniques investigated the crystal structure that affects dielectric properties. The phenomena of polarization in the crystal structure of compounds also were studied in order to characterize via bond length and bond angle.

2. Experimental Procedure

Synthesis of $Cu_{(2-x)}Mg_xP_2O_7$ (x = 0.00, 0.50, 1.00, 1.50, and 2.00) was conducted using the conventional method. High purity $(NH_4)_2HPO_4$ (99%) CuO (99.9%), and MgO (99.9%), were used as starting materials. Stoichiometric mixtures of raw materials were homogenized by vibratory milling with Yttria stabilized zirconia media in ethanol for 4 hrs. These were calcined at 800°C/24 hrs for x = 0.00, and 950°C/3 days for x = 0.50 – 2.00. The calcined powders were ball-milled again, pressed uniaxially into small pellets at the pressure of 1000 kg/cm^2 and sintered at 1000°C for 24h. The theoretical density of all ceramics observed was about 95–98%. Raman spectra were recorded in the range of 1300–100 cm^{-1} with eight scans on a thermo scientific DXR Raman microscope. The samples were excited with 488 nm light from an Ar^+ ion laser and the power of the incident beam was 12.5 mW. The crystal structure and crystallite sizes of the prepared samples were studied by X-ray powder diffraction with Cu K_α radiation(λ = 0.1546 nm). using a Bruker D8 AdvanceX-ray diffractometer (Bruker AXS, Karlsruhe, Germany) The dielectric properties were measured as a function of frequency (1–1000 kHz) and temperature (room temperature to 150°C) using an LCR meter (HP4284A; Hewlett-Packard, Palo Alto, CA).

Furthermore, substitutional solid solutions, in accordance with the Hume-Rothery rules, may form if the solute and solvent have: similar atomic radii; $R_{Cu(II)}$ = 0.73 Å and

$R_{Mg(II)}$ = 0.72 Å [13], similar electronegativities; Cu = 1.90 and Mg = 1.31, similar valency; Cu = : 2+ and Mg = 2+. And same crystal structure; β-$Cu_2P_2O_7$ = Monoclinic, C2/m and β-$Mg_2P_2O_7$ = Monoclinic, C2/m. These data show a high possibility of substitutional solid solution between Cu and Mg ions in pyrophosphate compounds. The X-ray absorption spectroscopy (XAS) was conducted on the beam line (BL8) of the National Synchrotron Research Center (Thailand). A double crystal Ge(220) was used for the EXAFS mono-chromator. X-ray absorption (XAS) spectra at the Cu K-edge were collected in transmission mode. The Cu foil, Cu_2O, CuO were used as a reference materials for X-ray absorption near-edge spectroscopy (XANES) measurements. The data from XANES were analyzed by aATHENA supporting program.

3. Results and Discussion

The Raman spectra of $Cu_{(2-x)}Mg_xP_2O_7$ are shown in Figure 1. It is clearly noticeable that the studied ceramics display more sharpness and splitting, especially in the low-frequency region (1300-100 cm^{-1}), indicating polymerization of $[PO_4{}^{3-}]$ to $[P_2O_7]^{4-}$. The vibration analysis of the $P_2O_7{}^{4-}$ ion which contains the O–P–O radical ($[PO_2]^-$) and the P–O–P bride ($[OPO]^-$) and approximate M–O stretching band were exhibited in Raman spectra. The Raman spectra are similar to those observed by Boonchom *et al.* [14]. The strong vibration bands around 1100 cm^{-1} are recognized to stretching of the PO_3 unit. The asymmetric (ν_{asym} POP) and symmetric stretch (ν_{sym} POP) bridge vibration for these samples are detected at about 960 and 730 cm^{-1}, respectively, while the asymmetric (δ_{asym} PO_3) and symmetric (δ_{sym} PO_3) bending vibration are observed at about 600 and 520 cm^{-1}, respectively. The metal oxide bonds are found in the 460–400 cm^{-1} region. When Cu^{2+} is replaced by Mg^{2+} in the $Cu_{(2-x)}Mg_xP_2O_7$ solid solutions, the Raman spectra show an important displacement of an absorption band found at about 420 cm^{-1}. This band can be assigned to the M–O bond lengths, which are responsible for the wave number increase from 411 to 458 cm^{-1} [15]. In composition x = 0.00 and 2.00 phases, three distinct bands that originate from the $\nu_{asym}(PO_3)$ vibrations are visible at 1214, 1146 and 1080 cm^{-1}. In

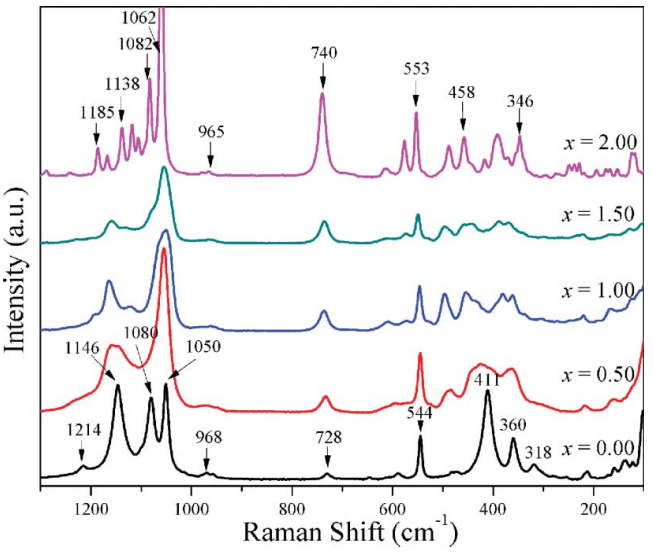

Figure 1. Raman spectra of $Cu_{(2-x)}Mg_xP_2O_7$; x = 0.00 –2.00.

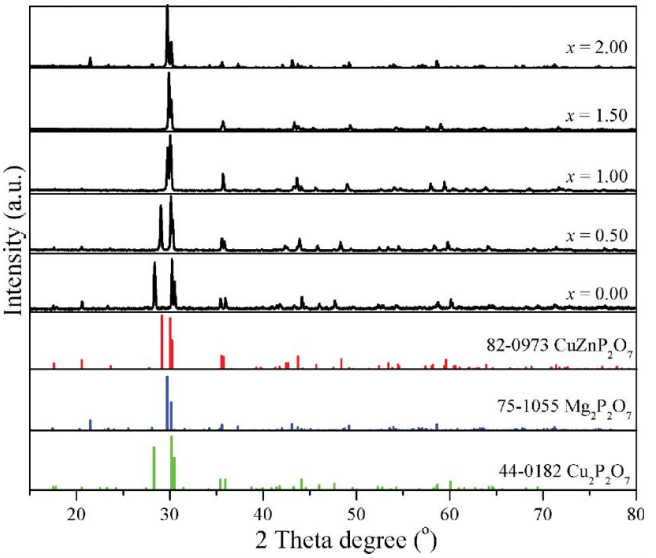

Figure 2. XRD patterns of $Cu_{(2-x)}Mg_xP_2O_7$; x = 0.00 –2.00.

the composition of $x = 0.50$, 1.00, and 1.50 phases, the bands remain at 1146 and 1080 cm^{-1}, but disappear at 1214 cm^{-1}. This indicates binary metal phosphates that closely resemble those of the β-$Mg_2P_2O_7$ phase, because the medium peak appears at around 1220 cm^{-1} only in the alpha phase [16].

Figure 2 shows the XRD patterns of $Cu_{(2-x)}Mg_xP_2O_7$ ($x = 0.00$, 0.50, 1.00, 1.50, and 2.00). Based on our analysis, the synthesized materials are solid solution and not a combination of the individual phases. These results indicate that the binary and the single metal compounds for $X_2P_2O_7$ (X = Ni, Mn, Zn, Mg, Cu, Co) types are isostructural. Consequently, all XRD pattern can be indexed distinctly based on a pure monoclinic phase with space group C2/c (Z = 4) for α-$Cu_2P_2O_7$, $P2_1/c$ (Z = 4) for α-$Mg_2P_2O_7$, and C2/m (Z = 2) for the samples as a function of x = 0.50 – 1.50, which noted to be similar to those of the standard XRD patterns of $M_2P_2O_7$ (PDF no. 44-0180 for Cu, PDF no. 75-1055 for Mg and PDF no.82-0973 for CuMg), respectively.

Table 1 presents the variation in these unit cell parameters with x. The half decreasing of lattice parameter c due to changing of space symmetry elements in the molecules from c (glide plane axis perpendicular to pincipal axis) to m (mirror plane perpendicular to pincipal axis) which show that increase symmetry in crystal structure. The lattice parameters a, c and β decrease. Parameter b increases, but the volume shows little change, due to the similar ionic radii of Mg and Cu($R_{Cu(II)} = 0.73$ Å and $R_{Mg(II)} = 0.72$ Å). These results indicated that when the crystal structure of α-$Cu_2P_2O_7$ was disturbed by different kinds of atom (Mg atoms). As a result the new crystal structure is stable at both low and high temperature. The average crystallite size of 72 ± 10 nm for α-$Cu_2P_2O_7$ sample was calculated from X-ray line broadening of the reflections of (002), (-112), (-202), (022), (112), (220), and (130), using Scherrer equation;

$$D = 0.89\lambda/\beta\cos\theta \quad (1)$$

where D is the mean size of the ordered (crystalline) domain, which may be smaller or equal to the grain size, θ is the diffraction angle,λ is the wavelength of X-ray radiation,

Table 1
Lattice parameters of $Cu_{(2-x)}Mg_xP_2O_7$; x = 0.00 – 2.00 calculated from XRD data

Composition (x)	Systems	a Å	b Å	c Å	β °	V Å^3
0.00	PDF no. 44-0182	6.88(0)	8.11(3)	9.16(1)	109.52(1)	482.30(0)
0.50	This work	6.75(1)	8.15(0)	4.54(4)	107.07(2)	238.75(2)
1.00		6.64(0)	8.21(4)	4.50(0)	106.52(0)	235.19(0)
1.50		6.57(4)	8.24(1)	4.48(2)	105.50(0)	233.71(1)
2.00	PDF no. 75-1055	6.94(0)	8.28(0)	9.04(0)	113.79(4)	476.47(4)

and β is the full width at half maximum (FWHM) [17], and were found to be 83 ± 9 nm for sample α-$Mg_2P_2O_7$ was calculated from X-ray line broadening of the reflections of (111), (002), (020), (212), (410) and (−422). The average crystallite size of 79 ± 9, 73 ± 6, and 61 ± 7 nm for binary metal pyrophosphates at $x = 0.50$, 1.00, and 1.50, respectively, were calculated from X-ray line broadening of the reflections of (110), (001), (−201), (021), (111), (220), and (130).The data of Raman and XRD results confirms that to single phase.

Normally, the oxidation state of Mg is two plus. However, the oxidation state of Cu can be one plus or two plus in phosphate form. So, X-ray absorption near the edge structure (XANES) technique was used to confirm oxidation state of copper in the $Cu_{(2-x)}Mg_xP_2O_7$ ($x = 0.0$, 0.5, 1.0, and 1.5) compounds. As XANES is very sensitive to both changes in the local geometry and the oxidation state, spectra collected at both edges could help in understanding Fourier transform evolutions. The XANES spectra of samples, as shown at the Cu K-edge in Figure 3, remain identical to the signal observed for

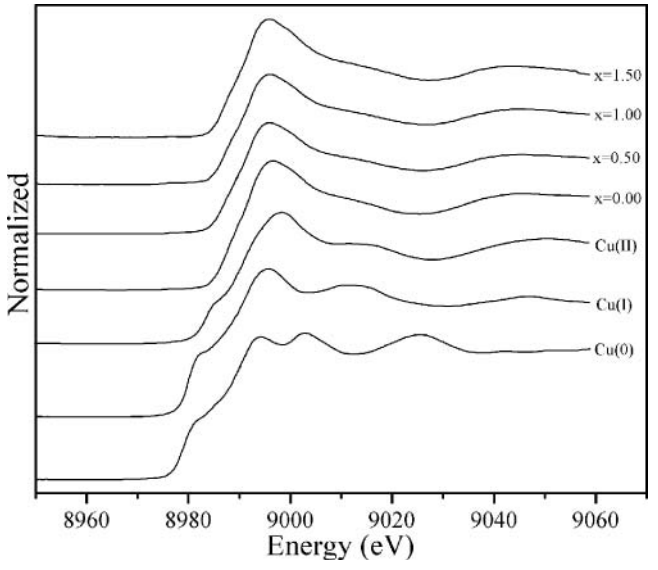

Figure 3. XANES spectra of $Cu_{(2-x)}Mg_xP_2O_7$; x = 0.00 –2.00.

Table 2
Energy positions of the absorption edges observed for measured samples

Compounds	Threshold value (E0)
Cu(0)	8979.27
Cu(I)	8979.91
Cu(II)	8986.25
0.00	8986.08
0.50	8986.65
1.00	8986.45
1.50	8986.69

Cu(II)O (Table 2), whatever the Cu content. Copper atoms thus remain Cu^{2+} in a monoclinic symmetry.

The relative permittivity(ε_r) and dielectric loss versus composition plots at 10, 100, and 1,000 kHz of $Cu_{(2-x)}Mg_xP_2O_7$are shown in Figure 4. The effect of porosity on the permittivity was eliminated by applying the Bosman and Havinga's correction [18], shown in Eq. (2), which can be used for dense ceramics having porosity lower than 5%:

$$\varepsilon_{r,\ \text{corrected}} = \varepsilon_{r,\ \text{measured}}(1 + 1.5P) \tag{2}$$

where $\varepsilon_{r,\ \text{measured}}$ and $\varepsilon_{r,\ \text{corrected}}$ are the measured and corrected relative permittivity, respectively, and P is fractional porosity and tabulated in Table 3. The bond angle and bond length were performed by the Raman scattering and EXAFS results for investigated phenomena of dielectric properties. Dielectric properties of the metal pyrophosphate group include two effects that comprise to shift of O atoms in the collinear P–O–P bridge and movement of M^{2+} ions in the octahedral MO_6. In the part of shifting of O atoms in the collinear P–O–P bridge. The sample as a function of $x = 0.50 - 1.50$, all compositions

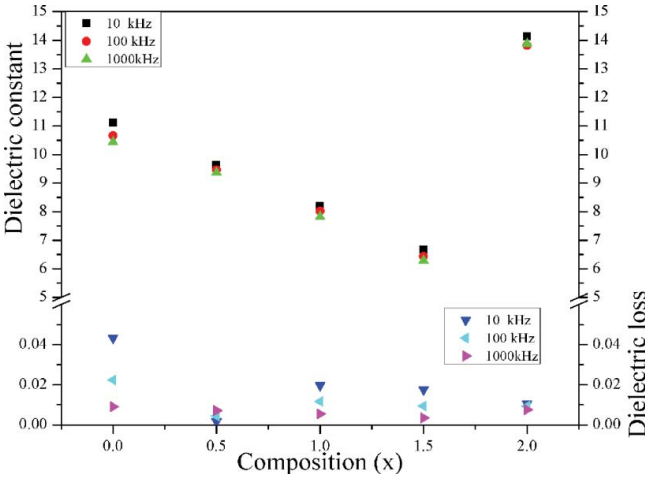

Figure 4. Plots of the relative permittivity and loss of $Cu_{(2-x)}Mg_xP_2O_7$; x = 0.00 –2.00.

Table 3
Relative permittivity and dielectric loss of samples

		Corrected relative permittivity			Dielectric loss		
Composition (x)	%TD	10k	100k	1000k	10k	100k	1000k
0.00	98.5	11.11	10.66	10.44	0.0432	0.0224	0.0091
0.50	96.7	9.64	9.46	9.36	0.0017	0.0045	0.0072
1.00	95.7	8.19	8.02	7.82	0.0196	0.0117	0.0055
1.50	96.4	6.67	6.43	6.29	0.0175	0.0095	0.0035
2.00	95.3	14.13	13.82	13.87	0.0105	0.0094	0.0076

have the space group C2/m. Previous researches reported that all of pyrophosphates compound which have monoclinic system with C2/m, the P–O–P angle are 180 degrees. Single metal pyrophosphates, α-$Cu_2P_2O_7$and α-$Mg_2P_2O_7$ were exhibited the P–O–P angle to157° [19] and 144° [20], respectively. In this case, the octahedral MO_6 site via bond strength or average bond length was considered by EXAFS data (Figure 5) and supported by Raman spectra in the wavenumber about 420 cm^{-1} (M-O stretching). As extended X-ray absorption fine structure (EXAFS) is very sensitive to change in local geometry, spectra collected at both edges could help in understanding Fourier transform evolutions. The data set were then analyzed by 'data processing' with ATHENA software [21]. The structure parameters of this analysis included approximate interatomic distances. The results demonstrated the asymmetry of CuO_6 octahedral due to the occurred of the little peak around last part of 1st shell introducing the Jahn-Teller distortion effect undergone by the copper octahedral centered site into the model or this peak may be the ghost peak [22]. The first shell was the consisting of six oxygen atoms, (M–O) with interatomic distances about2.10 Å. The next shell was described the combination of Cu-M (M = Cu/Mg), and Cu-P interaction. However, in this work was focus on 1st shell of M-O_6 octahedral. The relation of POP angle, M-O atomic distances from Raman and EXAFS were tabulated in Table 4. The average bond length of Mg-O_6 ($x = 2.00$) from XAS technic cannot be measured due to limitations of the instrument. Nevertheless, this data was supported by Raman result with increasing peak position which corresponded to decreasing bond length of EXAFS data Figure 5. The single metal pyrophosphate, $x = 2.00$ ($Mg_2P_2O_7$)

Table 4
Bond angle, M-O stretching position, and average bond length of samples

	POP angle	M-O_6	
Composition (x)	Angle(°)	Peak position (cm^{-1})	Bond length(Å)
0.00	157	411	2.18
0.50	180	420	2.16
1.00	180	431	2.13
1.50	180	442	2.09
2.00	144	458	—

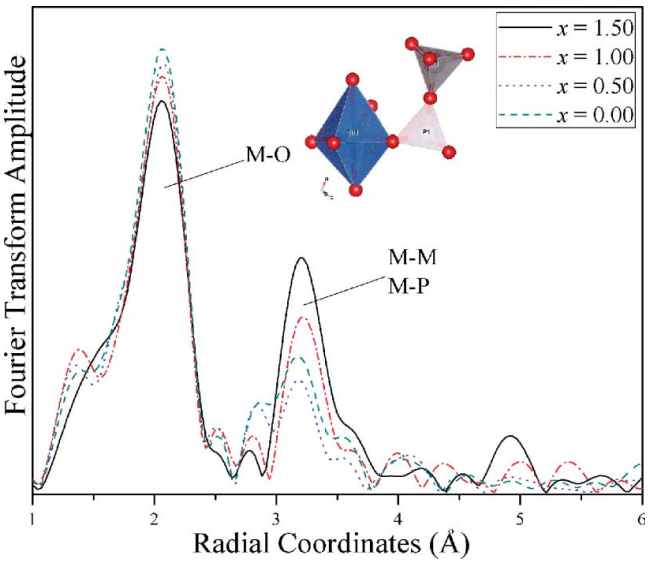

Figure 5. EXAFS patterns of $Cu_{(2-x)}Mg_xP_2O_7$; x = 0.00 –2.00.

was shown to be the highest ε_r and the least of P–O–P angles is 144 degrees, while $x = 0.00$ ($Cu_2P_2O_7$) was shown second ε_r and the second lowest of P–O–P angle is 157 degrees. Binary metal pyrophosphates, $x = 0.50 - 1.50$ with P–O–P angle is 180 degrees which exhibited ε_r less than single metal pyrophosphate compounds. These results show that the P–O–P angle is probably main factor for polarization of pyrophosphates group, by means of small P–O–P angle cause good polarization and good dielectric properties. Secondly, compounds having the same P–O–P angle (180 degrees), average bond length were considered. The samples as a function of $x = 0.50$, 1.00, and 1.50 displayed decreasing of ε_r when increasing Mg^{2+} compositions. These as a result of average M-O bond length decrease polarization. Therefore, dielectric permittivity tends to increase with increasing bond length, since decreasing bond strength, shows better polarization. The changing of dielectric loss of binary metal pyrophosphates at high frequency tends to be decreasing when x increases. Due to pyrophosphates compound are quite responsive in the high frequency range (microwave dielectric properties). But low frequency, the dielectric loss changing were difference may be caused by the extrinsic factors. Generally, high dielectric permittivity causes high dielectric loss. The Mg having lower EN (Electronegativity) than Cu [23] is introduced, positively charged defects will be destroyed thus decreasing the density of defect states of binary metal pyrophosphates, $Cu_{(2-x)}Mg_xP_2O_7$ system as compared to pure $Cu_2P_2O_7$. The addition of Mg to $Cu_2P_2O_7$ build up the amount of charged defect states that might affect the dielectric loss. Since the dielectric loss of these compounds depends upon the total amount of localized sites, the decrease of dielectric loss and the increase of Mg component can be understood in terms of the decreased density of defects on summing up of Mg to $Cu_2P_2O_7$. Due to the decreased number of dipoles (D^- and D^+) at higher component of Mg, the dielectric loss is also expected to decrease with Mg component as found in this study.

4. Conclusion

Metal pyrophosphates; $Cu_{(2-x)}Mg_xP_2O_7$ ($x = 0.0$-2.0) samples were prepared via solid state reaction to obtain information on solid solution formation, and characterized in the metal pyrophosphate group by Raman spectroscopy. XRD and Raman spectroscopy investigated the structure, which exhibited the compositions, $x = 0.50$ –1.50, as a copy structure of high temperature phase, β-$Cu_2P_2O_7$, with space group C2/m at both high and low temperature. The dielectric properties of the metal pyrophosphate group include two effects that comprise to shift of O atoms in the collinear P–O–P bridge and movement of M^{2+} ions in the octahedral MO_6. The experimental results were shown that P-O-P angle in $P_2O_7^{4-}$ ions is the main factor. Narrow angles will cause more polarization than wide angles. Furthermore, increasing bond length in the octahedral site (M-O) increases polarization, because it affects the bond strength of octahedral MO_6.The binary metal pyrophosphates have high dielectric permittivity and low dielectric loss, especially in $x = 0.50$.

Acknowledgment

We would like to thank the Synchrotron Light Research Institute (Public Organization) for XAS measurement.

Funding

This work was partially supported by the Thailand Research Fund (TRF) under Grant No. BRG5680006.

References

1. J. I. Bian, D. W. Kim, and K. S. Hong: Microwave dielectric properties of $A_{(2)}P_{(2)}O_{(7)}$ (A = Ca, Sr, Ba; Mg, Zn, Mn). *Jpn J Appl Phys.* **43**, 3521–3525 (2004).
2. J. J. Bian, D. Kim, and K. S. Hong: Microwave dielectric properties of $(Zn_{1-x}Mn_x)_{(2)}P_2O_7$. *J Mater Sci.* **40**, 1801–1803 (2005).
3. W. Wenwei, F. Yanjin, W. Xuehang, L. Sen, and L. Shushu: Preparation via solid-state reaction at room temperature and characterization of layered nanocrystalline $NH_4MnPO_4 \bullet H_2O$. *J Phys Chem Solids.* **70**, 584–587 (2009).
4. M. Weil, B: Stöger Crystal chemistry of transition metal diarsenates $M_2As_2O_7$ (M = Mn, Co, Ni, Zn): Variants of the thortveitite structure. *Acta Crystallographica Section B: Structural Science.* **66**, 603–614 (2010).
5. Z. W Xiao, G. R. Hu, Z. D. Peng, K. Du, and X. G. Gao: Solid state synthesis and characterization of iron(II) pyrophosphate $Fe_2P_2O_7$. *Chinese Chem Lett.* **18**, 1525–1527 (2007).
6. A. Bensalem, M. Ahluwalia, T. V. Vijayaraghavan, and YH Ko: Synthesis of amorphous $MgHPO_4 \bullet x(R)$ [R = Ethanol; Ethylene glycol] in anhydrous media. *Mater Res Bull.* **32**, 1473–1483 (1997).
7. C. Díaz, M. L. Valenzuela, V Lavayen, K Mendoza, DO Peña, and O'Dwyer C: Nanostructured copper oxides and phosphates from a new solid-state route. *Inorg Chim Acta.* **377**, 5–13 (2011).
8. D. Brandová, M. Trojan, M. Arnold, F. Paulik, and J. Paulik: Mechanism of dehydration and condensation of $CuHPO_4 \bullet H_2O$. *J Therm Anal.* **34**, 1449–1454 (1988).
9. D. Brandová, M. Trojan, F. Paulik, and J. Paulik: Mechanism of dehydration of $ZnHPO_4 \bullet H_2O$. *J Therm Anal.* **32**, 1923–1928 (1987).
10. A. Jouini, J. C. Gâcon, M. Ferid, and M. Trabelsi-Ayadi: Luminescence and scintillation properties of praseodymium poly and diphosphates. *Opt Mater.* **24**, 175–180 (2003).

11. T. Yang, and J. Lin: Hydrothermal syntheses and low temperature magnetic behaviors of $ACo_3(P_2O_7)_2$ (A = Ca, Sr, Ba, Pb). *J Solid State Chem.* **198**, 1–5 (2013).
12. C. H. Kim, and H. S. Yim: The effect of tetravalent metal on dielectric property in ZrP_2O_7 and TiP_2O_7. *Solid State Commun.* **110**, 137–142 (1999).
13. R. Shannon: Revised effective ionic radii and systematic studies of interatomic distances in halides and chalcogenides. *Acta Crystallogr A.* **32**, 751–767 (1976).
14. B. Boonchom, and N. Phuvongpha: Synthesis of new binary cobalt iron pyrophosphate $CoFeP_2O_7$. *Mater Lett.* **63**, 1709–1711 (2009).
15. H. Bih, I. Saadoune, H. Ehrenberg, and H. Fuess: Crystal structure, magnetic and infrared spectroscopy studies of the $LiCr_yFe_{1-y}P_2O_7$ solid solution. *J Solid State Chem.* **182**, 821–826 (2009).
16. K. Pogorzelec-Glaser, A. Pietraszko, B. Hilczer, and M. Połomska: Structure and phase transitions in $Cu_2P_2O_7$. *Phase Transit.* **79**, 535–544 (2006).
17. B. D. Cullity: Elements of X-ray Diffraction. London: Addison-Wesley Publishing (1977).
18. A. J. Bosman, EE Havinga: Temperature Dependence of Relative permittivitys of Cubic Ionic Compounds. *Phys Rev.* **129**, 1593–1600 (1963).
19. B. E. Robertson, and C. Calvo: The crystal structure and phase transformation of α-$Cu_2P_2O_7$. *Acta Crystallogr.* **22**, 665–672 (1967).
20. B. E. Robertson, and C. Calvo: Crystal structure of β-$Cu_2P_2O_7$. *CanJChemistry.* **46**, 605–612 (1968).
21. B. Ravel, and M. Newville: ATHENA, ARTEMIS, HEPHAESTUS: data analysis for X-ray absorption spectroscopy using IFEFFIT. *J Synchrotron Radiat.* **12**, 537–541 (2005).
22. J. A. Gomes, M. H. Sousa, G. J. da Silva, F. A. Tourinho, J. Mestnik-Filho, R. Itri, GdM Azevedo, and J. Depeyrot: Cation distribution in copper ferrite nanoparticles of ferrofluids: A synchrotron XRD and EXAFS investigation. *J Magn Magn Mater.* **300**, e213–e216 (2006).
23. L. Pauling: The nature of chemical bond. Calcutta: Oxford and IBH (1969).

Taylor & Francis
Taylor & Francis Group

Ferroelectrics

ISSN: 0015-0193 (Print) 1563-5112 (Online) Journal homepage: http://www.tandfonline.com/loi/gfer20

Phase Transition, Dielectric and Piezoelectric Properties of Lead-Free Piezoelectric $(K_{1/2}Na_{1/2})NbO_3 - Bi(Zn_{2/3}Nb_{1/3})O_3$ Ceramics

Manoon Sutapun, Rangson Muanghlua & Naratip Vittayakorn

To cite this article: Manoon Sutapun, Rangson Muanghlua & Naratip Vittayakorn (2016) Phase Transition, Dielectric and Piezoelectric Properties of Lead-Free Piezoelectric $(K_{1/2}Na_{1/2})NbO_3 - Bi(Zn_{2/3}Nb_{1/3})O_3$ Ceramics, Ferroelectrics, 490:1, 1-12, DOI: 10.1080/00150193.2015.1070649

To link to this article: http://dx.doi.org/10.1080/00150193.2015.1070649

Published online: 29 Jan 2016.

Ferroelectrics, 490: 1–12, 2016

ISSN: 0015-0193 print / 1563-5112 online
DOI: 10.1080/00150193.2015.1070649

Phase Transition, Dielectric and Piezoelectric Properties of Lead-Free Piezoelectric $(K_{1/2}Na_{1/2})NbO_3 - Bi(Zn_{2/3}Nb_{1/3})O_3$ Ceramics

MANOON SUTAPUN,[1] RANGSON MUANGHLUA,[2] AND NARATIP VITTAYAKORN[1,3,4,*]

[1]College of Nanotechnology, King Mongkut's Institute of Technology Ladkrabang, Bangkok 10520, Thailand
[2]Department of Electronics Engineering, Faculty of Engineering, King Mongkut's Institute of Technology Ladkrabang, Bangkok 10520, Thailand
[3]Advanced Materials Research Unit, Faculty of Science, King Mongkut's Institute of Technology Ladkrabang, Bangkok 10520, Thailand
[4]Nano-KMITL Center of Excellence on Nanoelectronic Devices, KMITL, Ladkrabang, Bangkok, 10520, Thailand

*The lead–free piezoelectric ceramics on the binary system of (1-x)$(K_{1/2}Na_{1/2})NbO_3$–x$Bi(Zn_{2/3}Nb_{1/3})O_3$ [(1-x)KNN–xBZnN]; x = 0.01–0.10 were fabricated by the solid state reaction method. The structure and phase transition were determined by X-ray diffraction.The results of XRD patterns suggested that $Bi(Zn_{2/3}Nb_{1/3})O_3$ completely diffuse into the $(K_{1/2}Na_{1/2})NbO_3$ lattices to form a solid solution. The crystal structure was in an orthorhombic phase for $x \leq 0.01$. When reaching $0.01 < x \leq 0.07$, crystal structure became a rhombohedral phase and transformed to a pseudo-cubic structure for $x > 0.07$. The dielectric data shows that the amount of $Bi(Zn_{2/3}Nb_{1/3})O_3$ added in the $(K_{1/2}Na_{1/2})NbO_3$ decreases the ferroelectric – paraelectric transition temperature progressively. Furthermore, optimum piezoelectric and ferroelectric properties were observed at the composition, x = 0.01: effective piezoelectric coefficients (d_{33} *) = 498 pm/V, remanent polarization (P_r) = 23.3 $\mu C/cm^2$, coercive field (E_c) = 14 kV/cm, maximum strain (S_{max}) = 0.3% and Curie temperature (T_C) = 380°C. The results of this study show that KNN with a small amount of $Bi(Zn_{2/3}Nb_{1/3})O_3$ (x = 0.01) can be one of lead-free piezoelectric ceramic candidate.*

Keywords Lead-free piezoelectric; phase transition; $(K_{1/2}Na_{1/2})NbO_3$-$Bi(Zn_{2/3}Nb_{1/3})O_3$

1. Introduction

Piezoelectric ceramics such as lead zirconate titanate ($PbZr_xTi_{1-x}O_3$; PZT) or PT-relaxor based compound are used widely in micro-actuators, piezoelectric sensors, transducers, and several piezoelectric devices [1,2]. Nevertheless, these materials contain about 60 wt% of lead oxide, which has been dangerous to our environment. Thus, there is a great

Received October 26, 2014; in final form February 15, 2015.
*Corresponding author. E-mail: naratipcmu@yahoo.com
Color versions of one or more of the figures in this article can be found online at www.tandfonline.com/gfer.

need for developing lead–free piezoelectric materials with excellent piezoelectric properties to instead lead-based materials for various applications. Many class of lead-free piezoelectric ceramic such as $Bi_{1/2}Na_{1/2}TiO_3$–based [3–5], Bi–layered structure [6,7], $BaTiO_3$–based [8–11] and alkaline niobate–based [12–23] have been investigated. Recently, research on lead–free piezoelectric materials had been focused mainly on $K_{1/2}Na_{1/2}NbO_3$ (KNN)–based ceramics because of their excellent piezoelectric, ferroelectric properties, and exhibited high Curie temperature. Nevertheless, it is difficult to achieve a dense ceramic of pure KNN from the normal sintering method due to the volatility of potassium at high temperature [12–15]. Thus, various techniques such as spark plasma sintering [16] hot forging press [17] and hot isostatic pressing [12], were used to improve density of KNN ceramics. However, these techniques were insufficient for the mass production industry. To improve the densification of KNN ceramics, many other perovskite structures was used to form the solid solution with KNN such as $BaTiO_3$ [18], $Bi_{1/2}Na_{1/2}O_3$ [19], $SrTiO_3$ [20], $LiTaO_3$ [21], $LiNbO_3$ [22], $LiSbO_3$ [23] and $Li(Nb,Sb)O_3$ [15].

Bi–based complex perovskite materials have been investigated extensively because Bi^{3+} has similar electronic configuration to Pb^{2+}. Recent work reported the solid solution between Bi–complex perovskites with lead titanate such as $PbTiO_3$–$Bi(Zn_{1/2}Ti_{1/2})O_3$ [24], $PbTiO_3$–$Bi(Mg_{1/2}Ti_{1/2})O_3$ [25] and $PbTiO_3$–$Bi(Ni_{1/2}Ti_{1/2})O_3$ [26] systems. These materials exhibited a high Curie temperature, which is of great advantage for high–temperature application. Thus, Bi–complex perovskite also can form solid solutions with lead–free piezoelectric ceramics. For example, Jarupoom *et al.* [27] published results on $(Bi_{1/2}Na_{1/2})TiO_3$–$(Bi_{1/2}K_{1/2})TiO_3$–$Bi(X_{1/2}Ti_{1/2})O_3$, where x = Mg and Ni system which reported large effective piezoelectric coefficients (d_{33} *) greater than 500 pm/V. Paterson *et al.* [28] observed a high remanent polarization ($P_r \sim 35\ \mu C/cm^2$) in the $(Bi_{1/2}Na_{1/2})TiO_3$–$Bi(Zn_{1/2}Ti_{1/2})O_3$ system. Many research groups focused on a solid solution between KNN with Bi–complex perovskite with the 1:1 of b–site ordering. Nevertheless, there were no systematic investigations on the Bi–complex perovskite with the 2:1 of b–site ordering. In this study, the amount of $Bi(X_{2/3}Nb_{1/3})O_3$, where X = Zn, was used partially to substitute KNN. The influence of $Bi(Zn_{2/3}Nb_{1/3})O_3$ (BZnN) addition on the sintering ability, crystal structure, phase transition, dielectric, ferroelectric and piezoelectric properties of the KNN ceramics being investigated.

2. Experimental Procedure

The (1-x)KNN–xBZnN (x = 0.01–0.10) ceramics were fabricated by the solid-state reaction method. Reagent–grade metal oxide, carbonate and bicarbonate powders: Na_2CO_3 (99.5%), $KHCO_3$ (99.50%), Nb_2O_5 (99.95%), Bi_2O_3 (99.95%) and ZnO (99.0%) were used as starting materials. Typically, the K_2CO_3 powder was used as a starting material. However, it is very difficult to take accurately weighing process coursed by K_2CO_3 has a highly hygroscopic property. This caused the non-stoichiometric of the K/Na ratio, resulting in poor electrical properties. The $KHCO_3$ powder was used as the starting material instead of K_2CO_3 powder because of its sensitivity to low hygroscopic property [29]. All powders were placed in an oven at 120°C for two days before using. All the starting powders were mixed with ethanol using vibro-milling process for 4 h with yttrium stabilized zirconia ball, and then dried at 80°C in oven. The mixed powders were calcined at 900°C for 2 h in covered crucibles, then ball milled again. The granulated powders were pressed into pellets with 11 mm of diameter, using 3 wt% polyvinyl alcohol (PVA) as a binder. After PVA burnout at 500°C for 2 h, the samples were sintered at between 1,100–

1,140°C for 2 h using heating/cooling rate of 5°C/min. All ceramic samples were sintered in sealed crucibles, which In order to reduce loss of the volatile components such as potassium, sodium and bismuth; all ceramic samples were sintered in sealed crucibles.

The structure of the sintered pellets was analyzed by X–ray diffraction (XRD) (D8 XRD Advance Bruker). The density of the ceramics was calculated by the Archimedes method [30]. The microstructure of the sintered pellets from fractured surfaces was observed by means of scanning electron microscopy (SEM, ZEISS, Evo-Ma10). Prior to the electrical measurements, the sintered ceramics were polished to achieve flat and parallel surfaces. And then, a silver paste was applied on both sides as the electrode and then the samples were fired at 650°C for 30 min. The dielectric properties were measured as a function of temperature using an LCR meter (HP4284A, Hewlett-Packard, Palo Alto, CA). A ferroelectric tester system (RT66B; Radient Technologies, Inc., Albuquerque, NM) was used to measure the polarization-electric field hysteresis (P–E) loop at 4 Hz at room temperature.

3. Results and Discussion

The x-ray diffraction patterns of sintered (1-*x*)KNN–*x*BZnN ceramics are shown in Figure 1. Pure perovskite structure was found in all compositions. Pyrochlore phase such as $K_4Nb_6O_{17}$ was not observed at all. The result indicates that the BZnN was diffused completely into the KNN lattices, with Bi^{3+} and Zn^{2+} entering the $(K_{1/2}Na_{1/2})^+$ and Nb^{5+} site, to form a new solid solution in the studied compositions. The detailed crystal structure was studied by analyzing XRD patterns using the Rietveld method and Full-prof software. All of the samples were refined, and they assumed three different structures: orthorhombic with space group *Amm2*, rhombohedral with space group *R3m* and pseudo–cubic with space group $Pm\bar{3}m$. The low χ^2 values obtained in this investigation indicate that the refinement was performed successfully in all parameters. Illustrations of the χ^2 index of (1-*x*)KNN–*x*BZnN ceramics are shown in Table 1. Figure 1 shows the optimum

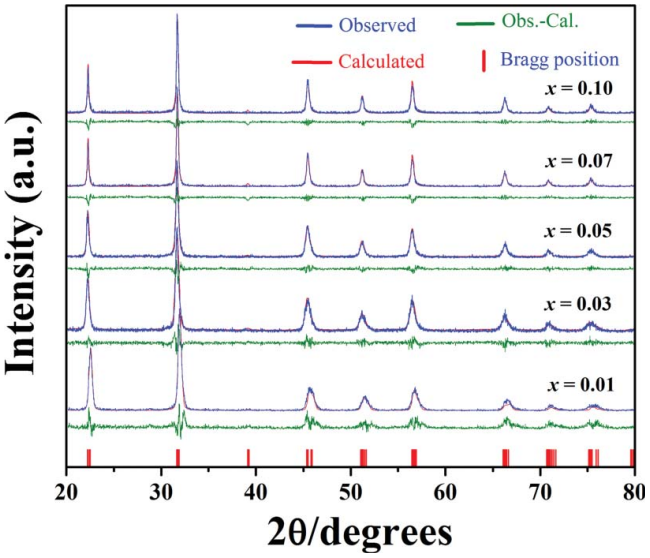

Figure 1. XRD patterns of (1-*x*)KNN–*x*BZnN ceramics.

Table 1
Crystal structure, χ^2, lattice parameters and unit cell volume of (1-x)KNN–xBZnN ceramics calculated from XRD data by the Rietveld method

Compositions (x)	Crystal structure	χ^2	Lattice parameter (nm)			V(nm^3)
			a	b	c	
0.00 [29]	O	–	3.9995	3.9490	3.9995	63.16
0.01	O	2.12	3.9934	3.9533	4.0033	63.20
	R	3.01	–	–	–	–
	P	3.14	–	–	–	–
0.03	O	1.90	–	–	–	–
	R	1.71	3.9830	–	–	63.23
	P	2.01	–	–	–	–
0.05	O	1.93	–	–	–	–
	R	1.87	3.9871	–	–	63.38
	P	2.01	–	–	–	–
0.07	O	2.06	–	–	–	–
	R	2.01	3.9872	–	–	63.39
	P	2.05	–	–	–	–
0.10	O	2.03	–	–	–	–
	R	2.04	–	–	–	–
	P	2.00	3.9884	–	–	63.44

O = orthorhombic; R = rhombohedral; P = pseudo–cubic.

refined structure for each composition. As observed, the experimental patterns fit well with the simulated patterns (calculated). The differences between the experimental and simulated patterns also are showed at the bottom of the individual pattern. At the composition, $x = 0.01$, the ceramic showed orthorhombic symmetry with space group *Amm2* because reflections of the phase fitted well, except at the calculated peak positions with $\chi^2 = 2.12$. However, with increasing BZnN content, the ceramics began to exhibit rhombohedral structure with space group *R3m* for the composition, $x < 0.01$, and transform to a pseudo-cubic structure when the composition, $x = 0.10$. The dielectric information described later further supports this hypothesis. In addition, most of the peaks were found to shift slightly to a lower angle with increasing BZnN content, which indicates a change in the cell parameters. The lattice parameters and unit cell volume calculated by the Rietveld method are presented in Table 1. The results indicated that the unit cell volume increased slightly with increasing BZnN content. In the A–site of perovskite structure, the Bi^{3+} is slightly smaller than $(K_{1/2}Na_{1/2})^{+}$ However, the unit cell volume increased due to the substitution of larger average ion size of B–site cation of Zn^{2+} (0.74Å) to Nb^{5+} (0.64Å). The crystal structure was in an orthorhombic phase for $x \leq 0.01$. When reaching $0.01 < x \leq 0.07$, crystal structure became a rhombohedral phase and transformed to a pseudo-cubic structure for $x > 0.07$. The same phenomenon has been observed in previous work [31]. By adding $Bi(Zn_{1/2}Ti_{1/2})O_3$ to KNN, the crystal structure transforms from orthorhombic to rhombohedral structure and changes slightly to pseudo–cubic structure.

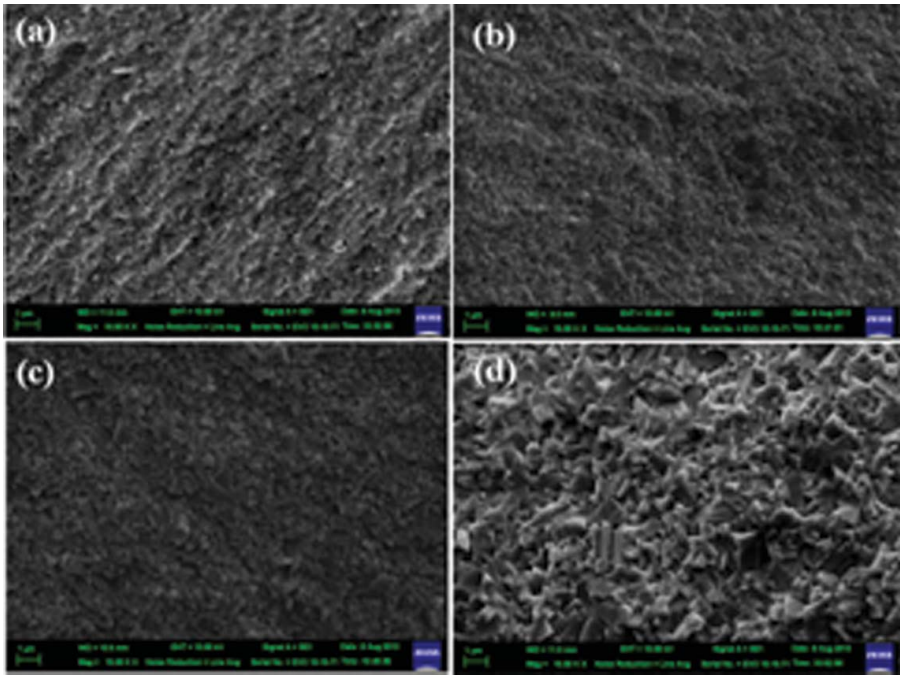

Figure 2. SEM micrographs of the fractured surface of (1-*x*)KNN–*x*BZnN ceramics at various compositions, (a) $x = 0.01$, (b) $x = 0.03$, (c) $x = 0.05$ and (d) $x = 0.10$.

Figure 2 demonstrates the SEM micrographs of the fracture surface of (1-*x*)KNN–*x*BZnN ceramics. No abnormal grains were found in any samples, indicating no formation of pyrochlore phase coursed by high volatility of K, Na or Bi element. All samples were well sintered and possessed dense ceramics. The average grain size increased when the BZnN content increased. The relative density of all ceramics was about 95.2–98.4%. The increasing in relative density can be described by the Bi^{3+} and Zn^{2+}, Nb^{5+}ion are considered to enter the A– and B–site, respectively, and many oxygen vacancies could be found in the ceramics. This phenomenon leads to expedite lattice diffusion, followed by increase of the density of the ceramic [32].

The temperature dependence of relative permittivity (ε_r) and loss tangent (tan δ) at 10 kHz of (1-*x*)KNN–*x*BZnN ceramics be displayed in Figure 3. The composition, $x = 0.01$, shows that the phase transitions at 120 and 380°C correspond to those from orthorhombic ferroelectric phase to tetragonal ferroelectric phase ($T_{O\text{-}T}$) and tetragonal ferroelectric to cubic paraelectric (T_C) phases, respectively. The phase transition behaviors of these ceramics and that of pure KNN were similar and observed at 200 and 420°C, respectively [12]. Nevertheless, both of these phase transitions shifted to a lower temperature with increasing BZnN content. At the composition in the range of $0.03 \leq x \leq 0.07$, the O–T phase transition disappeared, and the ceramic became a rhombohedral structure with a permittivity maximum transition temperature (T_m) of 340, 280 and 198°C at compositions $x = 0.03$, 0.05 and 0.07, respectively. Finally, the structure transforms to a pseudo–cubic structure in the composition $x = 0.10$ with T_m of 91°C. These dielectric data are consistent with XRD analysis. In addition, The T_m decreased with increasing BZnN content. The decreasing in the T_m is caused the substitution of the larger average size of B–site cation of Zn^{2+} to Nb^{5+}ion, causing a decreasing in the

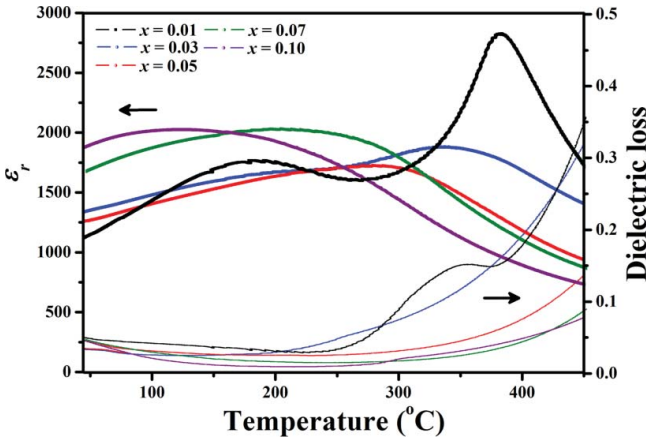

Figure 3. Dielectric permittivity as a temperature function of (1-*x*)KNN–*x*BZnN.

tolerance factor (*t*) [33]. For KNN has a value *t* is 1.012, when BZnN was added, the *t* value reduced to 1.006 at composition, $x = 0.10$.The *t* value was calculated using the ionic radii of Shannon and Prewitt [34]. Similar behavior has been observed in the $Bi_{1/2}K_{1/2}TiO_3$–KNN [33], $BiZn_{1/2}Ti_{1/2}O_3$–$BiScO_3$–$BaTiO_3$ [35] and KNN-$Bi(Zn_{1/2}Ti_{1/2})O_3$ ceramics [31]. Figure 4 illustrates the variation of the $1/\varepsilon_r$ as a function of temperature of (1-*x*)KNN–*x*BZnN; $x = 0.01$ ceramic at 10 kHz. The deviation degree from the Curie–Weiss law can be defined by the following ΔT_m:

$$\Delta T_m = T_{dev} - T_m \tag{1}$$

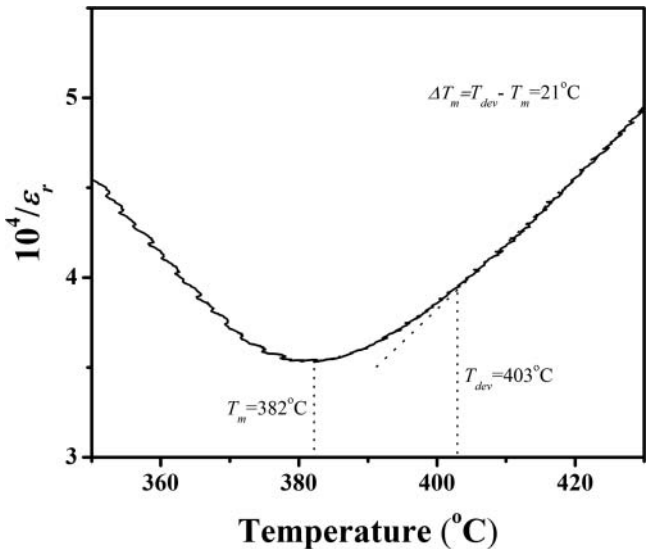

Figure 4. Variation of the $1/\varepsilon_r$ as a function of temperature at 10 kHz of (1-*x*)KNN–*x*BZnN; $x = 0.01$ ceramics.

where T_{dev} is at dielectric permittivity starts to deviate from the Curie–Weiss law. The T_m is the temperature at maximum permittivity. At the composition, $x = 0.01$, the ΔT_m is 21°C. The calculated ΔT_m increased from 21 to 230°C with increasing BZnN content, indicating enhanced diffuse phase transition behavior. The diffuseness of a phase transition can be determined by the following:

$$\frac{\varepsilon_m}{\varepsilon_r} = 1 + \frac{(T - T_m)^\gamma}{2\delta_\gamma^2} \quad (1 \le \gamma \le 2) \tag{2}$$

when ε_m is the maximum value of permittivity ε_r at T_m, δ_γ is as a measure of the degree of diffuseness of the peak. And γ is the degree of diffuseness. The γ value can have a ranging from 1 for a normal ferroelectric to 2 for an ideal relaxor ferroelectric material. The δ_γ value can be calculated from the slope of $\varepsilon_m/\varepsilon_r$ versus $(T\text{-}T_m)^2$ and the γ value can be calculated from the slope of $\ln(1/\varepsilon_r - 1/\varepsilon_m)$ versus $\ln(T - T_m)$, which both should be linear. Figure 5 displays the plots of $\ln(1/\varepsilon_r - 1/\varepsilon_m)$ versus $\ln(T - T_m)$ of (1-x)KNN–xBZnN ceramics. A linear relationship was observed in all ceramics. The data form Figure 5 was used to calculate γ and δ_γ values for each samples, as shown in Table 2 varies between 1.12 to 1.77 and 4.3 to 6.7, respectively. The γ and δ_γ values increases gradually with increasing BZnN content, suggesting that the ceramics have transformed from 1st order phase transition to diffuse phase transition. A diffuse phase transition has been explored in many perovskite structures such as $Bi_{1/2}Na_{1/2}TiO_3$–based ceramics [3], and KNN–$SrTiO_3$ [20] $BiZn_{1/2}Ti_{1/2}O_3$–$BiScO_3$–$BaTiO_3$ [35] and KNN–$Bi(Zn_{1/2}Ti_{1/2})O_3$ [31] systems. It is well known that not only differences in ionic radii but also the ionic charges of the cation in A– and B–site on the ABO_3 perovskite structure are favorable for the formation of an ordered structure in the A–site complex $(A'A'')BO_3$ or B–site complex $A(B'B'')O_3$ perovskite structure [36]. Regarding (1-x)KNN–xBZnN ceramics, Bi^{3+} (1.45 Å) substitutes Na^+ (1.39 Å) and K^+ (1.64 Å) in the A–site, while Zn^{2+} (0.74 Å) substitutes

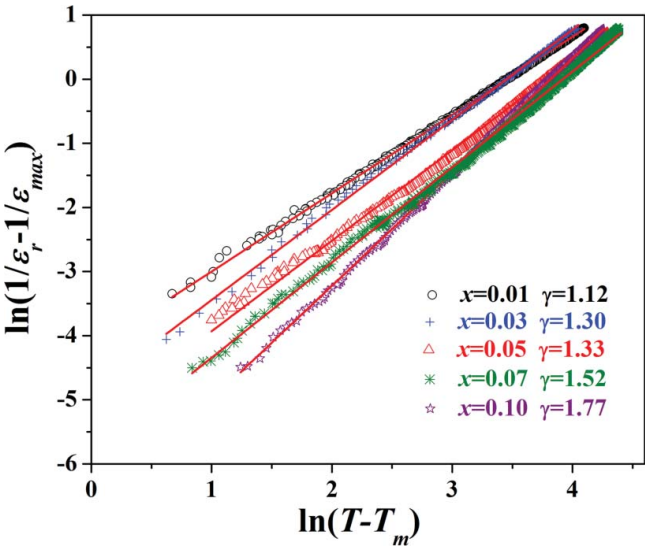

Figure 5. Plots of $\ln(1/\varepsilon_r - 1/\varepsilon_m)$ versus $\ln(T - T_m)$ of (1-x)KNN–xBZnN ceramics. The symbols denote the experimental data, while the solid lines denote the least–squares line that fits the modified Curie–Weiss law.

Table 2
Dielectric, ferroelectric and piezoelectric properties of (1-x)KNN–xBZnN ceramics

Compositions (x)	T_m (°C)	ΔT_m (°C)	ε_m	δ_γ	γ	P_r (μc/cm^2)	P_s (μc/cm^2)	E_c (kV/cm)	S_{max} (%)	d_{33} * pm/V
0.01	380	21	2850	4.3	1.12	23	26	14	0.30	498
0.03	340	57	1900	4.9	1.30	3	15	9	0.098	163
0.05	280	89	1750	5.4	1.33	3	13	9.5	0.083	138
0.07	198	135	2050	5.9	1.52	2	13	8	0.066	110
0.10	91	230	2040	6.7	1.77	1.3	12	5	0.057	95

Nb^{5+} (0.64 Å) in the B–site of the perovskite structure. The heterovalent ions and difference ionic radii lead the high degree of disorder and the local compositional fluctuation may increase in the perovskite structure, thus giving rise to a diffuse phase transition. Figure 6 illustrates the P–E hysteresis loops of (1-x)KNN–xBZnN ceramics. At the composition, $x = 0.01$, a well-saturated hysteresis loop was observed clearly. The remanent polarization (P_r) and a coercive field (E_c) value are of 23.3 μC/cm^2 and 14 kV/cm, respectively. However, when more BZnN was added the P_r and E_c values decreased dramatically, the slim hysteresis loop was dominated. The slim hysteresis behavior is explained by the high degree of disorder in the ABO_3 perovskite structure. Similar phenomena have been observed in $BaTiO_3$–$Bi(Zn_{1/2}Ti_{1/2})O_3$–$BaInO_3$ [37]. The unipolar strain versus electric field of (1-x)KNN–xBZnN ceramics at room temperature are shown in Figure 7. The high field piezoelectric strain coefficient (d_{33} *) was calculated by using the slope of these curves at 60 kV/cm, as shown in Table 2. The highest d_{33} * and maximum strain (S_{max}) value of this system was found in the composition, $x = 0.01$, where d_{33} * = 498 pm/V and $S_{max} = 0.3\%$. This significant strain enhancement may be due to mixed contribution between non-polar and ferroelectric phase transition. At the composition, $x = 0.01$, the generation of non-polar phase and the formation of defect dipoles in

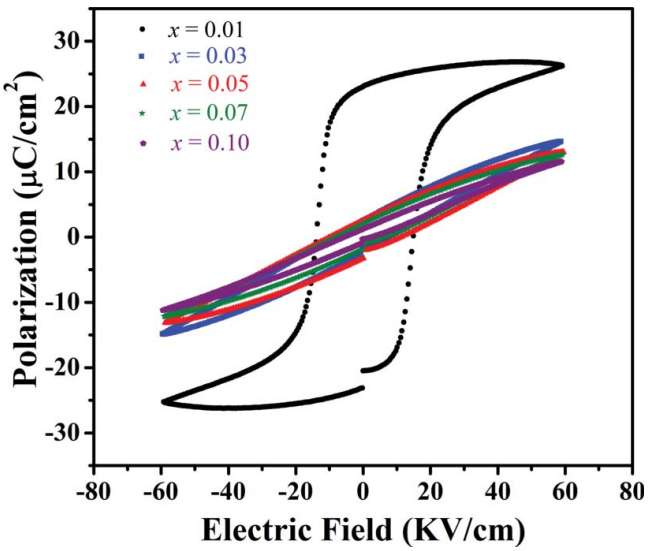

Figure 6. P–E hysteresis loops of (1-x)KNN–xBZnN ceramics.

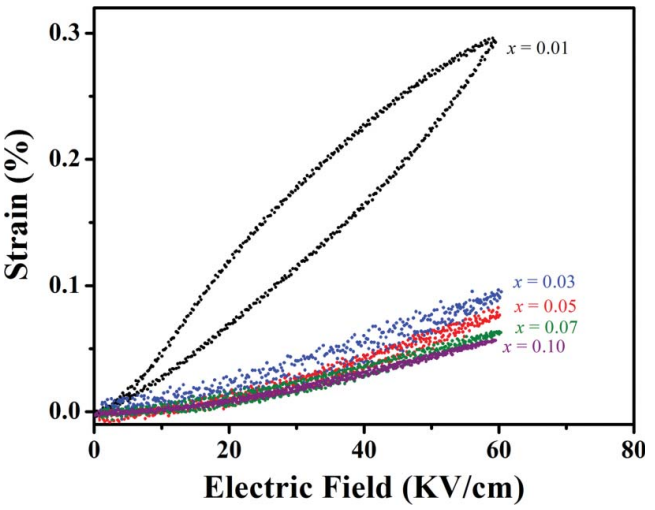

Figure 7. Unipolar strain $S(E)$ curves of (1-x)KNN–xBZnN ceramics.

ferroelectric material occurred. When the electric field was applied, the non-polar regions were induced reversible to ferroelectric phase formation, and lead to promote a large reversible domain switching. Finally, the large strain was obtained in this composition. When more amount of BZnN is added, the strain value decreased due to the non-polar phase dominated, thus the electric field induced phase transition could be difficultly achieved. Similar phenomena have been observed in the in other reports [38–40]. Table 3 presents the Comparison of the d_{33}* of our data with reported data on other lead-free piezoelectric ceramics. It is well known that the ferroelectric and piezoelectric properties in polycrystalline ceramics are caused by the intrinsic effect in connection with the change of the polarization and the extrinsic contribution effect [41, 42]. For the extrinsic effect, this effect is associated by grain size effect, defects, the secondary, densification and porosity of the ceramics. For the (1-x)KNN–xBZnN ceramics, the addition of BZnN can be promoted the grain growth of the KNN ceramics, which helps the domain movement. In addition, as the amount of BZnN is added, the ceramics became denser (%TD = 95–98% for KNN – BZnN system compared with %TD = 93% for pure KNN [31]). The enhancement of grain size and densification can be improved of ferroelectric and

Table 3
Comparison of the d_{33}* of our data with reported data on other lead–free piezoelectric ceramics

Materials	d_{33}* (pm/V)	Ref.
KNN-1%BZnN	498	This study
KNN-$LiSbO_3$	330	[23]
KNN-$LiTaO_3$	138	[21]
$BaTiO_3$-$Bi_{1/2}Na_{1/2}O_3$	240	[36]
$Bi_{1/2}Na_{1/2}O_3$-$Bi_{1/2}K_{1/2}O_3$-KNN	385–560	[36]
$Bi_{1/2}Na_{1/2}O_3$-$Bi_{1/2}K_{1/2}O_3$-$Bi(Mg_{1/2}Ti_{1/2})O_3$	570	[28]
$Bi_{1/2}Na_{1/2}O_3$-$Bi_{1/2}K_{1/2}O_3$-$Bi(Ni_{1/2}Ti_{1/2})O_3$	520	[28]
$Bi_{1/2}Na_{1/2}O_3$-$Bi_{1/2}K_{1/2}O_3$-$Bi(Zn_{1/2}Ti_{1/2})O_3$	460	[37]

piezoelectric properties. On the other hand, the intrinsic effect originates from the polarization and the ionic displacement. In KNN-based perovskite solid solution, the B-cation displacement and ferroelectric activity of Zn, Sc, Cd, Sn, W, Ce and Y cations were explored [43, 44]. The substitution of Zn^{2+} with Nb^{5+} would cause an increase of polarization and ferroelectric activity and lead the improvement of ferroelectric and piezoelectric properties in the solid solution. The large P_r, S_{max} and d_{33} * values were observed when amount of BZnN is added ($x = 0.01$). Nevertheless, when more amount of BZnN is added ($x > 0.01$), the concentration of heterovalent ions in the perovskite lattice were more changed lead to order/disorder state was altered. Due to increasing of random polarization with concentration of foreign ions, and lead to change of structure from long-range order to shot-range order state with increasing BZnN content, resulting the P_r, S_{max} and d_{33} * values decreased.

4. Conclusion

Lead–free piezoelectric (1-x)KNN–xBZnN ceramics was prepared by conventional solid-state reaction. The ceramics were observed a perovskite structure with orthorhombic phase at composition $x \leq 0.01$. When more BZnN was added in the range $0.01 < x \leq 0.07$, the crystal structure became a rhombohedral phase and transforms to a pseudo–cubic structure at $x > 0.07$. The dielectric data show that the amount of BZnN in the KNN solid solution slightly decreases the paraelectric cubic–ferroelectric phase transition temperature (T_C). Optimum ferroelectric and piezoelectric properties were observed at the composition, $x = 0.01$: Curie temperature (T_C) = 380°C, effective piezoelectric coefficients (d_{33} *) = 498 pm/V, remanent polarization (P_r) = 23.3 μC/cm^2, coercive field (E_c) = 14 kV/cm, and maximum strain (S_{max}) = 0.3%. The results show that KNN with a small amount of BZnN ($x = 0.01$) is a good lead-free piezoelectric ceramic. The results of this study indicate that (1-x)KNN–xBZnN forms a new class of environmental friendly candidate material for application in piezoelectric devices, and provides an alternative way of finding new lead–free piezoelectric materials.

Funding

R. Muanghlua would like to thank KMITL Research Fund under grant No. KREF045604 for the financial support and N. Vittayakorn acknowledges the support of The Thailand research Fund (TRF) under grant No. BRG5680006.

References

1. B. Jaffe, W. R. Cook, and H. Jaffe, Piezoelectric Ceramics. New York: Academic; 1971.
2. K. Uchino, Ferroelectric Devices. New York: Marcel Dekker, Inc.; 2000.
3. X. Wang, X. G. Tang, and H. L. W. Chan, Electromechanical and ferroelectric properties of $(Bi_{1/2}Na_{1/2})TiO_3$–$(Bi_{1/2}K_{1/2})TiO_3$–$BaTiO_3$ lead–free piezoelectric ceramics. *Appl Phys Lett*. **85**, 91–93 2004.
4. D. Lin, D. Xiao, J. Zhu, and P. Yu, Piezoelectric and ferroelectric properties of $[Bi_{0.5}(Na_{1-x-y}K_xLi_y)_{0.5}]TiO_3$ lead-free piezoelectric ceramics. *Appl Phys Lett*. **88**, 062901 2006.
5. E. A. Patterson, and D. P. Cann, Bipolar piezoelectric fatigue of $Bi(Zn_{0.5}Ti_{0.5})O_3$–$(Bi_{0.5}K_{0.5})TiO_3$–$(Bi_{0.5}Na_{0.5})TiO_3$ Pb–free ceramics. *Appl Phys Lett*. **101**, 042905 2012.
6. R. Jain, A. K. S Chauhan, V. Gupta, and K. Sreenivas, Piezoelectric properties of nonstoichiometric $Sr_{1-x}Bi_{2+2x/3}Ta_2O_9$ ceramics. *J Appl Phys*. **97**, 124101 2005.

7. W. Li, J. Gu, C. Song, D. Su, and J. Zhu, B-site doping effect on ferroelectric property of bismuth titanate ceramic. *J Appl Phys*. **98**, 114104 2005.
8. Z. Yu, C. Ang, R. Guo, and A. S. Bhalla, Piezoelectric and strain properties of $Ba(Ti_{1-x}Zr_x)O_3$ ceramics. *J Appl Phys*. **92**, 1489 2002.
9. B. W. Eerd, D. Damjanovic, N. Klein, N. Setter, and J. Trodahl, Structural complexity of $(Na_{0.5}Bi_{0.5})TiO_3$–$BaTiO_3$ as revealed by raman spectroscopy. *Phys Rev B*. **82**, 104112 2010.
10. D. Z. Xue, Y. M. Zhou, H. X. Bao, J. H. Gao, C. Zhou, and X. B. Ren, Large piezoelectric effect in Pb–free $Ba(Ti,Sn)O_3$–$x(Ba,Ca)TiO_3$ ceramics. *Appl Phys Lett*. **99**, 122901 2011.
11. W. F. Liu, and X. B. Ren, Large piezoelectric effect in Pb–Free ceramics. *Phys Rev Lett*. **103**, 257602 2009.
12. R. E. Jaeger, and L. Egerton, Hot pressing of potassium–sodium niobates. *J Am Ceram Soc*. **45**, 209–213 1962.
13. E. Ringgaard, and T. Wurlitzer, Lead–free piezoceramics based on alkali niobates. *J Eur Ceram Soc*. **25**, 2701–2706 2005.
14. Y. Saito, H. Takao, T. Tani, T. Nonoyama, K. Takatori, T. Homma, T. Nagaya, and M. Nakamura, Lead–free piezoceramics. *Nature*. **432**, 84–87 2004.
15. R. Muanghlua, S. Niemcharoen, M. Sutapun, B. Boonchom, and N. Vittayakorn, Phase transition behavior and electrical properties of lead–free $(K_{0.5}Na_{0.5})NbO_3$–$LiNbO_3$–$LiSbO_3$ piezoelectric ceramics. *Curr Appl Phys*. **11**, 434–437 2011.
16. Z. S. Ahn, and W. A. Schulze, Conventionally sintered $(Na_{0.5}K_{0.5})NbO_3$ with barium additions. *J Am Ceram Soc*. **70**, 18–21 1987.
17. B. Zhang, J. Li, K. Wang, and H. Zhang, Compositional dependence of piezoelectric properties in $Na_xK_{1-x}NbO_3$ lead–free ceramics prepared by spark plasma sintering. *J Am Ceram Soc*. **89**, 1605–1609 2006.
18. C. H. Choi, C. W. Ahn, and S. Nahma, $(1-x)BaTiO_3-x(Na_{0.5}K_{0.5})NbO_3$ ceramics for multilayer ceramic capacitors. *Appl Phys Lett*. **90**, 132905 2007.
19. R. Zuo, X. Fang, and C. Ye, Phase structures and electrical properties of new lead-free $(Na_{0.5}K_{0.5})NbO_3$–$(Bi_{0.5}Na_{0.5})TiO_3$ ceramics. *Appl Phys Lett*. **90**, 9290–9294 2007.
20. R. Wang, R. Xie, K. Hanada, K. Matsusaki, H. Bando, and M. Itoh, Phase diagram and enhanced piezoelectricity in the strontium titanate doped potassium–sodium niobate solid solution. *Phys Stat Sol*. **202**, R57–R59 2005.
21. Y. Dai, X. Zhang, and G. Zhou, Phase transitional behavior in $K_{0.5}Na_{0.5}NbO_3$–$LiTaO_3$ ceramics, *Appl Phys Lett*. **90**, 262903 2007.
22. Y. Guo, K. Kakimoto, and H. Ohsato, Phase transitional behavior and piezoelectric properties of $(Na_{0.5}K_{0.5})NbO_3$–$LiNbO_3$ ceramics. *Appl Phys Lett*. **85**, 4121–4123 2004.
23. S. Zhang, R. Xia, T. R. Shrout, and G. Zang, Characterization of lead free $(K_{0.5}Na_{0.5})NbO_3$–$LiSbO_3$ piezoceramic. *Solid State Commun*. **141**, 675–679 2007.
24. M. R. Suchomel, and P. K. Davids, Enhanced tetragonality in $(x)PbTiO_3$–$(1-x)Bi(Zn_{1/2}Ti_{1/2})O_3$ and related solid solution systems. *Appl Phys Lett*. **86**, 262905 2005.
25. J. Chen, X. Tan, W. Jo, and J. Rodel, Temperature dependence of piezoelectric properties of high–T_C $Bi(Mg_{1/2}Ti_{1/2})O_3$–$PbTiO_3$. *J Appl Phys*. **106**, 034109 2009.
26. S. M. Choi, C. J. Stringer, T. R. Shrout, and C. A. Randall, Structure and property investigation of a Bi–based perovskite solid solution: $(1-x)Bi(Ni_{1/2}Ti_{1/2})O_3$–$xPbTiO_3$. *J Appl Phys*. **95**, 034108 2005.
27. P. Jarupoom, E. Patterson, B. Gibbon, G. Rujijanagul, R. Yimnirun, and D. P. Cann, Lead-free ternary perovskite compounds with large electromechanical strains. *Appl Phys Lett.* **99**, 152901 2011.
28. E. Patterson, and D. P. Cann, Relaxor to Ferroelectric transitions in $(Bi_{1/2}Na_{1/2})TiO_3$–$Bi(Zn_{1/2}Ti_{1/2})O_3$ solid solutions. *J Am Ceram Soc.* **95**, 3509–3513 2012.
29. H. Nagata, S. Sato, Y. Hiruma, and T. Takenaka, Fabrication of dense $KNbO_3$ ceramics derived from $KHCO_3$ as a starting material. *Appl Phys Express*. **5**, 011502 2012.
30. J. S. Reed, Principles of Ceramics Processing. New York: Wiley Interscience; 1995.

31. M. Sutapun, C. C. Huang, D. P. Cann, and N. Vittayakorn, Phase transitional behavior and dielectric properties of lead free $(1\text{-}x)(K_{0.5}Na_{0.5})NbO_3-xBi(Zn_{0.5}Ti_{0.5})O_3$ ceramics. *J Alloy Compd.* **479**, 462–466 2009.
32. C. W. Ahn, S. Y. Noh, S. Nahm, J. Ryu, K. Uchino, S. J. Yoon, and J. S. Song, Low–temperature sintering and piezoelectric properties of ZnO added $0.41Pb(Ni_{1/3}Nb_{2/3})O_3$–$0.36PbTiO_3$–$0.23PbZrO_3$ ceramics. *Jpn J Appl Phys.* **42**, 5676–5680 2003.
33. A. Singh, and R. Chatterjee, Structural and electrical properties of BKT rich $Bi_{0.5}K_{0.5}TiO_3$–$K_{0.5}Na_{0.5}NbO_3$ system. *AIP Advances*. **3**, 032129 2013.
34. R. D. Shannon, Revised effective ionic radii and systematic studies of interatomic distances in halides and chalcogenides. *Acta Cryst A.* **32**, 751 1976.
35. C. C. Huang, D. P. Cann, X. Tan, and N. Vittayakorn, Phase transitions and ferroelectric properties in $BiScO_3$–$Bi(Zn_{1/2}Ti_{1/2})O_3$–$BaTiO_3$ solid solutions. *J Appl Phys.* **102**, 044103 2007.
36. N. Setter, L. E. Cross, The role of B–site cation disorder in diffuse phase transition behavior of perovskite ferroelectrics. *J Appl Phys.* **51**, 4356 1980.
37. N. Raengthon, and D. P. Cann, High temperature electronic properties of $BaTiO_3$–$Bi(Zn_{1/2}Ti_{1/2})O_3$–$BiInO_3$ for capacitor applications. *J Electroceram.* **28**, 165–171 2012.
38. A. Hussain, A. Zaman, Y. Iqbal, and M. H. Kim, Dielectric, ferroelectric and field induced strain properties of Nb-modified Pb-free $0.99Bi_{0.5}(Na_{0.82}K_{0.18})_{0.5}TiO_3$–$0.01LiSbO_3$ ceramics. *J Alloy Compd.* **574**, 320–324 2013.
39. A. Ullah, C. W. Ahn, A. Hussain, S. Y. Lee, J. S. Kim, and I. W. Kim, Effect of potassium concentration on the structure and electrical properties of lead-free $Bi_{0.5}(Na,K)_{0.5}TiO_3$–$BiAlO_3$ piezoelectric ceramics. *J Alloy Compd.* **509**, 3148–3154 2011.
40. P. Jaita, A. Watcharapasorn, D. P. Cann, and S. Jiansirisomboon, Dielectric, ferroelectric and electric field-induced strain behavior of $Ba(Ti_{0.9}Sn_{0.1})O_3$-modified $Bi_{0.5}(Na_{0.8}K_{0.2})_{0.5}TiO_3$ lead-free piezoelectrics. *J Alloy Compd.* **596**, 98–106 2014.
41. C. A. Randall, N. Kim, J. P. Kucera, W. Cao, and T. R. Shrout, Intrinsic and extrinsic size effects in fine-grained morphotropic phase boundary lead zirconate titanate ceramics. *J Am Ceram Soc.* **81**, 677–688 1998.
42. W. Cao, and C. A. Randall, Grain size and domain size relations in bulk ceramic ferroelectric materials. *J Phys Chem Solids.* **57**, 1499–1505 1996.
43. I. Grinberg, M. R. Suchomel, P. K. Davies, and A. M. Rappe, Predicting morphotropic phase boundary locations and transition temperatures in Pb- and Bi-based perovskite solid solutions from crystal chemical data and first-principles calculations. *J Appl Phys.* **98**, 094111 2005.
44. R. Zuo, and J. Rödel, Sintering and Electrical Properties of Lead-Free $Na_{0.5}K_{0.5}NbO_3$ Piezoelectric Ceramics. *J Am Ceram Soc.* **89**, 2010–2015 2006.

Ferroelectrics

ISSN: 0015-0193 (Print) 1563-5112 (Online) Journal homepage: http://www.tandfonline.com/loi/gfer20

Dielectric, Ferroelectric and Piezoelectric Properties of the Lead Free $0.9BaTiO_3$-$(0.1-x)Bi_{0.5}Na_{0.5}TiO_3$-$xBi(Mg_{0.5}Ti_{0.5})O_3$ Solid Solution

Jitkasem Mayamae, Usa Sukkha, Surasak Niemchareon, Rangson Muanghlua & Naratip Vittayakorn

To cite this article: Jitkasem Mayamae, Usa Sukkha, Surasak Niemchareon, Rangson Muanghlua & Naratip Vittayakorn (2016) Dielectric, Ferroelectric and Piezoelectric Properties of the Lead Free $0.9BaTiO_3$-$(0.1-x)Bi_{0.5}Na_{0.5}TiO_3$-$xBi(Mg_{0.5}Ti_{0.5})O_3$ Solid Solution, Ferroelectrics, 490:1, 23-35, DOI: 10.1080/00150193.2015.1070656

To link to this article: http://dx.doi.org/10.1080/00150193.2015.1070656

Published online: 29 Jan 2016.

Ferroelectrics, 490: 23–35, 2016

ISSN: 0015-0193 print / 1563-5112 online
DOI: 10.1080/00150193.2015.1070656

Taylor & Francis
Taylor & Francis Group

Dielectric, Ferroelectric and Piezoelectric Properties of the Lead Free $0.9BaTiO_3$-$(0.1\text{-}x)Bi_{0.5}Na_{0.5}TiO_3$-$xBi(Mg_{0.5}Ti_{0.5})O_3$ Solid Solution

JITKASEM MAYAMAE,[1] USA SUKKHA,[2] SURASAK NIEMCHAREON,[3] RANGSON MUANGHLUA,[3] AND NARATIP VITTAYAKORN[1,4,5,*]

[1]Electroceramic Research Laboratory, College of Nanotechnology, King Mongkut's Institute of Technology Ladkrabang, Bangkok 10520, Thailand
[2]Synchrotron Light Research Institute (Public Organization), 111 University Avenue, Muang District, Nakhon Ratchasima 30000, Thailand
[3]Department of Electronics Engineering, Faculty of Engineering, King Mongkut's Institute of Technology Ladkrabang, Bangkok 10520, Thailand
[4]Advanced Materials Research Unit, Faculty of Science, King Mongkut's Institute of Technology Ladkrabang, Bangkok 10520, Thailand
[5]Nano-KMITL Center of Excellence on Nanoelectronic Devices, KMITL, Ladkrabang, Bangkok 10520, Thailand

Solid solution of $0.9BaTiO_3$-$(0.1\text{-x})Bi_{0.5}Na_{0.5}TiO_3$-x$Bi(Mg_{0.5}Ti_{0.5})O_3$ (BT-BNT-xBMT) system, where x = 0.00, 0.02, 0.04, 0.06, 0.08, 0.10, was synthesized by the solid state reaction. Dense BT-BNT-xBMT ceramics were obtained by sintering at 1,150–1,250°C for 4 h. The effect of BMT on crystal structure and electrical property of BT-BNT ceramics was investigated as a function of composition, x, using X-ray diffraction, dielectric spectroscopy, hysteresis and strain measurements. The crystal structure of solid solution BT-BNT-xBMT, where x = 0.00-0.10, successively transforms from tetragonal to pseudocubic symmetry, with increased BMT concentration. Temperature dependence of dielectric constant (ε_r) and dielectric loss (tanδ) for BT-BNT-xBMT at various frequencies showed that phase transition of ceramics changed from ferroelectric to relaxor-like behavior as BMT content increased. Furthermore, remanent polarization (P_r), coercive field (E_c) and the normalized strain (d_{33}) of BT-BNT-xBMT ceramics tend to decrease with increasing BMT concentration.*

Keywords BT-BNT-*x*BMT; lead free piezoelectric; phase transition; electrical properties

1. Introduction

Lead zirconate titanate (PZT) ceramics have been used widely in many electronic devices such as piezoelectric sensor, actuators and transducers because of their excellence

Received October 26, 2014; in final form January 20, 2015.
*Corresponding author. E-mail: naratipcmu@yahoo.com
Color versions of one or more of the figures in this article can be found online at www.tandfonline.com/gfer.

piezoelectric properties [1]. However, PZT-based piezoelectric ceramics are not environmental friendly because more than 60% wt of these ceramics contains the lead toxicity. Furthermore, the EU legislation forced draft directives including Waste from Electrical and Electronic Equipment (WEEE) and Restriction of Hazardous Substances (RoHS). According to the environmental issues, lead free friendly piezoelectric ceramics have been received considerable attentions to replace lead-based piezoelectric materials.

Although no real lead free materials can be replaced the common use in lead-based ceramics for various applications, many potentially promising lead free materials have been developed. Among the lead free materials, Barium titanate ($BaTiO_3$; BT) has perovskite structure and good electrical properties such as ferroelectric and piezoelectric properties but low Curie temperature (T_c) [2]. In recent years, there are many researches about BT-base for example $Ba_{0.85}Ca_{0.15}Ti_{0.90}Zr_{0.10}O_3$ [3] and (1-x)$Ba_{0.98}Ca_{0.02}Ti_{0.94}Sn_{0.06}O_3$-x$Ba_{0.85}$-$Ca_{0.15}Ti_{0.90}$ -$Zr_{0.10}O_3$ [4]. Jiagang Wu *et al.* [4] found that BT-base ceramic by combining (1-x)$Ba_{0.98}Ca_{0.02}Ti_{0.94}Sn_{0.06}O_3$-x$Ba_{0.85}Ca_{0.15}Ti_{0.90}Zr_{0.10}O_3$((1-x)BCTS-xBCTZ) system has a phase boundary coexistence of orthorhombic and tetragonal phase at around 4 mol% BCTZ which show good dielectric and piezoelectric properties of dielectric constant ($\varepsilon_r \sim 5500$), dielectric loss ($\tan\delta \sim 0.3\%$) and piezoelectric constant ($d_{33} \sim 407$ pC/N). The binary system of $Bi_{0.5}Na_{0.5}TiO_3$-$BaTiO_3$ (BNT-BT) is an important candidate for replacing lead-based piezoelectric. In a few decades, BNT-BT solid solution was studied by various research groups [2, 5, 6]. Takenaka *et al.* [5] found that BNT-BT system has a morphotrobic phase boundary (MPB) between rhombohedral and tetragonal phases at around 6-7 mol% BT which shows the excellent properties including $\varepsilon_{33}^T/\varepsilon_0 = 580$, piezoelectric constant ($d_{33} = 125$ pC/N), Curie temperature ($T_c = 288°C$), dielectric loss ($tan\delta = 1.3\%$) and planar coupling coefficient ($k_{33} = 55.0\%$). Afterwards, researchers focused to develop BNT-BT binary material on the composition range of MPB by doing ternary solid solution such as KNN-modified BNT-BT [7,8] and BZr-modified BNT-BT [9]. Also, the BNT-BT-based systems on the BNT-rich side have been investigated extensively for example (0.94-x)BNT-0.06BT-xKNN [7], 0.865BNT–0.350BT–0.100BKT [8] and BZr-modified BNT-BT [9]. However, few works have investigated and developed BNT-BT on the BT-rich side. Recently, Wada et al. studied on the combination between $BaTiO_3$ and $Bi(Mg_{0.5}Ti_{0.5})O_3$ (BMT) and found that BMT can enhance Curie temperature (T_C) of BT with the highest T_C (about 360°C) for 0.5$BaTiO_3$-0.5BMT ceramics [10]. Moreover, Qi Wang et al. have studied lead free $Bi_{0.5}Na_{0.5}TiO_3$–$Bi(Mg_{0.5}Ti_{0.5})O_3$ systems and reported that BMT can improve piezoelectric properties and enhance T_C of BNT ceramic. The 0.95BNT-0.05$BMTO_3$ ceramic showed the highest d_{33} about 110pC/N and high T_C at 352°C [11].

This work dealt with the new ternary system of 0.9$BaTiO_3$-(0.1-*x*)$Bi_{0.5}Na_{0.5}TiO_3$-*x*Bi$(Mg_{0.5}Ti_{0.5})$ in order to get more information of BT-BNT-based on BT-rich side. BT-BNT-*x*BMT ceramics were prepared by the solid state reaction. The effect of BMT on crystal structure, phase transition and electrical properties were studied as a function of composition, *x*.

2. Experimental

Lead free 0.9$BaTiO_3$-(0.1-*x*)$Bi_{0.5}Na_{0.5}TiO_3$-*x*Bi$(Mg_{0.5}Ti_{0.5})O_3$ (BT-BNT-*x*BMT) ceramics, where $x = 0.00, 0.02, 0.04, 0.06, 0.08, 0.10$, were synthesized by the solid state reaction. Bi_2O_3 (99.9%, Sigma-Aldrich), $BaCO_3$ (98.5%, Fluka), Na_2CO_3 (99.8%, Riedel-deHaen), TiO_2 (99.9%, Sigma-Aldrich) and MgO (99%, Fluka) powders were used raw materials. First, stoichiometric amounts of raw materials were weighted and ball-milled with yttrium-stabilized zirconia in ethanol media for 18 hours. After drying the mixture for 24 h in an oven, the mixed

powder was calcined at 900°C for 4 hours with heating/cooling rate 10°C/min. In order to obtain fine particles prior to making a pellet, the calcined powders were ground and sieved. The fine powders were pressed into disks with 15 mm diameter. 5 wt% polyvinyl alcohol as a binder was used as binder. The disks were sintered at 1150-1250°C for 4 hours with heating/cooling rate 5°C/min. The crystal structure of ceramics was characterized using X-ray diffraction (Bruker-AXS D 8 Advance) with Cu(Kα) radiation in the 2θ scan range of 20°–80°. For electrical measurements, the samples were polished for both sides and made parallel before electrode coating with silver paste (C1000, Heraeus) on both surfaces. Silver paste was heated on at 750°C for 20 min with heating/cooling rate 5°C/min. The relative permittivity (ε_r) and dielectric loss (*tan*δ) were determined as a function of frequency (1-100 kHz) and temperature (room temperature to 250°C) using LCR meter (HP4284A, Hewlett-Packard, Palo Alto, CA). Polarization-electric field (P-E) hysteresis loop were determined at room temperature using Radiant Technologies, Inc (RT66A). The strain-electric field (S-E) curves were determined using MTI-2100 Fotonic sensor combined with Radiant Technologies. The peak field for P-E hysteresis loop and S-E curve measurements was maintained at 60 kV/cm during measurement. The surface morphology of ceramics was observed using scanning electron microscope (EVO®MA10).

3. Results and Discussion

The X-ray diffraction patterns of BT-BNT-*x*BMT ceramics, where $x = 0.00$, 0.02, 0.04, 0.06, 0.08, 0.1, are shown in Figure 1(a). It indicates that all samples are a single phase with the perovskite structure. The secondary and other phases were not observed in the XRD patterns, which indicating that all compositions in the BT-BNT-*x*BMT system can completely form solid solution with a perovskite structure. A (111) peak at around 39 was chosen to identify the crystal structure of BT-BNT-XBMT ceramics as shown in Figure 1(b). In the compositions, $0.00 \leq x \leq 0.08$, the crystal structure has a tetragonal symmetry, identified by a splitting of the (002) and (200) peaks. At the higher BMT content of $x = 0.1$, the doublet of (002) and (200) peaks become a single peak of (200) and the (111) peak still exhibits a single peak. These results indicated that the crystal structure changed to a pseudocubic symmetry.

The average ionic radius of A-site and B-site, calculated lattice parameters, the tetragonality c/a ratio and tolerance factor of each composition are listed in Table 1. The tetragonality c/a ratio is the important factor representing the lattice distortion of the tetragonal symmetry. It is seen that the c/a ratio decreases significantly with increasing BMT content. The ionic radii of Bi^{3+} (CN = 12, 1.40 Å) are smaller than the ionic radii of Ba^{2+} (CN = 12, 1.61 Å) resulting in the decreasing of average ionic radii at A-site [12]. Also, the substitution of Ti^{4+} ions (CN = 6, 0.605 Å) by Mg^{2+} (CN = 6, 0.72 Å) results in the increasing of average ionic radii at B-site as shown in Table 1. Then, it is reasonable to assume that the substitution of BMT into BT-BNT leads to the distortion and deformation of tetragonal structure. Furthermore, the tolerance factor (t) is important factor that reflecting the perovskite structure distortion, rotation and tilt of the BO_6 octahedra [13]. Generally, the perovskite structure is stable in the range of $0.880 < t < 1.090$ region [14] and the symmetry is higher as the t value is approach to 1. It is also noticed that the t for BT-BNT-*x*BMT ceramics tends to decrease with increasing BMT which corresponds well with the phase transition from tetragonal to pseudocubic symmetry.

Based on the XRD data, it could be said that the combination between BT-BNT and BMT could form completely crystalline solid solution of perovskite structure but the existence of BMT caused the tetragonality of BT-BNT decrease.

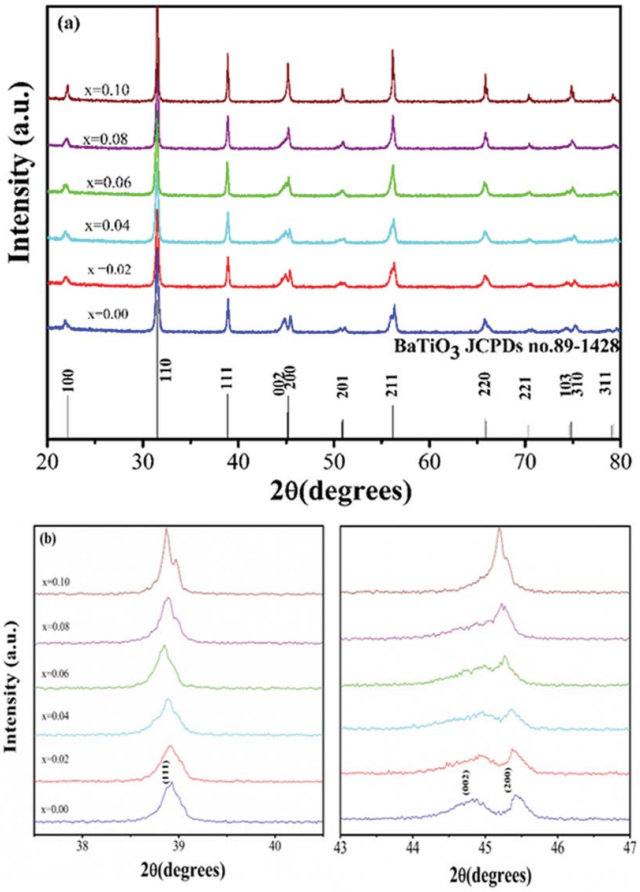

Figure 1. (a) X-ray diffraction patterns of 0.9BT-(0.1-x)BNT-(x)BMT ceramics with the composition $0.00 \leq x \leq 0.10$; (b) X-ray diffraction patterns for (111), (002) and (200) peaks of 0.9BT-(0.1-x)BNT-(x)BMT ceramics with the composition $0.00 \leq x \leq 0.10$.

Figure 2 illustrates the temperature dependence of the relative permittivity (ε_r) and dielectric loss ($tan\delta$) of BT-BNT-xBMT ceramics measured at various frequencies between 1 and 100 kHz. Regarding the composition, $x = 0.00$, the relative permittivity of 0.9BT-0.1BNT increased slowly until the temperature approached transition temperature, then it abruptly increased and passed through a maximum of about 178°C. This discontinuity of dielectric constant at phase transition is characteristic of the first order phase transition [15] and occurs from the change of the tetragonal ferroelectric (FE) phase into the cubic paraelectric (PE) phase, in agreement with previous reports [2]. The relative permittivity curves at the compositions, $0.02 \leq x \leq 0.10$, showed only one phase transition. The composition, $x = 0.02$, showed a broadening dielectric peak which much like the characteristic of relaxor ferroelectric, however the position of the peaks keep unchanged at various applied frequency. At higher composition, $0.04 \leq x \leq 0.10$, the diffuse phase transition behaviour with broad maximum and frequency dispersion became more self-evident when BMT concentration increased. Also, the transition temperature is dependent of frequency and increases with increasing frequency. These results indicated that BT-BNT-xBMT progressively change from normal ferroelectric to relaxor ferroelectric when

Table 1
Lattice parameters and lattice anisotropy of BT-BNT-XBMT ceramics with the composition $0.00 \leq x \leq 0.10$

		Ionic radii (Å)			Lattice parameter (Å)		
x	Crystal structure	A-site	B-site	Tolerance factor (t)	a	c	c/a
0.00	T	1.5910	0.605	1.0548	3.9590 ± 0.0792	4.1086 ± 0.2924	1.0378
0.02	T	1.5906	0.6062	1.0541	3.9847 ± 0.0518	4.0619 ± 0.1678	1.0194
0.04	T	1.5902	0.6073	1.0534	3.9792 ± 0.0500	4.0675 ± 0.1641	1.0222
0.06	T	1.5898	0.6085	1.0526	3.9969 ± 0.0421	4.0282 ± 0.0456	1.0078
0.08	T	1.5894	0.6096	1.0519	4.0017 ± 0.0159	4.0131 ± 0.0118	1.0029
0.10	PC	1.5890	0.6107	1.0511	4.0066 ± 0.0049	–	–

[539127

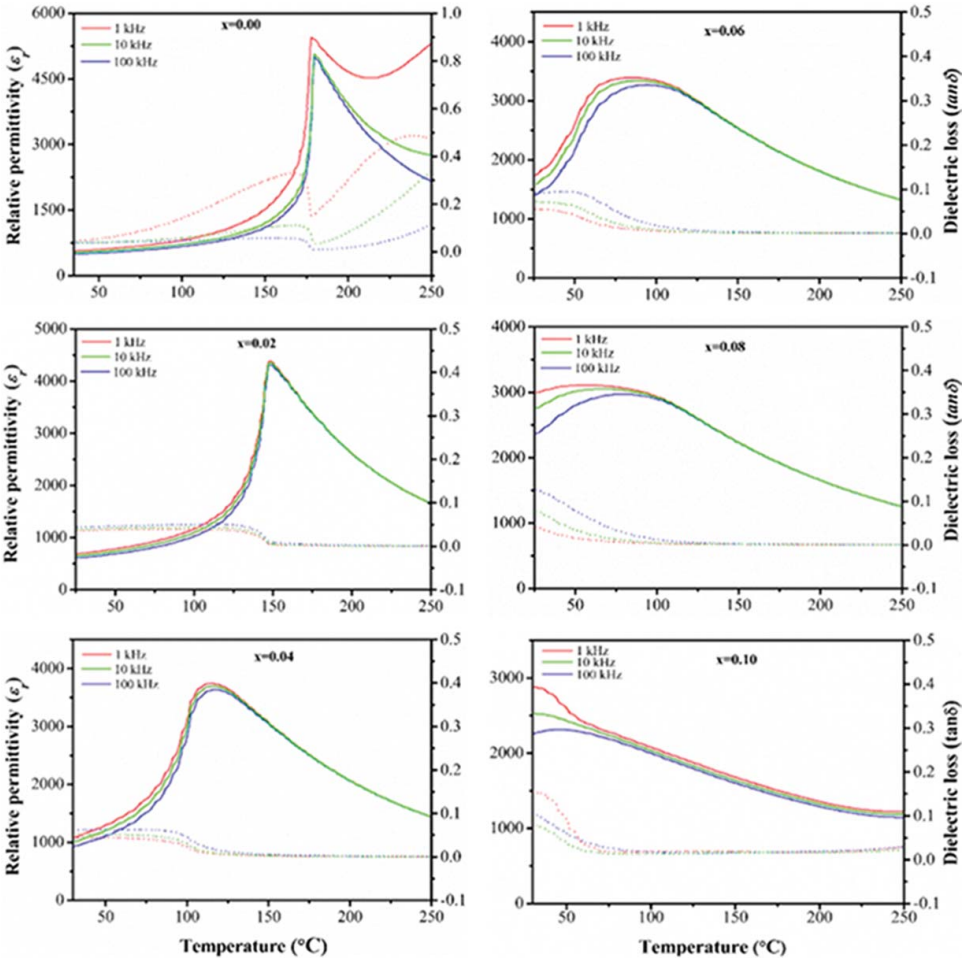

Figure 2. Relative permittivity (ε_r) and dielectric loss ($tan\delta$) as a temperature dependence of 0.9BT-(0.1-x)BNT-(x)BMT ceramics with the composition $0.00 \leq x \leq 0.10$.

BMT concentration increases. This phenomenon of BT-BNT-xBMT system resulted from the substitutions of Bi^{3+} ions for Na^{+} ions and Mg^{2+} ions for Ti^{4+}, which distort the unit cell and change dipole moment. For complex perovskite compound, the more cations occupy the equivalent crystallographic site of A or B, the more the chemical fluctuation and structural disorder in arrangement of cations are inhomogeneous at the nanometre scale, then the relaxation characteristic becomes more distinctly [16, 17].

In order to further characterize the relaxor behavior, a modified Curie–Weiss law in equation (1) was used for description a broad relative permittivity and diffuseness of phase transition [18, 19].

$$\frac{\varepsilon_m}{\varepsilon} = 1 + \frac{(T - T_m)^{\gamma}}{2\delta_{\gamma}} \tag{1}$$

where ε_m is the maximum value of relative permittivity and T_m is the temperature of dielectric maximum. The γ value expresses the degree of dielectric relaxation in relaxor

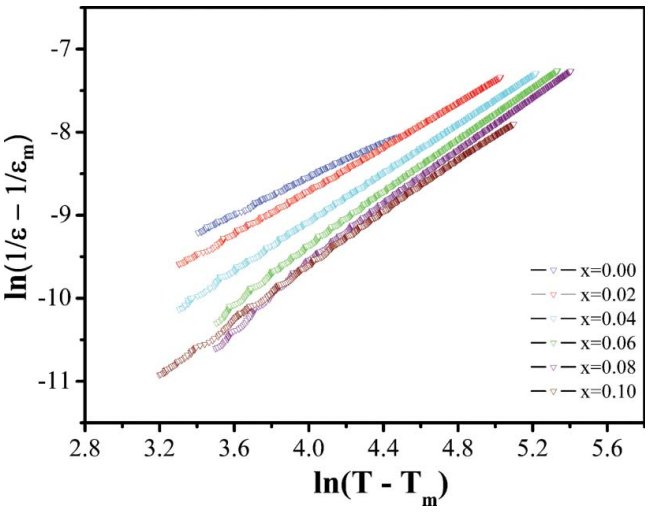

Figure 3. The relative plot between ln(1/ε–1/ε$_m$) and ln(T – T$_m$).

ferroelectric material which this value is in the range of $1 \leq \gamma \leq 2$. When γ value is equal 1, Eq. (1) becomes the classic Curie Weiss law valid in the case of normal ferroelectric. When γ value is equal 1, the ideal relaxor behavior with quadratic dependence is described. The parameter δ_γ is the diffuse parameter which can be used to determine the degree of diffuseness in the phase transition. The $\delta_{\boldsymbol{\gamma}}$ value can be observed from the slope of $\varepsilon'_m/\varepsilon'$ versus $(T\text{-}T_m)^2$, which should be linear. Plot of ln $(\frac{1}{\varepsilon} - \frac{1}{\varepsilon_m})$ as function of ln (T-T$_m$) at 100 kHz of BT-BNT-*x*BMT ceramics are displayed in figure 3. By plotting ln (1/ε–1/ε$_{max}$) versus ln(T-T$_m$), the γ value can be determined directly from the gradient. The γ and $\boldsymbol{\delta\gamma}$ values are determined and shown in Table 2. It is clearly seen that both δ_γ and γ values tend to increase with increasing of the BMT content, confirming the relaxor behavior in these solid solution. Based on the dielectric data, a slim P-E hysteresis loop in BT-BNT-*x*BMT ceramic at high BMT content is expected to observe at room temperature.

Curie temperature and maximum relative permittivity ($\varepsilon_{r\,max}$) at 100 kHz of BT-BNT-*x*BMT ceramics are determined and plotted as a function of composition in

Table 2
The dielectric and ferroelectric properties of BT-BNT-XBMT ceramics with the composition $0.00 \leq x \leq 0.10$

x	$\varepsilon_{r\ room}$ at 100 kHz	*tan*δ at 100 kHz	γ	δ_γ	P_r (μC/cm^2)	P_s (μC/cm^2)	E_c (kV/cm)	Squareness hysteresis loop (R_{sq})
0.00	524	0.038	1.08	12.88	15.52	19.72	29.47	1.56
0.02	663	0.039	1.32	13.98	12.87	18.04	24.31	1.38
0.04	1075	0.051	1.47	14.94	11.26	17.74	20.41	1.20
0.06	1684	0.071	1.60	15.77	8.30	17.30	13.64	0.88
0.08	2820	0.069	1.67	16.26	2.55	15.96	4.24	0.37
0.10	2526	0.080	1.59	15.97	1.63	11.77	3.48	0.33

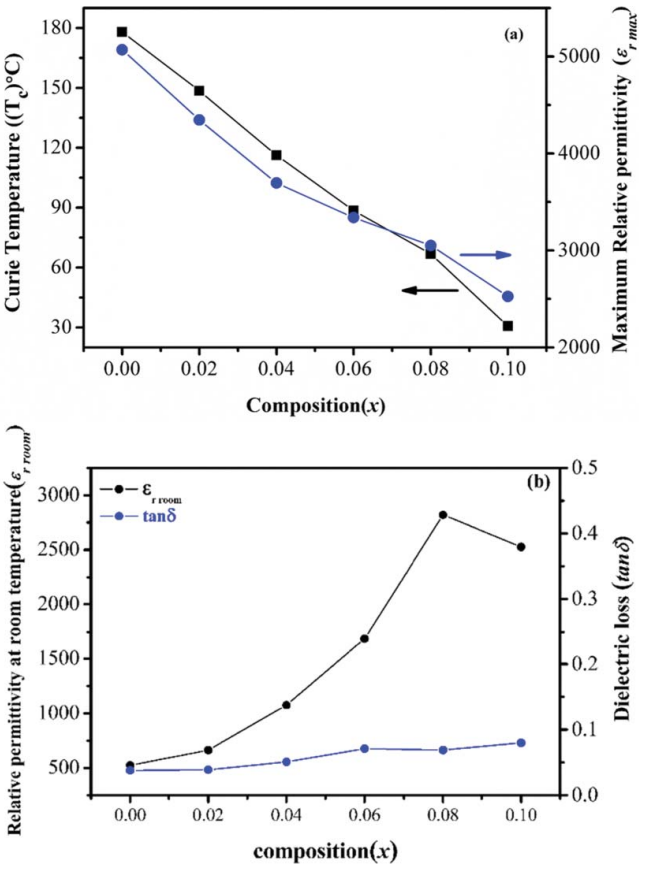

Figure 4. (a) The relative plot between Curie temperature and maximum relative permittivity ($\varepsilon_{r\,max}$) as a function of composition (x); (b) The relative plot between relative permittivity at room temperature ($\varepsilon_{r\ room}$) and dielectric loss ($tan\delta$) as a function of composition (x).

Figure 4(a). It was observed that Curie temperature decreased rapidly with further increase of BMT. As the previous works have reported that the rapidly decrease in transition can be caused by valence mismatch [20, 21]. In BT-BNT-xBMT system, the differences in valence of ions at A-site (Ba^{2+}, Na^{+}, Bi^{3+}) and B-site (Mg^{2+}, Ti^{4+}) might be result in valance mismatch, thus Curie temperature decrease with increasing BMT content. Similar behavior is also observed for the substitution of BMT in KNN structure [22]. Moreover, the maximum relative permittivity ($\varepsilon_{r\ max}$) of BT-BNT-XBMT ceramics tends to decrease with increasing BMT concentration. However, at room temperature the relative permittivity ($\varepsilon_{r\ room}$) tends to abruptly increase with increasing BMT, excepting the composition, $x = 0.10$. While, dielectric loss ($tan\delta$) tend to gradually increase with BMT increase as shown in Figure 4(b). The smooth increase of $\varepsilon_{r\ room}$ for the compositions, $0.02 \leq x \leq 0.08$, might be attributed to the decreasing of Curie temperature to room temperature. While, the $\varepsilon_{r\ \mathrm{room}}$ of composition, $x = 0.10$ is decrease might be the Curie temperature being below room temperature.

The composition dependence of polarization-electric field (P-E) hysteresis loops for BT-BNT-xBMT system was measured at room temperature with electric field of 60 kV/ cm, as shown in figure 5. It is evident that all ceramics display the saturated P-E

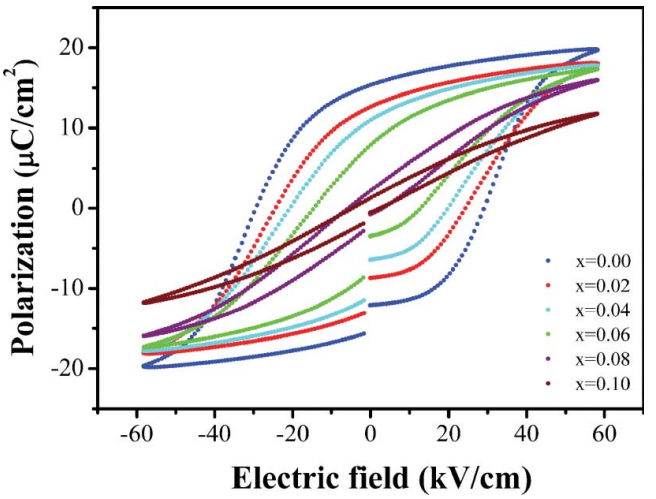

Figure 5. The relative plot of polarization (μC/cm^2) with electric field (kV/cm) of 0.9BT-(0.1-x) BNT-(x)BMT ($x = 0.00$-0.10) ceramics.

hysteresis loops. For 0.9BT-0.1BNT, a shape of hysteresis loop displays typically normal ferroelectric behavior with remanent polarization (P_r) and coercive field (E_c) of 15.52 μC/cm^2 and 29.47 kV/cm, respectively, which in good agreement with previous work [2]. Normal ferroelectric contains a long-range interaction between dipoles in the ferroelectric micro-domain state, giving a typical square hysteresis loops with high P_r and E_c. As expected for BT-BNT-xBMT ceramics, the substitution of BMT has significantly effect on the hysteresis loops shape and polarization and coercive field values. The more BMT concentration increases, the more the hysteresis loop shape becomes slim, identified the gradually drop of P_r, P_s and E_c values as summarized in Table 2. This result suggests that the long-range order of polarization in ferroelectric micro-domain was significantly broken down to polar nano-regions by adding BMT. Then, at high content of BMT, normal ferroelectric BT-BNT-xBMT ceramics become relaxor-like behavior exhibiting a slim P-E hysteresis loop with low P_r and E_c. For low content of BMT, the decreasing of P_r and E_c might be due to an easier of domain switching and domain wall motions [23] as well as tetragonality decreasing of crystal structure in this system [24]. The plots of P_r and E_c values against composition are given in figure 6. Again, a clearly smooth trend of decrease was seen in P_r and E_c with respect to BMT content, confirming the completely solid solution formation in BT-BNT-xBMT system.

To confirm the changes in hysteresis behavior, the empirical relationship between P_r, P_s and polarization at fields above the E_c proposed by Haertling and Zimmer was used for calculated the squareness of hysteresis loop [25]

$$R_{sq} = \frac{P_r}{P_s} + \frac{P_{1.1EC}}{P_r} \tag{2}$$

where R_{sq}, P_r and P_s are squareness of hysteresis loop, remanent polarization and saturation polarization, respectively. $P_{1.1Ec}$ is the polarization at an electric field equal to 1.1 times the coercive field (E_c). The squareness parameter reflects the quantification of changes P-E hysteresis loops. For an ideal P-E hysteresis loop, the R_{sq} is equal to 2. The calculated R_{sq} for all ceramics is listed in Table 2. It is clearly found that, as BMT content

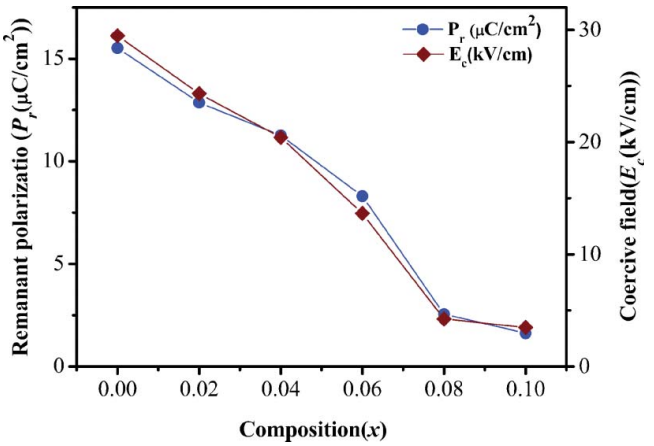

Figure 6. The composition (x) dependence of remanent polarization (P_r (μC/cm^2)) and coercive field (E_c(kV/cm)) in 0.9BT-(0.1-x)BNT-(x)BMT ceramics.

increase, the R_{sq} parameter decreases from 1.56 to 0.33 which implies that P-E hysteresis loop becomes more slanted. On the other words, the P-E loops changes from normal ferroelectric to relaxor behavior with increasing BMT concentration which is consistent with the dielectric result.

Combined with the ferroelectric, the dielectric and XRD results of BT-BNT-xBMT ceramic, all of changes such as the transformation of crystal structure, the decreasing of transition temperature and remanent polarization and ferroelectric – relaxor ferroelectric phase transition are so smooth. Therefore, it could be said that BT-BNT and BMT can completely form solid solution throughout the whole composition range.

Figure 7 illustrates the unipolar strain curves of BT-BNT-xBMT ceramics measured at room temperature with an external electric field of 60 kV/cm. It is clearly found the decreasing of unipolar strain of BT-BNT-xBMT ceramics from 0.2% to 0.09% when the

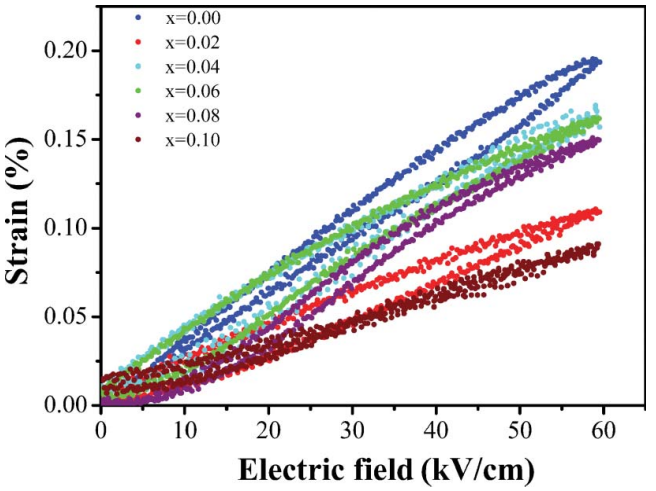

Figure 7. The relative plot of unipolar strain (%) as a function of electric field (kV/cm) in 0.9BT-(0.1-x)BNT-(x)BMT (x = 0.00-0.10) ceramics.

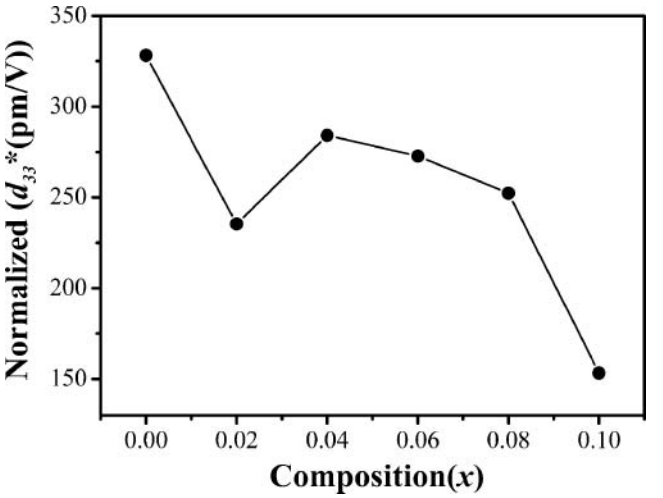

Figure 8. Normalized strain (d_{33} *(pm/V)) value of 0.9BT-(0.1-x)BNT-(x)BMT ceramics with the composition $0.00 \leq x \leq 0.10$.

composition of x was increased from 0.00 to 0.10. The normalized strain (d_{33}*) value of BT-BNT-XBMT ceramics was calculated from the S_{max}/E_{max} ratio for each composition. The composition dependence of normalized strain tends to decrease from 328 pm/V to 153 pm/V when composition of BMT increases, as represented in figure 8. This result has caused the approaching to the relaxor-like behavior with increasing of BMT [26].

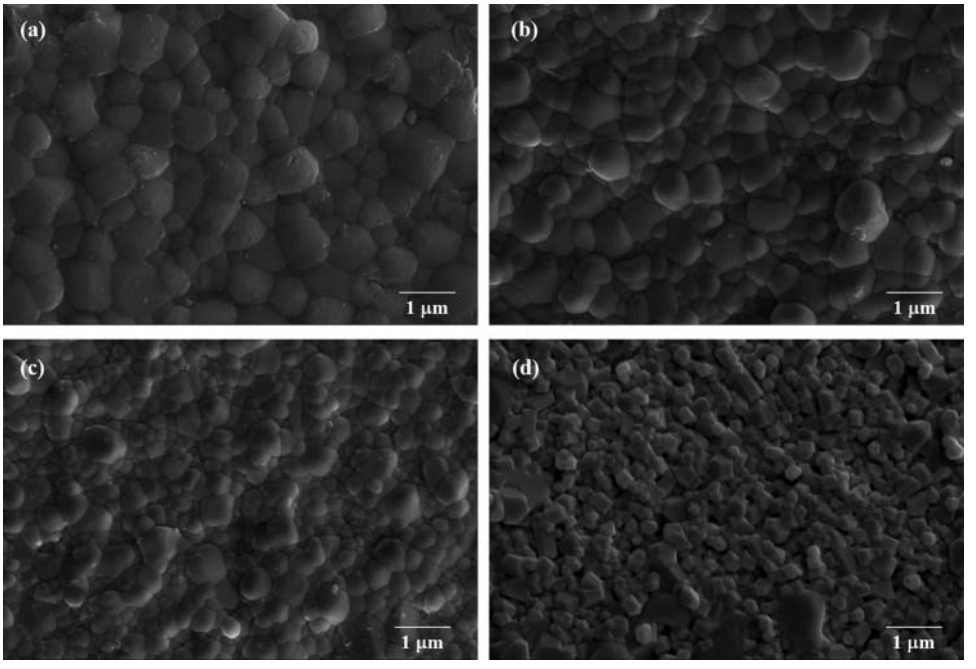

Figure 9. SEM micrographs of 0.9BT-(0.1-x)BNT-(x)BMT ceramics with various compositons (a) x = 0.00, (b) x = 0.02, (c) x = 0.04, and (d) x = 0.10.

The composition dependence of the level of induce strain is similar to result observation of BT-Bi($Ni_{1/2}Ti_{1/2}$)O_3 system [27].

Figure 9 displays SEM micrograph of the sintered surfaces of BT-BNT-*x*BMT ceramics at $x = 0.00$, 0.02, 0.04 and 0.10. The substitution of BMT directly effects on the average grain size of BT-BNT-*x*BMT ceramics. For the composition $x = 0.00$, the grain morphology shows and the average grain size is about 1.01 ± 0.14 μm. Homogeneous and uniformity feature microstructures were observed in the composition $x = 0.00$. The wide grain size distributions was observed in the composition $x = 0.02$ and 0.04. For the composition $x = 0.10$, more disorderly and unsystematic shaped grains are observed. A dramatic grain growth inhibition was founded with increasing BMT composition. The average grain size decreased significantly with increasing the composition *x*. The average grain size are about 0.72 ± 0.09 μm, 0.54 ± 0.09 μm, and 0.49 ± 0.07 μm for the composition $x = 0.02$, 0.04 and 0.10 respectively. This should be attributed to the effects arisen from the donor-type nature of BMT on inhibiting the grain growth [22]. The decreasing in piezoelectric properties in BNT-BT-xBMT system may be attributed to the inhibiting of the grain growth coursed by substitution of BMT in the BNT-BT system. The detailed mechanisms of the diminution in piezoelectric properties of BNT-BT-xBMT system are unclear and demands further study.

4. Conclusion

Lead free 0.9$BaTiO_3$-(0.1-*x*)$Bi_{0.5}Na_{0.5}TiO_3$-*x*Bi($Mg_{0.5}Ti_{0.5}$)O_3 (BT-BNT-*x*BMT; $x = 0.00 - 0.10$) piezoelectric ceramics were synthesized successfully by the solid state reaction. The crystal structure of BT-BNT-*x*BMT solid solution transforms from tetragonal to pseudocubic symmetry with increasing of BMT content. Combined with the ferroelectric and the dielectric results of BT-BNT-*x*BMT ceramic, phase transition of ceramics gradually changed from ferroelectric to relaxor-like behavior as BMT content increased. Also, BT-BNT and BMT can completely form solid solution throughout the whole composition range.

Funding

This work was supported by the Thailand Research Fund (TRF), under Grant No. BRG5680006.

References

1. J. Rödel, W. Jo, K. T. P. Seifert, E. M. Anton, and T. Granzow, D. Damjanovic, Perspective on the development of lead-free piezoceramics. *J Am Ceram Soc.* **92**, 1153–1177 (2009).
2. M. Rawat, and K. L. Yadav, Structural, dielectric and ferroelectric properties of $Ba_{(1-x)}(Bi_{0.5}Na_{0.5})xTiO_3$ ceramics. *Ceram Int.* **39**, 3627–3633 (2013).
3. J. Wu, D. Xiao, W. Wu, Q. Chen, Q. Zhu, Z. Yang, and J. Wang, Role of room-temperature phase transition in the electrical properties of (Ba, Ca)(Ti, Zr)O_3 ceramics. *Scripta Mater.* **65**, 771–774 (2011).
4. J. Wu, A. Habibul, X. Cheng, X. Wang, and B. Zhang, Orthorhombic–tetragonal phase coexistence and piezoelectric behavior in (1-x)(Ba,Ca)(Ti,Sn)O_3–x(Ba,Ca)(Ti,Zr)O_3 lead-free ceramics
5. T. Takenaka, K. Maruyama, and K. Sakata, ($Bi_{1/2}Na_{1/2}$)TiO_3-$BaTiO_3$ System for Lead Free Piezoelectric Ceramics. *Jpn J Appl Phys.* **30**, 2236–2239 (1991).

6. L. Gao, L. Huang, Y. Hu, and H. Du, Dielectric and ferroelectric properties of (1-x)$BaTiO_3$–x$Bi_{0.5}Na_{0.5}TiO_3$ ceramics. *Ceram Int.* **33**, 1041–1046 (2007).
7. S. Zhang, A. B. Kounga, E. Aulbach, T. Granzow, W. Jo, and H. Kleebe, Rödel J: Lead-free piezoceramics with giant strain in the system $Bi_{0.5}Na_{0.5}TiO_3$-$BaTiO_3$ - K $_{0.5}Na_{0.5}NbO_3$. I. Structure and room temperature properties. *J Appl Phys.* **103**, 034107 (2008).
8. J. F. Trelca, C. Courtois, M. Rguiti, A. Leriche, P. H. Duvigneaud, and T. Segato, Morphotropic phase boundary in the BNT–BT–BKT system. *Ceram Int.* **38**, 2823–2827 (2012).
9. J. U. Rahman, A. Hussain, A. Maqbool, G. H. Ryu, T K Song, W. Kim, and M. H. Kim, Field induced strain response of lead-free $BaZrO_3$-modified $Bi_{0.5}Na_{0.5}TiO_3$-$BaTiO_3$ ceramics. *J. Alloy Compd.* **593**, 97–102 (2014).
10. S. Wadda, K. Yamato, P. Pulpan, N. Kumada, B. Y. Lee, T. Iijima, C. Moriyoshi, and Y. Kuroiwa, Preparation of barium titanate–bismuth magnesium titanate ceramics with high Curie temperature and their piezoelectric properties. *J. Ceram Soc Jpn.* **118**(8), 683–687 (2010).
11. Q. Wang, J. Chen, L. Fan, L. Liu, L. Fang, and X. Xing, Preparation and Electric Properties of $Bi_{0.5}Na_{0.5}TiO_3$–$Bi(Mg_{0.5}Ti_{0.5})O_3$ Lead-Free Piezoceramics. *J. Am. Ceram. Soc.* **96**(4), 1171–1175 (2013).
12. R. D. Shannon, Revised effective ionic radii and systematic studies of interatomic distances in halides and chalcogenides. *Acta Crystallogr.,Sect. A: Cryst. Phys.,Diffr.,Theor. Gen. Crystallogr.* **A 32**, 751–767 (1976).
13. A. S. Bhalla, R. Guo, and R. Roy, The perovskite structure - a review of its role in ceramic science and technology. *Mater Res Innov.* **4**, 3–26 (2000).
14. O. Muller, and R. Roy, *The major ternary structural families.* (Springer-Verlag Berlin-Heidelberg-New/sYork (1974).
15. B. Jaffe, and W. R. Cook, *Piezoelectric ceramics.* (Academic Press, New York, (1971).
16. G. A. Smolenskii, Physical phenomena in ferroelectrics with diffuse phase transition. *Jpn. J. Phys. Soc.* **28**, 26–37 (1970).
17. S. K. Rout, E. Sinha, and S. Panigrahi, Dielectric properties and diffuse phase transition in $Ba_{(1-x)}Mg_xTi_{0.6}Zr_{0.4}O_3$ solid solutions. *Mater.Chem.Phys.* **101**, 428–432 (2007).
18. K. Uchino, and S. Nomura, Critical exponent of the dielectric constant in diffused-phase-transition crystals. *Ferroelectrics Lett.* **44**, 55 (1982).
19. R. Clarke, and J. C. Burfoot, The diffuse phase transition in potassium strontium niobate. *Ferroelectrics.* **48**, 505 (1974).
20. V. A. Isupov, Nonlinearity of the concentration dependence of the Curie temperature in ferroelectric perovskite solid solutions. *Phys Stat. Sol. (a).* **181**, 21 (2000).
21. R. J. Bratton, and T. Y. Tien, Phase Transitions in the System $BaTiO_3$—$KNbO_3$. *J Am Ceram Soc.* **50**, 90–93 (1967).
22. F. He, X. Chen, J. Chen, Y. Wang, H. Zhou, and L. Fang, $(K_{0.5}Na_{0.5})NbO_3$-$Bi(Mg_{0.5}Ti_{0.5})O_3$ solid solution: phase evolution, microstructure and electrical properties. *J Mater Sci-Mater El.* **24**, 4346–4350 (2013).
23. W. Bai, Y. Bian, J. Hao, B. Shen, and J. Zhai, The Composition and Temperature-Dependent Structure Evolution and Large Strain Response in (1-x)$(Bi_{0.5}Na_{0.5})TiO_3$-x$Ba(Al_{0.5}Ta_{0.5})O_3$ Ceramics. *J. Am. Ceram. Soc.* **96**(1), 246–252 (2013).
24. D. Xu, W. L. Li, L. D. Wang, W. Wang, W. P. Cao, and W. D. Fei, Large piezoelectric properties induced by doping ionic pairs in BaTiO3 ceramics. *Acta materialia.* **79**, 84–92 (2014).
25. G. H. Haertling, and W. J. Zimmer, Analysis of hot-pressing parameters for lead zirconate-lead titanate ceramics containing two atom percent bismuth. *Am. Ceram. Soc. Bull.* **45**, 1084–1089 (1966).
26. D. Xu, W. L. Li, L. D. Wang, W. Wang, W. P. Cao, and W. D. Fei, Large piezoelectric properties induced by doping ionic pairs in $BaTiO_3$ ceramics. *Acta mater.* **79**, 84–92 (2014).
27. I. Fujit, K. Nakashima, N. Kumada and S. Wada, Structural, Dielectric and piezoelectric properties of $BaTiO_3$–$Bi(Ni_{1/2}Ti_{1/2})O_3$ ceramics. *J. Ceram Soc Jpn.* **120**, 30–34 (2012).

Ferroelectrics

ISSN: 0015-0193 (Print) 1563-5112 (Online) Journal homepage: http://www.tandfonline.com/loi/gfer20

High Strain Response of the (1-x)($0.94Bi_{0.5}Na_{0.5}TiO_3$-$0.06BaTiO_3$)-x$BaSnO_3$ Lead Free Piezoelectric Ceramics System

Jira Janbua, Surasak Niemchareon, Rangson Muanghlua & Naratip Vittayakorn

To cite this article: Jira Janbua, Surasak Niemchareon, Rangson Muanghlua & Naratip Vittayakorn (2016) High Strain Response of the (1-x)($0.94Bi_{0.5}Na_{0.5}TiO_3$-$0.06BaTiO_3$)-x$BaSnO_3$ Lead Free Piezoelectric Ceramics System, Ferroelectrics, 490:1, 13-22, DOI: 10.1080/00150193.2015.1070655

To link to this article: http://dx.doi.org/10.1080/00150193.2015.1070655

Published online: 29 Jan 2016.

Ferroelectrics, 490: 13–22, 2016

ISSN: 0015-0193 print / 1563-5112 online
DOI: 10.1080/00150193.2015.1070655

High Strain Response of the $(1\text{-}x)(0.94Bi_{0.5}Na_{0.5}TiO_3\text{-}0.06BaTiO_3)\text{-}xBaSnO_3$ Lead Free Piezoelectric Ceramics System

JIRA JANBUA,[1] SURASAK NIEMCHAREON,[2] RANGSON MUANGHLUA,[2] AND NARATIP VITTAYAKORN[1,3,4,*]

[1]College of Nanotechnology, King Mongkut's Institute of Technology Ladkrabang, Bangkok 10520, Thailand
[2]Department of Electronics Engineering, Faculty of Engineering, King Mongkut's Institute of Technology Ladkrabang, Bangkok 10520, Thailand
[3]Advanced Materials Research Unit, Faculty of Science, King Mongkut's Institute of Technology Ladkrabang, Bangkok 10520, Thailand
[4]Nano-KMITL Center of Excellence on Nanoelectronic Devices, KMITL, Ladkrabang, Bangkok, 10520,Thailand

The system of lead free piezoelectric ceramics, (1-x)(0.94$Bi_{0.5}Na_{0.5}TiO_3$-0.06$BaTiO_3$)-x$BaSnO_3$ [abbreviated as BNT-BT-xBSn] with the compositions, x = 0.00, 0.02, 0.04, 0.06, 0.08 and 0.10 was synthesized via the conventional solid state reaction method. All the products from X-ray diffraction patterns showed diffraction peaks as a phase perovskite structure, with no secondary phases. Due to the composition-dependence of the ferroelectric, bipolar and unipolar strain properties were investigated in order to achieve a good new lead free piezoelectric ceramics system. It was noticeable that a large strain of around 0.4%, with a normalized strain value (d_{33}^*) of 669 pm/V at the x = 0.02composition, by applying an electric field of 60 kV/cm at room temperature. The results of this study showed that a new BNT-BT-xBSn ceramics system is a very promising candidate for creating a significantly large strain response, which is sufficiently effective for actuator material applications.

Keywords Perovskite; normalized strain (d_{33}^*); BNT-BT-*x*BSn

1. Introduction

Lead zirconate titanate (PZT) and PZT-based ceramics with a perovskite structure have been applied extensively for actuators, sensors and transducers in many electromechanical devices [1], due to the fact that of superb piezoelectric properties, the piezoelectric coefficient (d_{33}) is about 200-600 pC/N and strain 0.3% [2, 3]. Nevertheless, the high level of toxicity in lead (Pb) or lead oxide (PbO) from

Received October 26, 2014; in final form January 19, 2015.
*Corresponding author. E-mail: naratipcmu@yahoo.com
Color versions of one or more figures in this article can be found online at www.tandfonline.com/gfer.

component lead-based piezoelectric ceramics was brought about with severe environmental problems. In July 2006, the European Union (EU) legislated two directives including Waste Electrical and Electronic Equipment (WEEE) and Restriction of the use of certain Hazardous Substances in electrical and electronic equipment (RoHS) in order to protect human health and the environment by avoiding dangerous waste from electronic equipment and replacing it with less hazardous substances. Therefore, the current development of lead-free piezoelectric materials has been evaluated as a substitute for lead-based piezoelectric materials.

The lead free piezoelectric ceramics perovskite binary system, such as $Bi_{0.5}Na_{0.5}TiO_3$ -$BaTiO_3$ (abbreviated as BNT-BT), has been investigated as an important candidate for replacing Pb-based piezoelectric materials, which are used widely in industry. Bismuth sodium titanate ($Bi_{0.5}Na_{0.5}TiO_3$, BNT) was combined with barium titanate ($BaTiO_3$, BT) by Takenaka et al.in 1991 [4], and this (1-x) BNT-xBT binary system found a morphotropic phase boundary (MPB) between rhombohedral and tetragonal phases at the compositions, $x = 0.06$-0.07mol % BT. This composition has enhanced dielectric and piezoelectric properties such as $d_{33} = 125$ pC/N, $^{T}_{33}/\varepsilon_0 = 580$, $k_{33} = 55.0\%$, $\tan\delta = 1.3\%$, and $T_c = 288°$C. In order to develop these binary materials, previous researchers have attempted to improve their piezoelectric properties in order to provide high performance in applications that are comparable to equivalent Pb-based material by modifying via a solid state reaction method with several perovskite materials such as $Bi_{0.5}K_{0.5}TiO_3$ (BKT) [5], $K_{0.5}Na_{0.5}NbO_3$ (KNN) [6], $CaTiO_3$ (CT) [7], and $BaZrO_3$ (BZ) [8]. The concept of morphotropic phase boundary (MPB) is a preferred alternative for achieving excellent strain value that is promising for piezoelectric actuator applications. Recently, a large strain value was proposed for BNT-based solid solution ceramics, for example, the $1-x$$Bi_{0.5}Na_{0.5}TiO_3$–$x$$KNbO_3$ system; in which a very large reversible strain (0.40%) with a normalized strain value ($d_{33}^{*} = 498$ pm/V) was achieved at an MPB between ferroelectric rhombohedral and relaxor ferroelectric phases with pseudocubic phases. The large reversible strain was clarified by non-180° 71° and 109° domain switching of the field-induced ferroelectric rhombohedral phase [9]. Large strains also were obtained in the BNT-BT-based system. A large strain of 0.45% was reported for the (0.94-x)$Bi_{0.5}Na_{0.5}TiO_3$–0.06$BaTiO_3$–$x$$K_{0.5}Na_{0.5}NbO_3$ system at an applied electric field of 80 kV/cm with a normalized strain value (d_{33}^{*}) of 567 pm/V [6]. This was attributed to the structural lattice change by field-induced transition between antiferroelectric and ferroelectric phases. In addition, Jamil et al. [8] proposed the $BaZrO_3$-modified 0.935$Bi_{0.5}Na_{0.5}TiO_3$–0.065$BaTiO_3$ system, with a large strain of 0.38% and normalized strain (d_{33}^{*}) of 542 pm/V at an electric field of 70 kV/cm. The P–E and S–E loops exhibited transition from the ferroelectric to relaxor ferroelectric phase by passing through an intermediate phase that coexists in both ferroelectric and relaxor ferroelectric phases. $BaSnO_3$ (BSn), with a cubic unit crystal cell structure (the same as in $BaZrO_3$ and $SrTiO_3$), displays as lead-free perovskite materials, with applications such as gas sensors, semiconductors (n-type semiconductor with an energy band gap of 3.4 eV), and actuators [10–12].

This serves the purpose of synthesizing new solid solutions of the(1-x)(0.94$Bi_{0.5}Na_{0.5}TiO_3$-0.06$BaTiO_3$)-$x$$BaSnO_3$ system with the compositions, $x = 0.00$, 0.02, 0.04, 0.06, 0.08 and 0.10, and obtaining the MPB composition that causes a significantly promising large strain response that is sufficiently effective for actuator applications. The dielectric, ferroelectric (FE), bipolar and unipolar strain properties were measured as a function with different compositions.

2. Experimental Procedure

The (1-x)(0.94$Bi_{0.5}Na_{0.5}TiO_3$-0.06$BaTiO_3$)-$x$$BaSnO_3$ceramics were prepared by a conventional solid state reaction, with the compositions, $x = 0.00$-0.10. The powders with high purity of Bi_2O_3 (99.9%, Sigma-Aldrich), Na_2CO_3 (99.8%, Riedel-deHaen), TiO_2 (99.9%, Sigma-Aldrich), $BaCO_3$ (98.5%, Fluka) and SnO_2 (99.9%, Sigma-Aldrich) were used as starting raw materials. In first step, all powders were weighed according to the stoichiometric ratio of the product and ball-milled with zirconia balls in ethanol for 18 h. The mixed oxide powders were dried in an oven at 85°C and calcined at 850°C for 2 h, with a heating rate of 10°C/min. After that, the powders were sieved with 325-sized mesh for uniformed particle size screening before they were mixed with 5% polyvinyl alcohol and pressed uniaxially into circular disks, with a diameter of 10 mm. The sintering was carried out at 1,150°C for 2 h in air, in order to avoid vaporisation of the bismuth element. The as-prepared samples were examined for density by archimedes' principle. While the law of mixture was used for calculating the theoretical density of each composition, the densities of $Bi_{0.5}Na_{0.5}TiO_3$, $BaTiO_3$, and $BaSnO_3$ pure phases were 5.99 g/cm^3 (JCPDs No.36-0340), 6.012 g/cm^3 (JCPDs No.05-0626), and 7.238 g/cm^3 (JCPDs No.15-0780), respectively. The relative density of all sintered BNT-BT-xBSn ceramics was higher than 97%. The pellet samples were polished down to a smooth surface, and the phase purity and crystal structure of the pellet samples were investigated by X-ray diffraction (Bruker-AXS D 8 Advance), with Cu Kα_1 radiation and collection range of 2θ from 10° – 80°. Raman spectrophotometer (DXR smart Raman, Thermo scientific) was performed on pellets by using the 532 nm exciting line of a He–Ne laser recorded its wavelength range of between 100 and 1,000 cm^{-1}. In order to prepare the pellet samples for piezoelectric and ferroelectric measurement were polished down to approximately less than 0.65 mm. Ag paste electrodes were applied and then fired at 650°C for 30 min. Characterization of the ferroelectric hysteresis loops was performed in silicone oil at room temperature using a ferroelectric tester system (RT66B; Radient Technologies, Inc., Albuquerque, NM). The unipolar and bipolar strain characterization was measured by usingMTI-2100 Fotonic sensor combine with Radiant Technologies, Inc in silicone oil at room temperature.

3. Results and Discussion

Figure 1(a) shows the X-ray diffraction patterns of BNT-BT-xBSn ceramics with the compositions, $x = 0.00$–0.10. All of the diffraction peaks were observed clearly as a phase perovskite structure, without secondary phases. Peak enlargement at theta degrees (2θ) of around 39.5– 40°, 46– 46.5°, and 57–58° is exhibited in Figures 1(b to d), respectively. At the non-doped composition, x = 0.00, peak splitting is shown in the (003), with (021) at a 2θ of about 39.5 – 40°, and the (104), with (122) at a 2θ of about 57–58 °, which is in accordance to the rhombohedral phase. Furthermore, slight splitting can be seen at a 2θ of about 46– 46.5°, which assumes a (200) and (002) characteristic peak of the tetragonal phase. It is well known that the MPB between the rhombohedral (R) and tetragonal (T) phase was found in the composition of 0.94BNT-0.06BT[4]. Thus, BNT-BT-xBSn at the composition, $x = 0$ suggested an MPB of R-T. An increased concentration of BSn (x = 0.02–0.10) shows minor splitting in the (111), (200), and (211) peak, which resulted from Kα_2 (1.54439 Å) radiations. However, increasing the BSn content makes it become a pseudocubic symmetry structure. Additionally, the peak was seen to shift to lower angles with increasing BSn content. This leads to unit cell expansion, due to replacement of the larger ionic radius of Sn^{4+} (0.69 Å) when compared with Ti^{4+} (0.605 Å), which is similar to results observed in Sn-doped $BaTiO_3$ by K. Chandramani Singh et al. [13].

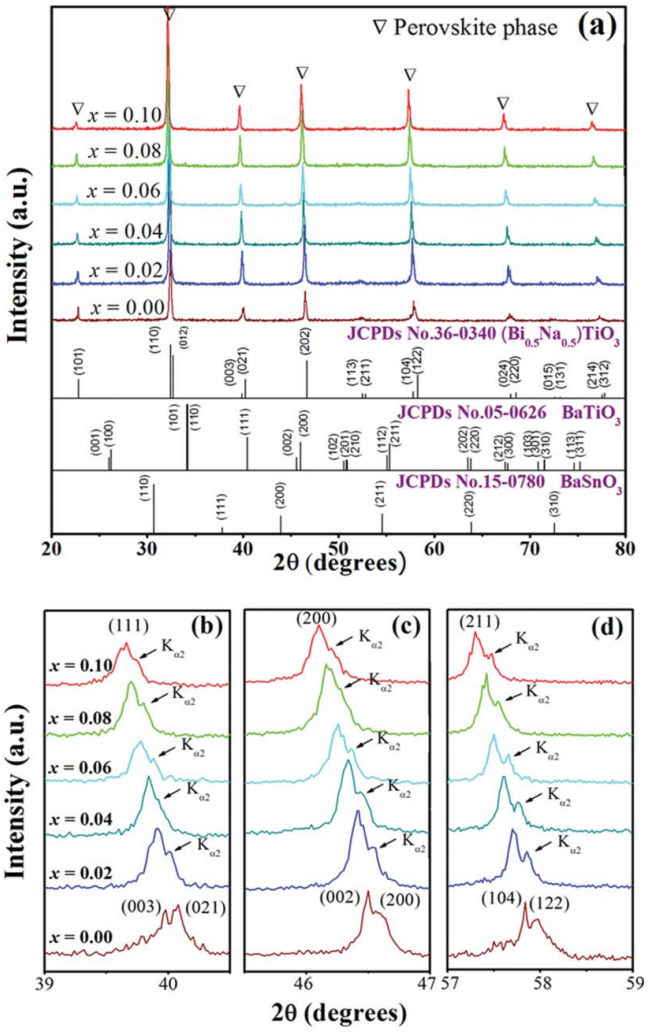

Figure 1 (a) X-ray diffraction patterns of the BNT-BT-*x*BSn ceramics system with the compositions, x = 0.00–0.10, and expanding chart of 2*θ*, (b) 39° – 40°, (c) 45° – 47° and (d) 57° – 59°.

In order to clarify the extreme composition-dependent phase transition behavior, Raman spectroscopy was used to determine the short length structure of local ionic configuration. Raman spectra of BNT-BT-*x*BSn ceramics were recorded at room temperature in the frequency range of 100 - 1,000 cm^{-1}, as plotted in Figure 2. The spectrum for pure 0.94BNT-0.06BT was reported previously in other data [14, 15]. Three modes distinguished broad peaks that were detected at around 268, 536, and 605 cm^{-1}, and associated with Ti-O vibrations in the TiO_6 octahedral [10]. The mode of high-frequency over 700 cm^{-1} was associated with E (longitudinal optical) and A_1 (longitudinal optical) overlap bands [16]. Increasing substitute BSn composition shows gently broadening peaks that begin to form into two peaks at 268 cm^{-1} mode, while further splitting occurs at 536 and 605 cm^{-1} mode, due to distortion of TiO_6octahedra. This is a result of substituting Sn^{4+} ion with a higher ionic radius at the Ti in B-site. Obviously, it is worth noting that the

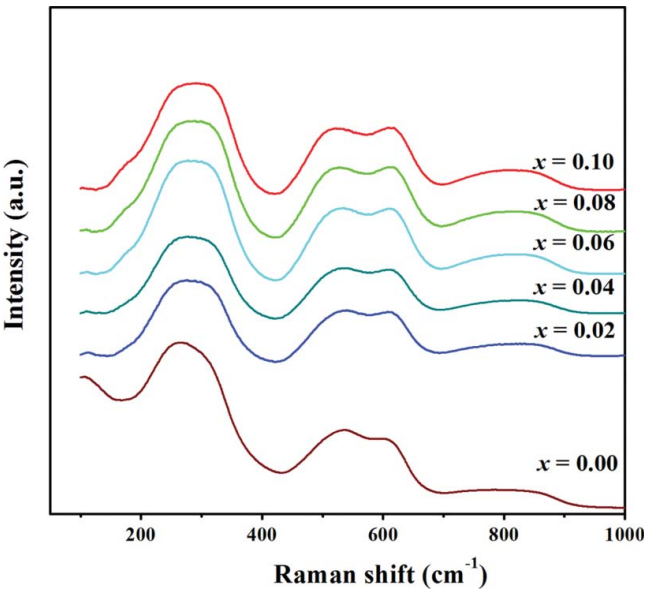

Figure 2 Raman spectra of BNT-BT-*x*BSn ceramics with different compositions.

composition, $x = 0.02$, started broadening at the 278 cm^{-1} mode and clearly split into two modes at 536 and 605 cm^{-1}, and transformed into a pseudocubic structure according to XRD results. However, the electric property measurement should be considered for confirming the structure evolution and phase mixture, specifically with ferroelectric (FE) and piezoelectric properties.

The plot of polarization with the electric field (P-E hysteresis loops) was investigated at room temperature for BNT-BT-*x*BSn ceramics with different compositions at 60 kV/cm and 10 kHz. Figure 3 shows the P-E hysteresis loops for the composition, $x = 0.00$, and reveals well saturation hysteresis loops of typical ferroelectric (FE) behavior with saturated polarization (P_s), remanent polarization (P_r), and coercive field (E_c) of 36 $\mu C/cm^2$, 35 $\mu C/cm^2$, and 37 kV/cm, respectively. As evidently seen, when the BSn content increases, P_s values decrease slightly and largely decrease in both P_r and E_c because when the applied electric field reaches E_c it relates easier to domain switching and domain wall motions. Figure 4 presents relationship of the P_r, P_s, and E_c values and BSn composition of BNT-BT-*x*BSn ceramics.

The results indicated that a sharp transition from non-ergodic relaxor (NR) state to ergodic relaxor (ER) state was observed with increasing BSn content. The dramatically decrease in P_r is caused by the lacks of long-range ferroelectric order in the sample. It is well known that, at above transition temperatures, relaxors ferroelectrics exist in a non-polar paraelectric state. Below the transition temperature, relaxors transform into an ergodic relaxor state at the Burns temperature nearly dynamic polar nano-regions (PNRs) with dipole moment directions randomly appear. With decreasing the temperature, the dynamics of PNR delay down until the PNRs become frozen and the relaxor transforms into a NR state which lacks of long-range ferroelectric order and be similar to a dipolar glass state.

The slim P-E hysteresis loops were observed clearly due to lower significant values of P_r and E_c for samples with a pseudocubic structure. It could be suggested that typical relaxor ferroelectric behavior and the results of this study are similar to the phase transition in BNT-based ceramics proposed by Hiruma et al.[9].This result is also similar to

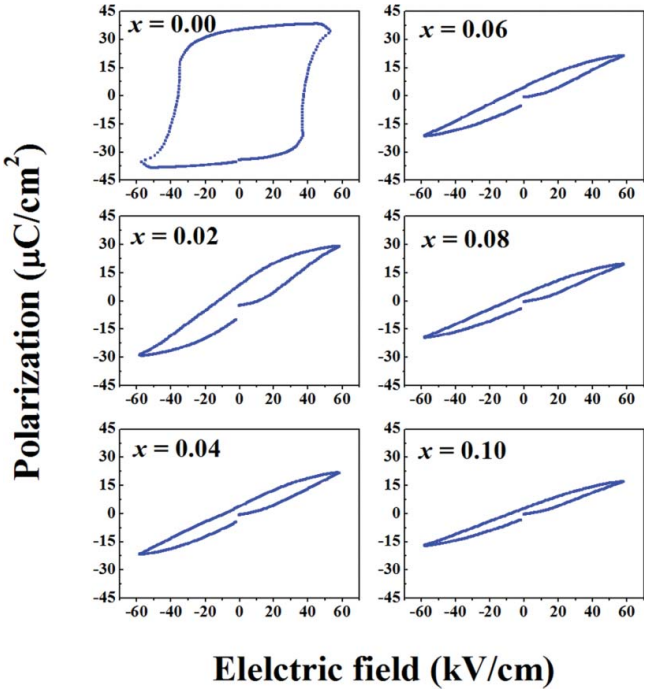

Figure 3 Polarization with the electric field (P-E hysteresis loops) of BNT-BT-*x*BSn ceramics with different compositions at room temperature under an applied electric field of 60 kV/cm.

observed by Jamil et al. that the P–E behavior of BNBT–BZ ceramics gently changed from ferroelectric to relaxor ferroelectrics [8]. Furthermore, NR state to ER relaxor cross-over behavior originated from the addition of KNN into the BNT-BT system and induced the giant strain, as also observed by Jo et al. [17, 18].

Figure 5 shows the bipolar electric-field with strain curves (S-E curve) of BNT-BT-*x*BSn ceramics, with different compositions measured at room temperature under an

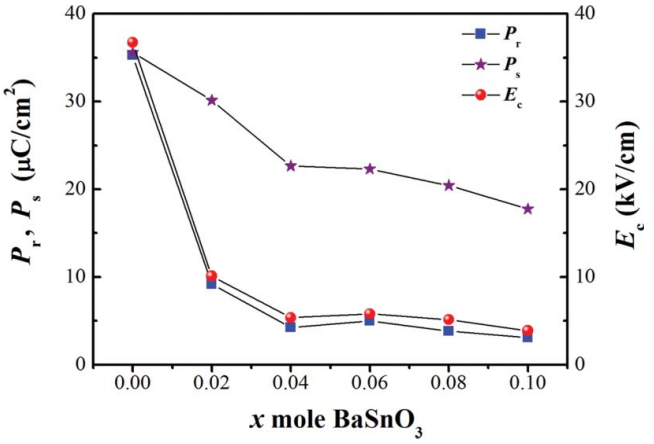

Figure 4 Polarization and coercive field values of BNT-BT-*x*BSn ceramics.

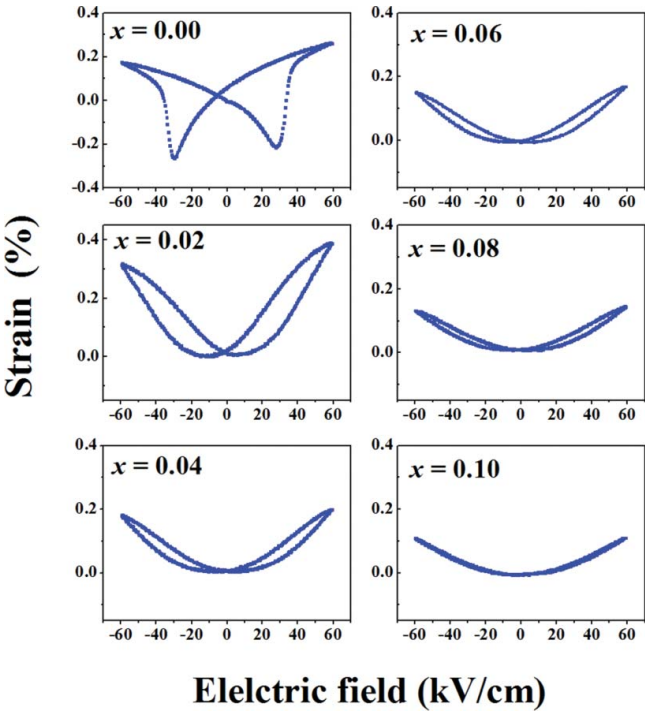

Figure 5 The bipolar electric-field with strain curves (S-E curve) of BNT-BT-*x*BSn ceramics.

applied electric field of 60 kV/cm. While Figure 6 shows the negative strain (S_n) values with BSn content, the S_n factor associates with domain back switching. This is a negative strain with a difference between the zero field and lowest strain. Pure 0.94BNT-0.06BT composition exhibits a well-defined typical butterfly S–E loop. In other compositions ($x > 0.02$), deviation from the butterfly S–E loops is accompanied by a significant reduction of negative strain. These results indicate different domain switching mechanisms induced by electric-field. Figure 6 shows decreasing S_n that suggests increasing the addition of BSn content proportionally, which deviates greatly from typical ER behavior. The pure 0.94BNT-0.06BT composition shows a large negative strain value of 0.27%, which corresponds with features typical for NR materials and coexistence between the rhombohedral (R) and tetragonal (T) phase. With a higher BSn content ($x > 0.02$), the S_n value approaches zero, which corresponds to a decreasing P_r value in the hysteresis loop curve for samples with a pseudocubic structure (as the relaxor ferroelectric phase relates to an almost invisible negative strain). It is believed that the transition boundary of the ER and NR relaxor phase in the composition, $x = 0.02$, results in displaying a large strain response. The highest strain of 0.4% was acquired with few negative strains at an electric field of 60 kV/cm. This result agrees well with other BNT-BT-based ceramics, for example, the BNT-BT-BZ3 system had a strain of 0.36% at an electric field of 70 kV/cm [8], the BNT-BT-KNN system had a strain of 0.45% at an electric field of 80 kV/ cm [6], the BNT-BT-SZ2 system had a strain of 0.39% at an electric field of 55 kV/cm [19], and the BNKT–BA3 system had a strain of 0.35% at an electric field of 60 kV/ cm [20].

To highlight the efficiency of this ceramic system for actuator applications, the unipolar electric-field with strain curves in the BNT-BT-*x*BSn system were investigated with

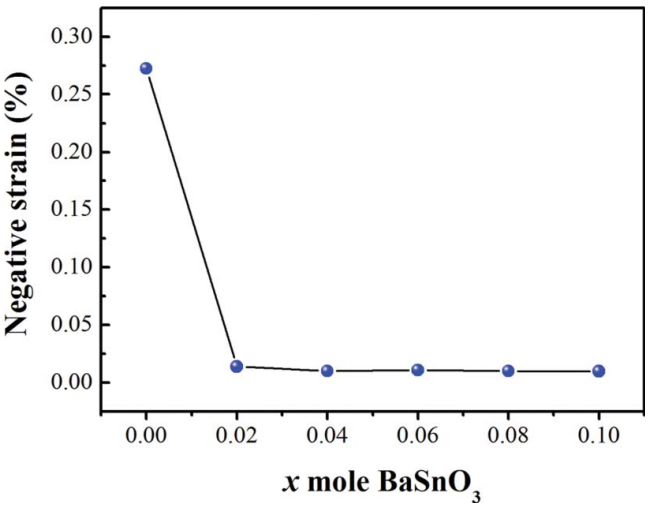

Figure 6 Negative strain (S_n) values with different contents of BSn composition.

various BSn concentrations at an applied electric field of 60 kV/cm, as plotted on the graph in Figure 7. A noticeably large strain of around 0.4% was obtained at the composition, $x = 0.02$, which is consistent with the results from strain curves of the bipolar electric-field. In addition, by increasing the amount of BSn ($x \geq 0.04$) further, the strain steadily decreases.

Figure 8 shows the normalized strain (d_{33}^*, pm/V) and maximum (%) strain values of all compositions in the BNT-BT-xBSn system. The normalized strain (d_{33}^*) can be calculated from the relationship of the S_{max}/E_{max}, d_{33}^* value. The composition, $x = 0.02$, has reached the maximum value of 669 pm/V, as a result of boundary between the NR and ER relaxor ferroelectric phases confirmed by the nature of P-E hysteresis loops. The concept of MPB or PPT is a preferred alternative for achieving a good, large strain that is promising for piezoelectric

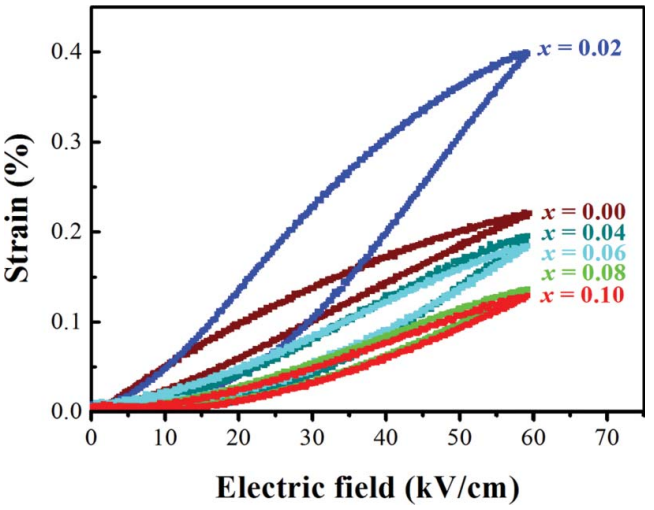

Figure 7 The unipolar electric-field with strain curves of BNT-BT-xBSn ceramics.

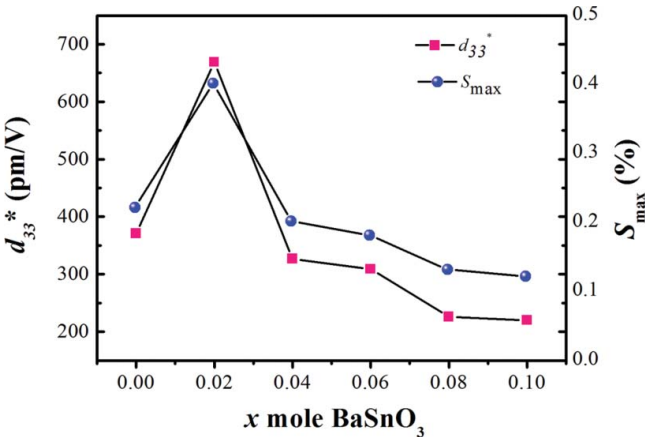

Figure 8 The normalized (d_{33}^*, pm/V) and maximum strain (%) values ofBNT-BT-xBSn ceramics.

actuator applications. This was the case in similar results from other BNT-BT-based ceramic researches such as those for BNT–BT6-KNN2 ($d_{33}^* = 567$ pm/V) [6], BNT–BT-BZ3 ($d_{33}^* =$ 542 pm/V) [8], BNT-BT-SZ2 ($d_{33}^* = 722$ pm/V) [19], BNKT–BA3($d_{33}^* = 592$ pm/V) [19], and comparable soft PZT ($d_{33}^* = 400$-590 pm/V) [21]. The results of this study propose that this BNT-BT-xBSn system is representative for lead-free piezoelectric materials, which are attractive and non-toxic in the environment.

4. Conclusion

The (1-x)(0.94$Bi_{0.5}Na_{0.5}TiO_3$-0.06$BaTiO_3$)-$xBaSnO_3$ system (abbreviated as BNT-BT-xBSn) with the composition, $x = 0.00 – 0.10$, was synthesized via the conventional solid state reaction method. The X-ray diffraction patterns of all the products showed diffraction peaks as a phase perovskite structure with no secondary phases. Results from the P-E hysteresis loops obtained showed a feature transition from square to narrow and slimmer loops with increased BSn content, which exhibited typical NR relaxor state and ER relaxor state behavior. It is believed that the transition of NR to ER relaxor ferroelectric phases results in displaying a large strain response. It is noticeable that large strains of around 0.4%, with a normalized strain value (d_{33}^*) of 669 pm/V at the $x = 0.02$ composition, to perform at room temperature under an applied electric field of 60 kV/cm. The results of this study showed that a new BNT-BT-xBSn ceramics system is a very promising candidate for creating a significantly large strain response, which is sufficiently useful for actuator material applications.

Funding

This work was supported by the Thailand Research Fund (TRF) under Grant No. BRG5680006.

References

1. J. Rödel, W. Jo, KTP Seifert, E. M. Anton, T. Granzow and D. Damjanovic : Perspective on the development of lead-free piezoceramics. *J Am Ceram Soc*. **92**, 1153–1177 (2009).

2. M. Dolgos, U. Adem, X. Wan, Z. Xu, A. J. Bell, T. P. Comyn, T. Stevenson, J. Bennett, J. B. Claridge and M. J. Rosseinsky: Chemical control of octahedral tilting and off-axis A cation displacement allows ferroelectric switching in a bismuth-based perovskite. *Chem Sci*. **3**: 1426–1435 (2012).
3. D. Damjanovic, N. Klein, J. Li and V. Porokhonskyy: What can be expected from lead-free piezoelectric materials?. *FunctMater Lett*. **3**: 5–13 (2010).
4. T. Takenaka, K. Maruyama and K. Sakata: $(Bi_{1/2}Na_{1/2})TiO_3$-$BaTiO_3$ system for lead free piezoelectric ceramics. *Jpn J Appl Phys*. **30**: 2236–2239 (1991).
5. J. Trelcat, C. Courtois, M. Rguiti, A. Leriche, P. Duvigneaud and T. Segato: Morphotropic phase boundary in the BNT-BT-BKT system. *Ceram Int*. **38**: 2823–2827 (2012).
6. S. Zhang, A. B. Kounga, E. Aulbach, T. Granzow, W. Jo and H. Kleebe, J Rödel : Lead-free piezoceramics with giant strain in the system $Bi_{0.5}Na_{0.5}TiO_3$-$BaTiO_3$ - $K_{0.5}Na_{0.5}NbO_3$. I. Structure and room temperature properties. *J Appl Phys.* **103**: 034107 (2008).
7. Y. Yuan, X. H. Zhou, C. J. Zhao, B. Li and S. R. Zhang: High-temperature capacitor based on Ca-doped $Bi_{0.5}Na_{0.5}TiO_3$-$BaTiO_3$ ceramics. *J Electron Mater*. **39**: 2471–2475(2010).
8. J. U. Rahman, A. Hussain, A. Maqbool, G. H. Ryu, T. K. Song, W. Kim and M. H. Kim: Field induced strain response of lead-free $BaZrO_3$-modified $Bi_{0.5}Na_{0.5}TiO_3$-$BaTiO_3$ ceramics. *J Alloy Compd*. **593**: 97–102(2014).
9. Y. Hiruma, H. Nagata and T. Takenaka: Phase diagrams and electrical properties of $(Bi_{1/2}Na_{1/2})TiO_3$-based solid solutions. *J Appl Phys*. **104**: 124106 (2008).
10. S. N. Tripathy, K. K. Mishra, S. Sen and D. K. Pradhan: Dielectric and raman spectroscopic studies of $Na_{0.5}Bi_{0.5}TiO_3$–$BaSnO_3$ ferroelectric system. *J Am Ceram Soc*. **97**: 1846–1854 (2014).
11. A. Aydi, H. Khemakhem, C. Boudaya, R. V. Mühll and A. Simon: New ferroelectric and relaxor ceramics in the mixed oxide system $NaNbO_3$-$BaSnO_3$. *Solid State Sci*. **6**: 333–337 (2004).
12. X. Han, X. Li, X. Long, H. Hea and Y. Cao: A dielectric and ferroelectric solid solution of (1-*x*) $BaSnO_3$-*x*$PbTiO_3$ with morphotropic phase boundary. *J. Mater Chem*. **19**: 6132–6136 (2009).
13. K. C. Singha, A. K. Nath, R. Laishram and O. P. Thakur: Structural, electrical and piezoelectric properties of nanocrystalline tin-substituted barium titanate ceramics, *Journal of Alloys and Compounds*, **509**: 2597–2601 (2011).
14. S. T. Zhang, A. B. Kounga, E. Aulbach and Y. Deng: Temperature-dependent electrical properties of $0.94Bi_{0.5}Na_{0.5}TiO_3$-$0.06BaTiO_3$ ceramics. *J Am Ceram Soc*. **91**: 3950–3954 (2008).
15. E. Aksel, J. S. Forrester, B. Kowalski, M. Deluca, D. Damjanovic and J. L. Jones: Structure and properties of La-modified $Na_{0.5}Bi_{0.5}TiO_3$ at ambient and elevated temperatures. *J Appl Phys*. **112**: 054111 (2012).
16. W. Jo, T. Granzow, E. Aulbach, J. Rödel and D. Damjanovic: Origin of the large strain response in $(K_{0.5}Na_{0.5})NbO_3$ -modified $(Bi_{0.5}Na_{0.5})TiO_3$-$BaTiO_3$ lead-free piezoceramics. *J Appl Phys*. **105**: 094102 (2009).
17. W. Jo, R. Dittmer, M. Acosta, J. Zang, C. Groh, E. Sapper, K. Wang and J. Rödel: Giant electric-field-induced strains in lead-free ceramics for actuator applications - Status and perspective. *JElectroceram*. **29**: 71–93 (2012).
18. A. Maqbool, A. Hussain, J. U. Rahman, T. KwonSong, W. J. Kim, J. Lee and M. H. Kim: Enhanced electric field-induced strainandferroelectricbehavior of $(Bi_{0.5s}Na_{0.5})TiO_3$-$BaTiO_3$-$SrZrO_3$ lead-free ceramics. *Ceram Int*. **40**: 11905–11914 (2014).
19. A. Ullah, C. W. Ahn, A. Hussain, S. Y. Lee, H. J. Lee and I. W. Kim: Phase transitions and large electric field-induced strain in $BiAlO_3$-modified$Bi_{0.5}(Na,K)_{0.5}TiO_3$ lead-free piezoelectric ceramics. *Curr Appl Phys*. **10**: 1174–1181 (2010).
20. P. Chen, C. Chen, C. Tu, C. Cheng and J. Cherng: Relaxor effect on electric field induced large strain in (1-*x*)$(Bi_{0.5}Na_{0.5})TiO_3$-*x*$BaTiO_3$ lead-free piezoceramics. *Ceram Int*. **40**: 6137–6142 (2014).

Materials and Design 110 (2016) 233–244

Contents lists available at ScienceDirect

Materials and Design

journal homepage: www.elsevier.com/locate/matdes

A facile one step conversion of the sub-micrometer to uniform nanopowder in tetragonal $BaTiO_3$ via a surface active etching salt

Thitirat Charoonsuk [a,b], Naratip Vittayakorn [a,b,c,d,*]

[a] Electroceramic Research Laboratory, College of Nanotechnology, King Mongkut's Institute of Technology Ladkrabang, Bangkok 10520, Thailand
[b] Advanced Material Research Unit, Faculty of Science, King Mongkut's Institute of Technology Ladkrabang, Bangkok 10520, Thailand
[c] Department of Chemistry, Faculty of Science, King Mongkut's Institute of Technology Ladkrabang, Bangkok 10520, Thailand
[d] Nano-KMITL Center of Excellence on Nanoelectronic Devices, King Mongkut's Institute of Technology Ladkrabang, Bangkok 10520, Thailand

HIGHLIGHTS

- The micro-scale $BaTiO_3$ precursor was conversed directly to nearly monodispersed nanoparticles in one step.
- Stoichiometry and crystal structure of the final nanoparticle products remained constant.
- A mechanism model for the formation of nanopowders was proposed and discussed in detail.
- This method is potentially useful for the preparation of other complex oxide systems with controlled size and scalability.

GRAPHICAL ABSTRACT

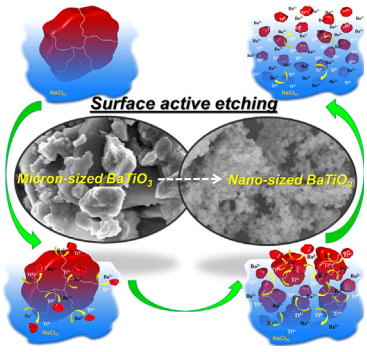

ARTICLE INFO

Article history:
Received 7 June 2016
Received in revised form 27 July 2016
Accepted 29 July 2016
Available online 01 August 2016

Keywords:
Barium titanate
Dielectric materials
Nanoparticles
Surface active etching
Ferroelectric materials

ABSTRACT

A reasonable design of nanoscale ferroelectric ceramic fillers, with well-controlled shape and size, has become very interesting in modern energy storage applications. A convenient "top-down" process was proposed to obtain nanoparticle products of tetragonal barium titanate ($BaTiO_3$) with highly accurate stoichiometry and morphological control. The key point of this work emphasized that a micrometer-sized precursor decreases to nanometer-sized product particles, and its irregular shape changes to nearly spherical with narrow size distribution. Both XRD and Raman results of $BaTiO_3$ nanoparticles indicated a tetragonal crystal structure. The 77.5 ± 2.5 nm sized $BaTiO_3$ powder product still polarized spontaneously at room temperature and the ferroelectric phase transition was confirmed at around 127 °C. Dielectric permittivity was found to be ~166.42 by Landauer-Bruggeman effective medium approximation (LB-RMA). Experimental procedures revealed a possible process mechanism observed within the etched surface and Oriented-attachment growth models, and this demonstrated approach could be used as an excellent platform for preparing ceramic nanoparticles. It also could be extended to synthesize complex oxide of functional materials for the preparation of other ceramic/polymer-based nanocomposites that achieve desirable properties.

* Corresponding author at: Electroceramic Research Laboratory, College of Nanotechnology, King Mongkut's Institute of Technology Ladkrabang, Bangkok 10520, Thailand.
E-mail address: naratip.vi@kmitl.ac.th (N. Vittayakorn).

http://dx.doi.org/10.1016/j.matdes.2016.07.137
0264-1275/

1. Introduction

Barium titanate ($BaTiO_3$) and its various doped derivatives have attracted much attention and become the most valuable lead-free ferroelectric material for a variety of industrial devices, such as multilayer capacitors, ferroelectric memories, thermistors, IR detectors, optical modulators, etc. [1–3]. To date, the nanoscale of $BaTiO_3$ has created increasing interest for the design of high-k gate dielectric ceramic-polymer nanocomposite films in flexible nanogenerators and flexible capacitors for energy storage applications [4–8]. The use of nanoscale filler particles not only decreases the thickness of nanocomposite films, but also improves high interfacial areas significantly, resulting in higher dielectric response and breakdown strength [4–8]. In addition to small-sized particles, the uniform shape and aggregate-free composites also play a critical role in the performance of nanocomposites, because various shapes and sizes usually lead to different interfacial polarization [4–6]. Besides size and shape dependence, the properties of binary and ternary complex oxides are highly sensitive to defects from non-stoichiometry [4–6]. Therefore, highly accurate control of shape, size, monodispersity and surface composition of nanoparticles, as filler for energy storage applications, is top priority in nanoscale synthesis.

"Bottom up" approaches via soft chemistry have been carried out in the synthesis of fine $BaTiO_3$ nanoparticles, including hydrothermal, solvothermal, sol-gel, and co-precipitation methods. A well-defined size and shape of $BaTiO_3$ nanoparticles could be obtained from the direct reaction of precursor ions through the hydrothermal method [9,10], while the solvothermal technique can produce more uniform nanoparticles, due to complex organic solvents preventing their agglomeration [11–13]. The sol-gel process shows outstanding control of a very small particle size (~10–50 nm) by using complex compound solution [14, 15]. Co-precipitation via oxalate [16] and citrates [17] can produce $BaTiO_3$ at a lower temperature easier than other methods. Alternative and modified techniques also were proposed such as sonochemical [18], supercritical fluid [19], sol-gel hydrothermal [20], Sol–gel combustion [21], microwave solvothermal [22], microwave-hydrothermal [23], etc. Much excellent work has been carried out by soft chemistry, but it usually requires the complicated step of experimental procedures, which need a highly purified, expensive precursor and specific equipment. It is too difficult to develop as a readily scalable method for synthesizing binary and ternary oxides in a large industrial volume. Notably, the most important problems caused via soft chemistry still emanate as much from low crystallinity and tetragonality of $BaTiO_3$ nanoproducts as decreased size, resulting in gradually decreasing spontaneous polarization and T_c. In the case of high basic solution, problems usually arise from hydroxylation incorporated in the oxygen sub-lattice, which stabilizes in a metastable cubic phase with non-ferroelectric properties [24,25]. The limitation of the chemical method motivates the search for other processes that produce high performing $BaTiO_3$ nanoparticles. These processes need to meet the industrial requirements based on geopolitical uncertainty, reproducibility, scarcity and cost. A recent method allowed for highly desirable properties for obtaining metals, metal sulfides, and even magnetic fine nanoparticles by using a digestive ripening process [26–30], which involved refluxing the poly-dispersed bulk precursor within the excess solution of complex capping agents, such as hexadecylamine (HDA), tetraoctyl-ammonium bromide (TOAB), hexadecyl-trimethyl-ammonium bromide (CTAB), etc. During the reflux process at over the melting point of the capping agent, larger particles were etched out as clusters, resulting in size reduction. These clusters were deposited simultaneously on another smaller particle, which preferred to grow by Ostwald ripening or other mechanisms in order to attain equilibrium of a specific size [26–30]. The final size and size distribution of nanoproducts are influenced mainly by the capping agent used [30]. To date, there has been no report on perovskite oxides, for example, $BaTiO_3$, $BaZrO_3$ or $Ba(Zr_xTi_{1-x})O_3$ because no suitable capping agents could be found or the reflux temperature was too low for breaking the surface particles of these materials.

This work demonstrates a possible way of obtaining tetragonal $BaTiO_3$ nanoparticles from microscale to nanoscale conversion via a convenient "top-down" process using NaCl salt. A simple process was performed without destroying the stoichiometry or crystallinity of the properties and crystal structure. The uniform shape and narrow-sized distribution of nanoparticles could be achieved by controlling the reaction temperature and time. The mechanism model of this process is proposed and discussed. This research shows the advantage of scale-up production, which does not require complex procedural steps, special apparatus or a specific purified precursor.

2. Experimental procedure

2.1. Conversion of $BaTiO_3$ nanopowder

The $BaTiO_3$ precursor was prepared by the solid state reaction between barium carbonate ($BaCO_3$) and titanium dioxide (TiO_2) at a calcination temperature of 1300 °C for 4 h. After calcination, the $BaTiO_3$ precursor was ground together with sodium chloride (NaCl) salt in a mortar at a weight ratio of 1:50 for 15 min. The NaCl salt of analytical grade (99.5%) was used as a surface etching agent without further purification. The mixture was then placed in a covered alumina crucible. The reaction was carried out at 700–900 °C for 3–72 h in air, with a heating/cooling rate of about 5 °C/min. After furnace cooling to room temperature, the powder products were washed with hot de-ionized water and filtered many times to confirm the complete removal of chloride ion (Cl-) residue. The amount of Cl- residue was checked by testing with 0.5 mol L^{-1} $AgNO_3$ reagent; until the white precipitation of AgCl disappeared. The powder products were dried at 90 °C overnight.

2.2. Characterization

The particle size and morphology of the powder products were determined by field-emission scanning electron microscope (FE-SEM, Hitachi 54700). An energy dispersive X-ray (EDX) analysis was used to identify the Ba:Ti stoichiometric ratio. The lattice fringes and electron diffraction patterns of the nanoparticles were observed by a transmission electron microscope (TEM; JEOL-JEM 2010, 80–200 kV). The phase purity, crystalline size and lattice strain of the products were examined by powder X-ray diffraction (XRD) with CuKα radiation source (Bruker D8 Advance diffractometer) in the 2θ range from 20–80° at an interval of 0.02°. The lattice parameters, atomic displacement, and degree of tetragonality were studied using powder XRD patterns collected on Rigaku, Miniflex600 in the 2θ range from 20–140° with a 0.02° step size. The $BaTiO_3$ crystal structure was refined by Rietveld analysis of the XRD data, using the JANA2006 program [31]. The induced strain arising from imperfect crystals was calculated by [32]:

$$\varepsilon = \beta_{hkl}/4\tan\theta \quad (1)$$

where β_{hkl} represents the corrected peak width at half-maximum intensity, as $\beta_{hkl} = [\beta^2_{hkl}\,\text{observed} - \beta^2_{hkl}\text{instrumental}]^{1/2}$, and θ is the diffraction angle. The lattice strain was modified and rearranged by Williamson and Hall in the following equation:

$$\beta_{hkl}\cos\theta = (k\lambda/D_{XRD}) + 4\varepsilon\tan\theta \quad (2)$$

where λ is the X-ray wavelength (0.154 nm), and k the constant value (0.89). The lattice strain was determined from the slope between the linear plots of $\beta_{hkl}\cos\theta$ and $4\tan\theta$, with the y-intercept used to calculate the crystalline size (D_{XRD}). Furthermore, Raman spectroscopy was used as a complimentary technique to investigate and confirm the phase formation and crystal structure of the powder products. The Raman spectra were collected by a DXR Raman microscope, Thermo Scientific, from a laser operating at 532 nm, 100× objective and nominal 10 μm laser spot size. In addition, differential scanning calorimetry (DSC; 2920 TA

Instrument) was used to study the $BaTiO_3$ phase transition. The DSC curves were recorded at 50–200 °C with a scanning rate of 10 °C/min. The dielectric measurements allowed determination of the phase transition temperature, relative permittivity value and dielectric loss. The dielectric properties of nanopowder were shaped into a disk by cold isostatic pressing, and measured as a function of temperature between 50 and 150 °C by an LCR analyzer (HP4284A, Hewlett-Packard, Palo Alto, CA) in the 100 Hz–10 kHz frequency range, with a heating/cooling rate of 2 °C/min.

3. Results and discussion

3.1. The mechanism model

This study used the mechanism model to convert the $BaTiO_3$ micron-sized precursor to nanoparticle products, as proposed with time dependence. A simple schematic is illustrated in Fig. 1. It can be assumed that a surface active etching by NaCl salt is an effective reaction for obtaining desirable nanoparticles, such as controllable morphology, stoichiometry and high crystallinity. At the early stage, the $BaTiO_3$ (micron-sized) precursor was placed into the environment of excess sodium chloride salt. Then, the sodium chloride salt melted completely when the reaction temperature reached 801 °C. The molten salts acted as a surface etching agent [33,34]. It is well known that BT powders synthesized by solid state reaction are polycrystalline, with random polyhedral crystallite orientation. Generally, the polycrystalline particles contain some defects such as stacking faults, dislocations or twin boundaries [35,36]. The presence of dislocations and twin boundaries in particles leads to lower lattice stabilization energy and higher chemical reactivity. The precursor particles also have a high density of surface defects, making them susceptible to attack by the molten NaCl. Therefore, the etching process occurs primarily together with these defects [35]. Consequently, when etching occurs all over the surface area of the precursor particles, several parts are ripped off to form smaller particles, and the precursor ions are dissolved into molten NaCl. This stage is illustrated in Fig. 1(a), with the bimodal distribution of the product particles being obtained. Upon further exposure [Fig. 1(b)], the process continues, which results in size-reduction of the precursor particles, higher concentration of solvated ions, and higher number of smaller etched-particles in the system. The etching rate tends to slow down with increasing time. Morpohology of the product particles becomes more uniform, and they acquire a near spherical shape with a narrow size distribution. The mechanism is illustrated in Fig. 1(c). It is noteworthy that up to this time the nanoparticle products maintain the original stoichiometry of the precursor. As the

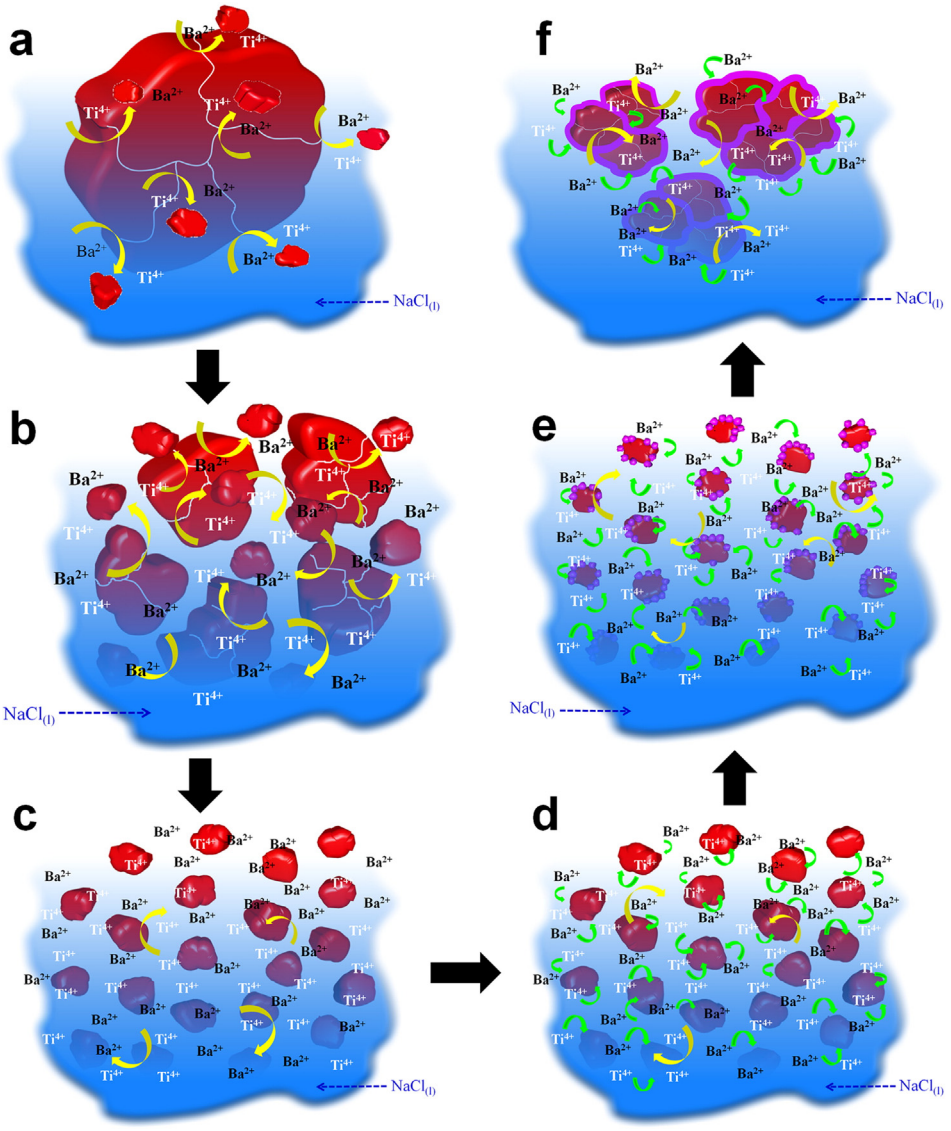

Fig. 1. Simple schematic diagram of the mechanism model.

reaction time is prolonged further, the concentration of precursor ions in salt flux is high enough to induce the supersaturation stage. These precursor ions diffuse and deposit directly over the surface of existing etched-particles, as illustrated in Fig. 1(d). The newly precipitated particles are called secondary particles, which occur and grow continuously over the surface area of the primary etched-nanoparticles. The outcome of this stage is represented in Fig. 1(e). It is worth noting that the formation mechanism of the secondary nanoparticles can be understood by invoking arguments similar to the rapid self-nucleation from the supersaturated solution, according to the La-Mer mechanism model [37]. When the reaction time is continued [Fig. 1(f)], the primary and secondary nanoparticles agglomerate tightly and fuse together. The spontaneous self-organization of contact particles grows by surface-interface solid particles. The nearest particles can attach to each other with a common crystallographic orientation. In this case, the morphology of the resultant product particles generally converts to irregular prismatic shapes with larger particle size and wide size distribution. The stoichiometry of product particles would be different from that in precursor particles. However, the etching process is still retained simultaneously, depending on prolonged reaction time, but this occurs at a lower reaction rate because of low assorted defect sites in small source particles. Therefore, the growth process arises at a higher rate than the etching process. If the reaction time were prolonged further, it is feasible that the particle product size would be big enough, and the digestion and growth mechanisms would reoccur in the same way.

3.2. Characterization of the $BaTiO_3$ precursor

In order to support the model in this study, the $BaTiO_3$ micron-sized precursor was prepared initially by the solid-state reaction method. The morphology and size of the particles were observed by FE-SEM, revealing that the $BaTiO_3$ precursor powder contained an irregular shape with particles of non-uniform size, which averaged 3.7 ± 1.5 μm. In order to confirm the homogeneity and stoichiometry of synthesized powder, EDX analysis was used to determine the Ba, Ti, and O content. Typical micrographs from the scanning electron microscope (SEM) with EDX analysis of the precursor powder are shown in Fig. 2(a) and (b). The EDX spectra taken from 2 different points demonstrated the Ba:Ti ratio of 24.89:24.88 and 25.31:24.37 for spectrum 1 and 2, respectively. Therefore, Ba:Ti stoichiometry was very close to 1:1.

The XRD and Raman techniques were used to investigate the phase purity and crystal structure. All of the diffraction profiles were refined by using Rietveld analysis. Both the precursor and nanopowder products were best refined with non-centrosymmetric *P*4*mm* space group from Crystallographic Information File no. 73,643 (see section on Supporting information). The example of the refined XRD pattern of precursor powder is shown in Fig. 2(c), and the enlarged plot is shown clearly in Supplementary data (S1). The refined parameters and quality of fit are listed in Table 1. The XRD refinement results in this study correlate with the analysis available in the literature [38]. The Raman spectrum of the precursor is shown in Fig. 2(d), and discussed using the point group analysis theory. The phonon modes of $BaTiO_3$ in cubic symmetry (*Pm*3*m*; Oh^1) are represented as $3F_{1u}$ (IR) + F_{2u} (inactive), with no Raman active modes. The off-centered Ti atom in the ferroelectric tetragonal (*P*4*mm*; $C4_v$) space group causes the *F* modes to split into transverse and longitudinal phonons of A_1 and *E* symmetry for F_{1u}, while the F_{2u} mode splits into B_1 and *E* modes, resulting in eight Raman-active modes of 4[*E*(TO) + *E*(LO)] (IR & R) + 3[A_1(TO) + A_1(LO)] (IR & R) + B_1 (R) [39]. All of the peaks for Raman spectra of the $BaTiO_3$ precursor in Fig. 2(d) matched well with

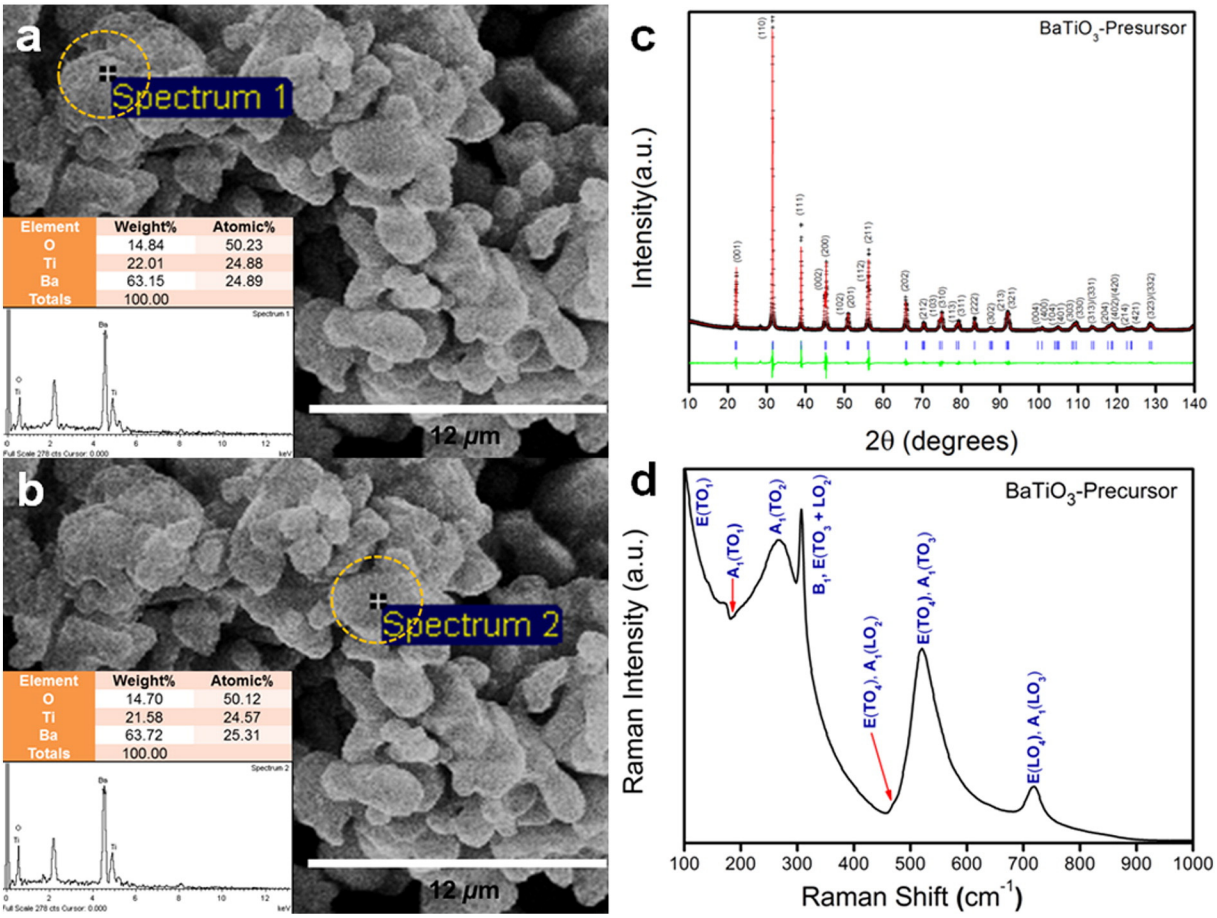

Fig. 2. SEM images with EDX analysis (a)–(b), Rietveld refinement X-ray fitting graphs (c), and Raman spectra (d) of the $BaTiO_3$ precursor.

Table 1
The corresponding fitting results from the Rietveld refinement data of the $BaTiO_3$ (μm) precursor and $BaTiO_3$ product particles after the process at 700-900 °C for 3 h.

	t-$BaTiO_3$ precursor	$BaTiO_{30}$ 700 °C	$BaTiO_3$ 800 °C	$BaTiO_3$ 900 °C
Crystal structure	Tetragonal	Tetragonal	Tetragonal	Tetragonal
Space group	*P4mm*	*P4mm*	*P4mm*	*P4mm*
a (Å)	3.9987(2)	3.9957(15)	3.9963(2)	3.9956(16)
c (Å)	4.0321(17)	4.0314(19)	4.0337(3)	4.0262(2)
c/*a*	1.0104(2)	1.0089 (8)	1.0083 (13)	1.0076 (5)
$V(Å)^3$	64.432(6)	64.364(5)	64.421(6)	64.278(5)
z(Ti)	0.52302(1)	0.52319(3)	0.51005(1)	0.519733(6)
z (O_1)	−0.05277(3)	−0.04919(8)	−0.05548(2)	−0.04548(2)
z (O_2)	0.48893(2)	0.50061(3)	0.52464(5)	0.49813(2)
R_{obs} (%)	1.19	2.77	1.95	1.73
R_p (%)	8.25	8.59	9.95	7.29
R_{wp} (%)	9.72	11.65	12.73	9.87
χ^2	1.17	1.36	1.28	1.35

$BaTiO_3$ in the *P4mm* tetragonal phase. The appearance of large damping at around 28–150 cm^{-1} was attributed to the $E(TO_1)$ soft mode [39]. It was suggested that the dip at 180 cm^{-1} represented the $A_1(TO_1)$ phonon mode, which appears in all ferroelectric phases of $BaTiO_3$. This $A_1(TO_1)$ phonon mode was explained as anti-resonance from the anharmonic coupling interference between three $A_1(TO)$ phonons [39]. A broad band at around 269 cm^{-1} was assigned to the transverse $A_1(TO_2)$ mode. The peaks at around 305 and a small peak at 473 cm^{-1} corresponded to the $[B_1, E(TO_3 + LO_2)]$ and $[E(TO_4) + A_1(LO_2)]$, respectively. Appearance of the 305 cm^{-1} Raman peak indicates a local order of asymmetric Ti—O vibration within the TiO_6 octahedra of tetragonal $BaTiO_3$, which disappears above the Curie temperature [39,40]. The 473 cm^{-1} peak of the $[E(TO_4) + A1(LO_2)]$ mode is appropriate for tetragonal representation [38]. In addition, the 521 and 702 cm^{-1} Raman peaks were assigned to $[E(TO_4), A_1(TO_3)]$ and $[E(LO_4) + A_1(LO_3)]$ phonon modes, respectively [39,40]. A Raman peak of 702 cm^{-1} at the highest frequency corresponded to the longitudinal mode of A_1 and *E* symmetry due to TiO_6 octahedral stretching [40]. Therefore, these results confirm the tetragonal crystal structure of precursor powders.

3.3. Effect of reaction temperature on morphology and phase stabilization

The effect of reaction temperature was investigated by focusing on the powder products in excess NaCl by varying the reaction temperature range from 700 to 900 °C. Morphology of the particles and their size were examined using FE-SEM, as illustrated in Figs. 3(a)–(d). The original $BaTiO_3$ precursor was shaped irregularly, with a particle size of about 3.7 ± 1.5 μm. After etching for 3 h at 700 °C, the particles were reduced to 385.5 ± 120.4 nm, with a more uniform shape than the precursor [Fig. 3(b)]. After etching at 800 °C, the morphology of the particles changed; with a dramatically reduced particle size of 87.3 ± 14.2 nm, and nearly spherical shape, as shown in Fig. 3(c). A small difference in the average particle size occurred when the reaction temperature increased from 800 to 900 °C: the average particle size slightly decreased from 87.3 ± 14.2 nm to 77.5 ± 4.1 nm, as illustrated in Fig. 3(d). Highly uniform particle morphology was obtained easily in this condition. Excess chloride salt plays an important role, and the reaction temperature influences the particle size and size distribution. Furthermore, the Ba:Ti stoichiometry in $BaTiO_3$ nanopowder products is confirmed by EDX analysis, as shown in Fig. 4. The composition analyzed in six different positions indicated an average atomic ratio of 1.01 ± 0.05 Ba/Ti, which is close to the Ba/Ti stoichiometry of the precursors. Therefore, it can be confirmed that the Ba:Ti stoichiometry of the powder product did not change notably from the stoichiometry of the precursors. In addition, other impurities, such as Na and Cl, were not detected. In contrast to soft chemistry methods, such as precipitation and hydrothermal techniques, the final Ba/Ti stoichiometry might be less than 1.0, due to the high dissolution rate of Ba^{2+} cations [41]. Therefore, it is vital to note that this research offers a novel preparation route, with an accurate compositional and morphological control of the final products. Furthermore, a TEM image of the nanopowder product obtained at 900 °C, with a uniform shape and particle size close to that estimated from the FE-SEM, is shown in Fig. 5(a). Clear lattice fringes are observed from the individual particle with inter-planar spacing of about 0.28 nm [Fig. 5(b)], which corresponds to the (110) crystal plane spacing of tetragonal $BaTiO_3$. The corresponding selected area electron diffraction (SAED) pattern reveals that the $BaTiO_3$ nanoparticles are single crystals and confirms the single crystalline nature of these nanoparticles. The SAED pattern in Fig. 5(c) displays the clean and sharp diffraction spots of (100) and (110) planes, which are characteristic of crystalline $BaTiO_3$. These results are consistent with analysis of the XRD pattern and Raman spectroscopy, confirming that the $BaTiO_3$ nanoparticles belong to tetragonal symmetry.

The XRD profiles of powder products were refined in order to confirm phase purity and crystal structure, and compare them with the precursor. The corresponding fitting results are shown in Fig. 6(a), and the enlarged plot is shown clearly in Supplementary data (S2). The results confirm the single phase for all of the products. Secondary phases were not found. The selected refinement parameters are listed in Table 1, which suggests a *P4mm* space group of the non-centrosymmetric tetragonal structure. The lattice parameters, *a* and *c*, show a slight decrease when compared to the precursor, but they remain independent from etching temperature within one standard deviation. It is known that cubic crystal structure becomes stabilized at room temperature with particle size decreasing to below ~30 nm [42,43]. No trend in decreasing *c*/*a* ratio was found in these nanopowder products, probably because $BaTiO_3$ products have a much larger average particle size than 30 nm. All nanopowder products consistent with the ferroelectric *P4mm* space group show the [001] displacement of Ti atoms, as shown in Table 1. This gives rise to spontaneous polarization in the ferroelectric tetragonal phase. Accordingly, spontaneous polarization can be calculated from relative ion displacement, as follows [44];

$$Ps = (e/V)\ \Sigma i\ Z''_i\ \Delta_i \quad (3)$$

where e is electron charge (μC), V is unit cell volume (cm^3), Z''_i is apparent charges of ion i (used from the work of A. W. Hewat [44]) and Δ_i is the displacement of ion i. The result shows calculated polarization slightly decreasing from 59.8 μC/cm^2 of the precursor to 44.6, 40.9 and 41.8 μC/cm^2 for nanopowders obtained at 700, 800 and 900 °C, respectively. These calculated polarization values exhibit a varied trend in the same way as those in tetragonality, as well as show a decreasing average particle size of the powder products. Furthermore, they can confirm the tetragonal structure and occurrence of ferroelectric phase in as-synthesized nanoparticles. The XRD data in Table 2 also show that the lattice strain increased with decreasing particle size. According to the Williamson-Hall (W-H) method, a 119 nm crystalline size of the precursor decreased to 114.7, 56.9 and 55.6 for powder at 700, 800 and 900, respectively. The crystalline size from the W-H method corresponded to a particle size from FE-SEM, which implies that the product particles are most likely the single crystal. This result is also in agreement with the electron diffraction patterns, collected by TEM.

This interesting result motivated this study to use a local probe analysis of Raman spectroscopy, which is sensitive to crystallographic defects and lattice distortions. Raman spectra of the $BaTiO_3$ precursor, compared with powder products obtained at various temperatures, are shown in Fig. 6(b). Powder products obtained at 700 °C showed Raman spectra that were similar to the precursor, which confirmed the stability of the tetragonal crystal structure. The difference in the Raman spectra ranging from 170 to 280 cm^{-1} was seen clearly for the powders at 800 and 900 °C. The most notable feature was the shape of the 180 cm^{-1} $A_1(TO_1)$ mode, which is attributed to the preferential orientation of the powder particles obtained at 800 and 900 °C, probably

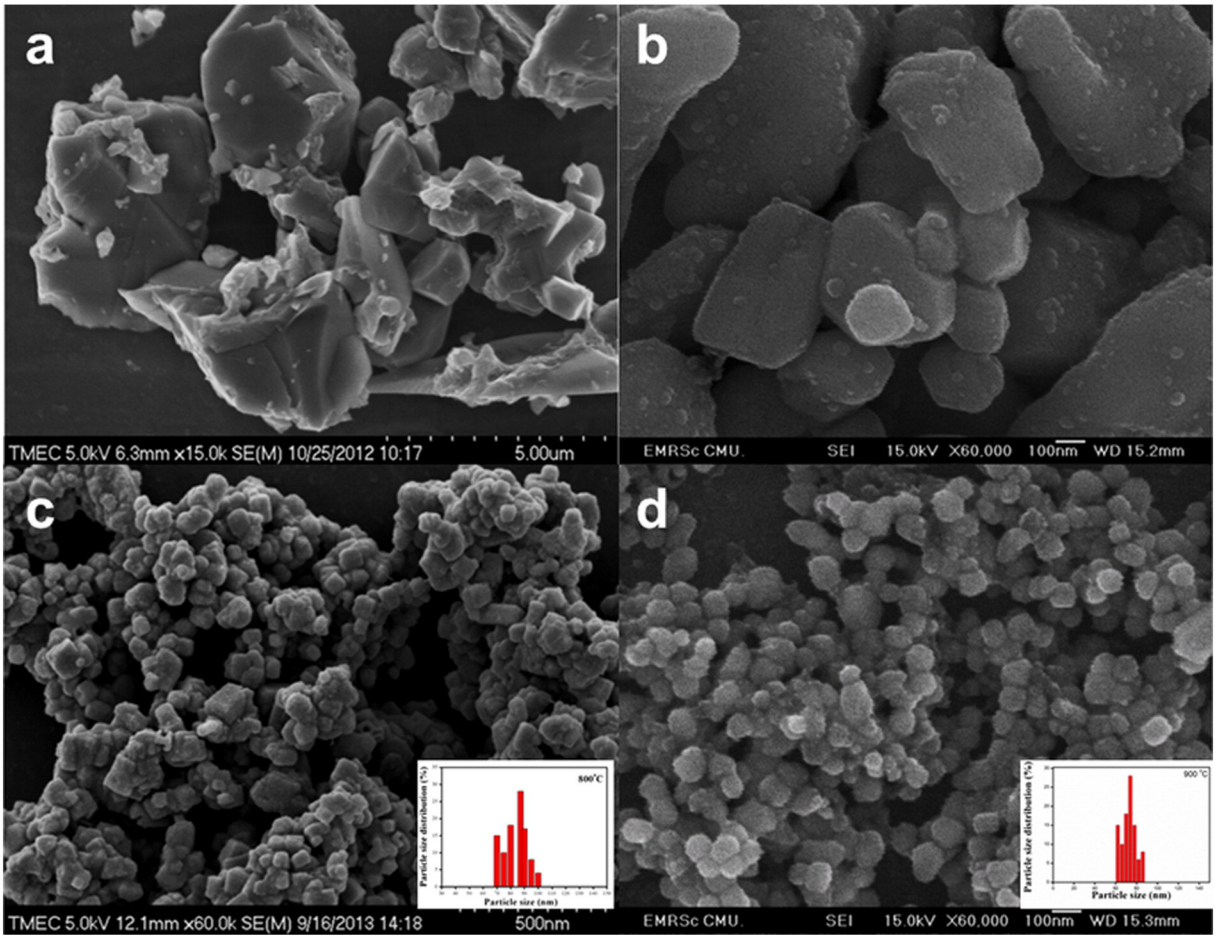

Fig. 3. FE-SEM micrographs of the $BaTiO_3$ (μm) precursor (a) and $BaTiO_3$ powder products after the reaction temperature of 700 (b), 800 (c) and 900 °C (d) for 3 h.

because of the decreasing size. As discussed in the literature, the intensity and shape of the $A_1(TO_1)$ mode strongly depends on the orientation of the crystal to the incident and reflected Raman light beam [41]. On the other hand, the spectral dip of $A_1(TO_1)$ may change to a positive peak of $[A_1(TO_1), E(TO_1 + LO_1)]$, due to the internal stress in nanoparticles, which can induce decoupling interaction of the $A1(TO_1)$, as also proposed in the literature [43,44]. According to Fig. 6(b), (c) and (d), all Raman peaks of the precursor also are defected in nanoparticle products.

3.4. Effect of reaction time on morphology and phase stabilization

In order to support the mechanism model of $BaTiO_3$ nanoparticles under the reaction system of melted chloride salt, a varied time series of experiments were performed. The influence of reaction time on the morphology and particle size is illustrated by the FE-SEM images in Figs. 7(a)–(f). The etching process was carried out at 900 °C for a reaction time ranging from 30 min to 72 h. The average particle size is reported in Table 2. During the first 30 min, the average particles size of the precursors decreased from 3.7 ± 1.5 μm to 1.53 ± 0.15 μm. Also, much smaller particles of around 5–10 nm were observed in the powder products, as shown in Fig. 7(a). Therefore, the bimodal size distribution could be seen, which corresponded to the mechanism step in Fig. 1(a). As the reaction time increased, the average particle size of the precursor powder decreased continuously. When the reaction time was extended to 3 h [Fig. 7(b)], mono-dispersed particles were obtained with an average particle size of about 77.5 ± 2.5 nm, and morphology of the particles became more spherical. This result corresponded to the mechanism represented in Fig. 1(c). The SEM images in Fig. 7(b) and (c) show that 3 to 8 h is a suitable reaction time for obtaining uniform nanopowders. A notable difference was observed after 12 h reaction time. As demonstrated in Fig. 7(d), the product particles were not mono-dispersed, but largely agglomerated into clusters with a non-uniform shape. The average particle size increased drastically from a minimum of 84.8 ± 2.5 nm at 8 h to 135.8 ± 17.5 nm, 155.3 ± 45.1 nm and 205.5 ± 65.0 nm at 12, 48 and 72 h, respectively. The results of prolonged etching revealed that the size of the secondary particle increases with increasing reaction time. The evidence from FE-SEM images showed that 12 to 72 h corresponded with the mechanism in Figs. 1(d)–(f).

Furthermore, in order to illustrate the relationship of particle size and morphology of powder products with reaction times more clearly, the matched plot with an SEM micrograph is shown in Fig. 8. The particle size tends to decrease with increasing reaction time until the optimum size and size distribution is achieved (marked with a blue circle). The particles change from an irregular shape to nearly spherical. The reaction time between 3 and 8 h did not lead to any significant change in morphology, size or even size distribution of the particles. The growth process after 8 h influences the morphology of product particles more than the etching process, resulting in a prismatic shape that forms with the poly-dispersity of the particle size. According to the growth process, the particle growth can occur generally in several ways such as Ostwald ripening [45], fast aggregated growth [46], orientation attachment [47], etc. The reaction time presented below in the analysis of this research favors the "orientation attachment (OA)" growth mechanism for approximately 12 to around 72 h. The growth

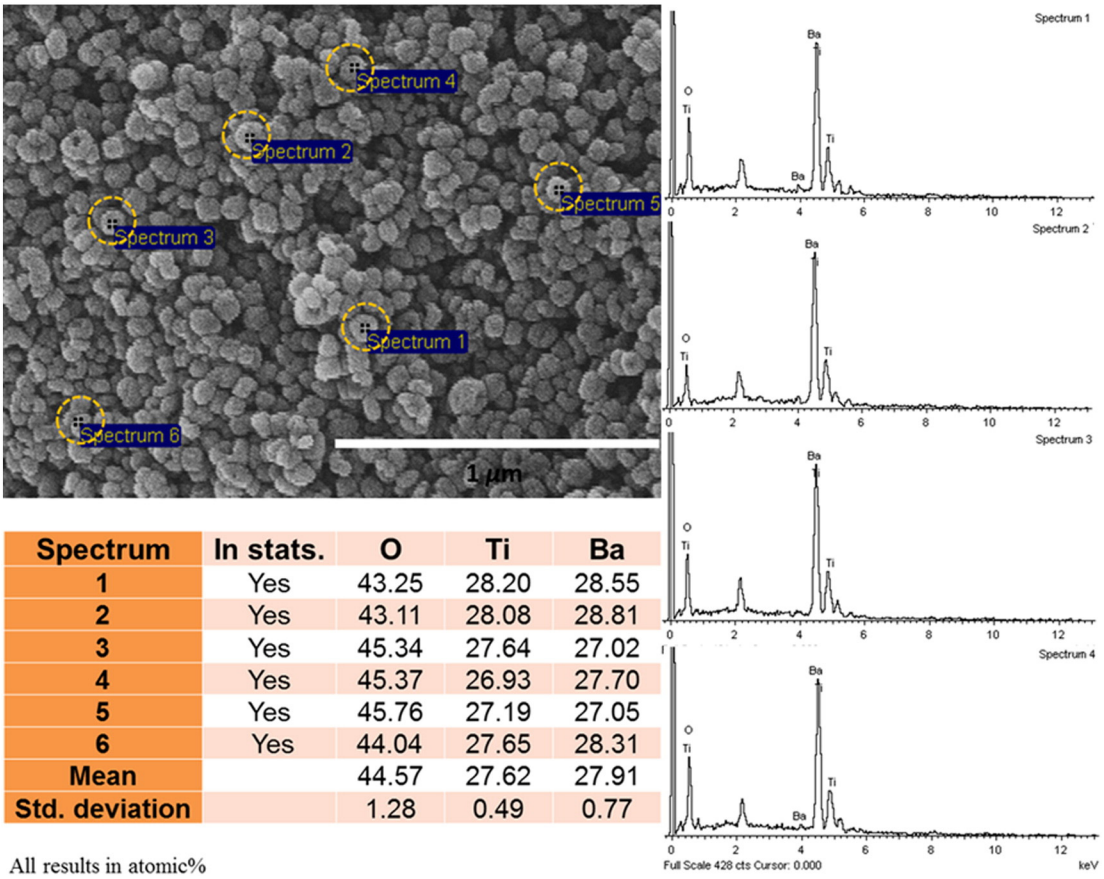

Spectrum	In stats.	O	Ti	Ba
1	Yes	43.25	28.20	28.55
2	Yes	43.11	28.08	28.81
3	Yes	45.34	27.64	27.02
4	Yes	45.37	26.93	27.70
5	Yes	45.76	27.19	27.05
6	Yes	44.04	27.65	28.31
Mean		44.57	27.62	27.91
Std. deviation		1.28	0.49	0.77

All results in atomic%

Fig. 4. SEM image with EDX analysis of $BaTiO_3$ powder products at 900 °C for 3 h.

curve of particle size could fit a modified kinetic Smoluchowski's equation [47] with Eq. (4), as follows:

$$d = d_{int}\ (mk_1\ t + 1)/(k_1\ t + 1) \tag{4}$$

where d_{int} and d represent the average particle size of the product particles at the reaction time of 12 h and average particle size at time t, respectively, while k_1 is a constant value, with m defined as the aggregated factor value. The enlarged resultant of the fitting plot between experimental data and calculation of Eq. (4) is shown in

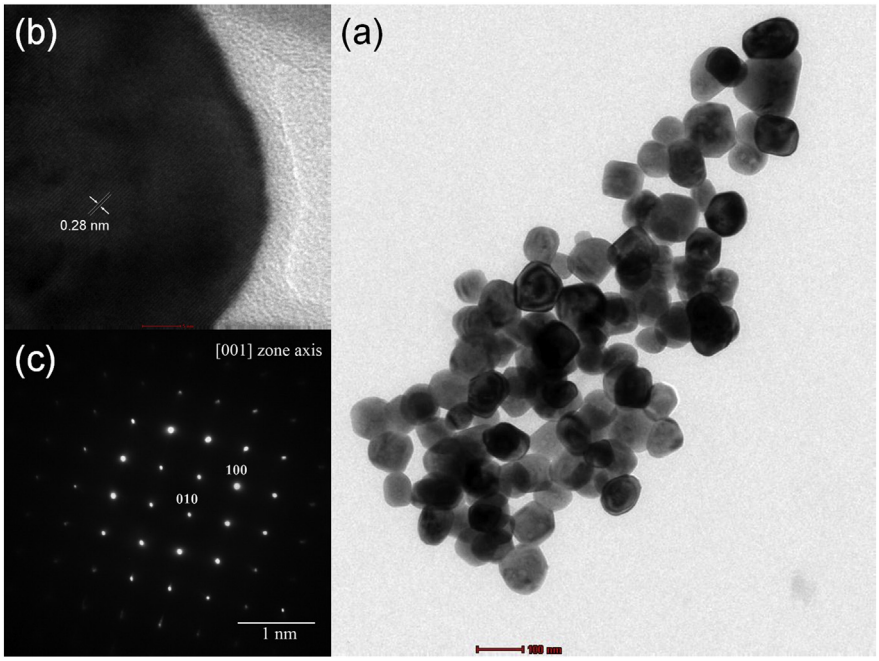

Fig. 5. TEM micrograph (a), lattice fringes (b) and selected area electron diffraction (SAED) pattern (c) of $BaTiO_3$ nanoparticle products at 900 °C for 3 h.

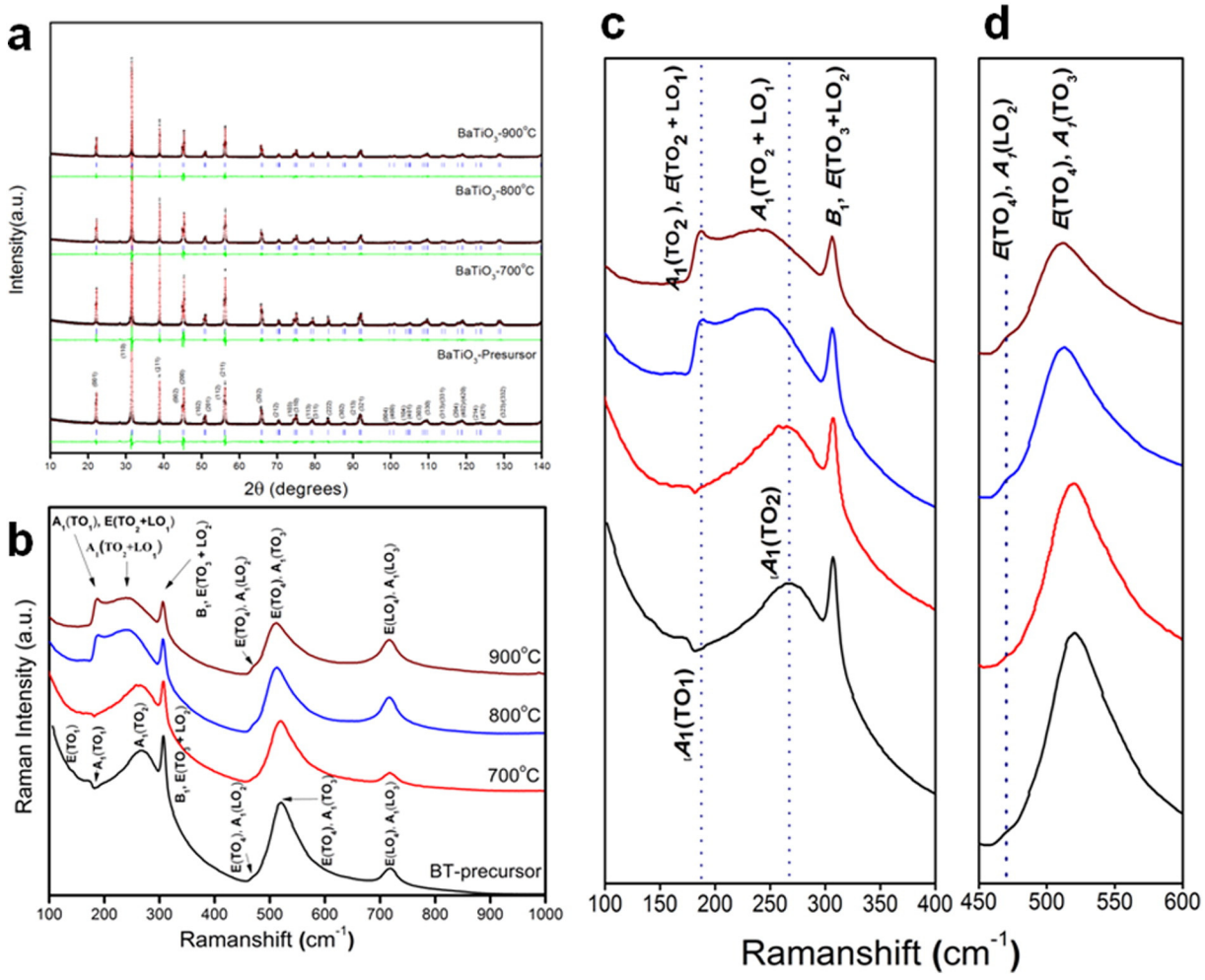

Fig. 6. Rietveld refinement X-ray fitting graphs (a), Raman spectra (b) and the enclosed-Raman spectra (c) and (d) of the $BaTiO_3$ (μm) precursor and powder products at 700, 800 and 900 °C for 3 h.

Supplementary data (S3). The plot corresponds well with the accepted R^2 value of about 0.9993.

The X-ray analysis has confirmed the single phase tetragonal structure of the product particles, as shown in Fig. 9(a). The crystalline size and lattice strain were calculated, as noted in Table 2. It was found that the crystalline size grew larger, and the lattice strain became weaker with increasing soaking time. Furthermore, all of the samples showed corresponding Raman active modes that were similar to those in precursor powder, as illustrated in Fig. 9(b). The slight difference in the peak shape at 180 cm^{-1} is associated with preferential orientation and the internal stress in nanoparticles, as mention above [40,43].

Table 2
Crystalline size, average particle size and lattice strain calculations of the $BaTiO_3$ precursor and powder products systematically synthesized with different conditions.

Samples		Williamson-Hall method		FE-SEM
Reaction temperature (°C)	Reaction time (hours)	Crystalline size (nm)	ε ($\times 10^{-3}$)	Average particle size (nm)
Precursor	–	119.4	1.8	3.7 ± 1.5 μm
700	3	114.7	2.2	385.5 ± 120.4
800	3	56.9	3.2	87.3 ± 14.2
900	3	55.6	3.3	77.5 ± 2.5
900	6	55.0	3.4	82.2 ± 3.2
900	8	60.8	3.1	84.8 ± 4.1
900	12	67.3	2.9	135.8 ± 17.5
900	24	69.5	2.6	140.6 ± 11.5
900	48	73.9	2.5	155.3 ± 45.1
900	72	75.2	2.3	205.5 ± 65.0

3.5. Ferroelectric phase transition

Ferroelectric phase transition behavior in $BaTiO_3$ nanopowder products was investigated at 900 °C for 3 and 24 h, and compared with the precursor by the mean results from a differential scanning calorimeter, as shown in Fig. 10. The endothermic peak, with well-defined phase transition, was observed at around 127.10, 127.00 and 129.40 °C for precursor and the powder products at 3 and 24 h, respectively, which corresponded with the ferroelectric tetragonal to paraelectric cubic phase transition. The evidence of an endothermic peak confirms the ferroelectricity in the nanopowder products after the etching process. The change in enthalpy (ΔH) associated with the phase transition is given by the area under the endothermic peak, which is calculated by DSC instrument software from a 2920 TA Instrument. The corresponding change in enthalpy (ΔH) of 637, 575 and 599 mJ/g was found for precursor and powder products at 3 and 24 h, respectively. The difference in enthalpy related to the average particle size [48]. Also, DSC is a highly sensitive technique for detecting the deviation from stoichiometry in $BaTiO_3$. According to the literature [49], nonstoichiometry in $BaTiO_3$ has a strong influence on thermal properties, ferroelectric phase transition and thermal fluctuation near the transition temperature. The results in Fig. 10 show that the endothermic peak of the nanopowder product had not shifted significantly from that of the precursor (127.00 °C from 127.10 °C). This small shift of 0.1 °C can be attributed

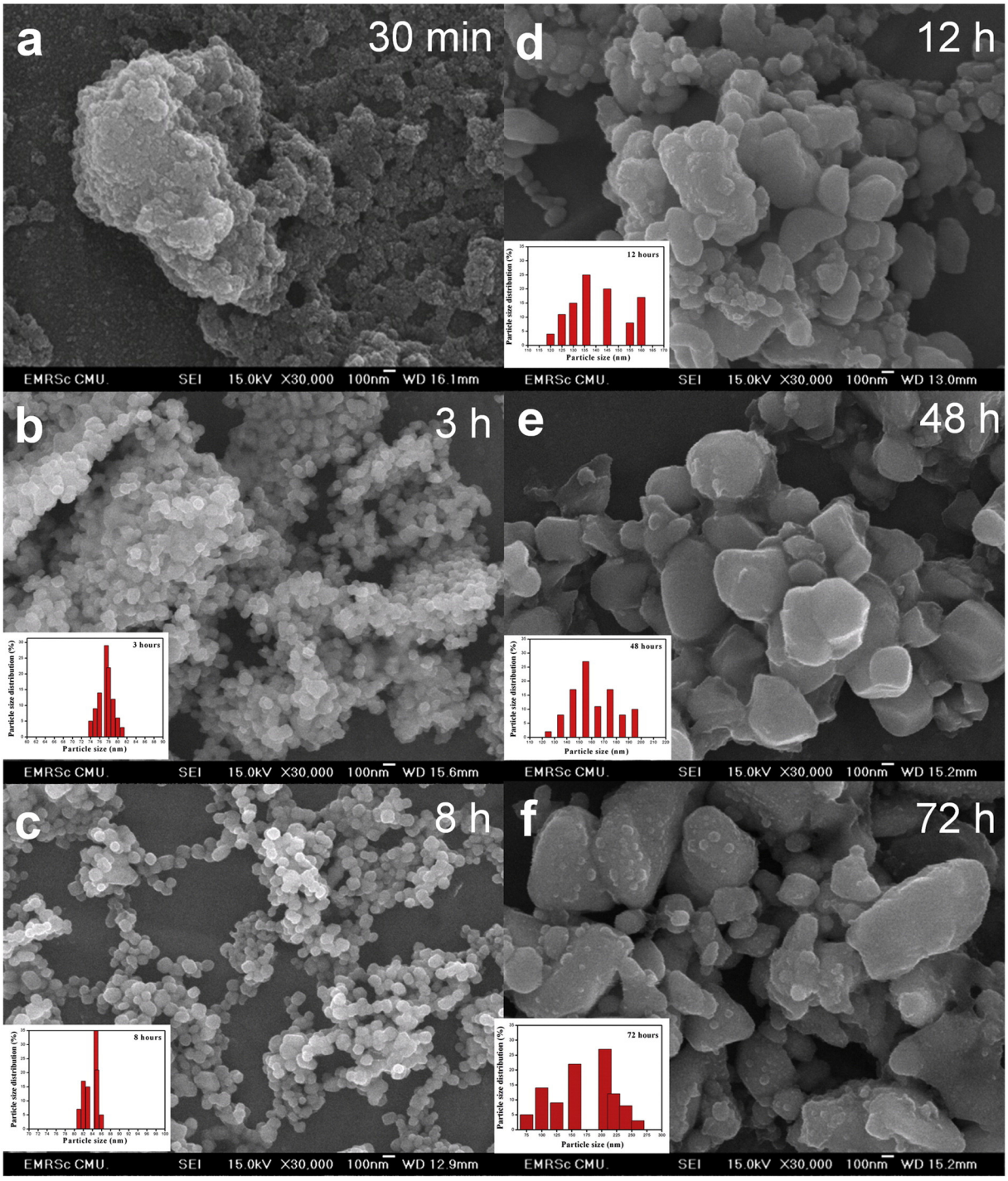

Fig. 7. FE-SEM micrograph of $BaTiO_3$ powder products (a)–(f) after the process at the reaction temperature of 900 °C from 30 min to 72 h.

to experimental error. Therefore, it can be confirmed that the stoichiometry of nanopowder products did not change at 3 h from that of the precursors. Nevertheless, the result of powder products at 24 h did show a difference. The endothermic peak position was found to increase to 129.4 °C, possibly due to residual stress. From the possible mechanism suggested above, the nucleation surface of secondary particles from primary ones can induce stresses that affect ferroelectric phase transition, based on a different thermal coefficient of expansion between these two phases [49]. On the other hand, according to Randell CA [50], the discontinuous shift of transition temperature of powder products comes from surface stresses, which may be caused by an evident low concentration of Ba-rich ($BaTi_{1-\delta}O_{3-2\delta}$) and Ti-rich ($Ba_{1-\delta}TiO_{3-\delta}$). Whereas, stresses on the non-stoichiometry surface of the $BaTiO_3$ particle [50] may be caused by an oriented attachment growth process when the surface particle is contacted.

3.6. Dielectric properties

As a high sintering temperature would induce hard agglomeration greatly and hardly change the nanostructure of $BaTiO_3$, the dielectric behavior of the nanoparticle product was measured from the porous bulk specimen at 900 °C/3 h, and prepared by cold-isostatic pressing without annealing or other heat treatment steps. The SEM micrograph of the surface specimen is shown in Fig. 11. Density of the bulk pellet was

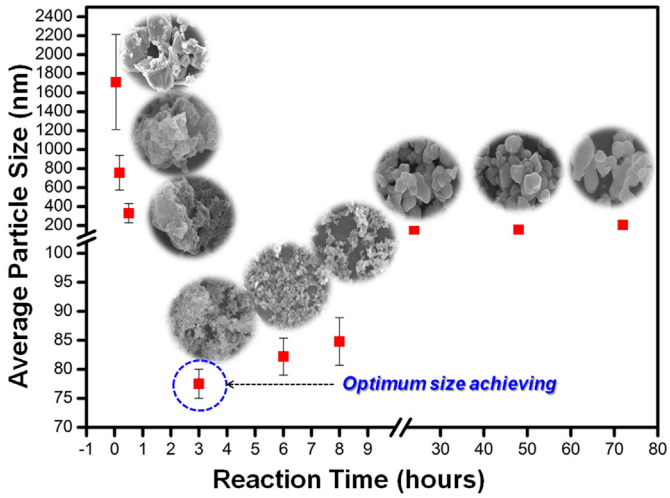

Fig. 8. Schematic illustrations of the average particle size and reaction times in relation to powder products from 30 min to 72 h.

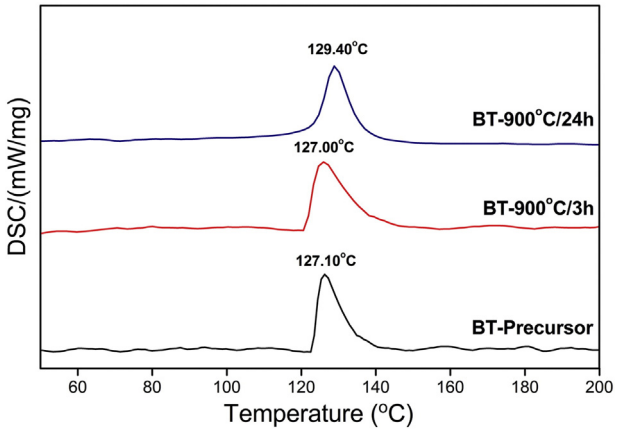

Fig. 10. DSC data results of the $BaTiO_3$ micrometer size precursor compared with the $BaTiO_3$ powder products at 900 °C for 3 and 24 h.

measured at 3.2401 g/cm^3 by Archimedes principle, which indicated around 53.88% when compared with the theoretical density of 6.0135 g/cm^3 from Rietveld refinement. The dependence of relative permittivity (ε_r) and dielectric loss (tan δ) on temperatures between 50 and 150 °C is shown in Fig. 12(a) and (b), respectively. The diffuse phase transition was found to be near 120 °C, with a broad maximum value of dielectric permittivity, and the small dissipation of dielectric loss (tan δ) was obtained at a low level of 0.01–0.06. The dielectric result confirmed that the 77.5 ± 2.5 nm of $BaTiO_3$ powder product was still in stabilized ferroelectric phase at room temperature, which agrees well with the XRD and DSC results. On the other hand, a lower tan δ of the bulk specimen is required for dielectric device applications because of the low heat produced [51]. According to the dielectric data, the measured dielectric permittivity of the specimen was found to be ~53 for 100 Hz, and it decreased slightly to ~51 and ~50 by increasing the frequency from 1 to 10 kHz. This dielectric permittivity can be considered as a composite value between the two phases of $BaTiO_3$ nanoparticle and air. The interfaces between nanoparticles and air could have hard effects on the dielectric behavior of the bulk specimen. Therefore, the Landauer-Bruggeman effective medium approximation (LB-EMA) was employed in this study to calculate the real dielectric permittivity value of $BaTiO_3$ nanoparticle products. The mathematical description of LB-EMA is given by [52];

$$v((\varepsilon_{air}-\varepsilon_r)/(\varepsilon_{air}+2\varepsilon_r))+(1-v)((\varepsilon_{BT}-\varepsilon_r)/(\varepsilon_{BT}+2\varepsilon_r))=0 \quad (5)$$

where v denotes the volume fraction of the pore in the specimen, which was determined as 46.12% by using a pore size analyzer (model MasterPore33). The ε_{BT}, $\varepsilon_{air,}$ and ε_r stand for the dielectric permittivity of $BaTiO_3$, air and bulk specimen, respectively. After calculation, the dielectric permittivity of $BaTiO_3$ becomes ~166.42, 160.33 and 141.66 for a frequency of 100 Hz, 1 kHz, and 10 kHz, respectively, which indicates exclusion of internal porosity. The estimated value of dielectric permittivity is shown in a similar way to that in reported data from the literature [53,54]. It is interesting to note that the real dielectric permittivity of the sample can be changed drastically in a wide range, which depends on introduction of the volume fraction of the pore. However, the real dielectric permittivity can be improved by the method for specimen preparation.

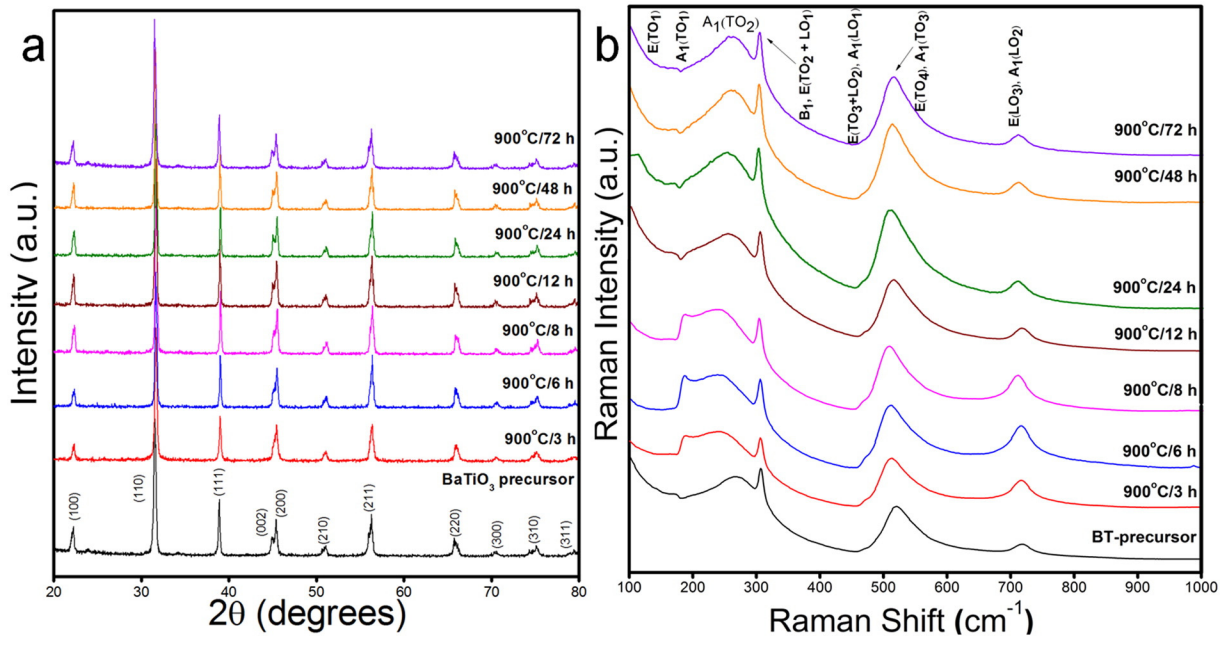

Fig. 9. X-ray diffraction patterns (a) and Raman spectra (b) of $BaTiO_3$ powder products after the reaction temperature at 900 °C for 3–72 h.

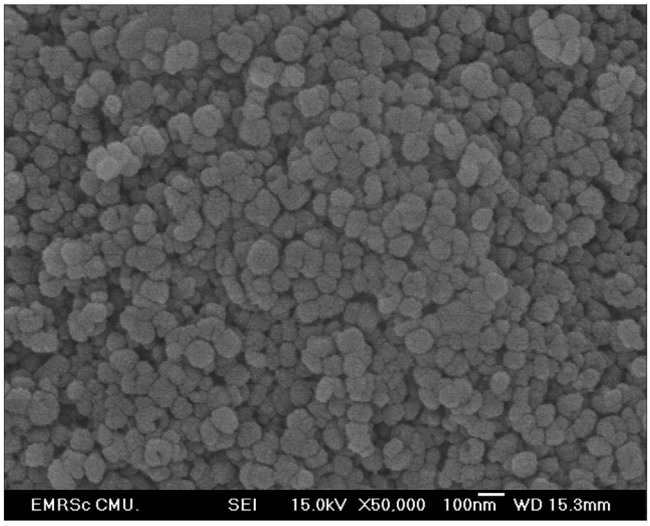

Fig. 11. SEM image on the surface of $BaTiO_3$ bulk specimen prepared by cold-isostatic pressing.

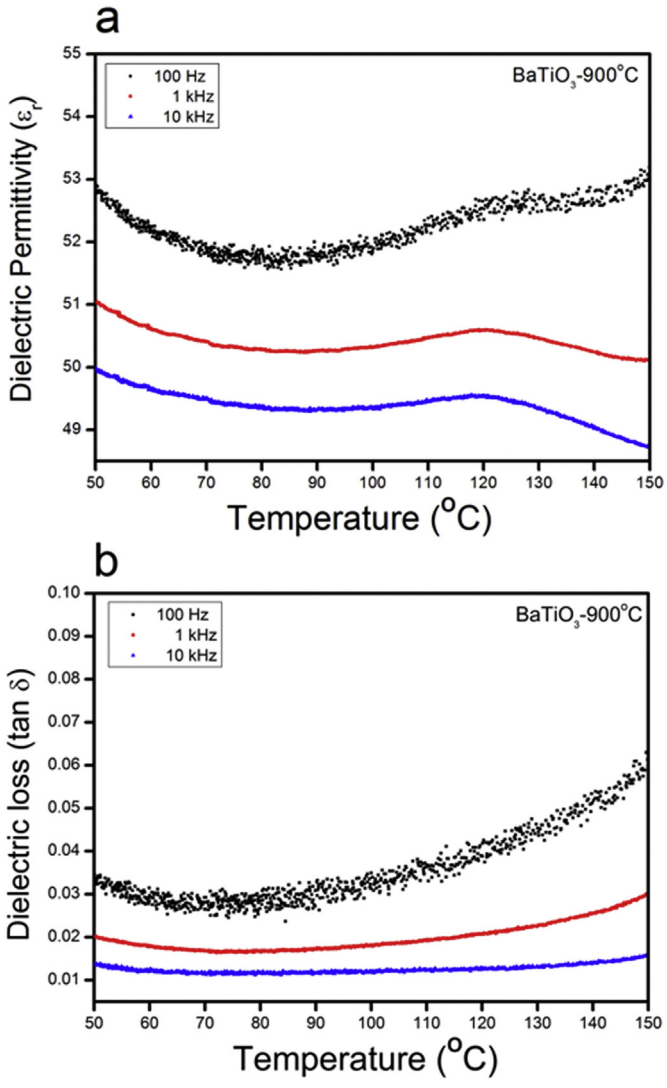

Fig. 12. (a) The relative permittivity and (b) the dielectric loss as a function of temperature of $BaTiO_3$ nanoparticle products at 900 °C for 3 h.

4. Conclusion

This research proposed a simple and convenient way for achieving uniform $BaTiO_3$ nanoparticles by direct conversion from an irregular-shaped $BaTiO_3$ micron sized precursor. A variation in temperature and time provides great thermodynamical control over the particle size and size distribution. A possible mechanism was proposed, starting with the term of precursor particles being etched from the whole surface area, until obtaining the optimal size of the product particles. The Oriented-attachment growth mechanism takes place to increase the particle size and form an irregular morphology. It is important that this research offers a novel preparation route, with an accurate compositional and morphological control of the final nanoparticle products. In addition, the $BaTiO_3$ nanoparticle product possesses a tetragonal crystal structure. The local symmetry remains non-centrosymmetric to a very small particle size of about 77.5 ± 2.5 nm, and thus allows ferroelectricity at room temperature. Hence, this method is highly recommended and potentially useful for the preparation of other complex oxide systems with controlled morphology, size, and surface composition by using a simple, easily scalable and highly versatile process.

Supplementary data to this article can be found online at http://dx.doi.org/10.1016/j.matdes.2016.07.137.

Acknowledgements

This research was supported by the Thailand Research Fund (TRF): No. BRG5680006. The authors would like to thank Dr. Taras Kolodiazhnyi for his valuable comments and discussions.

Appendix A. Supplementary data

Supplementary data comprise details of the crystallographic data for tetragonal $BaTiO_3$ in CIF format, an enlarged plot of Rietveld refinement X-ray fitting graphs of the tetragonal $BaTiO_3$ precursor (S1), the enlarged plot of Rietveld refinement X-ray fitting graphs of the $BaTiO_3$ precursor compared with the powder products at various temperature (S2), and the plot of particle size (nm) and time (h) between the experimental data and OA-mechanism fitting (S3). Supplementary data associated with this article can be found in the online version, at http://dx.doi.org/10.1016/j.matdes.2016.07.137.

References

[1] S.H. Shin, Y.H. Kim, M.H. Lee, J.Y. Jung, J. Nah, Hemispherically aggregated $BaTiO_3$ nanoparticle composite thin film for high-performance flexible piezoelectric nanogenerator, ACS Nano 8 (2014) 2766–2773.
[2] D. Yu, N.X. Xu, L. Hu, Q.L. Zhang, H. Yang, Nanocomposites with $BaTiO_3$–$SrTiO_3$ hybrid fillers exhibiting enhanced dielectric behaviors and energy-storage densities, J. Mater. Chem. C 3 (2015) 4016–4022.
[3] V.K. Prateek, R.K. Thakur, Gupta, recent progress on ferroelectric polymer-based nanocomposites for high energy density capacitors: synthesis, dielectric properties, and future aspects, Chem. Rev. 116 (2016) 4260–4317.
[4] C. Li, S. Yu, S. Luo, W. Yang, Z. Ge, H. Huang, R. Sun, C.P. Wong, Enhancement of dielectric performance up to GHz of the composites with polymer encapsulated hybrid $BaTiO_3$–Cu as fillers: multiple interfacial polarizations playing a key role, RSC Adv. 6 (2016) 36450–36458.
[5] Y. Hou, Y. Deng, Y. Wang, H.L. Gao, Uniform distribution of low content $BaTiO_3$ nanoparticles in poly (vinylidene fluoride) nanocomposite: toward high dielectric breakdown strength and energy storage density, RSC Adv. 5 (2015) 72090–72098.
[6] Y.N. Hao, X.H. Wang, S.O. Brien, J. Lombardi, L.T. Li, Flexible $BaTiO_3$/PVDF gradated multilayer nanocomposite film with enhanced dielectric strength and high energy density, J. Mater. Chem. C 3 (2015) 9740–9747.
[7] T. Gao, J. Liao, J. Wang, Y. Qiu, Q. Yang, M. Zhang, Y. Zhao, L. Qin, H. Xue, Z. Xiong, L. Chena, Q.M. Wang, Highly oriented $BaTiO_3$ self-assembled using an interfacial strategy and its application as a flexible piezoelectric generator for wind energy harvesting, J. Mater. Chem. A 3 (2015) 9965–9971.
[8] Z.D. Liu, Y. Feng, W.L. Li, High dielectric constant and low loss of polymeric dielectric composites filled by carbon nanotubes adhering $BaTiO_3$ hybrid particles, RSC Adv. 5 (2015) 29017–29021.
[9] Y. Ni, H. Zheng, N. Xiang, K. Yuana, J. Hong, Simple hydrothermal synthesis and photocatalytic performance of coral-like $BaTiO_3$ nanostructures, RSC Adv. 5 (2015) 7245–7252.

[10] Q. Ma, K. Kato, Crystallographic fusion behavior and interface evolution of monolayer $BaTiO_3$ nanocube arrangement, Cryst. Eng. Comm. 18 (2016) 1543–1549.
[11] D. Hu, H. Ma, Y. Tanaka, L. Zhao, Q. Feng, Ferroelectric mesocrystalline $BaTiO_3/SrTiO_3$ nanocomposites with enhanced dielectric and piezoelectric responses, Chem. Mater. 27 (2015) 4983–4994.
[12] J. Zhou, Z. Yang, Solvothermal growth of sub-10 nm monodispersed $BaTiO_3$ nanocubes, Cryst. Eng. Comm. 15 (2013) 8912–8914.
[13] H.T. Pham, J.H. Yang, D.S. Lee, B.H. Lee, H.D. Jeong, Ferroelectric/dielectric double gate insulator spin-coated using barium titanate nanocrystals for an indium oxide nanocrystal-based thin-film transistor, ACS Appl. Mater. Interfaces 8 (2016) 7248–7256.
[14] S. Liu, L. Huang, W. Li, X. Liu, S. Jing, J. Li, S. O'Brien, Green and scalable production of colloidal perovskite nanocrystals and transparent sols by a controlled self-collection process, Nanoscale 7 (2015) 11766–11776.
[15] K. Suematsu, M. Arimura, N. Uchiyama, S. Saita, T. Makino, High-performance dielectric thin film nanocomposites of barium titanate and cyanoethyl pullulan: controlling the barium titanate nanoparticle size using a sol–gel method, RSC Adv. 6 (2016) 20807–20813.
[16] C. Srilakshmi, G.M. Raob, R. Sarafa, Effect of the nature of a transition metal dopant in $BaTiO_3$ perovskite on the catalytic reduction of nitrobenzene, RSC Adv. 5 (2015) 45965–45973.
[17] T. Woldu, B. Raneesh, M.V.R. Reddy, N. Kalarikkal, Grain size dependent magnetoelectric coupling of $BaTiO_3$ nanoparticles, RSC Adv. 6 (2016) 7886–7892.
[18] S. Wirunchit, T. Charoonsuk, N. Vittayakorn, Facile sonochemical synthesis of near spherical barium zirconate titanate ($BaZr_{1-y}Ti_yO_3$; BZT); perovskite stability and formation mechanism, RSC Adv. 5 (2015) 38061–38074.
[19] G. Philippot, M. Albino, U.C. Chung, M. Josse, C. Elissalde, M. Maglione, C. Aymonier, Continuous $BaTi_{1-y}Zr_yO_3$ ($0 \le y \le 1$) nanocrystals synthesis in supercritical fluids for nanostructured lead-free ferroelectric ceramics, Mater. Des. 86 (2015) 354–360.
[20] J.H. Pan, C. Shen, I. Ivanova, N. Zhou, X. Wang, W.C. Tan, Q.H. Xu, D.W. Bahnemann, Q. Wang, Self-template synthesis of porous perovskite titanate solid and hollow submicrospheres for photocatalytic oxygen evolution and mesoscopic solar cells, ACS Appl. Mater. Interfaces 7 (2015) 14859–14869.
[21] M. Aghayana, A. Khorsand, M. Behdania, A. Manaf, Sol–gel combustion synthesis of Zr-doped $BaTiO_3$ nanopowders and ceramics: dielectric and ferroelectric studies, Ceram. Int. 40 (2014) 16141–16146.
[22] T.D. Nguyen-Phan, C.N. Huy, C.K. Kim, E.W. Shin, Facile microwave-assisted synthesis and controllable architecture of three-dimensional nickel titanate, Cryst. Eng. Comm. 17 (2015) 4562–4574.
[23] C. Srilakshmi, R. Saraf, V. Prashanth, G.M. Rao, C. Shivakumara, Structure and catalytic activity of Cr-doped $BaTiO_3$ nanocatalysts synthesized by conventional oxalate and microwave assisted hydrothermal methods, Inorg. Chem. 55 (2016) 4795–4805.
[24] C. Bogicevic, G. Thorner, F. Karolak, P. Haghi-Ashtianib, J.M. Kiata, Morphogenesis mechanisms in the solvothermal synthesis of $BaTiO_3$ from titanate nanorods and nanotubes, Nanoscale 7 (2015) 3594–3603.
[25] D. Caruntu, T. Rostamzadeh, T. Costanzo, S.S. Parizi, G. Caruntu, Solvothermal synthesis and controlled self assembly of monodisperse titanium-based perovskite colloidal nanocrystals, Nanoscale 7 (2015) 12955–12969.
[26] P. Sahu, B.L.V. Prasad, Fine control of nanoparticle sizes and size distributions: temperature and ligand effects on the digestive ripening process, Nanoscale 5 (2013) 1768–1771.
[27] S.P. Bhaskar, M. Vijayan, B.R. Jagirdar, Size modulation of colloidal Au nanoparticles *via* digestive ripening in conjunction with a solvated metal atom dispersion method: an insight into mechanism, J. Phys. Chem. C 118 (2014) 18214–18225.
[28] R. Moiraghi, O.A.D. Gallardo, E.A. Coronado, V.A. Macagno, M.A. Perez, Gold nucleation inhibition by halide ions: a basis for a seed-mediated approach, RSC Adv. 5 (2015) 19329–19336.
[29] A.H. Shaik, J. Chakraborty, Synthesis of monodisperse copper nanoparticles using a modified digestive ripening technique and formation of superlattices, RSC Adv. 5 (2015) 85974–85977.
[30] J. Seth, C.N. Kona, S. Das, B.L.V. Prasad, A simple method for the preparation of ultrasmall palladium nanoparticles and their utilization for the hydrogenation of terminal alkyne groups to alkanes, Nanoscale 7 (2015) 872–876.
[31] V. Petrick, M. Dusek, L. Palatinus, Crystallographic computing system JANA2006: general features, Kristallografiya 229 (2014) 345–352.
[32] A. Khorsand-Zak, W.H.A. Majid, M.E. Abrishami, R. Yousefe, X-ray analysis of ZnO nanoparticles by Williamson-Hall and size-strain plot methods, Solid State Sci. 13 (2011) 251–256.
[33] F. Huang, H.Z. Zhang, J.F. Banfield, Two-stage crystal-growth kinetics observed during hydrothermal coarsening of nanocrystalline ZnS, Nano Lett. 3 (2003) 373–378.
[34] S. Cingarapu, Z. Yang, C.M. Sorensen, K.J. Klabunde, Synthesis of indium nanoparticles: digestive ripening under mild conditions, Inorg. Chem. 50 (2011) 5000–5005.
[35] X.M. Lin, C.M. Sorensen, K.J. Klabunde, Digestive ripening, nanophase segregation and superlattice formation in gold nanocrystal colloids, J. Nanopart. Res. 2 (2000) 157–164.
[36] A. Polotai, K. Breece, E. Dickey, C.A. Randall, Novel approach to sintering nanocrystalline barium titanate ceramics, J. Am. Ceram. Soc. 88 (2005) 3008–3012.
[37] V.K. Lamer, R.H. Dinegar, Theory, production and mechanism of formation of monodispersed hydrosols, J. Am. Chem. Soc. 72 (1950) 4847–4854.
[38] G.H. Kwei, A. Lawson, S.J.L. Billinge, S.W. Chong, Structures of the ferroelectric phases of barium titanate, J. Phys. Chem. 97 (1993) 2368–2377.
[39] Y. Shiratori, C. Pithan, J. Domseiffer, R. Waser, Raman scattering studies on nanocrystalline $BaTiO_3$ part I – isolated particles and aggregates, J. Raman Spectrosc. 38 (2007) 1288–1299.
[40] A. Scalabrin, A.S. Chaves, D.S. Shim, S.P.S. Porto, Temperature dependence of the A_1 and E optical phonons in $BaTiO_3$, Phys. Status Solidi B 79 (1977) 731–741.
[41] S. Qin, D. Liu, H. Liu, Z. Zuo, Size-dependent selective etching mechanism: cavity formation on barium titanate nanocubes, J. Phys. Chem. C 112 (2008) 17171–17174.
[42] T.C. Huang, M.T. Wang, H.S. Sheu, W.F. Hsieh, Size-dependent lattice dynamics of barium titanate nanoparticles, J. Phys. Condens. Matter 19 (2007) 476212–476214.
[43] M.B. Smith, K. Page, T. Siegrist, P.L. Redmond, E.C. Walter, R. Seshadri, L.E. Brus, M.L. Steigerwald, Crystal structure and the paraelectric-to-ferroelectric phase transition of nanoscale $BaTiO_3$, J. Am. Chem. Soc. 130 (2008) 6955–6963.
[44] A.W. Hewat, Soft modes and the structure, spontaneous polarization and curie constants of perovskite ferroelectrics: tetragonal potassium niobate, J. Phys. C Solid State Phys. 6 (1973) 1074–1084.
[45] H. Zhang, X. Yong, C. Wang, C. Liang, M. Wu, Multiple growth stages and their kinetic models of anatase nanoparticles under hydrothermal conditions, J. Phys. Chem. C 114 (2010) 14461–14466.
[46] T.K. Nguyen, N. Maclean, S. Mahiddine, Mechanisms of nucleation and growth of nanoparticles in solution, Chem. Rev. 114 (2014) 7610–7630.
[47] J. Zhang, F. Huang, Z. Lin, Progress of nanocrystalline growth kinetics based on oriented attachment, Nanoscale 2 (2010) 18–34.
[48] S. Wada, H. Yasuno, T. Hoshina, S.M. Nam, T. Tsurumi, Preparation of nm-sized barium titanate fine particles and their powder dielectric properties, Jpn. J. Appl. Phys. 42 (2003) 6188–6195.
[49] S. Lee, C. Randall, A modified phase diagram for the barium oxide-titanium dioxide system for the ferroelectric barium titanate, J. Am. Ceram. Soc. 90 (2007) 2589–2594.
[50] S. Lee, Z.K. Liu, M.H. Kim, C.A. Randall, Influence of nonstoichiometry on ferroelectric phase transition in $BaTiO_3$, J. Appl. Phys. 101 (2007) 054119.
[51] J. Fu, Y. Hou, M. Zheng, Q. Wei, M. Zhu, H. Yan, Improving dielectric properties of PVDF composites by employing surface modified strong polarized $BaTiO_3$ particles derived by molten salt method, ACS Appl. Mater. Interfaces 7 (2015) 24480–24491.
[52] R. Landauer, The electrical resistance of binary metallic mixtures, J. Appl. Phys. 23 (1592) 779–784.
[53] Y. Wei, Y. Song, X. Deng, B. Han, X. Zhang, Y. Shen, Y. Lin, Dielectric and ferroelectric properties of $BaTiO_3$ nanofibers prepared *via* electrospinning, J. Mater. Sci. Technol. 30 (2014) 743–747.
[54] R.Z. Hou, P. Ferreira, M. Vilarinho, Nanoporous $BaTiO_3$ crystallites, Chem. Mater. 21 (2009) 3536–3541.

Subject:	Submission Confirmation for Lattice Evolution and Point Defects Chemistry in Ta-Doped Ceria (adfm.201603834)
From:	Advanced Functional Materials (em@editorialmanager.com)
To:	naratipcmu@yahoo.com;
Date:	Thursday, July 28, 2016 5:20 PM

You are being blind carbon copied ("bcc:'d") on an e-mail "To" "Taras V Kolodiazhnyi" kolodiazhnyi.taras@nims.go.jp

Dear Dr. Kolodiazhnyi,

Your submission entitled "Lattice Evolution and Point Defects Chemistry in Ta-Doped Ceria" has been received by journal Advanced Functional Materials. The manuscript number for your submission is adfm.201603834.

To view your submission, please login to http://afm-journal.edmgr.com/ by entering your username (********) and password and selecting the "Author Login" option.

This message has been sent to all named co-authors listed in the submission process to serve as notification of submission.

Thank you for submitting your work to the journal.

Kind regards,

Editorial Office
Advanced Functional Materials
E-mail:afm@wiley-vch.de
Tel: +49 (0) 6201 606 286

http://afm-journal.de/

*****
Please find a copy of the submission questions, which you answered during the submission, for your records:

Additional Information

3. Taras V Kolodiazhnyi, Ph.D.

Question	Response
	28 July, 2016 Editors Advanced Functional Materials Dear Editors, I would like to submit the

DOI: 10.1002/ ((please add manuscript number))
Article type: Full Paper

Lattice Evolution and Point Defect Chemistry in Ta-Doped Ceria

*Thitirat Charoonsuk, Naratip Vittayakorn and Taras V. Kolodiazhnyi**

T. Charoonsuk
Electroceramic Research Laboratory, College of Nanotechnology, King Mongkut's Institute of Technology Ladkrabang, Bangkok 10520, Thailand

Assoc. Prof. Dr. N. Vittayakorn
Advanced Material Research Unit, Faculty of Science, King Mongkut's Institute of Technology Ladkrabang, Bangkok 10520, Thailand
Department of Chemistry, Faculty of Science, King Mongkut's Institute of Technology Ladkrabang, Bangkok 10520, Thailand

Dr. T. Kolodiazhnyi
National Institute for Materials Science, 1-1 Namiki, Tsukuba, Ibaraki 305-0044, Japan
E-mail: kolodiazhnyi.taras@nims.go.jp

Keywords: ceria, lattice expansion, point defect equilibria, magnetochemistry

Understanding of the point defect chemistry of donor-doped ceria is important since it impacts the physical, chemical and electronic properties. This work reports on the point defects in Ta-doped ceria, relating the lattice evolution with the point defect concentration. The accurate Ce^{3+} quantification using magnetization method is a key factor in solving the defect equilibria. Combining the experimental data and lattice expansion models it is demonstrated that the extra positive charge of Ta^{5+} donors is compensated by both the Ce^{3+} and the oxygen interstitials An accurate quantitative analysis of the lattice expansion indicates that the theoretical calculations significantly overestimate the effect of the lattice response to oxygen interstitials. Furthermore, it is demonstrated that at high temperatures the anion Frenkel defects, whose concentration anomalously increases with the Ta substitution level, bring additional lattice expansion. The calculated enthalpy of formation of the anti-Frenkel defects

(H_{AF} = 3.27-4.24 eV) for Ta-doped ceria is in good agreement with the *ab-initio* calculations and with the experimental values for the U-doped ceria. These defects define the 'swelling' of the UO_2, PuO_2 and NpO_2 nuclear waste as well as the oxygen storage capacity for catalytic applications of chemically modified ceria.

1. Introduction

Cerium dioxide (CeO_2) and its substituted derivative materials have generated a lot of academic and industrial interest. These materials are used in the intermediate temperature (~500-1000 K) solid-oxide fuel cells (SOFCs),[1,2] gas sensors,[3] and automotive three way catalysts (TWCs).[4,5] Industrial applications of CeO_2 are attributed to its oxygen-storage capacity (OSC), which refer to the ability of exchanging oxygen by rapid $Ce^{4+} \leftrightarrow Ce^{3+}$ redox cycles.[6,7] CeO_2 is also used as a cheap surrogate material for modeling of point defects in isostructural nuclear waste materials, such as UO_2, PuO_2 and NpO_2.[8,9]

Undoped-ceria can deviate strongly from stoichiometry, depending on the temperature and oxygen partial pressure, pO_2.[10,11] The point defect chemistry of oxygen-deficient CeO_{2-x} has been studied both computationally[12,13] and experimentally,[10-11,14-15] arriving at the same conclusions. Using the Kröger-Vink notation, the oxygen deficiency leads to the $Ce^{4+} \rightarrow Ce^{3+}$ reduction, according to $[V_O^x] + [V_O^{\cdot}] + 2[V_O^{\cdot\cdot}] = [Ce'_{Ce}]$.[10-15] First-principles calculations estimate the formation energy for $[V_O^{\cdot\cdot}] + 2[Ce'_{Ce}]$ defect complex of about ~0.56 eV.[13] Other defects such as ceria vacancies, ceria interstitials and oxygen interstitials have much higher formation energy than the oxygen vacancies.[12-13,16] For oxygen-rich conditions, high voltage electron microscopy has found the oxygen interstitials on the surface[17] whereas the neutron diffraction based pair-distribution-function analysis has detected the oxygen interstitials in the octahedral void sites of ceria nanoparticles.[18] Meanwhile, the first-principles calculations of ceria at high pO_2 are somewhat controversial. Calculations by Zachele *et al.*[13] favor the oxygen vacancies as the dominant defects at high pO_2 but Xiao *et al.*,[19] and Keating *et al.*,[12]

find that the oxygen interstitials have lower defect formation energies and may be important high pO_2.

Ceria doped with acceptor ions, such as Gd^{3+}, Dy^{3+}, Sm^{3+}, etc., shows high ionic conductivity.[20,21] The defect chemistry model of acceptor-doped CeO_2 is now well understood.[12-13,22-24] At high pO_2 the acceptor ions are compensated by oxygen vacancies according to $[M'_{Ce}] = 2[V_O^{\cdot\cdot}]$, where (M = Gd^{3+}, Dy^{3+}, Sm^{3+}, etc.).[7,23-24] Decreasing pO_2 at high temperatures brings about ceria reduction, causing an increase in both the oxygen vacancies and conduction electrons according to $[V_O^x] + [V_O^{\cdot}] + 2[V_O^{\cdot\cdot}] = [Ce'_{Ce}]$.[23-25] The later reduction of ceria is one of the main problems limiting the application of CeO_2 as oxygen electrolyte in SOFC at high temperatures. On the other hand, it opens up other applications in the mixed electronic and ionic conductors, gas sensors and oxygen storage.[20-25]

Ceria doped with the donor ions, such as Nb^{5+}, Ta^{5+}, U^{5+}, W^{6+}, etc., shows significant electronic conductivity at high temperatures. Donor-doped ceria is explored as diffusion barrier for stainless-steel-supported SOFC[26] and as a catalytic additive for the $SrTiO_3$-based SOFC anodes.[27] The defect chemistry of Nb-substituted CeO_2 was first studied by electrical conductivity and thermogravimetric analysis (TGA) by Naik and Tien[28] who suggested that at high pO_2 Nb^{5+} ions are charge compensated by both Ce^{3+} and oxygen interstitials, O_i, according to $[Nb^{\cdot}_{Ce}] = [Ce'_{Ce}] + [O'_i] + 2[O''_i]$. Stratton and Tuller have arrived at the similar conclusions while studying CeO_2 – UO_2 solid solution.[29] Göbel *et. al.*,[30] investigated temperature and pO_2 dependence of electrical conductivity of $Ce_{0.98}Nb_{0.02}O_2$ epitaxial thin films and found that below T ≈ 573 K O''_i are the majority of the defects compensating Nb^{5+}. Moreover, the conductivity vs. pO_2 data also indicated a small admixture of singly ionized oxygen interstitials.[30] More recently, NMR analysis of Ta-doped CeO_2 has detected the oxygen interstitials in ceramics equilibrated at 873 K in the $^{17}O_2$ enriched atmosphere.[31] Remarkably, the first-principles calculations of the donor-doped CeO_2 are in disagreement

with the experiment as they predict electronic charge compensation of the donors (i.e., $[D_{Ce}^{\cdot}] = [Ce_{Ce}']$) at high pO_2.[13]

One of the problems in quantifying point defects in ceria is the lack of accurate estimate of the Ce^{3+} concentration. In most studies of the donor-doped CeO_2, the concentration, *c*, of Ce^{3+} ions is calculated from the measured electrical conductivity, σ, according to: $\boldsymbol{c = \frac{\sigma}{e\mu}}$, where μ is the electron mobility and *e* is the elementary charge. The large error in *c* comes from the uncertainty in electron mobility, which cannot be measured directly, but estimated from the electrical conductivity of CeO_{2-x} with 'known' concentration of the oxygen vacancies determined from the TGA.[28,32] Zhang *et al.*[33] and Fleming *et al*.,[34] pointed out that the X-ray photoelectron spectroscopy (XPS) significantly overestimates the Ce^{3+}/Ce^{4+} ratio. Yinglin and co-workers[35] showed photoluminescence (PL) spectra of the characteristic Ce^{3+} signals, however, it cannot be used to accurately determine the Ce^{3+} concentration. These difficulties preclude more accurate analysis of the defect concentration and defect formation energies in donor-doped ceria. Recently Kolodiazhnyi *et al*. introduced magnetochemical method to determine the low concentrations of Ce^{3+} with high accuracy in Nb-doped CeO_2.[36] It was shown that in ceramics equilibrated in air at 1923 K half of Nb^{5+} content is compensated by Ce^{3+} by forming a [Nb^{5+}-Ce^{3+}] defect complex while the rest of the Nb is compensated by the other defects, which could not be clearly identified.[36]

This contribution is focused on $Ce_{1-x}Ta_xO_2$ ceramics with $x \leq 0.03$ where we probe the point defect chemistry by combining the magnetochemical analysis and the lattice evolution as a function temperature and Ta^{5+} concentration. The accurate quantification of Ce^{3+} content from magnetic measurement and complimentary results from the lattice expansion lead to the consistent equilibrium defect model for $Ce_{1-x}Ta_xO_2$ at pO_2 = 0.2 atm. It is found that at least two types of defects, such as Ce_{Ce}' and O_i'' participate in the charge compensation of donor

ions. At higher temperatures, in addition to the above defects, a Frenkel disorder in anion sub-lattice contributes significantly to the lattice expansion.

2. Results and Discussion

There were two sets of $Ce_{1-x}Ta_xO_2$ samples studied in this work: A and B. The A-set consisted of ceramics equilibrated in air at 1923 K for 10 hours and fast-cooled to room temperature. With increasing *x* the sintered samples showed a change in color from light-blue to almost black. For the B-set of samples, the ceramics from the A-set were crushed into fine powder, compacted into pucks and equilibrated in air at 1273 K. After annealing at 1273 K the color of ceramics become light green-blue. We find that it is very important to crush the sintered ceramics into fine powder: Annealing of the 96 % dense ceramics (previously sintered at 1923 K) at 1273 K for 40 h brings almost no change in magnetization and color, while the X-ray diffraction shows some phase separation into two CeO_2 phases (major and minor) with a slightly different lattice parameters.

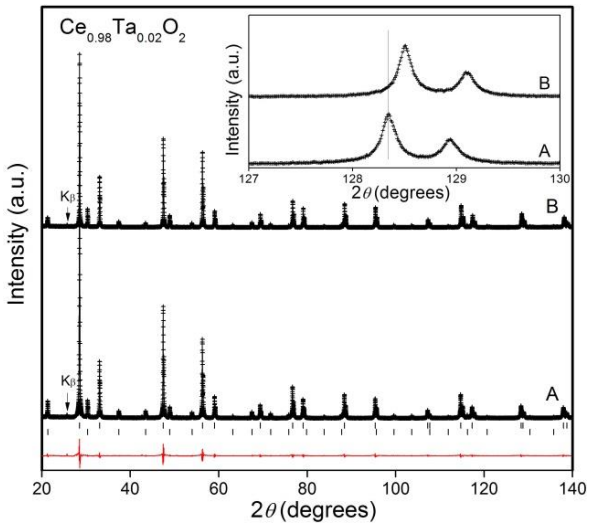

Figure 1. Rietveld refinement of the powder X-ray diffraction data of the A- and B-samples of $Ce_{0.98}Ta_{0.02}O_2$. Experimental data are shown as + symbols. The solid line is the fit, the vertical bars are the expected Bragg reflection positions for CeO_2 and for LaB_6 and the red line at the bottom is a difference between the fit and the experimental data for sample A only. The inset shows a large angle diffraction profile for A and B samples which demonstrates a change in the unit cell.

Figure 1 shows an example of the X-ray powder diffraction of the A- and B-samples of $Ce_{0.98}Ta_{0.02}O_2$ along with the Rietveld refinement of the cubic fluorite structure. In agreement with Ref.[37] no secondary phases were detected by the X-ray diffraction in both A- and B-sets for Ta content of $x \leq 0.03$. At higher x the traces of $CeTaO_4$ second phase were detected. Therefore, this work is limited to the $0.00 \leq x \leq 0.03$ compositions. For Ce^{3+} ion in a cubic crystal field environment, the total magnetic susceptibility is given by:

$$\chi = \chi_z + \chi_{\text{TIP}}, \quad (1)$$

where χ_{TIP} is temperature independent paramagnetism and χ_z is the magnetic susceptibility of Ce^{3+} ion cubic crystal field:[36]

$$x_z = \frac{N_A g_J^2 \mu_B^2 c}{4+2e^{-\frac{\Delta}{k_B T}}} \left\{ \frac{\frac{65}{9}+\frac{25}{18}e^{-\frac{\Delta}{k_B T}}}{k_B T} + \frac{80\left(1-e^{-\frac{\Delta}{k_B T}}\right)}{9\Delta} \right\} \quad (2)$$

where c is concentration of Ce^{3+} per formula unit, N_A is Avogrado number, g_J is the Landé g-factor, μ_B is the Bohr magneton, Δ is the energy gap between the Γ_8 and Γ_7 magnetic multiplets, k_B is the Boltzmann constant and T is the absolute temperature. The magnetic data and the fit for selected A- and B-samples are shown in **Figure 2.**

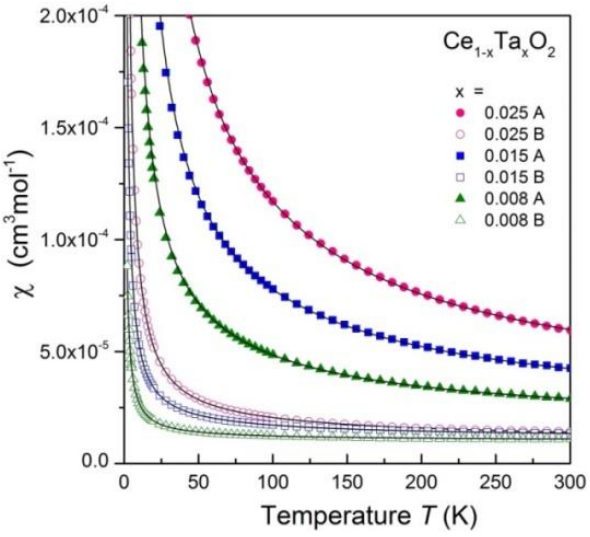

Figure 2. Temperature dependence of magnetic susceptibility of selected $Ce_{1-x}Ta_xO_2$ ceramics measured in 5000 Oe magnetic field. Solid and open symbols correspond to the samples of A- and B-set, respectively. Solid lines are the fits to the data.

The fitting parameters are summarized in **Figure 3**. The data in Figure 2a confirms a linear increase in the Ce^{3+} concentration with Ta substitution for A-samples. However, in contrast to the expected Ce^{3+}/Ta^{5+} ratio of 1:1, the data show that only half of Ta^{5+} ions are compensated by Ce^{3+}. This result is similar to the case of Nb-substituted CeO_2 reported in Ref.[36]

The data reveal a dramatic difference in the magnetization of the A- and B-set of samples. According to **Figure 3a**, the concentration of Ce^{3+} in B-samples is significantly lower than that in the A-samples.

The energy of the crystal field splitting Δ shows a tendency to increase with *x*, as shown in **Figure 3b**. In the case of the ideal solid solution of non-interacting Ce^{3+} and Ta^{5+} defects, the crystal field splitting is expected to be independent of *x* at low *x* values.[36] The small variation in the crystal field energy is attributed to the different local environment of the Ce^{3+} site because of the different concentration of point defects and possible formation of the [Ce^{3} - Ta^{5+}] defect complex.

Although pure CeO_2 is an insulating cubic fluorite, it shows substantial temperature-independent paramagnetism (x_{TIP})[36] which supports the idea of partially covalent nature of the chemical bonds.[38] The *x*-dependence of x_{TIP} shown in **Figure 3c** indicates a slight increase for A-samples, which is attributed to the partial population of the 4*f* band. For B-samples with depleted concentration of Ce^{3+} there appears an additional diamagnetic contribution which reduces the χ_{TIP} below the undoped CeO_2 value of $\chi_{TIP} = 1.45\times10^{-5}$ cm^3mol^{-1}. While the magnetic data clearly indicates that only a certain fraction of Ta^{5+} ions are compensated by Ce^{3+}, they cannot provide further information as to what kind of point defects compensate the remaining positive charge of the donor ions. To find the answer to this question we follow a well-established procedure[39,40] and analyze the effect of the ideal solution of the point defects on the lattice parameter of Ta-doped CeO_2.

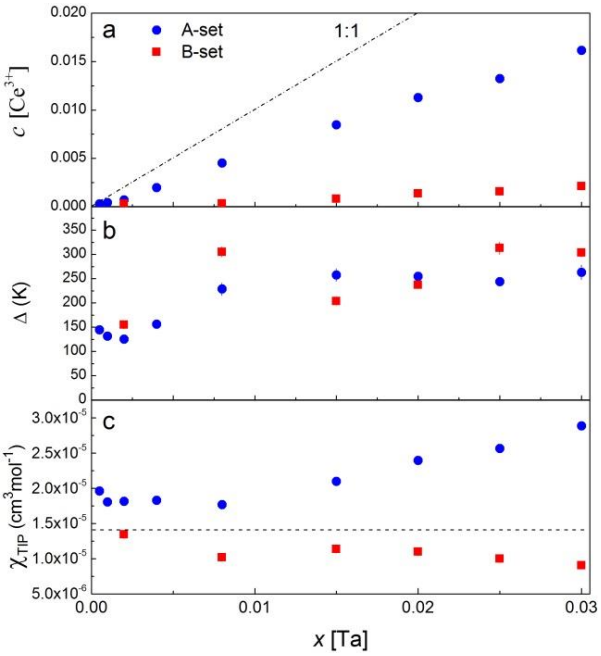

Figure 3. (a) Concentration of Ce^{3+} ions, *c*, obtained from the fit of magnetic susceptibility data, (b) Crystal field energy splitting between Γ_7 and Γ_8, and (c) Temperature independent paramagnetic susceptibility of A- and B-set of $Ce_{1-x}Ta_xO_2$ ceramics.

It is known that the ionic substitution or creation of any point defects will generally affect the lattice parameters. For example, formation of anion vacancy compensated by two Ce^{3+} cations causes lattice expansion in reduced ceria.[39] The lattice parameter of acceptor-doped ceria may either expand or contract depending on the radius of the rare-earth acceptor ion.[40] The total electro-neutrality condition for Ta-doped ceria is given by:[10-11,28,31-32,36,41]

$$[Ta_{ce}^{\cdot}] + 2[V_O^{\cdot\cdot}] + [V_O^{\cdot\cdot}] = 2[O_i''] + [O_i'] + 4[V_{ce}''''] + 3[V_{ce}'''] + 2[V_{ce}''] + [V_{ce}'] + [Ce_{ce}'] \quad (3)$$

Starting from the simplest scenario, we assume that all Ta^{5+} are compensated by Ce^{3+} according to:

$$[Ta_{ce}^{\cdot}] = [Ce_{ce}'] \quad (4)$$

The experimental unit cell, *a*, of CeO_2 with the cubic fluorite structure is given by:[36]

$$a = \frac{4}{\sqrt{3}}(r_{cation} + r_O) \times 0.99699, \quad (5)$$

where r_{cation} and r_{anion} are cation and anion radii, respectively. The coefficient 0.99699 is introduced in Eq. 5 to bring the ideal cubic fluorite cell in agreement with the experimental one.[40] When Ce is partially replaced by Ta, according to Eq. 4, the r_{cation} is given by:

$$r_{cation} = xr_{Ta^{5+}} + xr_{Ce^{3+}} + (1-2x)r_{Ce^{4+}}, \quad (6)$$

where $r_{Ta^{5+}}$ = 0.74 Å, $r_{Ce^{3+}}$ = 1.14 Å and $r_{Ce^{4+}}$ = 0.97 Å, based on the effective ionic radii model of Shanon[42] and *x* is the $[Ta^{5+}]$ concentration per formula unit.

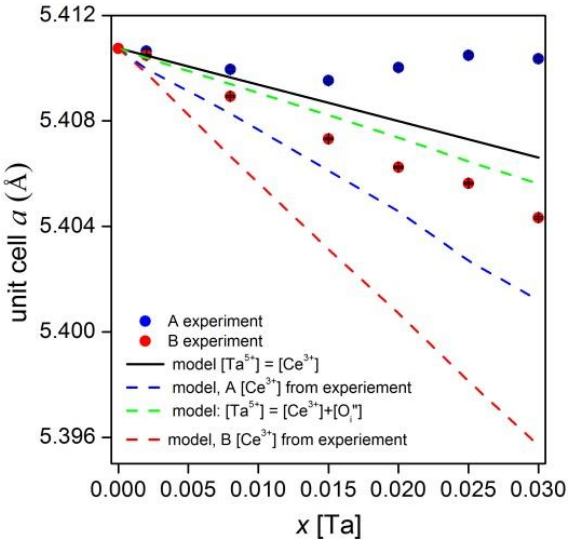

Figure 4. The variation in lattice parameter, *a* as a function of Ta^{5+} concentration, *x*, for A- and B-set of $Ce_{1-x}Ta_xO_2$. Black solid line is calculated unit cell according to the $[Ta_{ce}^{\cdot}] = [Ce_{ce}']$ model. Blue and red dash lines are calculated unit cells according to Equation 7 for A- and B-samples, respectively. Green-dash line is calculated unit cell for A-samples according to Equation 10.

The expected lattice parameters in the case of $[Ta_{ce}^{\cdot}] = [Ce_{ce}']$ compensation are shown as black line in **Figure 4** along with the experimental lattice parameters for A- and B-sets of samples. The unit cell of as-sintered (A-set) ceramic showed non-monotonic *x* dependence with *a* values significantly exceeding the predicted *a*(*x*) values at $x > 0.005$. The B-samples (i.e., annealed at 1273 K for 40 h) demonstrated almost linear lattice contraction with *a* values far below the expected ones (Figure 4). Thus the simple charge compensation mechanism of Equation 4 is inadequate to describe the experimental results. At the same time the *a*(*x*)

dependence concurs with the magnetic results and literature reports indicating that the charge compensation in Ta-doped ceria is far more complex than the simple $[Ta_{ce}^{\cdot}] = [Ce_{ce}']$ defect model.

Next we consider the $a(x)$ dependence for a real-case Ce^{3+} concentration obtained from the magnetic data and assuming that the other point defects do not cause any additional changes to the lattice parameter. In this case, the r_{cation} is given by:

$$r_{cation} = x r_{Ta^{5+}} + c r_{Ce^{3+}} + (1-x-c) r_{Ce^{4+}}, \quad (7)$$

where c is Ce^{3+} concentration estimated from the magnetic data (Figure 2). The unit cell calculated from Equation 5 and 7 is shown in Figure 4 by the blue dash and red dash lines for A-and B-samples, respectively. It can be seen that the experimental unit cells for both A- and B-sets are much larger than the calculated ones. Therefore, it can be concluded that the additional point defects compensating Ta^{5+} ions bring about significant lattice expansion.

According to the electro-neutrality condition (Equation 2), in addition to Ce^{3+} there are two other types of point defects that may need to be considered. These are cerium vacancies, V_{ce}'''', and oxygen interstitials, O_i''. We rule out cerium vacancies in further analysis for two reasons: First, we expect that the V_{ce}'''' must result in lattice contraction, and second, according to the first-principles calculations, cerium vacancies must have the highest formation energy among the point defects under the oxygen-rich conditions.[13,16] In contrast, the oxygen interstitials have much lower formation energies.[12-13,16] Furthermore, there is a solid experimental evidence of oxygen interstitials in both Nb- and Ta-doped CeO_2.[28,30-31] Assuming the O_i'' as an additional point defect in Ta-doped ceria, the modified charge neutrality conditions allow us to quantify the O_i'' concentration, b, from:

$$x[Ta_{Ce}^{\cdot}] = 2b[O_i''] + c[Ce_{Ce}']. \quad (8)$$

Taking the c values from the magnetic data, the b values for both the A-and B-sets of $Ce_{1-x}Ta_xO_2$ samples are summarized in **Figure 5**. It is clear from Figure 5 that for $Ce_{1-x}Ta_xO_2$

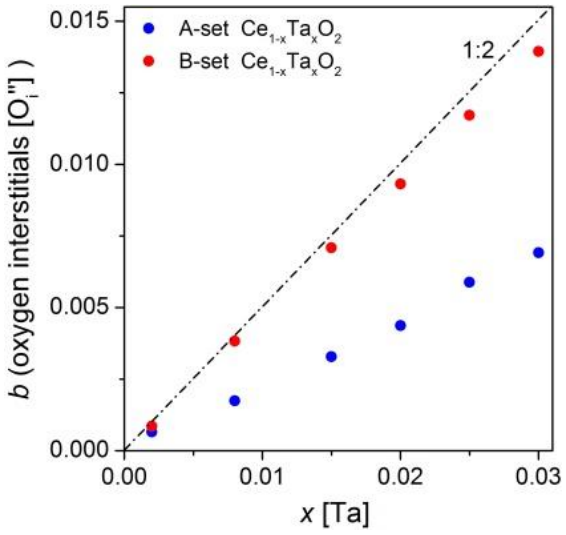

Figure 5. Concentration of oxygen interstitials as a function of Ta substitution for A- and B-sets of $Ce_{1-x}Ta_xO_2$ samples. The dash-dot line shows a 1:2 ratio for $[O_i'']$:[Ta^{5+}].

equilibrated at 1273 K for 40 hours almost all Ta^{5+} ions are compensated by oxygen interstitials for $x < 0.01$ with the rest of Ta^{5+} compensated by Ce^{3+}. For samples equilibrated at 1923 K only approximately half of the Ta^{5+} ions are compensated by O_i''. Although our results are in agreement with other experimental data, they are in contrast with the computational work of Zacherle *et al.*,[13] who claimed that at pO_2 = 0.2 atm the U-donor ions are compensated by Ce'_{Ce} at 1:1 ratio.

To estimate the effect of oxygen interstitials on the lattice expansion, we further make a reasonable assumption that the concentration of other intrinsic (i.e., Frenkel and Schottky) defects is negligibly small and can be ignored for B-set of samples. The lattice expansion upon incorporation of one O_i'' into a primitive unit cell is given by:

$$\varepsilon_i\ (\%) = \frac{a_{exp} - a_0}{b * a_0} \times 100, \qquad (9)$$

where a_{exp} is the experimental lattice parameter, a_0 is the lattice parameter with r_{cation} calculated from (7) and b is the concentration of O_i'' calculated from Equation 8. The results shown in **Figure 6** indicate that the primitive unit cell of $Ce_{1-x}Ta_xO_2$ expands by 11.8 ± 1.5 %

upon incorporation of O_i''. Along with the experimental data in Figure 6 we also include the first-principles results for incorporation of oxygen interstitial into the octahedral void formed by 8 oxygen ions.[19] It appears that the first-principles calculations overestimate the lattice expansion by a factor of ~1.68. At the same time, the significant difference between our experimental data and the *ab-initio* calculations of *ideal* (i.e., undoped) ceria reported in Ref.[19] may originate from the possible defect association, such as $[Ta_{Ce}^{\cdot}\text{-}O_i''\text{-}Ta_{Ce}^{\cdot}]$ or $[O_i''\text{-}Ta_{Ce}^{\cdot}]'$ in the $Ce_{1-x}Ta_xO_2$ samples equilibrated at 1273 K.

In the next step we used the calculated ε value to model the lattice expansion of the A-set of samples according to:

$$a^* = a_{cal}(1 + b \times \varepsilon), \quad (10)$$

where a_{cal} is given by the blue line in Figure 4 and b is the concentration of O_i'' determined from Equation 8. The $a^*(x)$ dependence for A-set of samples is shown in Figure 4 by the green dash line. Although the calculated unit cell values are close to the experimental ones for $x < 0.005$, the difference between the calculated and experimental data increases significantly at $x > 0.005$. This indicates that the excess positive charge compensation in A-set of $Ce_{1-x}Ta_xO_2$ is more complex than the one described by Equation 8, and an additional intrinsic point defects must be considered explicitly. These defects include the Schottky, Frenkel and anti-Frenkel disorder. Among them, the anti-Frenkel disorder is the most plausible one because of the lowest formation energy of the $V_O^{\cdot\cdot} + O_i''$ defect pair.[12-13,43-44] It is possible to estimate the concentration dependece of the anti-Frenkel defects in our A-set ceramics. The defect equilibria that includes the anti-Frenkel disorder is given by:

$$x[Ta_{Ce}^{\cdot}] = 2b[O_i''] + c[Ce_{Ce}'] + d\,[V_O^{\cdot\cdot} + O_i''], \quad (11)$$

where d is the concentration of the anti-Frenkel defects. Although the anti-Frenkel defects do not affect the charge neutrality conditions, they contribute to the change in the unit cell. This

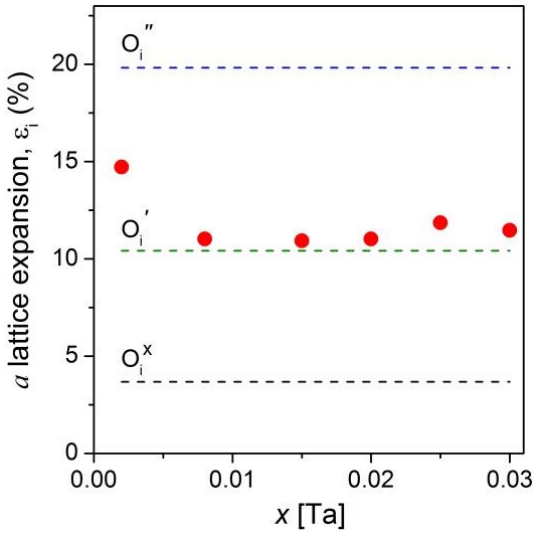

Figure 6. Lattice expansion normalized for incorporation of one O_i'' per primitive unit cell (i.e., per formula unit) calculated for several Ta^{5+} concentrations, *x*, of the B-set $Ce_{1-x}Ta_xO_2$ samples. The horizontal dash lines show lattice expansion upon incorporation of neutral, O_i^x, singly-, O_i', and doubly-ionized, O_i'', oxygen interstitials adapted from the first-principals calculations of Ref.[19]

change comes from the total effect of the lattice contraction caused by the oxygen vacancies and the lattice expansion caused by the oxygen interstitials:

$$\varepsilon_{AF} = \varepsilon_i + \varepsilon_v, \quad (12)$$

where ε_{AF} is the lattice expansion caused by creation of one anti-Frenkel defect pair, $V_O^{\cdot\cdot} + O_i''$, per primitive unit cell, ε_i = +11.8 %, calculated from Equation 9, and ε_v is the lattice contraction due to the incorporation of one oxygen vacancy per primitive unit cell. From experimental data and molecular dynamics simulations[39] the $\varepsilon_v \approx$ -4.0 %, which yeilds the total expansion $\varepsilon_{AF} \approx$ +7.8 %. Note that the latter value is valid only if the $V_O^{\cdot\cdot}$ and O_i'' defects formed by the anti-Frenkel disorder assume an ideal solid solution. If this condition holds for A-set of samples, the concetration of the anti-Frenkel defects, *d*, is calculated from:

$$a_{exp} = a^* (1 + d \times \varepsilon_{AF}), \quad (13)$$

where a_{exp} is experimental lattice parameter and a^* is defined in Equation 10.

The results summarized in **Figure 7** are remarkable in a way that they predict that the concentration of the anti-Frenkel defects increases with Ta substitution in $Ce_{1-x}Ta_xO_2$. While

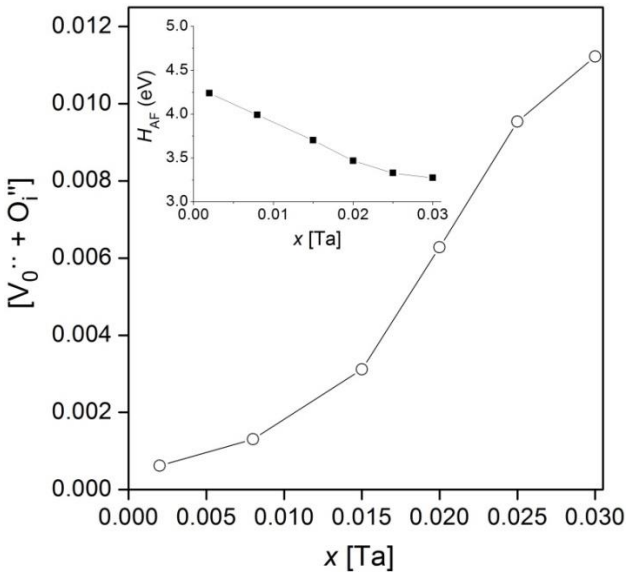

Figure 7. The concentration of $[V_O^{\cdot\cdot} + O_i'']$ anti-Frenkel defect pairs as a function of Ta^{5+} substitution (x) in A-set $Ce_{1-x}Ta_xO_2$ ceramics.

the absolute value of the $[V_O^{\cdot\cdot} + O_i'']$ in $Ce_{1-x}Ta_xO_2$ may have significant error bar due to several assumptions made, there is still a clear evidence of an increase in the anti-Frenkel defect concentration with x (Figure 7). It is important to note that qualitatively similar increase in anti-Frenkel defects with donor substitution has been proposed for Nb-doped ceria in Ref.[36]. There is significant uncertanty in the enthalpy of formation of the anti-Frenkel defect pairs in ceria, H_{AF} = 3.66-6.42 eV, reported in literature.[13,43-44] The H_{AF} can be estimated from the defect reaction equation:

$$[V_O^{\cdot\cdot}][O_i''] = K_{AF} \exp(-\frac{H_{AF}}{kT}), \quad (14)$$

where pre-factor $K_{AF} \approx 1.1\times10^{50}$ cm^{-6} is adapted from Ref.[29] The calculated H_{AF} dependence on Ta concentration is shown at the inset of Figure 7. The obtained enthalpy of the anti-Frenkel defect ranges from 3.27 to 4.24 eV. While these data are in reasonably good agreement with the values of 3.66 - 4.47 eV for U-doped CeO_2 reported by Stratton and Tuller[29] the reason for decrease of H_{AF} by almost 1 eV with an increase in Ta substitution x from 0.001 to 0.03 is not clear and requires further study.

3. Conclusions and future work

An accurate analysis of the Ce^{3+} concentration using magnetization data reveals rather complex picture of the point defect equilibria in Ta-doped ceria, which includes appreciable quantities of the charge-compensating O_i'', Ce_{Ce}' defects along with the intrinsic anti-Frenkel $V_O^{\cdot\cdot} + O_i''$ defect pairs. The results are in good agreement with other experimental data on Nb-, Ta- and U-doped ceria. The accurate experimental values of the lattice expansion caused by the oxygen interstitials obtained in this work can be used to further refine the first-principles calculations addressing the problem of the O_i''-induced swelling in CeO_2, PrO_2, UO_2 and PuO_2.

We also expect that the results will be used to further aid the first-principles calculations of the intrinsic (i.e., anti-Frenkel) and extrinsic defect formation energies in donor-doped ceria. Despite the enormous progress with accuracy and complexity of the *ab-initio* calculations, some of the experimental data related to the charge compensation mechanism in donor-doped CeO_2 are at variance with the theoretical simulations. In particular we demonstrate here that in the oxygen-rich atmosphere the Ta^{5+} ions are almost exclusively compensated by the oxygen interstitials at $T \leq 1273$ K, whereas at $T \geq 1923$ K, the charge compensation involves significant fraction of the Ce^{3+} ions. In addition to industrial interest, it is clear that the CeO_2 system will remain an excellent playground for testing the accuracy of the *ab-initio* calculations of the 4*f* electron systems.

4. Experimental Section

The $Ce_{1-x}Ta_xO_2$ with composition with x = 0.000-0.04 were prepared by solid state reaction method. The CeO_2 (99.99% purity, Tokai-Chemy, Japan) and Ta_2O_5 (99.99% purity, Cerac, USA) were used as the precursors. Mixed-precursor powders were ball-milled in ethanol for 24 h. The dried powders were sieved through a 250-mesh and calcined at 1473 K for 20 h in air. Small amount of 5% PVA binder was added before pressing them under 20 MPa in the WC (Fujilloy, Japan) pressing dies to obtain 7-10 mm diameter and approximately

2 mm thickness pellets. These pellets were stacked on top of each other above the CeO_2 powder layer and sintered at 1923 K for 10 h. The ceramics with 93-96 % relative density were obtained. Selected compositions were crushed into fine powder with Y-stabilized ZrO_2 mortar and pestle and pressed again into pellets which were annealed in air at 1273 K for 40 h followed by fast cooling to room temperature. The relative densities of these ceramics were 50-55 %.

Phase purity was determined by powder X-ray diffraction (Miniflex600 diffractometer, Rigaku, Japan) with CuKα radiation source. The LaB_6 (a = 4.1563(1) Å) powder was mixed with the samples as internal standard to refine unit cell parameters. The lattice parameters were obtained from Rietveld refinement of the X-ray diffraction data by using JANA2006 program. Magnetic moment was measured in 2-300 K range at 5000 Oe using Magnetic Property Measurement System (MPMS-XL, Quantum Design, USA) equipped with superconducting quantum interference devise.

Acknowledgements

This work was supported by Grant-in-Aid for Scientific Research 26400323 from JSPS provided to T. Kolodiazhnyi. The work of N.V. was supported by the Thailand Research Fund (TRF) under Grant No. BRG5680006.

Received: ((will be filled in by the editorial staff))

Revised: ((will be filled in by the editorial staff))

Published online: ((will be filled in by the editorial staff))

[1] D. J. L. Brett, A. Atkinson, N. P. Brandon, S. J. Skinner, *Chem. Soc. Rev.* **2008**, *37*, 1568.

[2] T. Jiang, Z. Wang, J. Zhang, X. Hao, D. Rooney, Y. Liu, W. Sun, J. Qiao, K. Sun, R. Hay, *J. Amer. Ceram. Soc.* **2015**, *98*, 1717.

[3] N. Izu, N. Oh-hori, M. Itou, W. Shin, I. Matsubara, N. Murayama, *Sens and Actuators B: Chem.* **2005**, *108*, 238.

[4] J. Kašpar, P. Fornasiero, M. Graziani, *Catal. Today* **1999**, *50*, 285.

[5] R. Di Monte, J. Kašpar, *Catal. Today* **2005**, *100*, 27.

[6] N. V. Skorodumova, S. I. Simak, B. I. Lundqvist, I. A. Abrikosov, B. Johansson, *Phys. Rev. Lett.* **2002**, *89*, 166601.

[7] J.-P. Eufinger, M. Daniels, K. Schmale, S. Berendts, G. Ulbrich, M. Lerch, H.-D. Wiemhofer, J. Janek, *Phys. Chem. Chem. Phys.* **2014**, *16*, 25583.

[8] M. C. Stennett, C. L. Corkhill, L. A. Marshall, N. C. Hyatt, *J. Nucl. Mater.* **2013**, *432*, 182.

[9] C. L. Tracy, M. Lang, J. M. Pray, F. Zhang, D. Popov, C. Park, C. Trautmann, M. Bender, D. Severin, V. A. Skuratov, R. C. Ewing, *Nat. Commun.* **2015**, *6*, 6133.

[10] H. L. Tuller, A. S. Nowick, *J. Electrochem. Soc.* **1979**, *126*, 209.

[11] R. J. Panlener, R. N. Blumenthal, J. E. Garnier, *J. Phys. Chem. Solids* **1975**, *36*, 1213.

[12] P. R. L. Keating, D. O. Scanlon, B. J. Morgan, N. M. Galea, G. W. Watson, *The J. of Phys. Chem. C* **2012**, *116*, 2443.

[13] T. Zacherle, A. Schriever, R. A. De Souza, M. Martin, *Phys. Rev. B* **2013**, *87*.

[14] Y. Namai, K.-I. Fukui, Y. Iwasawa, *Catal. Today* **2003**, *85*, 79.

[15] S. F. Friedrich Esch, Ling Zhou, Tiziano Montini, Cristina Africh, Paolo Fornasiero, Giovanni Comelli, Renzo Rosei, *Science* **2005**, *39*, 752.

[16] S. Grieshammer, T. Zacherle, M. Martin, *Phys. Chem. Chem. Phys.* **2013**, *15*, 15935.

[17] K. Yasunaga, K. Yasuda, S. Matsumura, T. Sonoda, *Nucl. Instr. Meth. Phys. Res. Sec. B: Beam Interac. Mater. and Atoms* **2006**, *250*, 114.

[18] E. Mamontov, T. Egami, *J. of Phys. and Chem. Solids* **2000**, *61*, 1345.

[19] H. Y. Xiao, Y. Zhang, W. J. Weber, *Acta Mater.* **2013**, *61*, 7639.

[20] F. Giannici, G. Gregori, C. Aliotta, A. Longo, J. Maier, A. Martorana, *Chem. Mater.* **2014**, *26*, 5994.

[21] V. Esposito, M. Zunic, E. Traversa, *Solid State Ionics* **2009**, *180*, 1069.

[22] J. Paier, C. Penschke, J. Sauer, *Chem. Rev.* **2013**, *113*, 3949.

[23] S. R. Bishop, T. S. Stefanik, H. L. Tuller, *Phys. Chem. Chem. Phys.* **2011**, *13*, 10165.

[24] H. Yoshida, H. Deguchi, K. Miura, M. Horiuchi, T. Inagaki, *Solid State Ionics* **2001**, *140*, 191.

[25] C. Xia, M. Liu, *Solid State Ionics* **2001**, *144*, 249.

[26] K. J. Kim, S. J. Kim, G. M. Choi, *ECS Transactions* **2013**, *57*, 897.

[27] C.-D. Savaniu, D. N. Miller, J. T. S. Irvine, *J. of the Amer. Ceram. Soc.* **2013**, *96*, 1718.

[28] I. K. Naik, T. Y. Tien, *J. Electrochem. Soc.* **1979**, *126*, 562.

[29] T. G. Stratton, H. L. Tuller, *J. Chem. Soc., Faraday Transac. 2: Molecular and Chem. Phys.* **1987**, *83*, 1143.

[30] M. C. Göbel, G. Gregori, J. Maier, *Solid State Ionics* **2012**, *215*, 45.

[31] R. Heinzmann, I. Issac, J.-P. Eufinger, G. Ulbrich, M. Lerch, J. Janek, S. Indris, *J. Phys. Chem. C* **2016**, *120*, 8568.

[32] I. K. Naik, T. Y. Tien, *J. Phys. Chem. Solids* **1978**, *39*, 311.

[33] F. Zhang, P. Wang, J. Koberstein, S. Khalid, S.-W. Chan, *Surf. Sci.* **2004**, *563*, 74.

[34] P. Fleming, S. Ramirez, J. D. Holmes, M. A. Morris, *Chem. Phys. Lett.* **2011**, *509*, 51.

[35] L. Yinglin, L. Zainovia, A. Azizan, M.-D. Judith, *J. Phys.: Condens. Matter* **2008**, *20*, 165201.

[36] T. Kolodiazhnyi, H. Sakurai, A. A. Belik, O. V. Gornostaeva, *Acta Mater.* **2016**, *113*, 116.

[37] P. V. Ananthapadmanabhan, Menon, S.B., Patil, D.S., Venkatramani, N., & Rohatgi, V.K. , *J. Mater. Sci. Lett.* **1992**, *11*, 501.

[38] F. Marabelli, P. Wachter, *Phys. Rev. B* **1987**, *36*, 1238.

[39] D. Marrocchelli, S. R. Bishop, H. L. Tuller, B. Yildiz, *Adv. Func. Mater.* **2012**, *22*, 1958.

[40] S. J. Hong, A. V. Virkar, *J. Amer. Ceram. Soc.* **1995**, *78*, 433.

[41] M. Mogensen, N. M. Sammes, G. A. Tompsett, *Solid State Ionics* **2000**, *129*, 63.

[42] R. Shannon, *Acta Crystallogr. Sec. A* **1976**, *32*, 751.

[43] M. Nakayama, M. Martin, *Phys. Chem. Chem. Phys.* **2009**, *11*, 3241.

[44] A. Walsh, S. M. Woodley, C. R. A. Catlow, A. A. Sokol, *Solid State Ionics* **2011**, *184*, 52.

ToC:

Point defects in the Ta-doped CeO_2 in the oxygen-rich conditions are studied using the dc magnetic susceptibility and the lattice parameter analysis. The extra positive charge of the donor ions is compensated by two types of defects: Ce^{3+} and oxygen interstitials, whose relative concentrations depend on the equilibrium temperature. In addition, anion Frenkel disorder starts to dominate at high temperatures.

Ceramics

T. Charoonsuk, N. Vittayakorn, T. Kolodiazhnyi*

Lattice Evolution and Point Defects Chemistry in Ta-Doped Ceria